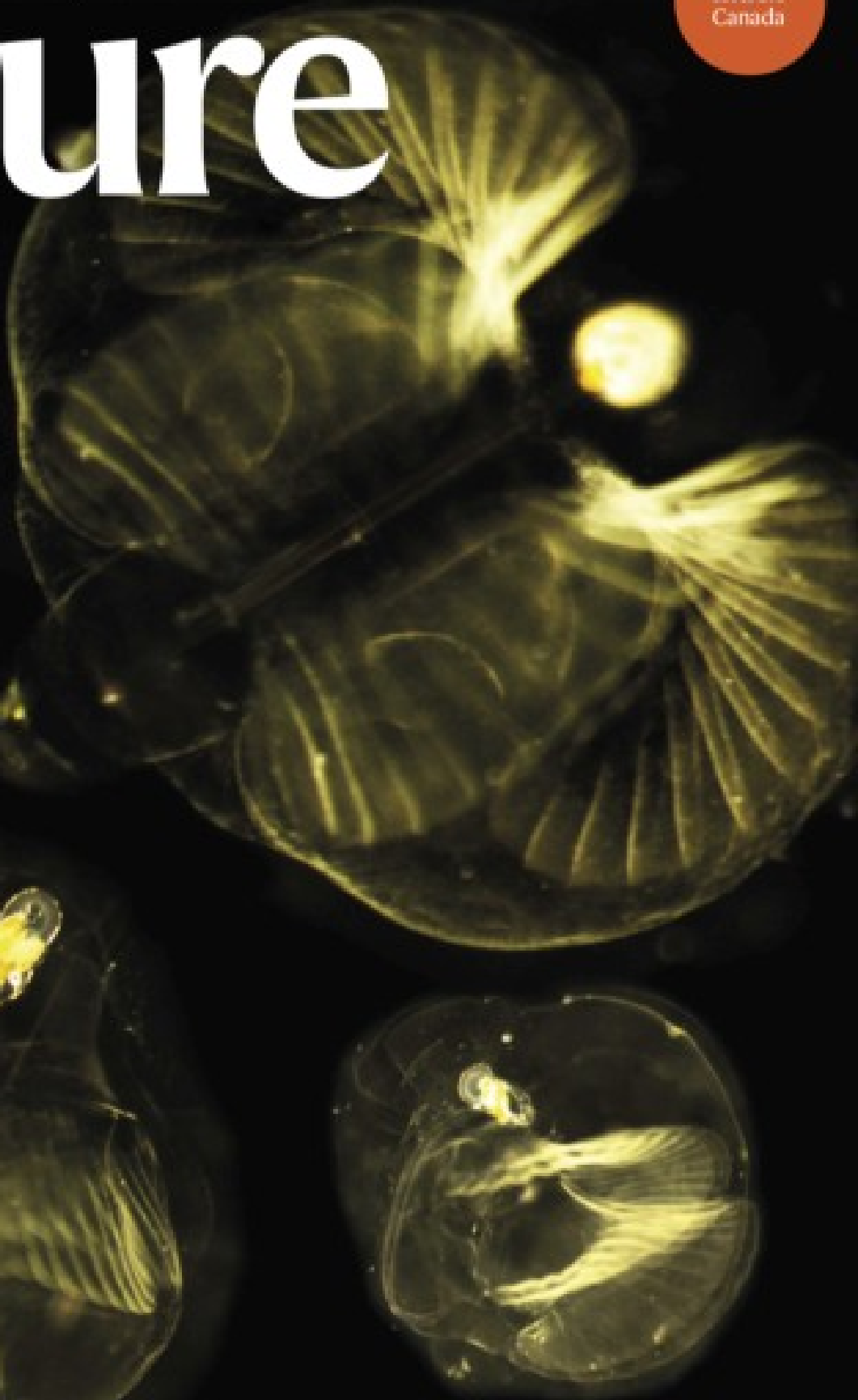


nature

MATTERS OF THE HEART

Deconstruction of cardiac development sheds light on tunicate evolution



Power play
Can industry deliver commercial nuclear fusion within 10 years?

Inherent bias
Genetic data of Roma people need better stewardship

I in the sky
Satellite with iodine-powered propulsion system takes to orbit

Nature.2021.11.20

[Sat, 20 Nov 2021]

- [This Week](#)
- [News in Focus](#)
- [Books & Arts](#)
- [Opinion](#)
- [Work](#)
- [Research](#)
- [Amendments & Corrections](#)

This Week

- **[COP26 didn't solve everything — but researchers must stay engaged](#)** [16 November 2021]
Editorial • The climate summit's organizers stopped researchers accessing the negotiations in Glasgow, UK. A zero-carbon world needs science and social science to bridge divides.
- **[Yes, science can weigh in on abortion law](#)** [16 November 2021]
World View • Why, as a scientist, I signed an amicus brief for the US Supreme Court's case on abortion.
- **[Bendable mini-scanner records every loop of a fingerprint](#)** [10 November 2021]
Research Highlight • A device that can fit in a person's palm has enough resolution to capture fingerprints for biometric identification.
- **[Weird crystal makes beetle a living jewel](#)** [10 November 2021]
Research Highlight • An insect owes its bright green covering to an unusual type of 'photonic crystal'.
- **[A cat can track its human by voice — if it can be bothered to](#)** [10 November 2021]
Research Highlight • Experiments involving 'impossible teleportation' reveal the cognitive powers of the house cat.
- **[Pandemic's plastic waste is choking the seas](#)** [08 November 2021]
Research Highlight • The onslaught of COVID-19 has generated millions of tonnes of plastic waste in the form of gloves, face masks and other items.
- **[Some of Earth's longest-lived fish show how to reach extreme ages](#)** [12 November 2021]
Research Highlight • Genomic analysis of Pacific rockfishes, which can survive for more than 200 years, provides insight into the biology of longevity.
- **[Nearly-fatal heat already affects people in 'informal' towns](#)** [10 November 2021]
Research Highlight • Temperatures in some settlements approach the limits of human survivability, even as Earth continues to warm.

- **Brightest X-rays on Earth expose COVID lung damage** [12 November 2021]

Research Highlight • Imaging technique can pick up micrometre-scale details of intact brains and other organs.

| [Next section](#) | [Main menu](#) |

- EDITORIAL
- 16 November 2021

COP26 didn't solve everything — but researchers must stay engaged

The climate summit's organizers stopped researchers accessing the negotiations in Glasgow, UK. A zero-carbon world needs science and social science to bridge divides.



Wealthy countries were criticized at COP26 for failing to meet a promise to provide US\$100 billion in financial help to low- and middle-income countries each year by 2020. Credit: Phil Noble/Reuters

The momentous and much-anticipated 26th United Nations Climate Change Conference of the Parties (COP26), intended to run for two weeks, ended on

13 November, 24 hours later than scheduled. There were some notable achievements. More countries announced pledges to go carbon neutral — including, for the first time, India, by 2070. Richer nations committed to doubling funding, known as adaptation finance, to help low- and middle-income countries (LMICs) deal with damaging climatic effects. Rules for carbon trading were agreed. And world leaders will report their progress on emissions cuts every year.

But a study for the Climate Action Tracker website, by Niklas Höhne at Wageningen University in the Netherlands and his colleagues, showed that, if pledges announced at the COP meeting are implemented, temperatures are still projected to rise 2.4 °C by 2100, well above the 1.5 °C target agreed at the 2015 Paris climate summit. The effects of this are likely to be catastrophic.



'COP26 hasn't solved the problem': scientists react to UN climate deal

Many researchers are frustrated at the lack of more meaningful measures to cut greenhouse-gas emissions. They have every right to be angry. But it would be a tragedy if that led them to disengage with the COP process and with humanity's fight to stop catastrophic climate change.

COP26 was the most important such event since Paris. But it is part of a much longer process: a stocktake of pledges made in Paris. COP26 also represented progress on several fronts, and it is not the final opportunity to

take action; the task continues at COP27 in Egypt next year. Researchers must take every opportunity to expand their role in that process, as it moves further into one of the planet's most critical decades.



[COP26 climate pledges: What scientists think so far](#)

The final agreement includes pledges, words and phrases that have not previously appeared in such texts. Besides the doubling of adaptation funding to US\$40 billion annually from 2025, high-income countries, including oil- and gas-exporting states, agreed for the first time to language that calls for reducing coal-fired power and an end to some types of public subsidy for other fossil fuels. High-income countries had wanted a total phase-out of coal; LMICs forced a compromise, pointing out that in many parts of the world, alternative energy sources do not yet exist.

High-income countries also agreed to set up an office to continue with research on a possible “loss and damage” fund, through which they could make payouts to LMICs that have been affected by climate change that they did not cause. And in the first week of COP26, more than 400 companies in the financial sector announced that they would be moving trillions of dollars of investments into firms that are committed to net-zero emissions.

These commitments were hard-fought — some have been more than 30 years in the making — and represent essential progress. But simmering below the surface are disagreements on definitions and on the detail of implementation — and that’s where the research community’s input will be

vital. For example, the text calls for reducing “unabated” coal, referring to coal without carbon capture and storage. But in reality, even coal plants equipped with carbon capture generate pollution. Researchers can spell this out.

Another crucial question concerns the impact of ‘net-zero’ commitments. This phrase is now commonly used as an indication of commitment to decarbonization. But [there's no agreed definition or measure of net zero](#). Without this, it is impossible to know if ‘net-zero’ pledges will actually stop global warming. There’s also no agreed definition of climate finance. Richer countries are providing around \$80 billion annually in climate finance to LMICs, but the lack of an agreed definition means the funds are dominated by loans and include elements such as development assistance (for example, funding for schools and clean water), which do not directly reduce carbon emissions.



[Net-zero emissions targets are vague: three ways to fix](#)

Research can inform all these questions, and the UN is inviting input. UN secretary-general António Guterres announced that he is asking a group of experts to “propose clear standards” to measure and analyse companies’ net-zero pledges. COP26 delegates also agreed that an expert group currently advising the UN climate convention on how to define climate finance must continue its work.

All advisers must be named as quickly as possible, because the time to act is short. They must span the range of disciplines: a group that is advising on standards for measuring net zero, for example, would need physical scientists working with economists and with researchers who study the methodology of creating financial indices. And it cannot be said loudly enough that researchers from institutions in the LMICs have to be heard.

If *Nature*'s experience of reporting from COP26 is anything to go by, researchers are not well integrated into climate policymaking. Indeed, researchers were frequently prevented by the conference organizers from accessing the rooms where negotiations were taking place. The UN allows researchers to observe negotiations directly so they can use these experiences as part of research projects or for teaching case studies. The UN climate convention office has promised to review how this obstruction happened. This experience must not be repeated in any future COP.

Stopping global warming will not happen without a partnership between nations, or a contract that all sides believe in, and buy into. Right now, countries with different levels of economic development and climate vulnerability are far apart. From the earliest COPs, researchers and their work have helped to bridge these divides. They must continue to do so now and in the future.

Nature **599**, 347 (2021)

doi: <https://doi.org/10.1038/d41586-021-03433-2>

This article was downloaded by **calibre** from <https://www.nature.com/articles/d41586-021-03433-2>

- WORLD VIEW
- 16 November 2021

Yes, science can weigh in on abortion law



Why, as a scientist, I signed an amicus brief for the US Supreme Court's case on abortion.

- [Diana Greene Foster](#) 0

The world is moving towards greater reproductive rights for women. More than 50 countries have liberalized their abortion laws in the past 25 years, informed by scientific research. Studies find that unsafe abortion is responsible for one in eight maternal deaths globally ([E. Ahman and I. H. Shah *Int. J. Gynaecol. Obstet.* 115, 121–126; 2011](#)), concentrated in low-income countries where abortion is illegal. Preventing unsafe abortion is a priority — 193 countries signed up to the United Nations Sustainable Development Goals, which call for reductions in maternal mortality.

Yet some countries, such as the United States, Poland and Nicaragua, are making access to abortion more difficult. Restrictions are passed on the basis of ideology or political motives, without considering scientific evidence about their impact. Science might not be able to decide philosophical questions about when life begins or when the rights of a fetus outweigh the agency of the person whose body is necessary for its growth and development. But it can tell us how access to abortion is affected by its legal status, and about the consequences when abortion is inaccessible. Science should weigh in on the often quoted yet seldom tested slogans of the abortion debate, because people's well-being is at stake.

Consider this argument: 'One cannot ban abortion; one can only ban safe abortion.' This can be tested. When abortion is illegal, pregnant people are more likely to resort to unsafe methods. But some circumvent the law in ways that are safe. Those with the means travel to places where abortion is legal, and others take safe medications, approved by the World Health Organization, to terminate their pregnancies outside the formal health system. In Latin America, where self-managed abortion is widespread, large decreases in mortality from unsafe abortion have been documented without widespread changes to restrictive abortion laws (see go.nature.com/3d6gspd).

But there's another consequence that should be investigated — when people are unable to get a legal abortion, they are more likely to carry unwanted pregnancies to term. It is estimated that 70% of unintended pregnancies end in abortion in places where it is legal, compared with about 50% where it is not (*J. Bearak et al. Lancet Glob. Health* **8**, E1152–E1161; 2020). I am a demographer who gathers data and creates quantitative models to assess how unintended pregnancies affect the well-being of women, children and families. My work shows that there are serious ramifications.

Most of my evidence is drawn from the Turnaway Study, which I led. My team and I followed almost 1,000 women for five years after they sought an abortion in the United States, comparing the health and socio-economic consequences of receiving an abortion or being denied one. We found serious physical health consequences from continued pregnancy and childbirth, including death. Women and their existing and subsequent

children also experienced greater economic and other hardship when abortion was denied. Women were more likely to continue to be exposed to intimate-partner violence, less likely to have an intended pregnancy under better circumstances later, and less likely to achieve their own aspirations.

Because I have found that the consequences of not getting a wanted abortion are worse than those experienced by women who get one, I worry that I seem to be taking a side in a political argument. But I have a duty to present my findings where they are relevant, which is why I was one of more than 100 social scientists who signed an amicus brief in the upcoming abortion-related US Supreme Court case *Dobbs v. Jackson Women's Health* (see [*Nature* 599, 187–189; 2021](#)).

Studies in other countries where abortion is legal — Colombia, Tunisia, South Africa and Nepal — have found that many women are turned away because of difficulties including a lack of trained clinicians and low knowledge of the law. Some get an abortion outside the legal system, sometimes with serious medical complications. Others plan to carry the pregnancy to term, and anticipate hardships. A woman in Tunisia remarked that she did not have clothes for a newborn. “Four children, and a fifth one on top! Where are we heading this way? Poverty and tyranny” ([S. Hajri et al. PLoS ONE 10, e0145338; 2015](#)). An 18-year-old in Colombia who would not be able to continue her studies once she had a baby said: “I will no longer be able to be young” ([T. DePiñeres et al. Reprod. Health 14, 133; 2017](#)).

There is much more science to be done on abortion access. What is the impact of gestational limits? Who crosses borders to get care? What information, support and services help people to use abortion medications safely, especially for the two in five women living in countries where abortion is restricted? What factors prevent people from recognizing pregnancy and seeking abortions earlier?

When a topic is controversial, the challenges to research increase. Stigma causes substantial under-reporting in national surveys and makes recruiting study participants difficult. Many funders fear the attention of abortion opponents or worry that supporting research is a political act. But the more

controversial a topic is, the more important it is that decisions are informed by rigorous evidence.

Issues such as climate change, vaccines and access to abortion are controversial and have a large impact on people's lives and well-being. That is why research to understand their impact is essential. Scientists, funders and journals should step up.

Nature **599**, 349 (2021)

doi: <https://doi.org/10.1038/d41586-021-03434-1>

This article was downloaded by **calibre** from <https://www.nature.com/articles/d41586-021-03434-1>

| [Section menu](#) | [Main menu](#) |

- RESEARCH HIGHLIGHT
- 10 November 2021

Bendable mini-scanner records every loop of a fingerprint

A device that can fit in a person's palm has enough resolution to capture fingerprints for biometric identification.



A normal image of a thermometer showing one side and a wrap-around image showing both sides

An image (left) taken with a flat sensor shows only one side of a thermometer, whereas a scan (right) taken by a wrap-around sensor shows both sides. Credit: A. J. J. M. van Breemen *et al.*/*Nature Electron*.

A high-resolution scanner roughly as thick as a human hair can be wrapped around objects about 1 centimetre in diameter, allowing it to image fingerprints as well as documents¹.

Access options

Subscribe to Journal

Get full journal access for 1 year

\$199.00

only \$3.90 per issue

[Subscribe](#)

All prices are NET prices.
VAT will be added later in the checkout.

Tax calculation will be finalised during checkout.

Rent or Buy article

Get time limited or full article access on ReadCube.

from \$8.99

[Rent or Buy](#)

All prices are NET prices.

Additional access options:

- [Log in](#)
- [Learn about institutional subscriptions](#)

Nature **599**, 350 (2021)

doi: <https://doi.org/10.1038/d41586-021-03075-4>

References

1. 1.

Van Breemen, A. J. J. M. *et al.* *Nature Electron.*
<https://doi.org/10.1038/s41928-021-00662-1> (2021).

This article was downloaded by **calibre** from <https://www.nature.com/articles/d41586-021-03075-4>

- RESEARCH HIGHLIGHT
- 10 November 2021

Weird crystal makes beetle a living jewel

An insect owes its bright green covering to an unusual type of ‘photonic crystal’.



The scales (pictured) of an African beetle species contain crystalline structures that colour the insect a brilliant green. Credit: Y. Kobayashi *et al./J. R. Soc. Interface*

An African beetle achieves its glittering green forewings thanks to a unique type of light-reflecting crystal in its scales¹.

Access options

Subscribe to Journal

Get full journal access for 1 year

\$199.00

only \$3.90 per issue

[Subscribe](#)

All prices are NET prices.

VAT will be added later in the checkout.

Tax calculation will be finalised during checkout.

Rent or Buy article

Get time limited or full article access on ReadCube.

from \$8.99

[Rent or Buy](#)

All prices are NET prices.

Additional access options:

- [Log in](#)
- [Learn about institutional subscriptions](#)

Nature **599**, 350 (2021)

doi: <https://doi.org/10.1038/d41586-021-03076-3>

References

1. 1.

Kobayashi, Y., Ohnuki, Y. & Yoshioka, S. *J. R. Soc. Interface*
<https://doi.org/10.1098/rsif.2021.0505> (2021).

This article was downloaded by **calibre** from <https://www.nature.com/articles/d41586-021-03076-3>

- RESEARCH HIGHLIGHT
- 10 November 2021
- Correction [12 November 2021](#)

A cat can track its human by voice — if it can be bothered to

Experiments involving ‘impossible teleportation’ reveal the cognitive powers of the house cat.



If it so wishes, a cat with its eyes closed can track its owners simply by following their voices. Credit: Yerlin Matu/Unsplash

Pet cats seem to be able to track their human companion’s every move — through sound¹.

Access options

Subscribe to Journal

Get full journal access for 1 year

\$199.00

only \$3.90 per issue

[Subscribe](#)

All prices are NET prices.

VAT will be added later in the checkout.

Tax calculation will be finalised during checkout.

Rent or Buy article

Get time limited or full article access on ReadCube.

from \$8.99

[Rent or Buy](#)

All prices are NET prices.

Additional access options:

- [Log in](#)
- [Learn about institutional subscriptions](#)

Nature **599**, 350 (2021)

doi: <https://doi.org/10.1038/d41586-021-03080-7>

Updates & Corrections

- **Correction 12 November 2021:** An earlier version of this story gave the wrong species name for the domestic cat. This has now been corrected.

References

1. 1.

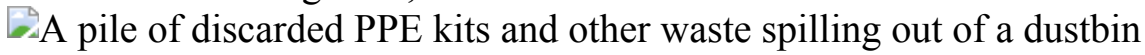
Takagi, S. *et al.* *PLoS ONE* **16**, e0257611 (2021).

This article was downloaded by **calibre** from <https://www.nature.com/articles/d41586-021-03080-7>

- RESEARCH HIGHLIGHT
- 08 November 2021

Pandemic's plastic waste is choking the seas

The onslaught of COVID-19 has generated millions of tonnes of plastic waste in the form of gloves, face masks and other items.



Protective equipment overflows a dustbin in Noida, India, during a COVID-19 surge. Credit: Sunil Ghosh/Hindustan Times/Getty

Disposable masks and gloves might have helped to relieve the COVID-19 pandemic, but they have worsened the world's plastic-waste crisis. Thousands of tonnes of plastic from hospital waste, face masks and other single-use items are flooding the oceans, a study shows¹.

Access options

Subscribe to Journal

Get full journal access for 1 year

\$199.00

only \$3.90 per issue

[Subscribe](#)

All prices are NET prices.

VAT will be added later in the checkout.

Tax calculation will be finalised during checkout.

Rent or Buy article

Get time limited or full article access on ReadCube.

from \$8.99

[Rent or Buy](#)

All prices are NET prices.

Additional access options:

- [Log in](#)
- [Learn about institutional subscriptions](#)

Nature **599**, 350 (2021)

doi: <https://doi.org/10.1038/d41586-021-03078-1>

References

1. 1.

Peng, Y., Wu, P., Schartup, A. T. & Zhang, Y. *Proc. Natl. Acad. Sci. USA* 118, e2111530118 (2021).

This article was downloaded by **calibre** from <https://www.nature.com/articles/d41586-021-03078-1>

- RESEARCH HIGHLIGHT
- 12 November 2021

Some of Earth's longest-lived fish show how to reach extreme ages

Genomic analysis of Pacific rockfishes, which can survive for more than 200 years, provides insight into the biology of longevity.



The copper rockfish (*Sebastodes caurinus*), has a respectable maximum lifespan of more than 50 years, but close relatives can last three times as long. Credit: Ralph Pace/Nature Picture Library

Cold-loving creatures known as Pacific Ocean rockfishes have wildly varying lifespans. The species *Sebastodes minor* lasts a mere 11 years; its cousin *Sebastodes aleutianus* can live for more than 2 centuries. Scientists have now pinpointed genes linked to this remarkable range¹.

Access options

Subscribe to Journal

Get full journal access for 1 year

\$199.00

only \$3.90 per issue

[Subscribe](#)

All prices are NET prices.
VAT will be added later in the checkout.

Tax calculation will be finalised during checkout.

Rent or Buy article

Get time limited or full article access on ReadCube.

from \$8.99

[Rent or Buy](#)

All prices are NET prices.

Additional access options:

- [Log in](#)
- [Learn about institutional subscriptions](#)

Nature **599**, 351 (2021)

doi: <https://doi.org/10.1038/d41586-021-03423-4>

References

1. 1.

Kolora, S. R. R. *et al.* *Science* **374**, 842–847 (2021).

This article was downloaded by **calibre** from <https://www.nature.com/articles/d41586-021-03423-4>

- RESEARCH HIGHLIGHT
- 10 November 2021

Nearly-fatal heat already affects people in ‘informal’ towns

Temperatures in some settlements approach the limits of human survivability, even as Earth continues to warm.



A house in an informal settlement in Makassar, Indonesia. Researchers studied a dozen such settlements in the city to predict how climate change will affect residents. Credit: Emma E. Ramsay

Informal, low-income settlements in tropical cities will be hit even harder than predicted by climate change, resulting in dire income losses and declining health¹.

Access options

Subscribe to Journal

Get full journal access for 1 year

\$199.00

only \$3.90 per issue

[Subscribe](#)

All prices are NET prices.

VAT will be added later in the checkout.

Tax calculation will be finalised during checkout.

Rent or Buy article

Get time limited or full article access on ReadCube.

from \$8.99

[Rent or Buy](#)

All prices are NET prices.

Additional access options:

- [Log in](#)
- [Learn about institutional subscriptions](#)

Nature **599**, 351 (2021)

doi: <https://doi.org/10.1038/d41586-021-03079-0>

References

1. 1.

Ramsay, E. E. *et al.* *iScience*
<https://doi.org/10.1016/j.isci.2021.103248> (2021).

This article was downloaded by **calibre** from <https://www.nature.com/articles/d41586-021-03079-0>

- RESEARCH HIGHLIGHT
- 12 November 2021

Brightest X-rays on Earth expose COVID lung damage

Imaging technique can pick up micrometre-scale details of intact brains and other organs.



The lung of a man who died from COVID-19 is depicted by a new type of scan showing open blood vessels in red, blocked blood vessels in yellow and air spaces in cyan. Credit: Paul Tafforeau

Researchers have harnessed the world's brightest X-rays to create intricate maps of human organs at various scales, from the entire organ down to individual cells ¹.

Access options

Subscribe to Journal

Get full journal access for 1 year

\$199.00

only \$3.90 per issue

[Subscribe](#)

All prices are NET prices.

VAT will be added later in the checkout.

Tax calculation will be finalised during checkout.

Rent or Buy article

Get time limited or full article access on ReadCube.

from \$8.99

[Rent or Buy](#)

All prices are NET prices.

Additional access options:

- [Log in](#)
- [Learn about institutional subscriptions](#)

Nature **599**, 351 (2021)

doi: <https://doi.org/10.1038/d41586-021-03077-2>

References

1. 1.

Walsh, C. L. *et al.* *Nature Methods* <https://doi.org/10.1038/s41592-021-01317-x> (2021).

This article was downloaded by **calibre** from <https://www.nature.com/articles/d41586-021-03077-2>

News in Focus

- **[New mineral, FDA chief and the pandemic's toll on research](#)** [17 November 2021]
News Round-Up • The latest science news, in brief.
- **['COP26 hasn't solved the problem': scientists react to UN climate deal](#)** [14 November 2021]
News • The Glasgow Climate Pact is a step forward, researchers say, but efforts to decarbonize are not enough to limit global temperature rises to 2 °C.
- **[Scientist Rebellion: researchers join protesters at COP26](#)**
[12 November 2021]
News • Scientists are among hundreds of demonstrators at the COP26 climate conference — and want more to join them.
- **[COVID antiviral pills: what scientists still want to know](#)**
[10 November 2021]
News Explainer • Drugs such as molnupiravir and Paxlovid could change the course of the pandemic if clinical trial results hold up in the real world.
- **[How protein-based COVID vaccines could change the pandemic](#)** [08 November 2021]
News • Jabs from Novavax and other biotech firms are coming. Scientists say they have a lot to offer.
- **[Scammers impersonate guest editors to get sham papers published](#)** [08 November 2021]
News • Hundreds of junk-science papers have been retracted from reputable journals after fraudsters used 'special issues' to manipulate the publication process. And the problem is growing.
- **[The start-ups chasing clean, carbon-free fusion energy](#)** [17 November 2021]
News Feature • An emerging industry of nuclear-fusion firms promises to have commercial reactors ready in the next decade.

- NEWS ROUND-UP
- 17 November 2021

New mineral, FDA chief and the pandemic's toll on research

The latest science news, in brief.



This diamond holds tiny black specks of davemaoite, a mineral formed at high temperature and pressure in the deep Earth. Credit: Aaron Celestian, Natural History Museum of Los Angeles County

Diamond delivers elusive mineral from deep Earth

Small black specks in a diamond from a Botswanan mine have turned out to be a [vital ingredient of the deep Earth](#), identified in nature for the first time after decades of searching.

The mineral forms at high temperatures and pressures in Earth's mantle, and normally cannot exist on the surface. But these particular specks were embedded inside a diamond that ferried the mineral intact from deep inside the planet ([O. Tschauner et al. Science 374, 891–894; 2021](#)).

The researchers who discovered the mineral named it davemaoite after Ho-kwang 'Dave' Mao, a scientist who made many pioneering discoveries in high-pressure geochemistry and geophysics. Davemaoite is mostly calcium silicate, but it can scavenge radioactive isotopes of uranium, thorium and potassium, which produce heat as they decay. This means the mineral plays a major part in heat flow deep inside Earth.

The davemaoite in the diamond has a perovskite crystal structure that forms only at the temperatures and pressures that exist between 660 and 900 kilometres deep. Scientists had synthesized it in the laboratory, and had theorized that it should be one of the main components of the lower mantle, but had never conclusively seen it in geological samples before.



Robert Califf was head of the US Food and Drug Administration for 11 months near the end of former president Barack Obama's presidency. Credit: Win McNamee/Getty

At last, Biden chooses FDA chief

After nearly ten months without appointing a permanent commissioner, US President Joe Biden has nominated Robert Califf (pictured), a former head of the Food and Drug Administration (FDA), to lead the regulatory agency again.

The FDA has been plagued by a series of missteps in the past decade — ranging from its approval of controversial drugs to perceived bowing to political pressure — that have undermined public confidence in it. Experts say that Califf will need to [prioritize restoring trust in the beleaguered agency](#) if he's confirmed by the US Senate.

A cardiologist, Califf had a long career at Duke University School of Medicine in Durham, North Carolina, where he founded the Duke Clinical

Research Institute, the world's largest academic clinical research centre. Since leaving the FDA in 2017, after less than 11 months as commissioner, he has led clinical policy and strategy at Verily, the life-sciences spin-off from Google's parent company, Alphabet.

Georges Benjamin, executive director of the American Public Health Association, an organization for US public-health officials in Washington DC, says that Califf is a shrewd choice. "He won't make some of the same rookie mistakes that someone who's never been in the agency might make."

Pandemic takes its toll on researcher productivity and mental health

The COVID-19 pandemic has dented researchers' productivity and mental health, according to [surveys of scientists in Europe and the United States](#). But the full impact might not be felt for years.

"The worst may be yet to come," says network scientist Dashun Wang at Northwestern University in Evanston, Illinois, who led 2 polls of nearly 7,000 principal investigators, conducted 9 months apart ([J. Gao et al. *Nature Commun.* 12, 6188; 2021](#)).

When the first poll was conducted in April 2020, scientists were already spending less time on research than before the pandemic. But in January 2021, when Wang's team conducted another poll, they found that this effect had largely abated (see 'Productivity problems').

The more recent poll also found that output fell for many last year, compared with 2019. Scientists who do not work on COVID-related projects reported that their new publications and submissions dropped by 9% and 15% during 2020. More troubling, says Wang, is that scientists launched fewer research projects overall in 2020, with an average drop of 26% compared with 2019.

Psychological factors could be at play. Under stress, Wang says, people have "tunnel vision, trying to focus on one thing instead of looking more broadly".

The [results of a separate survey](#) paint a bleak picture of academics' mental health, which researchers say could be affecting their enthusiasm to start new projects. Two thousand staff at UK higher-education institutions were surveyed in March and April this year by Education Support, a London-based charity. Nearly two-thirds reported feeling emotionally drained at least once a week, and more than one-quarter of respondents said they felt that way every day.

PRODUCTIVITY PROBLEMS

Surveys of researchers in the United States and Europe found that the COVID-19 pandemic adversely affected productivity, although there are signs of recovery.

How many hours a week do you spend on your job?

April 2020 (4,535 respondents)



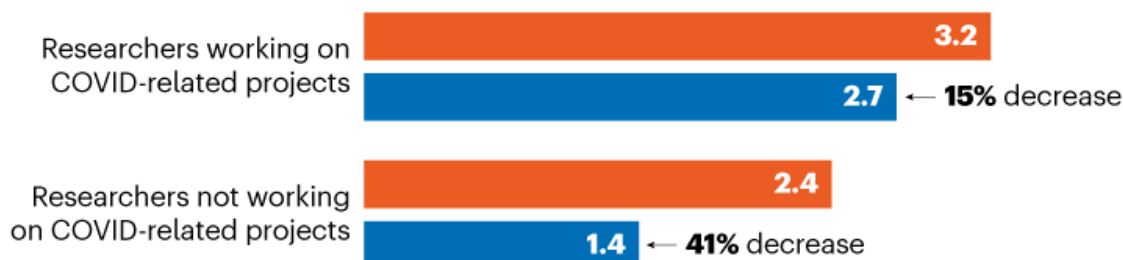
January 2021 (2,447 respondents)



How many new projects did you initiate this past year?

January 2021 (2,313 respondents)

■ Average 2019 ■ Average 2020



©nature

Source: J. Gao *et al. Nature Commun.* **12**, 6188 (2021)

Nature **599**, 353 (2021)

doi: <https://doi.org/10.1038/d41586-021-03435-0>

This article was downloaded by **calibre** from <https://www.nature.com/articles/d41586-021-03435-0>

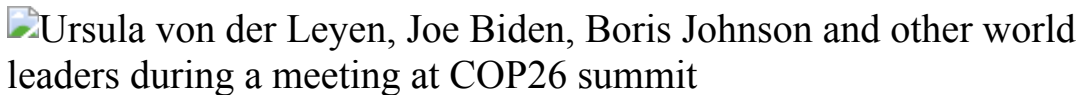
| [Section menu](#) | [Main menu](#) |

- NEWS
- 14 November 2021
- Correction [15 November 2021](#)

‘COP26 hasn’t solved the problem’: scientists react to UN climate deal

The Glasgow Climate Pact is a step forward, researchers say, but efforts to decarbonize are not enough to limit global temperature rises to 2 °C.

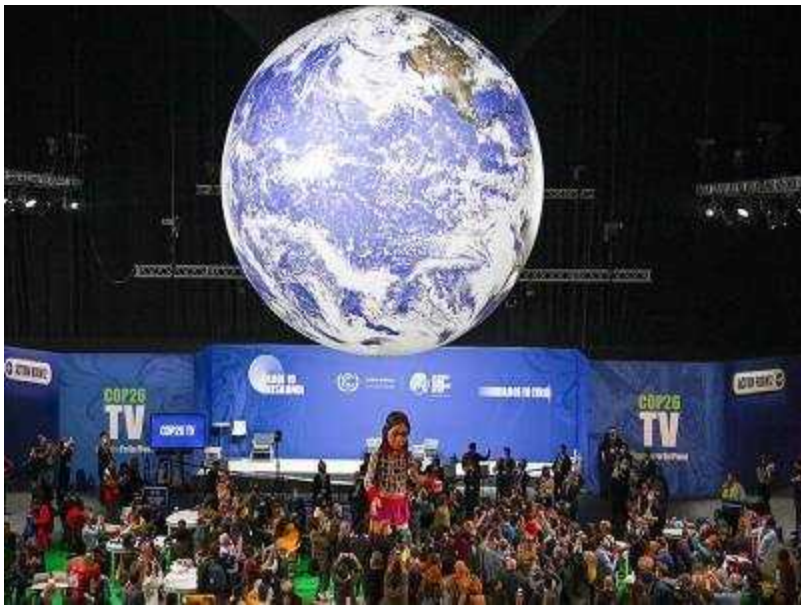
- [Ehsan Masood](#) &
- [Jeff Tollefson](#)



World leaders including European Commission president Ursula von der Leyen, US president Joe Biden and UK prime minister Boris Johnson at a meeting during COP26. Credit: Erin Schaff/New York Times/Redux/eyevine

Government ministers at the 26th United Nations Climate Change Conference of the Parties (COP26) have reached a deal on further steps to reduce greenhouse-gas emissions after discussions overran by 24 hours.

On 13 November, representatives from nearly 200 countries agreed the final text of the deal, which pledges further action to curb emissions, more frequent updates on progress and additional funding for low- and middle-income countries.



COP architects furious at lack of climate justice at pivotal summit

Researchers have expressed relief that the meeting did produce an agreement, but some left COP26 dissatisfied at the lack of stronger commitments to reduce emissions, and failure to agree “loss and damage” finance for countries that are vulnerable to climate change.

“COP26 has closed the gap, but it has not solved the problem,” [says Niklas Hoehne](#), a climate researcher at Wageningen University in the Netherlands. Countries now need to come forward with more ambitious pledges to tackle climate change, he adds.

Curbing emissions

The final 11-page document, called the [Glasgow Climate Pact](#), says that greenhouse-gas emissions must be reduced and carbon dioxide emissions must fall by 45% from 2010 levels by 2030 for global warming to be maintained at 1.5 °C above pre-industrial levels. It notes that, under existing emissions-reduction pledges, emissions will be nearly 14% higher by 2030 than in 2010.

Countries acknowledged the need to reduce emissions faster, and also agreed to report on progress annually. For the first time in a COP text,

nations agreed to begin reducing coal-fired power (without carbon capture) and to start to eliminate subsidies on other fossil fuels.

However, following objections from China and India, a promise in earlier drafts of the text to “phase out” coal was changed to “phase down”.

India’s climate and environment minister Bhupender Yadav told the conference that richer nations should not expect poorer countries to stop subsidizing fossil fuels such as gas. The lowest-income households rely on these to keep energy costs down, he said.



Scientists cheer India's ambitious carbon-zero climate pledge

The deal also includes [commitments](#) from some countries on ending deforestation, reducing methane emissions and a pledge from the financial sector to move trillions of dollars of investments into companies that are committed to net-zero emissions. However, modelling suggests that the promises will still not be enough to limit global warming to 2 °C above pre-industrial levels the goal stated in the 2015 Paris climate agreement.

If countries meet their 2030 targets, global temperatures will still [rise 2.4 °C above pre-industrial levels by 2100](#), according to an analysis by Hoehne and colleagues that was published on the website *Climate Action Tracker* during the first week of COP26.

“We are well aware that ambitions have fallen short of the commitments made in Paris,” COP26 president Alok Sharma told the conference in a speech shortly before the negotiations concluded. “We have kept 1.5 degrees alive. But its pulse is weak, and it will only survive if we keep our promises and translate commitments into rapid action.”

Charlie Gardner, a conservation biologist at the University of Kent in Canterbury, UK, who [joined demonstrations outside the conference](#) with the protest group Scientist Rebellion, says more radical action is needed, such as ending fossil-fuel production more quickly and transitioning economies away from constant growth.

Loss and damage

The issue of climate finance — funding from wealthy nations to help low- and middle-income countries transition away from fossil fuels — was heavily discussed during the meeting.

There was considerable anger over the [failure by high-income nations to meet an earlier pledge](#) to provide US\$100 billion in climate finance annually from 2020. “The message coming out of this COP is every country for themselves,” says Sara Jane Ahmed, a climate-finance researcher who advises the finance ministers of the V20, a group of 20 countries that are vulnerable to climate change.



The broken \$100-billion promise of climate finance – and how to fix it

However, the Glasgow Climate Pact includes a commitment to double ‘adaptation finance’ — funding to help the lowest-income countries improve climate resilience — to \$40 billion by 2025. Adaptation finance is around one-quarter of the \$80-billion climate finance currently available every year to low- and middle-income countries.

The deal also commits to continue work on a definition of climate finance that would be acceptable to all countries. This is essential if trust between developed and developing nations is to be regained, says Clare Shakya of the International Institute for Environment and Development, a London-based think tank. At the moment, different countries define climate finance in different ways. For example, some count development aid (which might include funding for clean water or schools) as climate finance. Some countries also count loans as climate finance, whereas others say climate finance should be provided as grants.

Nations failed to agree on whether to create a “loss and damage” fund, a kind of insurance policy that would compensate climate-vulnerable countries for damage resulting from emissions that they did not create. But the COP26 deal includes plans for an office connected to the United Nations — known as a technical assistance facility — that will continue to research the idea.

“On the ground, it is clear that countries are suffering loss and damage from climate change as we speak, and these costs are being borne disproportionately,” says conservationist Malik Amin Aslam, Pakistan’s minister for climate change. He is confident that such a fund will be created eventually, but thinks that there will be many more discussions first.

The price of carbon

COP26 negotiators also finalized the rules that govern international cooperation and carbon markets, ending a prolonged debate over how to implement this part of the 2015 Paris climate agreement. The new rules create an accounting system that is intended to prevent double-counting of emissions reductions. When one company or country invests in emissions reductions that take place in another, for example, the new framework ensures that the reductions are only recorded once when reported to the UN.



[COP26 climate summit: A scientists’ guide to a momentous meeting](#)

Most scientists and environmentalists applauded the outcome. “It’s basically as good as one could hope for,” says Robert Stavins, an economist at Harvard University in Cambridge, Massachusetts. A common accounting framework will enable separate trading schemes, such as those currently

operating in Europe, China and parts of the United States to connect with each other, creating a more international market.

But although the final text references the rights of Indigenous peoples who manage vast tracts of threatened tropical forest, some activists question whether the new rules go far enough. “We will have to watch closely the implementation of this new carbon scheme, as references to the rights of Indigenous peoples are relatively weak,” says Jennifer Tauli Corpuz, a lawyer from the Igorot people in the Philippines and chief policy lead at the non-profit advocacy group for Indigenous peoples, Nia Tero. “The good news is that we have more protections than we would have had under the rapidly growing voluntary carbon market.”

A recent analysis of the climate commitments put forward before COP26 estimated that the world would save around \$300 billion annually by 2030 if a global carbon market were in place¹. If those savings were reinvested in climate mitigation, it would more than double the projected annual emissions reductions in 2030, says James Edmonds, a co-author of the analysis, and a climate scientist at the US Department of Energy’s Pacific Northwest National Laboratory and the University of Maryland in College Park. “There are tremendous opportunities here,” Edmonds says.

Inclusivity issue

Although COP26 resulted in a final deal, the meeting drew criticism that many representatives of different non-governmental groups — including researchers — were prevented from observing the discussions.

There were nearly 12,000 such representatives categorized into nine constituencies, such as business, young people and researchers. Tracy Bach, an environmental lawyer who co-leads the researchers' group [Research and Independent Non-Governmental Organizations](#), says that for much of the conference only one representative from each constituency was allowed to observe negotiations inside the rooms. At previous COP summits many more observers have been permitted, she says.

The UK government had previously said that COP26 was the most inclusive COP summit ever, because around 40,000 people (including government delegates) were allowed to attend, compared with the 22,000 at COP25 in Madrid. “Most observers came to COP to engage in the negotiation process,” Bach says. “Giving more people a badge [to enter the conference centre] without letting them directly observe the negotiations is not engagement, and does not make this COP necessarily more inclusive,” she adds.

Patricia Espinosa, who heads the UN climate convention secretariat in Geneva, told the meeting that the experience of observers at COP26 will be reviewed immediately “to ensure greater inclusivity moving forward.”

Nature **599**, 355-356 (2021)

doi: <https://doi.org/10.1038/d41586-021-03431-4>

With additional reporting by Dan Fox, Nick Petrić Howe and Tosin Thompson.

Updates & Corrections

- **Correction 15 November 2021:** In an earlier version of this article, Malik Amin Aslam was incorrectly described as an adviser to Pakistan’s COP 26 delegation.

References

1. 1.

Edmonds, J. *et al.* *Clim. Change Econ.*
<https://doi.org/10.1142/S201000782150007X> (2021).

This article was downloaded by **calibre** from <https://www.nature.com/articles/d41586-021-03431-4>

- NEWS
- 12 November 2021

Scientist Rebellion: researchers join protesters at COP26

Scientists are among hundreds of demonstrators at the COP26 climate conference — and want more to join them.

- [Tosin Thompson](#)



Members of Scientist Rebellion, including Kyle Topfer (second from the left) and Charlie Gardner (far right), chained together on Glasgow's King George V Bridge. Credit: Mar Sala/Scientist Rebellion

It is about 1 p.m. on 11 November when I arrive at the rendezvous point: South Portland Street Suspension Bridge, a footbridge above the River Clyde in Glasgow, UK. On a dinghy floating across the river, a distant figure in a lab coat holds up a banner that reads: “Tell the truth or we will lose everything”. It is Tim Hewlett, an astrophysicist and co-founder of activist group Scientist Rebellion. I am told that he will continue to float across the river until he docks by the Scottish Event Campus, where the 26th United Nations Climate Change Conference of the Parties (COP26) is taking place, or until he’s arrested — whichever comes first.

For the past week, I have been speaking to scientists at COP26, where nations are trying to agree on how to fulfil their pledges to tackle climate change. Some of the researchers are advisers at the meeting or part of the delegations trying to negotiate a final deal. But others are among the hundreds of activists staging protests on the streets of Glasgow throughout the summit to demand stronger action.

Chained together

Scientist Rebellion has carried out various protests during COP26. On 6 November, activists blocked King George V bridge, one of the main routes connecting Glasgow city centre to the south side of the city. They chained padlocks around their necks and to each other to form a line. Hours of chain-cutting later, the police arrested 21 people — including 15 scientists, according to Scientist Rebellion.

“We believe this is the first ever mass arrest of scientists over the climate crisis,” says Charlie Gardner, a conservation biologist at the University of Kent in Canterbury, UK, who was among those arrested.



COP architects furious at lack of climate justice at pivotal summit

About six years ago, Gardner started teaching an undergraduate module on climate change. “That made me realize just how serious and impactful the climate crisis is for biodiversity,” he says. Gardner transitioned his research to focus on climate-change ecology, and used platforms including [a 2019 essay in *Nature Ecology & Evolution*](#)¹ to call on other academics to join civil-disobedience movements.

Gardner says Scientist Rebellion’s aim at COP26 is to highlight failures of the UN Framework Convention on Climate Change. He adds that he is not impressed with the [COP26 climate pledges](#) that have been made so far, and says that money and lobbying from sectors including the fossil-fuel industry have too much sway over governments. “There are a lot of very powerful vested interests that do not want us to rapidly decarbonize, as that will limit their ability to make profit.”

Some members of Scientist Rebellion even glued research papers describing the scale of climate change to a building. Among them was Kyle Topfer, an environmental scientist from Sydney, Australia, who also glued his left hand to a paper from *Frontiers in Conservation Science*. Topfer was eventually arrested — still stuck to the paper — and taken away in a police van.

Not getting involved

It has been difficult for scientists to persuade their peers to join in with protests, says Caroline Vincent, a London-based independent consultant for the pharmaceutical industry who is a member of XR Scientists — a branch of the organization Extinction Rebellion, which is known for disruptive protests.

“A lot of people in academia fear about their jobs because some institutions and universities frown upon people who engage in activism,” Vincent adds. “It’s ingrained in scientists to report in an impartial way and not take a view, a little bit like the queen.”



All aboard the climate train! Scientists join activists for COP26 trip

But Gardner thinks many scientists are put off protesting because “they’re just too busy”. Senior academics have high workloads and are under constant pressure to publish and secure grants, he says. And early- or mid-career researchers don’t want to get involved in activism because they have to concentrate on their research and publications. “To them I say, there are no professorships on a dead planet,” Gardner says. “All our hopes for the future are in jeopardy now, unless we take emergency action over the next few years.”

Although there are still relatively few scientists taking to the streets, Gardner has noticed a lot more discussions, particularly online, about the role of academics in going beyond teaching and research to engage in advocacy and activism. He hopes that this will be followed by more involvement in movements such as Scientist Rebellion.

“Climate change isn’t just a battle of information, but of power and influence,” says Gardner. “Writing scientific papers doesn’t influence the public or governments, whereas activism might.”

Despite his arrest, he intends to carry on protesting with Scientist Rebellion, and hopes to persuade more researchers to join him. “Leading by example is one of the most powerful ways to influence others,” he says.

Nature **599**, 357 (2021)

doi: <https://doi.org/10.1038/d41586-021-03430-5>

References

1. 1.

Gardner, C. J. & Wordley, C. F. R. *Nature Ecol. Evol.* **3**, 1271–1272 (2019).

This article was downloaded by **calibre** from <https://www.nature.com/articles/d41586-021-03430-5>

- NEWS EXPLAINER
- 10 November 2021

COVID antiviral pills: what scientists still want to know

Drugs such as molnupiravir and Paxlovid could change the course of the pandemic if clinical trial results hold up in the real world.

- [Heidi Ledford](#)



The antiviral drugs molnupiravir and Paxlovid can cut COVID-19 hospitalizations when people are treated soon after becoming infected with the coronavirus. Credit: Sergei Supinsky/AFP via Getty

'Tis the season of the antiviral. In just over a month, two antiviral drugs — both capable of being taken as a pill — have been found to cut COVID-19 hospitalizations and deaths in clinical trials of people treated soon after their initial infection.

On 4 November, the United Kingdom became the first country to approve molnupiravir, which was developed by Merck, based in Kenilworth, New Jersey, and Ridgeback Biotherapeutics in Miami, Florida. The approval came just over a month after the companies announced that the antiviral drug, which will be branded Lagevrio, [halved the risk of hospitalization](#) in people with mild or moderate forms of COVID-19. A day after the UK approval, Pfizer, based in New York City, announced that its antiviral drug Paxlovid cut hospitalizations by 89%.



[How antiviral pill molnupiravir shot ahead in the COVID drug hunt](#)

If the results hold up in the real world, the medicines could be game-changers for the pandemic. Previous antiviral options against COVID-19 [were expensive and had to be administered in a hospital](#). The new drugs are small molecules and can be taken at home. “They would be relatively cheap to manufacture,” says Charles Gore, executive director of the Medicines Patent Pool, a United Nations-backed organization based in Geneva, Switzerland, that works to increase access to medicines. “For large parts of the world that have not got good vaccine coverage, this is really a godsend.”

But little is known about how well the drugs will work, and how easily they could be used in the places that need them most. *Nature* looks at five key factors that could determine how the new COVID-19 antivirals shape the course of the pandemic.

How effective are the new antivirals?

Judging from the press releases, both drugs can slash hospitalizations — and potentially also deaths — from COVID-19 when they are given soon after infection takes hold. But until full reports of the clinical trials are released, some crucial details are missing.

Researchers will be looking at the ages and ethnicities of those who were enrolled in the trials, and at any other health conditions that they had, says John Mellors, an infectious-disease specialist at the University of Pittsburgh Medical Center in Pennsylvania.

Because antiviral drugs often need to be given early in the course of an infection for them to work effectively, Mellors will also be looking for more detail about when the drugs were given in the trials, and at how those timings correlated with efficacy. That information will provide a sense of when the window of opportunity for treatment closes. Neither trial had enough participants to enable firm conclusions to be drawn about the drugs' ability to prevent deaths, but no deaths occurred in their treatment arms.



The race for antiviral drugs to beat COVID — and the next pandemic

Researchers are also keen for any clue — including from further clinical trials — as to whether the drugs affect transmission of the coronavirus, or prevent illness in people who have been exposed to it.

If they do, the combination of vaccines and antiviral drugs could become a powerful tool in controlling outbreaks, says Jerome Kim, director-general of the International Vaccine Institute in Seoul. For example, if a worrying coronavirus variant emerges in a specific region, those who are most likely to be affected could be given an antiviral drug to supplement immunity from vaccines. This could clamp down on the virus and prevent its spread. “It opens up some new possibilities for the way we think about control,” Kim says. “This would have a really dramatic impact.”

Are the treatments safe?

Both Pfizer and Merck have reported that their antivirals were well tolerated by study participants, and that potential side effects were minor. But both drugs have features that could limit who would be able to take them.

Molnupiravir acts by introducing mutations into the viral genome during viral replication. A metabolite of the drug is picked up by a viral enzyme

called RNA-dependent RNA polymerase and incorporated into the viral genome, eventually causing so many errors that the virus can no longer survive.

Human cells have a DNA, rather than an RNA, genome, but some laboratory experiments have suggested that molnupiravir could cause mutations in human DNA as well¹.

A full course of treatment with molnupiravir is only five days long. But regulators might be cautious, particularly when it comes to treating pregnant people, says Kim. “There’s probably going to be warnings around the use of this antiviral because of the potential risk,” he says.



If clinical trial results hold up, drugs such as molnupiravir could be used alongside vaccines to control COVID-19 outbreaks.Credit: Merck & Co via Reuters

Paxlovid acts by inhibiting an enzyme that's needed to process some viral proteins into their final, functional form. But the drug is a combination of an antiviral and another drug, called ritonavir, which helps to prevent enzymes

in the liver from breaking down the antiviral before it has a chance to disable the coronavirus. Ritonavir, a component of some HIV treatment cocktails, can affect how some other medications are metabolized by the body. A wide range of drugs should not be given with it, including some that are commonly used to treat heart conditions, suppress the immune system and reduce pain.

This means that many people might not be able to tolerate the combination of Paxlovid and ritonavir. But Mellors notes that this antiviral drug regimen also lasts only a few days, and physicians might find ways to work around some drug-drug interactions. “There’s going to be a learning curve as to when it can be used, and when it can’t,” he says.

Will the drugs work against variants of concern?

In theory, the drugs should be effective against known coronavirus variants, including [the highly transmissible Delta variant](#). These variants are primarily characterized by mutations in the viral spike protein and other regions that are targeted by the immune system — and by vaccines.

The targets of molnupiravir and Paxlovid are different, but researchers will still need to show that the drugs work against variants, says Mellors. Merck has done laboratory studies indicating that molnupiravir is effective against Delta and other variants — including the Beta variant, which was first identified in South Africa.

Another concern is that the way in which molnupiravir generates mutations in the coronavirus genome could lead to the emergence of a new variant of concern. Although this is theoretically possible, Mellor thinks it’s unlikely. Laboratory studies have shown that molnupiravir generates a bevy of mutations in each viral genome, and the more mutations that the genome accumulates, the greater the likelihood that one of them will weaken the virus. “The chance that multiple mutations will enhance the virus is low,” Mellors says.

Could the coronavirus become resistant to antivirals?

Drug resistance is a familiar problem and is the reason that some viral infections, such as HIV and hepatitis C, are treated using combinations of antivirals. “The bottom line is that we’re going to need combination therapies,” says Katherine Soley-Radtke, a chemist who is developing antiviral drugs at the University of Maryland, Baltimore County.



[International COVID-19 trial to restart with focus on immune responses](#)

So far, molnupiravir and Paxlovid have been tested only as single therapies. A 5 November analysis by the science information and analytics firm Airfinity in London found only 16 COVID-19 trials that test combinations of antivirals and aim to enrol more than 100 participants. None involved molnupiravir or Paxlovid; most tested combinations with the malaria drug hydroxychloroquine, a drug that has repeatedly failed when tested as a single agent in rigorous clinical trials against COVID-19.

It will be important to look at people who don’t respond to molnupiravir or Paxlovid, to find out whether viral resistance is a factor, says Douglas Richman, an infectious-disease specialist at the University of California in San Diego. Researchers should also closely monitor people who receive the

drugs and have weakened immune systems. Because infections might last longer in these people, there could be more opportunity for resistance to emerge, says Richman.

Who will be able to access the new drugs?

Merck has signed an agreement with the Medicines Patent Pool to provide the intellectual-property licences needed to produce molnupiravir in low- and middle-income countries. Several generic-medicines companies have already started to manufacture the drug.

Gore says that the patent pool is in discussions with Pfizer. Both companies have committed to tier pricing to allow lower- and middle-income countries to pay less for the drugs than wealthier countries.

But intellectual property is not the only barrier to access. Another concern is testing: administering the antivirals early in the course of an infection means that countries will need an ample supply of COVID-19 tests. “There’s a huge gap in testing in some countries,” says Kim. “We don’t want someone to be prescribing this if someone has COVID-like symptoms, but it turns out to be the flu, not COVID-19.”

Meanwhile, wealthy countries are already placing large orders for the drugs, raising concerns that their stockpiles will soak up supplies and limit access in other parts of the world. The situation is all too familiar, says John Amuasi, leader of the Global Health and Infectious Diseases Research Group at the Kumasi Centre for Collaborative Research in Tropical Medicine in Ghana. “Look at what’s happened with the vaccines.”

Nature **599**, 358-359 (2021)

doi: <https://doi.org/10.1038/d41586-021-03074-5>

References

1. 1.

This article was downloaded by **calibre** from <https://www.nature.com/articles/d41586-021-03074-5>

| [Section menu](#) | [Main menu](#) |

- NEWS
- 08 November 2021
- Clarification [11 November 2021](#)

How protein-based COVID vaccines could change the pandemic

Jabs from Novavax and other biotech firms are coming. Scientists say they have a lot to offer.

- [Elie Dolgin](#)



A participant in Novavax's phase III trial receives a jab in early 2021. Credit: Kenny Holston/The New York Times/eyevine

Pamela Sherry is eager to become immunized against COVID-19. But she has put off getting a jab.

“I believe vaccines work,” she says. “I want the protection.” Yet she is prone to acute immune reactions and has blood circulation problems, so she has concerns about the shots available in the United States, where she lives — those based on messenger RNA (mRNA) and viral-vector technologies. Although safe for most of the population, they have been linked to rare but potentially severe side effects, including [heart inflammation](#) and [blood clots](#).



Mix-and-match COVID vaccines ace the effectiveness test

So Sherry has been waiting for the menu of vaccine options available to her to expand. In particular, she is holding out for a vaccine built from purified proteins. Unlike the relatively new technologies that the mRNA and viral-vector COVID-19 shots are based on, protein vaccines have been used for decades to protect people from hepatitis, shingles and other viral infections. To elicit a protective immune response, these shots deliver proteins, along with immunity-stimulating adjuvants, directly to a person’s cells, rather than a fragment of genetic code that the cells must read to synthesize the proteins themselves.

Although protein vaccines are not yet in widespread use for COVID-19, late-stage clinical-trial data so far look promising, demonstrating strong

protection with fewer side effects than other COVID-19 shots typically cause.

If such a shot were available, “I would go and get it right away,” says Sherry, who runs a stationery business out of her home in Prosper, Texas.

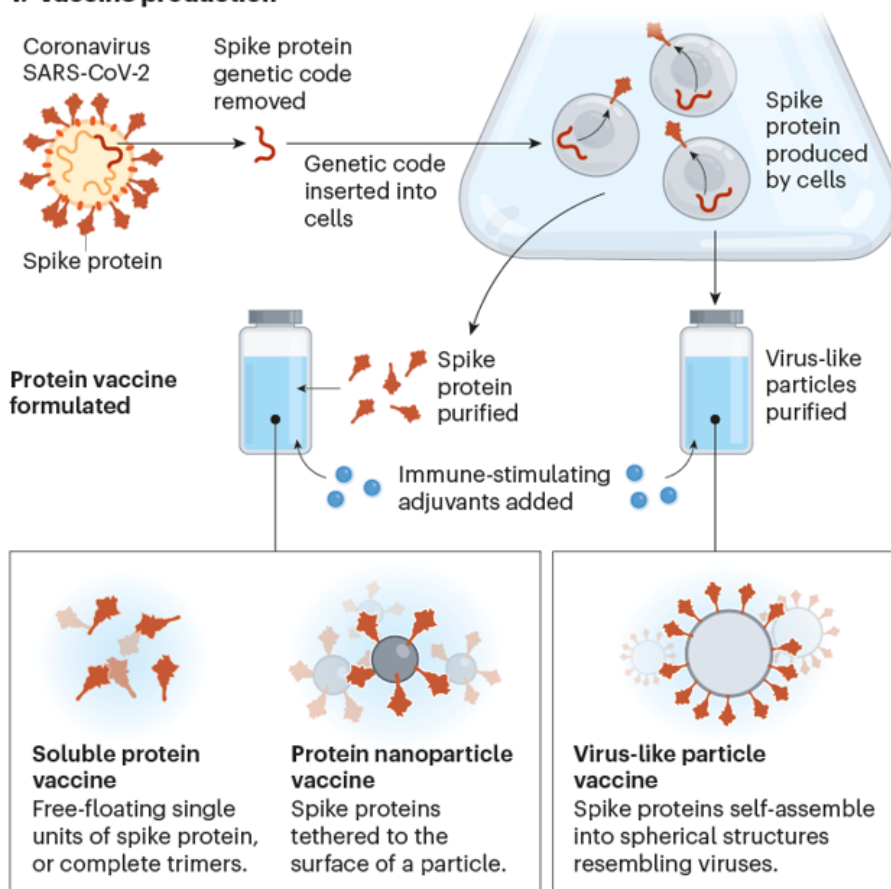
Sherry’s wait could soon be over. After months of quality-control setbacks and manufacturing delays, executives at biotechnology firm Novavax in Gaithersburg, Maryland, say they are poised to submit the company’s long-awaited application for their protein-based vaccine to US drug regulators before the end of the year. (On 1 November, Indonesia granted the company’s vaccine its first emergency authorization, and regulatory filings have already been made with government agencies in Australia, Canada, the United Kingdom, the European Union and elsewhere.) Meanwhile, two vaccine makers in Asia — Clover Biopharmaceuticals, based in Chengdu, China, and Biological E in Hyderabad, India — are similarly on track to file with various national authorities in the coming weeks and months.

PROTEIN VACCINES 101

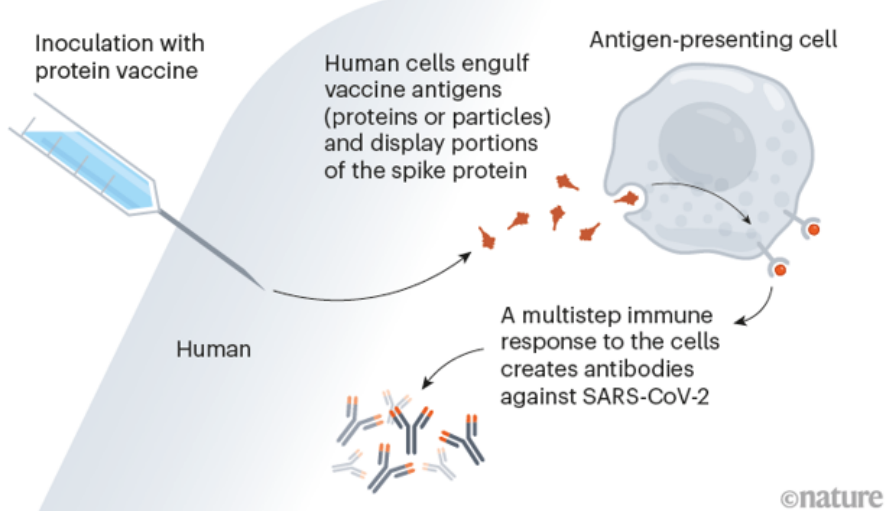
There are a number of ways to formulate a protein-based COVID-19 vaccine, including using free-floating protein or tethering protein to a nanoparticle.

Many vaccines are based on the coronavirus's spike protein, but some use only a key part of the protein, called the receptor-binding domain.

1. Vaccine production



2. Vaccine administration



©nature

Nik Spencer/*Nature*

In a few corners of the globe — Cuba, Taiwan, and elsewhere — home-grown protein shots are already playing a role in national vaccination efforts. Now, with a wave of more such products up for approval, the shots could allay the fears of vaccine hold-outs such as Sherry, serve as booster shots, and, importantly, help to fill a void in the global pandemic response.

So far, fewer than 6% of people in low-income countries have been vaccinated against COVID-19. Protein-based vaccines — with their inexpensive production protocols and logistical advantages, including stability at a broad range of temperatures — could help to narrow the immunization gap between rich and poor countries.

“The world needs these protein-based vaccines to reach those vulnerable populations,” says Nick Jackson, head of programmes and innovative technologies at the Coalition for Epidemic Preparedness Innovations, which has invested more than US\$1 billion in five protein-based COVID-19 vaccines in active development. The lion’s share is going to products made by Clover, Novavax and SK bioscience in Seongnam, South Korea. “Protein vaccines are going to beckon in a new era of COVID-19 immunization,” Jackson says.

Intrinsically slow

From the earliest days of the pandemic response, researchers anticipated that protein-based designs would be slower off the blocks than other vaccine technologies.

Companies know how to manufacture gobs of purified protein at scale — using genetically engineered cells from mammals, insects or microbes — but the process involves many steps, each of which has to be optimized for making a specific protein. “There’s an intrinsic slowness,” says Christian Mandl, a former industry executive who now consults on vaccine-development issues. Most of the protein-based vaccines currently in testing have been crafted around some version of the coronavirus SARS-CoV-2’s

spike protein, which helps the virus to enter cells (see ‘Protein vaccines 101’).



COVID vaccine boosters: the most important questions

Aside from the expected delays, however, vaccine manufacturers made some avoidable errors. When drug giants Sanofi and GlaxoSmithKline (GSK) teamed up on a protein vaccine project, for example, onlookers expected clinical development to move with great haste. But the companies initially relied on faulty reagents to characterize their product, resulting in a dosing miscalculation. Early trial participants received doses that were approximately one-fifth of the planned dose.

The mistake cost Sanofi and GSK around five months in their development timeline, because they had to repeat an exploratory study to find the optimal dose for late-stage testing. Their protein-based jab is now in a phase III trial that kicked off in late May, which involves thousands of participants in Africa, Asia and Latin America.

By comparison, large-scale trials from Novavax and Clover have already yielded efficacy data. According to a preprint published last month (that has not been peer reviewed)¹, the Novavax jab offered more than 90% protection against symptomatic COVID-19 in a 30,000-person study completed early in the year — before the Delta variant arrived, when only milder forms of the virus were in circulation.

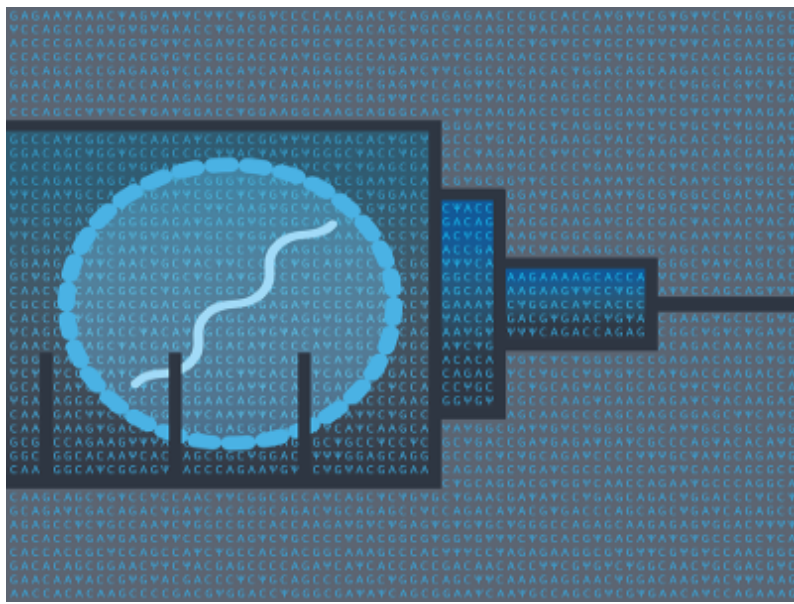
Ones to watch: Vaccine makers with protein jabs in late-stage clinical trials

Company	Location	Vaccine type	Cell manufacturing system
Biological E	Hyderabad, India	Soluble protein	Microbial cells (yeast)
Clover Biopharmaceuticals	Chengdu, China	Soluble protein	Mammalian cells (hamster ovary)
Medicago	Quebec City, Canada	Virus-like particle	Plant cells (tobacco-like <i>Nicotiana benthamiana</i>)
Novavax	Gaithersburg, Maryland	Protein nanoparticle	Insect cells (fall armyworm)
Sanofi/GlaxoSmithKline	Paris/Brentford, UK	Soluble protein	Insect cells (fall armyworm)
SK bioscience	Seongnam, South Korea	Protein nanoparticle	Mammalian cells (human)

Clover [reported somewhat lower efficacy](#) results for its protein-based jab — just 67% for symptomatic COVID-19 of any severity — but that number was probably deflated, because the vaccine was tested on populations grappling with more virulent strains of SARS-CoV-2, including the Delta

and Mu variants. Both vaccines elicited antibody levels on par with those induced by mRNA shots, which have emerged as some of the most efficacious in the pandemic^{2,3}.

The results show that making COVID-19 vaccines using proteins “is not a substandard approach just because it took longer,” says Ryan Spencer, chief executive of Dynavax Technologies of Emeryville, California, which makes the Clover vaccine’s adjuvant.



The tangled history of mRNA vaccines

The shots also appear to be safe. None of the 50 or so protein-based COVID-19 vaccines now in clinical testing around the world have elicited any major side effects. Even many of the reactions typically elicited by the mRNA or viral-vector jabs — headaches, fevers, nausea and chills — have proven far less common with the protein-based alternatives. For example, less than 1% of individuals who received a protein-based shot from Taiwan’s Medigen Vaccine Biologics Corporation, in Taipei City, developed fevers in clinical studies.

“The safety profile is very much like those of influenza vaccines,” says Szu-Min Hsieh, an infectious-disease specialist at the National Taiwan University Hospital in Taipei, who published phase II trial results last month⁴.

“That’s going to allow a lot of people not to fret as much,” adds Cindy Gay, an infectious-disease physician at the University of North Carolina School of Medicine in Chapel Hill, who co-led testing of the Novavax vaccine.

Design differences

Even if one protein-based vaccine succeeds — both in terms of its performance and in finding a market — there’s no reason to think they all will, however.

For one thing, the form of the spike protein they deploy varies greatly from one product to the next. Some use single proteins, others triads. Some use full-length spike protein, others just a fragment. Some proteins are free-floating, others are packaged together into nanoparticles.



Why is it so hard to investigate the rare side effects of COVID vaccines?

Many of them are also manufactured using different types of cell (see ‘Ones to watch’). Novavax and Sanofi/GSK use cells from the fall armyworm (*Spodoptera frugiperda*), a type of moth, to synthesize protein; Clover and Medigen rely on hamster ovary cells, a mainstay of therapeutic antibody production in the biotechnology industry. Plus, the leading candidates rely on different adjuvants, each of which prods the immune system in its own way, resulting in different kinds of vaccine responses.

All of this could translate into different efficacy and safety profiles, says Thomas Breuer, chief global health officer for GSK. “I could imagine that you will see differences, but time and the phase III trial results will give us the ultimate answer.”

Those results have the potential to shape booster programmes in wealthy countries, where large percentages of the population have already been vaccinated. Although mRNA jabs are currently being used as boosters in many of these places, tolerability concerns could drive people to seek out protein-based boosters once they’re available.

The technology is tried and true, and studies have shown that a mix-and-match strategy — in which a different COVID-19 vaccine is administered after the first — [are effective at preventing the disease](#), notes John Mascola, director of the Vaccine Research Center at the US National Institute of Allergy and Infectious Diseases. “We would need to see human data” confirming such a protein-based booster regimen is similarly safe and effective, Mascola says — but he and others expect that it will be. Trials evaluating the approach are ongoing.

Plugging the equity gap

Once authorized, protein shots are also expected to rapidly address supply shortages that have plagued efforts to vaccinate lower-income countries. Novavax and Clover, for example, have each pledged to donate hundreds of millions of doses of their jabs next year to COVAX, an initiative designed to distribute vaccines around the world.

The global health community [has also been arguing that equitable access](#) to COVID-19 vaccines could be achieved through local manufacturing of shots in the global south. To achieve this, more researchers should be looking to simple, inexpensive production systems that manufacturers in less-wealthy countries can readily implement, says Christopher Love, a chemical engineer at the Massachusetts Institute of Technology in Cambridge.



The fight to manufacture COVID vaccines in lower-income countries

Biological E is already taking advantage of one such system — yeast — to manufacture the vaccine it licensed from Baylor College of Medicine in Houston, Texas. According to Maria Elena Bottazzi, a Baylor virologist who helped to create the product, that makes it “probably the easiest and cheapest to scale” of all the COVID-19 vaccines on or nearing the market today.

In the earliest days of the COVID-19 crisis, vaccine platforms such as mRNA brought the advantage of speed, says Ralf Clemens, a vaccine-industry veteran and a scientific adviser to Clover. But now that a wave of protein-based vaccines is coming, he says, they will have a lot more to offer — and in the long run when it comes to protecting the world against coronavirus infections, “I think they will prevail.”

Nature **599**, 359-360 (2021)

doi: <https://doi.org/10.1038/d41586-021-03025-0>

Updates & Corrections

- **Clarification 11 November 2021:** This story was updated to acknowledge protein-based COVID-19 vaccines already in circulation in countries such as Cuba and Taiwan.

References

1. 1.

Dunkle, L. M. *et al.* Preprint at medRxiv
<https://doi.org/10.1101/2021.10.05.21264567> (2021).

2. 2.

Keech, C. *et al.* *N. Engl. J. Med.* **383**, 2320-2332 (2020).

3. 3.

Richmond, P. *et al.* *Lancet* [https://doi.org/10.1016/S0140-6736\(21\)00241-5](https://doi.org/10.1016/S0140-6736(21)00241-5) (2021).

4. 4.

Hsieh, S.-M. *et al.* *Lancet Resp. Med.* [https://doi.org/10.1016/S2213-2600\(21\)00402-1](https://doi.org/10.1016/S2213-2600(21)00402-1) (2021).

This article was downloaded by **calibre** from <https://www.nature.com/articles/d41586-021-03025-0>

| [Section menu](#) | [Main menu](#) |

- NEWS
- 08 November 2021

Scammers impersonate guest editors to get sham papers published

Hundreds of junk-science papers have been retracted from reputable journals after fraudsters used ‘special issues’ to manipulate the publication process. And the problem is growing.

- [Holly Else](#)



Scammers have impersonated researchers to gain access to reputable journals and publish special issues filled with nonsense papers. Credit: Getty

Hundreds of articles published in peer-reviewed journals are being retracted after scammers exploited the processes for publishing special issues to get poor-quality papers — sometimes consisting of complete gibberish — into established journals. In some cases, fraudsters posed as scientists and offered to guest-edit issues that they then filled with sham papers.

Elsevier is withdrawing 165 articles currently in press and plans to retract 300 more that have been published as part of 6 special issues in one of its journals, and Springer Nature is [retracting 62 articles](#) published in a special issue of one journal. The retractions come after the publishers each issued expressions of concern earlier this year, covering hundreds of articles.

Science-integrity experts expect that more investigations will come in the months ahead as other titles realize that they have been duped.



[Hundreds of gibberish papers still lurk in the scientific literature](#)

“It is very worrying,” says Guillaume Cabanac, a computer scientist at the University of Toulouse in France, who has worked to uncover nonsense science papers in special issues. He adds that it is shocking to see such papers in journals from ‘flagship’ publishers and that “it is not only predatory journals that publish bullshit”.

A Springer Nature spokesperson said that an investigation had revealed “deliberate attempts to subvert the trust-based editorial process and

manipulate the publication record”. They added that they did not yet know who was responsible (*Nature* is editorially independent of its publisher).

Elsevier says that it has put measures in place to stop similar problems happening in the future.

Special-issue scam

Many journals publish special issues — collections of articles that focus on a particular topic of relevance to their readers. These issues are often overseen by guest editors who are experts in the research topic, but are not usually involved in the day-to-day editorial work of the journal.

Fraudsters have been caught several times in recent years while trying to use special issues as a way to get low-quality papers published in legitimate journals — but the number of affected papers seems to be increasing.

In 2016, the website *Retraction Watch* reported that scammers had posed as a known scientist to trick *The Scientific World Journal*, published by Hindawi, into appointing them as the guest editor of a special issue on metaheuristics. A subsequent investigation by the publisher found that several peer-review reports for papers published in the special issue had come from compromised e-mail accounts belonging to other researchers. Hindawi told *Retraction Watch* that it had no idea who was behind the scam and said it had put measures in place to help prevent the problem from reoccurring.



The fight against fake-paper factories that churn out sham science

In December 2020, Springer Nature's *Journal of Nanoparticle Research* wrote that it had been "attacked in a new way by a sophisticated and organized network". A group of what seemed to be eminent computer scientists and engineers from well-known institutions in Germany and the United Kingdom wrote to the journal's editors suggesting a special issue about the role of nanotechnology in health care in September 2019. The editorial board accepted the proposal, created a special-issue entry in its editorial management system and gave three members of the group access to it so they could handle the manuscripts.

Months later, some members of the editorial board began to notice that most of the manuscripts submitted for the special issue were of poor quality or did not fit the theme. They launched an investigation, but by then 19 of the 80 submissions had already been accepted or published. These papers have since been retracted.

The investigation revealed that the people who had suggested the special issue were not who they claimed to be, but instead were scammers using Internet-domain names that looked very similar to the real scientists' institutional e-mail addresses. These included an e-mail suffix with 'univ' instead of 'uni' and '-ac.uk' instead of '.ac.uk'. There were also anomalies with the peer-reviewers' identities and peer-review reports.

“All of the evidence points to an organized network that tries — in this case successfully — to infiltrate scientific journals with the objective of easily publishing manuscripts from pseudo-scientists or less-productive researchers who want to appear in respectable journals,” wrote three members of the journal’s editorial board in the December article.

Unclear motivations

It is not yet clear why scammers are manipulating the system to publish sham articles. Cabanac suggests that it might be due to the pressure on researchers to publish papers to continue their careers. The ability to publish in specific journals — even if the papers are clearly nonsense — could allow some researchers to “get publications for their CV and a green card to stay in academia”, he says.

But the scammers’ motivations remain a mystery to Ivan Oransky, a journalist who runs *Retraction Watch*. Even the article titles, which would be listed as part of an individual’s publication record, often do not make sense, he says. “The papers are so obviously terrible, so why would you want them on your CV?” He adds that it is not clear whether special-issue scamming is becoming more common or whether it is just becoming more visible. “I do think that the journals are waking up to it, actually looking for it and having systems in place,” he says.



Predatory publishers' latest scam: bootlegged and rebranded papers

The latest retractions from Springer Nature and Elsevier suggest that the practice is becoming more sophisticated and prevalent. In July, Elsevier issued [expressions of concern for more than 400 papers](#) published in 6 special issues of *Microprocessors and Microsystems* after the title's editor had concerns about the integrity and peer review of the papers. Many of the papers were from authors based at Chinese institutions, and most contained nonsensical phrases that Elsevier thinks came from the use of reverse-translation software to disguise plagiarism.

Elsevier says that the issue occurred due to a temporary configuration error in their editorial system, which was corrected as soon as it was discovered. The publisher has withdrawn 165 papers in press and plans to retract 300 others. It says it validates the identities and qualifications of guest editors, and now asks the editor-in-chief or editorial-board members to confirm each paper's acceptance so that any irregularities are flagged as a special issue progresses.

The publisher is also working with Cabanac and his colleagues to develop open-source computerised tools that can flag when papers contain automatically generated scientific text.

Springer Nature has so far retracted 62 of the 436 papers published in 'topical collections' of the *Arabian Journal of Geoscience* that it flagged with [expressions of concern](#) in September. The prose in many of the affected papers switches between research on two seemingly unrelated topics. For example, 71 articles have abstracts or titles that contain the words 'dance', 'aerobics' or 'sports' in relation to geoscience, including the articles 'Sea level height based on big data of Internet of Things and aerobics teaching in coastal areas' and 'Rock stress and deformation characteristics based on SVM and sports high-intensity interval training'. A further 24 papers in a special issue of *Personal and Ubiquitous Computing* are also [being investigated](#) at Springer Nature.

The publisher says that in addition to putting extra checks in place, it is developing artificial-intelligence tools that can identify and prevent attempts to deliberately manipulate the system. It is also gathering evidence about

how the deceptions are carried out to share with other publishers. “We will not tolerate deliberate attempts to subvert the publication process,” a spokesperson said in a statement.

Oransky says that the big question now is what publishers do about special issues. They could pose a credibility problem, “even if it is guilt by association”. Whatever happens, he is certain that there are more retractions ahead.

Nature **599**, 361 (2021)

doi: <https://doi.org/10.1038/d41586-021-03035-y>

This article was downloaded by **calibre** from <https://www.nature.com/articles/d41586-021-03035-y>.

| [Section menu](#) | [Main menu](#) |

The chase for fusion energy

An emerging industry of nuclear-fusion firms promises to have commercial reactors ready in the next decade.

By Philip Ball
17 November 2021

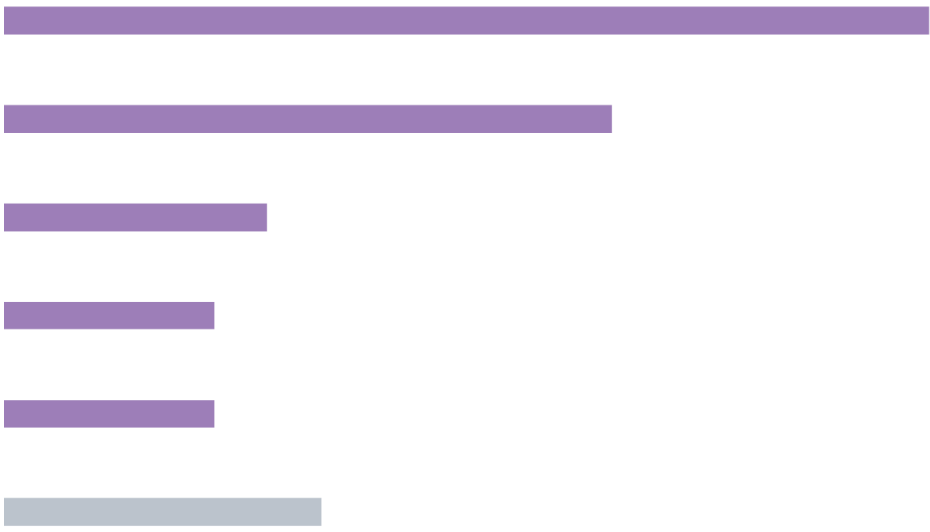


The ancient village of Culham, nestled in a bend of the River Thames west of London, seems an unlikely launching pad for the future. But next year, construction will start here on a gleaming building of glass and steel that could house what many people consider to be an essential technology to meet demand for clean energy in the twenty-first century and beyond.

Long derided as a prospect that is forever 30 years away, nuclear fusion seems finally to be approaching commercial viability. There are now more than 30 private fusion firms globally, according to an [October survey by the Fusion Industry Association \(FIA\) in Washington DC](#), which represents companies in the sector; the 18 firms that have declared their funding say they have attracted more than US\$2.4 billion in total, almost entirely from private investments (see ‘Fusion funding’). Key to these efforts are advances in materials research and computing that are enabling technologies other than the standard designs that national and international agencies have pursued for so long.

FUSION FUNDING

Private fusion firms have disclosed more than \$2.4 billion in funding.



TAE Technologies

880 US\$ million

Helion Energy

578

Commonwealth Fusion Systems

250

General Fusion

200

Tokamak Energy

200

Other (12 firms)

302

General Fusion

Commonwealth Fusion Systems

TAE Technologies

Helion Energy

Other

The latest venture at Culham — the hub of UK fusion research for decades — is a demonstration plant for General Fusion (GF), a company based in Burnaby, Canada. It is scheduled to start operating in 2025, and the company aims to have reactors for sale in the early 2030s. It “will be the first power-plant-relevant large-scale demonstration”, says GF’s chief executive Chris Mowry — unless, that is, its competitors deliver sooner.

Designed by British architect Amanda Levete, GF’s prototype plant illustrates the way fusion research has shifted from gargantuan state- or internationally funded enterprises to sleek, image-conscious affairs driven by private companies, often with state support. (GF will receive some UK government funding; it has not disclosed how much.)

TAE Technologies 880 US\$ million

Helion Energy 578

Commonwealth Fusion Systems 250

General Fusion 200

Tol

200

Oth

302



Artist's impression of General Fusion's planned plant at Culham, UK. Credit: AL_A for General Fusion. Lead image: The world's strongest high-temperature superconducting magnet will be used in a 2025 fusion reactor in Massachusetts. Credit: Gretchen Ertl, CFS/MIT-PSFC, 2021

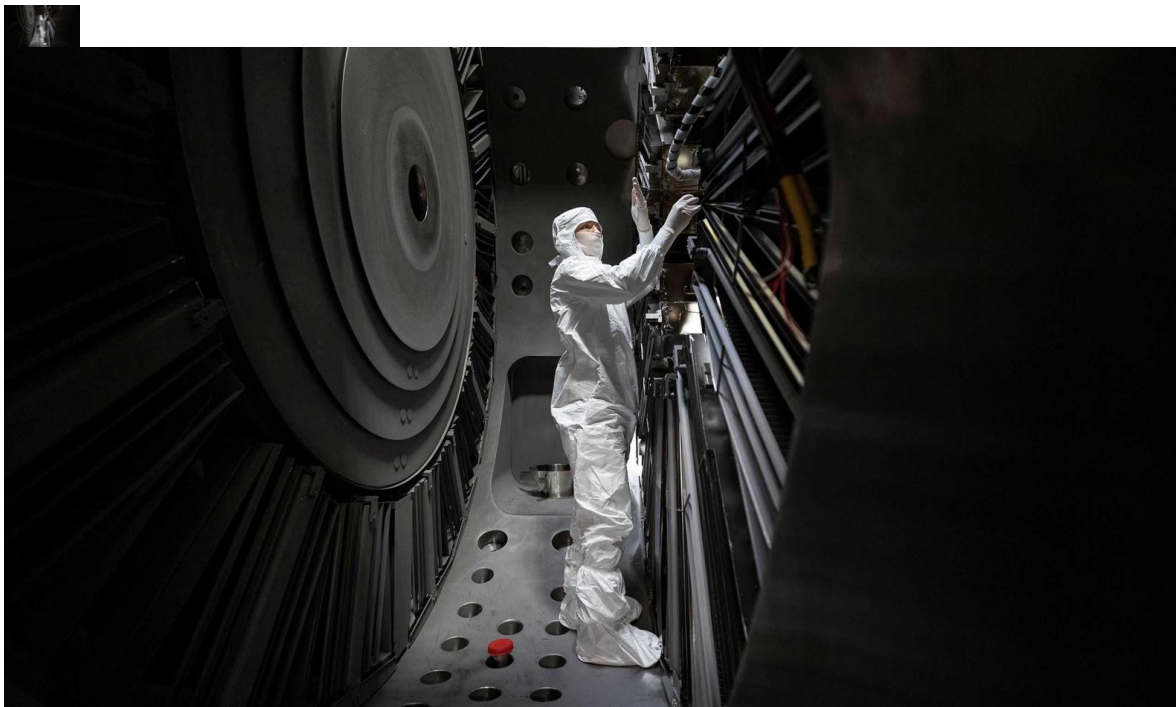
Artist's impression of General Fusion's planned plant at Culham, UK. Credit: AL_A for General Fusion. Lead image: The world's strongest high-temperature superconducting magnet will be used in a 2025 fusion reactor in Massachusetts. Credit: Gretchen Ertl, CFS/MIT-PSFC, 2021

In this respect, advocates of fusion technology say it has many parallels with the space industry. That, too, was once confined to government agencies but is now benefiting from the drive and imagination of nimble (albeit often state-assisted) private enterprise. This is “the SpaceX moment for fusion”, says Mowry, referring to Elon Musk’s space-flight company in Hawthorne, California.

“The mood has changed,” says Thomas Klinger, a fusion specialist at the Max Planck Institute for Plasma Physics (IPP) in Greifswald, Germany. “We can smell that we’re getting close.” Investors sense the real prospect of returns on their money: Google and the New York City-based investment bank Goldman Sachs, for instance, are among those funding the fusion company TAE Technologies, based in Foothill Ranch, California, which has raised around \$880 million so far. “Companies are starting to build things at the level of what governments can build,” says Bob Mumgaard, chief executive of Commonwealth Fusion Systems (CFS), based in Cambridge, Massachusetts.

And just as private space travel is now materializing, many industry observers are forecasting that the same business model will give rise to commercial fusion — desperately needed to decarbonize the energy economy — within a decade. “There’s a very good shot to get there within less than ten years,” says Michl Binderbauer, chief executive of TAE Technologies. In the FIA report, a majority

of respondents thought that fusion would power an electrical grid somewhere in the world in the 2030s.



A technician works inside TAE's 'Norman' demonstration fusion reactor. Credit: TAE Technologies

A technician works inside TAE's 'Norman' demonstration fusion reactor. Credit: TAE Technologies

Several fusion researchers who don't work for private firms told *Nature* that, although prospects are undeniably exciting, commercial fusion in a decade is overly optimistic. "Private companies say they'll have it working in ten years, but that's just to attract funders," says Tony Donné, programme manager of the Eurofusion consortium which conducts experiments at the state-run Joint European Torus, established at Culham in the late 1970s. "They all have stated constantly to be about ten years away from a working fusion reactor, and they still do."

Timelines that companies project should be regarded not so much as promises but as motivational aspirations, says Melanie Windridge, a plasma physicist who is the FIA's UK director of communications, and a communications consultant for the fusion firm Tokamak Energy, in Culham. "I think bold targets are necessary," she says. State support is also likely to be needed to build a fusion power plant that actually feeds electricity into the grid, adds Ian Chapman, chief executive of the UK Atomic Energy Authority (UKAEA).

But whether it comes from small-scale private enterprise, huge national or international fusion projects, or a bit of both, practical nuclear fusion finally seems to be on the horizon. "I'm convinced that it's going to happen", says Chapman. Chris Kelsall, chief executive of Tokamak Energy, agrees. "Sooner or later this will be cracked," he says. "And it will be transformative."

Seventy-year dream

Nuclear fusion, says Klinger, is “the only primary energy source left in the Universe” that we have yet to exploit. Ever since the process that powers the stars was harnessed in the 1950s for hydrogen bombs, technologists have dreamt of unlocking it in a more controlled manner for energy generation.

Existing nuclear power plants use fission: the release of energy when heavy atoms such as uranium decay. Fusion, by contrast, produces energy by merging very light nuclei, typically hydrogen, which can happen only at very high temperatures and pressures. Most efforts to harness it in reactors involve heating the hydrogen isotopes deuterium (D) and tritium (T) until they form a plasma — a fluid state of matter containing ionized atoms and other charged particles — and then fuse (see ‘Fuel mix’). For these isotopes, fusion starts at lower temperatures and densities than for normal hydrogen.

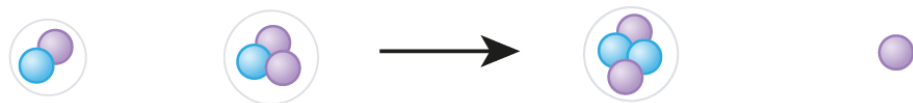
D–T fusion generates some radiation in the form of short-lived neutrons, but no long-lived radioactive waste, unlike fission. It is also safer than fission because it can be switched off easily: if the plasma is brought below critical thresholds of temperature or density, the nuclear reactions stop.

FUEL MIX

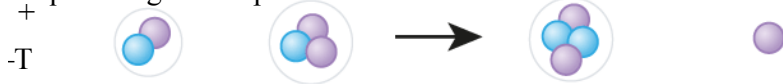
Many reactors fuse deuterium (D) with tritium (T) to release energy. This mix ignites, or creates a self-sustaining fusion reaction, at around 100 million kelvin. It produces neutrons, which can make the chamber radioactive.



+
+
T
·on
ium
4 (α)
·m



Other reactions, such as fusing protons (p) with boron-11 (^{11}B), don't produce neutrons, but ignition requires higher temperatures.



ror

riu

~~T~~(`

upm

+

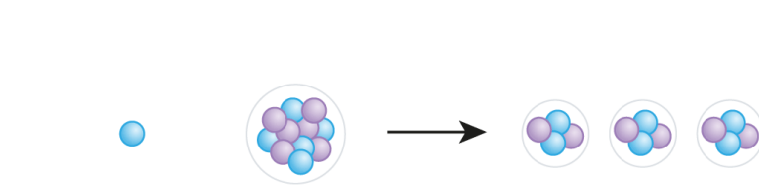
teriu

^{11}B

+

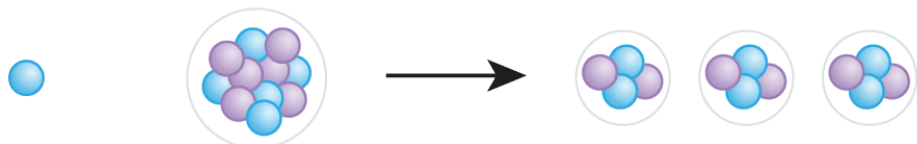
^{11}B -4

$^{1-11}$
itron
 $^{3\alpha}$



^{11}B

+



What makes it so difficult to conduct in a controlled manner, however, is the challenge of containing electrically charged plasma that is undergoing fusion at temperatures of around 100 million kelvin much hotter than the centre of the Sun. Generally, researchers use magnetic fields to confine and levitate the plasma inside the reactor. But instabilities in this infernal fluid make containment very

difficult, and have so far prevented fusion from being sustained for long enough to extract more energy than is put in to trigger it.

This is necessarily big science, and until this century, only state-run projects could muster the resources. The scale of the enterprise is reflected today in the world's biggest fusion effort: ITER, a fusion reactor being constructed in southern France and supported by 35 nations, including China, European Union member states, the United States, Russia, South Korea and Japan, with a price tag of at least \$22 billion.

A D-shaped magnetic coil (left) that will form part of the giant ITER fusion reactor in France.
B

A part of ITER's vacuum vessel, inside which plasma will be held.

Credit: [ITER Organization](#)

Although the first test runs are scheduled for 2025, [full D-T fusion is not scheduled until 2035](#), ultimately with the goal of continuously extracting 500 MW of power — comparable to the output of a modest coal-fired power plant — while putting 50 MW into the reactor. (These numbers refer only to the energy put directly into and drawn out of the plasma; they don't factor in other processes such as maintenance needs or the inefficiencies of converting the fusion heat output into electricity.)

A further series of big reactors might follow ITER: China, which has three fusion reactors feeding results into ITER, plans a China Fusion Engineering Testing Reactor (CFETR) in the 2030s, and both South Korea and the EU propose to build demonstration power plants that would follow on from ITER.

The big national and international efforts won't succeed soon enough to enable the decarbonization needed to address climate change, although fusion is expected to become a key part of the energy economy in the second half of the century. But private companies hope to have working and affordable devices sooner (see 'Fusion rush').

Fusion rush

Firms and governments are developing many kinds of fusion reactor. They all heat gas to create a plasma, confined at such high temperatures that atomic nuclei fuse, releasing energy that can be harnessed for electricity. Here are five prominent designs.

Illustrations by Tomáš Müller

Tokamak (ITER and other facilities)

Superconducting magnetic coils — cooled by liquid helium — hold plasma in a toroidal vessel.

Mini-tokamak (Tokamak Energy, Commonwealth Fusion Systems and others)

Magnets made of high-temperature superconductors produce stronger fields and can be cooled more easily, allowing more compact, spherical tokamaks to be built.

Linear (Colliding beams) reactor (TAE Technologies)

packets of plasma are fired into a central chamber and rotate rapidly inside a solenoid (coiled-wire electromagnet).

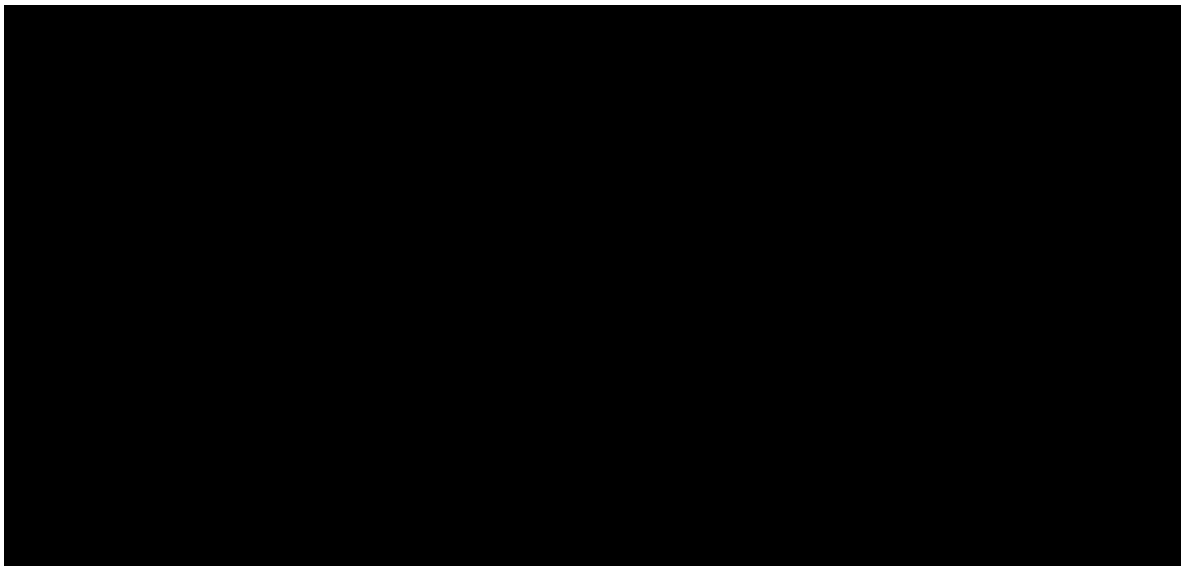
Magnetized Target Reactor (General Fusion)

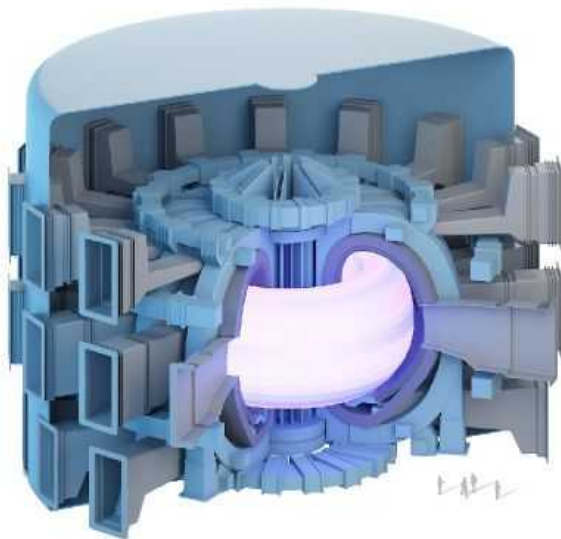
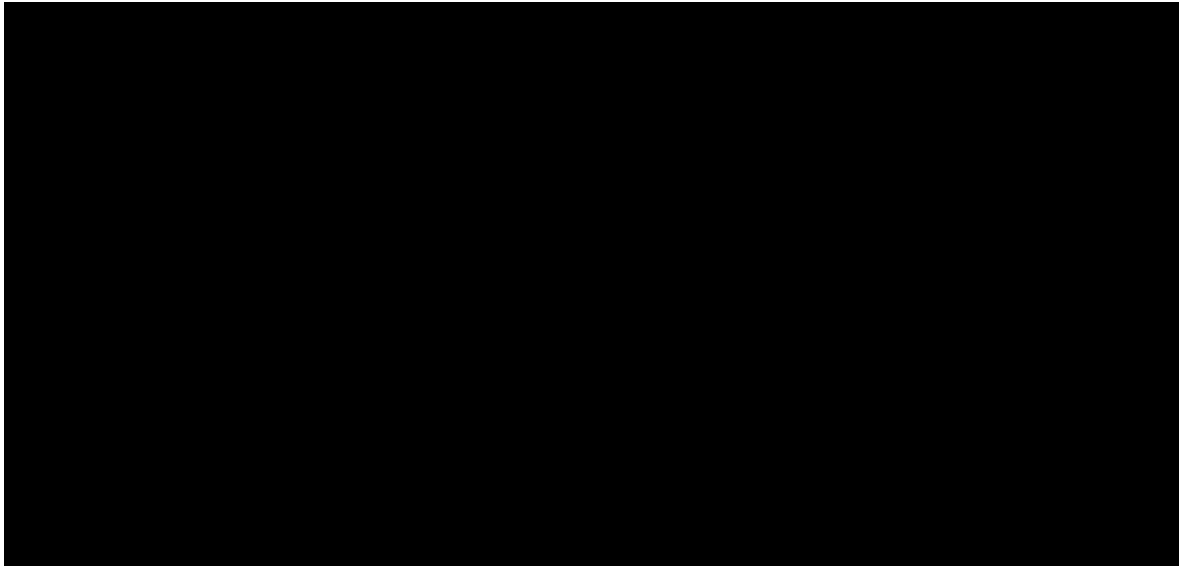
A spinning ball of liquid metal confines plasma; pistons then rapidly compress it. The plasma is allowed to expand, then compressed again.

Stellarator (Wendelstein 7-X)

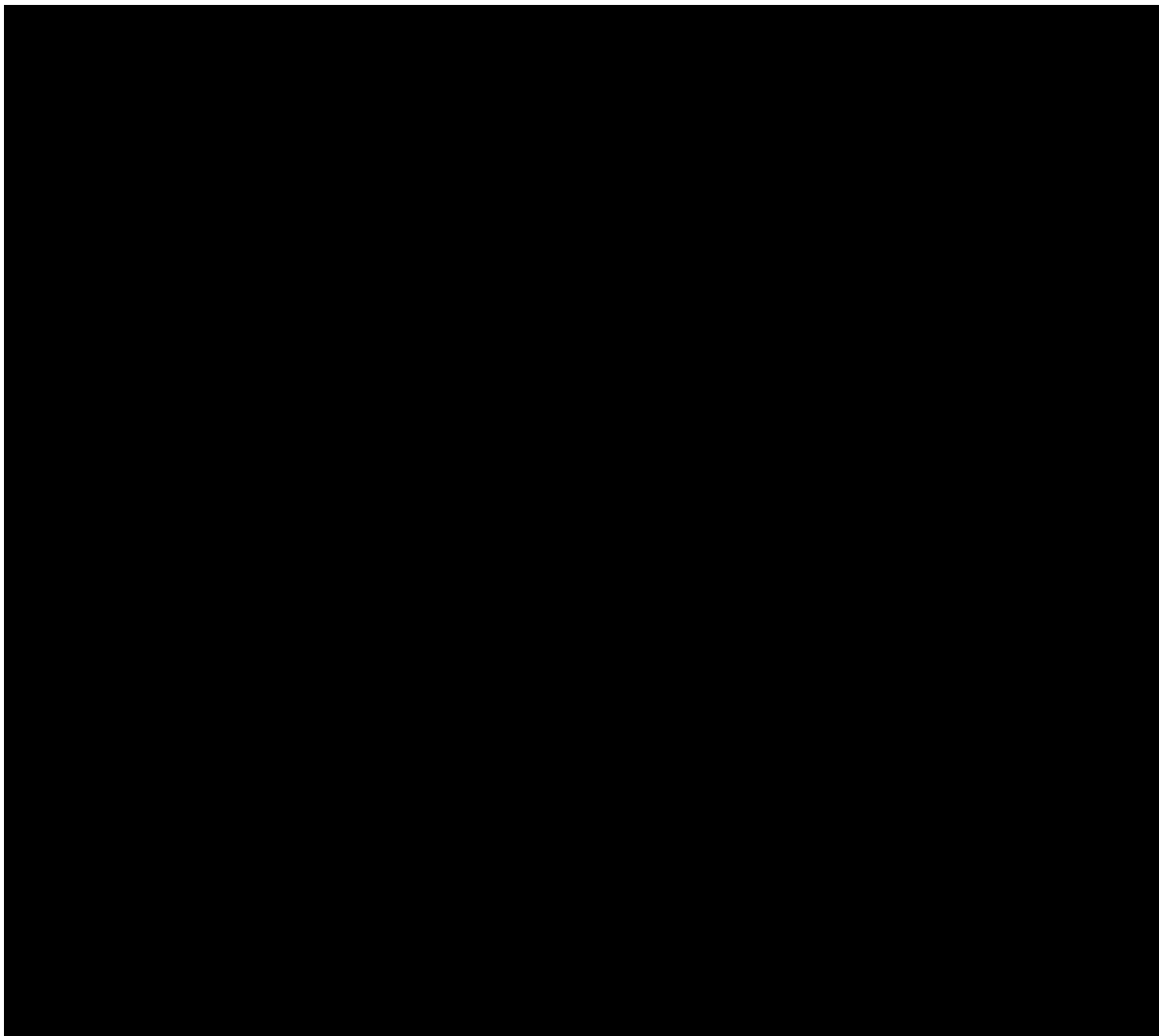
A complicated twisted loop of magnetic fields confines the plasma.

As with space exploration, one of the benefits of a private fusion sector is greater diversity of approaches than monolithic state enterprises can muster. ITER is using the most common approach to confining plasma, in a device called a tokamak, which uses powerful superconducting magnets to hold the plasma in a ring-shaped (toroidal) vessel. The flow of the electrically charged plasma particles themselves also generates a magnetic field that helps to confine the plasma.



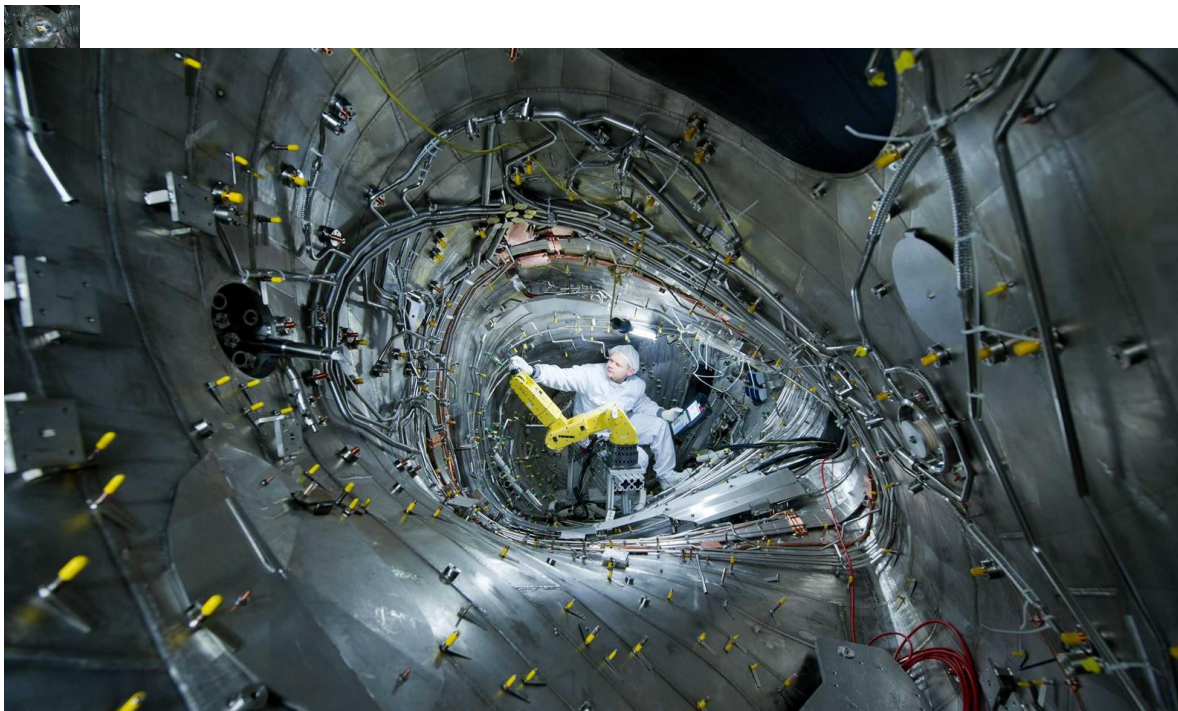


But a tokamak isn't the only option. In the early days of fusion, in the 1950s, US astrophysicist Lyman Spitzer showed that magnetic fields could be configured in a twisted loop, rather like a figure of eight, to make a 'magnetic bottle' that could be filled with plasma. This design was known as a stellarator. But solving the equations describing the plasma for this complex geometry was too computationally intensive, so the concept was mostly abandoned once tokamaks had been shown to work.



As supercomputers became available in the late 1980s, however, researchers revisited the idea. This led to a stellarator project at the IPP called the Wendelstein 7-X reactor. Costing more than €1 billion (US\$1.15 billion) to build, staff and operate up to its first plasma testing in 2015, with construction

costs of €370 million largely borne by the German government, Wendelstein 7-X will be completed by the end of this year. Then comes a long process of working out how to operate it routinely as a demonstration project.



An engineer works on the construction of the complex plasma vessel of Wendelstein 7-X, a reactor in Greifswald, Germany. Credit: Stefan Sauer/dpa via Alamy

An engineer works on the construction of the complex plasma vessel of Wendelstein 7-X, a reactor in Greifswald, Germany. Credit: Stefan Sauer/dpa via Alamy

Stellarators have the advantage that their plasma is more easily confined, with no need (as in tokamaks) to drive strong electric currents through it to keep a lid on instabilities, says fusion physicist Josefina Proll at Eindhoven University of Technology in the Netherlands. But it's not clear whether it will be possible to implement stellarator technology in a reactor in 20–30 years. “It seems not all that likely at this moment,” she says. “We have a lot of basic questions still to answer,” says Klinger. “This is a first-of-a-kind machine, so one must be patient and go step by step.” Private companies set shorter-term goals because they have to satisfy their stakeholders, he says — but that doesn't mean they can deliver.

Alternative designs

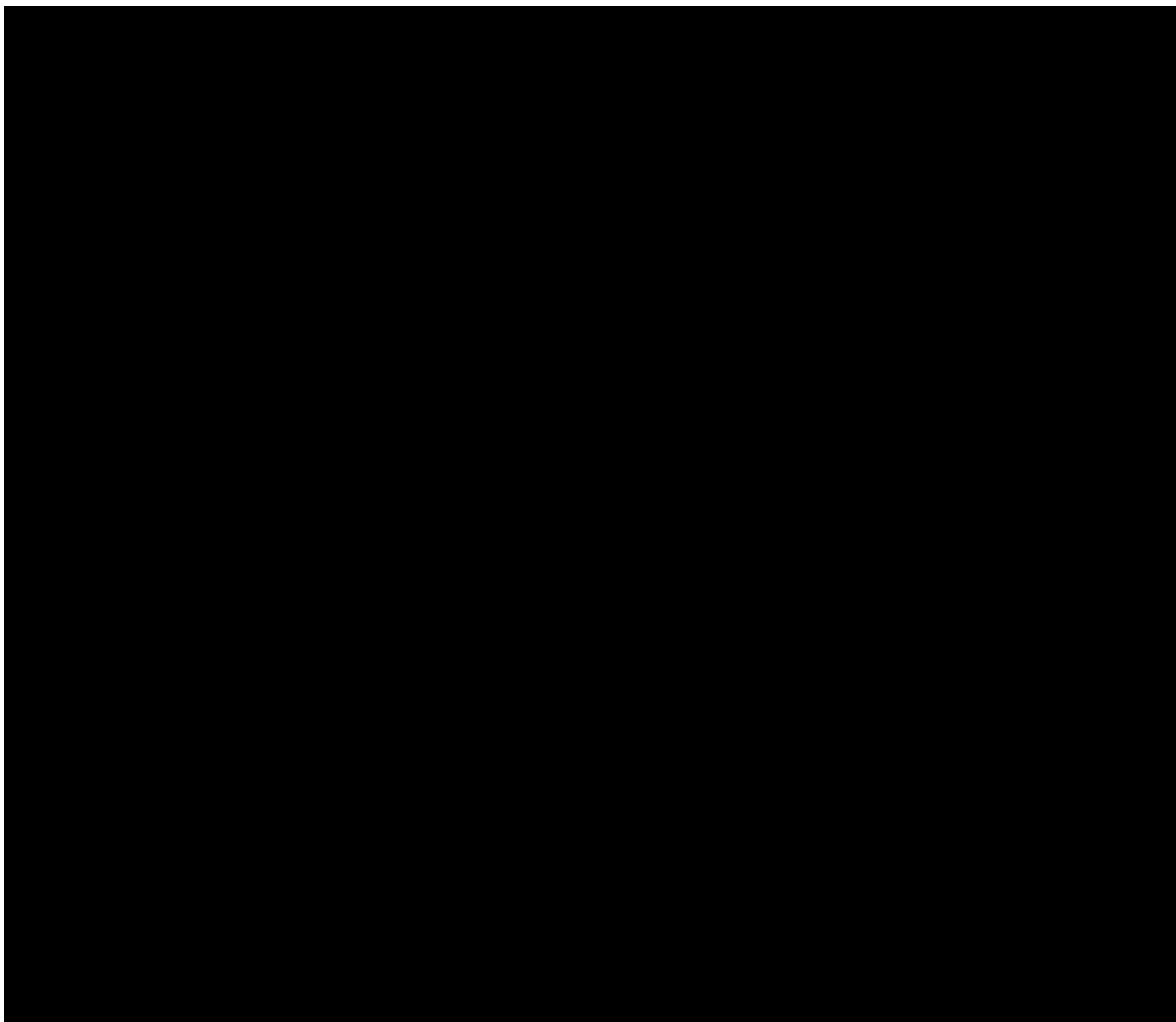
Some private fusion companies are sticking with the tokamak design, but scaled down. At Tokamak Energy, a team of around 165 employees is working on a spherical tokamak, shaped like an apple with its core removed. At 3.5 metres across, it will be many times smaller than the ITER tokamak, which, with surrounding cooling equipment, will be almost 30 metres wide and tall. Some state-funded schemes are considering the compact spherical design, too: the UKAEA, for example, has launched a project called STEP (Spherical Tokamak for Energy Production) that aims to create such

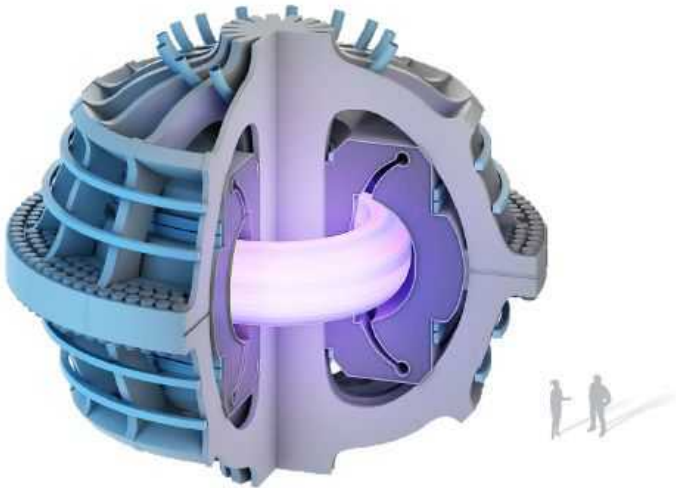
a device in a prototype plant that would deliver at least 100 MW to the national grid by 2040. The UKAEA has shortlisted five sites to host the plant, and expects the final choice to be made next year.

Hydrogen plasma in Tokamak Energy's ST40 spherical tokamak. This video has no sound.
Credit: Tokamak Energy Ltd

Hydrogen plasma in Tokamak Energy's ST40 spherical tokamak. This video has no sound.
Credit: Tokamak Energy Ltd

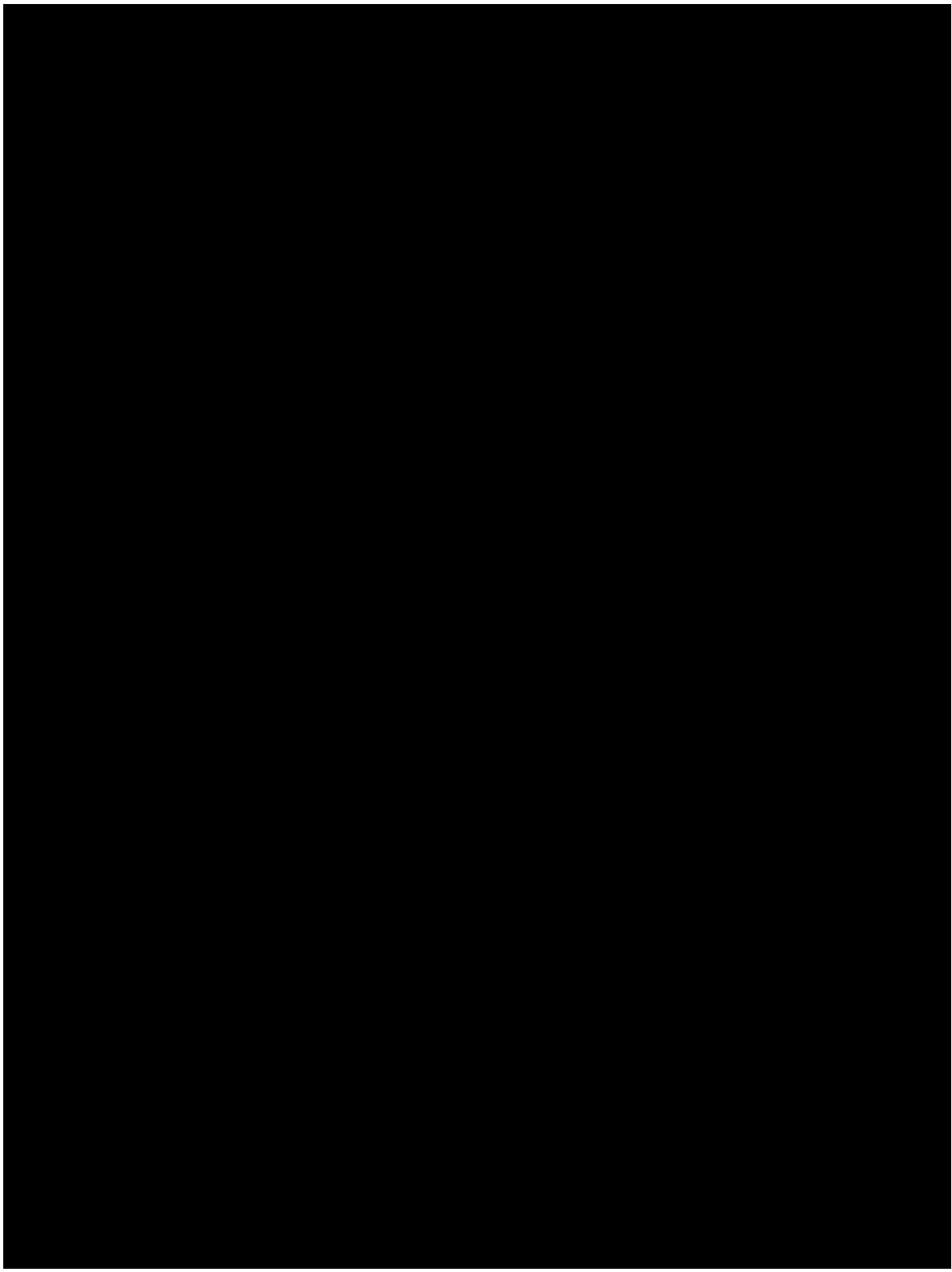
Key to these designs are new kinds of magnets made from ribbons of high-temperature superconducting materials, which should produce much stronger fields than the conventional superconducting magnets used by ITER. They are “a potential game-changer”, says Klinger — not just because of their higher fields, but also because conventional superconductors need liquid-helium cooling. That is an engineering nightmare: liquid helium’s viscosity is almost zero, allowing it to leak through any tiny cracks. High-temperature superconductors, by contrast, can be cooled with liquid nitrogen, which is abundant, cheap and easy to store.





Both Tokamak Energy (in collaboration with CERN, Europe’s particle-physics laboratory near Geneva, Switzerland) and CFS are banking on these new magnets. In August, CFS announced that it had made them in the form needed for its tokamaks — “on schedule and on budget”, Mumgaard says proudly.

In 2018, CFS was spun off from the Plasma Science and Fusion Center of the Massachusetts Institute of Technology (MIT) in Cambridge, and Klinger considers the firm “the most promising, most valuable and most thought-through private fusion initiative”. MIT and CFS together are preparing to build what Mumgaard calls “the first fusion machine that makes net energy” — producing more energy than goes into it. Named SPARC, it is being constructed in Devens, Massachusetts. Mumgaard says it will be running by the end of 2025, and will be “commercially relevant” because it will generate around 100 MW of power.





Researchers working on a magnet for the CFS/MIT ‘SPARC’ reactor. Credit: Gretchen Ertl, CFS/MIT-PSFC, 2021

Researchers working on a magnet for the CFS/MIT ‘SPARC’ reactor. Credit: Gretchen Ertl, CFS/MIT-PSFC, 2021

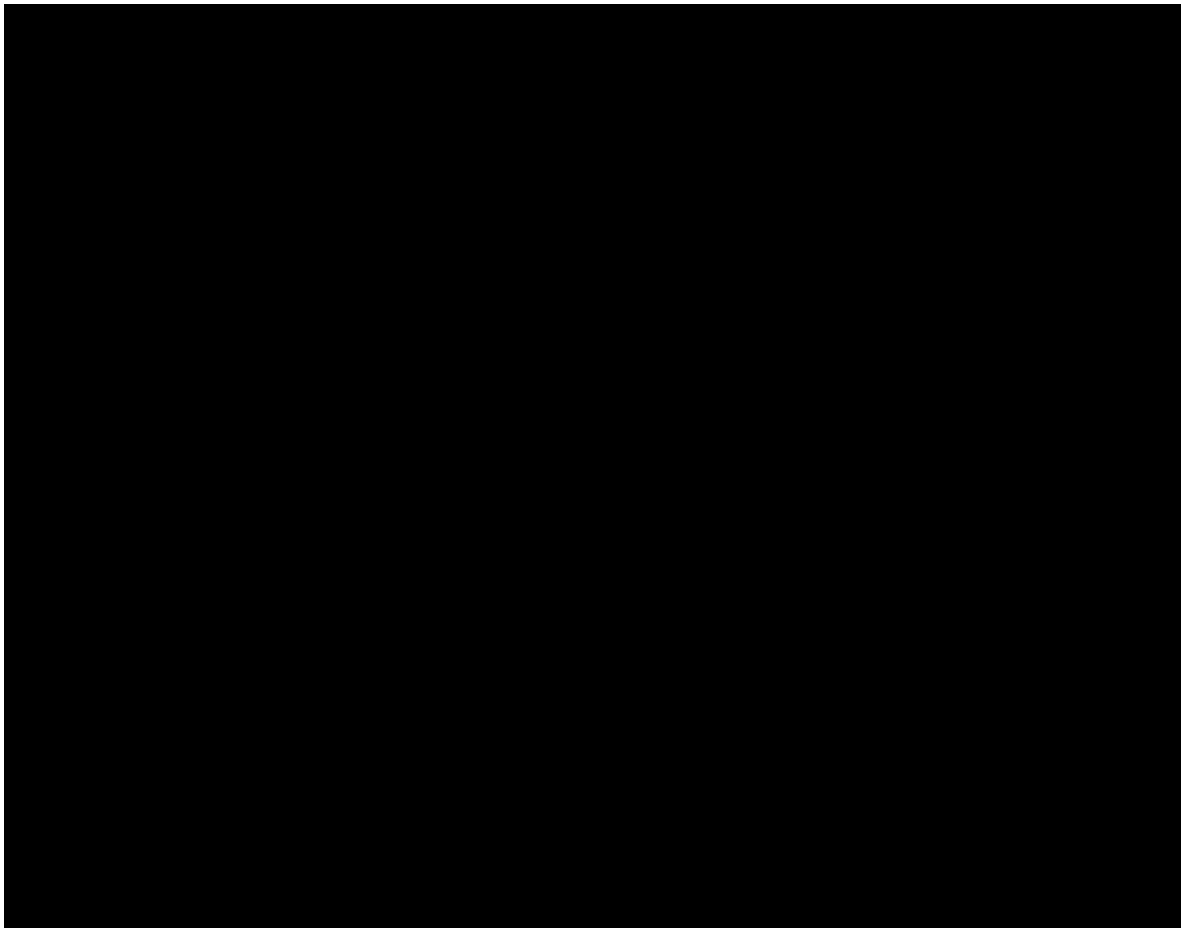
First Light Fusion, a company spun off from the University of Oxford, UK, in 2011, is pursuing a different strategy, called inertial confinement. Here, the fusion plasma isn’t held by magnetic fields: rather, a shock wave compresses it to the immense densities needed for fusion, and the plasma retains its shape just for a split second by inertia alone, before spreading out and dissipating its energy. The idea has been around since the 1950s, and is also being studied at the US National Ignition Facility (NIF) at Lawrence Livermore National Laboratory in California, where pea-sized plastic capsules of D-T fuel are imploded by nanosecond pulses of laser light to ignite fusion. In August, [NIF reported a laser shot that produced a fleeting energy output 8 times higher than it had ever before achieved](#) — and amounted to 70% of the energy that had gone into the reaction. That has raised hopes of net gain from inertial-confinement laser fusion, although such an energy-intensive process might be more useful for fundamental research than for large-scale power generation.

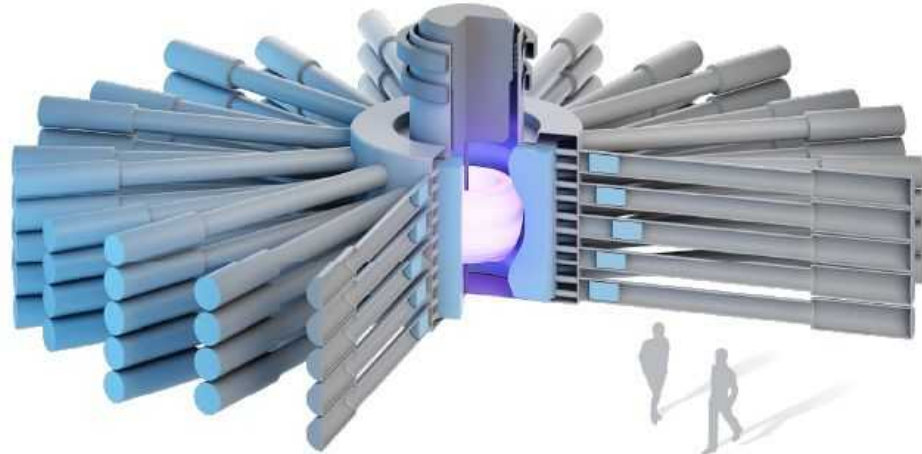
At First Light, the compression shock wave is created not by energy-hungry lasers, but by using an electromagnetic projectile gun to fire a small piece of material into a target containing the hydrogen isotopes. The company is keeping details of the process secret, but has said that to achieve fusion, it will need to fire the material at 50 kilometres per second — twice as fast as is typically achieved in current shock-wave experiments.

GF is taking yet another approach, called magnetized target fusion. It involves the plasma being compressed more slowly — for instance, using pistons — but with the aid of magnetic confinement

that prevents heat from dissipating as the plasma is squeezed. This idea, suggested in the early 1970s by researchers at the US Naval Research Laboratory in Washington DC, seeks an optimal compromise between the energy-intensive high magnetic fields needed to confine a tokamak plasma, and the energy-intensive shock waves, lasers or other methods used to rapidly compress plasma in inertial-confinement designs.

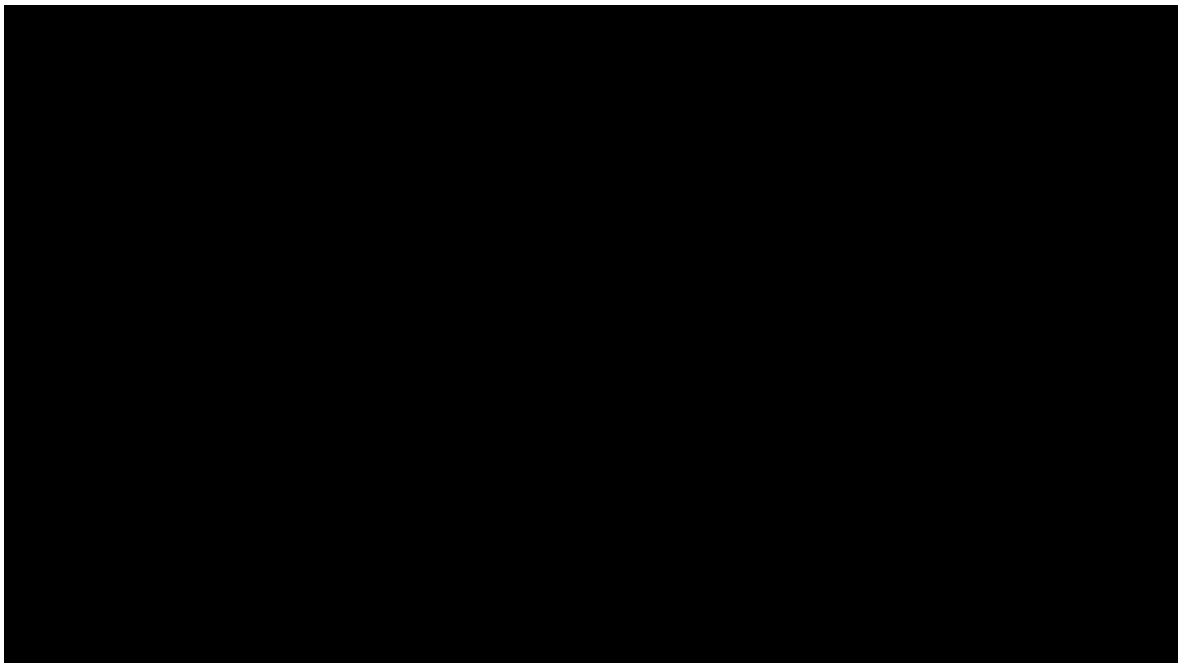
GF's design for its Culham reactor uses a centrifuge to spin a chamber filled with molten lead and lithium. That motion opens a cavity in the liquid metal, where the plasma sits. A piston system pumps more liquid metal into the chamber, compressing the plasma over a few tens of milliseconds. Fusion begins; then the pressure is released and the process repeated in pulses, about once a second.

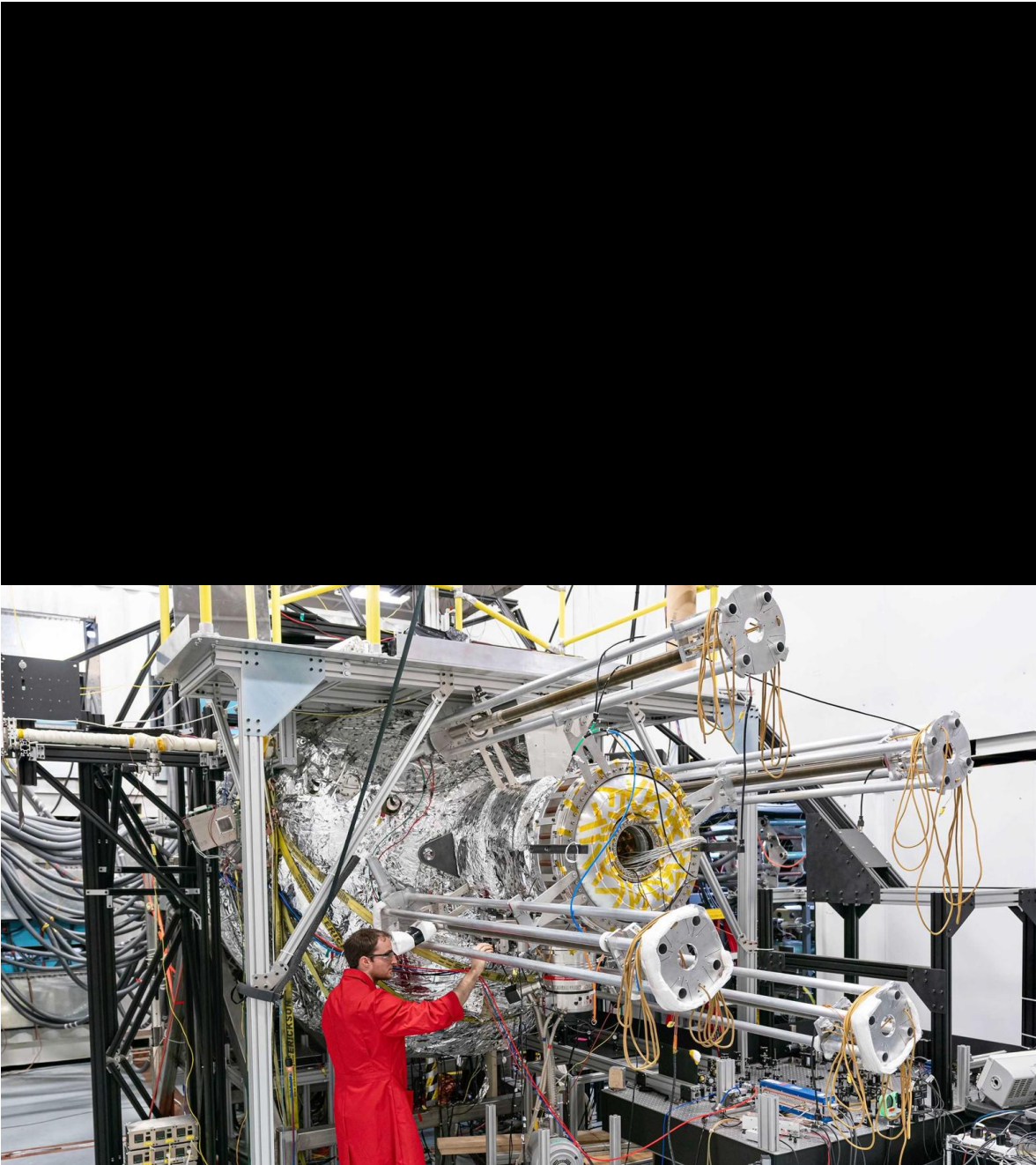




One especially neat aspect of this reactor is how it generates tritium fuel — a hugely expensive resource that can be made only in nuclear reactions, and decays rapidly. In ITER and other designs, tritium will be produced when neutrons escaping the reactor hit a lithium blanket lining the tokamak. In GF's design, tritium is made when neutrons hit lithium within the liquid-metal compression system itself.

GF has cracked key challenges only in the past few years — making a plasma target that lasts for long enough to be compressed, and smoothly and rapidly collapsing the liquid-metal cavity. The firm says, however, that after it has its UK demonstration plant operating in 2025, it will “power homes, businesses and industry with clean, reliable and affordable fusion energy by the early 2030s”.





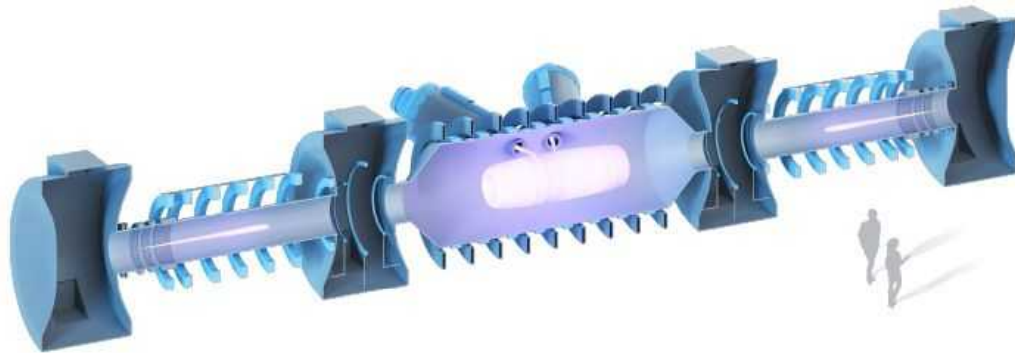
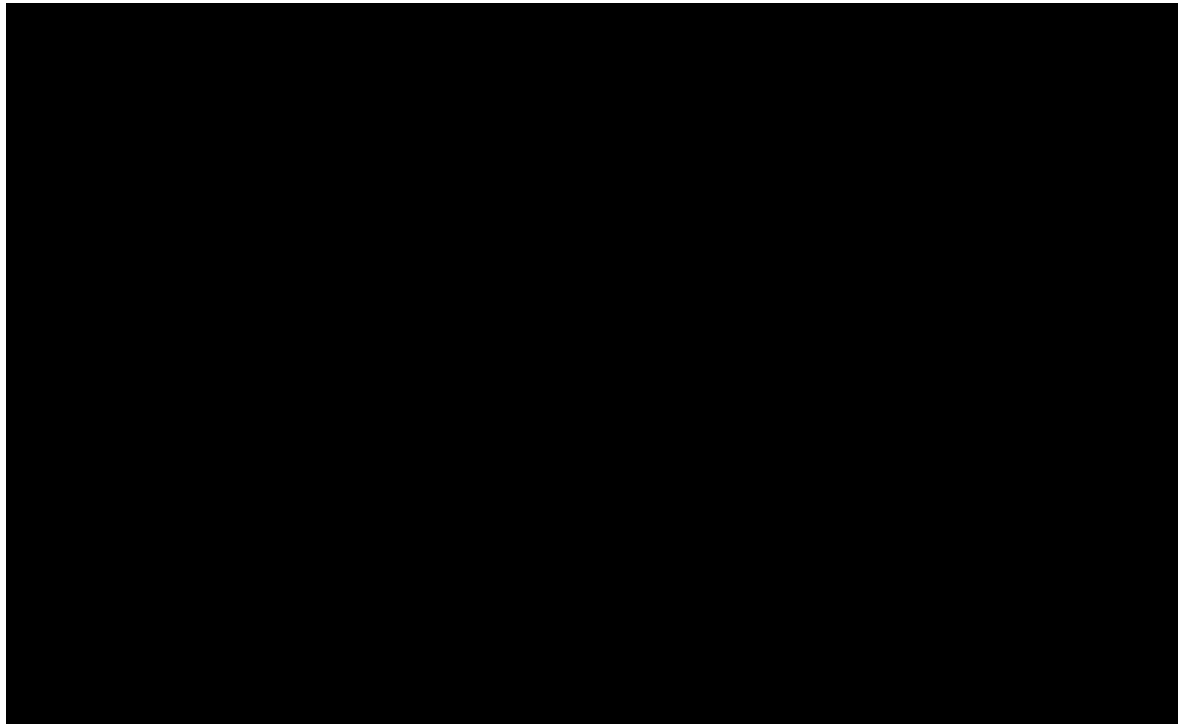
A General Fusion technician works on the plasma-injector system for one of the company's reactors.
Credit: General Fusion

A General Fusion technician works on the plasma-injector system for one of the company's reactors.
Credit: General Fusion

TAE Technologies has, in some ways, an even more audacious concept. It plans to abandon D-T fuel altogether, instead fusing boron-11 atoms with hydrogen-1 nuclei (protons). This idea, championed by TAE's co-founder, the Canadian plasma physicist Norman Rostoker, and dubbed p-¹¹B fusion, requires temperatures ten times greater than for D-T fusion: about one billion kelvin. The advantage

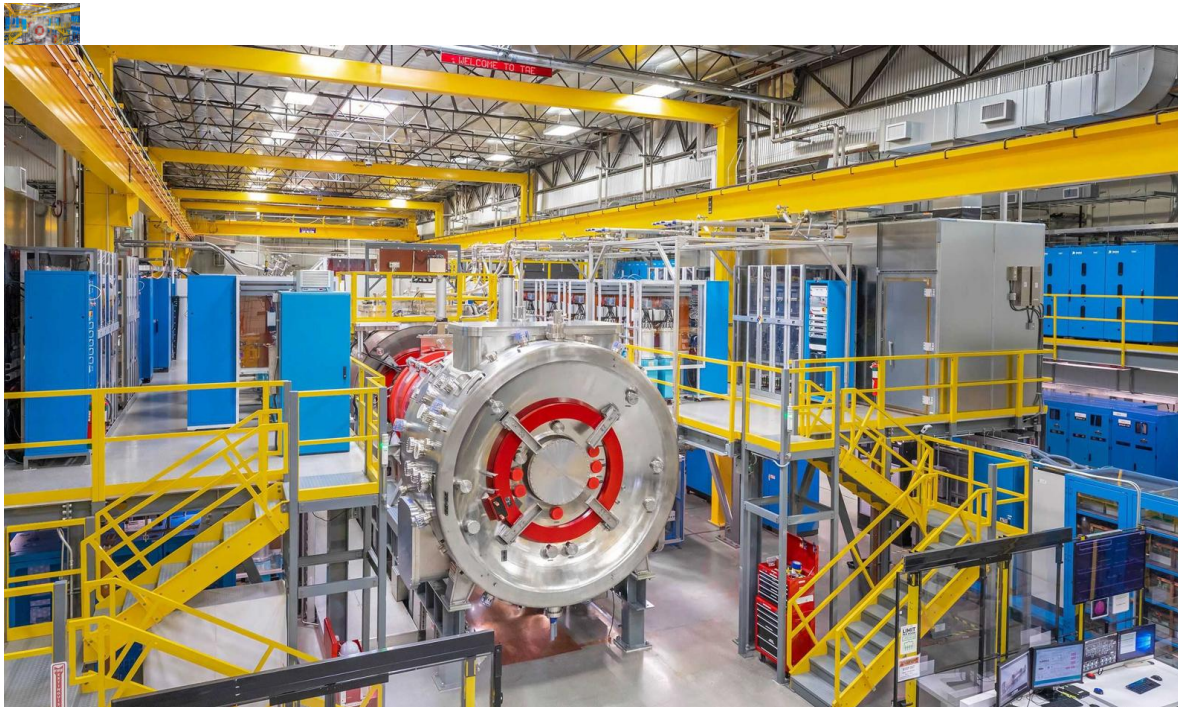
is that this reaction uses only abundantly available fuel, and generates no neutrons that could contaminate the reactor. Binderbauer says that the concept offers lowers maintenance costs and a much more sustainable end goal.

In TAE reactors, the plasma is confined inside a cylindrical magnetic field made by a solenoid — a design that draws on particle-accelerator technologies. The plasma rotates around the axis; that rotation, as in a spinning top, generates inherent stability. Confinement doesn't require strong external magnetic fields; those are mostly generated by the spinning plasma itself. To keep it rotating, tangential beams of boron inject angular momentum, rather as a top is torqued by a whip.



The company has made prototypes to demonstrate this set-up; since 2017, it has been working with a test system called Norman, and it is now starting work on a device called Copernicus that will run with normal hydrogen (or other non-fusing) plasmas to avoid producing neutrons. Computer simulations will show what energy would be generated if real fusion fuel were used. If TAE achieves the conditions needed for D-T fusion — which it hopes to do by around the middle of this decade — the company plans to license the technology to others who are pursuing those fuels. Binderbauer calls Copernicus a “stepping stone” to the temperatures needed for p-¹¹B fusion. “We’re convinced

that we can go to the billion-degree level,” he says — and he hopes to see this towards the end of the decade.



TAE’s ‘Norman’ test reactor. Credit: TAE Technologies

TAE’s ‘Norman’ test reactor. Credit: TAE Technologies

Among the many other private fusion firms, Helion Energy, in Everett, Washington, has attracted the most interest from investors: this month, it announced a \$500-million funding round, bringing its total to \$578 million. Its aim is to generate electricity directly from fusion, rather than using the process to heat fluids and drive turbines. Helion’s technique involves firing pulses of plasma together inside a linear reactor, then rapidly compressing the merged plasma with magnetic fields. When fusion occurs, the plasma expands and its magnetic field interacts with that surrounding the reactor to induce an electric current. Helion hopes to fuse a mixture of deuterium and helium-3, which would not produce neutrons as a by-product. But helium-3 itself would need to be produced by D–D fusion. The company is building a demonstration reactor called Polaris, which it aims to have in operation by 2024.

How Helion’s technology will generate electricity. This video has no sound. Credit: Helion Energy

How Helion’s technology will generate electricity. This video has no sound. Credit: Helion Energy

Cheaper reactors?

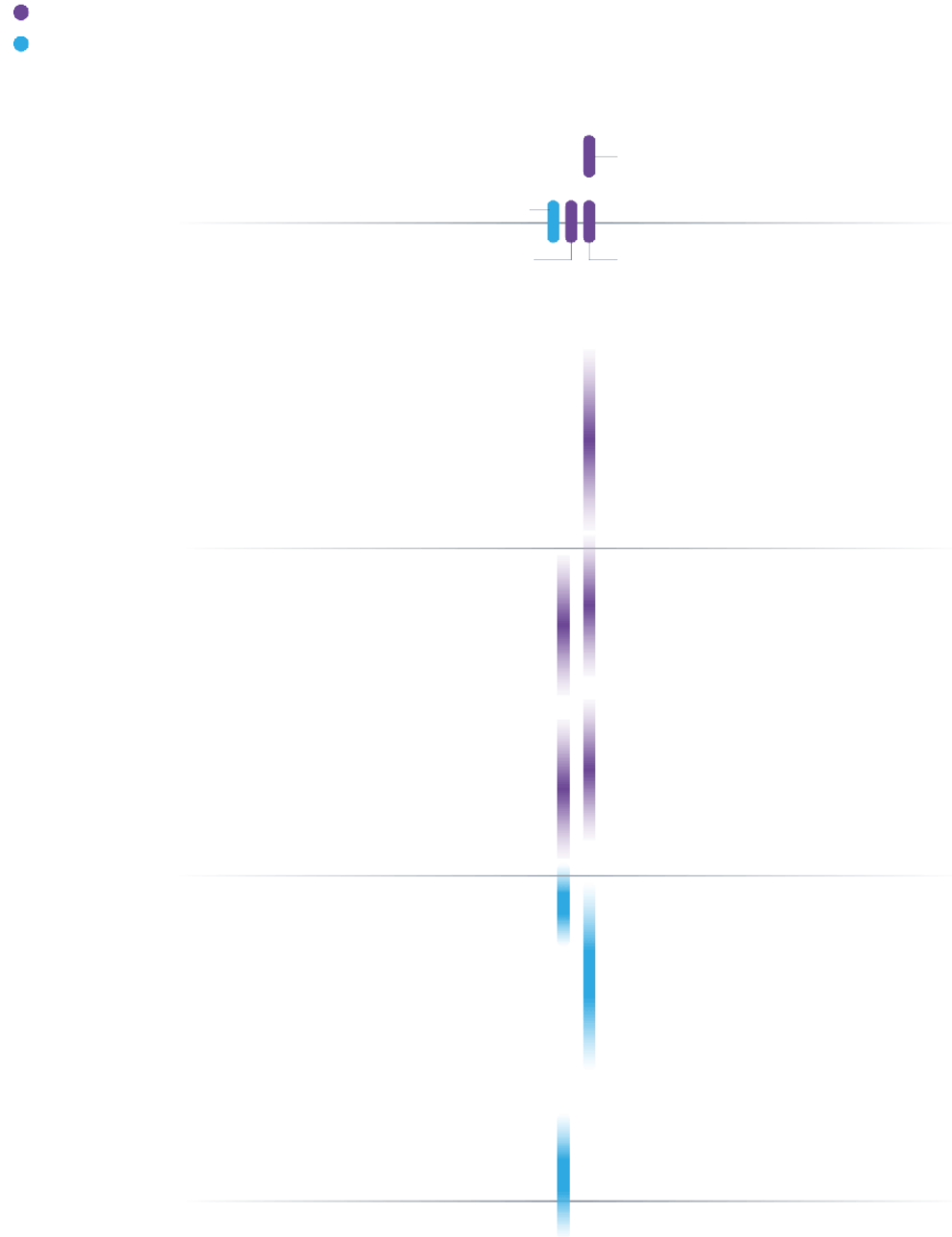
The reactors built by private companies, being smaller than ITER-scale projects, will be much more affordable. Tokamak Energy’s co-founder, David Kingham, envisages billion-dollar devices, and Binderbauer thinks TAE’s systems could be built for around \$250 million.

The aim is to make small fusion reactors that are compatible with existing energy grids. Kelsall says they could also serve industries that are particularly energy-intensive, such as metal smelting — a sector that can't be supplied by renewables. Mowry adds that shipping could be another important market: devices producing around 100 MW of power are “just the right size for a large container ship”.

Donné remains cautious about the prospects, however, saying that private companies “are working on aggressive time paths compared to publicly funded projects, but also have a much higher risk of potential failure”. All the same, TAE, for one, insists that it is still on the track that it promised in the mid-2010s, of having a fusion device ready for commercialization by around the end of this decade (see ‘Future promises’).

FUTURE PROMISES

Private firms are making bold promises about delivering commercial fusion reactors in the 2030s.



Private

State sponsored

Helion: Net electricity (small amounts) from Polaris reactor.

Giant international effort

ITER: test runs.

5

Commonwealth Fusion Systems (CFS):

First fusion machine expected to
generate more energy than it uses.

General Fusion: operate UK
demonstration plant.

TAE Technologies: reactors ‘ready for
commercialization’ by late 2020s.

0

CFS: aims to have 200 megawatt plant
supplying electricity grid in early 2030s.

General Fusion: targets reactors for
sale in early 2030s.

First Light Fusion: anticipates its first
power plant in 2030s.

Tokamak Energy: fusion power
plant (pilot) in 2030s.

5

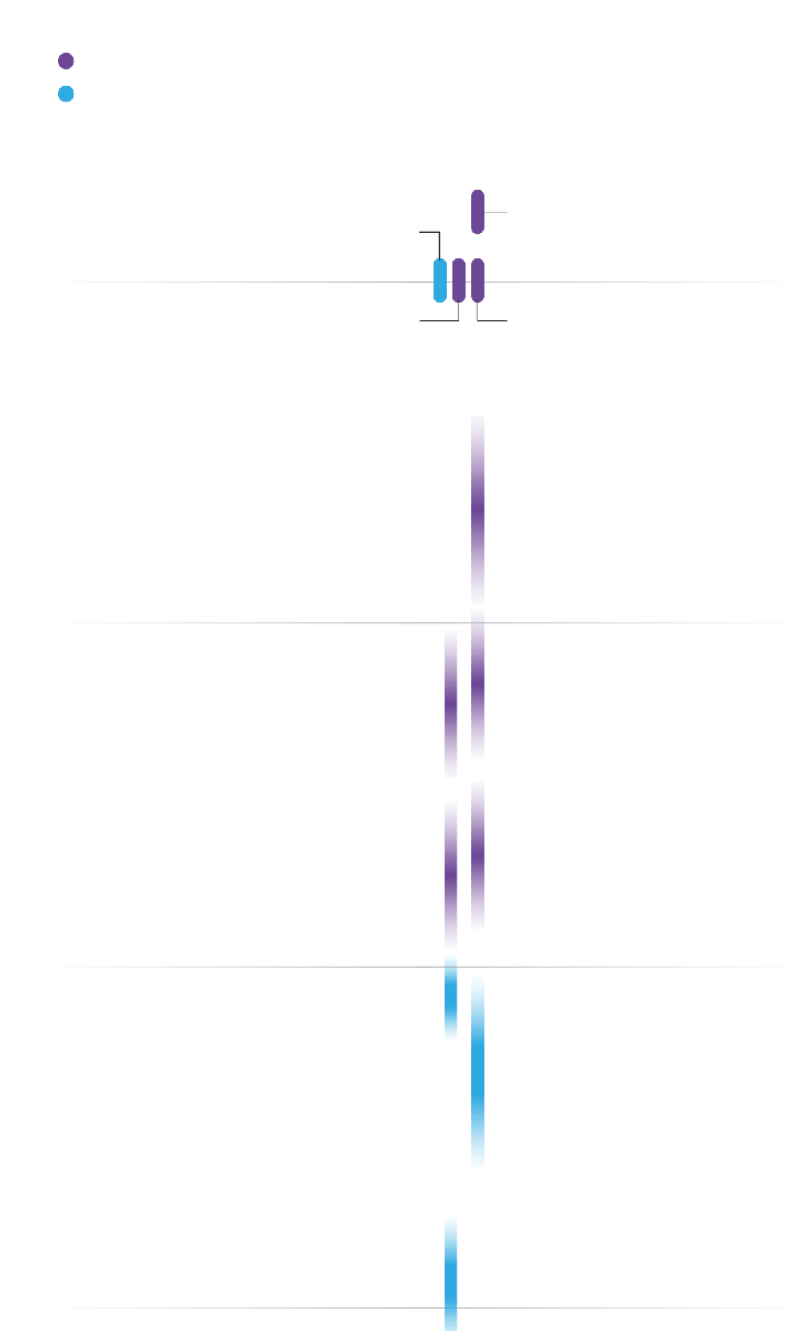
ITER: to run fusion with
deuterium–tritium fuel.

China Fusion Engineering Test
Reactor might complete
construction

in 2030s.

UK Atomic Energy Authority hopes STEP
fusion power plant can supply energy to
national grid.

0



Private

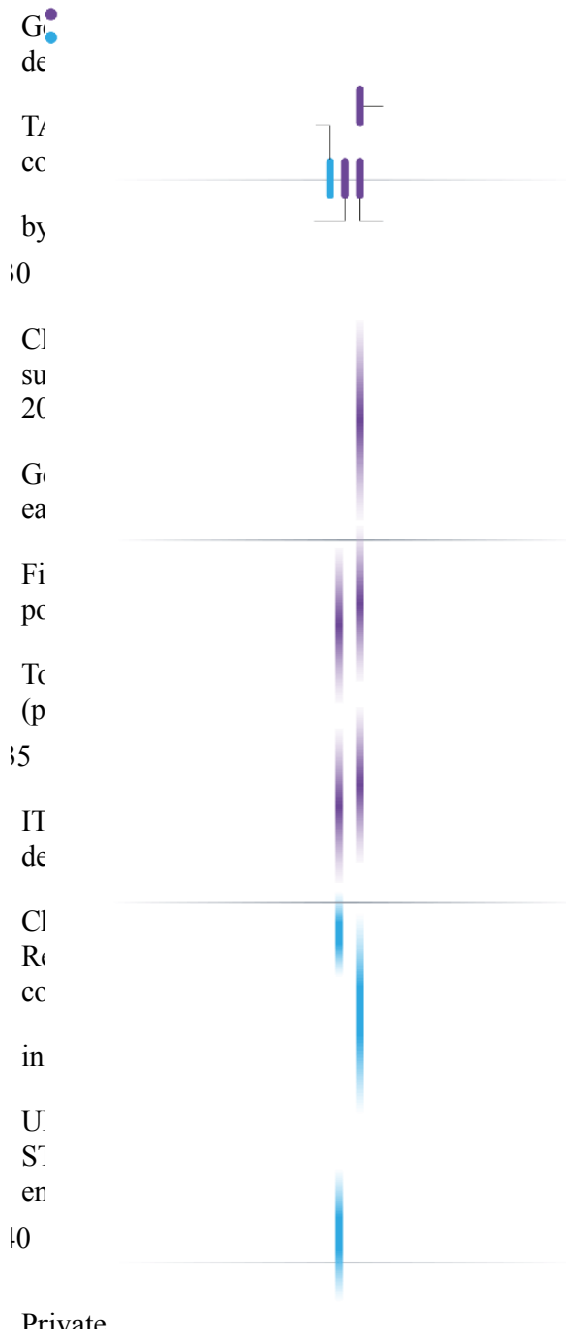
State sponsored
Helion: Net electricity

(small amounts)

from Polaris reactor.
Giant international

effort ITER: test runs.

Commonwealth Fusion Systems
(CFS): First fusion machine expected
to generate more energy than it uses.



test runs.
Helion Net

electricity (small
amounts) from

Polaris reactor.
Commonwealth
25
Fusion Systems

(CFS): First
fusion

machine expected
to generate more

energy than it
uses.

General Fusion:

Despite his scepticism, Donné adds: “I see the booming of private fusion companies as a good sign. There can be mutual benefits in keeping close ties between public and private fusion projects.”

That’s certainly happening. Not only is the private fusion industry building on years of state demonstration investment in projects such as ITER, but it is benefiting from governments that see value in supporting it — which is why the UK government and the US Department of Energy are also investing in firms such as Tokamak Energy, CFS and GF. Mowry thinks that such public-private partnerships are the way forward — as they were for COVID-19 vaccines. And, as with the reactors ready for vaccines, fusion will be needed everywhere, especially as energy use rises in lower-income countries commercialization

The vaccines showed “what you can do if you have the resources”, says Windridge. “If we had that kind of commitment in energy, I think it would be incredible to see what can be achieved.” As with the vaccines, too, society desperately needs more clean, carbon-free sources of energy. “This is an existential challenge,” says Mowry. “Fusion is the vaccine for climate change.”

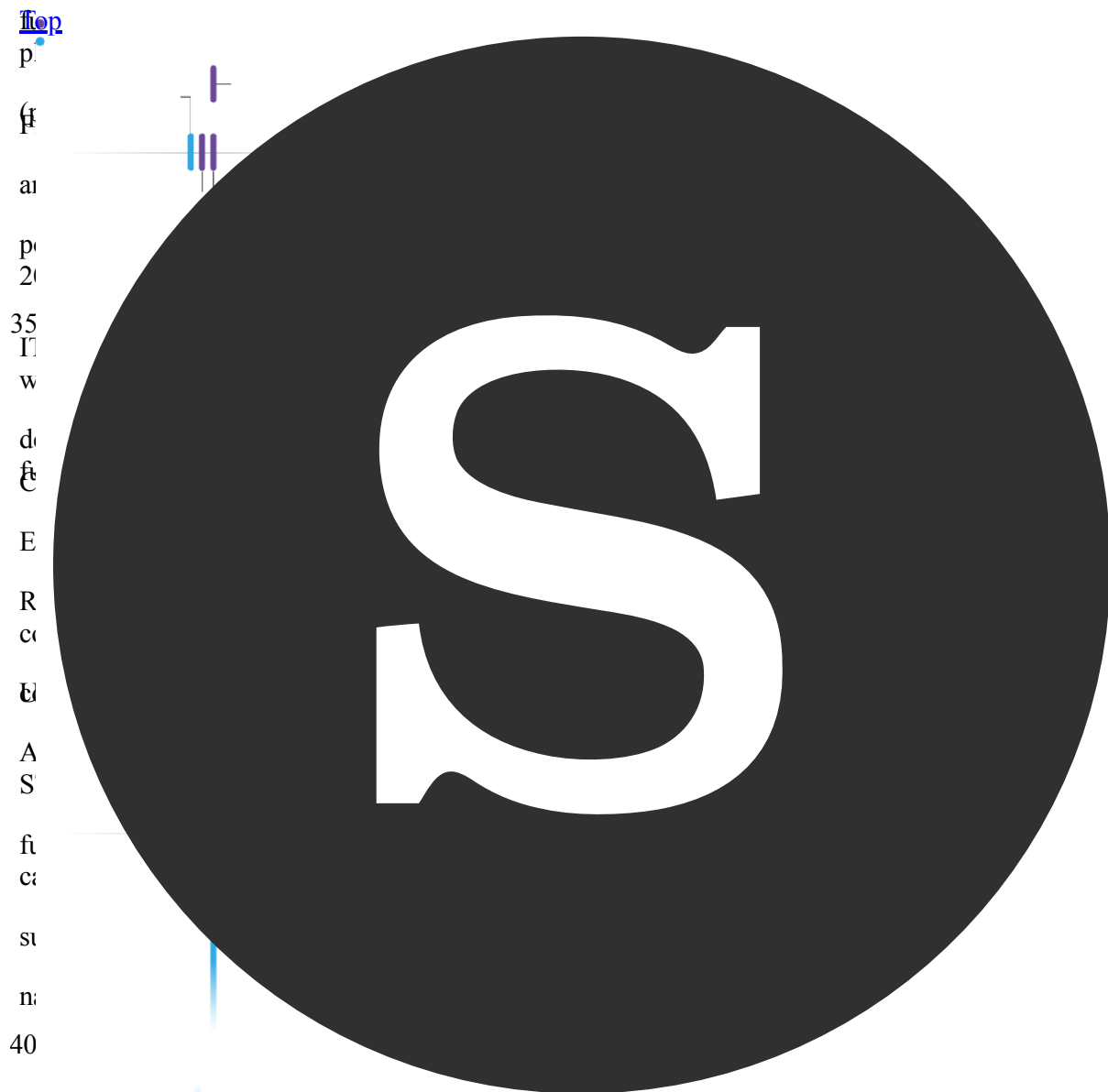
Philip Ball is a science writer in London.
plant

SPRINGER NATURE
Supplying
Springer Nature
electricity

grid in early 2030s.
General [Privacy Policy](#)
[Use of Cookies](#)

- [Legal notice](#)
- target [Terms & Conditions](#)
- [Accessibility statement](#)

sale in early
2030s Springer Nature Limited. All rights reserved.
Tokamak Energy:



[Built with Shorthand](#)

This article was downloaded by **calibre** from <https://www.nature.com/articles/d41586-021-03401-w>

Private

| [Section menu](#) | [Main menu](#) |

State
sponsored
Helion: Net

electricity
(small
amounts) from

Books & Arts

- **[Friction: from fingerprints to climate change](#)** [15 November 2021]

Book Review • An enthusiastic exploration of how surfaces interact both intrigues and frustrates.

- BOOK REVIEW
- 15 November 2021

Friction: from fingerprints to climate change

An enthusiastic exploration of how surfaces interact both intrigues and frustrates.

- [Anna Novitzky](#) ⁰



A water droplet on the hairs of a *Salvinia* fern.Credit: Frank Fox/SPL

Sticky: The Secret Science of Surfaces *Laurie Winkless* Bloomsbury Sigma (2021)

What links geckos' feet, plate tectonics, the winter sport curling and spacecraft re-entering the atmosphere? For physicist and science writer Laurie Winkless, the answer is: friction. Her eclectic, sometimes erratic, book *Sticky* touches on all these and much more as she investigates a force whose effects are felt in every moment of our lives, but which stubbornly resists attempts at theoretical explanation.

The study of friction is big business. Billions of dollars — and billions of tonnes of carbon emissions — could be saved if researchers and engineers could make cargo ships cut through the water more easily, or minimize car tyres' rolling resistance, rendering them more fuel-efficient. Yet the research, as Winkless presents it, is largely a business of trial and error. The effects that make things go faster, slow down, lodge in place or move smoothly arise from dozens of — often literal — moving parts, from the macroscopic scale to the atomic. As a result, it's a nightmare to isolate any single effect, let alone measure it. There's currently no way to predict from first principles a system's coefficient of friction — a measure of how much force is needed to slide one surface over another.



[From spoons to semiconductors — we are what we make](#)

This leads to some charmingly cobbled-together experiments as scientists attempt to approximate real-world conditions as closely as possible — with greater or lesser degrees of success. In one test to explore the drag-reducing properties of swimwear inspired by shark's skin, the swimmer must push against force-measuring paddles while doing the front crawl — with their legs tied together. In another, to investigate the aerodynamic properties of a golf ball, the projectile is placed in a glass-fronted wind tunnel and smoke is blown over it.

The seat-of-the-pants feel also applies to the book, as the chapters bounce from subject to subject. Earthquakes in New Zealand caused by strike-slip faults! How the different patterns of stitching on a baseball and a cricket ball affect their spin! Why humans have fingerprints! How pouring water onto sand might have helped the ancient Egyptians to move colossal blocks of stone! Winkless frequently drops an interesting titbit but fails to expand on it, which sent me down rabbit holes of Internet research (are the spikes on sharks' skin really made of the same materials as teeth? Apparently so, thanks to some nifty quirks of evolution). She encourages this independent investigation, supplying numerous suggestions for things to Google and online videos to watch, but the breathlessness makes it unsatisfying.

Sticky is most engaging when Winkless unpacks biomimetics. In this branch of materials science and design, researchers try to understand and replicate effects seen in nature. In discussing how geckos cling to sheer surfaces without the use of adhesives, she digs down layer by layer, from the ridges on the lizards' feet to the microscopic hairs that cover them, the nanostructures at the ends of the hairs and the atomic-level forces that act between those structures and the molecules of the surface. Similarly fractal explorations uncover how the leaves of the *Salvinia* fern stay dry even after weeks submerged in water. Tiny whisk-shaped hairs repel water, but the non-waxy tips of each hair attract it. “These minute hydrophilic patches actively pinned water in place, trapping air underneath,” she writes.



A journey through wine, spit and oil

The consequences of these mind-boggling intricacies could be transformative. Work on how the receptors in human fingertips register the texture of surfaces could lead to refreshable Braille displays for blind and partially sighted computer users. And a boat coated with paint that copies the fern’s “balance between hydrophobic repulsion and hydrophilic attraction”, Winkless relates, could travel the seas without ever getting wet or, importantly, being subject to the water’s drag. That could be hugely valuable in cutting emissions.

This and other snatches of topics that need much more funding provide the best hint of an overarching narrative. Each year, we learn, more than one-fifth of total global energy consumption goes on overcoming friction in its various forms. In the transport sector alone, 30% of energy is expended to fight friction — for example, to maintain the momentum of tyres against forces exerted by the road surface. Winkless discusses many areas of research that could tackle carbon emissions, but, she points out, “as with lots of conversations around climate change, the stumbling block might be ownership, rather than a lack of technical solutions”.

By operating globally, polluting industries such as shipping and ground transport transcend national regulation, and, paradoxically, the bigger the problem, the easier it seems to be to ignore. “If no country is held

responsible for emissions,” Winkless quotes from a 2018 report (see go.nature.com/3eybjk4), “no government will try to reduce them.” And if companies aren’t forced to act through regulations, none will spend the money to find solutions to the stickiest problem of them all.

In this way, scraps of story allude to an important picture, like the dozens of types of drag that contribute to a system’s coefficient of friction.

Nature **599**, 367 (2021)

doi: <https://doi.org/10.1038/d41586-021-03436-z>

This article was downloaded by **calibre** from <https://www.nature.com/articles/d41586-021-03436-z>

| [Section menu](#) | [Main menu](#) |

Opinion

- **Europe's Roma people are vulnerable to poor practice in genetics** [17 November 2021]
Comment • Analysis of how papers and databases are handled and interpreted shows that geneticists in Europe must stamp out unethical research practices at home, not just abroad.
- **Presidents of Royal Society live long lives** [16 November 2021]
Correspondence •
- **Link knowledge and action networks to tackle disasters** [16 November 2021]
Correspondence •
- **Funders need to credit open science** [16 November 2021]
Correspondence •
- **Reflections on a pioneer in electrical engineering** [16 November 2021]
Correspondence •

- COMMENT
- 17 November 2021

Europe's Roma people are vulnerable to poor practice in genetics

Analysis of how papers and databases are handled and interpreted shows that geneticists in Europe must stamp out unethical research practices at home, not just abroad.

- [Veronika Liphardt](#)⁰,
- [Mihai Surdu](#)¹,
- [Nils Ellebrecht](#)²,
- [Peter Pfaffelhuber](#)³,
- [Matthias Wienroth](#)⁴ &
- [Gudrun A. Rappold](#)⁵



A Roma woman on her balcony in an apartment building in Kosice, Slovakia. Credit: Sean Gallup/Getty

In the past few years, several media and scientific reports have raised awareness about unethical uses of DNA databases. Perhaps the most alarming is the [Chinese government's use of DNA to monitor the Uyghur minority ethnic population](#), which is predominantly Muslim, in Xinjiang province.

Yet problems with DNA databases are more widespread and entrenched than many geneticists either realize or want to acknowledge.

For many samples, either there is no record of consent being obtained from individuals whose DNA was collected, or the procedures used to obtain consent were inadequate. This applies to numerous studies involving Indigenous communities, including Australia's Aboriginal and Torres Strait Islander people, Native American communities in the United States and the

San people in southern Africa¹. Moreover, people often have little or no say in how their DNA will be used, and rarely benefit from the studies¹.

Now, our analysis of several hundred publications and five databases points to multiple issues with the handling and interpretation of DNA data from Roma people. The [Roma are the largest minority group in Europe](#).

In our view, research and peer-review practices must change across a broad array of disciplines, from forensic genetics to molecular anthropology. Failure to correct past and ongoing mistakes puts more people at risk of harm from the collection of DNA. It also threatens the reputation of human genetics — and of science in general.

The Roma in Europe

Around 10 million to 12 million Roma people currently live in Europe. The term Roma was introduced in the 1980s to replace labels such as ‘Gypsy’ or ‘Zigeuner’ (used in Germany) — words perceived in many European countries to be extremely insulting. Here, we use ‘Roma people’ to describe individuals who self-define as Roma or who are referred to as Roma by the European Union and European nation states. Yet we acknowledge that the term is problematic and can have reifying effects².



Forensic database challenged over ethics of DNA holdings

The same holds for the history and ethnicity ascribed to this group. Many scientists claim that the ancestors of Europe's Roma originated in India, and that Roma people have largely remained genetically isolated for the past 300–600 years^{3–5}. Many Roma people, however, do not see themselves as having a separate ethnicity from Europeans, and today their ancestry, cultural practices and history are extremely diverse⁶.

We chose to focus on genetic studies of Roma people because they have suffered from social discrimination for hundreds of years. Between 1935 and 1945, hundreds of thousands of Roma people were deported, sent into forced labour or killed⁷. Today, in many countries of the European Union, particularly Bulgaria and Slovakia, many Roma people live in segregated settlements. They have lower incomes and less access to quality education, housing, food and health care than does the rest of the population⁸. In 2016, one in three Roma people across nine EU member states lived without drinking water, and one in ten lived without electricity⁹.

DNA has been collected from thousands of Roma people across Europe, mainly since the 1990s. (The collection of blood samples from which DNA could in principle be extracted goes back to the 1970s.)



Children play outside in an Inuit and Cree community in eastern Canada. Credit: Iva Zimova/Panos

Over the past 5 years, we have assessed more than 450 papers, published between 1921 and 2021. Roughly two-thirds of these publications appeared in the past three decades. We have also checked DNA data from Roma people in five public databases. These are the Y-STR Haplotype Reference Database (YHRD; a Y-STR, or short tandem repeat, is a repeated nucleotide sequence on the Y chromosome), the Allele Frequency Net Database (AFND), the Allele Frequency Database (ALFRED), the Estonian Biocentre Human Genome Diversity Panel (EGDP) and the European DNA Profiling Group's Mitochondrial DNA Population Database (EMPOP). In the case of EMPOP, users must register before they can access the data, but they are required to provide only an e-mail address, name and affiliation. YHRD and EMPOP are also accessed by (but not owned by) law-enforcement agencies.

Our aim was to better understand how geneticists, medical researchers and molecular anthropologists, among others, have obtained this DNA. We also

wanted to interrogate how researchers have conducted and interpreted their analyses. As part of our analysis, we interviewed and e-mailed 10 researchers, 3 ethics committees and 13 research and funding institutions and journal editors about their methods and policies. Throughout our study, we sought guidance from Anja Reuss, a political adviser at and spokesperson for the Central Council of German Sinti and Roma, an advocacy group based in Heidelberg.

Consent and labels

In many cases, especially in the late twentieth century, samples have been collected from people (including prisoners) without adequate consent or any record of consent, then shared across research groups or deposited in public databases. In others, participants seem to have given some kind of consent, but it is unclear whether they understood exactly what their DNA would be used for. From two interviews with geneticists, we even learnt that, in some medical studies, various incentives were offered to Roma people — a practice considered unacceptable by most human geneticists. Participants, who in some cases gave only their spoken consent, were told that their data would reveal whether they were carriers of genetic diseases — but not that their genetic information would end up in public databases (such as EMPOP and YHRD) that can also be accessed by law-enforcement agencies, which is what happened in some cases.



Genomics is failing on diversity

In other studies, Roma people were recruited by medical practitioners who gave individual data sets an ethnic label and then shared people's personal data with researchers. Such secondary usage violates the ethical norms set out in Article 31 of the United Nations Declaration on the Rights of Indigenous Peoples, as well as the research regulations and legislation of the European Union and several countries, including Switzerland, the United States and Canada.

In tens of publications on the genetics of Roma people, researchers use words such as 'Gypsies', 'inbred' or 'consanguineous', or refer to Roma people as a 'genetic high-risk group'. For Roma people, these are disrespectful and pejorative terms in themselves. Moreover, such broad extrapolation is stigmatizing for such a large population. Use of these terms has declined over the past ten years, but 'Gypsy' continues to be used in a few academic publications. One of the public databases we looked at removed this label only in 2020.

Even the methodological approaches used in many of these studies are questionable. Recruiting individuals from the most isolated communities or from the patient registers of medical geneticists runs the risk of biased sampling, which distorts scientific results. In fact, using various methods, researchers have frequently tried to avoid sampling people whom they consider to have 'non-Roma' and mixed ancestry¹⁰. Even today, some researchers remove individual data sets if an analysis indicates mixed ancestry. This might be appropriate for certain research questions concerning a specific community. But, often, such data are used to support claims made about all European Roma people.

Forensic genetics

Perhaps most problematic is the use of these data in forensic genetics research.

Only since 2010 have leading forensic genetics journals required publications to include evidence of appropriate procedures, such as the use

of written informed consent or approval from an ethics committee (see, for example, refs 11,12). Yet data collected even decades earlier continue to be widely used. Also, if the police or military forces have helped to collect them, the data might not be published in a journal at all — and so not be subject to editorial checks. A German law-enforcement institution, the Baden Württemberg State Office of Criminal Investigation in Stuttgart, for example, collected data from dozens of people from Afghanistan and Romania and uploaded them in 2017 to the YHRD public database [without indicating whether individuals had consented to their data being used in this way](#)¹³.

Roma people are over-represented in the databases accessed by law-enforcement agencies — both because of biases in criminal-justice systems and because geneticists have sought data from communities thought to be genetically isolated. In the ‘national database’ of Bulgaria held in the YHRD, for instance, 52.7% of data sets are categorized as ‘Romani’, 36.9% as ‘Bulgarian’ and 10.3% as ‘Turks’, even though Roma people make up only 4.9% of the Bulgarian population (see ‘A biased picture?’).

A BIASED PICTURE?

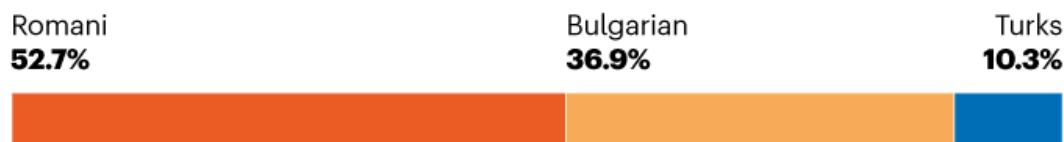
Roma people are over-represented in databases such as the YHRD*, which is accessed by law-enforcement agencies. Without thorough evaluation, the effects of this over-representation are unclear.

Bulgaria

Population (2011 census[†])



Samples in YHRD



Hungary

Population (2016 microcensus[‡])



Samples in YHRD



*YHRD, Y-STR Haplotype Reference Database. **All ethnic-group labels are those used by the YHRD and population censuses. YHRD data as of 11 November 2021. [†]Total is <100%: some respondents did not identify with an ethnic group. [‡]Total is >100%: respondents could select more than one ethnic category.

©nature

Sources: Natl Statistical Inst. of Bulgaria/YHRD/Hungarian Central Statistical Office

Some forensic geneticists argue that this over-representation might actually benefit members of minority populations. According to them, reducing the rarity of any one person's DNA profile in a database increases the chances of that person being exonerated in court. But such a claim cannot be made

without assessment of the relevant technology — the use of methodological, sociological, ethical, philosophical and legal analyses to evaluate the impacts of implementing a technology in society. And this evaluation would have to include all possible uses of the databases, such as genetic-ancestry testing or the de-anonymization of families, in which relatives' identities can be revealed through cross-referencing using other available data.

For several reasons, many people from genetically isolated communities are vulnerable when it comes to de-anonymization — especially those who have rare genetic diseases¹⁴. Users of the YHRD or the AFND cannot easily search for individual data. But the YHRD, for example, displays allele frequencies in specific geographical locations (sometimes down to village names) and further cultural information is provided in the referenced publications. Indeed, one can make inferences about certain communities and families even if genetic markers are used rather than full DNA sequences.

It seems unlikely that Roma people, along with many vulnerable groups, will benefit from their DNA being collected¹⁵. The development of medications for rare diseases on the basis of data from genetically isolated communities could, in principle, benefit members of those communities^{16,17}. Yet, in the case of Roma people, we have not been able to find an example of research that has been conducted in a truly cooperative way — such as involving members of the community or efforts to improve the community's access to health services, including therapies that might already be available.

The problems we have identified with respect to Roma people are highly likely to apply to other groups. From looking at publications and following the data, we know that large genetics projects or databases such as the Human Genome Diversity Project and the YHRD, and the Kidd Lab private database, run by geneticist Kenneth Kidd at Yale University in New Haven, Connecticut, include data and samples taken decades ago from Indigenous peoples and populations considered genetically isolated, such as the San people and the Karitiana of western Brazil¹⁸ (see 'What the database keepers say'). These data and materials have been used and shared by researchers around the world for more than 20 years. A broad verbal consent for

research uses, taken and considered acceptable 30 years ago, cannot cover all reuses of data and samples that are technologically feasible today.

What the database keepers say

Four out of six database coordinators responded to requests for comment.

Geneticist Kenneth Kidd at Yale University in New Haven, Connecticut, who runs the Allele Frequency Database (ALFRED), agrees that “in the past, inadequate consent was a problem”.

Jean-François Deleuze, scientific director of the Human Polymorphism Study Center (CEPH) in Paris, which holds the cell lines and data for the Human Genome Diversity Project, notes that since Europe’s General Data Protection Regulation came into force, “CEPH only distributes global allelic frequencies of genetic markers”, making “the re-identification of samples now impossible”.

Andrew Jones at the University of Liverpool, UK, who co-runs the Allele Frequency Net Database, accepts that the organization has “a responsibility to ‘curate’ data or metadata where there are problems”.

Kristiina Tambets, head of the Estonian Biocentre Human Genome Diversity Panel, states that those working for the database always make sure that they “have the ethical permits in place when [they] deal with human subjects”.

No responses were received from the European DNA Profiling Group’s Mitochondrial DNA Population Database or the Y-STR Haplotype Reference Database.

Course correction

Some researchers and journal editors are trying to make changes, owing in part to increased awareness worldwide of the injustices experienced by minority populations. In the past year, two journals — the *International Journal of Legal Medicine* and *Human Genetics* (both published by Springer Nature, the publisher of *Nature*) — have retracted six papers that use DNA

from Chinese minority ethnic groups. We know of another journal that is currently investigating a study that uses DNA from Roma people.

These are welcome steps. But much more must be done. In our view, resolving these problems requires four actions.

Establish an international oversight board. Human and forensic geneticists, bioethicists, medical scientists, anthropologists and scholars from the social sciences and humanities — as well as community advocates — need to investigate all the DNA data held in public databases that has been obtained from oppressed groups. As a first step, an oversight board could create a list of ‘at-risk’ populations for which problems with DNA data have been identified. Researchers, editors, members of the communities, forensic investigators and so on could then check to see whether the population they are working with or concerned about is on the list.

The European Society of Human Genetics could lead this effort, joined by societies from around the world. Such a board could establish how DNA has been collected, analysed and interpreted (much as we have done for Roma people, but more systematically); the nature of the consent given (if at all); and any resulting harms or benefits affecting the groups from which the data have been collected. In other words, it would extend the ethical diligence that is better established in medical genetics to research on all human genetic data.

The International Society for Forensic Genetics is already setting up an oversight board to examine cases in which consent is unclear. This is promising. But what we are calling for would be broader. Because different ethical standards between different research communities is part of the problem, forensic geneticists cannot solve the problem alone; they need guidance from other disciplines and stakeholders. Such analyses must be co-produced with members of the communities affected, as well as with scholars who understand the political and societal contexts facing these populations.

Retract unethical work and improve publishing practices. More pressure must be put on journal editors and publishers to investigate and, if necessary,

retract problematic studies. In principle, researchers could flag ethically troublesome research to the oversight board, which could then take up the issue with the journal. For new submissions involving DNA data from at-risk populations, reviewer panels must include bioethicists or other experts who know the communities involved and the societal challenges they face. If a reviewer has concerns, the communities must be consulted. It should also be mandatory for researchers to publish blank versions of the informed-consent forms (or equivalent) used for DNA data collection. Institutions, funders and researchers can put further pressure on journal editors and publishers by refusing to support, peer review or reward studies that fail to meet agreed standards.



A San woman walks through her community in the southern Kalahari desert in South Africa. Credit: Dan Kitwood/Getty

Encouragingly, a statement this year by the Committee on Publication Ethics, a non-profit advisory organization, emphasizes the need for editors and publishers to give [special protection to “vulnerable populations”](#). The

[CARE Principles for Indigenous Data Governance](#) also offer some guidance on this, but editors and reviewers need to apply these principles to all at-risk populations, not just to those described as Indigenous.

Numerous non-governmental groups, lawyers and scholars now advocate for many Indigenous groups regarding their DNA rights, particularly in the United States, Australia and Canada. This is not the case for Roma people and other migrant, stateless, nomadic or displaced populations around the world, including Tibetan people in China, Kurdish communities in Turkey or Ethiopian Jewish individuals (all of whom are represented in DNA databases). People in these groups are perceived by many to be foreign in their home countries.

Improve scientific training. In our analysis, we were surprised by the patchy awareness among researchers and institutions of the ethical problems of collecting genetic data from marginalized communities. Some were quick to realize the issues. Others were less willing to engage. In one e-mail, a journal editor joked to the employee of a publisher that they would need to “organise a time traveling machine and go back in time and make these better”.

Undergraduates and postgraduates studying human genetics should be taught about potential harms to participants of genetics studies, and how to avoid such damage. PhD students should be required to take courses, ideally involving members of oppressed communities. And workshops to bring senior researchers up to date with current best practice should be mandatory. Several scholars have demonstrated how this training could be achieved, including anthropologists Kim TallBear at the University of Alberta in Edmonton, Canada, and Emma Kowal at Deakin University in Melbourne, Australia, as well as geneticists Deborah Bolnick at the University of Connecticut in Storrs and Keolu Fox at the University of California, San Diego.

Encourage community participation. Individuals whose DNA might be studied must be involved in research projects from the outset. At the very least, this means researchers engaging in a two-way dialogue with people about the benefits and returns they can personally expect (or not), and about the risks of DNA donation. It also means providing community members

with ways to stay informed about the uses of their data (perhaps through a smartphone app), or to withdraw their DNA from a project at any time. The international board we are proposing could help to oversee this. Even better would be to [train community members in genomics](#) so that people in marginalized communities can identify research questions that are relevant to them.

Again, examples of such cooperative approaches already exist. Kowal established the [world's first Indigenous-governed genome facility](#) — Australia's National Centre for Indigenous Genomics, hosted at the Australian National University in Canberra. There, members of Indigenous communities decide what research questions should be asked and how data should be handled.

Sensitive approach

Over the past decade or so, several scientists have [urged researchers to collect more DNA data from minority populations](#), warning that genomics medicine could benefit only a privileged few if this doesn't happen^{19,20}. We commend these calls. Yet minority populations will be harmed in other ways if DNA collections and analyses are not methodologically sound, or are conducted without awareness of and sensitivity to the societal challenges people face.

Geneticists in Europe need to face up to the fact that unethical research practices are still happening on home soil — not just on other continents. Indeed, political actors have been using genetic studies on Roma people to bolster discriminatory policies. For example, in 2015, the [European Commission launched infringement proceedings against the Slovakian government](#) for its policy, established in the 1970s and reinforced after 1990, of segregating Roma children in schools for those with “mild mental disabilities”. In its response, the [Slovakian government cited “genetically determined disorders” associated with “inbreeding”](#).

Such policies are concerning for two reasons. Policies for many Roma children might be being shaped by the health conditions of a few. Also, any child with additional needs requires more educational and emotional

support, not less. Slovakia's schools for those with "mild mental disabilities" are notorious for providing a poor standard of education²¹. Only last year, after a change of government, did Slovakia acknowledge that this segregation is a problem and begin an investigation.

Meanwhile, more human geneticists globally must take on truly collaborative work across disciplinary and societal boundaries. This would ensure that communities or families whose members experience disproportionate rates of rare genetic diseases are treated with care and respect — not just as a 'unique research tool' or 'precious resource', as some geneticists write in their publications. Given our long history of misrepresenting human genetic variation, these challenges must be met if people's trust in science, as well as in health care, policing and criminal justice, is to be retained — or, in some cases, restored.

Nature **599**, 368–371 (2021)

doi: <https://doi.org/10.1038/d41586-021-03416-3>

References

1. 1.

Claw, K. G. *et al.* *Nature Commun.* **9**, 2957 (2018).

2. 2.

Yıldız, C. & De Genova, N. *Soc. Identities* **24**, 425–441 (2018).

3. 3.

Gresham, D. *et al.* *Am. J. Hum. Genet.* **69**, 1314–1331 (2001).

4. 4.

Mendizabal, I. *et al.* *Curr. Biol.* **22**, 2342–2349 (2012).

5. 5.

Martínez-Cruz, B. *et al.* *Eur. J. Hum. Genet.* **24**, 937–943 (2016).

6. 6.

Surdu, M. *Those Who Count: Expert Practices of Roma Classification* (Central European Univ. Press, 2016).

7. 7.

Müller-Hill, B. *Murderous Science: Elimination by Scientific Selection of Jews, Gypsies, and Others, Germany, 1933–1945* (Oxford Univ. Press, 1988).

8. 8.

van Baar, H. *Social Identities* **24**, 442–458 (2018).

9. 9.

European Union Agency for Fundamental Rights. *Second European Union Minorities and Discrimination Survey. Roma — Selected Findings* (European Union, 2016).

10. 10.

Lipphardt, V., Rappold, G. & Surdu, M. Preprint at ResearchGate
<https://doi.org/10.13140/RG.2.2.13286.04165> (2020).

11. 11.

Carracedo, A. *et al.* *Forensic Sci. Int. Genet.* **4**, 145–147 (2010).

12. 12.

Parson, W. & Roewer, L. *Int. J. Legal Med.* **124**, 505–509 (2010).

13. 13.

Lipphardt, V. & Surdu, M. Preprint at ResearchGate
<https://doi.org/10.13140/RG.2.2.16641.48484> (2021).

14. 14.

Mascalzoni, D. *et al.* *Eur. J. Hum. Genet.* **18**, 296–302 (2010).

15. 15.

Kalaydjieva, L., Gresham, D. & Calafell, F. *BMC Med. Genet.* **2**, 5 (2001).

16. 16.

Reardon, J. *The Postgenomic Condition: Ethics, Justice & Knowledge After the Genome* (Univ. Chicago Press, 2017).

17. 17.

Fox, K. *N. Engl. J. Med.* **383**, 411–413 (2020).

18. 18.

Munsterhjelm, M. *Int. J. Semiot. Law* **28**, 289–316 (2014).

19. 19.

Peterson, R. E. *et al.* *Cell* **179**, 589–603 (2019).

20. 20.

Popejoy, A. & Fullerton, S. *Nature* **538**, 161–164 (2016).

21. 21.

Amnesty International and European Roma Rights Centre. *A Lesson in Discrimination* (Amnesty & ERRC, 2017).

- CORRESPONDENCE
- 16 November 2021

Presidents of Royal Society live long lives

- [Oscar S. Wilson](#) ⁰ &
- [Herbert E. Huppert](#) ¹

The records of the UK Royal Society indicate that its presidents are generally long-lived — possibly more so than their high-ranking contemporaries in British society.

Access options

Subscribe to Journal

Get full journal access for 1 year

\$199.00

only \$3.90 per issue

[Subscribe](#)

All prices are NET prices.

VAT will be added later in the checkout.

Tax calculation will be finalised during checkout.

Rent or Buy article

Get time limited or full article access on ReadCube.

from \$8.99

Rent or Buy

All prices are NET prices.

Additional access options:

- [Log in](#)
- [Learn about institutional subscriptions](#)

Nature **599**, 372 (2021)

doi: <https://doi.org/10.1038/d41586-021-03420-7>

This article was downloaded by **calibre** from <https://www.nature.com/articles/d41586-021-03420-7>

| [Section menu](#) | [Main menu](#) |

- CORRESPONDENCE
- 16 November 2021

Link knowledge and action networks to tackle disasters

- [Jim Falk](#)⁰,
- [Rita R. Colwell](#)¹,
- [Charles F. Kennel](#)² &
- [Cherry A. Murray](#)³

Earth's climate, ecological and human systems could converge into a comprehensive crisis within our children's lifetimes, driven by factors such as inequality, inadequate health infrastructure and food insecurity (see consensus statement, [J. Falk et al. Sustain. Sci. https://doi.org/g5bd; 2021](#)). As the COVID-19 pandemic has revealed, national military and economic security provide inadequate protection against global catastrophes.

Access options

Subscribe to Journal

Get full journal access for 1 year

\$199.00

only \$3.90 per issue

[Subscribe](#)

All prices are NET prices.

VAT will be added later in the checkout.

Tax calculation will be finalised during checkout.

Rent or Buy article

Get time limited or full article access on ReadCube.

from \$8.99

[Rent or Buy](#)

All prices are NET prices.

Additional access options:

- [Log in](#)
- [Learn about institutional subscriptions](#)

Nature **599**, 372 (2021)

doi: <https://doi.org/10.1038/d41586-021-03419-0>

This article was downloaded by **calibre** from <https://www.nature.com/articles/d41586-021-03419-0>

| [Section menu](#) | [Main menu](#) |

- CORRESPONDENCE
- 16 November 2021

Funders need to credit open science

- [Hans de Jonge](#) ⁰,
- [Maria Cruz](#) ¹ &
- [Stephanie Holst](#) ²

Researchers are increasingly expected to pursue open science in the form of open-access publication and data sharing. To help promote this movement, the Dutch Research Council set up an Open Science Fund for research projects that are specifically designed to stimulate open-science practices (go.nature.com/3mtupbd).

The response from the Dutch research community has been overwhelming. We received 167 eligible proposals, of which 26 were funded in the first round. The projects include the development of innovative publication practices and of open-source tools and software that facilitate open science; devising and setting standards for data sharing; and promoting a cultural shift towards open science.

For open science to become the norm (see <https://doi.org/g47b>), we suggest that funders need to recognize and encourage researchers' participation in open science. Earlier this year, the European Commission announced a move in this direction: open science will be assessed as part of the scientific methodology under the excellence criterion of Horizon Europe's research-funding programme (see go.nature.com/3kioeq).

Nature **599**, 372 (2021)

doi: <https://doi.org/10.1038/d41586-021-03418-1>

This article was downloaded by **calibre** from <https://www.nature.com/articles/d41586-021-03418-1>

| [Section menu](#) | [Main menu](#) |

- CORRESPONDENCE
- 16 November 2021

Reflections on a pioneer in electrical engineering

- [Polina Bayvel](#) 

When Eric Ash (1928–2021) joined University College London’s department of electronic engineering in 1963, the institution’s annual report noted that he was an “acquisition of very special significance”. And so it proved to be. Some of his most important contributions were made during his 22 years here.

Access options

Subscribe to Journal

Get full journal access for 1 year

\$199.00

only \$3.90 per issue

[Subscribe](#)

All prices are NET prices.

VAT will be added later in the checkout.

Tax calculation will be finalised during checkout.

Rent or Buy article

Get time limited or full article access on ReadCube.

from \$8.99

Rent or Buy

All prices are NET prices.

Additional access options:

- [Log in](#)
- [Learn about institutional subscriptions](#)

Nature **599**, 372 (2021)

doi: <https://doi.org/10.1038/d41586-021-03417-2>

This article was downloaded by **calibre** from <https://www.nature.com/articles/d41586-021-03417-2>

| [Section menu](#) | [Main menu](#) |

Work

- **Stagnating salaries present hurdles to career satisfaction**

[16 November 2021]

Career Feature • Fewer than half of respondents to Nature's 2021 salary and satisfaction survey feel positive about their prospects.

- **The greener route to indigo blue** [15 November 2021]

Where I Work • Tammy Hsu is finding a way to produce fabric dye with a lower environmental impact.

- CAREER FEATURE
- 16 November 2021

Stagnating salaries present hurdles to career satisfaction

Fewer than half of respondents to *Nature*'s 2021 salary and satisfaction survey feel positive about their prospects.

- [Chris Woolston](#) ✉

[Find a new job](#)

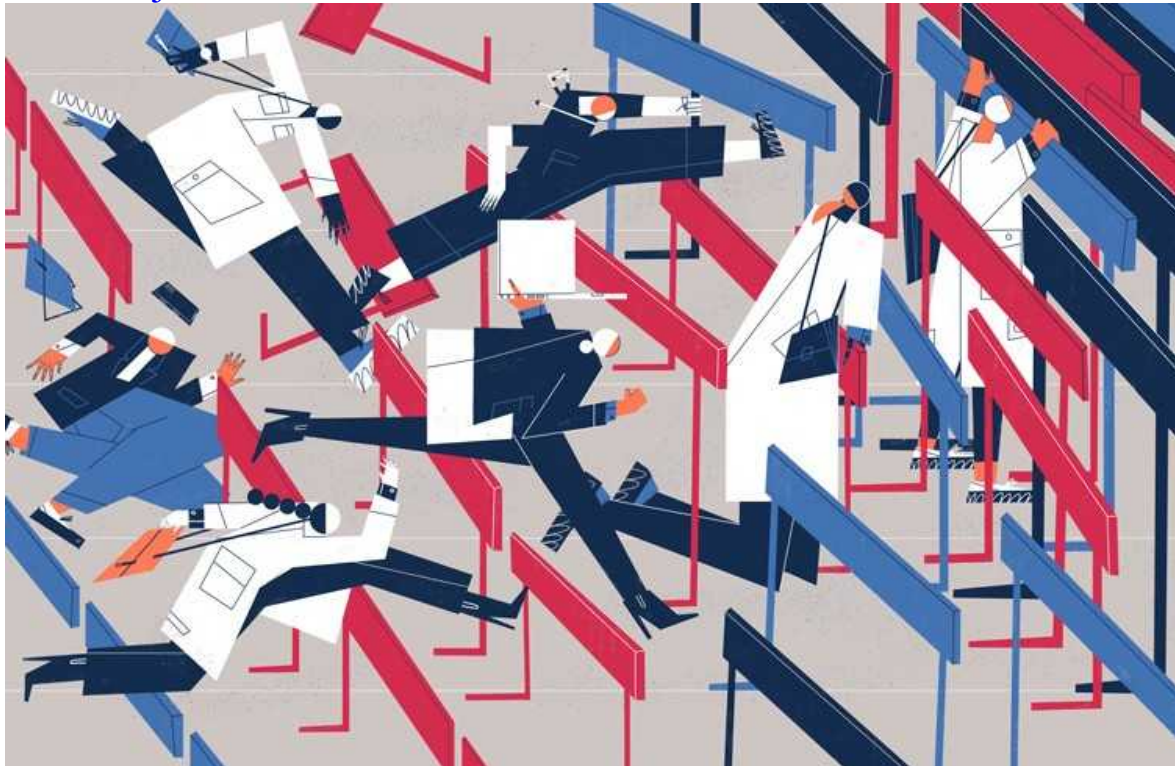


Illustration by Antonio Rodríguez

Last month, Jucelaine Haas returned home to Brazil after spending a year as a visiting scientist at the Helmholtz Centre for Environmental Research in

Leipzig, Germany. Now at the Federal University of Technology in Paraná, Haas says her tenure-track position offers some security but she has little opportunity for advancement. “I’m a university professor,” she says. “It’s such a nice title.”

Haas laments that a lack of resources and opportunities in Brazil have made it difficult for her to collect the sorts of accomplishment that would make her competitive for faculty jobs in other countries. “When you look at my CV, I don’t have many qualifications. I’ve made the most of what I have,” she says.

Haas’s gloomy outlook is not unusual. Fewer than half of respondents to *Nature*’s 2021 salary and satisfaction survey reported feeling positively about their career prospects, a clear sign of pessimism at a time of widespread funding shortages, intense competition for jobs and the disruptions of a global pandemic (see ‘*Nature*’s salary and job survey’). By comparison, the proportion was nearly 60% in 2018, when the last survey took place.

The self-selected survey drew responses from more than 3,200 working scientists around the world. Slightly more than one-third came from North America. Roughly one-quarter came from Europe, with another 14% coming from the United Kingdom and 10% from Asia. Almost two-fifths work in biomedical and clinical science, the most for any field. Close to two-thirds work in academia, 15% in industry, 9% in government and 5% at non-profit organizations. Respondents spanned the spectrum of job titles, including professors and lecturers (32%), postdoctoral researchers (22%) and staff scientists (19%). Almost 80% have a PhD. Female and male researchers responded in roughly equal numbers, but the choice of gender wasn’t binary, and 2% of researchers identified as non-binary or preferred not to say.

Nature’s salary and job survey

This article is the second of four linked to *Nature*’s global salary and job satisfaction survey. Further articles are scheduled for the following weeks, exploring job satisfaction, diversity and inclusion and other aspects of scientific life.

The salary survey runs every three years and [last took place in 2018](#). It was created together with Shift Learning, a market-research company in London, and was advertised on nature.com, in Springer Nature digital products and through e-mail campaigns. It was offered in English, Mandarin Chinese, Spanish, French and Portuguese. The full survey data sets are available at go.nature.com/3eqcpk9.

Optimism about job prospects seems to be waning. Whereas 59% of researchers felt positively about their futures in 2018, just 47% felt that way this year. Exactly half of respondents said that their prospects were worse than those of previous generations, a number essentially unchanged from 2018.

For Haas, one downside of staying in Brazil is that academics there often have to take on many other duties beyond research and teaching. For instance, she once had to evaluate applications from students who were claiming financial hardships. In addition to all her other tasks and responsibilities, she found herself reviewing financial documents and interviewing students to make sure they were as poor as they claimed. “I don’t see how that’s related to my research,” she says.

Andie Hall, a research assistant at the Natural History Museum in London, is unsure about her long-term prospects. She’s been at the same institution for 17 years, enough time to establish a niche sequencing specimens including freshly collected bryozoans and 200-year-old lacewings. “My job is quite different from everyone else in the museum,” she says. “I’m part technician and part researcher. It’s interesting, but it’s also a challenge.”

If she ever did want to move on, she knows her options would be limited by the fact that she did not go further than a master’s degree. “I often see jobs — and even training courses — advertised that I know I could do, but they require a PhD,” she says. “If you’re a technician who’s at the bench solving problems, I don’t think that a PhD is necessarily as important as experience.”

A closer look at the results shows that career optimism isn’t evenly distributed. People who identified as male (49%) were somewhat more likely than those who identified as female (45%) to have a positive view of

their job prospects. Among the 10 countries with the most respondents, prospects seemed especially gloomy in Brazil, where only 33% felt positively. People were slightly more positive in Australia (37%) and Spain (38%). Optimism was more abundant in China (50%), the United States (52%) and India (57%). A biomedical postdoc in Australia shared her thoughts: “As a dedicated scientist with over 15 years experience, I am completely disillusioned about research. Many of my friends have left research and I am about to drop off as well. Not because of lack of skills or passion for research but rather because of the constant fighting to stay in the game (which is costing me my mental health).”

The sectors in which scientists are based strongly colour their views of the future. Respondents in industry (64%) are much more likely than those in academia (42%) to feel positively. A project manager in the United States wrote, “I am now an evangelist for all of my friends still in academia to get out and join biotech or any other professional industry.”

Respondents in the fields of health care and engineering were especially likely to see good things ahead, at 59% and 55%, respectively. By contrast, only 38% of those working in ecology and evolution and 40% of those in geology and environmental science feel positive. The pandemic probably contributed to both optimism and pessimism in different fields. A biomedical postdoc in the United States stated: “I’m hopeful that [the pandemic] will result in more funding opportunities in biomedical sciences, but I also think it has significantly slowed down any research that is not related to SARS-CoV-2.”

A positive outlook was more common in early- or mid-career researchers (49%) than in researchers in the later stages of their careers (39%). Predictably, optimism is also in greater supply in people in full-time permanent jobs (53%) than in those on full-time contracts (36%).

Fixed-term contracts are clouding the future of Edmond Sanganyado, an environmental chemist at Shantou University in China. “In China, there’s no pathway to a permanent job,” says Sanganyado, who is originally from Zimbabwe. “You have to keep renewing your contract every three years. It’s difficult for a foreigner to have long-term goals.”

The widespread negativity uncovered by the survey is a bit surprising for people with so much to offer, says Jim Vigoreaux, a biologist and vice-provost for faculty affairs at the University of Vermont in Burlington. Vigoreaux co-authored an article in June that offers advice for scientists seeking faculty positions at research-intensive institutions ([J. O. Vigoreaux and M. J. Leibowitz *BMC Proc.* **15**, 4; 2021](#)). He acknowledges that faculty positions are in short supply and that the odds of success are low for any particular application. But he also notes that people with scientific skills have a growing number of options both inside and outside academia. Complex issues such as sustainability, social justice and health care will require a vast and committed research workforce, he says. “There are big challenges ahead of us, really interesting questions in so many areas of science and technology. I don’t quite get all of this pessimism.”

Vigoreaux encourages researchers on the job market to take a wide view of the possibilities in science, whether in academia or beyond. But that doesn’t mean they should take a scatter-gun approach to applying for jobs. “The prevailing mentality is to throw everything at the wall and see what sticks,” he says. “I encourage people to refrain from doing that. They should be more selective. And when they identify an opportunity, they should go full steam ahead.”

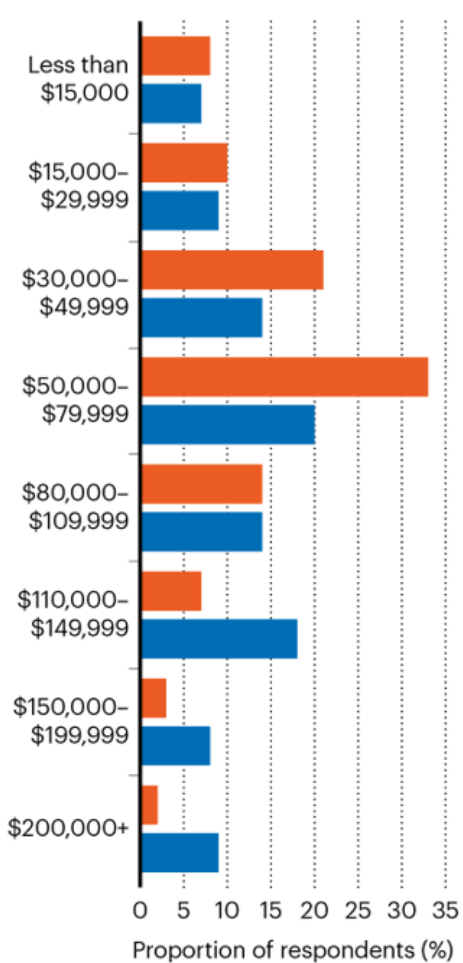
Respondents had their reasons for doubt. When asked to identify the biggest barriers to career progression, more than one-third cited competition for funding as one their top concerns, and 31% noted an overall lack of funding (see ‘Salaries and prospects’). Funding shortfalls were a particularly common complaint in Spain (44%), Australia (53%) and Brazil (64%). Overall, 9% of respondents said they were held back by a lack of skills. When asked to specify their shortcomings, those respondents were especially concerned about a lack of ‘hard’ skills, such as proficiency in specific experimental techniques and computational know-how.

SALARIES AND PROSPECTS

Scientific salaries vary widely, with higher wages generally found in industry. A slim majority of scientists are satisfied with their salaries, but they are less certain about their futures.

Salary comparison (US\$)

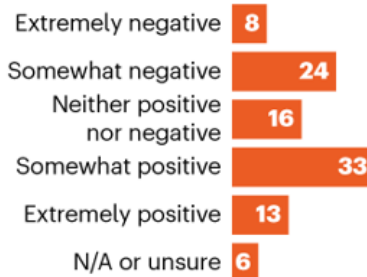
■ Academia ■ Industry



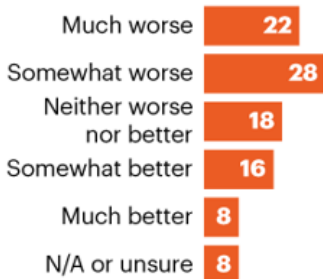
How satisfied are you with your salary/compensation?



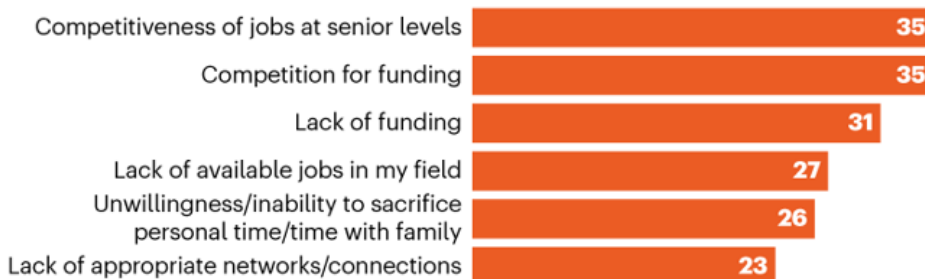
How do you feel about your future job prospects?



Do you feel that your prospects are better or worse than past generations?



What do you think is the biggest challenge for your personal career progression?



Pay disparities

The survey found stark pay disparities driven by factors such as field of study, job type and geography. Overall, about one-third of respondents reported making at least US\$80,000 a year, including 7% who make \$150,000 or more. That's up from 2018, when 23% reported making more than \$80,000 and 5% reported making more than \$150,000. At the other end of the spectrum, 19% reported earning less than \$30,000 in the 2021 survey, including 9% who make less than \$15,000.

High salaries proved to be more common in industry than academia. Seventeen per cent of respondents in industry reported making more than \$150,000 each year, but only 5% of academics reached those heights. A bioinformatician in the United States says she makes “around 50% of what I was offered for industry positions during my job search. It would be nice if academia could be more competitive with industry, but I love what I do and where I live so I can't really complain.”

Unsurprisingly, salaries vary by country. More than half of US respondents reported making at least \$80,000. But that mark was reached by only 19% in the United Kingdom, 6% in China and a mere 3% in Brazil. Haas says that as a full professor in Brazil, she makes less than most PhD students elsewhere. Overall, 27% of respondents whose job involves mainly teaching reported⁴ earning less than \$15,000. Notably, 7% of full professors also reported making less than \$15,000 a year, a troubling situation for accomplished academics. A full biomedical professor in Argentina lamented that she pockets about \$300–400 per month after a series of cutbacks at her institution. “Science in Argentina has been awful for many years,” she wrote. “It keeps getting worse.”

As with previous *Nature* surveys, male and female researchers generally reported similar earnings, especially at the early stages of their careers. However, there is a gender gap in high earners in senior positions. Among those who identified as late-career scientists, 40% of male researchers and 36% of female researchers reported earning at least \$110,000. This trend echoes that found in the 2018 survey, with 33% for men and 23% for women.

Salaries seem to be stagnating. Just 38% of respondents reported receiving a salary increase in the past year, down from 51% who reported a boost in 2018. Nine per cent reported a decrease in salary. When asked to identify the reason for the salary cut, 40% blamed cutbacks at their institutions. This particular complaint was almost twice as common in academia (44%) as in industry (23%).

Even though relatively few respondents reported rises compared with previous surveys, just over half said they were happy with their overall levels of compensation. That's up from 43% in 2018. Levels of satisfaction were especially high (62%) in respondents working in industry. For those in academia, fewer than half were satisfied.

Very low lows

Many scientists have reason for complaint. A full-time staff scientist physicist in Russia noted that his yearly salary is less than \$5,000. "There is regional discrimination in Russia," he wrote. "A scientist's salary in Moscow is about the same as in Europe." He says that salaries in the Republic of Dagestan, where he lives, are particularly low, with his as a prime example.

High salaries don't always translate to contentment. A project manager at a US biotech firm indicated that she's "neither satisfied nor dissatisfied" with her salary of more than \$200,000. She pointed out some issues at her company that transcend salary, including "a lack of long-term institutional goals, turnover of personnel, poor decision-making process and top-down communication".

Sometimes, a change of scenery can significantly improve a scientist's financial situation. Physicist Ana Rakonjac says that she struggled with relatively low salaries during more than five years of postdoctoral work in the United Kingdom, but things started to look up when she took an industry job as a senior research scientist at Atomionics, an atomic physics start-up in Singapore. "The salary was much higher, which relieved a lot of personal stress," she says. "Postdoc salaries are OK, but it was a difficult situation for

saving money. I never felt great financial security. If something went wrong, I'd have to rely on my parents."

Postdoctoral training doesn't always pay well in the short term, but it can be a worthwhile investment in the future, especially for those who wish to remain in academia, says Joyce Main, a higher-education researcher at Purdue University in West Lafayette, Indiana. Main co-authored a paper earlier this year that used a National Science Foundation database to track career outcomes for US postdocs in the social sciences and science, technology, engineering and medicine (STEM) fields ([J. Wang and J. B. Main Stud. Grad. Postdoc. Educ. 12, 384–402; 2021](#)). The study found that completing a postdoc in either a social-science or a STEM field increased the odds of landing a tenure-track faculty position seven to nine years after finishing the PhD. "In terms of developing your research programme, a postdoc can be helpful because it gives you an opportunity to focus on research and publishing papers," she says.

Vigoreaux says that scientists who aren't focused in their job search are less likely to get the salaries they deserve. "The crux of the problem is that they're just jumping at the first thing that's given them because they feel insecure," he says. "They don't come prepared with skills to negotiate a good starting salary." He explains that job-seekers who are focused in their quest will have clearer expectations of what they can expect to earn.

Overall, the survey highlighted the wide diversity of scientific lives (see 'How do you feel about your salary and career prospects'). The obvious struggles of many stand in contrast to the success of others. A social scientist in the United States who makes more than \$110,000 working in government summed up her perspective. "I am content and optimistic about my own career, but [I'm] very aware that I am lucky in comparison to the majority of PhDs in my field."

How do you feel about your salary and career prospects?

Free-text comments in *Nature*'s salary and job satisfaction survey highlight some of the issues scientists face over their pay and their future. Comments have been edited for length and clarity and, when necessary, translated into English.

- I've been a relatively successful postdoc in academia, but my future career prospects are not great. There are simply not enough jobs beyond postdoctoral levels. Industries always decline my application because I need industry experience, and I've been a postdoc for way too long. *Postdoc in biomedical field, Denmark.*
- I work in a government laboratory in the UK. Pay was frozen from 2010 to 2015 and has not caught up with industry/academia. Another pay freeze has been introduced. If I didn't need to work to top up my pension, I would retire. *Team leader in biomedical government lab, UK.*
- I'm lucky to have found a job that pays as much as it does. But I feel stuck. If I get a PhD I'll be in more debt and making the same. Progression feels impossible. I can't imagine going back to study full-time and finding a way to pay for it either. I want to do my own research but I don't think that will ever happen. I have to consider making enough money to survive. *Staff scientist for microbiology company, USA.*
- Improve the culture, the job security, and stabilize funding, and people with talent will flock to science. Until the basic humanity of this profession is improved, change cannot occur. We do not need any more surveys. We need to act at a global and collective level. *Government staff scientist in chemistry, USA.*
- Research in India is mostly dependent on government funding, and it will not improve unless private funding and research initiatives fill the gap. Societal research and the low-cost development of technology to improve welfare should be the priority for Indian research. *Government staff scientist in biomedical field, India.*
- The management at my institute pays me for one day a week but expects me to work full time. As a dedicated scientist with over 15 years experience, I am completely disillusioned about research. Many of my friends have left research and I am about to drop off as well. The vast majority of us are just considered as cheap labor. Researchers need not only money to live and perform at their best potential but also recognition for their hard work. Something has to change. *Postdoc in biomedical field, Australia.*

- Salaries for postdocs are a disgrace, considering the amount and the quality of work that we do. No university can sustain itself without a postdoc workforce. Postdocs living in major cities shouldn't have to pay taxes. They can't afford to live alone in their 30s so they have to live with others. Academia is turning into a milling machine with no regard for life/work balance and fair compensation. *Postdoc in biomedical field, USA.*

- As a civil servant in France, I haven't had had a rise in more than 10 years. That makes a scientific career less and less attractive. I can feel it in my standard of living because housing costs have continued to increase. In addition, this depreciation of salaries makes it more and more difficult for us to recruit brilliant young colleagues. I fully understand that they are going to look elsewhere where they will be better paid and have more resources.

Research director in agriculture and food, France. (Translated from French.)

Nature **599**, 519-521 (2021)

doi: <https://doi.org/10.1038/d41586-021-03041-0>

This article was downloaded by **calibre** from <https://www.nature.com/articles/d41586-021-03041-0>

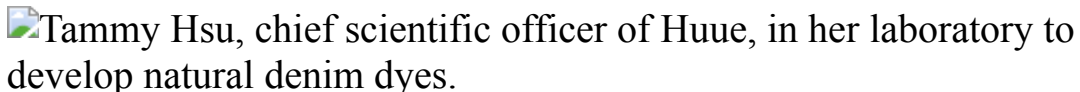
| [Section menu](#) | [Main menu](#) |

- WHERE I WORK
- 15 November 2021

The greener route to indigo blue

Tammy Hsu is finding a way to produce fabric dye with a lower environmental impact.

- [James Mitchell Crow](#) ⁰



Tammy Hsu is chief scientific officer and co-founder of Huue in Berkeley, California. Credit: Helynn Ospina for *Nature*

My work focuses on creating clean colour. Many conventional fabric dyes are made using unsustainable processes. Indigo dye, for example, is usually made from petroleum-derived aniline in a high-temperature process that involves formaldehyde and cyanide. Globally, around 20% of industrial water pollution comes from fabric dyeing.

I want to make dyes using microbial fermentation instead. At Huue, the early-stage start-up I co-founded in Berkeley, California, we look at how dye molecules are made in nature. We study the biochemical pathways, then program *Escherichia coli* bacteria to make our dye in the same way. Instead of using toxic chemicals, we feed the microbes and they make the dye.

We chose indigo to work on, because it is so iconic. The way indigo bonds with the cotton in denim, building up on the outside of the fibre, is special. When the dye wears down, the white core of the fibres is revealed, which is how denim gets its faded look.

At the University of California, Berkeley, I worked on inserting the indigo biochemical pathway into microbes. Commercial denim brands became

interested; so, just before I graduated, my business partner Michelle Zhu and I set up Huue. We went through a start-up accelerator to get seed funding, and then we were off to the races.

This photo was taken just after we moved into our own laboratory space. I'm standing in front of the fermentation station. The tanks of dark liquid are growing our microbes. All the instrumentation is used to fine-tune the growing conditions, which we are experimenting with to find out how to produce the most dye.

We have demonstrated that we can make a high-quality product, and are now working with dye mills to see what quality of fabric we can obtain. Depending on the launch schedule of the denim brands, we hope to see products dyed with our indigo on the market within a year.

Nature **599**, 524 (2021)

doi: <https://doi.org/10.1038/d41586-021-03437-y>

This article was downloaded by **calibre** from <https://www.nature.com/articles/d41586-021-03437-y>.

| [Section menu](#) | [Main menu](#) |

Research

- **[Iodine powers low-cost engines for satellites](#)** [17 November 2021]
News & Views • Solid iodine transforms directly into gas when heated — a property that has been used to create cheap, compact engines that could make large networks of small satellites commercially viable.
- **[GABA molecules made by B cells can dampen antitumour responses](#)** [03 November 2021]
News & Views • Analysis of immune cells shows that, unexpectedly, B cells secrete GABA, a molecule best known as a neurotransmitter. B-cell-derived GABA can modulate immune responses against tumours, raising the prospect of new therapies.
- **[Fifty years of the brain's sense of space](#)** [04 November 2021]
News & Views • Neurons in a brain region called the hippocampus were found to be selectively active when rats are in a specific spatial location during natural navigation. The discovery launched research efforts into how the brain supports spatial memory.
- **[A mediator of metabolic signals influences puberty and growth](#)** [03 November 2021]
News & Views • Variants of the melanocortin 3 receptor are associated with delayed puberty and reduced growth, suggesting that this receptor might integrate signals of metabolic status that affect body growth and sexual maturation.
- **[Californium—carbon bond captured in a complex](#)** [17 November 2021]
News & Views • The scarcity and high radioactivity of the heaviest actinide elements, such as californium, make their study a formidable challenge. A landmark report describes the first structural characterization of a californium—carbon bond.
- **[Role of bile acids and gut bacteria in healthy ageing of centenarians](#)** [06 October 2021]
News & Views • A study in humans indicates that certain bile acids that are produced by bacteria and commonly found in people over 100 boost gut health and protect against infection. These findings shed light on the contributors to healthy ageing.
- **[Excitons and emergent quantum phenomena in stacked 2D semiconductors](#)** [17 November 2021]
Review Article • This Review discusses the exciton physics of transition metal dichalcogenides, focusing on moiré patterns and exciton many-body physics, and outlines

future research directions in the field.

- **Observation of Stark many-body localization without disorder** [17 November 2021]

Article • Experiments with a trapped-ion quantum simulator observe Stark many-body localization, in which the quantum system evades thermalization despite having no disorder.

- **Measuring phonon dispersion at an interface** [17 November 2021]

Article • Four-dimensional electron energy-loss spectroscopy measurements of the vibrational spectra and the phonon dispersion at a heterointerface show localized modes that are predicted to affect the thermal conductance and electron mobility.

- **Approaching the intrinsic exciton physics limit in two-dimensional semiconductor diodes** [17 November 2021]

Article • Two-dimensional transition metal dichalcogenide diodes with defect-free van der Waals contacts allows minimization of the extrinsic interfacial disorder-dominated recombination and access to the intrinsic excitonic behaviour in two-dimensional semiconductor devices.

- **In-orbit demonstration of an iodine electric propulsion system** [17 November 2021]

Article • The successful in-orbit operation of an electric space propulsion system based on iodine, rather than the more expensive and difficult-to-store xenon, is demonstrated.

- **Exploding and weeping ceramics** [17 November 2021]

Article • A study demonstrates that a range of different behaviours—from reversible, through weeping, to explosive—can be exhibited by a chemically homogeneous ceramic system by manipulating conditions of compatibility in unusual ways.

- **Isolation and characterization of a californium metallocene** [17 November 2021]

Article • Chemical experiments on californium are stymied by isotope availability and radioactivity considerations, but are advanced here with synthesis and characterization of an organometallic complex.

- **Widespread changes in surface temperature persistence under climate change** [17 November 2021]

Article • A survey of climate change simulations from different models indicates widespread changes in surface temperature persistence under global warming that may be attributable to a broad range of physical processes.

- **Cardiopharyngeal deconstruction and ancestral tunicate sessility** [17 November 2021]

Article • The heart of appendicularians has evolved by 'deconstructing' an ancestral ascidian-like gene regulatory network.

- **MC3R links nutritional state to childhood growth and the timing of puberty** [03 November 2021]

Article • MC3R deficiency is associated with a delay in the onset of puberty, and a reduction in growth and lean mass.

- **Linking hippocampal multiplexed tuning, Hebbian plasticity and navigation** [20 October 2021]

Article • Episodic memory and allocentric spatial navigation are interwoven in the activity of hippocampal neuron ensembles via Hebbian plasticity, which allows rats to encode journey-specific episodes.

- **The orbitofrontal cortex maps future navigational goals**

[27 October 2021]

Article • Dedicated cells in the hippocampus and entorhinal cortex map an animal's instantaneous position in space; by contrast, its future goal location is represented in the orbitofrontal cortex, a structure within the broader circuit.

- **Temporal controls over inter-areal cortical projection neuron fate diversity** [09 November 2021]

Article • Combined analysis of the connectome and transcriptome in the mouse cortex indicates that dynamic differences in expression levels of largely generic sets of genes regulate differential targeting within neuronal subtypes.

- **Novel bile acid biosynthetic pathways are enriched in the microbiome of centenarians** [29 July 2021]

Article • The microbiota of centenarians (aged 100 years and older) comprise gut microorganisms that are capable of generating unique secondary bile acids, including isoallolithocholic acid, a bile acid with potent antimicrobial effects against Gram-positive—but not Gram-negative—multidrug-resistant pathogens.

- **Fc-engineered antibody therapeutics with improved anti-SARS-CoV-2 efficacy** [21 September 2021]

Article • Optimization of monoclonal antibodies against SARS-CoV-2 for enhanced Fc-effector function increase their effectiveness for prevention and treatment of COVID-19 in multiple animal models of SARS-CoV-2 infection.

- **B cell-derived GABA elicits IL-10+ macrophages to limit anti-tumour immunity** [03 November 2021]

Article • A paper in Nature demonstrates that B cell-derived GABA promotes monocyte differentiation into anti-inflammatory macrophages able to limit anti-tumour T cell cytotoxicity.

- **Cross-HLA targeting of intracellular oncoproteins with peptide-centric CARs** [03 November 2021]

Article • Targeting peptides from unmutated cancer drivers that are expressed in tumours but not in normal tissues using peptide-centric chimeric antigen receptors shows potential as treatment for cancer.

- **Dietary palmitic acid promotes a prometastatic memory via Schwann cells** [10 November 2021]

Article • Palmitic acid induces stable transcriptional and chromatin changes that lead to long-term stimulation of metastasis in orthotopic models of cancer through the secretion by tumour-associated Schwann cells of a specialized proregenerative extracellular matrix, the ablation of which inhibits metastasis initiation.

- **AKIRIN2 controls the nuclear import of proteasomes in vertebrates** [28 October 2021]

Article • Using time-controlled CRISPR screens, the authors identify AKIRIN2 as a factor involved in the nuclear import of the proteasome.

- **Target site selection and remodelling by type V CRISPR-transposon systems** [10 November 2021]

Article • Structural studies on *Scytonema hofmanni* CRISPR-associated transposon protein complexes indicate a mechanism for RNA-guided DNA transposition involving Cas12k, TnsC and TnsB.

- **Nucleation landscape of biomolecular condensates** [22 September 2021]

Article • Experiments using endogenous and biomimetic condensates in cells show that nucleation in cells resembles the physical process in inanimate materials, but is tuned by biomolecular features.

- **A synthetic antibiotic class overcoming bacterial multidrug resistance** [27 October 2021]

Article • Structure-guided design and component-based synthesis are used to produce iboxamycin, a novel ribosome-binding antibiotic with potent activity against Gram-positive and Gram-negative bacteria.

- **Architecture and assembly mechanism of native glycine receptors** [23 September 2021]

Article • Cryo-electron microscopy structures of pig glycine receptors indicate that they are predominantly assembled with 4 α :1 β stoichiometry via α -homotrimer and homotetramer intermediates.

- NEWS AND VIEWS
- 17 November 2021

Iodine powers low-cost engines for satellites

Solid iodine transforms directly into gas when heated — a property that has been used to create cheap, compact engines that could make large networks of small satellites commercially viable.

- [Igor Levchenko](#) ⁰ &
- [Kateryna Bazaka](#) ¹

Satellites organized in flexible networks known as constellations are more agile and resilient than are those operating alone. Manoeuvring satellites into such constellations requires inexpensive, reliable and efficient engines. Many networked satellites have electric propulsion thrusters, which generate thrust by using electrical energy to accelerate the ions of a propellant gas. However, the choice of gas presents a problem. Ionizing xenon requires a relatively small amount of energy, but xenon gas is expensive and needs to be compressed in high-pressure tanks to fit on board a satellite. Krypton is cheaper, but still requires a complex and heavy gas-storage and -supply system. [Writing in Nature](#), Rafalskyi *et al.*¹ report a successful demonstration of an iodine-ion thruster in space — offering a cheaper and simpler alternative to xenon or krypton.

Access options

Subscribe to Journal

Get full journal access for 1 year

\$199.00

only \$3.90 per issue

[Subscribe](#)

All prices are NET prices.

VAT will be added later in the checkout.

Tax calculation will be finalised during checkout.

Rent or Buy article

Get time limited or full article access on ReadCube.

from \$8.99

[Rent or Buy](#)

All prices are NET prices.

Additional access options:

- [Log in](#)
- [Learn about institutional subscriptions](#)

Nature **599**, 373-374 (2021)

doi: <https://doi.org/10.1038/d41586-021-03384-8>

References

1. 1.

Rafalskyi, D. *et al.* *Nature* **599**, 411–415 (2021).

2. 2.

Goebel, D. M. & Katz, I. *Fundamentals of Electric Propulsion: Ion and Hall Thrusters* (Wiley, 2008).

3. 3.

Levchenko, I. *et al. Nature* **562**, 185–187 (2018).

4. 4.

Parfenov, V. A. *et al. Sci. Adv.* **6**, eaba4174 (2020).

This article was downloaded by **calibre** from <https://www.nature.com/articles/d41586-021-03384-8>

| [Section menu](#) | [Main menu](#) |

- NEWS AND VIEWS
- 03 November 2021

GABA molecules made by B cells can dampen antitumour responses

Analysis of immune cells shows that, unexpectedly, B cells secrete GABA, a molecule best known as a neurotransmitter. B-cell-derived GABA can modulate immune responses against tumours, raising the prospect of new therapies.

- [Daniel L. Kaufman](#) ✉

Efforts to better understand how immune cells function hold the promise of providing information that might lead to improved clinical treatments.

[Writing in Nature](#), Zhang *et al.*¹ present results that point the way to the development of new approaches to enhance anticancer therapies.

Access options

Subscribe to Journal

Get full journal access for 1 year

\$199.00

only \$3.90 per issue

[Subscribe](#)

All prices are NET prices.

VAT will be added later in the checkout.

Tax calculation will be finalised during checkout.

Rent or Buy article

Get time limited or full article access on ReadCube.

from \$8.99

[Rent or Buy](#)

All prices are NET prices.

Additional access options:

- [Log in](#)
- [Learn about institutional subscriptions](#)

Nature **599**, 374-376 (2021)

doi: <https://doi.org/10.1038/d41586-021-02953-1>

References

1. 1.

Zhang, B. *et al.* *Nature* <https://doi.org/10.1038/s41586-021-04082-1> (2021).

2. 2.

Deidda, G., Bozarth, I. F. & Cancedda, L. *Front. Cell. Neurosci.* **8**, 119 (2014).

3. 3.

Mendu, S. K. *et al.* *Mol. Immunol.* **48**, 399–407 (2011).

4. 4.

Tian, J., Song, M. & Kaufman, D. L. *Sci. Rep.* **11**, 5402 (2021).

5. 5.

Tian, J. *et al.* *ImmunoHorizons* **3**, 498–510 (2019).

6. 6.

Tian, J., Middleton, B. & Kaufman, D. L. *Viruses* **13**, 966 (2021).

7. 7.

Soltani, N. *et al.* *Proc. Natl Acad. Sci. USA* **108**, 11692–11697 (2011).

8. 8.

Bhat, R. *et al.* *Proc. Natl Acad. Sci. USA* **107**, 2580–2585 (2010).

9. 9.

Tian, J., Yong, J., Dang, H. & Kaufman, D. L. *Autoimmunity* **44**, 465–470 (2011).

10. 10.

Alam, S., Laughton, D. L., Walding, A. & Wolstenholme, A. *J. Mol. Immunol.* **43**, 1432–1442 (2006).

11. 11.

Zhang, Y., Morgan, R., Podack, E. R. & Rosenblatt, J. *Immunol. Res.* **57**, 115–124 (2013).

12. 12.

Akrami, M. *et al.* *Proc. Natl Acad. Sci. USA* **117**, 23674–23683 (2020).

13. 13.

Soghomonian, J.-J. & Martin, D. L. *Trends Pharmacol. Sci.* **19**, 500–505 (1998).

This article was downloaded by **calibre** from <https://www.nature.com/articles/d41586-021-02953-1>

| [Section menu](#) | [Main menu](#) |

- NEWS AND VIEWS
- 04 November 2021

Fifty years of the brain's sense of space

Neurons in a brain region called the hippocampus were found to be selectively active when rats are in a specific spatial location during natural navigation. The discovery launched research efforts into how the brain supports spatial memory.

- [Isabel I. C. Low](#)⁰ &
- [Lisa M. Giocomo](#)¹

Nearly all of our conscious experiences incorporate a sense of space: the restaurant where we ate, our route home, where we found our teacup, navigating to our favourite chair. This sense of space is how we know where we are, remember where we have been and plan where we want to go. But how the brain generates this sense and uses it for memory or navigation remained a mystery for many years. [A landmark paper in 1971](#) by John O'Keefe and Jonathan Dostrovsky, published in *Brain Research*, offered the first glimpse into how neurons in the mammalian brain compute an animal's sense of space¹.

Access options

Subscribe to Journal

Get full journal access for 1 year

\$199.00

only \$3.90 per issue

Subscribe

All prices are NET prices.
VAT will be added later in the checkout.
Tax calculation will be finalised during checkout.

Rent or Buy article

Get time limited or full article access on ReadCube.

from \$8.99

Rent or Buy

All prices are NET prices.

Additional access options:

- [Log in](#)
- [Learn about institutional subscriptions](#)

Nature **599**, 376–377 (2021)

doi: <https://doi.org/10.1038/d41586-021-03010-7>

References

1. 1.

O'Keefe, J. & Dostrovsky, J. *Brain Res.* **34**, 171–175 (1971).

2. 2.

Kimble, D. P. *J. Comp. Physiol. Psychol.* **56**, 273–283 (1963).

3. 3.

Scoville, W. B. & Milner, B. *J. Neurol. Neurosurg. Psychiatry* **20**, 11–21 (1957).

4. 4.

Tolman, E. C. *Psychol. Rev.* **55**, 189–208 (1948).

5. 5.

Turner, C. H. *J. Comp. Neurol. Psychol.* **17**, 367–434 (1907).

6. 6.

O'Keefe, J. *Exp. Neurol.* **51**, 78–109 (1976).

7. 7.

Muller, R. U., Bostock, E., Taube, J. S. & Kubie, J. L. *J. Neurosci.* **14**, 7235–7251 (1994).

8. 8.

Bostock, E., Muller, R. U. & Kubie, J. L. *Hippocampus* **1**, 193–205 (1991).

9. 9.

Muller, R. U., Kubie, J. L. & Ranck, J. B. Jr *J. Neurosci.* **7**, 1935–1950 (1987).

10. 10.

Ziv, Y. *et al. Nature Neurosci.* **16**, 264–266 (2013).

11. 11.

Wood, E. R., Dudchenko, P. A. & Eichenbaum, H. *Nature* **397**, 613–616 (1999).

12. 12.

Aronov, D., Nevers, R. & Tank, D. W. *Nature* **543**, 719–722 (2017).

13. 13.

Omer, D. B., Maimon, S. R., Las, L. & Ulanovsky, N. *Science* **359**, 218–224 (2018).

14. 14.

Payne, H. L., Lynch, G. F. & Aronov, D. *Science* **373**, 343–348 (2021).

15. 15.

Las, L. & Ulanovsky, N. in *Space, Time and Memory in the Hippocampal Formation* (eds Derdikman, D. & Knierim, J. J.) 431–461 (Springer, 2014).

16. 16.

Moser, E. I., Moser, M.-B. & McNaughton, B. L. *Nature Neurosci.* **20**, 1448–1464 (2017).

17. 17.

Deshmukh, S. S. & Knierim, J. J. *Front. Behav. Neurosci.* **5**, 69 (2011).

18. 18.

Tsao, A. *et al.* *Nature* **561**, 57–62 (2018).

19. 19.

Seelig, J. D. & Jayaraman, V. *Nature* **521**, 186–191 (2015).

20. 20.

Robinson, N. T. M. *et al.* *Cell* **183**, 1586–1599 (2020).

This article was downloaded by **calibre** from <https://www.nature.com/articles/d41586-021-03010-7>

| [Section menu](#) | [Main menu](#) |

- NEWS AND VIEWS
- 03 November 2021

A mediator of metabolic signals influences puberty and growth

Variants of the melanocortin 3 receptor are associated with delayed puberty and reduced growth, suggesting that this receptor might integrate signals of metabolic status that affect body growth and sexual maturation.

- [Alejandro Lomniczi](#) 0

Body growth and the onset of puberty are regulated by neurons located in a part of the brain called the hypothalamus. In the central hypothalamus, signalling by hormones called melanocortins relays metabolic information to downstream growth and reproductive centres. However, the molecular and cellular targets of these signals have not been completely elucidated.

[Writing in Nature](#), Lam *et al.*¹ describe previously unreported mutations in the gene encoding the human melanocortin 3 receptor (MC3R) protein that seem to disrupt the receptor's function. They found that these mutations are associated with a delay in the onset of puberty as well as with reduced childhood growth, adult height and lean body mass.

Access options

Subscribe to Journal

Get full journal access for 1 year

\$199.00

only \$3.90 per issue

Subscribe

All prices are NET prices.
VAT will be added later in the checkout.
Tax calculation will be finalised during checkout.

Rent or Buy article

Get time limited or full article access on ReadCube.

from \$8.99

Rent or Buy

All prices are NET prices.

Additional access options:

- [Log in](#)
- [Learn about institutional subscriptions](#)

Nature **599**, 377-379 (2021)

doi: <https://doi.org/10.1038/d41586-021-02954-0>

References

1. 1.

Lam, B. Y. H. *et al. Nature* <https://doi.org/10.1038/s41586-021-04088-9> (2021).

2. 2.

Kennedy, G. C. *J. Endocrinol.* **16**, 9–17 (1957).

3. 3.

Kennedy, G. C. & Mitra, J. *J. Physiol. (Lond.)* **166**, 408–418 (1963).

4. 4.

Hill, J. W. & Faulkner, L. D. *Neuroendocrinology* **104**, 330–346 (2017).

5. 5.

Chen, A. S. *et al. Transgenic Res.* **9**, 145–154 (2000).

6. 6.

Vaisse, C., Clement, K., Guy-Grand, B. & Froguel, P. *Nature Genet.* **20**, 113–114 (1998).

7. 7.

Farooqi, I. S. *et al. N. Engl. J. Med.* **348**, 1085–1095 (2003).

8. 8.

Chen, A. S. *et al. Nature Genet.* **26**, 97–102 (2000).

9. 9.

Uenoyama, Y. *et al. Front. Endocrinol.* **10**, 312 (2019).

10. 10.

Steyn, F. J., Tolle, V., Chen, C. & Epelbaum, J. *Compr. Physiol.* **6**, 687–735 (2016).

11. 11.

Hauspie, R. C., Vercauteren, M. & Susanne, C. *Acta Paediatr.* **86** (Suppl. 423), 20–27 (1997).

This article was downloaded by **calibre** from <https://www.nature.com/articles/d41586-021-02954-0>

| [Section menu](#) | [Main menu](#) |

- NEWS AND VIEWS
- 17 November 2021

Californium—carbon bond captured in a complex

The scarcity and high radioactivity of the heaviest actinide elements, such as californium, make their study a formidable challenge. A landmark report describes the first structural characterization of a californium–carbon bond.

- [Julie E. Niklas](#)⁰ &
- [Henry S. La Pierre](#)¹

The detailed study of a class of organometallic compounds known as the metallocenes has driven crucial developments in areas such as catalysis, electrochemistry and nano-technology. [Writing in Nature](#), Goodwin *et al.*¹ report the synthesis and characterization of a metallocene complex of californium, a member of the actinide series of elements (Fig. 1a). Substantial technical challenges had to be overcome to handle this air-sensitive complex of a highly radioactive element — just two milligrams of californium were used in the work. Remarkably, the authors report the first crystallographic measurement of a californium–carbon bond.

Organometallic complexes of actinide ions have emerged as a frontier of research that challenges accepted models of bonding in coordination complexes (compounds consisting of a central atom or ion bound to ligands). Goodwin and colleagues' findings will help to map periodic trends of physico-chemical properties across the heavy actinides.

Access options

Subscribe to Journal

Get full journal access for 1 year

\$199.00

only \$3.90 per issue

[Subscribe](#)

All prices are NET prices.

VAT will be added later in the checkout.

Tax calculation will be finalised during checkout.

Rent or Buy article

Get time limited or full article access on ReadCube.

from \$8.99

[Rent or Buy](#)

All prices are NET prices.

Additional access options:

- [Log in](#)
- [Learn about institutional subscriptions](#)

Nature **599**, 379-380 (2021)

doi: <https://doi.org/10.1038/d41586-021-03385-7>

References

1. 1.

Goodwin, C. A. P. *et al.* *Nature* **599**, 421–424 (2021).

2. 2.

Morss, L. R., Edelstein, N. M. & Fuger, J. (eds) *The Chemistry of the Actinide and Transactinide Elements* 4th edn, Vols 1–6 (Springer, 2011).

3. 3.

Streitwieser, A. Jr & Mueller-Westerhoff, U. *J. Am. Chem. Soc.* **90**, 7364 (1968).

4. 4.

Minasian, S. G. *et al. Chem. Sci.* **5**, 351–359 (2014).

5. 5.

Windorff, C. J. *et al. J. Am. Chem. Soc.* **139**, 3970–3973 (2017).

6. 6.

Apostolidis, C. *et al. Angew. Chem. Int. Edn* **56**, 5066–5070 (2017).

7. 7.

Goodwin, C. A. P. *et al. Angew. Chem. Int. Edn* **58**, 11695–11699 (2019).

8. 8.

Laubereau, P. G. & Burns, J. H. *Inorg. Chem.* **9**, 1091–1095 (1970).

9. 9.

Polinski, M. J. *et al. Nature Chem.* **6**, 387–392 (2014).

10. 10.

Cary, S. K. *et al. Nature Commun.* **6**, 6827 (2015).

This article was downloaded by **calibre** from <https://www.nature.com/articles/d41586-021-03385-7>

| [Section menu](#) | [Main menu](#) |

- NEWS AND VIEWS
- 06 October 2021

Role of bile acids and gut bacteria in healthy ageing of centenarians

A study in humans indicates that certain bile acids that are produced by bacteria and commonly found in people over 100 boost gut health and protect against infection. These findings shed light on the contributors to healthy ageing.

- [Bipin Rimal](#)⁰ &
- [Andrew D. Patterson](#)¹

As we age, we are more likely to develop ageing-related illnesses such as cardiovascular disease, cancer and type 2 diabetes. Yet centenarians — people who are more than 100 years old — are less susceptible to such conditions than are ageing individuals who do not live as long^{1,2} (see go.nature.com/3csogm6). For some centenarians, answers to this conundrum might lie in the gut. [Writing in Nature](#), Sato *et al.*³ identify a previously unknown connection between healthy ageing in humans over the age of 100, and gut bacteria and bile acids (Fig. 1).

Access options

Subscribe to Journal

Get full journal access for 1 year

\$199.00

only \$3.90 per issue

Subscribe

All prices are NET prices.
VAT will be added later in the checkout.
Tax calculation will be finalised during checkout.

Rent or Buy article

Get time limited or full article access on ReadCube.

from \$8.99

Rent or Buy

All prices are NET prices.

Additional access options:

- [Log in](#)
- [Learn about institutional subscriptions](#)

Nature **599**, 380–381 (2021)

doi: <https://doi.org/10.1038/d41586-021-02196-0>

References

1. 1.

Hirata, T. *et al.* *Nature Commun.* **11**, 3820 (2020).

2. 2.

Sebastiani, P. *et al.* *Aging* **5**, 653–661 (2013).

3. 3.

Sato, Y. *et al.* *Nature* **599**, 458–464 (2021).

4. 4.

Hofmann, A. F. & Hagey, L. R. *J. Lipid Res.* **55**, 1553–1595 (2014).

5. 5.

Quinn, R. A. *et al. Nature* **579**, 123–129 (2020).

6. 6.

Devlin, A. S. & Fischbach, M. A. *Nature Chem. Biol.* **11**, 685–690 (2015).

This article was downloaded by **calibre** from <https://www.nature.com/articles/d41586-021-02196-0>

| [Section menu](#) | [Main menu](#) |

- Review Article
- [Published: 17 November 2021](#)

Excitons and emergent quantum phenomena in stacked 2D semiconductors

- [Nathan P. Wilson^{1,2,3}](#),
- [Wang Yao ORCID: orcid.org/0000-0003-2883-4528^{4,5}](#),
- [Jie Shan ORCID: orcid.org/0000-0003-1270-9386⁶](#) &
- [Xiaodong Xu ORCID: orcid.org/0000-0003-0348-2095^{1,7}](#)

Nature volume **599**, pages 383–392 (2021)

- 1687 Accesses
- 11 Altmetric
- [Metrics details](#)

Subjects

- [Electronic properties and materials](#)
- [Two-dimensional materials](#)

Abstract

The design and control of material interfaces is a foundational approach to realize technologically useful effects and engineer material properties. This is especially true for two-dimensional (2D) materials, where van der Waals stacking allows disparate materials to be freely stacked together to form

highly customizable interfaces. This has underpinned a recent wave of discoveries based on excitons in stacked double layers of transition metal dichalcogenides (TMDs), the archetypal family of 2D semiconductors. In such double-layer structures, the elegant interplay of charge, spin and moiré superlattice structure with many-body effects gives rise to diverse excitonic phenomena and correlated physics. Here we review some of the recent discoveries that highlight the versatility of TMD double layers to explore quantum optics and many-body effects. We identify outstanding challenges in the field and present a roadmap for unlocking the full potential of excitonic physics in TMD double layers and beyond, such as incorporating newly discovered ferroelectric and magnetic materials to engineer symmetries and add a new level of control to these remarkable engineered materials.

Access options

Subscribe to Journal

Get full journal access for 1 year

\$199.00

only \$3.90 per issue

[Subscribe](#)

All prices are NET prices.

VAT will be added later in the checkout.

Tax calculation will be finalised during checkout.

Rent or Buy article

Get time limited or full article access on ReadCube.

from \$8.99

[Rent or Buy](#)

All prices are NET prices.

Additional access options:

- [Log in](#)
- [Access through your institution](#)
- [Learn about institutional subscriptions](#)

Fig. 1: Excitons in TMD double layers.



Fig. 2: Moiré excitons.

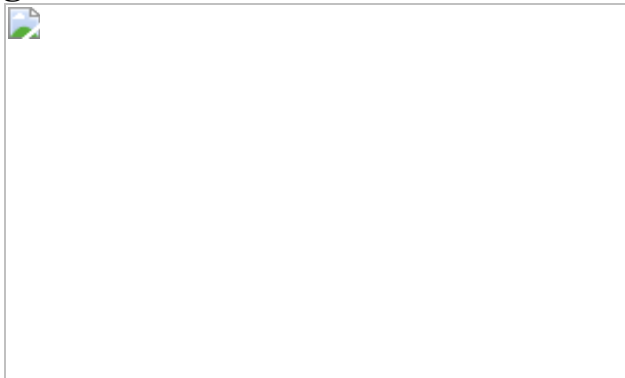


Fig. 3: Many-body physics of IX.

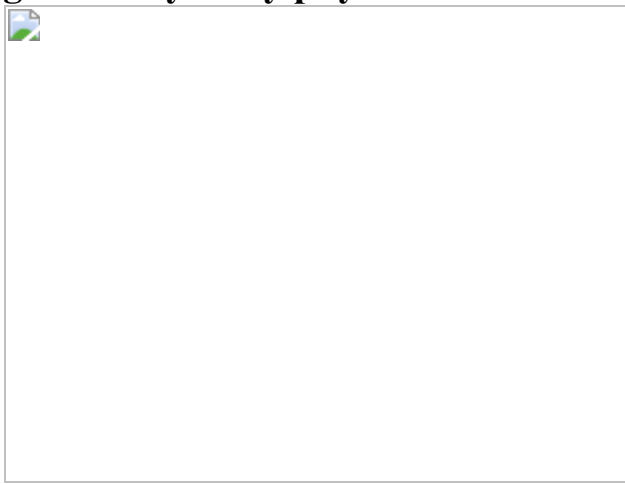


Fig. 4: Correlated states in superlattices.

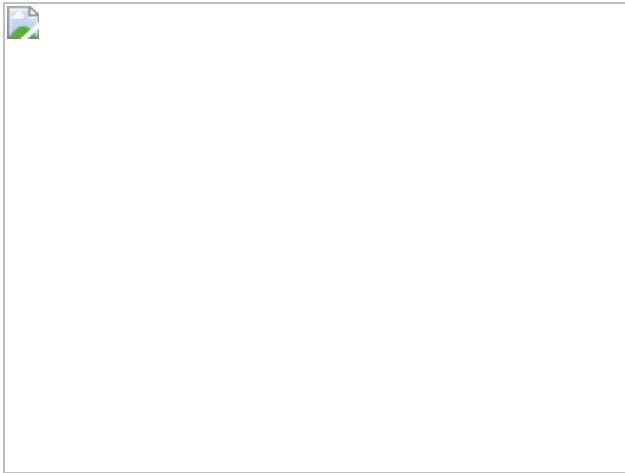
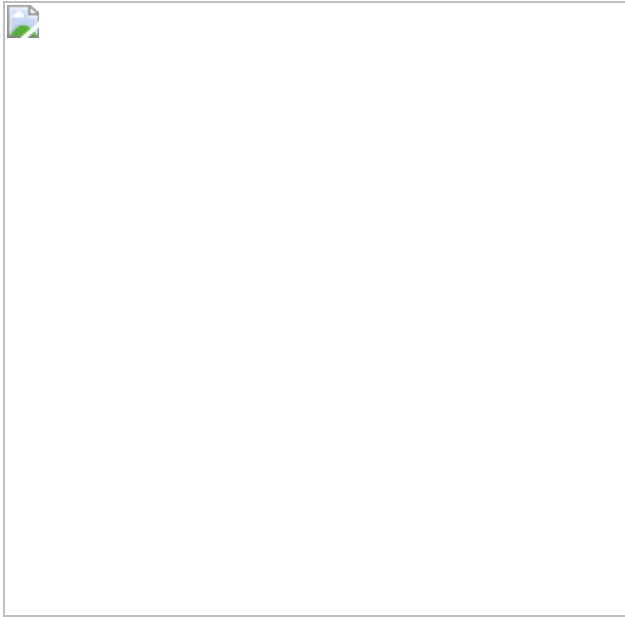


Fig. 5: Control of superlattice geometry.



References

1. 1.

Butov, L. V., Zrenner, A., Abstreiter, G., Böhm, G. & Weimann, G. Condensation of indirect excitons in coupled AlAs/GaAs quantum wells. *Phys. Rev. Lett.* **73**, 304–307 (1994).

2. 2.

Zhu, X., Littlewood, P. B., Hybertsen, M. S. & Rice, T. M. Exciton condensate in semiconductor quantum well structures. *Phys. Rev. Lett.* **74**, 1633–1636 (1995).

3. 3.

Eisenstein, J. P. & MacDonald, A. H. Bose–Einstein condensation of excitons in bilayer electron systems. *Nature* **432**, 691–694 (2004).

4. 4.

Kleemans, N. A. J. M. et al. Many-body exciton states in self-assembled quantum dots coupled to a Fermi sea. *Nat. Phys.* **6**, 534–538 (2010).

5. 5.

Byrnes, T., Recher, P. & Yamamoto, Y. Mott transitions of exciton polaritons and indirect excitons in a periodic potential. *Phys. Rev. B* **81**, 205312 (2010).

6. 6.

Biolatti, E., Iotti, R. C., Zanardi, P. & Rossi, F. Quantum information processing with semiconductor macroatoms. *Phys. Rev. Lett.* **85**, 5647–5650 (2000).

7. 7.

Chen, P., Piermarocchi, C. & Sham, L. J. Control of exciton dynamics in nanodots for quantum operations. *Phys. Rev. Lett.* **87**, 067401 (2001).

8. 8.

De Rinaldis, S. et al. Intrinsic exciton-exciton coupling in GaN-based quantum dots: Application to solid-state quantum computing. *Phys. Rev. B* **65**, 081309(R) (2002).

9. 9.

Aharonovich, I., Englund, D. & Toth, M. Solid-state single-photon emitters. *Nat. Photon.* **10**, 631–641 (2016).

10. 10.

Ghosh, S. & Liew, T. C. H. Quantum computing with exciton-polariton condensates. *npj Quant. Inf.* **6**, 16 (2020).

11. 11.

Butov, L. V., Gossard, A. C. & Chemla, D. S. Macroscopically ordered state in an exciton system. *Nature* **418**, 751–754 (2002).

12. 12.

High, A. A. et al. Spontaneous coherence in a cold exciton gas. *Nature* **483**, 584–588 (2012).

13. 13.

Lai, C. W., Zoch, J., Gossard, A. C. & Chemla, D. S. Phase diagram of degenerate exciton systems. *Science* **303**, 503–506 (2004).

14. 14.

Remeika, M., Fogler, M. M., Butov, L. V., Hanson, M. & Gossard, A. C. Two-dimensional electrostatic lattices for indirect excitons. *Appl. Phys. Lett.* **100**, 061103 (2012).

15. 15.

Remeika, M. et al. Measurement of exciton correlations using electrostatic lattices. *Phys. Rev. B* **92**, 115311 (2015).

16. 16.

Leonard, J. R. et al. Pancharatnam-Berry phase in condensate of indirect excitons. *Nat. Commun.* **9**, 2158 (2018).

17. 17.

Smolka, S. et al. Cavity quantum electrodynamics with many-body states of a two-dimensional electron gas. *Science* **346**, 332–335 (2014).

18. 18.

Edelberg, D. et al. Approaching the intrinsic limit in transition metal diselenides via point defect control. *Nano Lett.* **19**, 4371–4379 (2019).

19. 19.

Ivanov, A. L., Haug, H. & Keldysh, L. V. Optics of excitonic molecules in semiconductors and semiconductor microstructures. *Phys. Rep.* **296**, 237–336 (1998).

20. 20.

Van Tuan, D., Yang, M. & Dery, H. Coulomb interaction in monolayer transition-metal dichalcogenides. *Phys. Rev. B* **98**, 125308 (2018).

21. 21.

Mak, K. F., Lee, C., Hone, J., Shan, J. & Heinz, T. F. Atomically thin MoS₂: a new direct-gap semiconductor. *Phys. Rev. Lett.* **105**, 136805 (2010).

22. 22.

He, K. et al. Tightly bound excitons in monolayer WSe₂. *Phys. Rev. Lett.* **113**, 026803 (2014).

23. 23.

Wang, G. et al. Giant enhancement of the optical second-harmonic emission of WSe₂ monolayers by laser excitation at exciton resonances. *Phys. Rev. Lett.* **114**, 097403 (2015).

24. 24.

Stier, A. V., McCreary, K. M., Jonker, B. T., Kono, J. & Crooker, S. A. Exciton diamagnetic shifts and valley Zeeman effects in monolayer WS₂ and MoS₂ to 65 tesla. *Nat. Commun.* **7**, 10643 (2016).

25. 25.

Berkelbach, T. C., Hybertsen, M. S. & Reichman, D. R. Theory of neutral and charged excitons in monolayer transition metal dichalcogenides. *Phys. Rev. B* **88**, 045318 (2013).

26. 26.

Xiao, D., Liu, G.-B., Feng, W., Xu, X. & Yao, W. Coupled spin and valley physics in monolayers of MoS₂ and other group-VI dichalcogenides. *Phys. Rev. Lett.* **108**, 196802 (2012).

27. 27.

Xiao, D. et al. Coupled spin and valley physics in monolayers of MoS₂ and other group-VI dichalcogenides. *Phys. Rev. Lett.* **108**, 196802 (2012).

28. 28.

Mak, K. F., He, K., Shan, J. & Heinz, T. F. Control of valley polarization in monolayer MoS₂ by optical helicity. *Nat. Nanotechnol.* **7**, 494–498 (2012).

29. 29.

Jones, A. M. et al. Optical generation of excitonic valley coherence in monolayer WSe₂. *Nat. Nanotechnol.* **8**, 634–638 (2013).

30. 30.

Xu, X., Yao, W., Xiao, D. & Heinz, T. F. Spin and pseudospins in layered transition metal dichalcogenides. *Nat. Phys.* **10**, 343–350 (2014).

31. 31.

Mak, K. F. et al. Tightly bound trions in monolayer MoS₂. *Nat. Mater.* **12**, 207–211 (2013).

32. 32.

Ross, J. S. et al. Electrically tunable excitonic light-emitting diodes based on monolayer WSe₂ p–n junctions. *Nat. Nanotechnol.* **9**, 268–272 (2014).

33. 33.

Raja, A. et al. Coulomb engineering of the bandgap and excitons in two-dimensional materials. *Nat. Commun.* **8**, 15251 (2017).

34. 34.

Chaves, A. et al. Bandgap engineering of two-dimensional semiconductor materials. *npj 2D Mater. Appl.* **4**, 29 (2020).

35. 35.

Peimyoo, N. et al. Engineering dielectric screening for potential-well arrays of excitons in 2D materials. *ACS Appl. Mater. Interfaces* **12**, 55134–55140 (2020).

36. 36.

Sidler, M. et al. Fermi polaron-polaritons in charge-tunable atomically thin semiconductors. *Nat. Phys.* **13**, 255–261 (2017).

37. 37.

Efimkin, D. K. & MacDonald, A. H. Many-body theory of trion absorption features in two-dimensional semiconductors. *Phys. Rev. B* **95**, 035417 (2017).

38. 38.

Keldysh, L. V. Coulomb interaction in thin semiconductor and semimetal films. *J. Exp. Theor. Phys.* **29**, 658–661 (1979).

39. 39.

Chernikov, A. et al. Exciton binding energy and nonhydrogenic Rydberg series in monolayer WS₂. *Phys. Rev. Lett.* **113**, 076802 (2014).

40. 40.

Stier, A. V., Wilson, N. P., Clark, G., Xu, X. & Crooker, S. A. Probing the influence of dielectric environment on excitons in monolayer WSe₂: insight from high magnetic fields. *Nano Lett.* **16**, 7054–7060 (2016).

41. 41.

Stier, A. V. et al. Magneto optics of exciton Rydberg states in a monolayer semiconductor. *Phys. Rev. Lett.* **120**, 057405 (2018).

42. 42.

Raja, A. et al. Dielectric disorder in two-dimensional materials. *Nat. Nanotechnol.* **14**, 832–837 (2019).

43. 43.

Xu, Y. et al. Correlated insulating states at fractional fillings of moiré superlattices. *Nature* **587**, 214–218 (2020).

44. 44.

Novoselov, K. S. et al. Electric field in atomically thin carbon films. *Science* **306**, 666–669 (2004).

45. 45.

Kim, K. et al. Van der Waals Heterostructures with High Accuracy Rotational Alignment. *Nano Lett.* **16**, 1989–1995 (2016).

46. 46.

Frisenda, R. et al. Recent progress in the assembly of nanodevices and van der Waals heterostructures by deterministic placement of 2D materials. *Chem. Soc. Rev.* **47**, 53–68 (2018).

47. 47.

Kinoshita, K. et al. Dry release transfer of graphene and few-layer h-BN by utilizing thermoplasticity of polypropylene carbonate. *npj 2D Mater. Appl.* **3**, 22 (2019).

48. 48.

Moon, P. & Koshino, M. Energy spectrum and quantum Hall effect in twisted bilayer graphene. *Phys. Rev. B* **85**, 195458 (2012).

49. 49.

Dean, C. R. et al. Hofstadter’s butterfly and the fractal quantum Hall effect in moiré superlattices. *Nature* **497**, 598–602 (2013).

50. 50.

Sharpe, A. L. et al. Emergent ferromagnetism near three-quarters filling in twisted bilayer graphene. *Science* **365**, 605–608 (2019).

51. 51.

Cao, Y. et al. Unconventional superconductivity in magic-angle graphene superlattices. *Nature* **556**, 43–50 (2018).

52. 52.

Serlin, M. et al. Intrinsic quantized anomalous Hall effect in a moiré heterostructure. *Science* **367**, 900–903 (2020).

53. 53.

Chen, G. et al. Tunable correlated Chern insulator and ferromagnetism in a moiré superlattice. *Nature* **579**, 56–61 (2020).

54. 54.

Seyler, K. L. et al. Signatures of moiré-trapped valley excitons in MoSe₂/WSe₂ heterobilayers. *Nature* **567**, 66–70 (2019).

Demonstration of quantum-dot-like PL from moiré IXs.

55. 55.

Jin, C. et al. Observation of moiré excitons in WSe₂/WS₂ heterostructure superlattices. *Nature* **567**, 76–80 (2019).

Demonstration of intralayer moiré excitons and moiré minibands through reflectance spectroscopy.

56. 56.

Tran, K. et al. Evidence for moiré excitons in van der Waals heterostructures. *Nature* **567**, 71–75 (2019).

57. 57.

Alexeev, E. M. et al. Resonantly hybridized excitons in moiré superlattices in van der Waals heterostructures. *Nature* **567**, 81–86 (2019). **Demonstration and analysis of resonant interlayer hybridization in twisted TMD heterobilayers.**

58. 58.

Tang, Y. et al. Simulation of Hubbard model physics in WSe₂/WS₂ moiré superlattices. *Nature* **579**, 353–358 (2020). **Realization of Hubbard-model correlated antiferromagnetism in the moiré pattern of a TMD double layer.**

59. 59.

Wang, L. et al. Correlated electronic phases in twisted bilayer transition metal dichalcogenides. *Nat. Mater.* **19**, 861–866 (2020).

60. 60.

Regan, E. C. et al. Mott and generalized Wigner crystal states in WSe₂/WS₂ moiré superlattices. *Nature* **579**, 359–363 (2020).
Realization of generalized Wigner crystals in TMD heterobilayers.

61. 61.

Shimazaki, Y. et al. Strongly correlated electrons and hybrid excitons in a moiré heterostructure. *Nature* **580**, 472–477 (2020).
Demonstration of hybrid inter/intralayer excitons and moiré excitons in a TMD homobilayer.

62. 62.

Wu, F. C., Xue, F. & Macdonald, A. H. Theory of two-dimensional spatially indirect equilibrium exciton condensates. *Phys. Rev. B* **92**, 165121 (2015).

63. 63.

Fogler, M. M., Butov, L. V. & Novoselov, K. S. High-temperature superfluidity with indirect excitons in van der Waals heterostructures. *Nat. Commun.* **5**, 4555 (2014).

64. 64.

Liu, K. et al. Evolution of interlayer coupling in twisted molybdenum disulfide bilayers. *Nat. Commun.* **5**, 4966 (2014).

65. 65.

Calman, E. V. et al. Indirect excitons in van der Waals heterostructures at room temperature. *Nat. Commun.* **9**, 1895 (2018).

66. 66.

Matthews, J. W. & Blakeslee, A. E. Defects in epitaxial multilayers: I. Misfit dislocations. *J. Cryst. Growth* **27**, 118–125 (1974).

67. 67.

Matthews, J. W. & Blakeslee, A. E. Defects in epitaxial multilayers. II. Dislocation pile-ups, threading dislocations, slip lines and cracks. *J. Cryst. Growth* **29**, 273–280 (1975).

68. 68.

Matthews, J. W. & Blakeslee, A. E. Defects in epitaxial multilayers. III. Preparation of almost perfect multilayers. *J. Cryst. Growth* **32**, 265–273 (1976).

69. 69.

Rivera, P. et al. Observation of long-lived interlayer excitons in monolayer MoSe₂–WSe₂ heterostructures. *Nat. Commun.* **6**, 6242 (2015). **Demonstration of IX PL and dynamics in a TMD heterobilayer.**

70. 70.

Heo, H. et al. Interlayer orientation-dependent light absorption and emission in monolayer semiconductor stacks. *Nat. Commun.* **6**, 7372 (2015).

71. 71.

Latini, S., Winther, K. T., Olsen, T. & Thygesen, K. S. Interlayer excitons and band alignment in MoS₂/hBN/WSe₂ van der Waals heterostructures. *Nano Lett.* **17**, 938–945 (2016).

72. 72.

Jauregui, L. A. et al. Electrical control of interlayer exciton dynamics in atomically thin heterostructures. *Science* **366**, 870–875 (2019).

Demonstration of Stark effect and doping control of IX species, their spectra and their dynamics.

73. 73.

Liu, G. B., Xiao, D., Yao, Y., Xu, X. & Yao, W. Electronic structures and theoretical modelling of two-dimensional group-VIB transition metal dichalcogenides. *Chem. Soc. Rev.* **44**, 2643–2663 (2015).

74. 74.

Ross, J. S. et al. Interlayer exciton optoelectronics in a 2D heterostructure p-n junction. *Nano Lett.* **17**, 638–643 (2017).

75. 75.

Kim, J. et al. Observation of ultralong valley lifetime in WSe₂/MoS₂ heterostructures. *Sci. Adv.* **3**, e1700518 (2017).

76. 76.

Miller, B. et al. Long-lived direct and indirect interlayer excitons in van der Waals heterostructures. *Nano Lett.* **17**, 5229–5237 (2017).

77. 77.

Rivera, P. et al. Valley-polarized exciton dynamics in a 2D semiconductor heterostructure. *Science* **351**, 688–691 (2016). **Study of many-body interactions of valley-polarized IX populations.**

78. 78.

Jin, C. et al. Imaging of pure spin-valley diffusion current in WS₂-WSe₂ heterostructures. *Science* **360**, 893–896 (2018).

79. 79.

Zhu, H. et al. Interfacial charge transfer circumventing momentum mismatch at two-dimensional van der Waals heterojunctions. *Nano Lett.* **17**, 3591–3598 (2017).

80. 80.

Tang, Y. et al. Tuning layer-hybridized moiré excitons by the quantum-confined Stark effect. *Nat. Nanotechnol.* **2**, 52–57 (2020).

81. 81.

Ruiz-Tijerina, D. A. & Fal'ko, V. I. Interlayer hybridization and moiré superlattice minibands for electrons and excitons in heterobilayers of transition-metal dichalcogenides. *Phys. Rev. B* **99**, 125424 (2019).

82. 82.

Zhang, L. et al. Twist-angle dependence of moiré excitons in WS₂/MoSe₂ heterobilayers. *Nat. Commun.* **11**, 5888 (2020).

83. 83.

Luican, A. et al. Single-layer behavior and its breakdown in twisted graphene layers. *Phys. Rev. Lett.* **106**, 126802 (2011).

84. 84.

Yu, H. et al. Moiré excitons: from programmable quantum emitter arrays to spin-orbit-coupled artificial lattices. *Sci. Adv.* **3**, e1701696 (2017). **Calculation of the properties of moiré excitons in TMD**

heterobilayers, and derivation of quantum-optical properties of moiré excitons.

85. 85.

Rosenberger, M. R. et al. Twist angle-dependent atomic reconstruction and moiré patterns in transition metal dichalcogenide heterostructures. *ACS Nano* **14**, 4550–4558 (2020).

86. 86.

Zhang, C. et al. Interlayer couplings, moiré patterns, and 2D electronic superlattices in MoS₂/WSe₂ hetero-bilayers. *Sci. Adv.* **3**, e1601459 (2017).

87. 87.

Woods, C. R. et al. Commensurate-incommensurate transition in graphene on hexagonal boron nitride. *Nat. Phys.* **10**, 451–456 (2014).

88. 88.

Flores, M., Cisternas, E., Correa, J. D. & Vargas, P. Moiré patterns on STM images of graphite induced by rotations of surface and subsurface layers. *Chem. Phys.* **423**, 49–54 (2013).

89. 89.

Zhang, Z. et al. Flat bands in twisted bilayer transition metal dichalcogenides. *Nat. Phys.* **16**, 1093–1096 (2020).

90. 90.

Lee, K. et al. Ultrahigh-resolution scanning microwave impedance microscopy of moiré lattices and superstructures. *Sci. Adv.* **6**, eabd1919 (2020).

91. 91.

McGilly, L. J. et al. Visualization of moiré superlattices. *Nat. Nanotechnol.* **15**, 580–584 (2020).

92. 92.

Van Der Donck, M. & Peeters, F. M. Interlayer excitons in transition metal dichalcogenide heterostructures. *Phys. Rev. B* **98**, 115104 (2018).

93. 93.

Jung, J., Raoux, A., Qiao, Z. & Macdonald, A. H. Ab initio theory of moiré superlattice bands in layered two-dimensional materials. *Phys. Rev. B* **89**, 205414 (2014).

94. 94.

Guinea, F. & Walet, N. R. Continuum models for twisted bilayer graphene: effect of lattice deformation and hopping parameters. *Phys. Rev. B* **99**, 205134 (2019).

95. 95.

Wu, F., Lovorn, T., Tutuc, E. & MacDonald, A. H. Hubbard model physics in transition metal dichalcogenide moiré bands. *Phys. Rev. Lett.* **121**, 026402 (2018).

96. 96.

Yu, H., Wang, Y., Tong, Q., Xu, X. & Yao, W. Anomalous light cones and valley optical selection rules of interlayer excitons in twisted heterobilayers. *Phys. Rev. Lett.* **115**, 187002 (2015).

97. 97.

Baek, H. et al. Highly energy-tunable quantum light from moiré-trapped excitons. *Sci. Adv.* **6**, 8526–8537 (2020). **Demonstration of single photon emission from moiré excitons and electric-field tunability of moiré excitons.**

98. 98.

Mucha-Kruczyński, M., Wallbank, J. R. & Fal’Ko, V. I. Moiré miniband features in the angle-resolved photoemission spectra of graphene/hBN heterostructures. *Phys. Rev. B* **93**, 085409 (2016).

99. 99.

Xie, S. et al. Direct observation of distinct minibands in moiré superlattices. Preprint at <https://arxiv.org/abs/2010.07806> (2020).

100. 100.

Brem, S. et al. Hybridized intervalley moiré excitons and flat bands in twisted WSe₂ bilayers. *Nanoscale* **12**, 11088–11094 (2020).

101. 101.

Wallbank, J. R. et al. Excess resistivity in graphene superlattices caused by umklapp electron–electron scattering. *Nat. Phys.* **15**, 32–36 (2019).

102. 102.

Shahnazaryan, V., Iorsh, I., Shelykh, I. A. & Kyriienko, O. Exciton-exciton interaction in transition-metal dichalcogenide monolayers. *Phys. Rev. B* **96**, 115409 (2017).

103. 103.

Wang, Z. et al. Evidence of high-temperature exciton condensation in two-dimensional atomic double layers. *Nature* **574**, 76–80 (2019).

Study of a degenerate gas of electrically pumped IX through electroluminescence.

104. 104.

Sigl, L. et al. Signatures of a degenerate many-body state of interlayer excitons in a van der Waals heterostack. *Phys. Rev. Res.* **2**, 042044

(2020).

105. 105.

Zhu, Q., Tu, M. W. Y., Tong, Q. & Yao, W. Gate tuning from exciton superfluid to quantum anomalous Hall in van der Waals heterobilayer. *Sci. Adv.* **5**, eaau6120 (2019).

106. 106.

Paik, E. Y. et al. Interlayer exciton laser of extended spatial coherence in atomically thin heterostructures. *Nature* **576**, 80–84 (2019).

107. 107.

Liu, Y. et al. Room temperature nanocavity laser with interlayer excitons in 2D heterostructures. *Sci. Adv.* **5**, eaav4506 (2019).

108. 108.

Latini, S., Ronca, E., De Giovannini, U., Hübener, H. & Rubio, A. Cavity control of excitons in two-dimensional materials. *Nano Lett.* **19**, 3473–3479 (2019).

109. 109.

Zhang, L. et al. Van der Waals heterostructure polaritons with moiré-induced nonlinearity. *Nature* **591**, 61–65 (2021).

110. 110.

Dagotto, E. & Riera, J. Superconductivity in the two-dimensional t-J model. *Phys. Rev. B* **46**, 12084(R) (1992).

111. 111.

Greiner, M., Mandel, O., Esslinger, T., Hänsch, T. W. & Bloch, I. Quantum phase transition from a superfluid to a Mott insulator in a gas of ultracold atoms. *Nature* **415**, 39–44 (2002).

112. 112.

Liu, E. et al. Signatures of moiré trions in WSe₂/MoSe₂ heterobilayers. *Nature* **594**, 46–50 (2021).

113. 113.

Huang, X. et al. Correlated insulating states at fractional fillings of the WS₂/WSe₂ moiré lattice. *Nat. Phys.* **17**, 715–719 (2021).

114. 114.

Nagler, P. et al. Interlayer exciton dynamics in a dichalcogenide monolayer heterostructure. *2D Mater.* **4**, 025112 (2017).

115. 115.

Böning, J., Filinov, A. & Bonitz, M. Crystallization of an exciton superfluid. *Phys. Rev. B* **84**, 75130 (2011).

116. 116.

Suris, R. A. Gas-crystal phase transition in a 2D dipolar exciton system. *J. Exp. Theor. Phys.* **122**, 602–607 (2016).

117. 117.

Padhi, B., Chitra, R. & Phillips, P. W. Generalized Wigner crystallization in moiré materials. *Phys. Rev. B* **103**, 125146 (2021).

118. 118.

Jin, C. et al. Stripe phases in WSe₂/WS₂ moiré superlattices. *Nat. Mater.* **20**, 940–944 (2021)

119. 119.

Wang, F. et al. Imaging generalized Wigner crystal states in a WSe₂/WS₂ moiré superlattice. Preprint at <https://doi.org/10.21203/rs.3.rs-390032/v1> (2021).

120. 120.

Slobodkin, Y. et al. Quantum phase transitions of trilayer excitons in atomically thin heterostructures. *Phys. Rev. Lett.* **125**, 255301 (2020).

121. 121.

Tong, Q., Chen, M., Xiao, F., Yu, H. & Yao, W. Interferences of electrostatic moiré potentials and bichromatic superlattices of electrons and excitons in transition metal dichalcogenides. *2D Mater.* **8**, 025007 (2021).

122. 122.

Dicke, R. H. Coherence in spontaneous radiation processes. *Phys. Rev.* **93**, 99–110 (1954).

123. 123.

Yu, H. & Yao, W. Luminescence anomaly of dipolar valley excitons in homobilayer semiconductor moiré superlattices. *Phys. Rev. X* **11**, 021042 (2021).

124. 124.

Rezai, M., Wrachtrup, J. & Gerhardt, I. Polarization-entangled photon pairs from a single molecule. *Optica* **6**, 34–40 (2019).

125. 125.

Lezama, I. G. et al. Indirect-to-direct band gap crossover in few-layer MoTe₂. *Nano Lett.* **15**, 2336–2342 (2015).

126. 126.

Ribeiro-Palau, R. et al. Twistable electronics with dynamically rotatable heterostructures. *Science* **361**, 690–693 (2018). **Realization of in situ control of twist angle in a vdW heterostructure.**

127. 127.

Yao, K. et al. Enhanced tunable second harmonic generation from twistable interfaces and vertical superlattices in boron nitride homostructures. *Sci. Adv.* **7**, eabe8691 (2021).

128. 128.

Bai, Y. et al. Excitons in strain-induced one-dimensional moiré potentials at transition metal dichalcogenide heterojunctions. *Nat. Mater.* **19**, 1068–1073 (2020).

129. 129.

Song, T. et al. Switching 2D magnetic states via pressure tuning of layer stacking. *Nat. Mater.* **18**, 1298–1302 (2019).

130. 130.

Yankowitz, M. et al. Tuning superconductivity in twisted bilayer graphene. *Science* **363**, 1059–1064 (2019).

131. 131.

Xia, J. et al. Strong coupling and pressure engineering in WSe₂–MoSe₂ heterobilayers. *Nat. Phys.* **17**, 92–98 (2020).

132. 132.

Woods, C. R. et al. Charge-polarized interfacial superlattices in marginally twisted hexagonal boron nitride. *Nat. Commun.* **12**, 347 (2021).

133. 133.

Stern, M. V. et al. Interfacial ferroelectricity by van der Waals sliding. *Science* **372**, 1462–1466 (2021).

134. 134.

Yasuda, K., Wang, X., Watanabe, K., Taniguchi, T. & Jarillo-Herrero, P. Stacking-engineered ferroelectricity in bilayer boron nitride. *Science* **372**, 1458–1462 (2021).

135. 135.

Zhao, P., Xiao, C. & Yao, W. Universal superlattice potential for 2D materials from twisted interface inside h-BN substrate. *npj 2D Mater. Appl.* **5**, 38 (2021).

136. 136.

Weston, A. et al. Atomic reconstruction in twisted bilayers of transition metal dichalcogenides. *Nat. Nanotechnol.* **15**, 592–597 (2020).

137. 137.

Enaldiev, V. V., Ferreira, F., Magorrian, S. J. & Fal'ko, V. I. Piezoelectric networks and ferroelectric moiré superlattice domains in twistronic WS₂/MoS₂ and WSe₂/MoSe₂ bilayers. *2D Mater.* **8**, 025030 (2021).

138. 138.

Sung, J. et al. Broken mirror symmetry in excitonic response of reconstructed domains in twisted MoSe₂/MoSe₂ bilayers. *Nat. Nanotechnol.* **15**, 750–754 (2020).

139. 139.

Zhong, D. et al. Van der Waals engineering of ferromagnetic semiconductor heterostructures for spin and valleytronics. *Sci. Adv.* **3**,

e1603113 (2017).

140. 140.

Sivadas, N., Okamoto, S., Xu, X., Fennie, C. J. & Xiao, D. Stacking-dependent magnetism in bilayer CrI₃. *Nano Lett.* **18**, 7658–7664 (2018).

141. 141.

Tong, Q., Liu, F., Xiao, J. & Yao, W. Skyrmions in the Moiré of van der Waals 2D Magnets. *Nano Lett.* **18**, 7194–7199 (2018).

142. 142.

Xu, Y. et al. Emergence of a noncollinear magnetic state in twisted bilayer CrI₃. Preprint at <https://arxiv.org/abs/2103.09850> (2021).

143. 143.

Göser, O., Paul, W. & Kahle, H. G. Magnetic properties of CrSBr. *J. Magn. Magn. Mater.* **92**, 129–136 (1990).

144. 144.

Telford, E. J. et al. Layered antiferromagnetism induces large negative magnetoresistance in the van der Waals semiconductor CrSBr. *Adv. Mater.* **32**, 2003240 (2020).

145. 145.

Lee, K. et al. Magnetic order and symmetry in the 2d semiconductor CrSBr. *Nano Lett.* **21**, 3511–3517 (2021).

146. 146.

Wilson, N. P. et al. Interlayer electronic coupling on demand in a 2D magnetic semiconductor. *Nat. Mater.* <https://doi.org/10.1038/s41563-021-01070-8> (2021).

147. 147.

Wang, C. et al. A family of high-temperature ferromagnetic monolayers with locked spin-dichroism-mobility anisotropy: MnNX and CrCX (X = Cl, Br, I; C = S, Se, Te). *Sci. Bull.* **64**, 293–300 (2019).

148. 148.

Andersen, T. I. et al. Excitons in a reconstructed moiré potential in twisted WSe₂/WSe₂ homobilayers. *Nat. Mater.* **20**, 480–487 (2021).

149. 149.

Yoo, H. et al. Atomic and electronic reconstruction at the van der Waals interface in twisted bilayer graphene. *Nat. Mater.* **18**, 448–453 (2019).

150. 150.

Kennes, D. M. et al. Moiré heterostructures as a condensed-matter quantum simulator. *Nat. Phys.* **17**, 155–163 (2021).

151. 151.

Bloch, I. Ultracold quantum gases in optical lattices. *Nat. Phys.* **1**, 23–30 (2005).

152. 152.

Ismail, K., Chu, W., Yen, A., Antoniadis, D. A. & Smith, H. I. Negative transconductance and negative differential resistance in a grid-gate modulation-doped field-effect transistor. *Appl. Phys. Lett.* **54**, 460–462 (1989).

153. 153.

Forsythe, C. et al. Band structure engineering of 2D materials using patterned dielectric superlattices. *Nat. Nanotechnol.* **13**, 566–571 (2018).

154. 154.

Xu, Y. et al. Creation of moiré bands in a monolayer semiconductor by spatially periodic dielectric screening. *Nat. Mater.* **20**, 645–649 (2021).

155. 155.

Shanks, D. N. et al. Nanoscale trapping of interlayer excitons in a 2D semiconductor heterostructure. *Nano Lett.* **21**, 5641–5647 (2021).

Acknowledgements

N.P.W. would like to thank J. J. Finley for helpful discussions. X.X. and N.P.W. acknowledge support by the US Department of Energy, Office of Science, Basic Energy Sciences, under award number DE-SC0018171.

N.P.W. also acknowledges support from the Deutsche Forschungsgemeinschaft (DFG, German Research Foundation) under Germany’s Excellence Strategy—EXC-2111—390814868. W.Y. acknowledges support by the Croucher Foundation (Croucher Senior Research Fellowship), and the Research Grants Council of Hong Kong (AoE/P-701/20). J.S. acknowledges support by the US Department of Energy (DOE), Office of Science, Basic Energy Sciences (BES), under award number DE-SC0019481.

Author information

Affiliations

1. Department of Physics, University of Washington, Seattle, WA, USA

Nathan P. Wilson & Xiaodong Xu

2. Walter Schottky Institute, Technical University of Munich, Garching, Germany

Nathan P. Wilson

3. Munich Centre for Quantum Science and Technology, Munich,
Germany

Nathan P. Wilson

4. Department of Physics, University of Hong Kong, Hong Kong, China

Wang Yao

5. HKU-UCAS Joint Institute of Theoretical and Computational Physics
at Hong Kong, Hong Kong, China

Wang Yao

6. School of Applied and Engineering Physics, Cornell University,
Ithaca, NY, USA

Jie Shan

7. Department of Materials Science and Engineering, University of
Washington, Seattle, WA, USA

Xiaodong Xu

Contributions

X.X. and N.P.W. conceived this work. All authors contributed to the writing and preparation of the manuscript, supervised by X.X.

Corresponding author

Correspondence to [Xiaodong Xu](#).

Ethics declarations

Competing interests

The authors declare no competing interests.

Additional information

Peer review information *Nature* thanks Kristiaan De Greve, Tomasz Smolenski and the other, anonymous, reviewer(s) for their contribution to the peer review of this work.

Publisher's note Springer Nature remains neutral with regard to jurisdictional claims in published maps and institutional affiliations.

Rights and permissions

[Reprints and Permissions](#)

About this article

Cite this article

Wilson, N.P., Yao, W., Shan, J. *et al.* Excitons and emergent quantum phenomena in stacked 2D semiconductors. *Nature* **599**, 383–392 (2021). <https://doi.org/10.1038/s41586-021-03979-1>

- Received: 11 February 2021
- Accepted: 01 September 2021
- Published: 17 November 2021
- Issue Date: 18 November 2021
- DOI: <https://doi.org/10.1038/s41586-021-03979-1>

Share this article

Anyone you share the following link with will be able to read this content:

[Get shareable link](#)

Sorry, a shareable link is not currently available for this article.

[Copy to clipboard](#)

Provided by the Springer Nature SharedIt content-sharing initiative

This article was downloaded by **calibre** from <https://www.nature.com/articles/s41586-021-03979-1>

| [Section menu](#) | [Main menu](#) |

- Article
- [Published: 17 November 2021](#)

Observation of Stark many-body localization without disorder

- [W. Morong](#) [ORCID: orcid.org/0000-0003-4880-8159¹](#),
- [F. Liu](#) [ORCID: orcid.org/0000-0002-5690-4995¹](#),
- [P. Becker](#) [ORCID: orcid.org/0000-0002-7786-9447¹](#),
- [K. S. Collins](#) [ORCID: orcid.org/0000-0002-6159-8013¹](#),
- [L. Feng¹](#),
- [A. Kyprianidis¹](#),
- [G. Pagano²](#),
- [T. You¹](#),
- [A. V. Gorshkov](#) [ORCID: orcid.org/0000-0003-0509-3421¹](#) &
- [C. Monroe¹](#)

Nature volume 599, pages 393–398 (2021)

- 922 Accesses
- 3 Altmetric
- [Metrics details](#)

Subjects

- [Quantum simulation](#)
- [Statistical physics](#)
- [Thermodynamics](#)
- [Ultracold gases](#)

Abstract

Thermalization is a ubiquitous process of statistical physics, in which a physical system reaches an equilibrium state that is defined by a few global properties such as temperature. Even in isolated quantum many-body systems, limited to reversible dynamics, thermalization typically prevails¹. However, in these systems, there is another possibility: many-body localization (MBL) can result in preservation of a non-thermal state^{2,3}. While disorder has long been considered an essential ingredient for this phenomenon, recent theoretical work has suggested that a quantum many-body system with a spatially increasing field—but no disorder—can also exhibit MBL⁴, resulting in ‘Stark MBL’⁵. Here we realize Stark MBL in a trapped-ion quantum simulator and demonstrate its key properties: halting of thermalization and slow propagation of correlations. Tailoring the interactions between ionic spins in an effective field gradient, we directly observe their microscopic equilibration for a variety of initial states, and we apply single-site control to measure correlations between separate regions of the spin chain. Furthermore, by engineering a varying gradient, we create a disorder-free system with coexisting long-lived thermalized and non-thermal regions. The results demonstrate the unexpected generality of MBL, with implications about the fundamental requirements for thermalization and with potential uses in engineering long-lived non-equilibrium quantum matter.

Access options

Subscribe to Journal

Get full journal access for 1 year

\$199.00

only \$3.90 per issue

[Subscribe](#)

All prices are NET prices.
VAT will be added later in the checkout.
Tax calculation will be finalised during checkout.

Rent or Buy article

Get time limited or full article access on ReadCube.

from \$8.99

[Rent or Buy](#)

All prices are NET prices.

Additional access options:

- [Log in](#)
- [Access through your institution](#)
- [Learn about institutional subscriptions](#)

Fig. 1: Experimental setup.



Fig. 2: Non-thermalization from Stark MBL.

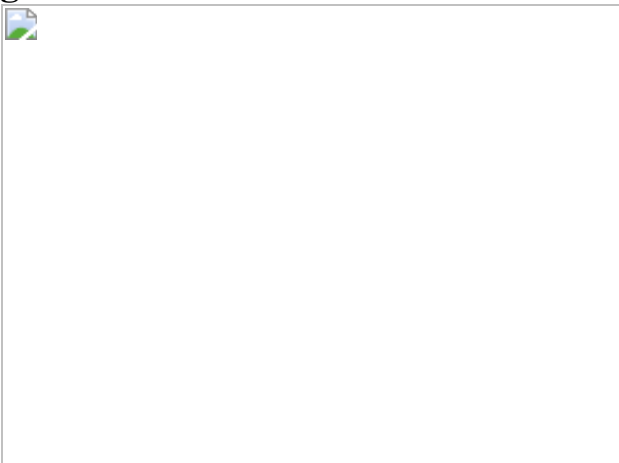


Fig. 3: DEER protocol.

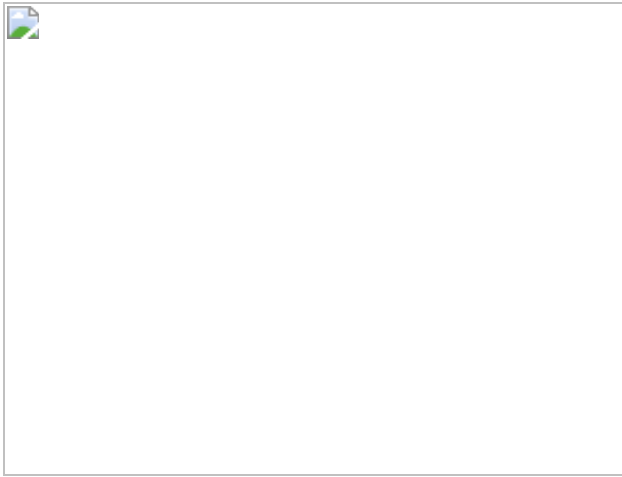
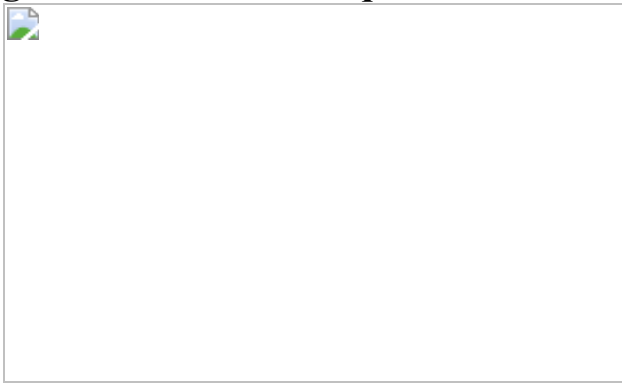


Fig. 4: Relaxation in a quadratic field.



Data availability

The data that support the findings of this study are available from the corresponding author upon request. [Source data](#) are provided with this paper.

Code availability

The code used for analyses is available from the corresponding author upon request.

References

1. 1.

Rigol, M., Dunjko, V. & Olshanii, M. Thermalization and its mechanism for generic isolated quantum systems. *Nature* **452**, 854–858 (2008).

2. 2.

Abanin, D. A., Altman, E., Bloch, I. & Serbyn, M. Colloquium: many-body localization, thermalization, and entanglement. *Rev. Mod. Phys.* **91**, 021001 (2019).

3. 3.

Nandkishore, R. & Huse, D. A. Many-body localization and thermalization in quantum statistical mechanics. *Annu. Rev. Condens. Matter Phys.* **6**, 15–38 (2015).

4. 4.

Van Nieuwenburg, E., Baum, Y. & Refael, G. From Bloch oscillations to many-body localization in clean interacting systems. *Proc. Natl Acad. Sci. USA* **116**, 9269–9274 (2019).

5. 5.

Schulz, M., Hooley, C. A., Moessner, R. & Pollmann, F. Stark many-body localization. *Phys. Rev. Lett.* **122**, 040606 (2019).

6. 6.

Anderson, P. W. Absence of diffusion in certain random lattices. *Phys. Rev.* **109**, 1492–1505 (1958).

7. 7.

Lee, P. A. Disordered electronic systems. *Rev. Mod. Phys.* **57**, 287–337 (1985).

8. 8.

Gornyi, I. V., Mirlin, A. D. & Polyakov, D. G. Interacting electrons in disordered wires: Anderson localization and low-T transport. *Phys. Rev. Lett.* **95**, 206603 (2005).

9. 9.

Basko, D. M., Aleiner, I. L. & Altshuler, B. L. Metal–insulator transition in a weakly interacting many-electron system with localized single-particle states. *Ann. Phys.* **321**, 1126–1205 (2006).

10. 10.

Serbyn, M., Papić, Z. & Abanin, D. A. Local conservation laws and the structure of the many-body localized states. *Phys. Rev. Lett.* **111**, 127201 (2013).

11. 11.

Huse, D. A., Nandkishore, R. & Oganesyan, V. Phenomenology of fully many-body-localized systems. *Phys. Rev. B* **90**, 174202 (2014).

12. 12.

Iyer, S., Oganesyan, V., Refael, G. & Huse, D. A. Many-body localization in a quasiperiodic system. *Phys. Rev. B* **87**, 134202 (2013).

13. 13.

Brenes, M., Dalmonte, M., Heyl, M. & Scardicchio, A. Many-body localization dynamics from gauge invariance. *Phys. Rev. Lett.* **120**, 030601 (2018).

14. 14.

Grover, T. & Fisher, M. P. A. Quantum disentangled liquids. *J. Stat. Mech: Theory Exp.* **2014**, P10010 (2014).

15. 15.

Yao, N. Y., Laumann, C. R., Cirac, J. I., Lukin, M. D. & Moore, J. E. Quasi-many-body localization in translation-invariant systems. *Phys. Rev. Lett.* **117**, 240601 (2016).

16. 16.

Alet, F. & Laflorencie, N. Many-body localization: an introduction and selected topics. *C. R. Phys.* **19**, 498–525 (2018).

17. 17.

Wannier, G. H. Dynamics of band electrons in electric and magnetic fields. *Rev. Mod. Phys.* **34**, 645–655 (1962).

18. 18.

Taylor, S. R., Schulz, M., Pollmann, F. & Moessner, R. Experimental probes of Stark many-body localization. *Phys. Rev. B* **102**, 054206 (2020).

19. 19.

Kshetrimayum, A., Eisert, J. & Kennes, D. M. Stark time crystals: symmetry breaking in space and time. *Phys. Rev. B* **102**, 195116 (2020).

20. 20.

Zhang, L., Ke, Y., Liu, W. & Lee, C. Mobility edge of Stark many-body localization. *Phys. Rev. A* **103**, 023323 (2021).

21. 21.

Chanda, T., Yao, R. & Zakrzewski, J. Coexistence of localized and extended phases: many-body localization in a harmonic trap. *Phys. Rev. Res.* **2**, 032039 (2020).

22. 22.

Singh Bhakuni, D. & Sharma, A. Stability of electric field driven many-body localization in an interacting long-range hopping model. *Phys. Rev. B* **102**, 085133 (2020).

23. 23.

Doggen, E. V. H., Gornyi, I. V. & Polyakov, D. G. Stark many-body localization: evidence for Hilbert-space shattering. *Phys. Rev. B* **103**, L100202 (2021).

24. 24.

Khemani, V., Hermele, M. & Nandkishore, R. Localization from Hilbert space shattering: from theory to physical realizations. *Phys. Rev. B* **101**, 174204 (2020).

25. 25.

Yao, R., Chanda, T. & Zakrzewski, J. Nonergodic dynamics in disorder-free potentials. *Ann. Phys.* <https://doi.org/10.1016/j.aop.2021.168540> (in the press).

26. 26.

Guardado-Sanchez, E. et al. Subdiffusion and heat transport in a tilted two-dimensional Fermi-Hubbard system. *Phys. Rev.* **10**, 011042 (2020).

27. 27.

Scherg, S. et al. Observing non-ergodicity due to kinetic constraints in tilted Fermi-Hubbard chains. *Nat. Commun.* **12**, 4490 (2021).

28. 28.

Guo, Q. et al. Stark many-body localization on a superconducting quantum processor. Preprint at <https://arxiv.org/abs/2011.13895> (2020).

29. 29.

Sala, P., Rakovszky, T., Verresen, R., Knap, M. & Pollmann, F. Ergodicity breaking arising from hilbert space fragmentation in dipole-conserving Hamiltonians. *Phys. Rev.* **10**, 011047 (2020).

30. 30.

Smith, J. et al. Many-body localization in a quantum simulator with programmable random disorder. *Nat. Phys.* **12**, 907–911 (2016).

31. 31.

Xu, K. et al. Emulating many-body localization with a superconducting quantum processor. *Phys. Rev. Lett.* **120**, 050507 (2018).

32. 32.

Chiaro, B. et al. Direct measurement of non-local interactions in the many-body localized phase. Preprint at <https://arxiv.org/abs/1910.06024> (2019).

33. 33.

Brydges, T. et al. Probing Rényi entanglement entropy via randomized measurements. *Science* **364**, 260–263 (2019).

34. 34.

Mølmer, K. & Sørensen, A. Multiparticle entanglement of hot trapped ions. *Phys. Rev. Lett.* **82**, 1835–1838 (1999).

35. 35.

Lee, A. C. et al. Engineering large Stark shifts for control of individual clock state qubits. *Phys. Rev. A* **94**, 042308 (2016).

36. 36.

Oganesyan, V. & Huse, D. A. Localization of interacting fermions at high temperature. *Phys. Rev. B* **75**, 155111 (2007).

37. 37.

Schreiber, M. et al. Observation of many-body localization of interacting fermions in a quasi-random optical lattice. *Science* **349**, 842–845 (2015).

38. 38.

Bernien, H. et al. Probing many-body dynamics on a 51-atom quantum simulator. *Nature* **551**, 579–584 (2017).

39. 39.

Tan, W. L. et al. Domain-wall confinement and dynamics in a quantum simulator. *Nat. Phys.* **17**, 742–747 (2021).

40. 40.

Gromov, A., Lucas, A. & Nandkishore, R. M. Fracton hydrodynamics. *Phys. Rev. Res.* **2**, 033124 (2020).

41. 41.

Wu, Y.-L. & Das Sarma, S. Understanding analog quantum simulation dynamics in coupled ion-trap qubits. *Phys. Rev. A* **93**, 022332 (2016).

42. 42.

Pino, M. Entanglement growth in many-body localized systems with long-range interactions. *Phys. Rev. B* **90**, 174204 (2014).

43. 43.

Safavi-Naini, A., Wall, M. L., Acevedo, O. L., Rey, A. M. & Nandkishore, R. M. Quantum dynamics of disordered spin chains with power-law interactions. *Phys. Rev. A* **99**, 033610 (2019).

44. 44.

Lukin, A. et al. Probing entanglement in a many-body-localized system. *Science* **364**, 256–260 (2019).

45. 45.

Serbyn, M. et al. Interferometric probes of many-body localization. *Phys. Rev. Lett.* **113**, 147204 (2014).

46. 46.

De Roeck, W. & Huvaneers, F. Stability and instability towards delocalization in many-body localization systems. *Phys. Rev. B* **95**, 155129 (2017).

47. 47.

Léonard, J. et al. Signatures of bath-induced quantum avalanches in a many-body-localized system. Preprint at <https://arxiv.org/abs/2012.15270> (2020).

48. 48.

Kondov, S. S., McGehee, W. R., Xu, W. & DeMarco, B. Disorder-induced localization in a strongly correlated atomic Hubbard gas. *Phys. Rev. Lett.* **114**, 083002 (2015).

49. 49.

Agarwal, K. et al. Rare-region effects and dynamics near the many-body localization transition. *Ann. Phys.* **529**, 1600326 (2017).

50. 50.

Moudgalya, S., Prem, A., Nandkishore, R., Regnault, N. & Bernevig, B. A. Thermalization and its absence within Krylov subspaces of a constrained Hamiltonian in *Memorial Volume for Shoucheng Zhang*

(eds Lian, B. et al.) 147–209 (World Scientific, 2021);
https://doi.org/10.1142/9789811231711_0009.

51. 51.

Else, D. V., Monroe, C., Nayak, C. & Yao, N. Y. Discrete time crystals. *Annu. Rev. Condens. Matter Phys.* **11**, 467–499 (2020).

52. 52.

Islam, R. et al. Onset of a quantum phase transition with a trapped ion quantum simulator. *Nat. Commun.* **2**, 377 (2011).

53. 53.

Zhang, J. et al. Observation of a discrete time crystal. *Nature* **543**, 217–220 (2017).

54. 54.

Zhang, J. et al. Observation of a many-body dynamical phase transition with a 53-qubit quantum simulator. *Nature* **551**, 601–604 (2017).

55. 55.

Monroe, C. et al. Programmable quantum simulations of spin systems with trapped ions. *Rev. Mod. Phys.* **93**, 025001 (2021).

56. 56.

Wei, X., Cheng, C., Xianlong, G. & Mondaini, R. Investigating many-body mobility edges in isolated quantum systems. *Phys. Rev. B* **99**, 165137 (2019).

57. 57.

Guo, Q. et al. Observation of energy-resolved many-body localization. *Nat. Phys.* **17**, 234–239 (2021).

58. 58.

Luitz, D. J. & Bar Lev, Y. The ergodic side of the many-body localization transition. *Ann. Phys.* **529**, 1600350 (2017).

59. 59.

Nauts, A. & Wyatt, R. E. New approach to many-state quantum dynamics: the recursive-residue-generation method. *Phys. Rev. Lett.* **51**, 2238–2241 (1983).

60. 60.

Titum, P., Iosue, J. T., Garrison, J. R., Gorshkov, A. V. & Gong, Z.-X. Probing ground-state phase transitions through quench dynamics. *Phys. Rev. Lett.* **123**, 115701 (2019).

61. 61.

Lanyon, B. P. et al. Universal digital quantum simulation with trapped ions. *Science* **334**, 57–61 (2011).

62. 62.

Zhu, D. et al. Probing many-body localization on a noisy quantum computer. *Phys. Rev. A* **103**, 032606 (2021).

63. 63.

Ponte, P., Papic', Z., Huvaneers, F. & Abanin, D. A. Many-body localization in periodically driven systems. *Phys. Rev. Lett.* **114**, 140401 (2015).

64. 64.

Richerme, P. et al. Non-local propagation of correlations in quantum systems with long-range interactions. *Nature* **511**, 198–201 (2014).

65. 65.

Schrieffer, J. R. & Wolff, P. A. Relation between the Anderson and Kondo Hamiltonians. *Phys. Rev.* **149**, 491–492 (1966).

66. 66.

Yang, Z. C., Liu, F., Gorshkov, A. V. & Iadecola, T. Hilbert-space fragmentation from strict confinement. *Phys. Rev. Lett.* **124**, 207602 (2020).

67. 67.

Atas, Y. Y., Bogomolny, E., Giraud, O. & Roux, G. Distribution of the ratio of consecutive level spacings in random matrix ensembles. *Phys. Rev. Lett.* **110**, 084101 (2013).

68. 68.

Neyenhuis, B. et al. Observation of prethermalization in long-range interacting spin chains. *Sci. Adv.* **3**, e1700672 (2017).

69. 69.

Li, W.-H., Deng, X. & Santos, L. Hilbert space shattering and disorder-free localization in polar lattice gases. Preprint at <https://arxiv.org/abs/2103.13780> (2021).

70. 70.

Hyllus, P. et al. Fisher information and multiparticle entanglement. *Phys. Rev. A* **85**, 022321 (2012).

Acknowledgements

We acknowledge helpful discussions with A. Migdall and R. Nandkishore. This work is supported by the DARPA Driven and Non-equilibrium Quantum Systems (DRINQS) Program (D18AC00033), the NSF Practical Fully-Connected Quantum Computer Program (PHY-1818914), the DOE Basic Energy Sciences: Materials and Chemical Sciences for Quantum

Information Science program (DE-SC0019449), the DOE High Energy Physics: Quantum Information Science Enabled Discovery Program (DE-0001893), the DoE Quantum Systems Accelerator, the DOE ASCR Quantum Testbed Pathfinder program (DE-SC0019040), the DoE ASCR Accelerated Research in Quantum Computing program (DE-SC0020312), the AFOSR MURI on Dissipation Engineering in Open Quantum Systems (FA9550-19-1-0399), and the Office of Naval Research (Award N00014-20-1-2695). The authors acknowledge the University of Maryland supercomputing resources made available for conducting the research reported in this work.

Author information

Affiliations

1. Joint Quantum Institute and Joint Center for Quantum Information and Computer Science, University of Maryland and NIST, College Park, MD, USA

W. Morong, F. Liu, P. Becker, K. S. Collins, L. Feng, A. Kyprianidis, T. You, A. V. Gorshkov & C. Monroe

2. Department of Physics and Astronomy, Rice University, Houston, TX, USA

G. Pagano

Contributions

F.L., L.F. and W.M. proposed the experiment. W.M., P.B., K.S.C., A.K., G.P., T.Y. and C.M. contributed to experimental design, data collection and analysis. F.L. and A.V.G. contributed supporting theory and numerics. All authors contributed to the manuscript.

Corresponding authors

Correspondence to [W. Morong](#) or [F. Liu](#).

Ethics declarations

Competing interests

The authors declare competing financial interests: C.M. is co-founder and chief scientist at IonQ, Inc.

Additional information

Peer review information *Nature* thanks the anonymous reviewers for their contribution to the peer review of this work.

Publisher's note Springer Nature remains neutral with regard to jurisdictional claims in published maps and institutional affiliations.

Extended data figures and tables

Extended Data Fig. 1 Experimental noise model.

a, b, Noiseless (**a**) and noisy (**b**) numerics for an initial Néel state with $g/J_0 = \{0.24, 1.2, 1.8\}$ (light to dark), corresponding to the data in Fig. [2c](#). Compared to the ideal numerics, the noisy numerics show overall lower imbalances, primarily due to the SPAM errors, and damped oscillations, primarily due to variations in the individual local effective B^z fields. However, these noise sources do not strongly affect the stability of the imbalance. **c**, Individual noisy realizations corresponding to the highest gradient shown above. **d**, Noise-averaged DEER simulations corresponding to Fig. [3b](#).

Extended Data Fig. 2 Trotterization scheme.

a, Numerics comparison of the imbalance dynamics for the averaged Hamiltonian of equation [\(13\)](#) (solid blue line) with the full Trotter evolution (dashed orange), for the case of an initial Néel state ($N = 15$) and parameters corresponding to the strongest experimental field gradient. **b**, Difference

(averaged - Trotter) between the plots in **a**, showing that the Trotter error over experimental timescales is on the order of one percent. **c**, Experimental examples (top row) of continuous and Trotterized evolution, both at $g/J_0 = 1.5$, compared to simulations (bottom row) using the (slightly different) parameters of the individual experimental realizations. Although the Trotterized evolution lasts nearly twice as much time in absolute units, since the averaged J_0 is roughly half as large, it nonetheless shows a substantial reduction in decoherence and improvement in fidelity to the desired Hamiltonian. An initial state with one spin flip is chosen for this comparison, as it makes the effect of decoherence due to phonons more pronounced compared with a state near zero net magnetization.

Extended Data Fig. 3 Histograms of r .

Probability density distributions of r , the ratio of adjacent energy level spacings, for the experimental Hamiltonian (equation (1) of the main text) at various values of g/J_0 and $N=15$. Numerics are compared with the distribution expected for either a Poisson level distribution (blue lines in **a** and **d**) or a Wigner–Dyson distribution (red lines in **b**, **c**). The level statistics in the absence of a field gradient are near the Poissonian limit, which may reflect the proximity to an integrable limit for the low-energy sector⁶⁸. A small gradient results in statistics near the Wigner–Dyson limit, followed by an approach to Poisson statistics as the gradient is increased.

Extended Data Fig. 4 Dependence of $\langle r \rangle$ on α and g/J_0 .

Dependence of $\langle r \rangle$ on α and g/J_0 ($N=13$, $B^z/J_0=5$), for the power-law Hamiltonian (equation (30)). In the experiments presented in the main text $\alpha \approx 1.3$.

Extended Data Fig. 5 Dependence of $\langle r \rangle$ on system size.

Level statistics for $N=\{9, 11, 13, 15\}$ (light to dark), for $\alpha=1.3$ and $B^z/J_0=5$ and for the power-law Hamiltonian (equation (30)).

Extended Data Fig. 6 Dependence of $\langle \bar{I} \rangle$ on system size and time.

a, Numerics showing $\langle \bar{I} \rangle$ for the Néel state with $N = \{9, 15, 25\}$ (light to dark). As the system increases from $N = 9$ to $N = 25$, the largest change is in a sharpening feature near $g/J_0 = 1$. These numerics do not include experimental noise. **b**, Experimental data for $N = 15$ and $N = 25$, reproduced from Fig. 2, shows a similar dip for the larger size. **c**, Expanded view of numerics from **a**. Especially for gradient values above $g/J_0 = 1$, the imbalance shows little finite-size dependence. **d**, Numerical comparison of $\langle \bar{I} \rangle$ ($N = 15$) for the experimental time and for an extended time of $100tJ_0$ (dashed). While at small gradients the finite-time effects on the imbalance are substantial, including the dip feature in the left plots, a steady state is largely achieved in the experimental window for gradients $g/J_0 > 1$. For all numerics shown, $B^{z0}/J_0 = 4.4(1 + 3g/(5J_0))$ (the experimental scaling resulting from equation (13) with Δt_1 varied) and $\alpha = 1.3$.

Extended Data Fig. 7 Long-term stability of Stark MBL.

a, b, Numerical study of the long-time dynamics of the initial states realized in Fig. 2, using exact diagonalization. For this finite-size realization, in a strong gradient ($g/J_0 = 2$, solid lines), the imbalance and bipartite entanglement entropy show some slow dynamics but apparently never approach the thermal value, in contrast with a weak gradient ($g/J_0 = 0.25$, dashed line). **c**, Numerical study of the finite-size and initial-state dependence of Stark MBL imbalance dynamics. States with one-block (Néel) and two-block domain walls are shown for $g/J_0 = 2$ and $N = 12, N = 16$, and $N = 20$ (light to dark solid lines, $N = 20$ for the two-block state only). The two-block initial state shows faster decay and greater finite-size effects, as is expected from the effective Hamiltonian in a large tilt (equation (26)). With a stronger gradient (dashed line, $g/J_0 = 5$ and $N = 12$), this instability can be arbitrarily postponed. To show the long-term trend clearly, a moving average with a window of $5J_0$ has been applied to these numerics. **d**, Experimental data for the one and two-block domains.

Consistent with numerics, state-dependent instability is manifested as a slow differential increase in the decay of the two-block state compared to the Néel state. These data were taken consecutively to ensure identical experimental parameters and decoherence rates. Each point is an average over 200 experimental repetitions, with error bars smaller than the symbol size. **e**, Numerical studies of stability in a quadratic field ($N=16$, $\gamma=2$) do not show this state-dependent instability over the same timescale. To show the long-term trend clearly, a moving average with a window of $5J_0$ has been applied to these numerics. **f**, Cartoon of the setup for numerics in **e** (shown with $N=8$ for clarity). The quadratic potential is chosen to have a minimum shifted away from the system centre by one-quarter site to avoid a fine-tuned reflection symmetry. For all numerics shown, $B^{z0}/J_0=4.5$ and $\alpha=1.3$.

Extended Data Fig. 8 QFI.

Normalized QFI for a Néel state ($N=15$) with $g/J_0=0.24$ (white) and $g/J_0=2.4$ (blue), corresponding to the lowest- and highest-gradient data in Fig. 2d. Points are experimental observations, averaged over 200 repetitions, with lines as guides to the eye. A value greater than one (dashed line) is an entanglement witness. After the initial fast dynamics up to $tJ_0 \approx 1$, the QFI is consistent with saturation for the small gradient, and with slow entanglement growth for the large gradient, with behaviour very similar to that previously observed in disordered MBL³⁰.

Extended Data Fig. 9 Additional DEER data.

DEER Difference signal for $R=\{1, 2, 3\}$ (light to dark), compared with the imbalance $\langle \{\mathcal{I}(t)\} \rangle$ for the same parameters. Data are offset for clarity but otherwise share the same axes. $\langle \{\mathcal{I}\} \rangle$ is taken from the same dataset as the $R=1$ spin-echo data, with the probe spin excluded from the imbalance calculation. After $tJ_0 \approx 2$, the imbalance is essentially constant at the low but finite steady-state value corresponding to this gradient strength. However, correlation dynamics are still progressing—in particular, correlations as measured by the difference signal only begin to develop for $R=2$ after this point. This is similar to the disordered MBL

state, in which slow entanglement dynamics continue after the locally conserved populations have reached a steady state^{10,11,44}. Points are averaged over 2,000 repetitions, with error bars representing statistical uncertainty of the mean (1σ s.e.m.).

Extended Data Fig. 10 Critical slope in quadratic field.

As the quadratic curvature is varied, the division between thermalizing and nonthermal regions is largely consistent with a critical slope near $g/J_0 = 0.5$. However, the strongest curvature of $\gamma = 3.6$ deviates from this rule. For the lowest two values of γ the system was completely delocalized, and thus only the lower bound is meaningful. Points are averaged over 200 experimental repetitions. Error bars (aside from the first two points) denote a variation of ± 1 spin location.

Source data

Source Data Fig. 1

Source Data Fig. 2

Source Data Fig. 3

Source Data Fig. 4

Rights and permissions

Reprints and Permissions

About this article

Cite this article

Morong, W., Liu, F., Becker, P. *et al.* Observation of Stark many-body localization without disorder. *Nature* **599**, 393–398 (2021).
<https://doi.org/10.1038/s41586-021-03988-0>

- Received: 12 February 2021
- Accepted: 01 September 2021
- Published: 17 November 2021
- Issue Date: 18 November 2021
- DOI: <https://doi.org/10.1038/s41586-021-03988-0>

Share this article

Anyone you share the following link with will be able to read this content:

[Get shareable link](#)

Sorry, a shareable link is not currently available for this article.

[Copy to clipboard](#)

Provided by the Springer Nature SharedIt content-sharing initiative

This article was downloaded by **calibre** from <https://www.nature.com/articles/s41586-021-03988-0>

- Article
- [Published: 17 November 2021](#)

Measuring phonon dispersion at an interface

- [Ruishi Qi^{1,2,3}](#) na1,
- [Ruochen Shi^{1,2}](#) na1,
- [Yuehui Li^{1,2}](#),
- [Yuanwei Sun^{1,2}](#),
- [Mei Wu^{1,2}](#),
- [Ning Li^{1,2,4}](#),
- [Jinlong Du¹](#),
- [Kaihui Liu](#) [ORCID: orcid.org/0000-0002-8781-2495](#)^{5,6,7},
- [Chunlin Chen](#) [ORCID: orcid.org/0000-0003-1985-1940](#)⁸,
- [Ji Chen^{5,6}](#),
- [Feng Wang](#) [ORCID: orcid.org/0000-0001-8369-6194](#)³,
- [Dapeng Yu^{1,9}](#),
- [En-Ge Wang^{2,10,11}](#) &
- [Peng Gao](#) [ORCID: orcid.org/0000-0001-9868-2115](#)^{1,2,6,7,12}

[Nature](#) volume **599**, pages 399–403 (2021)

- 2071 Accesses
- 42 Altmetric
- [Metrics details](#)

Subjects

- [Nanoscale materials](#)

- [Surfaces, interfaces and thin films](#)
- [Transmission electron microscopy](#)

Abstract

The breakdown of translational symmetry at heterointerfaces leads to the emergence of new phonon modes localized at the interface¹. These modes have an essential role in thermal and electrical transport properties in devices, especially in miniature ones wherein the interface may dominate the entire response of the device². Although related theoretical work began decades ago^{1,3,4,5}, experimental research is totally absent owing to challenges in achieving the combined spatial, momentum and spectral resolutions required to probe localized modes. Here, using the four-dimensional electron energy-loss spectroscopy technique, we directly measure both the local vibrational spectra and the interface phonon dispersion relation for an epitaxial cubic boron nitride/diamond heterointerface. In addition to bulk phonon modes, we observe modes localized at the interface and modes isolated from the interface. These features appear only within approximately one nanometre around the interface. The localized modes observed here are predicted to substantially affect the interface thermal conductance and electron mobility. Our findings provide insights into lattice dynamics at heterointerfaces, and the demonstrated experimental technique should be useful in thermal management, electrical engineering and topological phononics.

Access options

Subscribe to Journal

Get full journal access for 1 year

\$199.00

only \$3.90 per issue

[Subscribe](#)

All prices are NET prices.
VAT will be added later in the checkout.
Tax calculation will be finalised during checkout.

Rent or Buy article

Get time limited or full article access on ReadCube.

from \$8.99

[Rent or Buy](#)

All prices are NET prices.

Additional access options:

- [Log in](#)
- [Access through your institution](#)
- [Learn about institutional subscriptions](#)

Fig. 1: Experimental setup and interface structure.

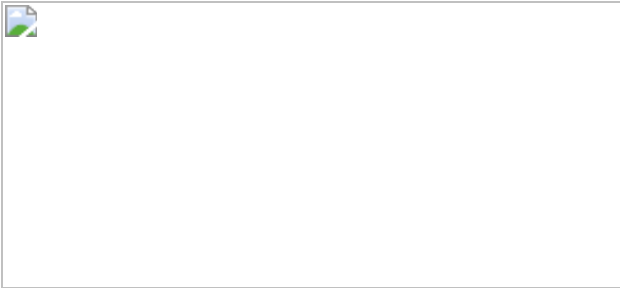


Fig. 2: Interface phonon measurements at the atomic scale.

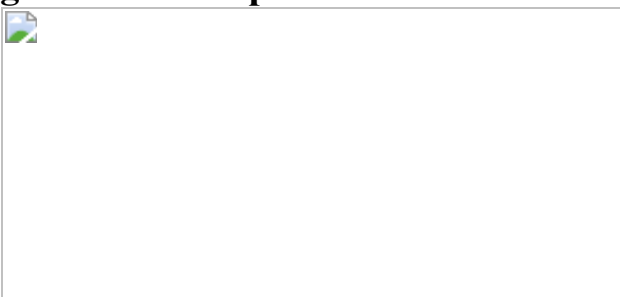


Fig. 3: Phonon dispersion measurements at the interface.



Data availability

The experimental 3D EELS and 4D EELS datasets are available in the Open Science Framework repository at <https://osf.io/8mp4t>. The other data that support the findings of this study are available from the corresponding author upon request.

Code availability

A GUI version of the MATLAB code for the EELS data processing can be found on GitHub at <https://github.com/ruishiqi/EELS>.

References

1. 1.

Masri, P. Surface and interface phonons and related topics. *Surf. Sci. Rep.* **9**, 293–369 (1988).

2. 2.

Giri, A. & Hopkins, P. E. A review of experimental and computational advances in thermal boundary conductance and nanoscale thermal transport across solid interfaces. *Adv. Funct. Mater.* **30**, 1903857 (2020).

3. 3.

Djafari-Rouhani, B., Masri, P. & Dobrzynski, L. Vibrational properties of a bicrystal interface: different-interface phonons and the low-temperature specific heat. *Phys. Rev. B* **15**, 5690–5711 (1977).

4. 4.

Masri, P. Interface phonons: effects of crystal size. *J. Phys. C* **14**, 2265–2278 (1981).

5. 5.

Tamine, M., Boumrar, H. & Rafil, O. Interface and step localized phonon modes between two truncated thin films. *Surf. Rev. Lett.* **11**, 155–165 (2004).

6. 6.

Girvin, S. & Yang, K. *Modern Condensed Matter Physics* (Cambridge Univ. Press, 2019).

7. 7.

Gordiz, K. & Henry, A. Phonon transport at interfaces: determining the correct modes of vibration. *J. Appl. Phys.* **119**, 015101 (2016).

8. 8.

Luh, D. A., Miller, T., Paggel, J. J. & Chiang, T. C. Large electron–phonon coupling at an interface. *Phys. Rev. Lett.* **88**, 256802 (2002).

9. 9.

Cahill, D. G. et al. Nanoscale thermal transport. *J. Appl. Phys.* **93**, 793–818 (2003).

10. 10.

Chu, C. W. et al. Interface-induced and interface-enhanced superconductivity. *J. Supercond. Nov. Magn.* **32**, 7–15 (2018).

11. 11.

Wang, Q.-Y. et al. Interface-induced high-temperature superconductivity in single unit-cell FeSe films on SrTiO₃. *Chin. Phys. Lett.* **29**, 037402 (2012).

12. 12.

Gordiz, K. & Henry, A. Phonon transport at crystalline Si/Ge interfaces: the role of interfacial modes of vibration. *Sci. Rep.* **6**, 23139 (2016).

13. 13.

Burkel, E. Phonon spectroscopy by inelastic X-ray scattering. *Rep. Prog. Phys.* **63**, 171–232 (2000).

14. 14.

Lee, J., Crampton, K. T., Tallarida, N. & Apkarian, V. A. Visualizing vibrational normal modes of a single molecule with atomically confined light. *Nature* **568**, 78–82 (2019).

15. 15.

Chen, X. et al. Modern scattering-type scanning near-field optical microscopy for advanced material research. *Adv. Mater.* **31**, 1804774 (2019).

16. 16.

Szeftel, J. Surface phonon dispersion, using electron energy loss spectroscopy. *Surf. Sci.* **152/153**, 797–810 (1985).

17. 17.

Krivanek, O. L. et al. Vibrational spectroscopy in the electron microscope. *Nature* **514**, 209–212 (2014).

18. 18.

Egerton, R. F. *Electron Energy-loss Spectroscopy in the Electron Microscope* 3rd edn (Springer, 2011).

19. 19.

Hage, F. S. et al. Nanoscale momentum-resolved vibrational spectroscopy. *Sci. Adv.* **4**, eaar7495 (2018).

20. 20.

Lagos, M. J., Trugler, A., Hohenester, U. & Batson, P. E. Mapping vibrational surface and bulk modes in a single nanocube. *Nature* **543**, 529–532 (2017).

21. 21.

Qi, R. et al. Four-dimensional vibrational spectroscopy for nanoscale mapping of phonon dispersion in BN nanotubes. *Nat. Commun.* **12**, 1179 (2021).

22. 22.

Li, N. et al. Direct observation of highly confined phonon polaritons in suspended monolayer hexagonal boron nitride. *Nat. Mater.* **20**, 43–48 (2021).

23. 23.

Govyadinov, A. A. et al. Probing low-energy hyperbolic polaritons in van der Waals crystals with an electron microscope. *Nat. Commun.* **8**, 95 (2017).

24. 24.

Venkatraman, K., Levin, B. D. A., March, K., Rez, P. & Crozier, P. A. Vibrational spectroscopy at atomic resolution with electron impact scattering. *Nat. Phys.* **15**, 1237–1241 (2019).

25. 25.

Hage, F. S., Radtke, G., Kepaptsoglou, D. M., Lazzeri, M. & Ramasse, Q. M. Single-atom vibrational spectroscopy in the scanning transmission electron microscope. *Science* **367**, 1124–1127 (2020).

26. 26.

Yan, X. et al. Single-defect phonons imaged by electron microscopy. *Nature* **589**, 65–69 (2021).

27. 27.

Senga, R. et al. Position and momentum mapping of vibrations in graphene nanostructures. *Nature* **573**, 247–250 (2019).

28. 28.

Dwyer, C. et al. Electron-beam mapping of vibrational modes with nanometer spatial resolution. *Phys. Rev. Lett.* **117**, 256101 (2016).

29. 29.

Hachtel, J. A. et al. Identification of site-specific isotopic labels by vibrational spectroscopy in the electron microscope. *Science* **363**, 525–528 (2019).

30. 30.

Hage, F. S., Kepaptsoglou, D. M., Ramasse, Q. M. & Allen, L. J. Phonon spectroscopy at atomic resolution. *Phys. Rev. Lett.* **122**, 016103 (2019).

31. 31.

Plotkin-Swing, B. et al. Hybrid pixel direct detector for electron energy loss spectroscopy. *Ultramicroscopy* **217**, 113067 (2020).

32. 32.

Nicholls, R. J. et al. Theory of momentum-resolved phonon spectroscopy in the electron microscope. *Phys. Rev. B* **99**, 094105 (2019).

33. 33.

Fritsch, J., Pavone, P. & Schröder, U. Ab initio calculation of the phonon dispersion in bulk InP and in the InP(110) surface. *Phys. Rev. B* **52**, 11326–11334 (1995).

34. 34.

Benedek, G. et al. Theory of surface phonons at metal surfaces: recent advances. *J. Phys. Condens. Matter* **22**, 084020 (2010).

35. 35.

Little, W. A. The transport of heat between dissimilar solids at low temperatures. *Can. J. Phys.* **37**, 334–349 (1959).

36. 36.

Swartz, E. T. & Pohl, R. O. Thermal boundary resistance. *Rev. Mod. Phys.* **61**, 605–668 (1989).

37. 37.

Mingo, N. & Yang, L. Phonon transport in nanowires coated with an amorphous material: an atomistic Green's function approach. *Phys. Rev. B* **68**, 245406 (2003).

38. 38.

Gordiz, K. & Henry, A. A formalism for calculating the modal contributions to thermal interface conductance. *New J. Phys.* **17**, 103002 (2015).

39. 39.

Ohtomo, A. & Hwang, H. Y. A high-mobility electron gas at the LaAlO₃/SrTiO₃ heterointerface. *Nature* **427**, 423–426 (2004).

40. 40.

Chen, C. et al. Misfit accommodation mechanism at the heterointerface between diamond and cubic boron nitride. *Nat. Commun.* **6**, 6327 (2015).

41. 41.

Süsstrunk, R. & Huber, S. D. Observation of phononic helical edge states in a mechanical topological insulator. *Science* **349**, 47–50 (2015).

42. 42.

Li, J. et al. Computation and data driven discovery of topological phononic materials. *Nat. Commun.* **12**, 1204 (2021).

43. 43.

Liu, Y., Xu, Y., Zhang, S.-C. & Duan, W. Model for topological phononics and phonon diode. *Phys. Rev. B* **96**, 064106 (2017).

44. 44.

T. Taniguchi, & S. Yamaoka. Heteroepitaxial growth of cubic boron nitride single crystal on diamond seed under high pressure. *Mater. Res. Soc. Symp. Proc.* **472**, 379–383 (1997).

45. 45.

Chen, K. et al. Ultrahigh thermal conductivity in isotope-enriched cubic boron nitride. *Science* **367**, 555–559 (2020).

46. 46.

Wei, L., Kuo, P. K., Thomas, R. L., Anthony, T. R. & Banholzer, W. F. Thermal conductivity of isotopically modified single crystal diamond. *Phys. Rev. Lett.* **70**, 3764–3767 (1993).

47. 47.

Huang, X. & Guo, Z. High thermal conductance across c-BN/diamond interface. *Diam. Relat. Mater.* **108**, 107979 (2020).

48. 48.

Zhou, J. et al. Observing crystal nucleation in four dimensions using atomic electron tomography. *Nature* **570**, 500–503 (2019).

49. 49.

Dabov, K., Foi, A., Katkovnik, V. & Egiazarian, K. Image denoising by sparse 3-D transform-domain collaborative filtering. *IEEE Trans. Image Process.* **16**, 2080–2095 (2007).

50. 50.

Batson, P. E. & Lagos, M. J. Interpretation of meV resolution phonon EELS data. *Microsc. Microanal.* **24**, 412–413 (2018).

51. 51.

Williams, D. B. & Carter, C. B. *Transmission Electron Microscopy: A Textbook for Materials Science* Vol. 2 (Springer Science & Business Media, 2008).

52. 52.

Giannozzi, P. et al. Quantum ESPRESSO: a modular and open-source software project for quantum simulations of materials. *J. Phys. Condens. Matter* **21**, 395502 (2009).

53. 53.

Giannozzi, P. et al. Advanced capabilities for materials modelling with Quantum ESPRESSO. *J. Phys. Condens. Matter* **29**, 465901 (2017).

54. 54.

Perdew, J. P. & Zunger, A. Self-interaction correction to density-functional approximations for many-electron systems. *Phys. Rev. B* **23**, 5048–5079 (1981).

55. 55.

Vanderbilt, D. Soft self-consistent pseudopotentials in a generalized eigenvalue formalism. *Phys. Rev. B* **41**, 7892–7895 (1990).

56. 56.

Vila, F. D., Rehr, J. J., Rossner, H. H. & Krappe, H. J. Theoretical X-ray absorption Debye–Waller factors. *Phys. Rev. B* **76**, 014301 (2007).

57. 57.

Waasmaier, D. & Kirfel, A. New analytical scattering-factor functions for free atoms and ions. *Acta Crystallogr. A* **51**, 416–431 (1995).

58. 58.

Plimpton, S. Fast parallel algorithms for short-range molecular dynamics. *J. Comput. Phys.* **117**, 1–19 (1995).

59. 59.

Kınacı, A., Haskins, J. B., Sevik, C. & Çağın, T. Thermal conductivity of BN-C nanostructures. *Phys. Rev. B* **86**, 115410 (2012).

60. 60.

Seyf, H. R., Gordiz, K., DeAngelis, F. & Henry, A. Using Green–Kubo modal analysis (GKMA) and interface conductance modal analysis

(ICMA) to study phonon transport with molecular dynamics. *J. Appl. Phys.* **125**, 081101 (2019).

61. 61.

Togo, A., Chaput, L. & Tanaka, I. Distributions of phonon lifetimes in Brillouin zones. *Phys. Rev. B* **91**, 094306 (2015).

Acknowledgements

This work was supported by the National Key R&D Program of China (2019YFA0708200), the National Natural Science Foundation of China (11974023, 52021006, 52125307, 12004010, 11888101), the Key-Area Research and Development Program of Guangdong Province (2018B030327001, 2018B010109009), the Strategic Priority Research Program of Chinese Academy of Sciences (XDB33000000), the ‘2011 Program’ from the Peking-Tsinghua-IOP Collaborative Innovation Center of Quantum Matter, the Youth Innovation Promotion Association of CAS, and the Introduced Innovative R&D Team Project of ‘The Pearl River Talent Recruitment Program’ of Guangdong Province (2019ZT08C321). We acknowledge the Electron Microscopy Laboratory of Peking University for the use of electron microscopes. We acknowledge the High-performance Computing Platform of Peking University for providing computational resources for the DFPT and molecular dynamics calculations. We thank J. Feng, Q. Gu, A. Gabourie, Z. Fan, C. Shi and T. Lovejoy for helpful discussions; and T. Taniguchi at NIMS in Japan for providing the samples.

Author information

Author notes

1. These authors contributed equally: Ruishi Qi, Ruochen Shi

Affiliations

1. Electron Microscopy Laboratory, School of Physics, Peking University, Beijing, China

Ruishi Qi, Ruochen Shi, Yuehui Li, Yuanwei Sun, Mei Wu, Ning Li, Jinlong Du, Dapeng Yu & Peng Gao

2. International Center for Quantum Materials, Peking University, Beijing, China

Ruishi Qi, Ruochen Shi, Yuehui Li, Yuanwei Sun, Mei Wu, Ning Li, En-Ge Wang & Peng Gao

3. Physics Department, University of California at Berkeley, Berkeley, CA, USA

Ruishi Qi & Feng Wang

4. Academy for Advanced Interdisciplinary Studies, Peking University, Beijing, China

Ning Li

5. State Key Laboratory for Mesoscopic Physics, School of Physics, Peking University, Beijing, China

Kaihui Liu & Ji Chen

6. Collaborative Innovation Center of Quantum Matter, Beijing, China

Kaihui Liu, Ji Chen & Peng Gao

7. Interdisciplinary Institute of Light-Element Quantum Materials and Research Center for Light-Element Advanced Materials, Peking University, Beijing, China

Kaihui Liu & Peng Gao

8. Shenyang National Laboratory for Materials Science, Institute of Metal Research, Chinese Academy of Sciences, Shenyang, China

Chunlin Chen

9. Shenzhen Institute for Quantum Science and Engineering (SIQSE),
Southern University of Science and Technology, Shenzhen, China

Dapeng Yu

10. Songshan Lake Materials Lab, Institute of Physics, Chinese Academy
of Sciences, Dongguan, China

En-Ge Wang

11. School of Physics, Liaoning University, Shenyang, China

En-Ge Wang

12. Beijing Graphene Institute, Beijing, China

Peng Gao

Contributions

R.Q. and R.S. contributed equally to this work (order determined by a random process upon completion of the manuscript). P.G., R.S. and R.Q. conceived the project. C.C. prepared the TEM sample. R.S. designed and performed the EELS measurements. R.Q. wrote the data processing codes and analysed the data. R.S. and R.Q. performed DFPT calculations of phonon dispersion, scattering cross-section and electron–phonon coupling under the direction of E.-G.W. R.Q., Y.L. and R.S. performed molecular dynamics simulations with the guidance from J.C. Y.S., M.W. and Y.L. acquired atomic-resolution iDPC images. N.L., J.D., K.L., F.W. and D.Y helped the data interpretation. R.Q., R.S. and P.G. finalized the manuscript with inputs from F.W. All authors contributed to this work through useful discussion and/or comments to the manuscript. P.G. supervised the project.

Corresponding author

Correspondence to [Peng Gao](#).

Ethics declarations

Competing interests

The authors declare no competing interests.

Additional information

Peer review information *Nature* thanks Juan-Carlos Idrobo, Lucas Lindsay and the other, anonymous, reviewer(s) for their contribution to the peer review of this work. Peer reviewer reports are available.

Publisher's note Springer Nature remains neutral with regard to jurisdictional claims in published maps and institutional affiliations.

Extended data figures and tables

[Extended Data Fig. 1 Spatial resolution estimation for 4D EELS.](#)

a, b, Spatial resolution as a function of convergence semi-angle for 60 kV (**a**) and 30 kV (**b**) beam energy. Solid line, diffraction limit. Dashed line, theoretical beam size considering both the diffraction limit and the beam source size. Scatters with error bars are experimental fitted resolution as shown in the following panels, where vertical error bars represent the standard deviation of the fitted resolutions from multiple images and horizontal ones are estimated by the roundness of the central diffraction spot. See [Methods](#) for detail. **c**, Momentum resolution as a function of convergence semi-angle. Inset with light-grey shadow schematically shows the diffraction spot size (yellow circles) relative to the BZ size in our 4D EELS measurements. Dashed horizontal lines mark the ratio to the distance between Γ and X. **d**, HAADF image of gold nanoparticles taken with 35 mrad (nominal value) convergence semi-angle with 60 kV beam energy, serving as a reference image. **e–g**, Above the yellow line are typical HAADF images taken with 5 mrad, 3 mrad and 2 mrad convergence semi-

angles, respectively. Below the yellow line are the reference image convoluted with a Gaussian kernel with FWHM indicated in the title (fitting result), which agrees nicely with the acquired images above the yellow line. **h–k**, same as **d–g**, but taken with 30 kV beam energy. Convergence semi-angles are 40 mrad (reference image), 7.5 mrad, 3 mrad, and 2 mrad respectively.

Extended Data Fig. 2 Interface component of the spectra extracted by finding the minimum difference between the measured spectrum and all possible linear combinations of two bulk spectra.

The fitting was performed by minimizing $\|\langle S(\omega) - \{a\}_1 S_1 - \{a\}_2 S_2 \rangle\|$, where $S(\omega)$ is the measured spectrum (Fig. 2b), $\langle S(\omega) \rangle$ with subscripts means the bulk spectra, and $\{a\}_1, \{a\}_2$ are adjusted coefficients. **a**, Line profile of the fitting residual. Since the fitting gives the linear combination that is closest to the measured spectrum, the residual represents the interface component that cannot be obtained from bulk modes. Near the interface, three red peaks correspond to three interfacial modes in Fig. 2g. The blue region at 160 meV is due to the isolated mode with reduced vibration at the interface. **b**, Norm (root sum squared) of residuals as a function of position (left axis), and the fitting coefficients $\{a\}_1$ and $\{a\}_2$ (right axis). The residual is sharply peaked at the interface (FWHM = 1.8 nm), indicating new vibrational features are highly localized at the interface.

Extended Data Fig. 3 3D EELS data acquired in different regions.

a, A low-magnification annular dark field image showing where the datasets were acquired. Boxes with labels ‘3D’ and ‘4D’ correspond to the scanning regions of the 3D EELS and 4D EELS datasets discussed in the main text. **b–e**, Four EELS line profiles acquired under the same experimental conditions except different pixel sizes and different scanning regions (marked in **a**). **b**, **c** and **d**, **e** were acquired in two experiments that

were two weeks apart. All datasets give consistent results as the one shown in Fig. 2.

Extended Data Fig. 4 Off-axis EELS measurements.

a, A schematic of the diffraction plane and EELS aperture placement. The colormap illustrates the diffraction plane viewed from $\langle [1\bar{1}2] \rangle$ zone axis, with 60 kV beam energy and 35 mrad convergence semi-angle. The diffraction spot size (35 mrad) is larger than the distance between adjacent spots, so they partially overlap. The green circle marks the position of the aperture, which is displaced away from the central spot. **b**, The EELS line profile acquired with off-axis geometry. Main spectral features are consistent with those acquired with on-axis geometry (Fig. 2b, Extended Data Fig. 3). **c**, Corresponding simulation result. **d**, EELS maps at selected energies. One of the interfacial modes has a better contrast than the on-axis result. **e–h**, same as **a–d**, but the beam is travelling along $\langle [1\bar{1}0] \rangle$ direction.

Extended Data Fig. 5 Phonon dispersion diagrams measured with 3 mrad convergence semi-angle.

a, A schematic of the bulk BZ (truncated octahedron) and the interface two-dimensional BZ (yellow hexagon). Upper-case and lower-case letters mark the high-symmetry points of the bulk BZ and interface BZ, respectively. **b**, Measured dispersion diagrams along the Γ – Σ – K – X line with 3 mrad convergence semi-angle. Dashed curves are calculated bulk phonon dispersion. Although smaller convergence semi-angles give better momentum resolution and hence nicer dispersion diagrams, insufficient spatial resolution makes it hard to extract localized features at the interface.

Extended Data Fig. 6 EELS line profiles at five momentum transfers.

a, A schematic of the diffraction plane and EELS aperture placement. The colormap illustrates the diffraction plane viewed from $\langle [1\bar{1}2] \rangle$ zone axis, with 30 kV beam energy and 7.5 mrad convergence semi-angle. The

diffraction spot size is drawn to scale, indicating our momentum resolution. The green rectangle marks the position of the slot aperture. **b–f**, Line profiles with momentum transfers from Γ (**b**) through the Σ line (**c, d**) to K (**e**) and finally X (**f**). The intensity decrease of the highest-frequency optical phonon is observable in most panels (green arrows), which corresponds to the negative-intensity line at 150–160 meV in Fig. [3c, d](#). The interfacial mode is directly observable in some panels (white arrows).

Extended Data Fig. 7 Projected bulk phonon bands.

a, b, Bulk phonon band of cBN and diamond projected onto (111) surface.

Extended Data Fig. 8 Modal contribution to ITC.

a, ITC decomposed into the mode-mode correlation integrals ([Methods](#)), with modes binned by their frequency. 8640 eigen modes are divided into 100 frequency bins. Main panel, pseudo-colour map of ITC component $G_{nn'}$ from heat flux correlation between n th and n' th frequency bin. Colour scale is in units of $\text{GW m}^{-2} \text{K}^{-1}$. Qualitatively it gives a measure of how strong two modes interact with each other. Right panel shows modal thermal conductance G_n in the n th frequency bin, i.e., projecting the $G_{nn'}$ map along one dimension. Top panel is a scatter plot showing the frequency versus interface vibration amplitude for each eigen mode. Interfacial modes show strong correlation with almost all other modes (red arrows), while isolated modes have almost no correlation with any other modes (green arrow) **b**, ITC decomposed into the mode-mode correlation integrals, with modes sorted by their interfacial amplitudes. The same set of eigen modes are sorted by their amplitudes at the interface, aiming to visualize the relation between interfacial amplitudes and modal thermal conductance. For clarity, eigenvectors are normalized such that the squared norm of each eigenvector is the number of atoms (this is just an overall scaling of all eigenvectors), so an interfacial amplitude greater than one means an enhanced vibration at the interface and a value smaller than one means a reduced vibration at the interface. Main panel shows the per-mode (i.e., divided by the number of modes in each bin) contribution to ITC from the modal heat flux correlation between n th and n' th amplitude bin. Colour scale is in units of MW m^{-2}

K^{-1} . Modes with enhanced amplitudes at the interface show strong correlation with all other modes, while modes with reduced amplitudes at the interface show little correlation with other modes. Top panel gives the scatter plot of frequency versus interfacial amplitude again.

[Extended Data Fig. 9 Electron-phonon coupling at the interface calculated by DFPT.](#)

a, Phonon linewidth due to electron-phonon coupling mapped on the phonon dispersion. Compared with bulk modes, the interfacial optical modes couple strongly with electrons (note that the colour map is in log scale) because both the interfacial phonon modes and the two-dimensional electron gas are highly confined at the interface. **b**, Electronic band structure. Three RGB channels represent electron wavefunctions projected onto atomic orbitals in the interface region (red), in cBN (green) and in diamond (blue). Dashed horizontal line is the Fermi level, which crosses a band localized near the interface, meaning the system becomes metallic due to carriers at the interface.

Supplementary information

[Peer Review File](#)

[Supplementary Video 1](#)

Four-dimensional EELS dataset across the interface. The top panel shows the energy-filtered EELS map between 120 meV and 140 meV at the Γ point, which includes the TO phonon of cBN but no phonon modes of diamond. The red dot or red vertical line indicates the beam position. The bottom panel compares the experimental and calculated dispersion diagram as the beam scans on the sample.

Rights and permissions

[Reprints and Permissions](#)

About this article

Cite this article

Qi, R., Shi, R., Li, Y. *et al.* Measuring phonon dispersion at an interface. *Nature* **599**, 399–403 (2021). <https://doi.org/10.1038/s41586-021-03971-9>

- Received: 08 March 2021
- Accepted: 31 August 2021
- Published: 17 November 2021
- Issue Date: 18 November 2021
- DOI: <https://doi.org/10.1038/s41586-021-03971-9>

Share this article

Anyone you share the following link with will be able to read this content:

[Get shareable link](#)

Sorry, a shareable link is not currently available for this article.

[Copy to clipboard](#)

Provided by the Springer Nature SharedIt content-sharing initiative

This article was downloaded by **calibre** from <https://www.nature.com/articles/s41586-021-03971-9>

- Article
- [Published: 17 November 2021](#)

Approaching the intrinsic exciton physics limit in two-dimensional semiconductor diodes

- [Peng Chen](#) ORCID: [orcid.org/0000-0001-8527-1210^{1,na1}](https://orcid.org/0000-0001-8527-1210),
- [Timothy L. Atallah^{1,na1}](#),
- [Zhaoyang Lin](#) ORCID: [orcid.org/0000-0002-6474-7184¹](https://orcid.org/0000-0002-6474-7184),
- [Peiqi Wang¹](#),
- [Sung-Joon Lee²](#),
- [Junqing Xu³](#),
- [Zhihong Huang](#) ORCID: [orcid.org/0000-0002-5927-5995²](https://orcid.org/0000-0002-5927-5995),
- [Xidong Duan](#) ORCID: [orcid.org/0000-0002-4951-901X⁴](https://orcid.org/0000-0002-4951-901X),
- [Yuan Ping³](#),
- [Yu Huang](#) ORCID: [orcid.org/0000-0003-1793-0741^{2,5}](https://orcid.org/0000-0003-1793-0741),
- [Justin R. Caram](#) ORCID: [orcid.org/0000-0001-5126-3829^{1,5}](https://orcid.org/0000-0001-5126-3829) &
- [Xiangfeng Duan](#) ORCID: [orcid.org/0000-0002-4321-6288^{1,5}](https://orcid.org/0000-0002-4321-6288)

[Nature](#) volume **599**, pages 404–410 (2021)

- 1997 Accesses
- 17 Altmetric
- [Metrics details](#)

Subjects

- [Electronic devices](#)

- [Photonic devices](#)
- [Two-dimensional materials](#)

Abstract

Two-dimensional (2D) semiconductors have attracted intense interest for their unique photophysical properties, including large exciton binding energies and strong gate tunability, which arise from their reduced dimensionality^{1,2,3,4,5}. Despite considerable efforts, a disconnect persists between the fundamental photophysics in pristine 2D semiconductors and the practical device performances, which are often plagued by many extrinsic factors, including chemical disorder at the semiconductor–contact interface. Here, by using van der Waals contacts with minimal interfacial disorder, we suppress contact-induced Shockley–Read–Hall recombination and realize nearly intrinsic photophysics-dictated device performance in 2D semiconductor diodes. Using an electrostatic field in a split-gate geometry to independently modulate electron and hole doping in tungsten diselenide diodes, we discover an unusual peak in the short-circuit photocurrent at low charge densities. Time-resolved photoluminescence reveals a substantial decrease of the exciton lifetime from around 800 picoseconds in the charge-neutral regime to around 50 picoseconds at high doping densities owing to increased exciton–charge Auger recombination. Taken together, we show that an exciton-diffusion-limited model well explains the charge-density-dependent short-circuit photocurrent, a result further confirmed by scanning photocurrent microscopy. We thus demonstrate the fundamental role of exciton diffusion and two-body exciton–charge Auger recombination in 2D devices and highlight that the intrinsic photophysics of 2D semiconductors can be used to create more efficient optoelectronic devices.

Access options

Subscribe to Journal

Get full journal access for 1 year

\$199.00

only \$3.90 per issue

[Subscribe](#)

All prices are NET prices.

VAT will be added later in the checkout.

Tax calculation will be finalised during checkout.

Rent or Buy article

Get time limited or full article access on ReadCube.

from \$8.99

[Rent or Buy](#)

All prices are NET prices.

Additional access options:

- [Log in](#)
- [Access through your institution](#)
- [Learn about institutional subscriptions](#)

Fig. 1: Atomically thin WSe₂ p–n diode with atomically clean vdW contacts.

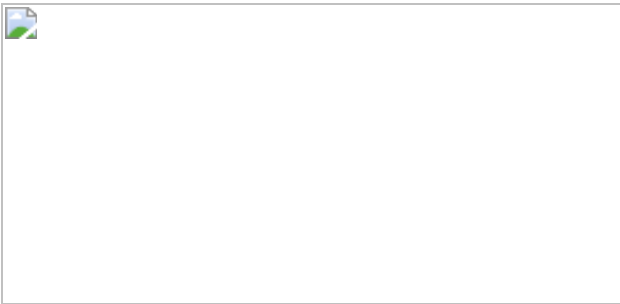


Fig. 2: Doping-dependent optoelectronic performance of a 2D WSe₂ p–n diode.

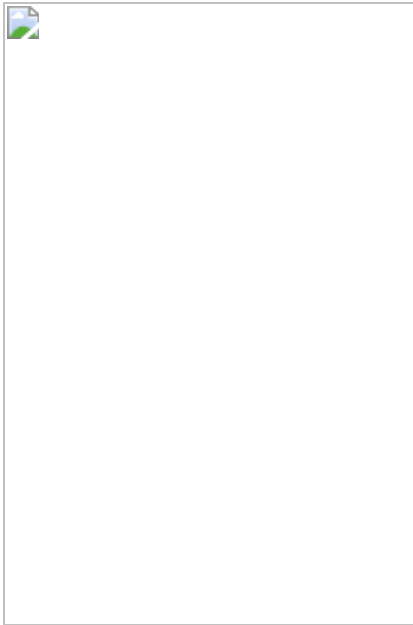
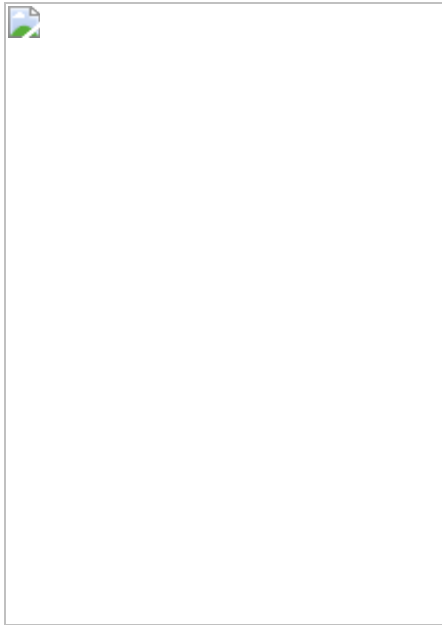


Fig. 3: Doping-dependent TRPL and exciton–charge Auger.



Fig. 4: Correlation between photocurrent and exciton lifetime.



Data availability

The data that support the plots within this paper and other findings of this study are available from the corresponding authors upon reasonable request.

References

1. 1.

Ross, J. S. et al. Electrical control of neutral and charged excitons in a monolayer semiconductor. *Nat. Commun.* **4**, 1474 (2013).

2. 2.

He, K. et al. Tightly bound excitons in monolayer WSe₂. *Phys. Rev. Lett.* **113**, 026803 (2014).

3. 3.

Chernikov, A. et al. Exciton binding energy and nonhydrogenic Rydberg series in monolayer WS₂. *Phys. Rev. Lett.* **113**, 076802 (2014).

4. 4.

Yuan, L. & Huang, L. Exciton dynamics and annihilation in WS₂ 2D semiconductors. *Nanoscale* **7**, 7402–7408 (2015).

5. 5.

Paul, K. K., Kim, J.-H. & Lee, Y. H. Hot carrier photovoltaics in van der Waals heterostructures. *Nat. Rev. Phys.* **3**, 178–192 (2021).

6. 6.

Ross, J. S. et al. Electrically tunable excitonic light-emitting diodes based on monolayer WSe₂ p–n junctions. *Nat. Nanotechnol.* **9**, 268–272 (2014).

7. 7.

Baugher, B. W., Churchill, H. O., Yang, Y. & Jarillo-Herrero, P. Optoelectronic devices based on electrically tunable p–n diodes in a monolayer dichalcogenide. *Nat. Nanotechnol.* **9**, 262–267 (2014).

8. 8.

Pospischil, A., Furchi, M. M. & Mueller, T. Solar-energy conversion and light emission in an atomic monolayer p–n diode. *Nat. Nanotechnol.* **9**, 257–261 (2014).

9. 9.

Cheng, R. et al. Electroluminescence and photocurrent generation from atomically sharp WSe₂/MoS₂ heterojunction p–n diodes. *Nano Lett.* **14**, 5590–5597 (2014).

10. 10.

Lee, C.-H. et al. Atomically thin p–n junctions with van der Waals heterointerfaces. *Nat. Nanotechnol.* **9**, 676–681 (2014).

11. 11.

Li, M.-Y. et al. Epitaxial growth of a monolayer WSe₂–MoS₂ lateral p–n junction with an atomically sharp interface. *Science* **349**, 524–528 (2015).

12. 12.

Zhang, Z. et al. Robust epitaxial growth of two-dimensional heterostructures, multiheterostructures, and superlattices. *Science* **357**, 788–792 (2017).

13. 13.

Massicotte, M. et al. Dissociation of two-dimensional excitons in monolayer WSe₂. *Nat. Commun.* **9**, 1633 (2018).

14. 14.

Wen, X., Xu, W., Zhao, W., Khurgin, J. B. & Xiong, Q. Plasmonic hot carriers-controlled second harmonic generation in WSe₂ bilayers. *Nano Lett.* **18**, 1686–1692 (2018).

15. 15.

Livache, C. et al. A colloidal quantum dot infrared photodetector and its use for intraband detection. *Nat. Commun.* **10**, 2125 (2019).

16. 16.

Khan, Q. et al. Overcoming the electroluminescence efficiency limitations in quantum-dot light-emitting diodes. *Adv. Opt. Mater.* **7**, 1900695 (2019).

17. 17.

Hong, X. et al. Ultrafast charge transfer in atomically thin MoS₂/WS₂ heterostructures. *Nat. Nanotechnol.* **9**, 682–686 (2014).

18. 18.

Yuan, L., Wang, T., Zhu, T., Zhou, M. & Huang, L. Exciton dynamics, transport, and annihilation in atomically thin two-dimensional semiconductors. *J. Phys. Chem. Lett.* **8**, 3371–3379 (2017).

19. 19.

Steinhoff, A. et al. Biexciton fine structure in monolayer transition metal dichalcogenides. *Nat. Phys.* **14**, 1199–1204 (2018).

20. 20.

Zhu, X.-Y. How to draw energy level diagrams in excitonic solar cells. *J. Phys. Chem. Lett.* **5**, 2283–2288 (2014).

21. 21.

Pólya, G. Über eine Aufgabe der Wahrscheinlichkeitsrechnung betreffend die Irrfahrt im Straßennetz. *Math. Ann.* **84**, 149–160 (1921).

22. 22.

Doyle, P. G. *Application of Rayleigh's Short-cut Method to Polya's Recurrence Problem*. PhD thesis, Dartmouth College (1982).

23. 23.

Dean, C. R. et al. Boron nitride substrates for high-quality graphene electronics. *Nat. Nanotechnol.* **5**, 722–726 (2010).

24. 24.

Chen, P. et al. Band evolution of two-dimensional transition metal dichalcogenides under electric fields. *Appl. Phys. Lett.* **115**, 083104 (2019).

25. 25.

Liu, Y. et al. Approaching the Schottky–Mott limit in van der Waals metal–semiconductor junctions. *Nature* **557**, 696–700 (2018).

26. 26.

Chow, C. M. E. et al. Monolayer semiconductor Auger detector. *Nano Lett.* **20**, 5538–5543 (2020).

27. 27.

Wang, Y. et al. Van der Waals contacts between three-dimensional metals and two-dimensional semiconductors. *Nature* **568**, 70–74 (2019).

28. 28.

Luque, A. & Hegedus, S. *Handbook of Photovoltaic Science and Engineering* 2nd edn (John Wiley, 2011).

29. 29.

Allen, T. G., Bullock, J., Yang, X., Javey, A. & De Wolf, S. Passivating contacts for crystalline silicon solar cells. *Nat. Energy* **4**, 914–928 (2019).

30. 30.

Das, S., Gupta, G. & Majumdar, K. Layer degree of freedom for excitons in transition metal dichalcogenides. *Phys. Rev. B* **99**, 165411 (2019).

31. 31.

Lien, D.-H. et al. Electrical suppression of all nonradiative recombination pathways in monolayer semiconductors. *Science* **364**, 468–471 (2019).

32. 32.

David, A., Young, N. G., Lund, C. & Craven, M. D. The physics of recombinations in III-nitride emitters. *ECS J. Solid State Sci. Technol.* **9**, 016021 (2019).

33. 33.

Elbaz, G. A. et al. Unbalanced hole and electron diffusion in lead bromide perovskites. *Nano Lett.* **17**, 1727–1732 (2017).

34. 34.

Chuang, S. L. *Physics of Optoelectronic Devices* (John Wiley, 1995).

35. 35.

Passari, L. & Susi, E. Recombination mechanisms and doping density in silicon. *J. Appl. Phys.* **54**, 3935–3937 (1983).

36. 36.

Altermatt, P. P., Schmidt, J., Heiser, G. & Aberle, A. G. Assessment and parameterisation of Coulomb-enhanced Auger recombination coefficients in lowly injected crystalline silicon. *J. Appl. Phys.* **82**, 4938–4944 (1997).

37. 37.

Richter, A., Glunz, S. W., Werner, F., Schmidt, J. & Cuevas, A. Improved quantitative description of Auger recombination in crystalline silicon. *Phys. Rev. B* **86**, 165202 (2012).

38. 38.

Kadlec, E. et al. Effects of electron doping level on minority carrier lifetimes in n-type mid-wave infrared InAs/InAs_{1-x}Sb_x type-II superlattices. *Appl. Phys. Lett.* **109**, 261105 (2016).

39. 39.

Cadiz, F. et al. Exciton diffusion in WSe₂ monolayers embedded in a van der Waals heterostructure. *Appl. Phys. Lett.* **112**, 152106 (2018).

40. 40.

Mouri, S. et al. Nonlinear photoluminescence in atomically thin layered WSe₂ arising from diffusion-assisted exciton–exciton annihilation. *Phys. Rev. B* **90**, 155449 (2014).

41. 41.

Uddin, S. Z. et al. Neutral exciton diffusion in monolayer MoS₂. *ACS Nano* **14**, 13433–13440 (2020).

42. 42.

Martin, J. et al. Observation of electron–hole puddles in graphene using a scanning single-electron transistor. *Nat. Phys.* **4**, 144–148 (2008).

43. 43.

Chen, K. et al. Experimental evidence of exciton capture by mid-gap defects in CVD grown monolayer MoSe₂. *npj 2D Mater. Appl.* **1**, 15 (2017).

44. 44.

Liu, E. et al. Gate tunable dark trions in monolayer WSe₂. *Phys. Rev. Lett.* **123**, 027401 (2019).

45. 45.

Nguyen, P. V. et al. Visualizing electrostatic gating effects in two-dimensional heterostructures. *Nature* **572**, 220–223 (2019).

46. 46.

Tea, E. & Hin, C. Charge carrier transport and lifetimes in n-type and p-type phosphorene as 2D device active materials: an ab initio study. *Phys. Chem. Chem. Phys.* **18**, 22706–22711 (2016).

47. 47.

Palummo, M., Bernardi, M. & Grossman, J. C. Exciton radiative lifetimes in two-dimensional transition metal dichalcogenides. *Nano Lett.* **15**, 2794–2800 (2015).

48. 48.

Ye, Z. et al. Efficient generation of neutral and charged biexcitons in encapsulated WSe₂ monolayers. *Nat. Commun.* **9**, 3718 (2018).

49. 49.

Sundararaman, R. et al. JDFTx: Software for joint density-functional theory. *SoftwareX* **6**, 278–284 (2017).

50. 50.

Schlipf, M. & Gygi, F. Optimization algorithm for the generation of ONCV pseudopotentials. *Comput. Phys. Commun.* **196**, 36–44 (2015).

51. 51.

Perdew, J. P., Burke, K. & Ernzerhof, M. Generalized gradient approximation made simple. *Phys. Rev. Lett.* **77**, 3865–3868 (1996).

52. 52.

Grimme, S. Semiempirical GGA-type density functional constructed with a long-range dispersion correction. *J. Comput. Chem.* **27**, 1787–1799 (2006).

53. 53.

Groenendijk, D. J. et al. Photovoltaic and photothermoelectric effect in a double-gated WSe₂ device. *Nano Lett.* **14**, 5846–5852 (2014).

Acknowledgements

Xiangfeng Duan acknowledges the support from the Office of Naval Research through Award N00014-18-1-2707. J.R.C. acknowledges NSF Career grant number 1945572. Y.H. acknowledges the financial support from the Office of Naval Research through award N00014-18-1-2491. Y.P. acknowledges the support from Air Force Office of Scientific Research under AFOSR award no. FA9550-YR-1-XYZQ.

Author information

Author notes

1. These authors contributed equally: Peng Chen, Timothy L. Atallah

Affiliations

1. Department of Chemistry and Biochemistry, University of California, Los Angeles, Los Angeles, CA, USA

Peng Chen, Timothy L. Atallah, Zhaoyang Lin, Peiqi Wang, Justin R. Caram & Xiangfeng Duan

2. Department of Materials Science and Engineering, University of California, Los Angeles, Los Angeles, CA, USA

Sung-Joon Lee, Zhihong Huang & Yu Huang

3. Department of Chemistry and Biochemistry, University of California Santa Cruz, Santa Cruz, CA, USA

Junqing Xu & Yuan Ping

4. State Key Laboratory for Chemo/Biosensing and Chemometrics,
College of Chemistry and Chemical Engineering, Hunan University,
Changsha, China

Xidong Duan

5. California NanoSystems Institute, University of California, Los Angeles, Los Angeles, CA, USA

Yu Huang, Justin R. Caram & Xiangfeng Duan

Contributions

Xiangfeng Duan and P.C. conceived the research. P.C., T.L.A., J.R.C. and Xiangfeng Duan designed the experiment. P.C. fabricated the devices and performed optoelectrical measurements. Z.L., P.W., S.-J.L., Z.H., Xidong Duan and Y.H. contributed to materials, device fabrications, measurements and discussions. J.X. and Y.P. conducted band structure calculations. T.L.A. and P.C. conducted the time-resolved photoluminescence and photocurrent scanning measurements. P.C., T.L.A., J.R.C. and Xiangfeng Duan performed the data analysis. P.C., T.L.A., J.R.C. and Xiangfeng Duan co-wrote the manuscript. All authors discussed the results and commented on the manuscripts.

Corresponding authors

Correspondence to [Justin R. Caram](#) or [Xiangfeng Duan](#).

Ethics declarations

Competing interests

The authors declare no competing interests.

Additional information

Peer review information *Nature* thanks Andrey Chaves, Lain-Jong Li and the other, anonymous, reviewer(s) for their contribution to the peer review of this work.

Publisher's note Springer Nature remains neutral with regard to jurisdictional claims in published maps and institutional affiliations.

Extended data figures and tables

Extended Data Fig. 1 Band diagram and photocurrent generation in diode.

a, The carriers generated by the Schottky barrier are blocked by the barrier at the p–n interface. **b**, The carriers generated by the p–n junction may tunnel through the Schottky junction and contribute to the photocurrent.

Extended Data Fig. 2 Fitting the I_{DS} - V_{DS} characteristic of p–n junction diode.

Black dot: experimental data; solid red line: fit of diode equation. **a**, The fit of p–n configuration; we extract the $R_S = 36 \text{ M}\Omega$, $R_{SH} = 47 \text{ G}\Omega$, $I_S = 4.6 \times 10^{-22} \text{ A}$ and $\eta = 1.18$; **b**, The fit of NP configuration; we extract the $R_S = 28 \text{ M}\Omega$, $R_{SH} = 35 \text{ G}\Omega$, $I_S = 8.1 \times 10^{-21} \text{ A}$ and $\eta = 1.3$.

Extended Data Fig. 3 Apparent external quantum efficiency (EQE) of 2D diodes by assuming the device area as the active area.

a, EQE dependence on charge density for the evap-diode (red dots) and the vdW-diode (black dots) at $V_{G1} = -5 \text{ V}$. The line serves as a guide for the eyes. **b**, EQE dependence on charge density for the evap-diode (red dots) and the vdW-diode (black dots) at $V_{G1} = 5 \text{ V}$. The EQE is calculated as $\text{EQE} = I_{SC}E_{ph}/(eP_{in})$, where I_{SC} is the short circuit photocurrent, E_{ph} is the energy per photon, e is the elementary charge and P_{in} is the input power.

$P_{\text{in}} = \text{power density } (P_d) \times \text{illuminated exciton-collection area } (A)$. Note we estimated the apparent EQE by using the device area (the entire WSe₂ area between the source and drain electrodes) as A for simplicity, which may lead to a considerably underestimated EQE value as the device area is usually larger than the active area. If we consider the exciton diffusion model with a total exciton collection length of $\sim 1 \mu\text{m}$, the maximum EQE is estimated $\sim 21\%$.

Extended Data Fig. 4

Fitting lifetimes and doping dependence of relative PL intensity and lifetime for different components. **a**, An example of biexponential fit: ($V_G = -0.8 \text{ V}$, $P = 244 \text{ nW}$). The top panel is the residuals of tri-exponential fitting. The middle panel is the residuals of bi-exponential fitting. The bi-exponential residual is identical to the tri-exponential implying the tri-exponential is an over-fit confirmed by the error in k_3 being larger than the value of k_3 (Extended Data Table 1); therefore, we used the bi-exponential fit. The bottom panel is the TRPL data and bi-exponential and tri-exponential fitting curve. **b**, An example of triexponential fit: ($V_G = -4 \text{ V}$, $P = 244 \text{ nW}$). The top panel is the residuals of tri-exponential fitting. The middle panel is the residuals of bi-exponential fitting. The tri-exponential residual is better than the bi-exponential without fit errors larger than the fit values; there we used the tri-exponential fit. The bottom panel is the TRPL data and bi-exponential and tri-exponential fitting curve. **c**, Doping dependence of relative PL intensity for different components. There are three components, which are t_1 , t_2 and t_3 . **d**, Doping dependence of the PL lifetime for different components. The inset shows the lifetime of t_3 .

Extended Data Fig. 5 A highly simplified band diagram showing the relevant states for band-edge carriers in WSe₂.

$E_{F,0}$ denotes the Fermi level of undoped system; $E_{F,t}$ denotes the Fermi level at turning point.

Extended Data Fig. 6 Deconvolution of the exciton diffusion from scanning photocurrent microscopy studies.

Specifically, we used $V_{G1} = 4$ V and $V_{G2} = -4$ V (black line) as our measure of laser spot size since the photocurrent collection is exclusively from the diode interface, which is much smaller than our laser spot size (instrument response function, IRF) and fit (red dashed line) it to a single Gaussian function. We fit (pink dashed line) $V_{G1} = 4$ V and $V_{G2} = -0.4$ V (blue line) with a function being convolution of the IRF Gaussian with an exponential centred at the middle of the interface ($X = 0$ μm) for the low-doping limit. The decay constant for the fit corresponds to exciton diffusion length $L_{\text{exc}} = 0.72 \pm 0.10$ μm . The yellow square denotes the position of electrodes.

Extended Data Fig. 7 Gate dependent I_{SC} in monolayer, bilayer and four-layer WSe₂ vdW-diodes.

a, $I_{\text{DS}} - V_{\text{DS}}$ curve of the monolayer WSe₂ diode under illumination. **b**, $I_{\text{DS}} - V_{\text{DS}}$ curve of the bilayer WSe₂ diode under illumination. **c**, $I_{\text{DS}} - V_{\text{DS}}$ curve of the four-layer WSe₂ diode under illumination. **d**, Gate dependent I_{SC} in monolayer diode. **e**, Gate dependent I_{SC} in bilayer diode. **f**, Gate dependent I_{SC} in four-layer diode.

Extended Data Fig. 8

Power dependent apparent EQE in a bilayer diode at $V_{G1} = 5$ V and different V_{G2} .

Extended Data Table 1 Fitting parameters for Extended Data Fig. 4a, 4b

Extended Data Table 2 Summary of the diode parameters in different studies

Rights and permissions

[Reprints and Permissions](#)

About this article

Cite this article

Chen, P., Atallah, T.L., Lin, Z. *et al.* Approaching the intrinsic exciton physics limit in two-dimensional semiconductor diodes. *Nature* **599**, 404–410 (2021). <https://doi.org/10.1038/s41586-021-03949-7>

- Received: 03 February 2021
- Accepted: 24 August 2021
- Published: 17 November 2021
- Issue Date: 18 November 2021
- DOI: <https://doi.org/10.1038/s41586-021-03949-7>

Share this article

Anyone you share the following link with will be able to read this content:

[Get shareable link](#)

Sorry, a shareable link is not currently available for this article.

[Copy to clipboard](#)

Provided by the Springer Nature SharedIt content-sharing initiative

This article was downloaded by **calibre** from <https://www.nature.com/articles/s41586-021-03949-7>

- Article
- Open Access
- [Published: 17 November 2021](#)

In-orbit demonstration of an iodine electric propulsion system

- [Dmytro Rafalskyi](#)¹,
- [Javier Martínez Martínez](#)¹,
- [Lui Habl](#) [ORCID: orcid.org/0000-0003-4259-9894](#)^{1,2},
- [Elena Zorzoli Rossi](#)¹,
- [Plamen Proynov](#)¹,
- [Antoine Boré](#)¹,
- [Thomas Baret](#)¹,
- [Antoine Poyet](#)¹,
- [Trevor Lafleur](#) [ORCID: orcid.org/0000-0002-9926-2187](#)¹,
- [Stanislav Dudin](#) [ORCID: orcid.org/0000-0001-9161-4654](#)¹ &
- [Ane Aanesland](#)¹

[Nature](#) volume **599**, pages 411–415 (2021)

- 2182 Accesses
- 275 Altmetric
- [Metrics details](#)

Subjects

- [Aerospace engineering](#)
- [Applied physics](#)
- [Plasma-based accelerators](#)

Abstract

Propulsion is a critical subsystem of many spacecraft^{1,2,3,4}. For efficient propellant usage, electric propulsion systems based on the electrostatic acceleration of ions

formed during electron impact ionization of a gas are particularly attractive^{5,6}. At present, xenon is used almost exclusively as an ionizable propellant for space propulsion^{2,3,4,5}. However, xenon is rare, it must be stored under high pressure and commercial production is expensive^{7,8,9}. Here we demonstrate a propulsion system that uses iodine propellant and we present in-orbit results of this new technology. Diatomic iodine is stored as a solid and sublimated at low temperatures. A plasma is then produced with a radio-frequency inductive antenna, and we show that the ionization efficiency is enhanced compared with xenon. Both atomic and molecular iodine ions are accelerated by high-voltage grids to generate thrust, and a highly collimated beam can be produced with substantial iodine dissociation. The propulsion system has been successfully operated in space onboard a small satellite with manoeuvres confirmed using satellite tracking data. We anticipate that these results will accelerate the adoption of alternative propellants within the space industry and demonstrate the potential of iodine for a wide range of space missions. For example, iodine enables substantial system miniaturization and simplification, which provides small satellites and satellite constellations with new capabilities for deployment, collision avoidance, end-of-life disposal and space exploration^{10,11,12,13,14}.

[Download PDF](#)

Main

Spacecraft require propulsion to perform manoeuvres in space, such as orbit transfers, avoidance of collisions, orbit maintenance to compensate for aerodynamic or gravitational perturbations, and end-of-life disposal¹. The choice of propulsion technology, in particular its exhaust speed, determines the propellant mass needed. Electric propulsion^{5,15} uses electric power to accelerate a propellant (via electric and/or magnetic fields) and can achieve exhaust speeds that are an order of magnitude higher than chemical propulsion (which uses energy from chemical reactions for propellant acceleration). Some of the most successful electric propulsion systems include gridded ion and Hall thrusters⁵, which create a plasma through electron impact ionization of a gas⁶ and electrostatically accelerate ions to generate thrust. In addition to being used by many commercial satellites orbiting the Earth, such propulsion systems are also used for space exploration. Examples include the European Space Agency's SMART-1 mission to the Moon², NASA's Dawn mission that studied the protoplanets Ceres and Vesta in the asteroid belt between Mars and Jupiter¹⁶, and the Japanese Aerospace Exploration Agency's Hayabusa1 and Hayabusa2 sample-return missions to the near-Earth asteroids 25143 Itokawa¹⁷ and 162173 Ryugu¹⁸.

As spacecraft are power limited, electric propulsion systems must maximize their thrust-to-power ratio, which for electrostatic accelerators requires a propellant with a

low ionization threshold and a high atomic mass⁵. At present, the propellant of choice is xenon. However, xenon is very rare (less than one part per ten million in the atmosphere), and commercial production is both expensive and limited^{7,8,9}. There are also competing applications that use xenon, including lighting and imaging, anaesthetics in hospitals^{9,19} and etching in the semiconductor industry²⁰. With the rise of satellite mega-constellations^{21,22,23}, the demand for xenon may outpace supply within the next ten years. A further disadvantage is that xenon must be stored at very high pressures (typically 10–20 MPa), which requires specialized loading equipment and trained personnel, making it incompatible with the ‘new space’ paradigm. For the long-term sustainability of the space industry, it is critical that a replacement propellant be found.

A possible alternative is iodine^{24,25}, which is much more abundant and cheaper than xenon²⁶ ([Methods](#)) and can be stored unpressurized as a solid. In addition, both atomic and diatomic iodine have a lower ionization threshold, and diatomic iodine has a relative mass that is almost twice that of xenon. Although iodine is viewed as a game-changing propellant and has been investigated by companies^{27,28}, universities^{29,30,31} and space agencies³² around the world, no system has previously been tested in space. Here we describe the development and testing of an iodine electric propulsion system (the NPT30-I2, with a nominal power and thrust of 55 W and 0.8 mN, respectively) and present results of the in-space operation of this new technology.

Solid diatomic iodine is stored in a tank connected to an inductively coupled plasma source tube terminated by two high-voltage, multi-aperture grids (Fig. 1). Heaters connected to the tank cause iodine sublimation and subsequent gas flow into the source tube. An iodine plasma is created by electron impact ionization using a radio-frequency (RF) inductive antenna, and positive plasma ions are extracted and accelerated by the grids to high speeds (about 40 km s^{-1}) to produce thrust. A cathode filament downstream of the grids thermionically emits electrons to charge neutralize the ion beam. The propulsion system includes all subsystems for operation (Extended Data Fig. 1a), such as propellant storage, delivery and control, the gridded ion thruster, electron-emitting neutralizers, the power processing unit and passive thermal management³³. See [Methods](#) for further details of the electrical system and cathode neutralizer. Iodine enables substantial miniaturization, and with the innovations discussed below, the total mass (including propellant) and volume are 1.2 kg and 96 mm × 96 mm × 106 mm, respectively.

Fig. 1: Schematic of the NPT30-I2 iodine electric propulsion system.

figure1

Solid iodine (darker green region) is located in a storage tank upstream of the plasma source tube (blue region). Heating causes sublimation and a low-pressure gas (lighter green region) enters the source tube (green arrow). A plasma (purple region) is created by a RF antenna, and iodine ions (I^+ , I_2^+ and I^{2+}) are accelerated by a set of grids. A cathode emits electrons (e^-) to neutralize the ion beam. Waste heat is conducted towards the iodine tank and structural frame (solid blue arrows) or radiated away (blue dashed arrows).

The use of iodine creates unique design and operational challenges. Iodine has a high electronegativity that can lead to corrosion with many common materials. Technical ceramics (aluminium oxide and zirconium oxide) are used for the source tube and some interface components, and all vulnerable metal surfaces are coated with a polymer film. The iodine sublimation rate is controlled by monitoring and adjusting the tank temperature to maintain the desired saturation pressure in the range of 2–6 kPa. The operating temperature of the tank is kept between 80 °C and 100 °C to avoid local melting of iodine, and the tank is directly integrated upstream of the plasma source tube. When the propulsion system is not firing, iodine gas cools and deposits

within a small orifice ([Methods](#)) between the tank and source tube blocking further flow without the need for a control valve.

Vibrations during launch and spacecraft motion once in orbit can cause solid iodine to break into pieces, which may damage the propulsion system or lead to poor thermal contact during heating. To prevent this, iodine is embedded into a porous aluminium oxide ceramic block with a porosity of 95% placed inside the tank (the tank-to-propellant mass fraction is 54%). During assembly, iodine is heated above its melting temperature to form a liquid, which is poured into the block ([Methods](#)). Once cooled, the iodine solidifies and is safely held. When the propulsion system fires, plasma heat losses to the walls of the source tube and heat losses in the power electronics are directed towards the storage tank (Fig. 1). This allows reuse of waste heat so that less than 1 W of additional power is needed from heaters during steady-state operation. All other heat losses are channelled to the front and side panels of the propulsion system and either radiated or conducted to the spacecraft. See [Methods](#) for further thermal design details.

For plasma creation and ion acceleration, the use of iodine leads to important differences over xenon, as in addition to the molecular ion I_2^+ , direct dissociative ionization²⁹ and two-step dissociation and ionization reactions allow the formation of the atomic ion I^+ . Multiply charged ions, such as I^{2+} , are also possible. Ground testing has been conducted to characterize the system before launch ([Methods](#)). Using time-of-flight spectrometry with an electrostatic diagnostic system in the thruster plume, mass-to-charge ratio spectra are measured (Fig. 2a) and the beam composition is determined, as shown in Fig. 2b. The dominant ion species are I_2^+ and I^+ , and their relative fractions change with RF generator output power. As the mass flow rate is fixed, higher iodine dissociation occurs at higher powers owing to an increased plasma density. Gas depletion at these powers also results in more energetic electrons, which affects the rate factors of collisional processes²⁹.

Fig. 2: Beam composition and ionization efficiency.

 **figure2**

a, Example mass-to-charge ratio, m/z , spectrum obtained with the TOF diagnostic system. The labels indicate the ions I^{2+} , I^+ and I_2^+ . **b**, Relative current concentration of iodine species in the ion beam as a function of RF generator output power. **c**, Ion-beam current extracted from the plasma source as a function of RF power with iodine and xenon propellants. The black curve shows results of a numerical plasma discharge model ([Methods](#)). **d**, Propellant mass utilization efficiency as a function of total power for different iodine mass flow rates. The error bars represent estimates of measuring equipment precision and accuracy limitations.

[Source data](#)

Despite diatomic gases having additional energy-loss mechanisms associated with molecular dissociation and the excitation of vibrational and rotational states³⁴, the

ionization efficiency of iodine in our propulsion system is higher than that of xenon, as shown in Fig. 2c. For the experiments with xenon, the system was temporarily modified to inject gas into the source tube from an external high-pressure storage tank. The iodine mass flow rate is inferred from measurements of the entire propulsion system mass before and after operation. In Fig. 2c, for the same mass flow rate and RF power, an almost 50%-higher beam current is extracted from the plasma source with iodine. This improvement is consistent with previous experimental and numerical results^{29,30} and occurs because of the lower ionization threshold of iodine ions (10.5 eV for I^+ and 9.3 eV for I_2^+) compared with xenon (12.1 eV for Xe^+) and the different collisional processes and reaction cross-sections. This results in a lower electron temperature and lower consequent plasma losses to the source tube walls³⁴. The results for xenon are in agreement with a numerical model ([Methods](#)). A common ionization performance metric^{5,35} is the propellant mass utilization efficiency (Fig. 2d), $\eta_m = \frac{(\dot{m}_i)}{(\dot{m}_s)}$, where \dot{m}_i is the ion mass flow rate and \dot{m}_s is the sublimation mass flow rate. At the highest performance in our system, $\eta_m \approx 60\%$ for iodine and $\eta_m \approx 40\%$ for xenon (not shown).

Ions in the plasma source are extracted and accelerated by voltages between 800 V and 1,300 V applied across the grids. Measurements of the ion flux distributions ([Methods](#)) in Fig. 3a confirm the presence of high-energy ions with an average energy close to the net accelerating voltage, V_n , of 900 V and 1,300 V, respectively. By measuring the ion-beam current ([Methods](#)) an indirect measurement of the thrust is obtained from, $F = \alpha \gamma I_{beam} \sqrt{2M_I}$. Here I_{beam} is the beam current, M_I and q_I are the mass and charge of atomic iodine ions, respectively, and γ and α are correction factors: $\gamma = \cos\theta_{div}$, where θ_{div} is the beam divergence half-angle, and $\alpha = \beta \gamma^{2+}$, where $\beta = \frac{\sqrt{2}}{\sqrt{2+}}$, where $\beta = \frac{\sqrt{2}}{\sqrt{2+}}$, and $\gamma = \frac{\sqrt{2}}{\sqrt{2+}}$ are the relative current contributions for each ion species and the pre-factors represent the square root of the relative mass-to-charge ratio. An example of the thrust correction factor, $\alpha\gamma$, is shown in Extended Data Fig. 3b. The propulsion system electronics continually perform these indirect thrust estimates during operation. Direct thrust measurements are obtained using a thrust balance ([Methods](#)). Figure 3b shows the measured thrust range achievable, and a comparison between direct and indirect measurements.

Fig. 3: Propulsion system performance.

 **figure3**

a, Ion flux distribution functions (IFDF) in the plume for acceleration voltages of 900 V and 1,300 V. **b**, Direct thrust measurements from a thrust balance compared with indirect thrust measurements estimated from the ion-beam current, applied grid voltage, and extrapolated beam divergence and beam composition data. **c**, Measured ion-beam divergence half-angle with iodine and xenon. The normalized perveance, p/p_{\max} , is a measure of the ion space charge ([Methods](#)). **d**, Thrust and specific impulse performance map of the propulsion system within the operating total power range, and for different iodine mass flow rates. The error bars represent 1 s.d. (**b**) or estimates of measuring equipment precision and accuracy limitations (**c**).

[Source data](#)

By carefully designing the grids ([Methods](#), Extended Data Fig. [3a, d](#)), ions are well focused with a low divergence between 10° and 15°, as shown in Fig. [3c](#). The beam

divergence has been measured with an automated array of electrostatic probes ([Methods](#)). The iodine divergence is slightly lower than that of xenon because of the improved ionization efficiency, which reduces unionized neutrals in the plume and lowers the ion-neutral collision frequency. An important performance metric is the specific impulse⁵, $\{I\}_{\rm sp} = F \cdot m / (g_0 \cdot t)$, which represents how effectively propellant is used (here g_0 is the gravitational acceleration equal to 9.81 m s⁻²). The performance map of the propulsion system is shown in Fig. [3d](#) (see also Extended Data Fig. [3c,e](#)), where the maximum thrust and specific impulse are about 1.3 mN and 2,500 s, respectively, for total powers (which includes RF power, acceleration power, neutralizer power, propellant heating power, electronics power and all losses) below 65 W. The total impulse that can be delivered to a spacecraft at the maximum specific impulse is 5,500 Ns (corresponding to a burn time of about 1,500 h).

The propulsion system has undergone extensive qualification to meet in-space conditions and launch-vehicle requirements ([Methods](#)), and a flight model was recently integrated into the Beihangkongshi-1 satellite operated by Spacety (Extended Data Fig. [1b](#)). The 12-unit CubeSat (with a mass of approximately 20 kg) was launched into space onboard a Long March 6 rocket on 6 November 2020. The satellite was injected into a circular, Sun-synchronous orbit with an altitude of approximately 480 km.

Figure [4a](#) summarizes all test firings performed up until 28 February 2021 and shows the mean semi-major axis of the satellite as predicted from a theoretical model, GPS data from the satellite, numerical simulations (using the General Mission Analysis Tool, GMAT³⁶), and independent tracking data of the satellite (satellite catalogue number 46838) produced by the Space Surveillance Network (SSN) operated by the US Space Command³⁷. The arrows indicate 11 firings over the displayed time period. Tests 1A and 1B represent firings to check the overall system operation. Subsequent firings 2A–2I test the repeatability and ignition cycling. The direction of the thrust vector has been varied during some firings (by reorienting the satellite using its onboard attitude control system). The duration of each test is between 80 min and 90 min (including 10–20 min for iodine heating and plasma ignition, which results in a small propellant mass loss of 12 mg before thrust generation), which for each firing gives an altitude change between 200 m and 400 m at a thrust and power of about 0.8 mN and 55 W, respectively. As an example, Fig. [4b](#) shows GPS data, GMAT simulations and theoretical predictions for firing 1B, and Fig. [4c](#) shows the estimated thrust and power consumption from telemetry data during the manoeuvre (see also Extended Data Fig. [4c](#)). See [Methods](#) and Extended Data Table 1 for further orbital analysis details.

Fig. 4: In-orbit manoeuvres performed by an iodine electric propulsion system.

 **figure4**

a, Mean semi-major axis of the Beihangkongshi-1 satellite from the SSN³⁸ and GPS data, and as predicted using numerical simulations and theory. The arrows indicate separate firings. **b**, Mean semi-major axis as a function of time during manoeuvre 1B. The green region indicates when the propulsion system is firing. **c**, Thrust and total power telemetry during manoeuvre 1B. **d**, Comparison between ion-beam current, *b*, electron neutralizer current, *e*, and current to the accel grid, *a*, during ground, *g*, and in-flight, *f*, operation for manoeuvre 1B. The GPS data have an accuracy of approximately 20 m.

Source data

The results in Fig. 4a, b shows definite orbit changes correlated with the known propulsion system start times. At present, the firings have demonstrated a cumulative altitude change above 3 km. Additional downloaded propulsion system telemetry data are shown in Fig. 4d (see also Extended Data Fig. 4a, b), which is compared with corresponding ground measurement data taken during qualification. These measurements confirm that sufficient ion beam neutralization occurs (the electron emission current is larger than the ion current) and that ground testing conditions reproduce the space environment.

The linear decay between firings in Fig. 4a represents residual aerodynamic drag on the satellite¹. Manoeuvres 1A and 1B demonstrate that the propulsion system can be used for orbit maintenance to compensate for this drag. In addition, all firings are representative of collision avoidance manoeuvres. Given the rapid growth of small satellites in low Earth orbit³⁸, a miniaturized propulsion system enabled by the use of iodine will provide such satellites with the capability to avoid potential collisions and to deorbit at end of life to prevent the build-up of space debris: actions that will prove vital for the long-term sustainability of the space industry³⁹.

In conclusion, we have described an iodine electric propulsion system and presented in-orbit results demonstrating this new technology. Our work shows that iodine is not only a viable replacement propellant for xenon but also gives enhanced performance. For large satellites and satellite constellations, the use of a more abundant propellant that can be stored unpressurized will help simplify satellite design and propulsion system integration and reduce the market demand for xenon, which may have benefits in other sectors^{9,24}. For smaller satellites, iodine provides high impulse capability giving new options for deployment, collision avoidance and deorbiting, and advanced space exploration missions^{10,11,12,13,14}.

Methods

Propellant cost comparison

High-purity iodine is not needed in our propulsion system, and the total propellant cost for a purity of 99.5% was approximately US\$60, with an additional cost below US\$200 for iodine-related hardware. The propulsion system qualification cost was just under US\$4,000. A modified version of our propulsion system using xenon propellant has also been developed. For the same mass of propellant, the cost of xenon was US\$1,275, and owing to the high-pressure titanium tank, flow control valves, pipe and sensors, the hardware cost was about 100 times higher than that for iodine. The qualification cost also increased to approximately US\$9,000.

The high cost of xenon is one of the reasons that SpaceX has instead chosen krypton as an alternative propellant for their Starlink satellites⁴⁰. However, krypton has a higher ionization threshold and lower atomic mass than both xenon and iodine, and the required propulsion system power increases by more than 25% to achieve the same thrust level. Furthermore, the storage density of krypton is approximately three times lower than that of xenon (and nine times lower than that of iodine)⁴¹, which increases the volume and mass of the propellant tank. Krypton is used in a number of competing industries, such as window insulation applications, which account for more than 50% of the market share, and which is expected to grow rapidly⁴² due to the demand for energy-efficient buildings. Considering a Starlink constellation size between 12,000 and 42,000 satellites, each requiring of the order of 10 kg of propellant⁴⁰, a substantial amount of krypton will be needed in the coming years.

Plasma modelling

Owing to the similarity in physical properties between xenon and iodine, and the wider availability and accuracy of important physical data (such as reaction cross-sections), xenon has been used in numerical modelling to aid the design, development and

testing of the propulsion system. The model (which is similar to that in ref. [43](#)) is self-consistent and considers mass flow conservation, and volume-averaged ionization and power balance within the thruster summarized by the following steady-state conservation equations

$$\dot{m} = \dot{m}_i + \dot{m}_n \quad (1)$$

$$A_{\text{eff}} u_B = n_n K_{iz} V \quad (2)$$

$$P_{\text{RF}} = \frac{n_p u_B A_{\text{eff}}}{\eta_{\text{rf}}} \quad (3)$$

Here \dot{m} is the total input propellant mass flow rate, \dot{m}_i is the mass flow rate of ions extracted from the plasma source, \dot{m}_n is the mass flow rate of any unionized neutral gas, A_{eff} is the effective surface area for plasma loss inside the source tube, $u_B = \sqrt{q T_e / M}$ is the Bohm velocity^{[34](#)}, q and M are the ion charge and mass, respectively, T_e is the electron temperature, n_n is the average neutral gas density in the source tube, K_{iz} is the ionization rate factor, V is the volume of the source tube, P_{RF} is the RF power, n_p is the average plasma density inside the plasma source, η_{rf} is the antenna–plasma power transfer efficiency. The equations above implicitly include relevant electron-neutral reaction processes (such as elastic scattering, and inelastic excitation and ionization processes), RF antenna–plasma coupling and plasma-wall sheath physics^{[34,43](#)}.

Ion optics

One of the key elements of a gridded ion thruster are the ion optics, which in our case consists of a two-grid assembly. Particle-in-cell (PIC) simulations (using the open-source code XOPIC^{[44](#)}) have been used to model ion extraction and acceleration by the grids. Extended Data Fig. [3d](#) shows a PIC simulation of ion acceleration through a single set of grid holes. Ions are well focused through the holes with no direct impingement, and only low-energy ions generated by ion-neutral charge-exchange collisions and possible downstream electron-neutral ionization with unionized neutral gas in the plume, strike the second grid (called the accel grid), as is typical in gridded ion thrusters^{[5](#)}.

For given grid dimensions, if the total accelerating voltage is too low, the space charge of the ions between the grids can lead to under-focusing and direct impingement on the upstream surface of the second grid. This results in rapid sputter erosion, and possible shorting of the grids by sputtered material. The well known Child–Langmuir law³⁴ can be used to estimate this space-charge-limited current, I_{CL} , which in our case gives

$$\text{I}_{\text{CL}} = \frac{4\pi\varepsilon_0 N A_s}{9\sqrt{\frac{2qM}{V_T}}} \left(\frac{V_T}{L_{\text{eff}}} \right)^{3/2} \quad (4)$$

where ε_0 is the permittivity of free space, N is the number of grid apertures, A_s is the area of each aperture in the upstream grid (called the screen grid), V_T is the total accelerating voltage across the grids and $L_{\text{eff}} = \sqrt{(t_s + L_g)^2 + r_s^2}$ is the effective grid gap length with t_s and r_s the screen grid thickness and aperture radius, respectively, and L_g the physical grid gap length. A useful metric for quantifying the level of space charge between the grids is the perveance, $p = I_{\text{beam}}/V_T^{3/2}$. When the ion beam current is equal to the space-charge-limited current, the maximum perveance, p_{max} , of the grids is reached. For the grids used in our propulsion system, $p_{\text{max}} = 1.7 \times 10^{-6} \text{ A V}^{-3/2}$ for singly charged atomic iodine ions. If the total accelerating voltage is instead too high, the cross-over limit⁵ is reached and ions are over-focused, again leading to erosion. The space-charge and cross-over limits are indicated in Extended Data Fig. 3a.

Thermionic cathode neutralizer

Conventional electric propulsion systems typically make use of hollow cathode plasma bridge neutralizers⁵, which are capable of emitting a high electron current and are well suited to neutralizing large ion-beam currents. As our propulsion system operates at low power, and to further enable system miniaturization, two thermionic carburized thoriated tungsten filament neutralizers are used instead with a total estimated lifetime of 3,600 h.

Electrical system design

The electronics system is separated into modules as shown in Extended Data Fig. 2a. A main control unit coordinates the operation of the propulsion system, whereas each of the other modules controls a functional component by providing local regulation

and monitoring of relevant parameters. The propulsion system is supplied by an unregulated voltage bus in the range 10–30 V and requires a power between 30 W and 70 W depending on the operating mode. A common mode filter on the power line reduces electromagnetic interference. The main communication channel with the satellite is a redundant Controller Area Network bus operating at data rates between 250 kbit and 1 Mbit. In addition, an inter-integrated circuit interface can also be used. Galvanic isolation is implemented on all communication channels.

The propulsion system uses five microcontrollers: one main processor and four second-level controllers managing local subsystems. The main microcontroller implements global control and safety algorithms, and also provides the interface with the satellite's onboard computer (OBC). A real-time operating system with multiple tasks is used, where each task has a priority assigned and the scheduler decides which should be executed depending on the given priority.

After receiving a firing request from the OBC, the propulsion system switches on the subsystems, carries out built-in self-tests and proceeds with the plasma ignition sequence. Each microcontroller implements a bootloader allowing the OBC to reprogramme the user application in flight. This bootloader has several safety measures, such as redundancy or a triple voting algorithm, to avoid possible corruption caused by single-event upsets.

Thermal design

Heat is generated by ohmic losses in the power electronics and plasma losses to the source tube walls. The internal components of the gridded ion thruster reach the highest temperatures (up to 170 °C), whereas all other components and subassemblies are below 80 °C. The amount of heat needed for iodine sublimation is given by

$$Q = \dot{m} \cdot \Delta H_s \quad (7)$$

where \dot{m} is the mass flow rate and ΔH_s is the sublimation enthalpy of iodine (62.4 KJ mol⁻¹). For a typical mass flow rate of 0.07 mg s⁻¹, the sublimation power is less than 0.02 W. Owing to the reuse of waste heat, less than 1 W of additional power is needed by the flow management system to compensate for conductive and radiative losses and keep the propellant flow path sufficiently hot to prevent iodine deposition. Both the tank and flow path to the source tube have heaters maintaining the target temperature during start-up, ignition and steady-state operation. For a cold start, approximately 10 min is needed to heat the iodine to the required temperature.

Propellant valve

To enhance miniaturization and eliminate moving parts, the propulsion system does not use a conventional solenoid control valve. Instead, controlled iodine deposition and blocking of a submillimetre hole between the propellant tank and source tube is used. When the propulsion system is not operating, the temperature of the orifice causes deposition, which blocks the hole. At this deposition temperature, the resulting sublimation rate is very low. In addition, the effective gas flow conductance is substantially reduced owing to the design of the orifice, the gas distribution head, source tube and acceleration grid themselves, so that iodine leakage is low. Ground-based experiments with the propulsion system stored under vacuum for over two weeks show an upper limit leakage rate of less than $0.08 \mu\text{g s}^{-1}$.

Propellant loading

Iodine is filled into the porous matrix, which is placed inside the propellant storage tank before the filling process. To improve thermal conductivity, a polymeric thermal pad is placed between the matrix and the walls of the tank. Although iodine does not have a strong chemical affinity with oxygen under normal conditions, owing to its oxidizing nature the tanks are purged with argon before propellant filling to remove any residual gases that could contaminate the plasma during operation.

Iodine is melted at a temperature close to 120°C in a separate reservoir and immediately poured into the matrix. This improves the packing factor over typical solid iodine crystals, and helps to minimize the formation of voids. The absolute pressure in the reservoir is just above atmospheric pressure with the argon partial pressure kept close to 100 kPa. A saturated state is maintained inside the tank as the vapour pressure of iodine is close to 14 kPa at 120°C (ref. [45](#)).

Diagnostics for ground testing

Vacuum chamber testing

Performance and plume characterization was performed by operating the propulsion system inside a cylindrical vacuum chamber with a length of 0.83 m and a diameter of 0.6 m. The chamber was pumped with a combination of rotary, turbo-molecular and cryogenic (operated at -75°C) pumps. The pressure was measured with a MKS Baratron 627B absolute pressure transducer and a cold cathode Balzers IKR 050 gauge (with gas-specific correction factors applied). The chamber base pressure was better than 5×10^{-4} Pa, with a background pressure below 1.4×10^{-3} Pa maintained during operation. Although the neutral iodine gas dissociation fraction is not well known in

the chamber, the effective pumping speed is estimated to be between 700 l s^{-1} and $1,400 \text{ l s}^{-1}$.

Automated beam diagnostic system

Ion-beam current and divergence measurements are performed with a semi-circular, automated, beam diagnostic system⁴⁶ that includes an array of 15 planar electrostatic probes. Motors at each end of the semi-circular arm precisely control the azimuthal arm position, which allows spatial measurements of the ion-beam current density over a two-dimensional hemispherical surface. The probes are biased at -40 V to reflect electrons and any possible negative iodine ions in the plume. The measured current is corrected to account for secondary electron emission due to ion bombardment of the probes and plasma sheath expansion around each probe due to the applied voltage⁴⁶. The total ion-beam current, I_{beam} , and effective beam divergence half-angle, θ_{div} , are obtained by integrating the measured current density profiles according to the following equations

$$\$ \$ \{ I \} _{\{ \rm beam \}} = \{ R \} ^{2} \{ \int \} _{-\frac{\pi}{2}}^{\frac{\pi}{2}} \{ \frac{1}{2} \} ^{\frac{1}{2}} \{ \frac{1}{2} \} ^{\frac{1}{2}} \{ \frac{1}{2} \} \{ \varPhi \} \{ \int \} _{-\frac{\pi}{2}}^{\frac{\pi}{2}} \{ \frac{1}{2} \} ^{\frac{1}{2}} \{ \frac{1}{2} \} \{ \varPhi \} \{ \theta \} \{ J_i \} \{ \varPhi , \theta \} \$ \$$$

(9)

$$\$ \$ \{ \theta \} _{\{ \rm div \}} = \{ \cos \} ^{-1} \left[\frac{\int \{ -\frac{1}{2} \} \{ \varPhi \} \{ \theta \} \{ J_i \} \{ \varPhi , \theta \} }{\int \{ -\frac{1}{2} \} \{ \varPhi \} \{ \theta \} \{ J_i \} \{ \varPhi , \theta \} } \right] ^{\frac{1}{2}} \{ \frac{1}{2} \} ^{\frac{1}{2}} \{ \frac{1}{2} \} ^{\frac{1}{2}} \{ \frac{1}{2} \} \{ \varPhi \} \{ \cos \} \{ \varPhi , \cos \} ^{2} \{ \theta \} \{ \int \} _{-\frac{\pi}{2}}^{\frac{\pi}{2}} \{ \frac{1}{2} \} ^{\frac{1}{2}} \{ \frac{1}{2} \} ^{\frac{1}{2}} \{ \frac{1}{2} \} \{ \varPhi \} \{ \theta \} \{ J_i \} \{ \varPhi , \theta \} \$ \$$$

(10)

where R is the radius of the semi-circular probe arm, \varPhi and θ are the probe azimuthal and latitude angles, respectively, and J_i is the ion beam current density.

Time-of-flight probe

Time-of-flight (TOF) measurements were performed using a molybdenum disk with a diameter of 7 cm placed in the plume, and located 54 cm downstream of the accel grid. The probe was biased at -100 V to reflect electrons and any possible negative iodine ions²⁹ in the plume, and the current collected by the probe was measured with a digital oscilloscope using short, low-impedance, connections. The time constant of the probe is much less than the ion transit time and is of the order of $1 \mu\text{s}$. During measurements,

both grids of the propulsion system are initially grounded before a rectangular voltage pulse with an amplitude and width of 1,000 V and 4.5 μ s, respectively, is applied (with rising and falling times of approximately 0.5 μ s). This causes an instantaneous extraction and acceleration of positive ions from the plasma source, and the appearance of distinct peaks in the measured TOF probe current due to the different ion transit times, τ , to the probe

$$\$ \$ \tau = \frac{L}{\sqrt{2qV_n/M}} \quad (11)$$

where L is the distance between the exit of the propulsion system and the TOF probe, V_n is the net accelerating voltage and q/M is the ion charge-to-mass ratio. Owing to pulse-shape limitations, probe current peaks show a certain spread. Individual ion species contributions are determined by fitting exponential Gaussian functions and integrating to find the average current.

Retarding field energy analyser

A Semion 2500 Retarding Field Energy Analyzer (RFEA) from Impedans is used to measure the distribution function of beam ions. The RFEA has a diameter of 50 mm and includes a single grounded front grid, two internal grids with a controlled bias voltage and a biased collector plate. The RFEA is located 30 cm downstream of the propulsion system and is connected to an automated Semion Electronics Unit scanning system. The first derivative of the collector current as a function of the swept bias voltage⁴⁷, V_{bias} , on the second grid then gives the ion flux distribution function, $h(V_{bias})$, defined such that

$$\$ \$ h(V_{bias}) \propto \frac{dI_{RFEA}}{dV_{bias}} \quad (12)$$

where I_{RFEA} is the collector current measured by the RFEA.

Indirect thrust measurements

The integrated electronics in the propulsion system includes current and voltage measurement sensors that continually measure the applied accelerating voltage, and the current to both grids. For gridded ion thrusters, the ion-beam current that is extracted from the plasma source is balanced by an electron current to the first grid to maintain charge balance (Extended Data Fig. 2b). This current, after subtracting off the small current from the accel grid, then matches the net electron current emitted by

the thermionic cathode neutralizer. During ground testing, and operation in space, the grid current and voltage measurements allow estimates of the extracted beam current and thrust to be made in real time.

Direct thrust measurements

Direct thrust measurements were performed with the propulsion system attached to a thrust balance placed inside the vacuum chamber. We developed a single pendulum thrust balance with a sensitivity of 0.03 mN that uses a force sensor to measure the thrust applied at the end of a moving arm. The force sensor and thrust vector location are shifted, which changes the respective pendulum lever arms and allows the measured force on the sensor to be magnified. The force sensor is an S256 load cell with an integral overload stop, which produces an analogue voltage output with a sensitivity of 1 mV V^{-1} at full-scale load (100 mN). To remove electrical interference, the low-level output voltage from the load cell is converted to a digital signal and sent to the measuring unit located outside of the chamber. The raw data are digitally smoothed with a second-order Savitzky–Golay filter. The thrust balance is calibrated with a set of known masses placed on a horizontal arm that produces a moment about the pendulum pivot balanced by the moment due to the force on the sensor.

Diagnostics for in-flight testing

The propulsion system includes eight thin-film platinum temperature sensors for measurement of the temperature (with an accuracy of 0.1°C) at key locations, including all electronic subsystems, the propellant tank, and the interface flange between the tank and plasma source tube. The input current and voltage from the satellite, as well as output currents and voltages from different subsystems, such as the cathode neutralizer, grids and RF antenna, are continuously measured. The data acquisition frequency is set by the satellite onboard computer and is equal to 1 Hz.

Flight qualification

The propulsion system has undergone extensive vibration, radiation, thermal and flow testing for flight qualification. Vibration testing consisted of sinusoidal, random and sine-burst (quasi-static acceleration testing) at levels set by the spacecraft launch vehicle. Sinusoidal vibrations include low-frequency tests (5–100 Hz) with accelerations up to 4.5 g. Random vibration tests ranged between 20 Hz and 2,000 Hz with a total root-mean-square acceleration of 6.7 g and a duration of 120 s per axis. Quasi-static tests were also performed for each axis with a maximum acceleration of 8.75 g. Additional shock tests were conducted at frequencies up to 5,000 Hz, with a shock response spectrum acceleration up to 1,500 g. Electronic components and electromechanical assemblies underwent single-event radiation testing (high-energy

proton bombardment) at energies up to 200 MeV, as well as gamma-ray testing for a total ionizing dose compatible with a qualification level of 15 krad for the unshielded assembly. The entire propulsion system underwent thermal exposure and thermal cycling campaigns in both ambient conditions and under vacuum conditions in a thermal vacuum chamber (with temperatures between -25°C and 60°C). Propulsion system operation in a vacuum chamber confirmed iodine sublimation and overall performance stability over extended firing times with multiple on–off cycles. Long-term propulsion system operation was tested with a qualification model for a total cumulative time of 120 h with 109 separate on–off ignition cycles.

Collection and analysis of in-flight data

The propulsion system electronics records approximately 50 telemetry parameters that are downloaded from the satellite after each in-orbit firing. The thrust and power depend on the operational mode selected, with different modes possible depending on the power, mass flow rate and applied grid voltage. Two modes have been tested during the in-orbit demonstration as shown in Extended Data Table 1, and denoted N1 and FS. The N1 mode has a thrust-locked feedback loop with a target thrust of 0.8 mN and an upper limit of 60 W, whereas the FS mode has a minimum thrust of 0.35 mN with an upper power limit of 50 W. In this last mode, the propulsion system has all feedback loops disabled, and data from secondary sensors are ignored. An automated self-test is performed before each firing.

Example system temperature measurements performed during in-orbit operation are compared with ground testing measurements in Extended Data Fig. 4b. The results are similar for all parameters, and again show that ground testing conditions replicate the space environment.

Orbit changes resulting from each firing were confirmed using both direct and indirect evidence. Direct evidence includes satellite tracking data from a GPS receiver onboard the satellite, and independent tracking data obtained from the SSN (see ref. 37 with satellite catalogue number 46838). Indirect evidence comes from a comparison of satellite orbital elements calculated from the GPS data with those predicted by numerical simulations using GMAT³⁶, and a simplified theoretical model based on low-thrust trajectories around a spherical Earth⁴⁸. The theoretical model uses the GPS mean semi-major axis just before manoeuvre 1A begins as an initial condition (backpropagating for earlier times). GMAT simulations use the JGM-3 geopotential model of degree and order 70×70 , as well as point mass perturbations for the Moon and Sun. Atmospheric drag is included using the MSISE90 model⁴⁹, as well as solar radiation pressure using a spherical spacecraft model³⁶. Simulations are initiated using times and positions from the GPS data before each firing begins, and use approximate thrust profiles taken from the downloaded telemetry.

Owing to gravitational perturbations, the osculating semi-major axis of the satellite shows oscillations with an amplitude of the order of 10 km. For this reason, mean orbital elements based on Brouwer theory⁵⁰ are used, which smooth out these high-frequency oscillations. The mean semi-major axis is deduced from the SSN data after converting from the Kozai to Brouwer mean motion convention⁵¹.

Data availability

The raw in-orbit data generated and/or analysed during this study are not publicly available as they are partially owned by ESA and Spacety, but are available from the corresponding author on reasonable request and with permission from ESA or Spacety. The SSN data in Fig. 4a that support the findings of this study are available from www.space-track.org (satellite catalogue number 46838). [Source data](#) are provided with this paper.

Code availability

The codes that support the findings of this study are available from the corresponding author upon reasonable request.

References

1. 1. Larson, W. J. & Wertz, J. R. (eds) *Space Mission Analysis and Design* (Microcosm Press, 2005).
2. 2. Foing, B. H. et al. SMART-1 mission to the Moon: status, first results and goals. *Adv. Space Res.* **37**, 6–13 (2006).
3. 3. Benkhoff, J. et al. BepiColombo—comprehensive exploration of Mercury: mission overview and science goals. *Planet. Space Sci.* **58**, 2–20 (2010).
4. 4. Rayman, M. D., Varghese, P., Lehman, D. H. & Livesay, L. L. Results from the Deep Space 1 technology validation mission. *Acta Astronaut.* **47**, 475–487 (2000).

5. 5.

Goebel, D. & Katz, I. *Fundamentals of Electric Propulsion: Ion and Hall Thrusters* (John Wiley, 2008).

6. 6.

Levchenko, I. et al. Perspectives, frontiers, and new horizons for plasma-based space electric propulsion. *Phys. Plasmas* **27**, 020601 (2020).

7. 7.

Kerry, F. G. *Industrial Gas Handbook: Gas Separation and Purification* (CRC Press, 2007).

8. 8.

Panarotto, M., Borgue, O. & Isaksson, O. Modelling flexibility and qualification ability to assess electric propulsion architectures for satellite megaconstellations. *Aerospace* **7**, 176 (2020).

9. 9.

Neice, A. E. & Zornow, M. H. Xenon anesthesia for all, or only a select few? *Anaesthesia* **71**, 1267–1272 (2016).

10. 10.

Mani, K. V., Cervone, A. & Topputo, F. Combined chemical-electric propulsion for a stand-alone Mars CubeSat. *J. Spacecr. Rockets* **56**, 1816–1830 (2019).

11. 11.

Douglas Liddle, J., Holt, A. P., Jason, S. J., O'Donnell, K. A. & Stevens, E. J. Space science with CubeSats and nanosatellites. *Nat. Astron.* **4**, 1026–1030 (2020).

12. 12.

Shkolnik, E. L. On the verge of an astronomy CubeSat revolution. *Nat. Astron.* **2**, 374–378 (2018).

13. 13.

Levchenko, I. et al. Explore space using swarms of tiny satellites. *Nature* **562**, 185–187 (2018).

14. 14.

Serjeant, S., Elvis, M. & Tinetti, G. The future of astronomy with small satellites. *Nat. Astron.* **4**, 1031–1038 (2020).

15. 15.

Larson, W. J., Henry, G. N. & Humble R. W. (eds) *Space Propulsion Analysis and Design* (McGraw-Hill, 1995).

16. 16.

Russell, C. & Raymond C. (eds) *The Dawn Mission to Minor Planets 4 Vesta and 1 Ceres* (Springer, 2012).

17. 17.

Kuninda, H. et al. Powered flight of electron cyclotron resonance ion engines on Hayabusa explorer. *J. Propuls. Power* **23**, 544–551 (2007).

18. 18.

Nishiyama, K., Hosoda, S., Tsukizaki, R. and Kuninaka, H. In-flight operation of the Hayabusa2 ion engine system on its way to rendezvous with asteroid 162173 Ryugu. *Acta Astronaut.* **166**, 69–77 (2020).

19. 19.

Franks, N. P., Dickinson, R., de Sousa, S. L. M., Hall, A. C. & Lieb, W. R. How does xenon produce anaesthesia. *Nature* **396**, 324 (1998).

20. 20.

Chu, P. B. et al. Controlled pulse-etching with xenon difluoride. In *Proc. International Solid State Sensors and Actuators Conference (Transducers '97)* 665–668 (IEEE, 1997).

21. 21.

Radtke, J., Kebschull, C. & Stoll, E. Interactions of the space debris environment with mega constellations—using the example of the OneWeb constellation. *Acta*

Astronaut. **13**, 55–68 (2017).

22. 22.

Massey, R., Lucatello, S. & Benvenuti, P. The challenge of satellite megaconstellations. *Nat. Astron.* **4**, 1022–1023 (2020).

23. 23.

Venkatesan, A., Lowenthal, J., Prem, P. & Vidaurre, M. The impact of satellite constellations on space as an ancestral global commons. *Nat. Astron.* **4**, 1043–1048 (2020).

24. 24.

Dressler, R., Chiu, Y.-H. & Levandier, D. Propellant alternatives for ion and Hall thrusters. In *Proc. 38th Aerospace Science Meeting and Exhibit AIAA-2000-0602* (AIAA, 2000).

25. 25.

Tverdokhlebov, O. S. & Semenkin, A. V. Iodine propellant for electric propulsion: to be or not to be. In *Proc. 37th AIAA/ASME/SAE/ASEE Joint Propulsion Conference AIAA-2001-3350* (AIAA, 2001).

26. 26.

Tatsuo, K. (ed.) *Iodine Chemistry and Applications* (John Wiley, 2014).

27. 27.

Szabo, J. et al. Performance evaluation of an iodine-vapor Hall thruster. *J. Propuls. Power* **28**, 848–857 (2012).

28. 28.

Tsay, M., Frongillo, J., Model, J., Zwahlen, J. & Paritsky, L. Maturisation of iodine-fueled BIT-3 RF ion thruster and RF neutralizer. In *Proc. 52nd AIAA/ASME/SAE/ASEE Joint Propulsion Conference AIAA-2016-4544* (AIAA, 2016).

29. 29.

Grondein, P., Lafleur, T., Chabert, P. & Aanesland, A. Global model of an iodine gridded plasma thruster. *Phys. Plasmas* **23**, 033514 (2016).

30. 30.

Holste, K. et al. Performance of an iodine-fueled radio-frequency ion-thruster. *Eur. Phys. J. D* **72**, 1–7 (2018).

31. 31.

Holste, K. et al. Ion thrusters for electric propulsion: scientific issues developing a niche technology into a game changer. *Rev. Sci. Instrum.* **91**, 061101 (2020).

32. 32.

Kamhawi, H. et al. Overview of iodine propellant Hall thruster development activities at NASA Glenn Research Center. In *Proc. 52nd AIAA/ASME/SAE/ASEE Joint Propulsion Conference* AIAA-2016-4729 (AIAA, 2016).

33. 33.

Rafalskyi, R. & Aanesland, A. Gridded ion thruster with integrated solid propellant. Patent no. WO2017037062A1 (2017).

34. 34.

Lieberman, M. A. & Lichtenberg, A. J. *Principles of Plasma Discharges and Materials Processing* (John Wiley, 2005).

35. 35.

Goebel, D. M., Wirz, R. E., & Katz, I. Analytical ion thruster discharge performance model. *J. Propuls. Power* **23**, 1055–1067 (2012).

36. 36.

General Mission Analysis Tool (GMAT), version R2018a (NASA Goddard Space Flight Center, 2020); <https://software.nasa.gov/software/GSC-18094-1>

37. 37.

Space-Track.org (United States Space Command and the Combined Force Space Component Command, 2021); <https://www.space-track.org>

38. 38.

Villela, T., Costa, C. A., Brandão, A. M., Bueno, F. T. & Leonardi, R. Towards the thousandth CubeSat: a statistical overview. *Int. J. Aerosp. Eng.* **2019**, 5063145 (2019).

39. 39.

Schaub, H., Jasper, L. E. Z., Anderson, P. V. & McKnight, D. S. Cost and risk assessment for spacecraft operation decisions caused by the space debris environment. *Acta Astronaut.* **113**, 66–79 (2015).

40. 40.

Fazio, N., Gabriel, S. B., Golosnoy, I. O. & Wollenhaupt, B. Mission cost for gridded ion engines using alternative propellants. In *36th International Electric Propulsion Conference IEPC-2019-831* (Electric Rocket Propulsion Society, 2019).

41. 41.

Szabo, J., Tedrake, R., Kolencik, G. & Pote, B. Measurements of a krypton fed 1.5 kW Hall effect thruster with a centrally located cathode. In *35th International Electric Propulsion Conference IEPC-2017-26* (Electric Rocket Propulsion Society, 2017).

42. 42.

Krypton Market Size, Share & COVID-19 Impact Analysis, by Type (N3, N4.5, and N5), by Application (Lighting, Window Insulation, Laser, and Others) and Regional Forecast, 2021–2028 Market Research Report (Fortune Business Insights, 2021).

43. 43.

Chabert, P., Arancibia Montreal, J., Bredin, J., Popelier, L. & Aanesland, A. Global model of a gridded-ion thruster powered by a radiofrequency inductive coil. *Phys. Plasmas* **19**, 073512 (2012).

44. 44.

Verboncoeur, J. P., Langdon, A. B. & Gladd, N. An object oriented electromagnetic PIC code. *Comput. Phys. Commun.* **87**, 199–211 (1995).

45. 45.

Stull, D. R. Vapor pressure of pure substances. Organic and inorganic compounds. *Ind. Eng. Chem.* **39**, 517–540 (1947).

46. 46.

Habl, L., Rafalskyi, D. & Lafleur, T. Ion beam diagnostic for the assessment of miniaturized electric propulsion systems. *Rev. Sci. Instrum.* **91**, 093501 (2020).

47. 47.

Chabert, P. & Braithwaite, N. *Physics of Radio-frequency Plasmas* (Cambridge Univ. Press, 2011).

48. 48.

Lafleur, T. & Apffel, N. Low-Earth-orbit constellation phasing using miniaturized low-thrust propulsion systems. *J. Spacecr. Rockets* **58**, 628–642 (2021).

49. 49.

Hedin, A. E. Extension of the MSIS thermosphere model into the middle and lower atmosphere. *J. Geophys. Res. Space Phys.* **96**, 1159–1172 (1991).

50. 50.

Brouwer, D. Solution of the problem of artificial satellite theory without drag. *Astron. J.* **64**, 378–396 (1959).

51. 51.

Hoots, F. R., Schumacher, P. W. Jr & Glover, R. A. History of analytical orbit modelling in the US space surveillance system. *J. Guid. Control Dynam.* **27**, 174–185 (2004).

Acknowledgements

We thank the European Space Agency (ESA) for supporting the in-orbit demonstration through the TURBO project, ARTES C&G programme, contract number 4000131883/20/NL/MM/can, the French Government (Ministère de l’Enseignement Supérieur, de la Recherche et de l’Innovation) for supporting this work through the i-Lab 2017 grant (le Grand Prix I-LAB 2017 – 19th Concours Nationale d’Aide à la

Création d'Entreprises des Technologies Innovantes), and the French National Space Agency (Centre National d'Etudes Spatiales) for support of the project through the INODIN grant, R&T action R-S19/PF-0002-108-92. We thank Spacety, and particularly J. Zheng, for mission support during the in-orbit demonstration. We also thank the Laboratoire de Physique des Plasmas at Ecole Polytechnique for funding open access of our paper.

Author information

Affiliations

1. ThrustMe, Verrières-le-Buisson, France

Dmytro Rafalskyi, Javier Martínez Martínez, Lui Habl, Elena Zorzoli Rossi, Plamen Proynov, Antoine Boré, Thomas Baret, Antoine Poyet, Trevor Lafleur, Stanislav Dudin & Ane Aanesland

2. Laboratoire de Physique des Plasmas, CNRS, Ecole Polytechnique, Sorbonne Université, Université Paris-Saclay, IP Paris, Route de Saclay, Palaiseau, France

Lui Habl

Contributions

D.R. conceived the original prototype and operational algorithms, and, together with A.A., elaborated the concept and development roadmap. T.B. and A.P. performed mechanical design and mechanical simulations of the system. J.M.M. performed thermal and fluid dynamics characterization of the system, and characterization of the chemical interaction of iodine with system components. D.R., E.Z.R., L.H. and A.B. performed experimental plasma and ion beam characterization and supported in-orbit testing and thruster telemetry data analysis. P.P., together with A.B., designed and developed the hardware and system software. S.D. developed the RF generation system, and, together with E.Z.R., contributed to the direct thrust measurements. L.H. and T.L. performed ion optics and plasma modelling. T.L. and J.M.M. performed orbital dynamics simulations and analysis of in-flight telemetry and GPS data obtained during the mission. D.R., T.L., L.H. and J.M.M. planned and coordinated the writing of the manuscript. All authors contributed to the design process and to the editing of the manuscript.

Corresponding author

Correspondence to [Trevor Lafleur](#).

Ethics declarations

Competing interests

D.R., J.M.M., L.H., E.Z.R., P.P., A.B., T.B., A.P., T.L. and A.A. are employees of ThrustMe. S.D. is a consultant working with ThrustMe. D.R. and A.A. hold a patent related to the propulsion system (patent no. WO2017037062A1).

Additional information

Peer review information *Nature* thanks Kristof Holste and the other, anonymous, reviewer(s) for their contribution to the peer review of this work. Peer reviewer reports are available.

Publisher's note Springer Nature remains neutral with regard to jurisdictional claims in published maps and institutional affiliations.

Extended data figures and tables

[Extended Data Fig. 1 Propulsion system architecture and integration with satellite.](#)

a, The propulsion system is a complete system that includes all necessary subsystems for operation. Power is supplied from the spacecraft (S/C) and used for flow control, plasma generation, ion acceleration, and beam neutralization. Solid iodine sublimates and enters the inductively coupled plasma source. An igniter initially strikes a plasma which is then maintained by an RF antenna wrapped around the outside of the source tube. Ions from the plasma are extracted and accelerated by the high-voltage grids, and the positive ion beam is neutralized by electrons thermionically emitted from the cathode filament. **b**, The propulsion system installed in the Beihangkongshi-1 satellite before launch. Photograph reproduced and adapted by the authors with permission from Spacety. © 2020 Spacety Co., Ltd. (Changsha).

[Extended Data Fig. 2 Electrical system architecture and thruster electrical schematic.](#)

a, The main control unit interfaces with the satellite onboard computer and implements global control and safety algorithms. The RF generator supplies power to the RF antenna via a matching network to match the impedance of the plasma and generator for efficient power transfer. The cathode supply controls and monitors the

electron-emitting cathode filament, the flow control unit manages the propellant tank and flow path heaters, the grid control unit manages the applied voltage to the acceleration grids, and the ignition unit controls the igniter needed for initial gas breakdown in the source tube to produce a plasma. **b**, General electrical circuit showing the high-voltage grids and electron-emitting cathode. Ions (denoted X^{z+}) from the upstream plasma source are extracted and accelerated by the voltage applied across the screen and accel grids. A small ion current, I_a , flows to the accel grid due to charge-exchange collisions with any unionized propellant in the plume. To maintain charge balance in the source tube, an electron current equal to the sum of the ion beam and accel grid currents flows to the screen grid, I_s . A current equal to the ion beam current is then emitted from the filament. The accel grid is biased negatively with respect to the filament to prevent electron backstreaming into the plasma source⁵.

[Extended Data Fig. 3 Ion optics simulations and propulsion system performance.](#)

a, Perveance (space-charge) and cross-over limits of the propulsion system grid set obtained from particle-in-cell (PIC) simulations. The black dash-dot line shows the perveance limit from the Child-Langmuir law (see [Methods](#)), while the green shaded region denotes the operating range of the propulsion system. **b**, Correction factor as a function of RF power applied to the indirect thrust measurements to account for ion beam divergence and the presence of multiple ion species. **c**, Thrust of the propulsion system as a function of total system power and iodine input mass flow rate. **d**, PIC simulation of a single set of grid apertures (black shaded regions) showing the steady-state spatial ion distribution. The simulation is 2D in cylindrical coordinates and the domain has been normalized by the axial and radial simulation dimensions. **e**, Specific impulse of the propulsion system as a function of total system power and iodine mass flow rate. Error bars represent estimates of the measuring equipment precision and accuracy limitations.

[Source data](#)

[Extended Data Fig. 4 Ground-flight data comparison and propulsion system operation timeline.](#)

a, Comparison between the ion beam current, I_b , electron neutralizer current, I_e , and current to the accel grid, I_a , during ground and in-flight operation for manoeuvre 1B. **b**, Measured electronic subsystem temperatures during propulsion system operation on the ground, and in space for manoeuvre 1B. The figure presents data for the main control unit, or Motherboard (MB), the Radio-Frequency Generator (RFG), the Grid Supply Unit (GSU), the Cathode Supply Unit (CSU), and the Flow Control Unit

(FCU). **c**, In-orbit telemetry data of the thrust and power as a function of time for manoeuvre 1B indicating the propellant heating, propulsion system operation and propellant cooling stages.

Source data

Extended Data Table 1 Summary of propulsion system firing tests and resulting orbit changes

Supplementary information

Peer Review File

Source data

Source Data Fig. 2

Source Data Fig. 3

Source Data Fig. 4

Source Data Extended Data Fig. 3

Source Data Extended Data Fig. 4

Rights and permissions

Open Access This article is licensed under a Creative Commons Attribution 4.0 International License, which permits use, sharing, adaptation, distribution and reproduction in any medium or format, as long as you give appropriate credit to the original author(s) and the source, provide a link to the Creative Commons license, and indicate if changes were made. The images or other third party material in this article are included in the article's Creative Commons license, unless indicated otherwise in a credit line to the material. If material is not included in the article's Creative Commons license and your intended use is not permitted by statutory regulation or exceeds the permitted use, you will need to obtain permission directly from the copyright holder. To view a copy of this license, visit <http://creativecommons.org/licenses/by/4.0/>.

Reprints and Permissions

About this article

Cite this article

Rafalskyi, D., Martínez, J.M., Habl, L. *et al.* In-orbit demonstration of an iodine electric propulsion system. *Nature* **599**, 411–415 (2021).
<https://doi.org/10.1038/s41586-021-04015-y>

- Received: 30 April 2021
- Accepted: 13 September 2021
- Published: 17 November 2021
- Issue Date: 18 November 2021
- DOI: <https://doi.org/10.1038/s41586-021-04015-y>

Share this article

Anyone you share the following link with will be able to read this content:

[Get shareable link](#)

Sorry, a shareable link is not currently available for this article.

[Copy to clipboard](#)

Provided by the Springer Nature SharedIt content-sharing initiative

[Sea squirts teach new lessons in evolution](#)

- Shamin Bundell
- Benjamin Thompson

Nature Podcast 17 Nov 2021

[Iodine powers low-cost engines for satellites](#)

- Igor Levchenko
- Kateryna Bazaka

News & Views 17 Nov 2021

This article was downloaded by **calibre** from <https://www.nature.com/articles/s41586-021-04015-y>

| [Section menu](#) | [Main menu](#) |

- Article
- [Published: 17 November 2021](#)

Exploding and weeping ceramics

- [Hanlin Gu](#) ¹ [na1](#),
- [Jascha Rohmer](#) [ORCID: orcid.org/0000-0001-9473-2947](#) ² [na1](#),
- [Justin Jetter](#) [ORCID: orcid.org/0000-0003-2725-8426](#) ²,
- [Andriy Lotnyk](#) [ORCID: orcid.org/0000-0002-0000-9334](#) ³ [nAff4](#),
- [Lorenz Kienle](#) ²,
- [Eckhard Quandt](#) [ORCID: orcid.org/0000-0002-2314-5179](#) ² &
- [Richard D. James](#) [ORCID: orcid.org/0000-0001-6019-6613](#) ¹

Nature volume **599**, pages 416–420 (2021)

- 843 Accesses
- 78 Altmetric
- [Metrics details](#)

Subjects

- [Actuators](#)
- [Ceramics](#)
- [Sensors and biosensors](#)

Abstract

The systematic tuning of crystal lattice parameters to achieve improved kinematic compatibility between different phases is a broadly effective strategy for improving the reversibility, and lowering the hysteresis, of solid–solid phase transformations^{[1](#),[2](#),[3](#),[4](#),[5](#),[6](#),[7](#),[8](#),[9](#),[10](#),[11](#)}. (Kinematic

compatibility refers to the fitting together of the phases.) Here we present an apparently paradoxical example in which tuning to near perfect kinematic compatibility results in an unusually high degree of irreversibility. Specifically, when cooling the kinematically compatible ceramic $(\text{Zr}/\text{Hf})\text{O}_2(\text{YNb})\text{O}_4$ through its tetragonal-to-monoclinic phase transformation, the polycrystal slowly and steadily falls apart at its grain boundaries (a process we term weeping) or even explosively disintegrates. If instead we tune the lattice parameters to satisfy a stronger ‘equidistance’ condition (which additionally takes into account sample shape), the resulting material exhibits reversible behaviour with low hysteresis. These results show that a diversity of behaviours—from reversible at one extreme to explosive at the other—is possible in a chemically homogeneous ceramic system by manipulating conditions of compatibility in unexpected ways. These concepts could prove critical in the current search for a shape-memory oxide ceramic^{[9,10,11,12](#)}.

Access options

Subscribe to Journal

Get full journal access for 1 year

\$199.00

only \$3.90 per issue

[Subscribe](#)

All prices are NET prices.

VAT will be added later in the checkout.

Tax calculation will be finalised during checkout.

Rent or Buy article

Get time limited or full article access on ReadCube.

from \$8.99

[Rent or Buy](#)

All prices are NET prices.

Additional access options:

- [Log in](#)
- [Access through your institution](#)
- [Learn about institutional subscriptions](#)

Fig. 1: Lattice correspondences and transformation stretch matrices.

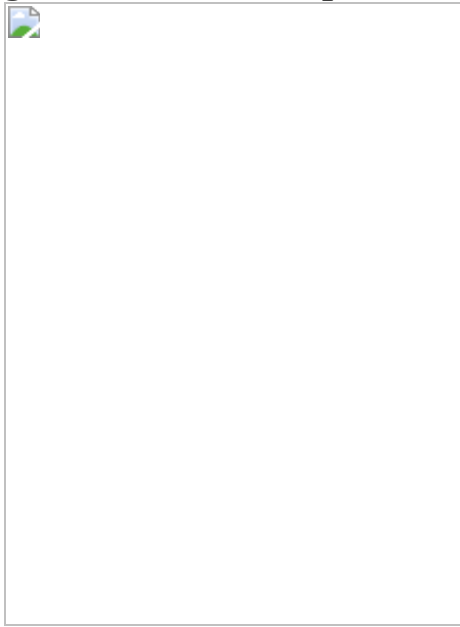
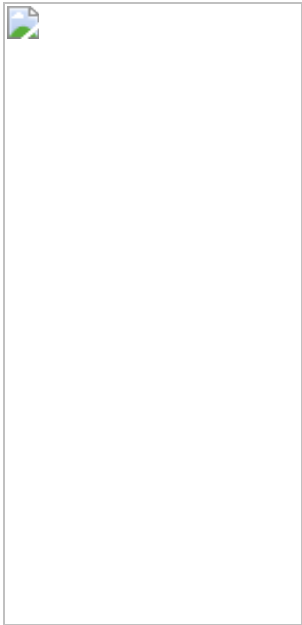


Fig. 2: Frame sequences of martensitic transformation.



Fig. 3: Thermal characterization and kinematic compatibility.



Data availability

The raw data that support the findings of this study are available at <https://archive.materialscloud.org> with the identifier<https://doi.org/10.24435/materialscloud:6c-hk>.

References

1. 1.

Chen, X., Srivastava, V., Dabade, V. & James, R. D. Study of the cofactor conditions: conditions of supercompatibility between phases. *J. Mech. Phys. Solids* **61**, 2566–2587 (2013).

2. 2.

Chluba, C. et al. Ultralow-fatigue shape memory alloy films. *Science* **348**, 1004–1007 (2015).

3. 3.

Delville, R. et al. Transmission electron microscopy study of phase compatibility in low hysteresis shape memory alloys. *Philos. Mag.* **90**, 177–195 (2010).

4. 4.

Della Porta, F. On the cofactor conditions and further conditions of supercompatibility between phases. *J. Mech. Phys. Solids* **122**, 27–53 (2019).

5. 5.

Niitsu, K., Kimura, Y., Omori, T. & Kainuma, R. Cryogenic superelasticity with large elastocaloric effect. *NPG Asia Mater.* **10**, e457 (2018).

6. 6.

Zarnetta, R. et al. Identification of quaternary shape memory alloys with near-zero thermal hysteresis and unprecedented functional stability. *Adv. Funct. Mater.* **20**, 1917–1923 (2010).

7. 7.

Gu, H., Bumke, L., Chluba, C., Quandt, E. & James, R. D. Phase engineering and supercompatibility of shape memory alloys. *Mater. Today* **21**, 265–277 (2018).

8. 8.

Jetter, J. et al. Tuning crystallographic compatibility to enhance shape memory in ceramics. *Phys. Rev. Mater.* **3**, 93603 (2019).

9. 9.

Wegner, M., Gu, H., James, R. D. & Quandt, E. Correlation between phase compatibility and efficient energy conversion in Zr-doped barium titanate. *Sci. Rep.* **10**, 3496 (2020).

10. 10.

Liang, Y. G. et al. Tuning the hysteresis of a metal-insulator transition via lattice compatibility. *Nat. Commun.* **11**, 3539 (2020).

11. 11.

Pang, E. L., McCandler, C. A. & Schuh, C. A. Reduced cracking in polycrystalline $\text{ZrO}_2\text{-CeO}_2$ shape-memory ceramics by meeting the cofactor conditions. *Acta Mater.* **177**, 230–239 (2019).

12. 12.

Lai, A., Du, Z., Gan, C. L. & Schuh, C. A. Shape memory and superelastic ceramics at small scales. *Science* **341**, 1505–1508 (2013).

13. 13.

Kohn, R. V. & Müller, S. Branching of twins near an austenite—twinned-martensite interface. *Philos. Mag. A* **66**, 697–715 (1992).

14. 14.

Burkart, M. W. & Read, T. A. Diffusionless phase change in the indium-thallium system. *Trans. Am. Inst. Min. Metall. Eng.* **197**, 1516–1524 (1953).

15. 15.

Ball, J. M. & James, R. D. in *Analysis and Continuum Mechanics: a Collection of Papers Dedicated to J. Serrin on His Sixtieth Birthday* 647–686 (Springer, 1989).

16. 16.

Yang, S. et al. A jumping shape memory alloy under heat. *Sci. Rep.* **6**, 21754 (2016).

17. 17.

Yadava, K. et al. Extraordinary anisotropic thermal expansion in photosalient crystals. *IUCrJ* **7**, 83–89 (2020).

18. 18.

Naumov, P., Chizhik, S., Panda, M. K., Nath, N. K. & Boldyreva, E. Mechanically responsive molecular crystals. *Chem. Rev.* **115**, 12440–12490 (2015).

19. 19.

Tong, F. et al. Photomechanical molecular crystals and nanowire assemblies based on the [2+2] photodimerization of a phenylbutadiene derivative. *J. Mater. Chem. C* **8**, 5036–5044 (2020).

20. 20.

Chandrasekar, S. & Chaudhri, M. M. The explosive disintegration of Prince Rupert's drops. *Philos. Mag. B* **70**, 1195–1218 (1994).

21. 21.

Gibbs, J.W. *On the equilibrium of heterogeneous substances* Vol. 1 (Longmans Green and Co., 1879)

22. 22.

Chen, X. et al. Direct observation of chemical short-range order in a medium-entropy alloy. *Nature* **592**, 712–716 (2021).

23. 23.

Hayakawa, M., Kuntani, N. & Oka, M. Structural study on the tetragonal to monoclinic transformation in arc-melted ZrO₂-2mol.%Y₂O₃—I. Experimental observations. *Acta Metall.* **37**, 2223–2228 (1989).

24. 24.

Hayakawa, M. & Oka, M. Structural study on the tetragonal to monoclinic transformation in arc-melted ZrO₂-2mol.%Y₂O₃—II. Quantitative analysis. *Acta Metall.* **37**, 2229–2235 (1989).

25. 25.

Chen, X. & Song, Y. *Structural Phase Transformation Web Tools* (StrucTrans, 2014); <http://www.structrans.org>

26. 26.

Ball, J. M. & James, R. D. A characterization of plane strain. *Proc. Math. Phys. Sci.* **432**, 93–99 (1991).

Acknowledgements

R.D.J. and H.G. were supported by the NSF (DMREF-1629026), the MURI programme (FA9550-18-1-0095 and FA9550-16-1-0566) and a Vannevar Bush Faculty Fellowship. R.D.J. also acknowledges a Mercator Fellowship for the support of this German–US collaboration. E.Q., J.R. and J.J. acknowledge funding by the Deutsche Forschungsgemeinschaft (DFG) through a Reinhart Koselleck Project (313454214), and the project “Search for compatible zirconium oxide-based shape memory ceramics” (453203767). We thank N. Wolff for preliminary TEM measurements, and A. Mill for her assistance in the preparation of specimens for TEM investigation.

Author information

Author notes

1. Andriy Lotnyk

Present address: Laboratory of Infrared Materials and Devices, The Research Institute of Advanced Technologies, Ningbo University, Ningbo, China

2. These authors contributed equally: Hanlin Gu, Jascha Rohmer

Affiliations

1. Department of Aerospace Engineering and Mechanics, University of Minnesota, Minneapolis, MN, USA

Hanlin Gu & Richard D. James

2. Institute for Materials Science, Faculty of Engineering, Kiel University, Kiel, Germany

Jascha Rohmer, Justin Jetter, Lorenz Kienle & Eckhard Quandt

3. Leibniz Institute of Surface Engineering (IOM), Leipzig, Germany

Andriy Lotnyk

Contributions

H.G. and J.R. contributed equally to the manuscript. J.R. synthesized and characterized the samples. E.Q., J.R. and J.J. designed the compositions and J.J. also aided in characterization. L.K. and A.L. contributed to our understanding of the chemical homogeneity in this system. H.G. and R.D.J. developed the theory of compatibility and identified the significance of the equidistance condition with input from all authors. R.D.J. wrote the manuscript with input from all authors. E.Q. and R.D.J. supervised the collaboration.

Corresponding authors

Correspondence to [Hanlin Gu](#), [Jascha Rohmer](#), [Justin Jetter](#), [Andriy Lotnyk](#), [Lorenz Kienle](#), [Eckhard Quandt](#) or [Richard D. James](#).

Ethics declarations

Competing interests

The authors declare no competing interests.

Additional information

Peer review information *Nature* thanks Jian Luo and the other, anonymous, reviewer(s) for their contribution to the peer review of this work.

Publisher's note Springer Nature remains neutral with regard to jurisdictional claims in published maps and institutional affiliations.

Extended data figures and tables

[Extended Data Fig. 1 Microstructure and grain size.](#)

(a) SEM image of the sample $y = 0.5$ with monoclinic twin laminated microstructure, showing the untreated sample surface directly after sintering, and (b) the fractured surface of the same sample. (c) Typical transformed material from a weeping sample that shows separation at the grain boundaries.

[Extended Data Fig. 2 Chemical homogeneity and absence of short-range ordering \(crushed\).](#)

The micrographs of the microstructural and nanoscale investigations are TEM and HRTEM images as well as SAED and NBED patterns of the $(\text{Zr}_{0.9} \text{Hf}_{0.1} \text{O}_2)_{0.775}$ ($\text{Y}_{0.5} \text{Nb}_{0.5} \text{O}_2)_{0.225}$ (weeping) sample prepared by crushing. No additional reflections are observed in SAED and NBED patterns beyond those due to dynamical double diffraction. Also no additional reflections are seen in the FFT images.

[Extended Data Fig. 3 Chemical homogeneity and absence of short-range ordering \(FIB\).](#)

The micrographs of the microstructural and nanoscale analysis are HAADF-STEM and HAADF-HRSTEM images as well as SAED and NBED patterns of the $(\text{Zr}_{0.9} \text{Hf}_{0.1} \text{O}_2)_{0.775} (\text{Y}_{0.5} \text{Nb}_{0.5} \text{O}_2)_{0.225}$ (weeping) sample, prepared by FIB. No additional reflections are observed in SAED, NBED patterns (only from dynamical double diffraction) as well as FFT images. Low-magnification HAADFM and atomic-scale HAADF micrographs are raw images, showing no significant intensity variation.

Extended Data Fig. 4 Chemical homogeneity, crushed sample.

Nanoscale chemical study of a $(\text{Zr}_{0.9} \text{Hf}_{0.1} \text{O}_2)_{0.775} (\text{Y}_{0.5} \text{Nb}_{0.5} \text{O}_2)_{0.225}$ (weeping) sample, prepared by crushing. The images are HAADF-HRSTEM micrograph and high resolution EDX elemental maps, suggesting a uniform distribution of elements.

Extended Data Fig. 5 Chemical homogeneity, FIB sample.

Nanoscale chemical analysis of a $(\text{Zr}_{0.9} \text{Hf}_{0.1} \text{O}_2)_{0.775} (\text{Y}_{0.5} \text{Nb}_{0.5} \text{O}_2)_{0.225}$ (weeping) sample prepared by FIB. The images are HAADF-HRSTEM micrograph and high resolution EDX elemental maps, suggesting a uniform distribution of elements.

Extended Data Fig. 6 Chemical homogeneity and structure at grain boundaries (FIB).

Nanoscale study and local chemical analysis of a grain boundary of a $(\text{Zr}_{0.9} \text{Hf}_{0.1} \text{O}_2)_{0.775} (\text{Y}_{0.5} \text{Nb}_{0.5} \text{O}_2)_{0.225}$ (weeping) sample prepared by FIB. The micrographs are HAADF-STEM and HAADF-HRSTEM images as well as high resolution EDX elemental maps of the sample. Atomic-resolution HAADF micrographs are raw images, showing no significant intensity variation along the grain boundary (GB). The high resolution EDX maps suggest no significant element segregation at the grain boundary.

Extended Data Fig. 7 Structure by X-Ray Diffraction with Rietveld Refinement.

XRD diffraction pattern and calculated fit after Rietveld refinement (Top) with Topas software. The diagram at the bottom (Residual) shows the difference in intensity between the measured and calculated diffraction pattern. The sample in plot a) has a phase transformation above room temperature (RT) and is in the monoclinic phase, whereas the phase transformation of the sample in plot b) is below RT, so the pattern shows the tetragonal crystal structure. The low R_{wp} values, representing the goodness of the fit, indicate the quality of the Rietveld refinement. Temperature dependent measurements were conducted with a graphite domed heating stage. In c) the sample $y = 0.9$ is in its monoclinic phase, while in d) the measurement was taken at $415\text{ }^{\circ}\text{C}$ following the monoclinic to tetragonal phase transition. The stage appears in the measured XRD pattern with additional peaks that were identified and excluded from the refinement done on the parameters of the physical phases. The resulting higher R_{wp} values compared to a) and b) can be explained by the reduced intensities due to limited transmissibility of the graphite dome used in these cases. Each measurement is refined up to 1000 times with different varied starting parameters with only the best fit being used for further calculations.

Extended Data Fig. 8 Temperature dependent XRD measurements.

Temperature dependent XRD measurement of the sample $y = 0.8$ with domed heating stage showing the phase transformation on heating and cooling. Upon heating, the characteristic tetragonal peak starts to grow at the austenitic start temperature and the monoclinic peaks are vanishing. At temperatures far above A_f we force transformation of the residual phase.

During cooling to $30\text{ }^{\circ}\text{C}$, we observe the reverse transformation (t-to-m) of the sample. These measurements are the basis to obtain the lattice parameter of the monoclinic and tetragonal phases by Rietveld refinement, to determine the temperature dependent change of these lattice parameters and to calculate the middle eigenvalues λ_2 of the transformation stretch matrix for the lattice Correspondences 1_a , 1_b and 2.

Extended Data Fig. 9 Frame sequence of explosive behaviour.

In a sequence of frames, the Fig. shows the path of a jumping ceramic confined to a cylinder. This jump is also shown in Supplementary Video [2](#).

Supplementary information

Supplementary Information

This file contains Supplementary Sections 1–3 including equations for the analysis of compatibility and a heat transfer analysis and Tables 1–4.

Supplementary Video 1

A sample at a high Zr/Hf ratio exhibiting explosive behaviour on cooling to the transformation temperature. See the main text for details.

Supplementary Video 2

The path of a sample at a high Zr content exhibiting jumping, confined to a graduated cylinder. See also the main text and Extended Data Fig. 9.

Supplementary Video 3

A sample at a high Zr/Hf ratio that exhibits weeping (that is, steady falling apart at the grain boundaries). See also the main text and Fig. 2.

Supplementary Video 4

Reversible motion of the interface in the context of a general cooling protocol. The sample closely satisfies the equidistance condition. See the main text and the caption of Fig. 2.

Supplementary Video 5

This video shows reversible motion of an interface close up, so the interface position is clear. The sample closely satisfies the equidistance condition. See also the main text and the caption of Fig. 2.

Supplementary Video 6

A sample that was held at a temperature a little above the transformation temperature for 94 days, and then cooled to the point of transformation. This supports the arguments given in the Methods (“Possible rate effects”) on the absence of a significant rate effect.

Rights and permissions

Reprints and Permissions

About this article

Cite this article

Gu, H., Rohmer, J., Jetter, J. *et al.* Exploding and weeping ceramics. *Nature* **599**, 416–420 (2021). <https://doi.org/10.1038/s41586-021-03975-5>

- Received: 22 September 2020
- Accepted: 31 August 2021
- Published: 17 November 2021
- Issue Date: 18 November 2021
- DOI: <https://doi.org/10.1038/s41586-021-03975-5>

Share this article

Anyone you share the following link with will be able to read this content:

[Get shareable link](#)

Sorry, a shareable link is not currently available for this article.

[Copy to clipboard](#)

Provided by the Springer Nature SharedIt content-sharing initiative

This article was downloaded by **calibre** from <https://www.nature.com/articles/s41586-021-03975-5>

| [Section menu](#) | [Main menu](#) |

- Article
- [Published: 17 November 2021](#)

Isolation and characterization of a californium metallocene

- [Conrad A. P. Goodwin](#) [ORCID: orcid.org/0000-0002-4320-2548¹](#) na1,
- [Jing Su](#) [ORCID: orcid.org/0000-0002-6895-2150^{2,3}](#) na1,
- [Lauren M. Stevens¹](#),
- [Frankie D. White¹](#),
- [Nickolas H. Anderson¹](#),
- [John D. Auxier II](#) [ORCID: orcid.org/0000-0001-6234-6451¹](#),
- [Thomas E. Albrecht-Schönzart⁴](#),
- [Enrique R. Batista](#) [ORCID: orcid.org/0000-0002-3074-4022²](#),
- [Sasha F. Briscoe⁵](#),
- [Justin N. Cross](#) [ORCID: orcid.org/0000-0003-1881-155X¹](#),
- [William J. Evans](#) [ORCID: orcid.org/0000-0002-0651-418X⁶](#),
- [Alyssa N. Gaiser](#) [ORCID: orcid.org/0000-0001-7063-359X⁴](#),
- [Andrew J. Gaunt](#) [ORCID: orcid.org/0000-0001-9679-6020¹](#),
- [Michael R. James¹](#),
- [Michael T. Janicke](#) [ORCID: orcid.org/0000-0002-3139-2882¹](#),
- [Tener F. Jenkins](#) [ORCID: orcid.org/0000-0002-9469-7405⁶](#),
- [Zachary R. Jones¹](#),
- [Stosh A. Kozimor](#) [ORCID: orcid.org/0000-0001-7387-0507¹](#),
- [Brian L. Scott](#) [ORCID: orcid.org/0000-0003-0468-5396⁷](#),
- [Joseph. M. Sperling⁴](#),
- [Justin C. Wedal⁶](#),
- [Cory J. Windorff](#) [ORCID: orcid.org/0000-0002-5208-9129⁴](#),
- [Ping Yang](#) [ORCID: orcid.org/0000-0003-4726-2860²](#) &
- [Joseph W. Ziller⁶](#)

[Nature](#) volume 599, pages 421–424 (2021)

- 2343 Accesses
- 36 Altmetric
- [Metrics details](#)

Subjects

- [Chemical bonding](#)
- [Coordination chemistry](#)
- [Organometallic chemistry](#)

Abstract

Californium (Cf) is currently the heaviest element accessible above microgram quantities. Cf isotopes impose severe experimental challenges due to their scarcity and radiological hazards. Consequently, chemical secrets ranging from the accessibility of 5*f*/6*d* valence orbitals to engage in bonding, the role of spin–orbit coupling in electronic structure, and reactivity patterns compared to other *f* elements, remain locked.

Organometallic molecules were foundational in elucidating periodicity and bonding trends across the periodic table^{1,2,3}, with a twenty-first-century renaissance of organometallic thorium (Th) through plutonium (Pu) chemistry^{4,5,6,7,8,9,10,11,12}, and to a smaller extent americium (Am)¹³, transforming chemical understanding. Yet, analogous curium (Cm) to Cf chemistry has lain dormant since the 1970s. Here, we revive air-/moisture-sensitive Cf chemistry through the synthesis and characterization of $[Cf(C_5Me_4H)_2Cl_2K(OEt_2)]_n$ from two milligrams of ^{249}Cf . This bent metallocene motif, not previously structurally authenticated beyond uranium (U)^{14,15}, contains the first crystallographically characterized Cf–C bond. Analysis suggests the Cf–C bond is largely ionic with a small covalent contribution. Lowered Cf 5*f* orbital energy versus dysprosium (Dy) 4*f* in the colourless, isoelectronic and isostructural $[Dy(C_5Me_4H)_2Cl_2K(OEt_2)]_n$ results in an orange Cf compound, contrasting

with the light-green colour typically associated with Cf compounds^{[16](#),[17](#),[18](#),[19](#),[20](#),[21](#),[22](#)}.

Access options

Subscribe to Journal

Get full journal access for 1 year

\$199.00

only \$3.90 per issue

[Subscribe](#)

All prices are NET prices.

VAT will be added later in the checkout.

Tax calculation will be finalised during checkout.

Rent or Buy article

Get time limited or full article access on ReadCube.

from \$8.99

[Rent or Buy](#)

All prices are NET prices.

Additional access options:

- [Log in](#)
- [Access through your institution](#)
- [Learn about institutional subscriptions](#)

Fig. 1: Synthesis and solid-state structure of 2-Cf.



Fig. 2: UV–vis–NIR spectra of 2-Cf.

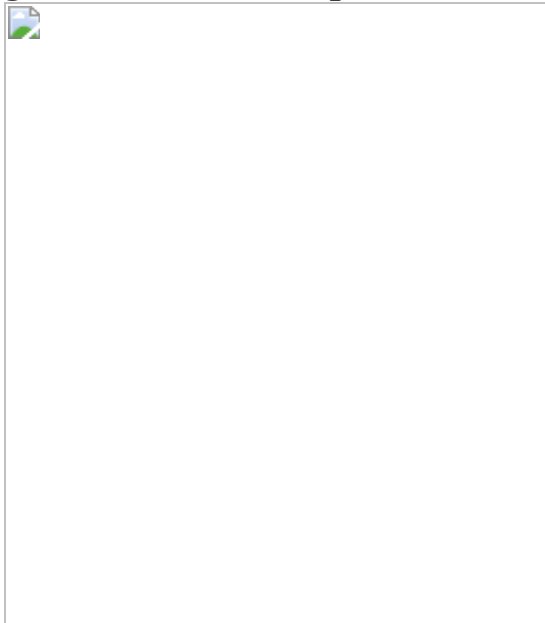
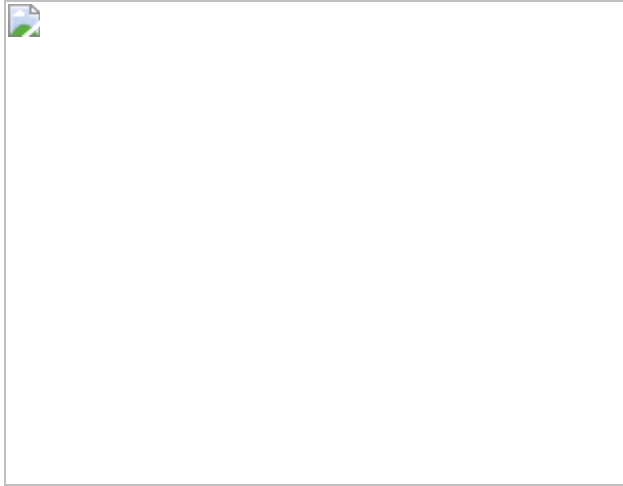


Fig. 3: Experimental solid-state and SO-NEVPT2 calculated absorption spectra of 2-Cf averaged for both *cis* and *trans* geometries.



Data availability

The data that support the findings of this study are available within the paper and its [Supplementary Information](#) files. Cambridge Crystallographic Data Centre (CCDC) deposition numbers are 2025245 (**1-²⁴¹Am**), 2058952 (**1-Ho**), 2025247 (**2-Cf**), 2025249 (**2-Gd^a**), 2092534 (**2-Gd^b**), 2025248 (**2-Dy**), 2063323 (**3**) and 2025250 (**4**). These data can be obtained free of charge from the CCDC via www.ccdc.cam.ac.uk/data_request/cif.

References

1. 1.

Mingos, M. & Crabtree, R. *Comprehensive Organometallic Chemistry III* (Elsevier, 2007).

2. 2.

Zalkin, A. & Raymond, K. N. Structure of di- π -cyclooctatetraeneuranium (uranocene). *J. Am. Chem. Soc.* **91**, 5667–5668 (1969).

3. 3.

Kealy, T. J. & Pauson, P. L. A new type of organo-iron compound. *Nature* **168**, 1039–1040 (1951).

4. 4.

Hartline, D. R. & Meyer, K. From chemical curiosities and trophy molecules to uranium-based catalysis: developments for uranium catalysis as a new facet in molecular uranium chemistry. *JACS Au* **1**, 698–709 (2021).

5. 5.

Pagano, J. K. et al. Actinide 2-metallabiphenylenes that satisfy Hückel’s rule. *Nature* **578**, 563–567, (2020).

6. 6.

Apostolidis, C., Dutkiewicz, M. S., Kovács, A. & Walter, O. Solid-state structure of tris-cyclopentadienide uranium(III) and plutonium(III). *Chem. Eur. J.* **24**, 2841–2844 (2018).

7. 7.

Windorff, C. J. et al. Identification of the formal +2 oxidation state of plutonium: synthesis and characterization of {Pu^{II}[C₅H₃(SiMe₃)₂]₃}⁻. *J. Am. Chem. Soc.* **139**, 3970–3973 (2017).

8. 8.

Formanuk, A. et al. Actinide covalency measured by pulsed electron paramagnetic resonance spectroscopy. *Nat. Chem.* **9**, 578–583 (2017).

9. 9.

Dutkiewicz, M. S., Apostolidis, C., Walter, O. & Arnold, P. L. Reduction chemistry of neptunium cyclopentadienide complexes: from structure to understanding. *Chem. Sci.* **8**, 2553–2561 (2017).

10. 10.

Apostolidis, C. et al. A structurally characterized organometallic plutonium(IV) complex. *Angew. Chem. Int. Ed.* **56**, 5066–5070 (2017).

11. 11.

Dutkiewicz, M. S. et al. Organometallic neptunium(III) complexes. *Nat. Chem.* **8**, 797–802 (2016).

12. 12.

Liddle, S. T. The renaissance of non-aqueous uranium chemistry. *Angew. Chem. Int. Ed.* **54**, 8604–8641 (2015).

13. 13.

Goodwin, C. A. P. et al. [Am(C₅Me₄H)₃]: an organometallic americium complex. *Angew. Chem. Int. Ed.* **58**, 11695–11699 (2019).

14. 14.

Sonnenberger, D. C. & Gaudiello, J. Synthesis and cyclic voltammetric study of bis(pentamethylcyclopentadienyl)neptunium dichloride. *J. Less-Common Met.* **126**, 411–414 (1986).

15. 15.

Laubereau, P. G. The formation of dicyclopentadienylberkeliumchloride. *Inorg. Nucl. Chem. Lett.* **6**, 611–616 (1970).

16. 16.

Cary, S. K. et al. A series of dithiocarbamates for americium, curium, and californium. *Dalton Trans.* **47**, 14452–14461 (2018).

17. 17.

Polinski, M. J. et al. Unusual structure, bonding and properties in a californium borate. *Nat. Chem.* **6**, 387–392 (2014).

18. 18.

Sykora, R. E., Assefa, Z., Haire, R. G. & Albrecht-Schmitt, T. E. First structural determination of a trivalent californium compound with oxygen coordination. *Inorg. Chem.* **45**, 475–477 (2006).

19. 19.

Carnall, W. T. A systematic analysis of the spectra of trivalent actinide chlorides in D_{3h} site symmetry. *J. Chem. Phys.* **96**, 8713–8726 (1992).

20. 20.

Carnall, W. T., Fried, S. & Wagner, F. Absorption spectrum of CfCl₃. *J. Chem. Phys.* **58**, 1938–1949 (1973).

21. 21.

Burns, J. H., Peterson, J. R. & Baybarz, R. D. Hexagonal and orthorhombic crystal structures of californium trichloride. *J. Inorg. Nucl. Chem.* **35**, 1171–1177 (1973).

22. 22.

Laubereau, P. G. & Burns, J. H. Microchemical preparation of tricyclopentadienyl compounds of berkelium, californium, and some lanthanide elements. *Inorg. Chem.* **9**, 1091–1095 (1970).

23. 23.

Streitwieser, A. & Müller-Westerhoff, U. Bis(cyclooctatetraenyl)uranium (uranocene). A new class of sandwich complexes that utilize atomic f orbitals. *J. Am. Chem. Soc.* **90**, 7364–7364 (1968).

24. 24.

Minasian, S. G. et al. New evidence for 5f covalency in actinocenes determined from carbon K-edge XAS and electronic structure theory. *Chem. Sci.* **5**, 351–359 (2014).

25. 25.

Evans, W. J. Tutorial on the role of cyclopentadienyl ligands in the discovery of molecular complexes of the rare-earth and actinide metals in new oxidation states. *Organometallics* **35**, 3088–3100 (2016).

26. 26.

Hayton, T. W. Recent developments in actinide-ligand multiple bonding. *Chem. Commun.* **49**, 2956–2973 (2013).

27. 27.

Jones, M. B. & Gaunt, A. J. Recent developments in synthesis and structural chemistry of nonaqueous actinide complexes. *Chem. Rev.* **113**, 1137–1198 (2013).

28. 28.

Baumgärtner, F., Fischer, E. O., Kanellakopulos, B. & Laubereau, P. Tri(cyclopentadienyl)americium(III). *Angew. Chem. Int. Ed.* **5**, 134–135 (1966).

29. 29.

Laubereau, P. G. & Burns, J. H. Tricyclopentadienyl-curium. *Inorg. Nucl. Chem. Lett.* **6**, 59–63 (1970).

30. 30.

Kirker, I. & Kaltsoyannis, N. Does covalency *really* increase across the 5f series? A comparison of molecular orbital, natural population, spin and electron density analyses of AnCp₃ (An = Th-Cm; Cp = η⁵-C₅H₅). *Dalton Trans.* **40**, 124–131 (2011).

31. 31.

Strittmatter, R. J. & Bursten, B. E. Bonding in tris(η⁵-cyclopentadienyl) actinide complexes. 5. A comparison of the bonding in neptunium, plutonium, and transplutonium compounds with that in lanthanide compounds and a transition-metal analog. *J. Am. Chem. Soc.* **113**, 552–559 (1991).

32. 32.

Kozimor, S. A. et al. Trends in covalency for d- and f-element metallocene dichlorides identified using chlorine K-edge X-ray absorption spectroscopy and time-dependent density functional theory. *J. Am. Chem. Soc.* **131**, 12125–12136 (2009).

33. 33.

Arney, D. S. J. & Burns, C. J. Synthesis and properties of high-valent organouranium complexes containing terminal organoimido and oxo

functional groups. A new class of organo-f-element complexes. *J. Am. Chem. Soc.* **117**, 9448–9460 (1995).

34. 34.

Apostolidis, C. et al. $[An(H_2O)_9](CF_3SO_3)_3$ ($An=U\text{-Cm, Cf}$): exploring their stability, structural chemistry, and magnetic behavior by experiment and theory. *Angew. Chem. Int. Ed.* **49**, 6343–6347 (2010).

35. 35.

Polinski, M. J. et al. Chirality and polarity in the f-block borates $M_4[B_{16}O_{26}(OH)_4(H_2O)_3Cl_4]$ ($M=Sm, Eu, Gd, Pu, Am, Cm, \text{ and } Cf$). *Chem. Eur. J.* **20**, 9892–9896 (2014).

36. 36.

Cary, S. K. et al. Emergence of californium as the second transitional element in the actinide series. *Nat. Commun.* **6**, 6827 (2015).

37. 37.

Galley, S. S. et al. Synthesis and characterization of tris-chelate complexes for understanding *f*-orbital bonding in later actinides. *J. Am. Chem. Soc.* **141**, 2356–2366 (2019).

38. 38.

Shannon, R. D. Revised effective ionic radii and systematic studies of interatomic distances in halides and chalcogenides. *Acta Crystallogr. A* **32**, 751–767 (1976).

39. 39.

Schumann, H., Glanz, M., Hemling, H. & Ekkehard Hahn, F. *Metallorganische Verbindungen der Lanthanoide*. 93 [1].

Tetramethylcyclopentadienyl-Komplexe ausgewählter 4f-Elemente. Z. Anorg. Allg. Chem. **621**, 341–345 (1995).

40. 40.

Jenkins, T. F. et al. Tetramethylcyclopentadienyl ligands allow isolation of Ln(II) ions across the lanthanide series in [K(2.2.2-cryptand)][(C₅Me₄H)₃Ln] complexes. *Organometallics* **37**, 3863–3873 (2018).

Acknowledgements

We thank I. May at Los Alamos National Laboratory (LANL) and G. P. Horne at Idaho National Laboratory for discussions. We acknowledge the US Department of Energy (DOE), Office of Science (SC), Basic Energy Sciences (BES) Heavy Element Chemistry Program (HEC) at LANL (E.R.B., A.J.G., S.A.K., Z.R.J., B.L.S., F.D.W., P.Y., J.S.; DE-AC52-06NA25396), at Florida State University (T.E.A.-S., A.N.G., J.M.S., C.J.W.; DE-FG02-13ER16414), and at the University of California at Irvine (W.J.E., T.F.J., J.C.W.; DE-SC0004739). C.A.P.G. was sponsored by a Distinguished J. R. Oppenheimer Postdoctoral Fellowship (LANL-LDRD, 20180703PRD1). We thank LANL-LDRD (L.M.S., A.J.G.; 20190091ER) for aspects of the ²⁴¹Am experimental work. Theoretical research was performed using EMSL (grid.436923.9), a DOE-SC User Facility sponsored by the Office of Biological and Environmental Research. J.S. also thanks the National Natural Science Foundation of China (22076130), and the Fundamental Research Funds for the Central Universities (20826041D4117) and start-up funds from Sichuan University. J.N.C. and J.D.A. acknowledge the DOE-SC, Isotope Development and Production for Research and Application subprogram within the Office of Nuclear Physics for ²⁴¹Am sample conditioning and dispensing. J.D.A. thanks the NNSA Plutonium Sustainment Program and the National Nuclear Security Administration (NNSA) Material Recycle and Recovery for funding. We thank E. R. Birnbaum and B. L. Ortiz for procurement of ²⁴¹Am through the National Isotope Development Center, purchased with LANL DOE-SC-BES-HEC funds.

Author information

Author notes

1. These authors contributed equally: Conrad A. P. Goodwin, Jing Su

Affiliations

1. Chemistry Division, Los Alamos National Laboratory, Los Alamos, NM, USA

Conrad A. P. Goodwin, Lauren M. Stevens, Frankie D. White, Nickolas H. Anderson, John D. Auxier II, Justin N. Cross, Andrew J. Gaunt, Michael R. James, Michael T. Janicke, Zachary R. Jones & Stosh A. Kozimor

2. Theoretical Division, Los Alamos National Laboratory, Los Alamos, NM, USA

Jing Su, Enrique R. Batista & Ping Yang

3. College of Chemistry, Sichuan University, Chengdu, China

Jing Su

4. Department of Chemistry and Biochemistry, Florida State University, Tallahassee, FL, USA

Thomas E. Albrecht-Schönzart, Alyssa N. Gaiser, Joseph. M. Sperling & Cory J. Windorff

5. Radiation Protection Division, Los Alamos National Laboratory, Los Alamos, NM, USA

Sasha F. Briscoe

6. Department of Chemistry, University of California, Irvine, CA, USA

William J. Evans, Tener F. Jenkins, Justin C. Wedal & Joseph W. Ziller

7. Materials Physics and Applications Division, Los Alamos National Laboratory, Los Alamos, NM, USA

Brian L. Scott

Contributions

E.R.B., W.J.E., A.J.G., S.A.K. and P.Y. devised the project and are corresponding authors. C.A.P.G. led lanthanide synthetic protocol development and performed Cf and Am synthetic work and characterization with oversight and help from A.J.G., along with expertise and support from L.M.S. and F.D.W. (UV–vis–NIR), M.T.J. (nuclear magnetic resonance (NMR) spectroscopy), T.F.J. (ligand preparation), B.L.S. (single-crystal XRD) and S.F.B. (radiological safety). S.A.K., N.H.A. and Z.R.J. prepared the LANL ^{249}Cf stock solution; A.N.G., J.M.S. and C.J.W. prepared the FSU ^{249}Cf stock solution; L.M.S., A.J.G., M.R.J. and J.N.C. prepared and characterized the ^{241}Am stock at LANL. J.C.W. provided supporting characterization of lanthanide compounds. J.S., E.R.B. and P.Y. performed and analysed all theoretical work. Principal manuscript writing was by C.A.P.G., J.S., A.J.G., S.A.K., W.J.E., E.R.B. and P.Y., with input and editing from all authors. A.J.G. was the submitting author.

Corresponding authors

Correspondence to [Enrique R. Batista](#), [William J. Evans](#), [Andrew J. Gaunt](#), [Stosh A. Kozimor](#) or [Ping Yang](#).

Ethics declarations

Competing interests

The authors declare no competing interests.

Additional information

Peer review information *Nature* thanks Weiqun Shi and the other, anonymous, reviewer(s) for their contribution to the peer review of this work. Peer reviewer reports are available.

Publisher's note Springer Nature remains neutral with regard to jurisdictional claims in published maps and institutional affiliations.

Extended data figures and tables

Extended Data Fig. 1 Outline of the complexes synthesized in this work.

a, The known **1-M** ($M = \text{Sm, Gd}$) complexes were chosen for their ionic radii similarities to Cf^{3+} ($\text{Sm, } 0.958 \text{ \AA}; \text{Gd, } 0.938 \text{ \AA}; \text{Cf, } 0.95 \text{ \AA}$). Complex **1- ^{241}Am** was synthesized following prior methodology for **1- ^{243}Am** to assess radiolytic effects. **b**, Complex **1-Dy** was synthesized as Dy^{3+} ($4f^9$) is valence isoelectronic to Cf^{3+} ($5f^9$), and **1-Ho** was synthesized as the ionic radius of Ho^{3+} (0.901 \AA) is significantly smaller than that of Cf^{3+} . **c**, Complexes **2-M** ($M = \text{Gd, Dy}$) were synthesized as comparisons to **2-Cf** and chosen for the metal having a similar ionic radius to Cf^{3+} (Gd) or for being valence isoelectronic (Dy). **d**, Eu^{3+} (0.947 \AA) is a better ionic radius match to Cf^{3+} than Sm or Gd; however, we were unable to isolate **1-Eu** using salt-metathesis protocols which instead led to reduction to a Eu^{2+} complex, **3**.

Extended Data Fig. 2 Geometric features of the ‘ $\{\text{Cf}(\text{Cp}^{\text{tet}})_2\text{Cl}_2\}^{1-}$, anions and polymeric chain propagation.

a, View from the top of the metallocene fragment for Cf(1) showing the *trans* disposition of the Cp^{tet} C–H groups and the Cl–Cf–Cl bond angle. **b**, View from the top of the metallocene fragment for Cf(2) showing the *cis* disposition of the Cp^{tet} C–H groups and the Cl–Cf–Cl bond angle. **c, d**, View down the crystallographic *c* axis, showing that the Cf(1) and Cf(2) chains propagate parallel to the *a* axis—note that the arrangement of the panels is not indicative of their relative spatial arrangement.

Extended Data Fig. 3 Example bonding orbitals from 2-Cf and 2-Dy.

The lowest occupied valence *f* orbitals of a'' symmetry of **2-Cf** (left, 27 a'') and **2-Dy** (right, 22 a'') (contour value of 0.03 a.u.; see Supplementary Table 19). This shows the greater mixing between metal 5*f* and C 2*p* orbitals in **2-Cf** compared to 4*f* and C 2*p* orbitals in **2-Dy**.

Extended Data Table 1 Mulliken charge (*q*) on metal atom, $(Cp^{tet})_2$ fragment and (Cl_2K) fragment in the $[M(Cp^{tet})_2Cl_2K]$ ($M = Cf, Dy$) compounds of C_s symmetry from DFT/PBE0 calculations

Extended Data Table 2 Bond distances and bond orders in $[M(Cp^{tet})_2Cl_2K]$ ($M = Cf, Dy$) complexes of C_s symmetry from DFT/PBE0 calculations^a

Extended Data Table 3 QTAIM analysis on $[M(Cp^{tet})_2Cl_2K]$ ($M = Cf, Dy$) complexes of C_s symmetry from DFT/PBE0 calculations, and previously reported data for $[An(Cp)_3]$ ($An = Th - Cm$)

Supplementary information

Supplementary Information

This file includes extensive experimental details on compounds synthesized in this work, photographs of select reactions and products, crystallographic data collection descriptions and comments on radiation-induced changes in crystals of **2-Cf**, visual representations of molecular structures, nuclear magnetic resonance, UV–vis–NIR, FT-IR spectra, and full computational details.

Peer Review File

Supplementary Data

Crystallographic information files for compounds **1-²⁴¹Am**, [²⁴¹Am(Cp^{tet})₃]; **1-Ho**, [Ho(Cp^{tet})₃]; **2-Cf**, [Cf(Cp^{tet})₂Cl₂K(OEt₂)]_n; **2-Gd^a**, α -[Gd(Cp^{tet})₂Cl₂K(OEt₂)]_n; **2-Gd^b**, β -[Gd(Cp^{tet})₂Cl₂K(OEt₂)]_n; **2-Dy**, [Dy(Cp^{tet})₂Cl₂K(OEt₂)]_n; **3**, [Eu(Cp^{tet})₂(THF)₂]; and **4**, [K(Et₂O)(Cp^{tet})]_n.

Rights and permissions

[Reprints and Permissions](#)

About this article

Cite this article

Goodwin, C.A.P., Su, J., Stevens, L.M. *et al.* Isolation and characterization of a californium metallocene. *Nature* **599**, 421–424 (2021).
<https://doi.org/10.1038/s41586-021-04027-8>

- Received: 15 April 2021
- Accepted: 15 September 2021
- Published: 17 November 2021
- Issue Date: 18 November 2021
- DOI: <https://doi.org/10.1038/s41586-021-04027-8>

Share this article

Anyone you share the following link with will be able to read this content:

[Get shareable link](#)

Sorry, a shareable link is not currently available for this article.

[Copy to clipboard](#)

Provided by the Springer Nature SharedIt content-sharing initiative

Californium—carbon bond captured in a complex

- Julie E. Niklas
- Henry S. La Pierre

News & Views 17 Nov 2021

This article was downloaded by **calibre** from <https://www.nature.com/articles/s41586-021-04027-8>

| [Section menu](#) | [Main menu](#) |

- Article
- [Published: 17 November 2021](#)

Widespread changes in surface temperature persistence under climate change

- [Jingyuan Li¹](#) &
- [David W. J. Thompson](#) ORCID: [orcid.org/0000-0002-5413-4376^{1,2}](https://orcid.org/0000-0002-5413-4376)

[Nature](#) volume **599**, pages 425–430 (2021)

- 921 Accesses
- 26 Altmetric
- [Metrics details](#)

Subjects

- [Atmospheric science](#)
- [Climate change](#)

Abstract

Climate change has been and will be accompanied by widespread changes in surface temperature. It is clear that these changes include global-wide increases in mean surface temperature and changes in temperature variance that are more regionally-dependent^{1,2,3}. It is less clear whether they also include changes in the persistence of surface temperature. This is important as the effects of weather events on ecosystems and society depend critically

on the length of the event. Here we provide an extensive survey of the response of surface temperature persistence to climate change over the twenty-first century from the output of 150 simulations run on four different Earth system models, and from simulations run on simplified models with varying representations of radiative processes and large-scale dynamics. Together, the results indicate that climate change simulations are marked by widespread changes in surface temperature persistence that are generally most robust over ocean areas and arise due to a seemingly broad range of physical processes. The findings point to both the robustness of widespread changes in persistence under climate change, and the critical need to better understand, simulate and constrain such changes.

Access options

Subscribe to Journal

Get full journal access for 1 year

\$199.00

only \$3.90 per issue

[Subscribe](#)

All prices are NET prices.

VAT will be added later in the checkout.

Tax calculation will be finalised during checkout.

Rent or Buy article

Get time limited or full article access on ReadCube.

from \$8.99

[Rent or Buy](#)

All prices are NET prices.

Additional access options:

- [Log in](#)
- [Access through your institution](#)
- [Learn about institutional subscriptions](#)

Fig. 1: Changes in surface temperature persistence in ESMs.



Fig. 2: Spatially averaged surface temperature persistence.



Fig. 3: Changes in persistence averaged over all four ESMs.

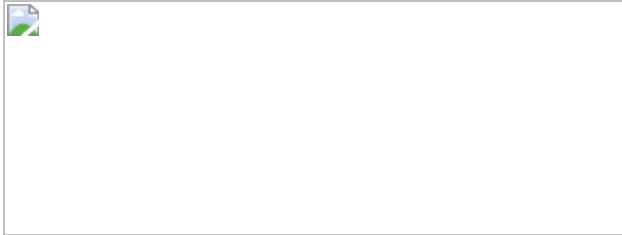


Fig. 4: Changes in persistence in slab-ocean numerical models.

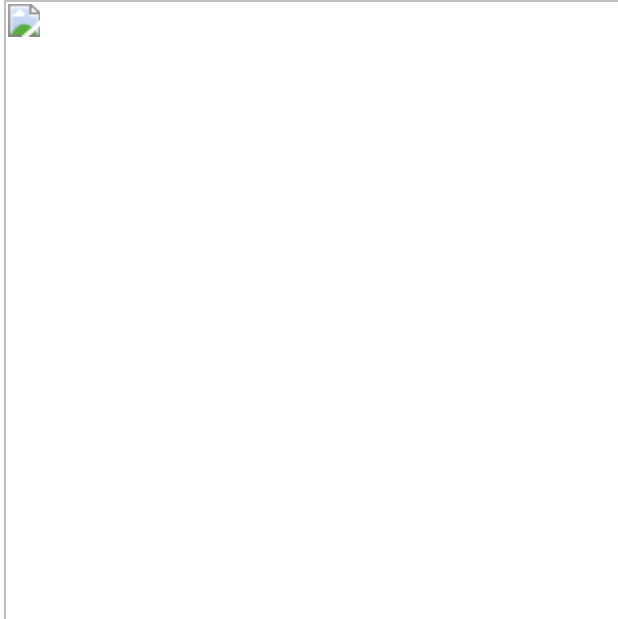
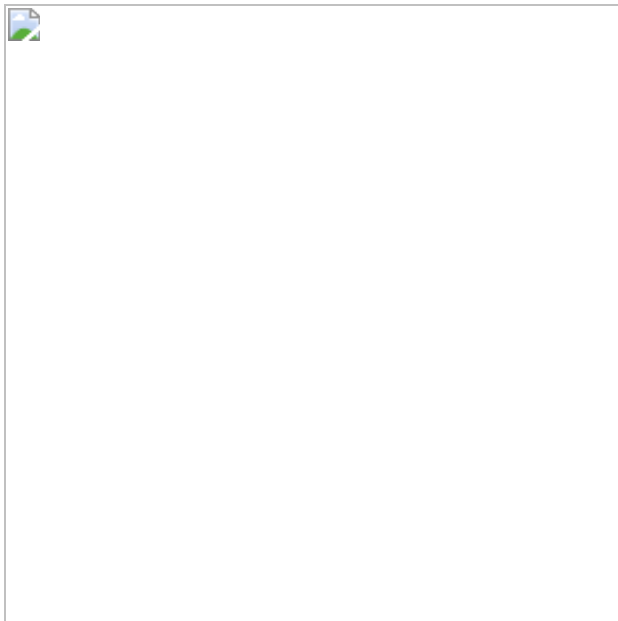


Fig. 5: Changes in persistence in a simplified ‘tropics-world’ simulation.



Data availability

The large-ensemble output is publicly available via the Multi-Model Large Ensemble Archive (MMLEA) at the National Center for Atmospheric Research (<https://doi.org/10.1038/s41558-020-0731-2>). The output from the

gray radiation and RRTMG simulations were provided by Zhihong Tan at the NOAA Geophysical Fluid Dynamics Laboratory; the output from the RCE simulations were provided by Gabor Drotos at the Institute for Cross-Disciplinary Physics and Complex Systems, Palma de Mallorca, Spain. All data used to construct the figures are archived in Figshare (<https://doi.org/10.6084/m9.figshare.15078807.v1>). All other data that support the findings of the study are available from the corresponding author upon reasonable request.

Code availability

Code that was used in this study is available from the corresponding author upon reasonable request.

References

1. 1.
Hartmann, D. L. et al. in *Climate Change 2013: The Physical Science Basis* (eds Stocker, T. F. et al.) Ch. 2 (IPCC, Cambridge Univ. Press, 2013).
2. 2.
Kirtman, B. et al. in *Climate Change 2013: The Physical Science Basis* (eds Stocker, T. F. et al.) Ch. 11 (IPCC, Cambridge Univ. Press, 2013).
3. 3.
Collins, M. et al. in *Climate Change 2013: The Physical Science Basis* (eds Stocker, T. F. et al.) Ch. 12 (IPCC, Cambridge Univ. Press, 2013).
4. 4.
Schar, C. et al. The role of increasing temperature variability in European summer heatwaves. *Nature* **427**, 332–336 (2004).

5. 5.

Seneviratne, S. I., Luthi, D., Litschi, M. & Schar, C. Land–atmosphere coupling and climate change in Europe. *Nature* **443**, 205–207 (2006).

6. 6.

Fischer, E. M. & Schar, C. Future changes in daily summer temperature variability: driving processes and role for temperature extremes. *Clim. Dyn.* **33**, 917–935 (2009).

7. 7.

Donat, M. G. & Alexander, L. V. The shifting probability distribution of global daytime and night-time temperatures. *Geophys. Res. Lett.* <https://doi.org/10.1029/2012GL052459> (2012).

8. 8.

Fischer, E. M., J. Rajczak, & Schar, C. Changes in European summer temperature variability revisited. *Geophys. Res. Lett.* **39**, 19 (2012).

9. 9.

Volodin, E. M. & Yurova, A. Y. Summer temperature standard deviation, skewness and strong positive temperature anomalies in the present day climate and under global warming conditions. *Clim. Dyn.* **40**, 1387–1398 (2013).

10. 10.

Lewis, S. C. & Karoly, D. J. Anthropogenic contributions to Australia’s record summer temperatures of 2013. *Geophys. Res. Lett.* **40**, 3705–3709 (2013).

11. 11.

Screen, J. A. Arctic amplification decreases temperature variance in northern mid- to high-latitudes. *Nat. Clim. Change* **4**, 577–582 (2014).

12. 12.

Schneider, T., Bischoff, T. & Plotka, H. Physics of changes in synoptic midlatitude temperature variability. *J. Climate* **28**, 2312–2331 (2015).

13. 13.

McKinnon, K. A., Rhines, A., Tingley, M. P. & Huybers,, P. The changing shape of Northern hemisphere summer temperature distributions. *J. Geophys. Res. Atm.* **121**, 8849–8868 (2016).

14. 14.

Tamarin-Brodsky, T., Hodges, K., Hoskins, B. J. & Shepherd, T. G. A dynamical perspective on atmospheric temperature variability and its response to climate change. *J. Climate* **32**, 1707–1724 (2019).

15. 15.

Tamarin-Brodsky, T., Hodges, K. I., Hoskins, B. J. & Shepherd, T. Changes in Northern Hemisphere temperature variability shaped by regional warming patterns. *Nat. Geosci.* **13**, 414–421 (2020).

16. 16.

Boulton, C. A. & Lenton, T. M. Slowing down of North Pacific climate variability and its implications for abrupt ecosystem change. *Proc. Natl Acad. Sci. USA* **112**, 11496–11501 (2015).

17. 17.

Lenton, T. M., Dakos, V., Bathiany, S. & Scheffer, M. Observed trends in the magnitude and persistence of monthly temperature variability. *Sci. Rep.* **7**, 5940 (2017).

18. 18.

Pfleiderer, P. & Coumou, D. Quantification of temperature persistence over the Northern Hemisphere land-area. *Clim. Dyn.* **51**, 627–637

(2018).

19. 19.

Di Cecco, G. J., Gouhier, T. C. Increased spatial and temporal autocorrelation of temperature under climate change. *Sci. Rep.* **8**, 14850 (2018).

20. 20.

Pfleiderer, P., Schleussner, C., Kornhuber, K. & Coumou, D. Summer weather becomes more persistent in a 2 C world. *Nat. Clim. Change* **9**, 666–671 (2019).

21. 21.

Fischer, E. M., Beyerle, U., Schleussner, C. F., King, A. D. & Knutti, R. Biased estimates of changes in climate extremes from prescribed SST simulations. *Geophys. Res. Lett.* **45**, 8500–8509 (2018).

22. 22.

Cohen, J. et al. Recent Arctic amplification and extreme mid-latitude weather. *Nat. Geosci.* **7**, 627–637 (2014).

23. 23.

Barnes, E. A. & Screen, J. The impact of Arctic warming on the midlatitude jet-stream: Can it? Has it? Will it? *WIREs Clim. Change* **6**, 277–286 (2015).

24. 24.

Graham, R. M. et al. Increasing frequency and duration of Arctic winter warming events. *Geophys. Res. Lett.* **44**, 6974–6983 (2013).

25. 25.

Tan, Z., Lachmy, O. & Shaw, T. A. The sensitivity of the jet stream response to climate change to radiative assumptions. *JAMES* **11**, 934–956 (2019).

26. 26.

Hall, A. & Manabe, S. The role of water vapor feedback in unperturbed climate variability and global warming. *J. Climate* **12**, 2327–2346 (1999).

27. 27.

Drotos, G., Becker, T., Mauritsen, T. & Stevens, B. Global variability in radiative-convective equilibrium with a slab ocean under a wide range of co₂ concentrations. *Tellus* **72**, 1–19 (2020).

28. 28.

Barnes, E. A. & Hartmann, D. L. Testing a theory for the effect of latitude on the persistence of eddy-driven jets using CMIP3 simulations, *Geophys. Res. Lett.* **37**, L15801 (2010).

29. 29.

Woollings, T. et al. Blocking and its response to climate change. *Curr. Clim. Change Rep.* **4**, 287–300 (2018).

30. 30.

Barnes, E. A. & Polvani, L. Response of the midlatitude jets and of their variability to increased greenhouse gases in the CMIP5 models. *J. Climate* **26**, 7117–7135 (2013).

31. 31.

Yulaeva, E. & Wallace, J. M. The signature of ENSO in global temperature and precipitation fields derived from the microwave sounding unit. *J. Climate* **7**, 1719–1736 (1994).

32. 32.

Alexander, M. A. et al. The atmospheric bridge: the influence of ENSO teleconnections on air–sea interaction over the global oceans. *J. Climate* **15**, 2205–2231 (2002).

33. 33.

Cai, W. et al. Increasing frequency of extreme El Nino events due to greenhouse warming. *Nat. Clim. Change* **4**, 111–116 (2014).

34. 34.

Kohyama, T., Hartmann, D. L. & Battisti, D. S. La Nina-like mean-state response to global warming and potential oceanic roles. *J. Climate* **30**, 4207–4225 (2017).

35. 35.

Frankignoul, C. & Hasselman, K. Stochastic climate models, Part II Application to sea-surface temperature variability and thermocline variability. *Tellus* **29**, 289–305 (1977).

36. 36.

Deser, C., Alexander, M. A. & Timlin, M. S. Understanding the persistence of sea surface temperature anomalies in midlatitudes. *J. Climate* **16**, 57–72 (2003).

37. 37.

Capotondi, A., Alexander, M. A., Bond, N. A., Curchitser, E. N. & Scott, J. D. Enhanced upper ocean stratification with climate change in the CMIP3 models. *J. Geophys. Res.* **117**, C04031 (2012).

38. 38.

Li, G. et al. Increasing ocean stratification over the past half-century. *Nat. Clim. Change* **10**, 1116–1123 (2020).

39. 39.

Amaya, D. J. et al. Are long-term changes in mixed layer depth influencing North Pacific marine heatwaves? *Bull. Am. Meteorol. Soc.* **102**, S59–S66 (2021).

40. 40.

Sallée, J. B. et al. Assessment of Southern Ocean water mass circulation and characteristics in CMIP5 models: historical bias and forcing response. *J. Geophys. Res. Oceans* **118**, 1830–1844 (2013).

41. 41.

Manabe, S., Stouffer, R. J., Spelman, M. J. & Bryan, K. Transient responses of a coupled ocean-atmosphere model to gradual changes of atmospheric CO₂. Part I. Annual mean response. *J. Climate* **4**, 785–818 (1991).

42. 42.

de Lavergne, C. et al. Cessation of deep convection in the open Southern Ocean under anthropogenic climate change. *Nat. Clim. Change* **4**, 278–282 (2014).

43. 43.

Kostov, Y. et al. Fast and slow responses of Southern Ocean sea surface temperature to SAM in coupled climate models. *Climate Dyn.* **48**, 1595–1609 (2017).

44. 44.

Bronselaer, B. et al. Change in future climate due to Antarctic meltwater. *Nature* **564**, 53–58 (2018).

45. 45.

Jia, G. et al. in *IPCC Special Report on Climate Change and Land* (eds Shukla, P. R. et al.) Ch. 2 (IPCC, 2019).

46. 46.

Frankignoul, C., Czaja, A. & L'Heveder, B. Air–sea feedback in the North Atlantic and surface boundary conditions for ocean models. *J. Climate* **11**, 2310–2324 (1998).

47. 47.

Hausmann, U., Czaja, A. & Marshall, J. Mechanisms controlling the sst air–sea heat flux feedback and its dependence on spatial scale. *Clim. Dyn.* **48**, 1297–1307 (2016).

48. 48.

Vargas Zeppetello, L. R., Donohoe, A. & Battisti, D. S. Does surface temperature respond to or determine downwelling longwave radiation? *Geophys. Res. Lett.* **46**, 2781–2789 (2019).

49. 49.

Barsugli, J. J. and D. S. Battisti, The basic effects of atmosphere–ocean thermal coupling on midlatitude variability. *J. Atmos. Sci.* **55**, 477–493 (1998).

50. 50.

Cronin, T. W. & Emanuel, K. A. The climate time scale in the approach to radiative-convective equilibrium. *JAMES* **5**, 843–849 (2013).

51. 51.

Kay, J. E. et al. The Community Earth System Model (CESM) Large Ensemble Project: a community resource for studying climate change in the presence of internal climate variability. *Bull. Amer. Meteor. Soc.* **96**, 1333–1349 (2015).

52. 52.

Jeffrey, S. et al. Australia's CMIP5 submission using the CSIRO-Mk3.6 model. *Aust. Meteorol. Ocean* **63**, 1–13 (2013).

53. 53.

Kirchmeier-Young, M., Zwiers, F. W. & Gillett, N. P. Attribution of extreme events in arctic sea ice extent. *J. Climate* **30**, 553–571 (2017).

54. 54.

Rodgers, K. B., Lin, J. & Frolicher, T. L. Emergence of multiple ocean ecosystem drivers in a large ensemble suite with an Earth system model. *Biogeosciences* **12**, 3301–3320 (2015).

55. 55.

Deser, C. et al. Insights from Earth system model initial-condition large ensembles and future prospects. *Nat. Clim. Change* **10**, 277–286 (2020).

56. 56.

Phillips, A. S., Deser, C., Fasullo, J., Schneider, D. P. & Simpson, I. R. Assessing climate variability and change in model large ensembles: a user's guide to the "climate variability diagnostics package for large ensembles" version 1.0 (2020).

57. 57.

Fraedrich, K. and Blender, R. Scaling of atmosphere and ocean temperature correlations in observations and climate models. *Phys. Rev. Lett.* **90**, 108501 (2003).

58. 58.

Franzke, C. L. E. et al. The structure of climate variability across scales. *Rev. Geophys.* **58**, e2019RG000657 (2020).

59. 59.

Wilks, D. S. “The stippling shows statistically significant grid points”: how research results are routinely overstated and overinterpreted, and what to do about it. *Bull. Amer. Meteor. Soc.* **97**, 2263–2273 (2016).

60. 60.

Frierson, D. M. W., Held, I. M. & Zurita-Gotor, P. A gray-radiation aquaplanet moist gcm. Part I: static stability and eddy scale. *J. Atmos. Sci.* **63**, 2548–2566 (2006).

61. 61.

Iacono, M. J., Mlawer, E. J., Clough, S. A. & Morcrette, J.-J. Impact of an improved longwave radiation model, RRTM, on the energy budget and thermodynamic properties of the NCAR community climate model, CCM3. *J. Geophys. Res.* **105**, 14873–14890 (2000).

62. 62.

Delworth, T. L., Broccoli, A. J., Stouffer, R. J., Balaji, V. & Beesley, J. A. GFDL’s CM2 global coupled climate models. Part I: Formulation and simulation characteristics. *J. Climate* **19**, 643–667 (2006).

63. 63.

Kang, S. M., Held, I. M., Frierson, D. M. W. & Zhao, M. The response of the ITCZ to extratropical thermal forcing: Idealized slab-ocean experiments with a GCM. *J. Climate* **21**, 3521–3532 (2008).

64. 64.

Mauritsen, T. et al. Developments in the MPI-M Earth System Model version 1.2 (MPI-ESM1.2) and its response to increasing CO₂. *JAMES* **11**, 998–1038 (2019).

Acknowledgements

We thank A. Philips at NCAR for assistance with the Climate Variability Diagnostics Package analyses of the MMLEA; M. Winton and K. Rodgers for discussion of the GFDL ESM2M output; Z. Tan for providing output from the gray radiation and RRTMG simulations, and comments on the text; G. Drotos for providing the output from the RCE simulations and comments on the text; and F. Lehner, A. Czaja and B. Medeiros for helpful discussions. The large-ensemble output was obtained from the MMLEA produced by the US CLIVAR Working Group on Large Ensembles. We also acknowledge high-performance computing support from Cheyenne (<https://doi.org/10.5065/D6RX99HX>) provided by NCAR's Computational and Information Systems Laboratory, sponsored by the National Science Foundation (NSF). All maps were made using the Proplot Matplotlib wrapper and map projections from the Cartopy Python package. J.L. and D.W.J.T. are supported by the NSF Climate and Large-Scale Dynamics program.

Author information

Affiliations

1. Department of Atmospheric Science, Colorado State University, Fort Collins, CO, USA

Jingyuan Li & David W. J. Thompson

2. School of Environmental Sciences, University of East Anglia, Norwich, UK

David W. J. Thompson

Contributions

D.W.J.T. led the writing. J.L. performed the analyses and produced the figures.

Corresponding author

Correspondence to [David W. J. Thompson](#).

Ethics declarations

Competing interests

The authors declare no competing interests.

Additional information

Peer review information *Nature* thanks Daniel Koll and Christian Franzke for their contribution to the peer review of this work. Peer reviewer reports are available.

Publisher's note Springer Nature remains neutral with regard to jurisdictional claims in published maps and institutional affiliations.

Extended data figures and tables

[Extended Data Fig. 1 The relationship between the autocorrelation and the average length of a warm event.](#)

The 2d density plot of the lag-one autocorrelation and the average length of warm events calculated as a function of grid box in the CESM1 historical output. Warm events are defined as periods when temperatures exceed one standard deviation. Panels (a-d) show results for four sample ensemble members in the CESM1. Each panel includes results from 55296 grid boxes. Data density is found using a Gaussian kernel density estimate.

[Extended Data Fig. 2 The ensemble-mean relationship between the autocorrelation and the average length of a warm event.](#)

(a) The 2d density plot of the lag-one autocorrelation and the average length of warm events calculated as a function of grid box in the CESM1 historical output. Results are calculated for each ensemble member and then averaged

over all ensemble members. Warm events are defined as periods when temperatures exceed one standard deviation. Each panel includes results from 55296 grid boxes. (b; shading) As in the top panel, but results are averaged over bins that span 0.001 on the abscissa. (b; black line) Results derived from randomly generated red-noise time series with autocorrelation specified on the abscissa. Data density is found using a Gaussian kernel density estimate.

Extended Data Fig. 3 Changes in variance explained by persistence as a function of lag.

The changes in persistence between the “historical” period 1970-1999 and the “future” period 2070-2099 calculated from 40 large-ensembles run on the NCAR CESM1. Warm (red) colours represent an increase in persistence from the Historical to Future periods, while cool (blue) colours represent a decrease in persistence over the same period. Results show the percent changes in the variance explained by the (a) lag 5, (b) lag 10, (c) lag 15, and (d) lag 20-day autocorrelations. That is, they show: $\frac{\{r_i^2\}_{\text{Future}} - \{r_i^2\}_{\text{Historical}}}{\{r_i^2\}_{\text{Historical}}} - 1$ where r_i^2 denotes the variance explained by the lag i -day autocorrelation. Note that the autocorrelations are calculated first for individual ensemble members and then averaged over all ensembles using the Fisher-z transformation. Stippling indicates grid points where at least 75% of the ensemble members agree on the sign of the change (a likelihood of $\sim 0.1\%$ by chance) and where the ensemble mean results exceed the 95% confidence threshold based on a two-tailed test of the t-statistic. Note that panel (b) is identical to Figure 1a. See [Methods](#) for details of the ESM output, analysis, statistical significance, and reproducibility.

Extended Data Fig. 4 Changes in persistence as a function of lag.

The changes in persistence between the “historical” period 1970-1999 and the “future” period 2070-2099 calculated from 40 large-ensembles run on the NCAR CESM1. Warm (cool) colors represent an increase (decrease) in persistence from the historical to future period. Results show the *actual*

changes in the variance explained by the (a) lag 5, (b) lag 10, (c) lag 15, and (d) lag 20-day autocorrelations, not the *percent* changes as shown in Extended Data Figure 3. That is, they show: $\langle \{r\}^2 \rangle_{\{i, \text{Future}\}} - \langle \{r\}^2 \rangle_{\{i, \text{Historical}\}}$ where r_i^2 denotes the variance explained by the lag i -day autocorrelation. The autocorrelations are calculated first for individual ensemble members and then averaged over all ensembles using the Fisher-z transformation. Stippling indicates grid points where at least 75% of the ensemble members agree on the sign of the change (a likelihood of $\sim 0.1\%$ by chance) and where the ensemble mean results exceed the 95% confidence threshold based on a two-tailed test of the t-statistic. See [Methods](#) for details of the ESM output, analysis, statistical significance, and reproducibility.

Extended Data Fig. 5 Testing the robustness of changes in persistence to lag.

(a) The results at lag i on the abscissa indicate the spatial correlation between 1) the spatial map formed as $\langle \{r\}^2 \rangle_{\{i, \text{Future}\}} - \langle \{r\}^2 \rangle_{\{i, \text{Historical}\}}$, where $\langle \{r\}^2 \rangle_{\{i, \text{Future}\}}$ and $\langle \{r\}^2 \rangle_{\{i, \text{Historical}\}}$ indicate the variance explained by the lag i -day autocorrelation in the Future and Historical periods, respectively, and the autocorrelations are calculated first for individual ensemble members and then averaged over all ensembles (e.g., the lag $i=10$ map is shown in Extended Data Figure 4b); and 2) the corresponding map calculated for lag $i+1$. (b) As in panel (a), but for the spatial correlations between 1) the map formed for lag i and 2) the map formed for lag $i=10$. Results are based on all members from the CESM1 output.

Extended Data Fig. 6 Climatological-mean autocorrelations of surface temperature in the historical and future periods.

The lag 10-day autocorrelations of surface temperature in large ensembles run on the four indicated ESMs for (top) the 1970-1999 historical period; (bottom) the 2070-2099 future period. The results are derived from (a, e) 40 ensemble members run on the NCAR CESM1, (b, f) 30 ensemble members

run on the CSIRO Mk3.6, (c, g) 50 ensemble members run on the CCCma CanESM2, and (d, h) 30 members run on the GFDL ESM2M.

[Extended Data Fig. 7 Assessing changes in ENSO in large ensembles run on four ESMs.](#)

Scatter plots of the standard deviation of the monthly mean Nino 3.4 index during the historical period 1970-1999 and the future period 2070-2099 derived from (a) 40 ensemble members run on the NCAR CESM1, (b) 30 ensemble members run on the CSIRO Mk3.6, (c) 50 ensemble members run on the CCCma CanESM2, and (d) 30 members run on the GFDL ESM2M. The black diagonal lines represent the 1:1 line. Dots indicate results from individual ensemble members. The output was obtained from the NCAR CVDP-LE.

[Extended Data Fig. 8 Southern Ocean temperatures and SH sea ice extent in large ensembles run on four ESMs.](#)

Monthly mean values of (left) Southern Ocean temperatures; (right) Southern Hemisphere sea ice extent in large ensembles from the indicated ESMs. Results are shown for individual ensemble members and smoothed for display purposes using a 13 month running mean. Results are derived from (a, b) 40 ensemble members run on the NCAR CESM1, (c, d) 30 ensemble members run on the CSIRO Mk3.6, (e, f) 50 ensemble members run on the CCCma CanESM2, and (g, h) 30 members run on the GFDL ESM2M. The output was obtained from the NCAR CVDP-LE.

Supplementary information

[Peer Review File](#)

Rights and permissions

[Reprints and Permissions](#)

About this article

Cite this article

Li, J., Thompson, D.W.J. Widespread changes in surface temperature persistence under climate change. *Nature* **599**, 425–430 (2021).
<https://doi.org/10.1038/s41586-021-03943-z>

- Received: 12 October 2020
- Accepted: 24 August 2021
- Published: 17 November 2021
- Issue Date: 18 November 2021
- DOI: <https://doi.org/10.1038/s41586-021-03943-z>

Share this article

Anyone you share the following link with will be able to read this content:

[Get shareable link](#)

Sorry, a shareable link is not currently available for this article.

[Copy to clipboard](#)

Provided by the Springer Nature SharedIt content-sharing initiative

This article was downloaded by **calibre** from <https://www.nature.com/articles/s41586-021-03943-z>

- Article
- [Published: 17 November 2021](#)

Cardiopharyngeal deconstruction and ancestral tunicate sessility

- [Alfonso Ferrández-Roldán](#) ORCID: [orcid.org/0000-0003-0632-9838^{1,2}](https://orcid.org/0000-0003-0632-9838),
- [Marc Fabregà-Torras](#) ORCID: [orcid.org/0000-0002-1446-5832^{1,2} na1](https://orcid.org/0000-0002-1446-5832),
- [Gaspar Sánchez-Serna](#) ORCID: [orcid.org/0000-0003-3889-8648^{1,2} na1](https://orcid.org/0000-0003-3889-8648),
- [Enya Duran-Bello](#) ORCID: [orcid.org/0000-0002-4461-7446^{1,2}](https://orcid.org/0000-0002-4461-7446),
- [Martí Joaquín-Lluís](#) ORCID: [orcid.org/0000-0001-5866-0042^{1,2}](https://orcid.org/0000-0001-5866-0042),
- [Paula Bujosa](#) ORCID: [orcid.org/0000-0002-5945-6227^{1,2}](https://orcid.org/0000-0002-5945-6227),
- [Marcos Plana-Carmona](#) ORCID: [orcid.org/0000-0002-1976-7506^{1,2}](https://orcid.org/0000-0002-1976-7506),
- [Jordi Garcia-Fernández](#) ORCID: [orcid.org/0000-0001-5677-5970^{1,3}](https://orcid.org/0000-0001-5677-5970),
- [Ricard Albalat](#) ORCID: [orcid.org/0000-0003-0282-9595^{1,2}](https://orcid.org/0000-0003-0282-9595) &
- [Cristian Cañestro](#) ORCID: [orcid.org/0000-0003-4623-8105^{1,2}](https://orcid.org/0000-0003-4623-8105)

[Nature](#) volume 599, pages 431–435 (2021)

- 2180 Accesses
- 206 Altmetric
- [Metrics details](#)

Subjects

- [Evolutionary developmental biology](#)
- [Gene expression](#)
- [Non-model organisms](#)

Abstract

A central question in chordate evolution is the origin of sessility in adult ascidians, and whether the appendicularian complete free-living style represents a primitive or derived condition among tunicates¹. According to the ‘a new heart for a new head’ hypothesis, the evolution of the cardiopharyngeal gene regulatory network appears as a pivotal aspect to understand the evolution of the lifestyles of chordates^{2,3,4}. Here we show that appendicularians experienced massive ancestral losses of cardiopharyngeal genes and subfunctions, leading to the ‘deconstruction’ of two ancestral modules of the tunicate cardiopharyngeal gene regulatory network. In ascidians, these modules are related to early and late multipotency, which is involved in lineage cell-fate determination towards the first and second heart fields and siphon muscles. Our work shows that the deconstruction of the cardiopharyngeal gene regulatory network involved the regressive loss of the siphon muscle, supporting an evolutionary scenario in which ancestral tunicates had a sessile ascidian-like adult lifestyle. In agreement with this scenario, our findings also suggest that this deconstruction contributed to the acceleration of cardiogenesis and the redesign of the heart into an open-wide laminar structure in appendicularians as evolutionary adaptations during their transition to a complete pelagic free-living style upon the innovation of the food-filtering house⁵.

Access options

Subscribe to Journal

Get full journal access for 1 year

\$199.00

only \$3.90 per issue

[Subscribe](#)

All prices are NET prices.
VAT will be added later in the checkout.
Tax calculation will be finalised during checkout.

Rent or Buy article

Get time limited or full article access on ReadCube.

from \$8.99

[Rent or Buy](#)

All prices are NET prices.

Additional access options:

- [Log in](#)
- [Access through your institution](#)
- [Learn about institutional subscriptions](#)

Fig. 1: *O. dioica* cardiogenesis.



Fig. 2: Comparison of the cardiopharyngeal cell lineage and GRN in ascidians and appendicularians.

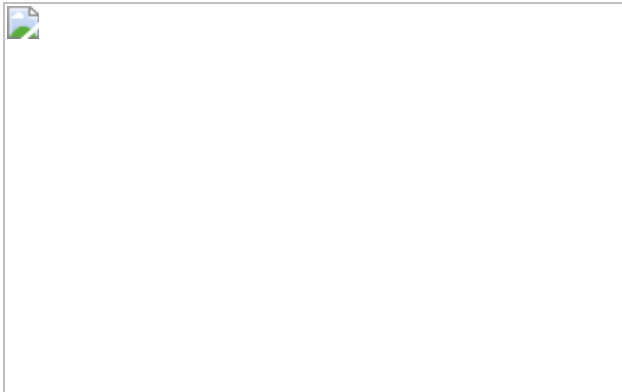
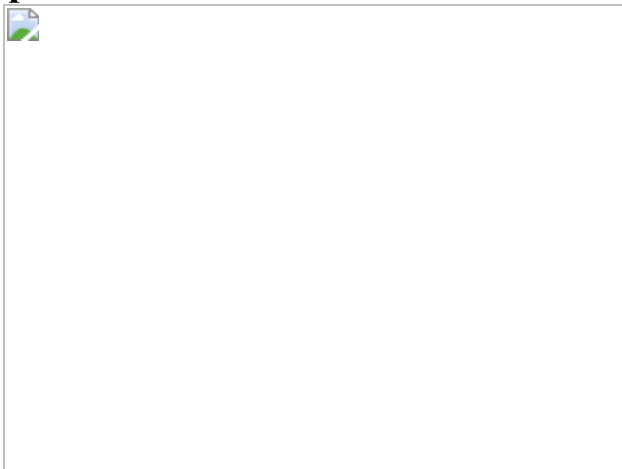


Fig. 3: Evolutionary scenario of the deconstruction of the cardiopharyngeal GRN and acquisition of an adult free-living style in appendicularians.



Data availability

Accession numbers and URLs of databases from publicly available sources are provided in the Methods, Supplementary Information and Supplementary Data [1](#).

References

1. 1.

Satoh, N. in *Chordate Origins and Evolution* (ed. Satoh, N.) 17–30 (Academic, 2016).

2. 2.

Diogo, R. et al. A new heart for a new head in vertebrate cardiopharyngeal evolution. *Nature* **520**, 466–473 (2015).

3. 3.

Razy-Krajka, F. & Stolfi, A. Regulation and evolution of muscle development in tunicates. *Evodevo* **10**, 1–34 (2019).

4. 4.

Stolfi, A. et al. Early chordate origins of the vertebrate second heart field. *Science* **565**, 565–569 (2010).

5. 5.

Mikhaleva, Y., Skinnes, R., Sumic, S., Thompson, E. M. & Chourrout, D. Development of the house secreting epithelium, a major innovation of tunicate larvaceans, involves multiple homeodomain transcription factors. *Dev. Biol.* **443**, 117–126 (2018).

6. 6.

Garstang, W. The morphology of the Tunicata, and its bearings on the phylogeny of the Chordata. *Quar. J. Micr. Sci.* **72**, 51–186 (1928).

7. 7.

Bourlat, S. J. et al. Deuterostome phylogeny reveals monophyletic chordates and the new phylum Xenoturbellida. *Nature* **444**, 85–88 (2006).

8. 8.

Delsuc, F., Brinkmann, H., Chourrout, D. & Philippe, H. Tunicates and not cephalochordates are the closest living relatives of vertebrates. *Nature* **439**, 965–968 (2006).

9. 9.

Swalla, B. J., Cameron, C. B., Corley, L. S. & Garey, J. R. Urochordates are monophyletic within the deuterostomes. *Syst. Biol.* **49**, 52–64 (2000).

10. 10.

Delsuc, F. et al. A phylogenomic framework and timescale for comparative studies of tunicates. *BMC Biol.* **16**, 39 (2018).

11. 11.

Kocot, K. M., Tassia, M. G., Halanych, K. M. & Swalla, B. J. Phylogenomics offers resolution of major tunicate relationships. *Mol. Phylogenet. Evol.* **121**, 166–173 (2018).

12. 12.

Braun, K., Leubner, F. & Stach, T. Phylogenetic analysis of phenotypic characters of Tunicata supports basal Appendicularia and monophyletic Ascidiacea. *Cladistics* **36**, 259–300 (2020).

13. 13.

Stach, T. Ontogeny of the appendicularian *Oikopleura dioica* (Tunicata, Chordata) reveals characters similar to ascidian larvae with sessile adults. *Zoomorphology* **126**, 203–214 (2007).

14. 14.

Nishida, H., Ohno, N., Caicci, F. & Manni, L. 3D reconstruction of structures of hatched larva and young juvenile of the larvacean *Oikopleura dioica* using SBF-SEM. *Sci. Rep.* **11**, 1–14 (2021).

15. 15.

Almazán, A., Ferrández-Roldán, A., Albalat, R. & Cañestro, C. Developmental atlas of appendicularian *Oikopleura dioica* actins provides new insights into the evolution of the notochord and the cardio-paraxial muscle in chordates. *Dev. Biol.* **448**, 260–270 (2019).

16. 16.

Stach, T., Winter, J., Bouquet, J.-M. M., Chourrout, D. & Schnabel, R. Embryology of a planktonic tunicate reveals traces of sessility. *Proc. Natl Acad. Sci. USA* **105**, 7229–7234 (2008).

17. 17.

Davidson, B. *Ciona intestinalis* as a model for cardiac development. *Semin. Cell Dev. Biol.* **18**, 16–26 (2007).

18. 18.

Christiaen, L., Stolfi, A. & Levine, M. BMP signaling coordinates gene expression and cell migration during precardiac mesoderm development. *Dev. Biol.* **340**, 179–187 (2010).

19. 19.

Wang, W. et al. A single-cell transcriptional roadmap for cardiopharyngeal fate diversification. *Nat. Cell Biol.* **21**, 674–686 (2019).

20. 20.

Racioppi, C., Wiechecki, K. A. & Christiaen, L. Combinatorial chromatin dynamics foster accurate cardiopharyngeal fate choices. *eLife* **8**, 1–33 (2019).

21. 21.

Lescroart, F. et al. Early lineage restriction in temporally distinct populations of Mesp1 progenitors during mammalian heart development. *Nat. Cell Biol.* **16**, 829–840 (2014).

22. 22.

Satou, Y., Imai, K. S. & Satoh, N. The ascidian Mesp gene specifies heart precursor cells. *Development* **131**, 2533–2541 (2004).

23. 23.

Davidson, B., Shi, W., Beh, J., Christiaen, L. & Levine, M. FGF signaling delineates the cardiac progenitor field in the simple chordate, *Ciona intestinalis*. *Genes Dev.* **20**, 2728–2738 (2006).

24. 24.

Bernadskaya, Y. Y., Brahmbhatt, S., Gline, S. E., Wang, W. & Christiaen, L. Discoidin-domain receptor coordinates cell-matrix adhesion and collective polarity in migratory cardiopharyngeal progenitors. *Nat. Commun.* **10**, 57 (2019).

25. 25.

Shi, Y., Katsev, S., Cai, C. & Evans, S. BMP signaling is required for heart formation in vertebrates. *Dev. Biol.* **224**, 226–237 (2000).

26. 26.

Davidson, B., Shi, W. & Levine, M. Uncoupling heart cell specification and migration in the simple chordate *Ciona intestinalis*. *Development* **132**, 4811–4818 (2005).

27. 27.

Schachterle, W., Rojas, A., Xu, S.-M. & Black, B. L. ETS-dependent regulation of a distal Gata4 cardiac enhancer. *Dev. Biol.* **361**, 439–449 (2012).

28. 28.

Wang, W., Razy-Krajka, F., Siu, E., Ketcham, A. & Christiaen, L. NK4 antagonizes Tbx1/10 to promote cardiac versus pharyngeal muscle fate in the ascidian second heart field. *PLoS Biol.* **11**, e1001725 (2013).

29. 29.

Delsman, H. C. Contributions on the ontogeny of *Oikopleura dioica*. *Verch. Rijksinst. Onderz. Zee* **3**, 1–24 (1910).

30. 30.

Fujii, S., Nishio, T. & Nishida, H. Cleavage pattern, gastrulation, and neurulation in the appendicularian, *Oikopleura dioica*. *Dev. Genes Evol.* **218**, 69–79 (2008).

31. 31.

Hogan, B. Deconstructing the genesis of animal form. *Development* **131**, 2515–2520 (2004).

32. 32.

Fenaux, R. in *The Biology of Pelagic Tunicates* (ed. Bone, Q.) 25–34 (Oxford Univ. Press, 1998).

33. 33.

Martí-Solans, J. et al. *Oikopleura dioica* culturing made easy: a low-cost facility for an emerging animal model in EvoDevo. *Genesis* **53**, 183–193 (2015).

34. 34.

Brozovic, M. et al. ANISEED 2017: extending the integrated ascidian database to the exploration and evolutionary comparison of genome-scale datasets. *Nucleic Acids Res.* **46**, D718–D725 (2018).

35. 35.

Naville, M. et al. Massive changes of genome size driven by expansions of non-autonomous transposable elements. *Curr. Biol.* **29**, 1161–1168 (2019).

36. 36.

Guindon, S. et al. New algorithms and methods to estimate maximum-likelihood phylogenies: assessing the performance of PhyML 3.0. *Syst. Biol.* **59**, 307–321 (2010).

37. 37.

Larsson, A. AliView: a fast and lightweight alignment viewer and editor for large datasets. *Bioinformatics* **30**, 3276–3278 (2014).

38. 38.

Conklin, E. G. The organization and cell lineage of the ascidian egg. *J. Acad. Nat. Sci. Phila.* **13**, 1–119 (1905).

39. 39.

Martí-Solans, J. et al. Coelimination and survival in gene network evolution: dismantling the RA-signaling in a chordate. *Mol. Biol. Evol.* **33**, 2401–2416 (2016).

40. 40.

Bassham, S. & Postlethwait, J. Brachyury (T) expression in embryos of a larvacean urochordate, *Oikopleura dioica*, and the ancestral role of T. *Dev. Biol.* **220**, 322–332 (2000).

41. 41.

Cañestro, C. & Postlethwait, J. H. Development of a chordate anterior–posterior axis without classical retinoic acid signaling. *Dev. Biol.* **305**, 522–538 (2007).

42. 42.

Schindelin, J. et al. Fiji: an open-source platform for biological-image analysis. *Nat. Methods* **9**, 676–682 (2012).

43. 43.

Torres-Águila, N. P. et al. Diatom bloom-derived biotoxins cause aberrant development and gene expression in the appendicularian chordate *Oikopleura dioica*. *Commun. Biol.* **1**, 121 (2018).

Acknowledgements

We thank all team members of the C.C. and R.A. laboratories for discussions; S. Artíme for assistance with the animal facility; and L. Christiaen and A. Elewa for reading and commenting on the manuscript. C.C. was supported by BFU2016-80601-P and PID2019-110562GB-I00, R.A. by BIO2015-67358-C2-1-P and J.G.-F. by BFU2017-861152-P and PID2020-117820GB-I00 grants from Ministerio de Ciencia y Innovación (Spain). C.C., R.A. and J.G.-F. were also supported by grant 2017-SGR-1665 from Generalitat de Catalunya. A.F.-R. was supported by FPU14/02654, G.S.-S. by FPU18/02414, M.P.-C. by colaboración-2015/16, P.B. by colaboración-2016/17 and M.J.-L. by colaboración-2019/20 fellowships from Ministerio de Educación Cultura y Deporte. M.F.-T. was supported by a PREDOC2020/58 fellowship from the University of Barcelona. M.P.-C. was supported by PPL1415, A.F.-R by PPL1314 and P.B. by PPLB1617 from Asociación Española Contra el Cáncer (AECC).

Author information

Author notes

1. These authors contributed equally: Marc Fabregà-Torrus and Gaspar Sánchez-Serna

Affiliations

1. Departament de Genètica, Microbiologia i Estadística, Facultat de Biologia, Universitat de Barcelona, Barcelona, Spain

Alfonso Ferrández-Roldán, Marc Fabregà-Torrus, Gaspar Sánchez-Serna, Enya Duran-Bello, Martí Joaquín-Lluís, Paula Bujosa, Marcos

Plana-Carmona, Jordi Garcia-Fernàndez, Ricard Albalat & Cristian Cañestro

2. Institut de Recerca de la Biodiversitat (IRBio), Universitat de Barcelona, Barcelona, Spain

Alfonso Ferrández-Roldán, Marc Fabregà-Torras, Gaspar Sánchez-Serna, Enya Duran-Bello, Martí Joaquín-Lluís, Paula Bujosa, Marcos Plana-Carmona, Ricard Albalat & Cristian Cañestro

3. Institut de Biomedicina (IBUB), Universitat de Barcelona, Barcelona, Spain

Jordi Garcia-Fernàndez

Contributions

A.F.-R. carried out the cardiac developmental atlas, genome surveys, phylogenetic analyses, WMISH experiments, cell lineage mapping and BMP inhibitory treatments. M.F.-T. contributed to the *Gata* genome survey and FWMISH. G.S.-S. and P.B. contributed to the *Fgf/Mapk* genome survey and FGF inhibitory treatments. E.D.-B. contributed to the *Tbx* genome survey and WMISH. M.J.-L. contributed to the *Ets* and *Tbx* phylogenies. M.P.-C. contributed to *Islet* characterization. A.F.-R. interpreted the data and made the figures. C.C. conceptualized the project. J.G.-F. and R.A. provided resources. R.A. and C.C. supervised the experiments. C.C. and A.F.-R. wrote the manuscript. All authors commented on the manuscript and agreed to its final version.

Corresponding author

Correspondence to [Cristian Cañestro](#).

Ethics declarations

Competing interests

The authors declare no competing interests.

Additional information

Peer review information *Nature* thanks Benoit Bruneau, Brad Davidson and the other, anonymous, reviewer(s) for their contribution to the peer review of this work. Peer reviewer reports are available.

Publisher's note Springer Nature remains neutral with regard to jurisdictional claims in published maps and institutional affiliations.

Extended data figures and tables

[Extended Data Fig. 1 4D-reconstruction of a virtual cardiac cell tracing, based on nuclear position from the 30-cell stage to tailbud stages of *O. dioica* embryos \(modified from Stach 2008\)](#)[16](#).

B8.9 appears as the first CPC. Blastomere nomenclature follows that of Conklin for ascidians (vegetal blastomeres in capital letters, animal blastomeres in small letters, and blastomeres from the right underlined)³⁸, and their fate are indicated in different colors: muscle+heart (purple), posterior tail muscle cells (yellow), anterior tail muscle cells (ATM, green), heart (red), germ-line (blue). Circles and hexagons represent blastomeres derived from right and left sides of the embryo, respectively. Dashes encircle sister cells resulting from a cell division.

[Extended Data Fig. 2 Mesp ML phylogenetic tree and Math and Neurogenin expression.](#)

a, Unrooted phylogenetic tree, represented in a rectangular layout for the sake of clarity, showing the presence of bHLH homologs of *Neurogenin* and *Math* in appendicularians, but the absence of *Mesp*. The presence of *Mesp* in cephalochordates, vertebrates and all analyzed ascidians suggests an ancestral loss of *Mesp* at the base of the appendicularian lineage after its

split from the lineage leading to ascidians. Bootstrap values are shown in the nodes. Scale bar indicates amino acid substitutions. Vertebrates (black): *Gallus gallus* (Gga), *Homo sapiens* (Hsa), *Latimeria chalumnae* (Lch), *Lepisosteus oculatus* (Loc); Ascidian tunicates (blue): *Botrylloides leachii* (Ble), *Botrylloides schlosseri* (Bsc), *Ciona robusta* (Cro), *Ciona savignyi* (Csa), *Halocynthia aurantium* (Hau), *Halocynthia roretzi* (Hro), *Molgula occidentalis* (Mocci), *Molgula occulta* (Moccu), *Molgula oculata* (Mocul), *Phallusia fumigata* (Pfu), *Phallusia mammillata* (Pma); Appendicularian tunicates (red): *Bathochordaeus* sp. (Bsp), *Fritillaria borealis* (Fbo), *Mesochordaeus erythrocephalus* (Mer), *Oikopleura albicans* (Oal), *Oikopleura dioica* (Odi), *Oikopleura longicauda* (Olo), *Oikopleura vanhoeffeni* (Ova); Cephalochordates (green): *Branchiostoma belcheri* (Bbe), *Branchiostoma floridae* (Bfl), *Branchiostoma lanceolatum* (Bla). **b–f**, Developmental expression pattern of *O. dioica* *Math* homolog. Whole mount *in situ* hybridization in different stages of *O. dioica* development showing expression in the notochord in tailbud and early-hatching embryos (red arrowheads) (**c, d**), in epidermis (blue arrowheads) (**c–f**), in the rectum domain in hatching stages (yellow arrowheads) (**d–f**), in later stages of neural system development (pink arrowheads) (**e, f**), and in later stages of digestive system development (green arrowheads) (**e, f**). **g–k**, Developmental expression pattern of *O. dioica* *Neurogenin* homolog. Whole mount *in situ* hybridization in different stages of *O. dioica* development shows that *Neurogenin* expression was restricted to nervous system in tailbud and early-hatching stages (pink arrowheads) (**h, i**) but no expression was detected in any region compatible with cardiac function. Images from tailbud in advance correspond to left lateral views orientated anterior towards the left and dorsal towards the top.

Extended Data Fig. 3 Ets ML phylogenetic tree and expression.

a, Unrooted phylogenetic tree of the *Ets* and *Erg* protein families showed a high bootstrap value separating both protein families what corroborated the existence of two *Ets1/2* genes in appendicularians. Scale bar indicates amino acid substitutions. Vertebrates (black): *Gallus gallus* (Gga), *Homo sapiens* (Hsa), *Latimeria chalumnae* (Lch), *Lepisosteus oculatus* (Loc); Ascidian tunicates (blue): *Botrylloides leachii* (Ble), *Botrylloides schlosseri* (Bsc), *Ciona robusta* (Cro), *Ciona savignyi* (Csa), *Halocynthia aurantium*

(Hau), *Halocynthia roretzi* (Hro), *Molgula occidentalis* (Mocci), *Molgula occulta* (Moccu), *Molgula oculata* (Mocul), *Phallusia fumigata* (Pfu), *Phallusia mammillata* (Pma); Appendicularian tunicates (red): *Bathochordaeus* sp. (Bsp), *Fritillaria borealis* (Fbo), *Mesochordaeus erythrocephalus* (Mer), *Oikopleura albicans* (Oal), *Oikopleura dioica* (Odi), *Oikopleura longicauda* (Olo), *Oikopleura vanhoeffeni* (Ova); Cephalochordates (green): *Branchiostoma belcheri* (Bbe), *Branchiostoma floridae* (Bfl), *Branchiostoma lanceolatum* (Bla). **b**, Phylogenetic analysis of chordate *Ets1/2*, using cephalochordate sequences as outgroup, suggested that the two *Ets1/2* genes of appendicularians were co-orthologs to the ascidian *Ets1/2a*. **c–h**, Whole mount *in situ* hybridization of *O. dioica* *Ets1/2a1* did not show any clear expression before hatchling stages (**c–f**). In early-hatchling stage *Ets1/2a1* revealed expression in the migratory endodermal strand cells (pink arrowheads) (**g**). In late-hatchling the expression signal was restricted to the buccal gland (green arrowheads) (**h**). **i, j**, *Ets1/2a2* did not show expression until tailbud stage. **k, l**, In tailbud embryos, expression signal was detected in tail muscle cells (orange arrowheads), the notochord (red arrowheads) and the epidermis of the trunk (blue arrowheads). **m**, In early-hatchling expression signal continued in the tail muscle and the notochord and increased in the anal domain (yellow arrowhead). **n**, In late-hatchling stage, the *Ets1/2a2* expression covered the entire oikoplasic epithelium, and continued in the muscle cells of the tail. Large images from tailbud in advance correspond to left lateral views oriented anterior towards the left and dorsal towards the top. Inset images are dorsal views of optical cross sections at the levels of dashed lines.

Extended Data Fig. 4 FGF/MAPK ML phylogenetic tree and expression.

a, ML phylogenetic tree of the *MEK* subfamilies in chordates revealing the loss of the *MEK4*, *MEK5* and *MEK1/2* subfamilies in appendicularians, but the surviving of *MEK3/6* and *MEK7* subfamilies. Scale bar indicates amino acid substitutions. Bootstrap values are shown in the nodes. Vertebrates (black): *Gallus gallus* (Gga), *Homo sapiens* (Hsa), *Latimeria chalumnae* (Lch), *Lepisosteus oculatus* (Loc); Ascidian tunicates (blue): *Botrylloides leachii* (Ble), *Botrylloides schlosseri* (Bsc), *Ciona robusta* (Cro), *Ciona savignyi* (Csa), *Halocynthia aurantium* (Hau), *Halocynthia roretzi* (Hro),

Molgula occidentalis (Mocci), *Molgula occulta* (Moccu), *Molgula oculata* (Mocul), *Phallusia fumigata* (Pfu), *Phallusia mammillata* (Pma); Appendicularian tunicates (red): *Bathochordaeus* sp. (Bsp), *Fritillaria borealis* (Fbo), *Mesochordaeus erythrocephalus* (Mer), *Oikopleura albicans* (Oal), *Oikopleura dioica* (Odi), *Oikopleura longicauda* (Olo), *Oikopleura vanhoeffeni* (Ova); Cephalochordates (green): *Branchiostoma belcheri* (Bbe), *Branchiostoma floridae* (Bfl), *Branchiostoma lanceolatum* (Bla). **b–g**, Whole mount in situ hybridization of *ERK* homolog in different stages of *O. dioica* development did not detect expression in any studied stage (**b–f**) until late-hatching when expression was detected in an specific central domain in the oikoplasic epithelium (blue arrowheads) (**g**). **h–m**, Whole mount in situ hybridization of *MEK7* homolog in *O. dioica* revealed expression in the developing neural tissue in tailbud stages (pink arrowheads) (**i, j**), and in the esophagus (green arrowhead) and the oikoplasic epithelium (blue arrowheads) in the late-hatching stage (**m**). **n–s**, Whole mount in situ hybridization of *MEK3/6* homolog in different stages of *O. dioica* development did not show any obvious tissue specific expression domain in the trunk, but the signal was generalized, with the exception of muscle cells in the tail at late-hatching stages. Images from tailbud in advanced correspond to left lateral views orientated anterior towards the left and dorsal towards the top.

Extended Data Fig. 5 Gata and FoxF ML phylogenetic trees in chordates.

a, *Gata* ML phylogenetic tree reveals the loss of the *Gata4/5/6* in appendicularians, but the surviving and lineage specific duplications of *Gata1/2/3* in appendicularians. **b**, *FoxF* ML phylogenetic tree reveals the presence of an ortholog of *FoxF* in appendicularians. The sister *FoxQ* subfamily was used as outgroup to root the tree. Scale bar indicates amino acid substitutions. Bootstrap values are shown in the nodes. Vertebrates (black): *Gallus gallus* (Gga), *Homo sapiens* (Hsa), *Latimeria chalumnae* (Lch), *Lepisosteus oculatus* (Loc); Ascidian tunicates (blue): *Botrylloides leachii* (Ble), *Botrylloides schlosseri* (Bsc), *Ciona robusta* (Cro), *Ciona savignyi* (Csa), *Halocynthia aurantium* (Hau), *Halocynthia roretzi* (Hro), *Molgula occidentalis* (Mocci), *Molgula occulta* (Moccu), *Molgula oculata* (Mocul), *Phallusia fumigata* (Pfu), *Phallusia mammillata* (Pma);

Appendicularian tunicates (red): *Bathochordaeus* sp. (Bsp), *Fritillaria borealis* (Fbo), *Mesochordaeus erythrocephalus* (Mer), *Oikopleura albicans* (Oal), *Oikopleura dioica* (Odi), *Oikopleura longicauda* (Olo), *Oikopleura vanhoeffeni* (Ova); Cephalochordates (Green): *Branchiostoma belcheri* (Bbe), *Branchiostoma floridae* (Bfl), *Branchiostoma lanceolatum* (Bla).

Extended Data Fig. 6 NK ML phylogenetic tree in chordates reveals the presence of an ortholog of Nk4 in appendicularians and two orthologs of the Nk2 subfamily.

Scale bar indicates amino acid substitutions. Bootstrap values are shown in the nodes. Vertebrates (black): *Gallus gallus* (Gga), *Homo sapiens* (Hsa), *Latimeria chalumnae* (Lch), *Lepisosteus oculatus* (Loc); Ascidian tunicates (blue): *Botrylloides leachii* (Ble), *Botrylloides schlosseri* (Bsc), *Ciona robusta* (Cro), *Ciona savignyi* (Csa), *Halocynthia aurantium* (Hau), *Halocynthia roretzi* (Hro), *Molgula occidentalis* (Mocci), *Molgula occulta* (Moccu), *Molgula oculata* (Mocul), *Phallusia fumigata* (Pfu), *Phallusia mammillata* (Pma); Appendicularian tunicates (red): *Bathochordaeus* sp. (Bsp), *Fritillaria borealis* (Fbo), *Mesochordaeus erythrocephalus* (Mer), *Oikopleura albicans* (Oal), *Oikopleura dioica* (Odi), *Oikopleura longicauda* (Olo), *Oikopleura vanhoeffeni* (Ova); Cephalochordates (Green): *Branchiostoma belcheri* (Bbe), *Branchiostoma floridae* (Bfl), *Branchiostoma lanceolatum* (Bla).

Extended Data Fig. 7 Hand ML phylogenetic tree suggests that member of this family in *O. dioica* is homologous to ascidian *Hand1/2*.

Despite the tree suggests that the second paralog of ascidian (*Hand-r*) arose by a duplication at the base of the tunicate clade, and therefore subsequently lost in appendicularians. The low node support –bootstrap and approximate likelihood-ratio test (aLRT)– and the presence of shared long amino acid domain rich in K between the *Hand1/2* and *Hand-r* in ascidians, but absent in appendicularians, do not allow us to discard the possibility that *Hand-r* was originated by a duplication within the ascidian lineage, and its basal branching in the tunicate clade is due to a long branch attraction

phenomenon. Scale bar indicates amino acid substitutions. Bootstrap values are shown in the nodes. Vertebrates (black): *Gallus gallus* (Gga), *Homo sapiens* (Hsa), *Latimeria chalumnae* (Lch), *Lepisosteus oculatus* (Loc); Ascidian tunicates (blue): *Botrylloides leachii* (Ble), *Botrylloides schlosseri* (Bsc), *Ciona robusta* (Cro), *Ciona savignyi* (Csa), *Halocynthia aurantium* (Hau), *Halocynthia roretzi* (Hro), *Molgula occidentalis* (Mocci), *Molgula occulta* (Moccu), *Molgula oculata* (Mocul), *Phallusia fumigata* (Pfu), *Phallusia mammillata* (Pma); Appendicularian tunicates (red): *Bathochordaeus* sp. (Bsp), *Fritillaria borealis* (Fbo), *Mesochordaeus erythrocephalus* (Mer), *Oikopleura albicans* (Oal), *Oikopleura dioica* (Odi), *Oikopleura longicauda* (Olo), *Oikopleura vanhoeffeni* (Ova); Cephalochordates (green): *Branchiostoma belcheri* (Bbe), *Branchiostoma floridae* (Bfl), *Branchiostoma lanceolatum* (Bla).

Extended Data Fig. 8 Developmental coexpression patterns of *ActnM1* and potential cardiac transcription factors.

Double fluorescent in situ hybridization of *ActnM1* with *Nk4*, *Hand1/2*, *FoxF*, *Gata1/2/3b* and *Gata1/2/3d*. *Nk4* expression signal was detected in ventral epidermis and the CPC (B8.9) from the incipient-tailbud stage (**a**) until the early-tailbud (**a'**). In later stages, we only detected expression in the epidermis, but not in the cardiac precursors (**a''–a'''**). *Hand1/2* was specifically expressed in the cardiac progenitors from late-tailbud to hatchling stages (**b''–b'''**). We did not detect expression of *FoxF*, *Gata1/2/3b* nor *Gata1/2/3d* in cardiac precursors, but they were expressed in different epidermal domains (**c–e'''**). The images correspond to the overlay of a stack of confocal sections with expression of the different genes. The small overlapping color in **e'''** is due to the overlay of the stack, and not to actual co-expression. White arrowheads indicate co-expression of *ActnM1* with the corresponding gene in cardiac progenitors. Incipient- and early-tailbud stages correspond to ventral views oriented anterior towards the top. Late-tailbud and early-hatching stages correspond to lateral views oriented anterior towards the left and dorsal towards the top.

Extended Data Fig. 9 FGF, MEK and BMP inhibition during heart development of *O. dioica*.

a–g', Whole mount in situ hybridization of *ActnM1* in DMSO-control (**a**) and treated embryos with inhibitors of FGFR (SU5402 and AZD4547), MEK3/6 (Gossypetin), MEK7 (5Z-7-Oxozeaenol) and BMP inhibitors (LDN and Dorsomorphin) from 2-cell stage up to early-tailbud stage (**b–g'**). Embryos treated with FGFR and MEK inhibitors affected gastrulation and caused abnormal phenotypes in which mesodermal derivatives showed either abnormal domains (**b'–e'**) or complete absence (**b''–e''**). However, those treated embryos that reached fairly normal incipient morphologies (**b–g**), showed the presence of CPCs (red arrowheads). **h–n'**, Whole mount in situ hybridization of *NK4+ Brachyury* in DMSO-control (**h**) and treated embryos with FGFR, MEK and BMP inhibitors (**i–n'**) from 32-cell stage to early-tailbud stage. A majority of the treated embryos showed the *Nk4* expression in the CPCs (**i–n**), even in some with obvious abnormalities in the notochord (**i**). Only in embryos with severe abnormal morphologies or arrested, we could not distinguish the CPCs from other *Nk4* expression domains (**i'–n'**). **o–t'**, Whole mount in situ hybridization of *ActnM1* in DMSO-control (**o**) and treated embryos with FGFR, MEK and BMP inhibitors from 32-cell stage to early-hatching stage (**p–t'**). Most of the treated embryos showed abnormal tails (**p'–t'**), in which the elongation and rotation had been affected. Moreover, while the CPCs had converged near the midline into a single cardiac field, we observed that in many embryos with tail malformations, the CPCs had not converged and were still bilaterally separated at the right and left sides of the trunk (red numbers in brackets). These results suggests that FGF/MEK/MAPK and BMP signaling pathways may be involved in tail elongation/rotation and late cardiac organogenesis. Tailbud embryos images correspond to dorsal views with anterior to the left. Hatching images represent dorsal views with anterior to the top.

Extended Data Fig. 10 Tbx ML phylogenetic tree and *Islet*, *Ebf*, *MyoD* and *Dach* expression.

a, ML phylogenetic tree of the Tbx subfamilies in chordates reveals the loss of *Tbx1/10* and *Tbx21/Eomes/Tbr1* subfamilies in appendicularians and the ancestral loss of *Tbx4/5* subfamily in tunicates. Scale bar indicates amino acid substitutions. Bootstrap values are shown in the nodes. Vertebrates (black): *Gallus gallus* (Gga), *Homo sapiens* (Hsa), *Latimeria chalumnae*

(Lch), *Lepisosteus oculatus* (Loc); Ascidian tunicates (blue): *Botrylloides leachii* (Ble), *Botrylloides schlosseri* (Bsc), *Ciona robusta* (Cro), *Ciona savignyi* (Csa), *Halocynthia aurantium* (Hau), *Halocynthia roretzi* (Hro), *Molgula occidentalis* (Moocc), *Molgula occulta* (Mooccu), *Molgula oculata* (Moocul), *Phallusia fumigata* (Pfu), *Phallusia mammillata* (Pma); Ascidian appendicularians (red): *Bathochordaeus* sp. (Bsp), *Fritillaria borealis* (Fbo), *Mesochordaeus erythrocephalus* (Mer), *Oikopleura albicans* (Oal), *Oikopleura dioica* (Odi), *Oikopleura longicauda* (Olo), *Oikopleura vanhoeffeni* (Ova); Cephalochordates (green): *Branchiostoma floridae* (Bfl), *Branchiostoma lanceolatum* (Bla). **b–w**, Whole mount in situ hybridization of *O. dioica* *Islet*, *Ebf*, *MyoD* and *Dach* homologs. 64-cell embryos did not showed expression of *Islet* (**b**) which was only detected in the developing nervous system from tailbud to hatchling embryos (**c–f**). *Ebf* (*COE*) did not show expression in early stages (**g, h**) but we detected expression in the nervous system from tailbud to mid-hatchling stage (**i–k**) and in the oikoplasic epithelium of late-hatchling embryos (**l**). We did not detect expression of *MyoD* from 32-cell to hatchling embryos (**m–p**). In late-hatchling embryos *MyoD* was expressed in the oikoplasic epithelium (**q**). *Dach* expression started at the 64-cell stage in the developing nervous system (pink arrowheads) and continued until late-tailbud stage (**r–t**). In tailbud stages, *Dach* started expressing in the trunk epidermis (blue arrowheads) which was maintained until late-hatchling stages when it was expressed in the whole oikoplasic epithelium (blue arrowheads) (**s–v**). In mid-hatchling stage, beside the epidermis, *Dach* expression was also detected in the endostyle (green arrowheads) (**w**). Large images from tailbud in advance correspond to left lateral views oriented anterior towards the left and dorsal towards the top. Inset images are dorsal views of optical cross sections at the levels of dashed lines. Pink arrowheads indicate the developing nervous system. Blue arrowheads indicate the oikoplasic epithelium.

Supplementary information

Supplementary Information

This file contains the Supplementary Discussion and Supplementary References.

Reporting Summary

Supplementary Video 1

Ventral view of a late hatchling at 8.5 hours post fertilization showing the first heart beatings, before the rest of the organs of the trunk are fully developed.

Supplementary Data 1

Accession numbers and species abbreviations.

Supplementary Data 2

FGF/MEK and BMP inhibitory treatment results.

Supplementary Data 3

Cardiac cell-specific marker BLAST identification

Peer Review File

Rights and permissions

Reprints and Permissions

About this article

Cite this article

Ferrández-Roldán, A., Fabregà-Torras, M., Sánchez-Serna, G. *et al.* Cardiopharyngeal deconstruction and ancestral tunicate sessility. *Nature*

599, 431–435 (2021). <https://doi.org/10.1038/s41586-021-04041-w>

- Received: 10 February 2021
- Accepted: 17 September 2021
- Published: 17 November 2021
- Issue Date: 18 November 2021
- DOI: <https://doi.org/10.1038/s41586-021-04041-w>

Share this article

Anyone you share the following link with will be able to read this content:

[Get shareable link](#)

Sorry, a shareable link is not currently available for this article.

[Copy to clipboard](#)

Provided by the Springer Nature SharedIt content-sharing initiative

[Sea squirts teach new lessons in evolution](#)

- Shamini Bundell
- Benjamin Thompson

Nature Podcast 17 Nov 2021

This article was downloaded by **calibre** from <https://www.nature.com/articles/s41586-021-04041-w>

- Article
- [Published: 03 November 2021](#)

MC3R links nutritional state to childhood growth and the timing of puberty

- [B. Y. H. Lam](#) ORCID: [orcid.org/0000-0002-3638-9025^{1,2 na1}](https://orcid.org/0000-0002-3638-9025),
- [A. Williamson](#) ORCID: [orcid.org/0000-0002-7599-9301^{1,2,3 na1}](https://orcid.org/0000-0002-7599-9301),
- [S. Finer](#) ORCID: [orcid.org/0000-0002-2684-4653^{4 na1}](https://orcid.org/0000-0002-2684-4653),
- [F. R. Day](#) ORCID: [orcid.org/0000-0003-3789-7651³](https://orcid.org/0000-0003-3789-7651),
- [J. A. Tadross](#) ORCID: [orcid.org/0000-0002-8424-1252^{1,2,5}](https://orcid.org/0000-0002-8424-1252),
- [A. Gonçalves Soares⁶](#),
- [K. Wade](#) ORCID: [orcid.org/0000-0003-3362-6280⁶](https://orcid.org/0000-0003-3362-6280),
- [P. Sweeney⁷](#),
- [M. N. Bedenbaugh⁸](#),
- [D. T. Porter](#) ORCID: [orcid.org/0000-0002-8042-3251⁷](https://orcid.org/0000-0002-8042-3251),
- [A. Melvin^{1,2}](#),
- [K. L. J. Ellacott⁹](#),
- [R. N. Lippert¹⁰](#),
- [S. Buller^{1,2}](#),
- [J. Rosmaninho-Salgado¹¹](#),
- [G. K. C. Dowsett^{1,2}](#),
- [K. E. Ridley¹²](#),
- [Z. Xu¹²](#),
- [I. Cimino](#) ORCID: [orcid.org/0000-0003-1397-5408^{1,2}](https://orcid.org/0000-0003-1397-5408),
- [D. Rimmington^{1,2}](#),
- [K. Rainbow^{1,2}](#),
- [K. Duckett^{1,2}](#),
- [S. Holmqvist](#) ORCID: [orcid.org/0000-0001-6709-6666¹²](https://orcid.org/0000-0001-6709-6666),

- [A. Khan](#) ORCID: orcid.org/0000-0002-5189-6906⁴,
- [X. Dai](#)¹³,
- [E. G. Bochukova](#)¹³,
- [Genes & Health Research Team](#),
- [R. C. Trembath](#)¹⁴,
- [H. C. Martin](#) ORCID: orcid.org/0000-0002-4454-9084¹⁵,
- [A. P. Coll](#)^{1,2},
- [D. H. Rowitch](#) ORCID: orcid.org/0000-0002-0079-0060¹²,
- [N. J. Wareham](#) ORCID: orcid.org/0000-0003-1422-2993³,
- [D. A. van Heel](#) ORCID: orcid.org/0000-0002-0637-2265^{4,13},
- [N. Timpson](#) ORCID: orcid.org/0000-0002-7141-9189⁶,
- [R. B. Simerly](#) ORCID: orcid.org/0000-0001-5840-0152⁸,
- [K. K. Ong](#) ORCID: orcid.org/0000-0003-4689-7530^{3,12},
- [R. D. Cone](#) ORCID: orcid.org/0000-0003-3333-5651^{7,16},
- [C. Langenberg](#) ORCID: orcid.org/0000-0002-5017-7344^{3,17 na1},
- [J. R. B. Perry](#) ORCID: orcid.org/0000-0001-6483-3771^{3 na1},
- [G. S. Yeo](#) ORCID: orcid.org/0000-0001-8823-3615^{1,2 na1} &
- [S. O'Rahilly](#) ORCID: orcid.org/0000-0003-2199-4449^{1,2 na1}

Nature volume 599, pages 436–441 (2021)

- 8441 Accesses
- 1 Citations
- 469 Altmetric
- [Metrics details](#)

Subjects

- [Endocrinology](#)
- [Quantitative trait](#)
- [Reproductive biology](#)

Abstract

The state of somatic energy stores in metazoans is communicated to the brain, which regulates key aspects of behaviour, growth, nutrient partitioning and development¹. The central melanocortin system acts through melanocortin 4 receptor (MC4R) to control appetite, food intake and energy expenditure². Here we present evidence that MC3R regulates the timing of sexual maturation, the rate of linear growth and the accrual of lean mass, which are all energy-sensitive processes. We found that humans who carry loss-of-function mutations in *MC3R*, including a rare homozygote individual, have a later onset of puberty. Consistent with previous findings in mice, they also had reduced linear growth, lean mass and circulating levels of IGF1. Mice lacking *Mc3r* had delayed sexual maturation and an insensitivity of reproductive cycle length to nutritional perturbation. The expression of *Mc3r* is enriched in hypothalamic neurons that control reproduction and growth, and expression increases during postnatal development in a manner that is consistent with a role in the regulation of sexual maturation. These findings suggest a bifurcating model of nutrient sensing by the central melanocortin pathway with signalling through MC4R controlling the acquisition and retention of calories, whereas signalling through MC3R primarily regulates the disposition of calories into growth, lean mass and the timing of sexual maturation.

Access options

Subscribe to Journal

Get full journal access for 1 year

\$199.00

only \$3.90 per issue

[Subscribe](#)

All prices are NET prices.

VAT will be added later in the checkout.

Tax calculation will be finalised during checkout.

Rent or Buy article

Get time limited or full article access on ReadCube.

from \$8.99

[Rent or Buy](#)

All prices are NET prices.

Additional access options:

- [Log in](#)
- [Access through your institution](#)
- [Learn about institutional subscriptions](#)

Fig. 1: Non-synonymous variants of *MC3R* and association with phenotypes.

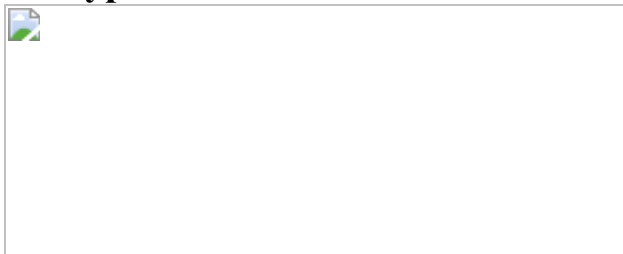


Fig. 2: Characteristics of an individual who is homozygous for the *MC3R* p.G240W mutation.

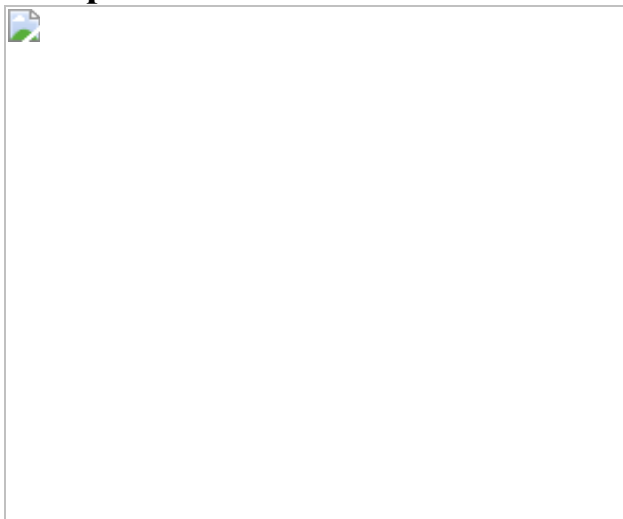


Fig. 3: The role of MC3R in sexual maturation and regulation of the oestrous cycle.

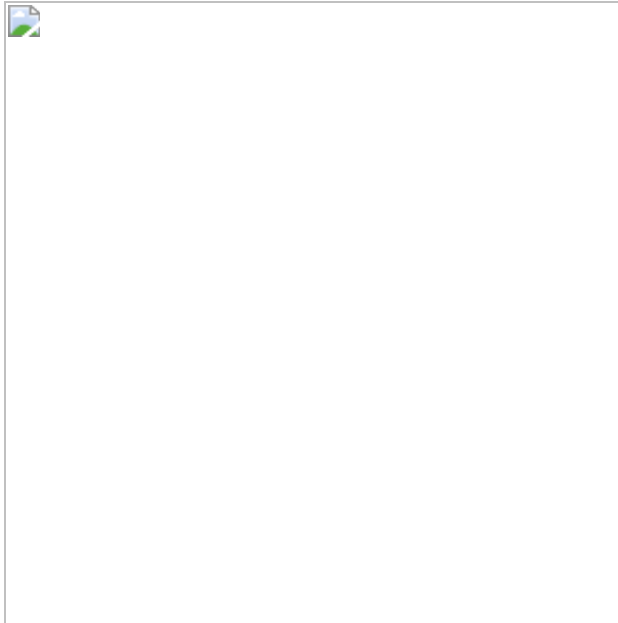
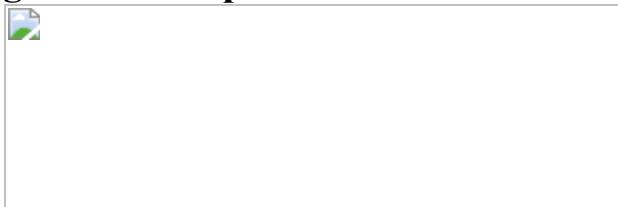


Fig. 4: *Mc3r* expression in the mouse hypothalamus.



Data availability

All data used in the genetic association analyses are available from the UKBB upon application (<https://www.ukbiobank.ac.uk>). Data from the Fenland cohort can be requested by bona fide researchers for specified scientific purposes via the study website (<https://www.mrc-epid.cam.ac.uk/research/studies/fenland/information-for-researchers/>). Data will either be shared through an institutional data sharing agreement or arrangements will be made for analyses to be conducted remotely without the necessity for data transfer. The EPIC-Norfolk data can be requested by bona fide researchers for specified scientific purposes via the study website (<https://www.mrc-epid.cam.ac.uk/research/studies/epic-norfolk/>). Data will either be shared through an institutional data sharing agreement or arrangements will be made for analyses to be conducted remotely without the need for data transfer. ALSPAC data are available through a system of

managed open access. Full details of the cohort and study design have been previously described and are available at <http://www.alspac.bris.ac.uk>. Please note that the study website contains details of all the data that are available through a fully searchable data dictionary and variable search tool (<http://www.bristol.ac.uk/alspac/researchers/our-data/>). Data for this project were accessed under the project number B2891. The application steps for ALSPAC data access are as follows: (1) please read the ALSPAC access policy, which describes the process of accessing the data in detail and outlines the costs associated with doing so. (2) You may also find it useful to browse the fully searchable research proposals database, which lists all research projects that have been approved since April 2011. (3) Please submit your research proposal for consideration by the ALSPAC Executive Committee. You will receive a response within 10 working days to advise you whether your proposal has been approved. If you have any questions about accessing data, please email alspac-data@bristol.ac.uk. For Genes & Health, data are available via <http://www.genesandhealth.org/>. Publicly available GWAS datasets utilized in the genome-wide association study analyses are available from the Neale laboratory (<http://www.nealelab.is/uk-biobank>), Open Targets Genetics (<https://genetics.opentargets.org/>), Global Biobank Engine (<https://biobankengine.stanford.edu/>), Open GWAS IEU (<https://gwas.mrcieu.ac.uk/>) and Phenoscanner (<http://www.phenoscanner.medschl.cam.ac.uk/>). Mouse single-cell RNA sequencing data are available from Gene Expression Omnibus (GEO) accessions [GSE93374](#), [GSE87544](#), [GSE92707](#) and [GSE74672](#).

Code availability

Programming scripts were written to assist in the execution of publicly available functions and computer programs in our compute environment. For access to these scripts, readers may contact the corresponding author.

References

1. 1.

Friedman, J. M. The function of leptin in nutrition, weight, and physiology. *Nutr. Rev.* **60**, S1–S14; discussion S68–S84, S85–S87 (2002).

2. 2.

Cone, R. D. Anatomy and regulation of the central melanocortin system. *Nat. Neurosci.* **8**, 571–578 (2005).

3. 3.

Cowley, M. A. et al. Leptin activates anorexigenic POMC neurons through a neural network in the arcuate nucleus. *Nature* **411**, 480–484 (2001).

4. 4.

Hill, J. W. et al. Direct insulin and leptin action on pro-opiomelanocortin neurons is required for normal glucose homeostasis and fertility. *Cell Metab.* **11**, 286–297 (2010).

5. 5.

Varela, L. & Horvath, T. L. Leptin and insulin pathways in POMC and AgRP neurons that modulate energy balance and glucose homeostasis. *EMBO Rep.* **13**, 1079–1086 (2012).

6. 6.

Chen, A. S. et al. Role of the melanocortin-4 receptor in metabolic rate and food intake in mice. *Transgenic Res.* **9**, 145–154 (2000).

7. 7.

Fan, W., Boston, B. A., Kesterson, R. A., Hruby, V. J. & Cone, R. D. Role of melanocortinergic neurons in feeding and the agouti obesity syndrome. *Nature* **385**, 165–168 (1997).

8. 8.

Vaisse, C., Clement, K., Guy-Grand, B. & Froguel, P. A frameshift mutation in human MC4R is associated with a dominant form of obesity. *Nat. Genet.* **20**, 113–114 (1998).

9. 9.

Yeo, G. S. et al. A frameshift mutation in MC4R associated with dominantly inherited human obesity. *Nat. Genet.* **20**, 111–112 (1998).

10. 10.

Huszar, D. et al. Targeted disruption of the melanocortin-4 receptor results in obesity in mice. *Cell* **88**, 131–141 (1997).

11. 11.

Farooqi, I. S. et al. Clinical spectrum of obesity and mutations in the melanocortin 4 receptor gene. *N. Engl. J. Med.* **348**, 1085–1095 (2003).

12. 12.

Krakoff, J. et al. Lower metabolic rate in individuals heterozygous for either a frameshift or a functional missense MC4R variant. *Diabetes* **57**, 3267–3272 (2008).

13. 13.

Brown, P. I. & Brasel, J. in *The Malnourished Child Nestlé Nutrition Workshop Series* (eds Lewinter-Suskind, L. & Suskind, R. M.) 213–228 (Nestlé Nutrition Institute and Vevey/Raven Press, 1990).

14. 14.

Clement, K. et al. A mutation in the human leptin receptor gene causes obesity and pituitary dysfunction. *Nature* **392**, 398–401 (1998).

15. 15.

Strobel, A., Issad, T., Camoin, L., Ozata, M. & Strosberg, A. D. A leptin missense mutation associated with hypogonadism and morbid obesity. *Nat. Genet.* **18**, 213–215 (1998).

16. 16.

Roselli-Rehfuss, L. et al. Identification of a receptor for gamma melanotropin and other proopiomelanocortin peptides in the hypothalamus and limbic system. *Proc. Natl Acad. Sci. USA* **90**, 8856–8860 (1993).

17. 17.

Gantz, I. et al. Molecular cloning of a novel melanocortin receptor. *J. Biol. Chem.* **268**, 8246–8250 (1993).

18. 18.

Butler, A. A. et al. A unique metabolic syndrome causes obesity in the melanocortin-3 receptor-deficient mouse. *Endocrinology* **141**, 3518–3521 (2000).

19. 19.

Chen, A. S. et al. Inactivation of the mouse melanocortin-3 receptor results in increased fat mass and reduced lean body mass. *Nat. Genet.* **26**, 97–102 (2000).

20. 20.

Renquist, B. J. et al. Melanocortin-3 receptor regulates the normal fasting response. *Proc. Natl Acad. Sci. USA* **109**, E1489–E1498 (2012).

21. 21.

Wood, A. R. et al. Defining the role of common variation in the genomic and biological architecture of adult human height. *Nat. Genet.* **46**, 1173–1186 (2014).

22. 22.

Day, F. R. et al. Genomic analyses identify hundreds of variants associated with age at menarche and support a role for puberty timing in cancer risk. *Nat. Genet.* **49**, 834–841 (2017).

23. 23.

Demidowich, A. P., Jun, J. Y. & Yanovski, J. A. Polymorphisms and mutations in the melanocortin-3 receptor and their relation to human obesity. *Biochim. Biophys. Acta Mol. Basis Dis.* **1863**, 2468–2476 (2017).

24. 24.

Marouli, E. et al. Rare and low-frequency coding variants alter human adult height. *Nature* **542**, 186–190 (2017).

25. 25.

Mencarelli, M. et al. Rare melanocortin-3 receptor mutations with in vitro functional consequences are associated with human obesity. *Hum. Mol. Genet.* **20**, 392–399 (2011).

26. 26.

Zegers, D. et al. Identification of three novel genetic variants in the melanocortin-3 receptor of obese children. *Obesity (Silver Spring)* **19**, 152–159 (2011).

27. 27.

Lee, Y. S., Poh, L. K. & Loke, K. Y. A novel melanocortin 3 receptor gene (MC3R) mutation associated with severe obesity. *J. Clin. Endocrinol. Metab.* **87**, 1423–1426 (2002).

28. 28.

Studenski, S. A. et al. The FNIH Sarcopenia Project: rationale, study description, conference recommendations, and final estimates. *J. Gerontol. A Biol. Sci. Med. Sci.* **69**, 547–558 (2014).

29. 29.

Kim, T. N. et al. Comparisons of three different methods for defining sarcopenia: an aspect of cardiometabolic risk. *Sci. Rep.* **7**, 6491 (2017).

30. 30.

Boyd, A. et al. Cohort profile: the ‘children of the 90s’-the index offspring of the Avon Longitudinal Study of Parents and Children. *Int. J. Epidemiol.* **42**, 111–127 (2013).

31. 31.

Wade, K. H. et al. Loss-of-function mutations in the melanocortin 4 receptor in a UK birth cohort. *Nat. Med.* **27**, 1088–1096 (2021).

32. 32.

Lotta, L. A. et al. A cross-platform approach identifies genetic regulators of human metabolism and health. *Nat. Genet.* **53**, 54–64 (2021).

33. 33.

Khaw, K. T. et al. Combined impact of health behaviours and mortality in men and women: the EPIC-Norfolk prospective population study. *PLoS Med.* **5**, e12 (2008).

34. 34.

Pietzner, M. et al. Plasma metabolites to profile pathways in noncommunicable disease multimorbidity. *Nat. Med.* **27**, 471–479 (2021).

35. 35.

Tapanainen, J. et al. Short and long term effects of growth hormone on circulating levels of insulin-like growth factor-I (IGF-I), IGF-binding protein-1, and insulin: a placebo-controlled study. *J. Clin. Endocrinol. Metab.* **73**, 71–74 (1991).

36. 36.

Finer, S. et al. Cohort profile: East London Genes & Health (ELGH), a community-based population genomics and health study in British Bangladeshi and British Pakistani people. *Int. J. Epidemiol.* **49**, 20–21i (2020).

37. 37.

de Onis, M. et al. Development of a WHO growth reference for school-aged children and adolescents. *Bull. World Health Organ.* **85**, 660–667 (2007).

38. 38.

Campbell, J. N. et al. A molecular census of arcuate hypothalamus and median eminence cell types. *Nat. Neurosci.* **20**, 484–496 (2017).

39. 39.

Sweeney, P. et al. The melanocortin-3 receptor is a pharmacological target for the regulation of anorexia. *Sci. Transl. Med.* **13**, eabd6434 (2021).

40. 40.

Lam, B. Y. H. et al. Heterogeneity of hypothalamic pro-opiomelanocortin-expressing neurons revealed by single-cell RNA sequencing. *Mol. Metab.* **6**, 383–392 (2017).

41. 41.

Romanov, R. A. et al. Molecular interrogation of hypothalamic organization reveals distinct dopamine neuronal subtypes. *Nat.*

Neurosci. **20**, 176–188 (2017).

42. 42.

Chen, R., Wu, X., Jiang, L. & Zhang, Y. Single-cell RNA-seq reveals hypothalamic cell diversity. *Cell Rep.* **18**, 3227–3241 (2017).

43. 43.

Backholer, K. et al. Kisspeptin cells in the ewe brain respond to leptin and communicate with neuropeptide Y and proopiomelanocortin cells. *Endocrinology* **151**, 2233–2243 (2010).

44. 44.

Cocchi, D., De Gennaro Colonna, V., Bagnasco, M., Bonacci, D. & Muller, E. E. Leptin regulates GH secretion in the rat by acting on GHRH and somatostatinergic functions. *J. Endocrinol.* **162**, 95–99 (1999).

45. 45.

Tannenbaum, G. S., Gurd, W. & Lapointe, M. Leptin is a potent stimulator of spontaneous pulsatile growth hormone (GH) secretion and the GH response to GH-releasing hormone. *Endocrinology* **139**, 3871–3875 (1998).

46. 46.

Wang, L. & Moenter, S. M. Differential roles of hypothalamic AVPV and arcuate kisspeptin neurons in estradiol feedback regulation of female reproduction. *Neuroendocrinology* **110**, 172–184 (2020).

47. 47.

Dunger, D. B., Ahmed, M. L. & Ong, K. K. Effects of obesity on growth and puberty. *Best Pract. Res. Clin. Endocrinol. Metab.* **19**, 375–390 (2005).

48. 48.

Hauspie, R. C., Vercauteren, M. & Susanne, C. Secular changes in growth and maturation: an update. *Acta Paediatr. Suppl.* **423**, 20–27 (1997).

49. 49.

Kuhnen, P. et al. Proopiomelanocortin deficiency treated with a melanocortin-4 receptor agonist. *N. Engl. J. Med.* **375**, 240–246 (2016).

50. 50.

Roa, J. & Herbison, A. E. Direct regulation of GnRH neuron excitability by arcuate nucleus POMC and NPY neuron neuropeptides in female mice. *Endocrinology* **153**, 5587–5599 (2012).

51. 51.

Manfredi-Lozano, M. et al. Defining a novel leptin–melanocortin–kisspeptin pathway involved in the metabolic control of puberty. *Mol. Metab.* **5**, 844–857 (2016).

52. 52.

Salomon, F., Cuneo, R. C., Hesp, R. & Sonksen, P. H. The effects of treatment with recombinant human growth hormone on body composition and metabolism in adults with growth hormone deficiency. *N. Engl. J. Med.* **321**, 1797–1803 (1989).

53. 53.

Doherty, T. J. Invited review: aging and sarcopenia. *J. Appl. Physiol.* **95**, 1717–1727 (2003).

54. 54.

McCance, R. A. & Widdowson, E. M. The determinants of growth and form. *Proc. R. Soc. Lond. B Biol. Sci.* **185**, 1–17 (1974).

55. 55.

Sudlow, C. et al. UK Biobank: an open access resource for identifying the causes of a wide range of complex diseases of middle and old age. *PLoS Med.* **12**, e1001779 (2015).

56. 56.

Eastwood, S. V. et al. Algorithms for the capture and adjudication of prevalent and incident diabetes in UK Biobank. *PLoS ONE* **11**, e0162388 (2016).

57. 57.

Powell, R. M. et al. Development and validation of total and regional body composition prediction equations from anthropometry and single frequency segmental bioelectrical impedance with DEXA. Preprint at *medRxiv* <https://doi.org/10.1101/2020.12.16.20248330> (2020).

58. 58.

Zhao, Y. et al. GIGYF1 loss of function is associated with clonal mosaicism and adverse metabolic health. *Nat. Commun.* **12**, 4178 (2021).

59. 59.

McLaren, W. et al. The Ensembl variant effect predictor. *Genome Biol.* **17**, 122 (2016).

60. 60.

Rentzsch, P., Witten, D., Cooper, G. M., Shendure, J. & Kircher, M. CADD: predicting the deleteriousness of variants throughout the human genome. *Nucleic Acids Res.* **47**, D886–D894 (2019).

61. 61.

Loh, P. R. et al. Efficient Bayesian mixed-model analysis increases association power in large cohorts. *Nat. Genet.* **47**, 284–290 (2015).

62. 62.

Chang, C. C. et al. Second-generation PLINK: rising to the challenge of larger and richer datasets. *Gigascience* **4**, 7 (2015).

63. 63.

Van Hout, C. V. et al. Exome sequencing and characterization of 49,960 individuals in the UK Biobank. *Nature* **586**, 749–756 (2020).

64. 64.

Bycroft, C. et al. The UK Biobank resource with deep phenotyping and genomic data. *Nature* **562**, 203–209 (2018).

65. 65.

Millard, L. A. C., Davies, N. M., Gaunt, T. R., Davey Smith, G. & Tilling, K. Software application profile: PHESANT: a tool for performing automated phenotype scans in UK Biobank. *Int. J. Epidemiol.* **47**, 29–35 (2018).

66. 66.

Ghoussaini, M. et al. Open Targets Genetics: systematic identification of trait-associated genes using large-scale genetics and functional genomics. *Nucleic Acids Res.* **49**, D1311–D1320 (2021).

67. 67.

Elsworth, B. et al. The MRC IEU OpenGWAS data infrastructure. Preprint at *bioRxiv* <https://doi.org/10.1101/2020.08.10.244293> (2020).

68. 68.

McInnes, G. et al. Global Biobank Engine: enabling genotype–phenotype browsing for biobank summary statistics. *Bioinformatics* **35**, 2495–2497 (2019).

69. 69.

Kamat, M. A. et al. PhenoScanner V2: an expanded tool for searching human genotype–phenotype associations. *Bioinformatics* **35**, 4851–4853 (2019).

70. 70.

Howe, L. D. et al. Changes in ponderal index and body mass index across childhood and their associations with fat mass and cardiovascular risk factors at age 15. *PLoS ONE* **5**, e15186 (2010).

71. 71.

Frysz, M., Howe, L. D., Tobias, J. H. & Paternoster, L. Using SITAR (superimposition by translation and rotation) to estimate age at peak height velocity in Avon Longitudinal Study of Parents and Children. *Wellcome Open Res.* **3**, 90 (2018).

72. 72.

Li, H. Aligning sequence reads, clone sequences and assembly contigs with BWA-MEM. Preprint at *arXiv* <https://export.arxiv.org/abs/1303.3997> (2013).

73. 73.

Koboldt, D. C. et al. VarScan 2: somatic mutation and copy number alteration discovery in cancer by exome sequencing. *Genome Res.* **22**, 568–576 (2012).

74. 74.

Wade, K. H. et al. Loss-of-function mutations in the melanocortin 4 receptor in a UK birth cohort. *Nat. Med.* **27**, 1088–1096 (2021).

75. 75.

Lindsay, T. et al. Descriptive epidemiology of physical activity energy expenditure in UK adults (the Fenland study). *Int. J. Behav. Nutr. Phys. Act.* **16**, 126 (2019).

76. 76.

Williams, S. A. et al. Plasma protein patterns as comprehensive indicators of health. *Nat. Med.* **25**, 1851–1857 (2019).

77. 77.

Pietzner, M. et al. Genetic architecture of host proteins involved in SARS-CoV-2 infection. *Nat. Commun.* **11**, 6397 (2020).

78. 78.

Willer, C. J., Li, Y. & Abecasis, G. R. METAL: fast and efficient meta-analysis of genomewide association scans. *Bioinformatics* **26**, 2190–2191 (2010).

79. 79.

Day, N. et al. EPIC-Norfolk: study design and characteristics of the cohort. European Prospective Investigation of Cancer. *Br. J. Cancer* **80**, 95–103 (1999).

80. 80.

Narasimhan, V. M. et al. Health and population effects of rare gene knockouts in adult humans with related parents. *Science* **352**, 474–477 (2016).

81. 81.

Bayraktar, O. A. et al. Astrocyte layers in the mammalian cerebral cortex revealed by a single-cell *in situ* transcriptomic map. *Nat. Neurosci.* **23**, 500–509 (2020).

82. 82.

Bankhead, P. et al. QuPath: open source software for digital pathology image analysis. *Sci. Rep.* **7**, 16878 (2017).

83. 83.

Schmidt, U., Weigert, M., Broaddus, C. & Myers, G. Cell Detection with Star-Convex Polygons in *MICCAI 2018* 265–273 (Springer Nature Switzerland, 2018)

84. 84.

Widmann, J. et al. RNASTAR: an RNA structural alignment repository that provides insight into the evolution of natural and artificial RNAs. *RNA* **18**, 1319–1327 (2012).

85. 85.

Stuart, T. et al. Comprehensive integration of single-cell data. *Cell* **177**, 1888–1902.e21 (2019).

Acknowledgements

MC3R genetic analysis, next-generation sequencing and functional analysis were supported by the UK Medical Research Council (MRC) Metabolic Diseases Unit (MC_UU_00014/1), Wellcome (WT 095515/Z/11/Z) and the National Institute for Health Research (NIHR) Cambridge Biomedical Research Centre. K.R., K.D., D.R., I.C., A.P.C. and G.S.Y. are supported by the MRC Metabolic Disease Unit (MC_UU_00014/1). S.O. is supported by a Wellcome Investigator award (WT 095515/Z/11/Z) and the NIHR Cambridge Biomedical Research Centre. B.Y.H.L. is supported by a Biotechnology and Biological Sciences Research Council (BBSRC) Project Grant (BB/S017593/1). A.W. and S.B. hold PhD studentships supported by Wellcome. J.A.T. is supported by an NIHR Clinical Lectureship (CL-2019-14-504). A.M. holds a PhD studentship supported jointly by the University of Cambridge Experimental Medicine Training Initiative programme in

partnership with AstraZeneca (EMI-AZ). G.K.C.D. is supported by the BBSRC Doctoral Training Programme. Next-generation sequencing was performed via Wellcome–MRC IMS Genomics and transcriptomics core facility supported by the MRC (MC_UU_00014/5) and the Wellcome (208363/Z/17/Z) and the Cancer Research UK Cambridge Institute Genomics Core. The histology core is supported by the MRC (MC_UU_00014/5). We thank P. Barker and K. Burling of the Cambridge NIHR Biomedical Research Centre Clinical Biochemistry Assay Laboratory for their assistance with biochemical assays. The EPIC-Norfolk study (<https://doi.org/10.22025/2019.10.105.00004>) has received funding from the MRC (MR/N003284/1 and MC-UU_12015/1) and Cancer Research UK (C864/A14136). The genetics work in the EPIC-Norfolk study was funded by the MRC (MC_PC_13048). Metabolite measurements in the EPIC-Norfolk study were supported by the MRC Cambridge Initiative in Metabolic Science (MR/L00002/1) and the Innovative Medicines Initiative Joint Undertaking under EMIF grant agreement no. 115372. We are grateful to all of the participants who have been part of the project and to the many members of the study teams at the University of Cambridge who have enabled this research. The Fenland study (<https://doi.org/10.22025/2017.10.101.00001>) is funded by the MRC (MC_UU_12015/1). We are grateful to all of the volunteers and to the general practitioners and practice staff for assistance with recruitment. We thank the Fenland study investigators, Fenland study co-ordination team and the Epidemiology Field, Data and Laboratory teams. We further acknowledge support for genomics and metabolomics from the MRC (MC_PC_13046). Proteomic measurements were supported and governed by a collaboration agreement between the University of Cambridge and Somalogic. F.R.D., N.J.W., K.K.O., C.L. and J.R.B.P. are funded by the MRC (MC_UU_12015/1, MC_UU_12015/2, MC_UU_00006/1 and MC_UU_00006/2). N.J.W. is an NIHR Senior Investigator. We are grateful for funding to the BIA prediction equations, supported by the NIHR Biomedical Research Centre Cambridge (IS-BRC-1215-20014). The NIHR Cambridge Biomedical Research Centre is a partnership between Cambridge University Hospitals NHS Foundation Trust and the University of Cambridge, funded by the NIHR. The views expressed are those of the authors and not necessarily those of the NHS, the NIHR or the Department of Health and Social Care. We thank A. Mesut Erzurumluoglu, L.

Wittemans, E. Wheeler, I. Stewart, M. Pietzner, M. Koprulu, E. De Lucia Rolfe, R. Powell and N. Kerrison for providing help with and access to GWAS meta-analysis summary statistics for body composition measures and biomarkers in the UKBB, metabolomics measures in the EPIC-Norfolk study, proteomics measures in the MRC Fenland study, as well as help with genotype quality control in the Fenland study and the UKBB. The MRC, Wellcome (217065/Z/19/Z) and the University of Bristol provide core support for ALSPAC. Genome-wide association data were generated by sample logistics and genotyping facilities at Wellcome Sanger Institute and LabCorp (Laboratory Corporation of America) using support from 23andMe. A.G.S. was supported by the study of 'Dynamic longitudinal exposome trajectories in cardiovascular and metabolic non-communicable diseases' (H2020-SC1-2019-Single-Stage-RTD, project ID 874739). K.W. was supported by the Elizabeth Blackwell Institute for Health Research, University of Bristol and the Wellcome Institutional Strategic Support Fund (204813/Z/16/Z). N.T. is a Wellcome Trust Investigator (202802/Z/16/Z), is the principal investigator of the ALSPAC (MRC & WT 217065/Z/19/Z), is supported by the University of Bristol NIHR Biomedical Research Centre (BRC-1215-2001), the MRC Integrative Epidemiology Unit (MC_UU_00011) and works within the Cancer Research UK Integrative Cancer Epidemiology Programme (C18281/A19169). We are extremely grateful to all of the families who took part in the ALSPAC study, the midwives for their help in recruiting them, and the whole ALSPAC team, which includes interviewers, computer and laboratory technicians, clerical workers, research scientists, volunteers, managers, receptionists and nurses. The Rowitch laboratory receives funding from Wellcome and the ERC Advanced Grant (REP-789054-1). Genes & Health is/has recently been core funded by Wellcome (WT102627 and WT210561), the MRC (M009017), Higher Education Funding Council for England Catalyst, Barts Charity (845/1796), Health Data Research UK (for London substantive site), and research delivery support from the NHS NIHR Clinical Research Network (North Thames). Additional funding for recall was provided by a pump priming award to S.F. (SCA/PP/12/19) from the Diabetes Research and Wellness Foundation. E.G.B. and X.D. are supported by the Wellcome (208987/Z/17/Z) and Barts Charity (project grant to E.G.B.). We thank Social Action for Health, Centre of The Cell, members of our Community Advisory Group, and staff who have recruited and collected

data from volunteers; the NIHR National Biosample Centre (UK Biocentre), the Social Genetic and Developmental Psychiatry Centre (King's College London), Wellcome Sanger Institute, and Broad Institute for sample processing, genotyping, sequencing and variant annotation; Barts Health NHS Trust, NHS Clinical Commissioning Groups (Hackney, Waltham Forest, Tower Hamlets and Newham), East London NHS Foundation Trust, Bradford Teaching Hospitals NHS Foundation Trust, and Public Health England (especially D. Wyllie) for GDPR-compliant data sharing; and most of all, we thank all of the volunteers participating in Genes & Health. R.D.C. receives funding from US National Institutes of Health (NIH) grants DK070332 and DK126715. P.S. is funded by NIH F32HD095620 and K99DK127065. R.B.S. receives funding from the NIH (DK106476). M.N.B. is funded by the NIH (F32DK123879). This research has been conducted using data from UK Biobank, a major biomedical database (<https://www.ukbiobank.ac.uk>), application numbers 32974 and 44448.

Author information

Author notes

1. These authors contributed equally: B. Y. H. Lam, A. Williamson, S. Finer, C. Langenberg, J. R. B. Perry, G. S. Yeo and S. O'Rahilly
2. A full list of members and their affiliations appears in the Supplementary Information

Affiliations

1. MRC Metabolic Diseases Unit, Wellcome–MRC Institute of Metabolic Science, University of Cambridge, Cambridge, UK
B. Y. H. Lam, A. Williamson, J. A. Tadross, A. Melvin, S. Buller, G. K. C. Dowsett, I. Cimino, D. Rimmington, K. Rainbow, K. Duckett, A. P. Coll, G. S. Yeo & S. O'Rahilly
2. NIHR Cambridge Biomedical Research Centre, Cambridge, UK

B. Y. H. Lam, A. Williamson, J. A. Tadross, A. Melvin, S. Buller, G. K. C. Dowsett, I. Cimino, D. Rimmington, K. Rainbow, K. Duckett, A. P. Coll, G. S. Yeo & S. O'Rahilly

3. MRC Epidemiology Unit, Wellcome–MRC Institute of Metabolic Science, University of Cambridge, Cambridge, UK

A. Williamson, F. R. Day, N. J. Wareham, K. K. Ong, C. Langenberg & J. R. B. Perry

4. Wolfson Institute of Population Health, Barts and the London School of Medicine and Dentistry, Queen Mary University of London, London, UK

S. Finer, A. Khan & D. A. van Heel

5. Department of Pathology, University of Cambridge, Cambridge, UK

J. A. Tadross

6. MRC Integrative Epidemiology Unit and Population Health Sciences, Bristol Medical School, University of Bristol, Bristol, UK

A. Gonçalves Soares, K. Wade & N. Timpson

7. Life Sciences Institute, University of Michigan, Ann Arbor, MI, USA

P. Sweeney, D. T. Porter & R. D. Cone

8. Department of Molecular Physiology and Biophysics, School of Medicine, Vanderbilt University, Nashville, TN, USA

M. N. Bedenbaugh & R. B. Simerly

9. Institute of Biomedical and Clinical Sciences, University of Exeter Medical School, Exeter, UK

K. L. J. Ellacott

10. Department of Neurocircuit Development and Function, German Institute of Human Nutrition, Potsdam, Germany

R. N. Lippert

11. Medical Genetics Unit, Hospital Pediátrico, Centro Hospitalar e Universitário de Coimbra, Coimbra, Portugal

J. Rosmaninho-Salgado

12. Department of Paediatrics, University of Cambridge, Cambridge, UK

K. E. Ridley, Z. Xu, S. Holmqvist, D. H. Rowitch & K. K. Ong

13. Blizard Institute, Barts and The London School of Medicine and Dentistry, Queen Mary University London, London, UK

X. Dai, E. G. Bochukova & D. A. van Heel

14. School of Basic and Medical Biosciences, Faculty of Life Sciences and Medicine, King's College London, London, UK

R. C. Trembath

15. Wellcome Sanger Institute, Hinxton, Cambridge, UK

H. C. Martin

16. Department of Molecular and Integrative Physiology, School of Medicine, University of Michigan, Ann Arbor, MI, USA

R. D. Cone

17. Computational Medicine, Berlin Institute of Health at Charité–Universitätsmedizin Berlin, Berlin, Germany

C. Langenberg

Consortia

Genes & Health Research Team

Contributions

B.Y.H.L., A.W., S.F., A.M., K.W., N.T., K.K.O., C.L., J.R.B.P., G.S.Y. and S.O. designed the study. B.Y.H.L., A.W., K.D., A.M., S.B. and J.R.-S. planned and performed the in vitro experiments. B.Y.H.L. and A.W. conducted the bioinformatic and genetic analyses on the UKBB and Genes & Health data. A.W., F.R.D., N.J.W., K.K.O., J.R.B.P. and C.L. conducted the genotype–phenotype association on the UKBB, Fenland and EPIC data. K.R. and K.D. conducted the next-generation sequencing for ALSPAC and Sanger sequencing for ALSPAC and Genes & Health. B.Y.H.L. and A.M. conducted genetics and bioinformatic analyses of ALSPAC. A.G.S., K.W. and N.T. lead the analysis of phenotypic association in ALSPAC. P.S., D.T.P., K.L.J.E., R.N.L. and R.D.C. performed the study on *Mc3r*-null mice. B.Y.H.L. performed the single-cell data analysis. I.C., D.R. and A.P.C. lead the mouse studies in Cambridge. J.A.T., G.K.C.D., K.E.R., S.H., Z.X., D.H.R., M.N.B. and R.B.S. conducted the histology, single-molecule fluorescent in situ hybridization and imaging analyses. S.F., A.K., R.C.T., H.C.M., D.A.v.H. and the Genes & Health team managed the cohort. D.A.v.H., H.C.M., E.G.B. and X.D. led the genetic analysis. S.F. coordinated and conducted the clinical recall. B.Y.H.L., A.W., S.F., F.R.D., A.G.S., K.W., N.T., K.K.O., C.L., J.R.B.P., G.S.Y. and S.O. wrote the manuscript and it was reviewed by all authors. This publication is the work of the authors, and C.L., J.R.B.P., G.S.Y. and S.O. will serve as guarantors for the contents of this paper.

Corresponding author

Correspondence to [S. O'Rahilly](#).

Ethics declarations

Competing interests

S.O. has undertaken remunerated consultancy work for Pfizer, AstraZeneca, GSK and ERX Pharmaceuticals. D.A.v.H. has an unrestricted research grant from Alnylam Pharmaceuticals. P.S. and R.D.C. hold equity in Courage Therapeutics Inc. and are inventors of intellectual property optioned to Courage Therapeutics Inc. R.D.C. chairs the Scientific Advisory Board at Courage Therapeutics Inc. All remaining authors declare no competing interests.

Additional information

Peer review information *Nature* thanks the anonymous reviewers for their contribution to the peer review of this work. Peer reviewer reports are available.

Publisher's note Springer Nature remains neutral with regard to jurisdictional claims in published maps and institutional affiliations.

Extended data figures and tables

[Extended Data Fig. 1 Functionally characterised MC3R mutations.](#)

Complete, partial loss-of-function (LoF) and wild-type like mutations are marked in purple, dark yellow and green respectively. Coloured rectangles indicate cohort(s) in which mutations were identified: Red = UK Biobank (UKBB); Blue = Avon Longitudinal Study of Parents & Children (ALSPAC); Light Brown = Genes & Health (G&H).

[Extended Data Fig. 2 PheWAS analysis of MC3R genetic risk score.](#)

A CADD-weighted MC3R genetic risk score was constructed (see [Methods](#)) and used to conduct a genome-wide analysis (pheWAS) with publicly available summary statistics. Solid black line indicates Bonferroni multiple-testing threshold of $p < 1.046\text{e-}4$, dashed line indicates nominal significance threshold $p < 0.05$.

Extended Data Fig. 3 Effect of MC3R Loss-of-Function mutations on height (cm) across time.

Carriers of MC3R LoF mutations (dark blue) had lower height throughout early life course compared to the reference group (light blue) after adjusting for sex and age. Figures only show results where the mutation group was represented by at least one individual at all time points between birth and 24 years. Mean \pm 95% CI shown, N and p-values are listed in Supplementary Table 4.

Extended Data Fig. 4 MC3R is essential for normal cycle length and for fasting-induced suppression of the reproductive axis.

a, b, Representative traces of progression through the oestrous cycle in WT (**a**) and *Mc3r*^{-/-} (**b**) mice following an overnight fast. D = Dioestrous; M = Metoestrous; E = Oestrous.

Extended Data Fig. 5 *Mc3r* is expressed in several cell populations in the mouse hypothalamus.

a, T-SNE plot showing 28 neuronal clusters (0–27) of the mouse hypothalamus from a combined dataset consisting of 18,427 neurons from 4 published studies. **b**, *Mc3r* is expressed in several neuronal populations (\log_2 normalised expression in dark red). **c**, Multiplexed smFISH showing the co-expression of *Mc3r* (white) *Kiss1* (red) and *Tac2* (green) in the arcuate nucleus. (Representative example shown, n = 3 mice, scale bar = 20 μ m). **d**, Venn diagram showing the number of cells expressing *Kiss1* (left, red), *Tac2* (right, green), or both (KNDy, centre). **e**, Violin plots showing the number of *Mc3r* mRNA puncta in *Kiss1* only, KNDy, and *Tac2* only cells. Mean percentages of cells \pm SEM with detected *Mc3r* are shown, data collected from 3 mice.

Extended Data Fig. 6 Expression of *Mc3r* and *Lepr* in KNDy and GHRH neurons.

a, b, *Mc3r* expression is more prominent compared to *Mc4r* and *Lepr* in *Tac2* (KNDy) (cluster 7, blue) (**a**) and GHRH neurons (cluster 15, green) (**b**). **c**, Violin plots showing expression of *Kiss1*, *Tac2*, *Ghrh*, *Mc3r* and *Lepr* in KNDy and Ghrh neurons in the Campbell³⁸ and the Chen⁴² dataset separately. The Lam⁴⁰ and Romanov⁴¹ datasets are not shown due to low cell count (<10).

Extended Data Fig. 7 Human smFISH showing the co-expression of *MC3R*, *KISS1*, and *GHRH* in the human hypothalamic arcuate nucleus.

a, Annotated overview *MC3R* and *KISS1* co-expression: *MC3R* = grey, *KISS* = magenta and *MC3R+KISS1* = white (scale bar = 200μm). High-powered micrograph (squared area) below shows the staining of *MC3R* (white) and *Kiss1* (magenta) mRNA punta in 2 representative cells (teal = DAPI, scale bar = 10μm). N = 2 slides. **b**, Annotated overview of *MC3R* and *GHRH* co-expression: *MC3R* = grey, *GHRH* = green and *MC3R+KISS1* = white (scale bar = 200μm). High-powered micrograph (squared area) below shows the staining of *MC3R* and *GHRH* mRNA punta in a representative cell (teal = DAPI, scale bar = 4μm). N = 2 slides.

Extended Data Fig. 8 *Mc3r* expression in kisspeptin neurons in the mouse hypothalamus at P16, P28 and P48.

a–c, Representative smFISH showing the co-expression of *Mc3r* and *Kiss1* in the anteroventral periventricular nucleus (AVPV) at P16 (**a**); P28 (**b**) and P48 (**c**) (N = 3 mice for all age groups): *Mc3r* = green, *Kiss1* = red (scale bar = 20μm).

Supplementary information

Supplementary Information

This file contains a note of the effect of *MC3R* complete loss-of-function (cLoF) mutations on trajectories of BMI and height in the Avon

Longitudinal Study of Parents and Children (ALSPAC), and members of the Genes & Health Research Team.

Reporting Summary

Peer Review File

Supplementary Tables

This file contains Supplementary Tables 1–15.

Rights and permissions

Reprints and Permissions

About this article

Cite this article

Lam, B.Y.H., Williamson, A., Finer, S. *et al.* MC3R links nutritional state to childhood growth and the timing of puberty. *Nature* **599**, 436–441 (2021). <https://doi.org/10.1038/s41586-021-04088-9>

- Received: 17 December 2020
- Accepted: 01 October 2021
- Published: 03 November 2021
- Issue Date: 18 November 2021
- DOI: <https://doi.org/10.1038/s41586-021-04088-9>

Share this article

Anyone you share the following link with will be able to read this content:

[Get shareable link](#)

Sorry, a shareable link is not currently available for this article.

[Copy to clipboard](#)

Provided by the Springer Nature SharedIt content-sharing initiative

Further reading

- [**A mediator of metabolic signals influences puberty and growth**](#)

◦ Alejandro Lomniczi

Nature (2021)

[**A mediator of metabolic signals influences puberty and growth**](#)

- Alejandro Lomniczi

News & Views 03 Nov 2021

This article was downloaded by **calibre** from <https://www.nature.com/articles/s41586-021-04088-9>

| [Section menu](#) | [Main menu](#) |

- Article
- [Published: 20 October 2021](#)

Linking hippocampal multiplexed tuning, Hebbian plasticity and navigation

- [Jason J. Moore](#) ORCID: orcid.org/0000-0002-4209-3896^{1,2},
- [Jesse D. Cushman](#)^{1,2},
- [Lavanya Acharya](#)^{1,3},
- [Briana Popeney](#)^{1,2} &
- [Mayank R. Mehta](#) ORCID: orcid.org/0000-0003-2005-2468^{1,2,4,5}

Nature volume **599**, pages 442–448 (2021)

- 5292 Accesses
- 103 Altmetric
- [Metrics details](#)

Subjects

- [Hippocampus](#)
- [Spatial memory](#)

Abstract

Three major pillars of hippocampal function are spatial navigation¹, Hebbian synaptic plasticity² and spatial selectivity³. The hippocampus is also implicated in episodic memory⁴, but the precise link between these

four functions is missing. Here we report the multiplexed selectivity of dorsal CA1 neurons while rats performed a virtual navigation task using only distal visual cues⁵, similar to the standard water maze test of spatial memory¹. Neural responses primarily encoded path distance from the start point and the head angle of rats, with a weak allocentric spatial component similar to that in primates but substantially weaker than in rodents in the real world. Often, the same cells multiplexed and encoded path distance, angle and allocentric position in a sequence, thus encoding a journey-specific episode. The strength of neural activity and tuning strongly correlated with performance, with a temporal relationship indicating neural responses influencing behaviour and vice versa. Consistent with computational models of associative and causal Hebbian learning^{6,7}, neural responses showed increasing clustering⁸ and became better predictors of behaviourally relevant variables, with the average neurometric curves exceeding and converging to psychometric curves. Thus, hippocampal neurons multiplex and exhibit highly plastic, task- and experience-dependent tuning to path-centric and allocentric variables to form episodic sequences supporting navigation.

Access options

Subscribe to Journal

Get full journal access for 1 year

\$199.00

only \$3.90 per issue

[Subscribe](#)

All prices are NET prices.

VAT will be added later in the checkout.

Tax calculation will be finalised during checkout.

Rent or Buy article

Get time limited or full article access on ReadCube.

from \$8.99

[Rent or Buy](#)

All prices are NET prices.

Additional access options:

- [Log in](#)
- [Access through your institution](#)
- [Learn about institutional subscriptions](#)

Fig. 1: Good performance but impaired spatial selectivity in a VNT.

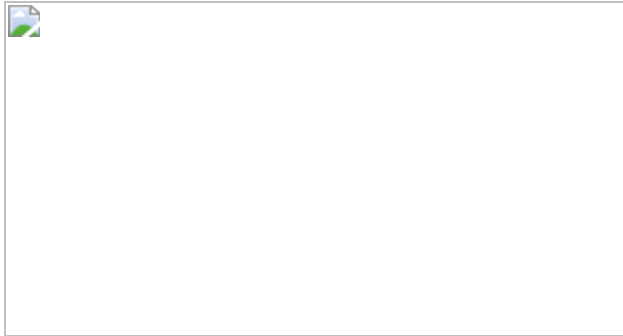


Fig. 2: Allocentric, path-centric and angular tuning.

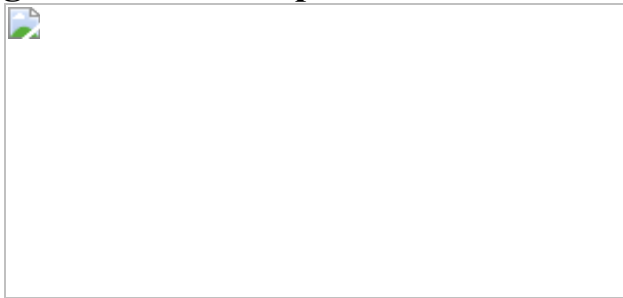


Fig. 3: Tuning is correlated with behaviour.

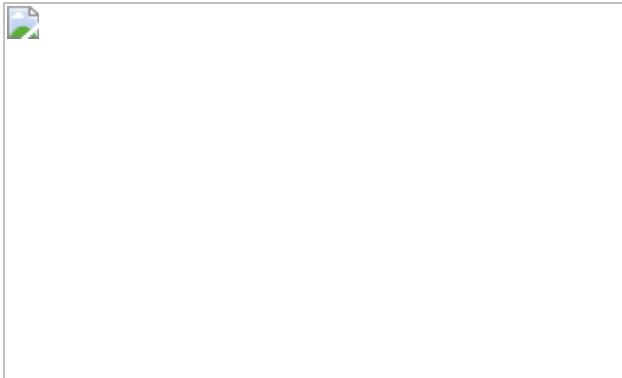
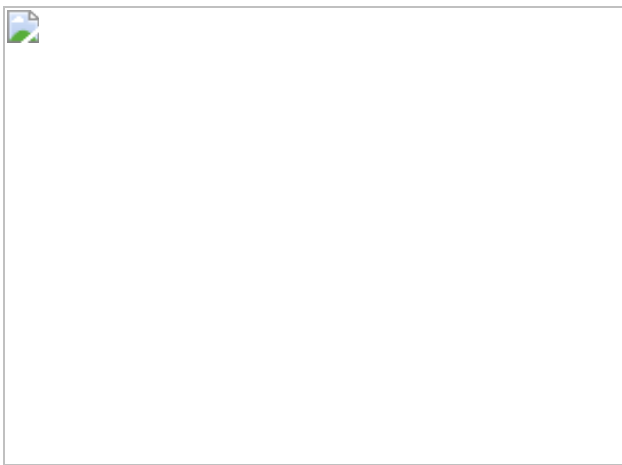


Fig. 4: Increased neural clustering correlated with improved behaviour within a session.



Data availability

The data that support the findings of this study are available from the corresponding authors upon reasonable request.

Code availability

All analyses were performed using custom-written code in MATLAB version 9.5 (R2018b). Codes necessary to reproduce the figures in this study are available from the corresponding authors upon reasonable request.

References

1. 1.

Morris, R. G. M. Synaptic plasticity and learning: selective impairment of learning in rats and blockade of long-term potentiation in vivo by the *N*-methyl-d-aspartate receptor antagonist AP5. *J. Neurosci.* **9**, 3040–3057 (1989).

2. 2.

Bliss, T. V. P. & Lømo, T. Long-lasting potentiation of synaptic transmission in the dentate area of the anesthetized rabbit following stimulation of the perforant path. *J. Physiol.* **232**, 331–356 (1973).

3. 3.

O'Keefe, J. & Dostrovsky, J. The hippocampus as a spatial map. Preliminary evidence from unit activity in the freely-moving rat. *Brain Res.* **34**, 171–175 (1971).

4. 4.

Scoville, W. B. & Milner, B. Loss of recent memory after bilateral hippocampal lesions. *J. Neurol. Neurosurg. Psychiatry* **20**, 11–21 (1957).

5. 5.

Cushman, J. D. et al. Multisensory control of multimodal behavior: do the legs know what the tongue is doing? *PLoS ONE* **8**, e80465 (2013).

6. 6.

Blum, K. I. & Abbott, L. F. A model of spatial map formation in the hippocampus of the rat. *Neural Comp.* **8**, 85–93 (1996).

7. 7.

Mehta, M. R., Quirk, M. C. & Wilson, M. A. Experience-dependent asymmetric shape of hippocampal receptive fields. *Neuron* **25**, 707–715 (2000).

8. 8.

Tsodyks, M. & Sejnowski, T. Associative memory and hippocampal place cells. *Int. J. Neural Syst.* **6**, 81–86 (1995).

9. 9.

McNaughton, B. L. et al. Deciphering the hippocampal polyglot: the hippocampus as a path integration system. *J. Exp. Biol.* **199**, 173–185 (1996).

10. 10.

Buzsáki, G. & Moser, E. I. Memory, navigation and theta rhythm in the hippocampal–entorhinal system. *Nat. Neurosci.* **16**, 130–138 (2013).

11. 11.

Hollup, S. A., Molden, S., Donnett, J. G., Moser, M. B. & Moser, E. I. Accumulation of hippocampal place fields at the goal location in an annular watermaze task. *J. Neurosci.* **21**, 1635–1644 (2001).

12. 12.

Pfeiffer, B. E. & Foster, D. J. Hippocampal place-cell sequences depict future paths to remembered goals. *Nature* **497**, 74–79 (2013).

13. 13.

Xu, H., Baracskay, P., O’Neill, J. & Csicsvari, J. Assembly responses of hippocampal CA1 place cells predict learned behavior in goal-directed spatial tasks on the radial eight-arm maze. *Neuron* **101**, 119–132 (2019).

14. 14.

Mehta, M. R., Barnes, C. A. & McNaughton, B. L. Experience-dependent, asymmetric expansion of hippocampal place fields. *Proc.*

Natl Acad. Sci. USA **94**, 8918–8921 (1997).

15. 15.

Mehta, M. R. & McNaughton, B. L. Expansion and shift of hippocampal place fields: evidence for synaptic potentiation during behavior. *Comput. Neurosci. Trends Res.* 741–745 (1997).

16. 16.

Mehta, M. R. From synaptic plasticity to spatial maps and sequence learning. *Hippocampus* **25**, 756–762 (2015).

17. 17.

Tulving, E. Episodic memory: from mind to brain. *Annu. Rev. Psychol.* **53**, 1–25 (2002).

18. 18.

Baraduc, P. & Wirth, S. Schema cells in the macaque hippocampus. *Science* **363**, 635–639 (2019).

19. 19.

Pastalkova, E., Itskov, V., Amarasingham, A. & Buzsáki, G. Internally generated cell assembly sequences in the rat hippocampus. *Science* **321**, 1322–1327 (2008).

20. 20.

Ravassard, P. et al. Multisensory control of hippocampal spatiotemporal selectivity. *Science* **340**, 1342–1346 (2013).

21. 21.

Aghajan, Z. M. et al. Impaired spatial selectivity and intact phase precession in two-dimensional virtual reality. *Nat. Neurosci.* **18**, 121–128 (2015).

22. 22.

Villette, V., Malvache, A., Tressard, T., Dupuy, N. & Cossart, R. Internally recurring hippocampal sequences as a population template of spatiotemporal information. *Neuron* **88**, 357–366 (2015).

23. 23.

Sarel, A., Finkelstein, A., Las, L. & Ulanovsky, N. Vectorial representation of spatial goals in the hippocampus of bats. *Science* **355**, 176–180 (2017).

24. 24.

Markram, H., Lübke, J. & Frotscher, M. Regulation of synaptic efficacy by coincidence of postsynaptic APs and EPSPs. *Science* **275**, 213–215 (1997).

25. 25.

Bi, G. & Poo, M. Synaptic modifications in cultured hippocampal neurons: dependence on spike timing, synaptic strength, and postsynaptic cell type. *J. Neurosci.* **18**, 10464–10472 (1998).

26. 26.

Mehta, M. R. & Wilson, M. A. From hippocampus to V1: effect of LTP on spatio-temporal dynamics of receptive fields. *Neurocomputing* **32–33**, 905–911 (2000).

27. 27.

Kentros, C. et al. Abolition of long-term stability of new hippocampal place cell maps by NMDA receptor blockade. *Science* **280**, 2121–2126 (1998).

28. 28.

Ekstrom, A. D., Meltzer, J., McNaughton, B. L. & Barnes, C. A. NMDA receptor antagonism blocks experience-dependent expansion of hippocampal ‘place fields’. *Neuron* **31**, 631–638 (2001).

29. 29.

Sato, M. et al. Hippocampus-dependent goal localization by head-fixed mice in virtual reality. *eNeuro* **4**, ENEURO.0369-16.2017 (2017).

30. 30.

Rowland, L. H. et al. Selective cognitive impairments associated with NMDA receptor blockade in humans. *Neuropsychopharmacology* **30**, 633–639 (2005).

31. 31.

Dupret, D., O’Neill, J., Pleydell-Bouverie, B. & Csicsvari, J. The reorganization and reactivation of hippocampal maps predict spatial memory performance. *Nat. Neurosci.* **13**, 995–1002 (2010).

32. 32.

Gothard, K. M., Skaggs, W. E. & McNaughton, B. L. Dynamics of mismatch correction in the hippocampal ensemble code for space: interaction between path integration and environmental cues. *J. Neurosci.* **16**, 8027–8040 (1996).

33. 33.

Acharya, L., Aghajan, Z. M., Vuong, C., Moore, J. J. & Mehta, M. R. Causal influence of visual cues on hippocampal directional selectivity. *Cell* **164**, 197–207 (2016).

34. 34.

Ziv, Y. et al. Long-term dynamics of CA1 hippocampal place codes. *Nat. Neurosci.* **16**, 264–266 (2013).

35. 35.

Howard, L. R. et al. The hippocampus and entorhinal cortex encode the path and euclidean distances to goals during navigation. *Curr. Biol.* **24**, 1331–1340 (2014).

36. 36.

MacDonald, C. J., Lepage, K. Q., Eden, U. T. & Eichenbaum, H. Hippocampal ‘time cells’ bridge the gap in memory for discontiguous events. *Neuron* **71**, 737–749 (2011).

37. 37.

Gauthier, J. L. & Tank, D. W. A dedicated population for reward coding in the hippocampus. *Neuron* **99**, 179–193 (2018).

38. 38.

Leutgeb, S. et al. Independent codes for spatial and episodic memory in hippocampal neuronal ensembles. *Science* **309**, 619–623 (2005).

39. 39.

Rolls, E. T., Treves, A., Robertson, R. G., Georges-François, P. & Panzeri, S. Information about spatial view in an ensemble of primate hippocampal cells. *J. Neurophysiol.* **79**, 1797–1813 (1998).

40. 40.

Miller, J. F. et al. Neural activity in human hippocampal formation reveals the spatial context of retrieved memories. *Science* **342**, 1111–1114 (2013).

41. 41.

Jacobs, J., Kahana, M. J., Ekstrom, A. D., Mollison, M. V. & Fried, I. A sense of direction in human entorhinal cortex. *Proc. Natl Acad. Sci. USA* **107**, 6487–6492 (2010).

42. 42.

Aronov, D. & Tank, D. W. Engagement of neural circuits underlying 2D spatial navigation in a rodent virtual reality system. *Neuron* **84**, 442–456 (2014).

43. 43.

Chen, G., King, J. A., Lu, Y., Cacucci, F. & Burgess, N. Spatial cell firing during virtual navigation of open arenas by head-restrained mice. *eLife* **7**, e34789 (2018).

44. 44.

Resnik, E., McFarland, J. M., Sprengel, R., Sakmann, B. & Mehta, M. R. The effects of GluA1 deletion on the hippocampal population code for position. *J. Neurosci.* **32**, 8952–8968 (2012).

45. 45.

Tse, D. et al. Schemas and memory consolidation. *Science* **316**, 76–82 (2007).

46. 46.

Rubin, A., Yartsev, M. M. & Ulanovsky, N. Encoding of head direction by hippocampal place cells in bats. *J. Neurosci.* **34**, 1067–1080 (2014).

47. 47.

Shahi, M. et al. A generalized linear model approach to dissociate object-centric and allocentric directional responses in hippocampal place cells. *Soc. Neurosci. Abstr.* **1**, (2017).

48. 48.

Jercog, P. E. et al. Heading direction with respect to a reference point modulates place-cell activity. *Nat. Commun.* **10**, 2333 (2019).

49. 49.

Cabral, H. O., Fouquet, C., Rondi-Reig, L., Pennartz, C. M. A. & Battaglia, F. P. Single-trial properties of place cells in control and CA1 NMDA receptor subunit 1-KO mice. *J. Neurosci.* **34**, 15861–15869 (2014).

50. 50.

Mehta, M. R. Neuronal dynamics of predictive coding. *Neurosci.* **7**, 490–495 (2001).

51. 51.

Harvey, C. D., Collman, F., Dombeck, D. A. & Tank, D. W. Intracellular dynamics of hippocampal place cells during virtual navigation. *Nature* **461**, 941–946 (2009).

52. 52.

Safaryan, K. & Mehta, M. Enhanced hippocampal theta rhythmicity and emergence of eta oscillation in virtual reality. *Nat. Neurosci.* **24**, 1065–1070 (2021).

53. 53.

Kumar, A. & Mehta, M. R. Frequency-dependent changes in NMDAR-dependent synaptic plasticity. *Front. Comput. Neurosci.* **5**, 38 (2011).

54. 54.

Wang, S. H. & Morris, R. G. M. Hippocampal-neocortical interactions in memory formation, consolidation, and reconsolidation. *Annu. Rev. Psychol.* **61**, 49–79 (2010).

55. 55.

Mehta, M. R. Cortico-hippocampal interaction during up-down states and memory consolidation. *Nat. Neurosci.* **10**, 13–15 (2007).

56. 56.

Brun, V. H. et al. Place cells and place recognition maintained by direct entorhinal–hippocampal circuitry. *Science* **296**, 2243–2246 (2002).

57. 57.

Ahmed, O. J. & Mehta, M. R. The hippocampal rate code: anatomy, physiology and theory. *Trends Neurosci.* **32**, 329–338 (2009).

58. 58.

Mehta, M. R. Contribution of I_h to LTP, place cells, and grid cells. *Cell* **147**, 968–970 (2011).

59. 59.

Moore, J. J. et al. Dynamics of cortical dendritic membrane potential and spikes in freely behaving rats. *Science* **355**, eaaj1497 (2017).

60. 60.

Mehta, M. R. Cooperative LTP can map memory sequences on dendritic branches. *Trends Neurosci.* **27**, 69–72 (2004).

61. 61.

Wolbers, T., Wiener, J. M., Mallot, H. A. & Büchel, C. Differential recruitment of the hippocampus, medial prefrontal cortex, and the human motion complex during path integration in humans. *J. Neurosci.* **27**, 9408–9416 (2007).

62. 62.

Hahn, T. T. G., McFarland, J. M., Berberich, S., Sakmann, B. & Mehta, M. R. Spontaneous persistent activity in entorhinal cortex modulates cortico-hippocampal interaction in vivo. *Nat. Neurosci.* **15**, 1531–1538 (2012).

63. 63.

Wang, C. et al. Egocentric coding of external items in the lateral entorhinal cortex. *Science* **362**, 945–949 (2018).

64. 64.

Friedman, J., Hastie, T. & Tibshirani, R. Regularized paths for generalized linear models via coordinate descent. *J. Stat. Softw.* **33**, 1–22 (2008).

65. 65.

Boyd, J. P. *Chebyshev and Fourier Spectral Methods*. 2nd revised edn (Dover Publications, 2000).

Acknowledgements

We thank C. Vuong, D. Aharon and B. Willers for help with initial development of the experimental paradigm and early data collection; N. Agarwal and F. Quezada for help with training and behaviour; A. Kees and P. Ravassard for surgical assistance; and K. Choudhary for data management support. This work was supported by grants to M.R.M. from the W.M. Keck Foundation, AT&T, NSF 1550678 and NIH 1U01MH115746 to M.R.M. Some results presented in this manuscript were presented in abstract form at the annual Society for Neuroscience conference in 2015 (632.16), 2016 (263.03), 2017 (523.11), 2018 (508.06) and 2019 (083.85).

Author information

Affiliations

1. W.M. Keck Center for Neurophysics, University of California at Los Angeles, Los Angeles, CA, USA

Jason J. Moore, Jesse D. Cushman, Lavanya Acharya, Briana Popeney & Mayank R. Mehta

2. Department of Physics and Astronomy, University of California at Los Angeles, Los Angeles, CA, USA

Jason J. Moore, Jesse D. Cushman, Briana Popeney & Mayank R. Mehta

3. Biomedical Engineering Interdepartmental Program, University of California at Los Angeles, Los Angeles, CA, USA

Lavanya Acharya

4. Department of Neurology, University of California at Los Angeles, Los Angeles, CA, USA

Mayank R. Mehta

5. Department of Electrical and Computer Engineering, University of California at Los Angeles, Los Angeles, CA, USA

Mayank R. Mehta

Contributions

J.D.C., L.A. and M.R.M. designed the experiments. J.J.M. and M.R.M. designed the analyses. J.D.C. and L.A. performed the electrophysiology experiments. B.P. performed the NMDAR block experiments. J.J.M. performed all analyses with input from M.R.M. J.J.M and M.R.M. wrote the manuscript with input from J.D.C. and L.A.

Corresponding authors

Correspondence to [Jason J. Moore](#) or [Mayank R. Mehta](#).

Ethics declarations

Competing interests

The authors declare no competing interests.

Additional information

Peer review information *Nature* thanks the anonymous reviewers for their contribution to the peer review of this work.

Publisher's note Springer Nature remains neutral with regard to jurisdictional claims in published maps and institutional affiliations.

Extended data figures and tables

[Extended Data Fig. 1 Rats use a place navigation strategy to solve the task.](#)

a, Performance, measured by rewards/meter, consistently improved across subsequent sessions in different session blocks ($p = 0.02$, two-sided Wilcoxon sign-rank test on difference between % Improvement across consecutive days without a gap, $n = 27$ differences). Thin gray lines indicate individual session blocks, with the thick black line indicating the mean ($n = 12$ session blocks). **b**, Top, left, individual trials (thin colored lines) and mean path from each start position (thick black lines) for a single behavioral session with 4 start positions. Paths are color coded based on start position. Right, all mean paths rotated to begin at the same point and heading, illustrating that rats take unique paths from each start position. Paths are color coded to match the colors in the left panel. Bottom, same as top but for a different behavioral session with 8 start positions. **c**, The path correlation (see [Methods](#)) was significantly smaller ($p = 1.9 \times 10^{-7}$, one-sided Wilcoxon sign-rank test) across start positions (0.58, [0.53, 0.63]) compared to within start positions (0.81, [0.77, 0.84], $n = 34$ sessions for all statistics). Values are reported as median and 95% confidence interval of

the median here and in **d**. **d**, As in **c**, the across start position correlation was smaller than the within start position correlation for each individual rat in the study. Rat 1: Across (0.58, [0.51, 0.68]) vs Within (0.88, [0.80, 0.89]), $p = 2.4 \times 10^{-4}$, $n = 12$ sessions). Rat 2: Across (0.53, [0.44, 0.63]) vs Within (0.82, [0.74, 0.85]), $p = 2.4 \times 10^{-4}$, $n = 12$ sessions). Rat 3: Across (0.56, [0.50, 0.69]) vs Within (0.76, [0.73, 0.84]), $p = 1.6 \times 10^{-2}$, $n = 6$ sessions). Rat 4: Across (0.61, [0.47, 0.66]) vs Within (0.78, [0.73, 0.81]), $p = 0.06$, $n = 4$ sessions). One-sided Wilcoxon sign-rank test used throughout.

Extended Data Fig. 2 Further behavioral quantification.

a, The percentage of time rats spent in the goal-containing northeast (NE) quadrant (36, [33, 39]%) was significantly greater than chance ($p = 2.8 \times 10^{-4}$, two-sided Wilcoxon sign-rank test), and greater than all other quadrants (NW: 20, [19, 22]%; SE: 26, [23, 28]%; SW: 17, [16, 18]%). **b**, Left: The median performance was 0.43, [0.38, 0.47] reward/meter; Middle: The median trial distance was 230, [210, 260] cm; Right: The median trial time was 10, [9.5, 11] s of movement. **c**, Quadrant occupancy as in **a**, split between 4-start sessions and 8-start sessions, exhibiting similar characteristics. **d**, Behavioral measures from **b**, split between 4-start sessions and 8-start sessions. No significant differences exist between the conditions in any measure. Rewards/meter: 4-start (0.46, [0.34, 0.49]), 8-start (0.40, [0.35, 0.46]), $p = 0.35$. Trial Distance: 4-start (220, [205, 267]), 8-start (252, [217, 297]), $p = 0.30$. Trial Time: 4-start (9.75, [8.47, 12.0]), 8-start (10.5, [9.9, 11.7]), $p = 0.27$. **e**, Left, occupancy index ([Supplementary Information](#)) as a function of radial distance from the goal location. $p = 1.3 \times 10^{-12}$, 34 sessions; one-way repeated-measures ANOVA. Right, population average, showing rats spend more time near the goal than expected by chance. Lines and shading indicate the median and 95% confidence interval of the median, color coded as in **c**. **f**, Left, speed index ([Supplementary Information](#)) as a function of radial distance from the goal location. $p = 2.0 \times 10^{-9}$, 34 sessions; one-way repeated-measures ANOVA. Right, population average, showing rats run slower near the goal than expected by chance. Color conventions are as in **e**. $n = 34$ sessions for all combined statistics; $n = 20$ sessions for 4-start statistics; $n = 14$ for 8-start

statistics. Values are reported as median and 95% confidence interval of the median.

Extended Data Fig. 3 NMDAR antagonist impairs virtual navigation task performance.

a, Top, black lines, trajectories from 6 rats injected with saline, on the first day in a new environment. The goal heading index (GHI, [Supplementary Information](#)) for each rat is indicated above. Bottom, green lines, full trajectories during a probe trial (see [Methods](#)) immediately following the session above, demonstrating rats preferentially spent time near the learned reward site (open black circles). The large green dot indicates the starting position for the probe trial. Scale is as in Fig. 1. **b**, Top, red lines, trajectories from 6 rats injected with the NMDA antagonist (R)-CPPene (see [Methods](#)). Bottom, purple lines, trajectories from a probe trial immediately following the sessions in red. **c**, GHI is strongly positively correlated with rewards/meter ($R = 0.89$, $p = 1.08 \times 10^{-12}$, two-sided t test, $n = 34$ sessions). **d**, Top, there was no significant difference ($p = 1$, two-sided Wilcoxon sign-rank test) in rewards/meter between the saline (SAL, black, 0.19, [0.14, 0.24], $n = 6$ rats) and CPP (red, 0.22, [0.15, 0.25], $n = 6$ rats) conditions. Bottom, trial length was not significantly different between the two conditions ($p = 0.41$, two-sided Wilcoxon rank-sum test; SAL: 3.7 [3.3, 4.1] m, $n = 282$ trials; CPP: 3.8, [3.1, 5.1] m, $n = 69$ trials). **e**, Top, rats traveled less distance overall in the CPP sessions (64, [15, 105] m, $n = 6$ rats) compared to SAL sessions (260, [150, 300] m, $n = 6$ rats; $p = 0.03$, two-sided Wilcoxon sign-rank test). Bottom, rats traveled less distance in the CPP probe trials (1.5, [0.12, 3.6] m, $n = 6$ rats) compared to SAL probe trials (9.6, [4.9, 12] m, $n = 6$ rats; $p = 0.03$, two-sided Wilcoxon sign-rank test). **f**, Top, rats spent more time moving in the SAL sessions compared to CPP sessions ($p = 2.9 \times 10^{-13}$, 2-way ANOVA with Saline/CPP group as a categorical variable and time (19 bins) as a continuous variable). Bottom, rats spent less time moving in the CPP probe trials compared to the SAL probe trials ($p = 1.7 \times 10^{-3}$, 2-way ANOVA with Saline/CPP group as a categorical variable and time (12 bins) as a continuous variable). **g**, GHI was significantly greater than 0 in the SAL full session (0.11, [0.09, 0.28], $n = 6$ rats, $p = 0.02$, Right-tailed (one-sided) Wilcoxon sign-rank test throughout this panel) and SAL probe trials (0.08, [0.002, 0.14], $n = 6$ rats,

$p = 0.03$), as well as the CPP full session (0.10, [0.05, 0.17], $n = 6$ rats, $p = 0.02$), indicating movement directed towards the reward zone. Goal heading index in the CPP probe trials was not significantly greater than 0 (-0.19 , $[-0.33, 0.09]$, $n = 4$ rats, $p = 0.88$), indicating equivalent time spent moving towards or away from the reward zone. 2 sessions were excluded due to insufficient movement.

Extended Data Fig. 4 Additional examples of spatial tuning in 4- and 8-start navigation tasks using the binning method.

a, Example units as in Fig. 1b–c. **b**, Example units as in **a** but for sessions with 8 start positions rather than 4.

Extended Data Fig. 5 Differences between binning and GLM-derived maps; quantification of stability of GLM results for space, distance, and angle tuning.

a, 4 example units demonstrating the differences between binned (top) and GLM (bottom) maps. **b**, Sparsity of spatial, distance, and angular maps using the binning method versus the sparsity using the GLM. For allocentric space and episodic distance, but not allocentric angle, the binning method estimated larger sparsity on average than the GLM (Space: $p = 7.3 \times 10^{-29}$; Distance: $p = 7.4 \times 10^{-3}$; Angle: $p = 0.06$; $n = 384$ units, two-sided Wilcoxon sign-rank test for all). **c**, Top, example rate maps for two units from the first (top row) and second (middle row) halves of a session. Bottom, the stability of tuned spatial rate maps (0.25, [0.14, 0.40], $n = 111$ units) was significantly higher than both the stability of untuned maps (0.14, [0.08, 0.23], $n = 273$ units; $p = 0.02$, two-sided Wilcoxon rank-sum test here and throughout the figure) and the stability expected from random shuffles of first and second half maps (-0.00 , $[-0.06, 0.08]$, $n = 384$ units; $p = 3.7 \times 10^{-7}$). Untuned maps were also more stable than chance ($p = 5.2 \times 10^{-4}$). **d**, Example path distance rate maps for two units from the first and second halves of a session. Bottom, the stability of tuned path distance maps (0.38, [0.30, 0.44], $n = 181$ units) was significantly higher than the stability of untuned maps (0.10, [0.03, 0.20], $n = 203$ units; $p = 5.1 \times 10^{-8}$) and of shuffled controls (-0.02 , $[-0.10, 0.03]$, $n = 384$ units; $p =$

1.8×10^{-19}). Untuned distance maps were also more stable than chance ($p = 3.2 \times 10^{-3}$). **e**, Example angle rate maps for two units from the first and second halves of a session. Bottom, the stability of tuned path angle maps (0.37, [0.28, 0.43], $n = 155$ units) was significantly higher than the stability of untuned maps (0.09, [0.05, 0.17], $n = 229$ units; $p = 1.9 \times 10^{-8}$) and of shuffled controls (0.02, [−0.04, 0.05], $n = 384$ units; $p = 3.4 \times 10^{-17}$). Untuned distance maps were also more stable than chance ($p = 1.7 \times 10^{-3}$). No adjustments were made for multiple comparisons in **c–e**.

Extended Data Fig. 6 Distance coding cells show similar selectivity across start positions.

a, Spikes as a function of rat's position, for two different cells (top and bottom) are color coded based on the start position. **b**, Spikes as a function of the distance traveled, with trials from different start positions grouped together. The maps look qualitatively similar from all four start positions. The variations in firing rates could occur due to other variables, e.g. direction selectivity. **c**, Hence, we used the GLM method (see [Methods](#)) using data from all the trials. Spikes are shown as a function of the path distance and time elapsed. The GLM estimate of firing rate as a function of distance alone is shown by thick line.

Extended Data Fig. 7 Examples of path distance tuning for longer distances in 4- and 8-start navigation tasks; additional properties of path distance tuning.

a, Example units as in Fig. [2b](#). **b**, Example units as in **a** but for sessions with 8 start positions rather than 4. **c**, The distance sparsity of units in 4-start sessions (0.13, [0.12, 0.14], $n = 183$ units) was slightly but significantly greater ($p = 0.03$, two-sided Wilcoxon rank-sum test) than the distance sparsity in 8-start sessions (0.11, [0.09, 0.13], $n = 181$ units). **d**, The effect in **c** was not present when controlling for the total number of spikes ($p = 0.43$, two-way ANOVA, see [Methods](#)). **e**, The distribution of occupancy times was skewed toward earlier distances, with a center of mass at 115 cm. **f**, Left, sample distance tuning curve (black) overlaid with the sum of two fitted Gaussians (green). Right, the individual Gaussians that

were fitted. **g**, The median goodness of fit (correlation coefficient between the original and fitted curve) was quite high (0.97, [0.96, 0.98], n = 181 units), with no unit having a fit less than 0.89. **h**, Distribution of the number of significant peaks in distance maps. 50% of units had more than one peaks, with a mean of 1.7, [1.5, 1.8] peaks. Error bars represent the 95% confidence interval of the mean obtained from a binomial distribution using the Matlab function *binofit()*. **i**, The peak index (peak amplitude of a fitted Gaussian divided by constant offset) of distance curves (2.2, [2.0, 2.4], n = 300 peaks) was significantly higher ($p = 2.1 \times 10^{-69}$, two-sided Wilcoxon rank-sum test) than for shuffled data (0.63, [0.57, 0.68], n = 463 peaks). **j**, The width of fitted Gaussian components (width at half-max; 20, [18, 21] cm, n = 300 peaks) was slightly but significantly smaller ($p = 0.03$, two-sided Wilcoxon rank-sum test) than for shuffled data (22, [21, 23] cm, n = 463 peaks). Details of the fitting procedure and quantification of field properties are available in the [Supplementary Information](#).

Extended Data Fig. 8 Path distance tuning is not easily explained by selectivity to time or distance to the goal.

a, Path distance (top row) and path time (bottom row) rate maps for three sample cells. s_d and s_t represent the sparsity of rate maps for distance and time, respectively. Column 1 depicts a cell that is well-tuned in both the distance and time domains. Column 2 shows a cell that is better tuned in the distance domain. Column 3 shows a cell that is better tuned in the time domain. **b**, Rate maps in **a** are overlaid in the bottom row for ease of comparison. Distance between 0 and 200 cm and time between 0 and 10 s are normalized from 0 to 1 for visualization. **c**, Left, sparsity of Path Time maps versus sparsity of Path Distance maps. Right, sparsity index (defined as $(s_d - s_t)/(s_d + s_t)$) was slightly but significantly greater than 0 (0.03, [0.02 0.05], n = 384 cells; $p = 1.5 \times 10^{-6}$, two-sided Wilcoxon sign-rank test). **d**, Path distance (top row) and goal distance (bottom row) rate maps for three sample cells. s_d and s_g represent the sparsity of rate maps for path distance and goal distance, respectively. Column 1 depicts a cell that is well-tuned in both the frames of reference. Column 2 shows a cell that is better tuned in the path distance frame. Column 3 shows a cell that is better tuned in the goal distance domain. **e**, Rate maps in **d** are overlaid in the bottom row for

ease of comparison. Distance between 0 and 200 cm and time between -200 and 0 cm are normalized from 0 to 1 for visualization. **f**, Left, sparsity of Goal Distance maps versus sparsity of Path Distance maps. Right, sparsity index (defined as $(s_d - s_g)/(s_d + s_g)$) was significantly greater than 0 (0.27, [0.23 0.31], n = 384 cells; p = 7.8×10^{-37} , two-sided Wilcoxon sign-rank test).

Extended Data Fig. 9 Examples of angular tuning in 4- and 8-start navigation tasks; additional properties of angular tuning.

a, Example units as in Fig. 2c. **b**, Example units as in a but for sessions with 8 start positions rather than 4. **c**, The angular sparsity of units in 4-start sessions (0.10, [0.09, 0.12], n = 155 units) was not significantly different (p = 0.77, two-sided Wilcoxon rank-sum test) than the angular sparsity in 8-start sessions (0.11, [0.09, 0.12], n = 155 units). **d**, There was no significant difference when controlling for the total number of spikes (p = 0.06, two-way ANOVA, see [Methods](#)). **e**, The distribution of occupancy times was skewed toward the north-east direction, with a mean vector pointing towards 56°. **f**, Left, sample angle tuning curve (black) overlaid with the sum of four fitted Von Mises curves (red). Right, the individual Von Mises curves that were fitted. **g**, The median goodness of fit (correlation coefficient between the original and fitted curve) was quite high (0.98, [0.97, 0.98], n = 155 units). **h**, Distribution of the number of significant peaks in angle maps. 83% of units had more than one peak, with a mean of 2.7, [2.5, 2.8] peaks. Error bars represent the 95% confidence interval of the mean obtained from the Matlab function *binofit()*. **i**, The peak index (peak amplitude of a fitted Von Mises curve divided by constant offset; 1.8, [1.7, 2.0], n = 411 peaks) was significantly higher (p = 2.1×10^{-35} , two-sided Wilcoxon rank-sum test) than for shuffled data (0.77 [0.72, 0.84], n = 476 peaks). **j**, The width of fitted Von Mises curves (width at half-max; 47, [46, 49]°, n = 411 peaks) was not significantly different (p = 0.70, two-sided Wilcoxon rank-sum test) than for shuffled data (45, [44, 48]°, n = 476 peaks). Details of the fitting procedure and quantification of field properties are available in the [Supplementary Information](#).

Extended Data Fig. 10 Episodic relationship between space, distance, and angle selectivity.

a, Sparsity for rate maps in allocentric space (left), path distance (middle), and allocentric angle (right) versus the center distance coordinate (see [Methods](#)) for each cell. Significantly tuned cells are marked with large, colored dots and cells that are not significantly tuned are marked with small, black dots. **b**, The percentage of cells significantly tuned as a function of their center distance coordinate for space (blue), distance (green), and angle (red). The combined plot at the far right is the same as Fig. [2h](#). **c**, Cross-correlations between the curves in **b**, overlaid with shuffled control cross-correlations, demonstrate that the relative ordering of parameter tuning – Distance, then Space, then Angle – is greater than expected by chance. Dotted black lines indicate the median and 95% range of the cross-correlation of the curves in **b** constructed from shuffled data (see [Methods](#)). Cross-correlation peaks above this range (Left, cyan, 11.25 cm indicating Distance leads Space; Middle, magenta, -150 cm indicating Space leads Angle; Right, orange, -161.3 cm indicating Distance leads Angle) indicate statistical significance at the $p < 0.05$ level.

Extended Data Fig. 11 Additional measures of performance correlate with neural tuning; speed does not correlate with performance.

a, Same values as in Fig. [3c](#) plotted as a function of Trial Latency (see [Methods](#)). Correlation values and p-values are shown above each figure. R_w and p_w represent the correlation value and p -value for the weighted best fit line. For unweighted fits, p -values are from a two-sided t test for each panel, with $n = 34$ sessions. For weighted fits, p -values are calculated through a resampling procedure (see [Methods](#)). **b**, Same as **a**, but plotted as a function of Trial Distance (see [Methods](#)). **c**, Same as **a**, but plotted as a function of within-start path correlation (Extended Data Fig. [1b-c](#), see [Methods](#)). **d**, Same as **a**, but plotted as a function of goal heading index (see [Methods](#)). **e**, Including sessions from all rats, the median speed in a session was not significantly correlated with behavioral performance as measured by rewards/meter, Trial Latency, Trial Distance, Path Correlation,

or Goal Heading Index. Correlation values and *p*-values are shown above each figure. *p*-values are from a two-sided *t* test for each panel, with n = 34 sessions.

Extended Data Fig. 12 Experience-dependent changes in behavior, neural activation, and shifts in single unit path distance tuning.

a, Trial latency (time spent running) decreased as a function of trial number (Effect of trial number on Trial Latency: $p = 5.0 \times 10^{-5}$, 34 sessions; one-way repeated-measures ANOVA). The thick line is the median, and the thin lines are the 95% confidence interval of the median. **b**, Mean speed did not significantly change as a function of trial number (Effect of trial number on Mean Speed: $p = 0.44$, 34 sessions; one-way repeated-measures ANOVA). The thick line is the median, and the thin lines are the 95% confidence interval of the median. **c**, The fraction of total cells active (rate in a 3-trial boxcar average > 0.2 Hz) increased with experience (correlation coefficient $R = 0.94$, $p = 2.7 \times 10^{-25}$, n = 52 trials, two-sided *t* test). **d**, Averaged across the ensemble, the firing rates were higher in later trials than early trials (Figure 4b). This was quantified on a cell-by-cell basis by computing the rate modulation index for each cell (see [Methods](#)), which was centered at 0.11, [0.08, 0.15], and significantly greater than 0 ($p = 1.8 \times 10^{-13}$, two-sided Wilcoxon sign-rank test, n = 384 units). **e**, Eight example cells with distance tuning curves exhibiting shifting with experience. Curves are estimated from the GLM using data only from trials 1–26 (light green) or 27–52 (dark green). The cells in the top three rows demonstrate backwards, or anticipatory, shifting. The cells in the bottom row demonstrate forwards shifting. **f**, Cross-correlation plots, sorted by the experiential shift (distance lag of the peak in the cross-correlation) of peak correlation, for all cells significantly tuned for distance but not angle, (n = 88; 91 cells met this criteria, but 3 were excluded for having insufficient spiking in one of the two halves). **g**, The median experiential shift (-7.5 , $[-15, 0]$ cm) was significantly different from 0 ($p = 0.014$, two-sided Wilcoxon sign-rank test).

Extended Data Fig. 13 Within-session clustering and forward movement of spatial, distance, and angle maps and their relationship with psychometric curves.

a, Left, distributions of peaks of allocentric spatial rate maps (top, blue) and spatial occupancy (bottom, gray) in early trials, showing dispersed, fairly uniform distributions. Right, distributions of spatial peaks (top) and spatial occupancy (bottom) in later trials, showing clear clustering near the goal location. **b**, The allocentric goal distance (see [Methods](#)) significantly decreased with increasing trial number (Neurons: $R = -0.63$, $p = 1.5 \times 10^{-3}$, two-sided t test, $n = 22$ trial blocks (every other trial from trial 5 to 47) here and for all other tests in this panel; Behavior: $R = -0.64$, $p = 1.2 \times 10^{-3}$, two-sided t test, $n = 22$ trial blocks), and the sparsity of these distributions increased with trial number (Neurons: $R = 0.67$, $p = 5.7 \times 10^{-4}$, two-sided t test, $n = 22$ trial blocks; Behavior: $R = 0.63$, $p = 1.8 \times 10^{-3}$, two-sided t test, $n = 22$ trial blocks). **c**, The center of the distribution of path-distance tuning curve peaks and behavior both moved closer to the trial beginning with increasing trial number (Neurons: $R = -0.91$, $p = 2.8 \times 10^{-9}$, two-sided t test; Behavior: $R = -0.69$, $p = 3.9 \times 10^{-4}$), and the sparsity of these distributions increased with trial number (Neurons: $R = 0.89$, $p = 2.6 \times 10^{-8}$; Behavior: $R = 0.89$, $p = 4.4 \times 10^{-8}$). **d**, The angle goal distance (see [Methods](#)) for angular tuning curve peaks and behavior decreased with increasing trial number (Neurons: $R = -0.86$, $p = 3.4 \times 10^{-7}$, two-sided t test, $n = 22$ trial blocks (every other trial from trial 5 to 47) here and for all other tests in this panel; Behavior: $R = -0.55$, $p = 7.6 \times 10^{-3}$); the sparsity of these distributions increased with trial number (Neurons: $R = 0.67$, $p = 7.1 \times 10^{-4}$; Behavior: $R = 0.65$, $p = 1.0 \times 10^{-3}$).

Extended Data Fig. 14 Temporal relationship between neural firing properties and behavior, split into high- and low-performing sessions.

a, Top, performance increased with trial number. This was true when including all cells (colored dots, same data as Fig. 4a, right), cells from sessions with high performance (top 50% of sessions, gray dots, “High”), or

cells from sessions with low performance (bottom 50% of sessions, black dots, “Low’). Solid lines are exponential fits to the data. Middle, the firing rate of active cells increased with trial number. Bottom, cross-correlation of the population firing rate with performance, for all sessions, high-performance sessions, and low-performance sessions. For all data and high-performance sessions, the lag of the peak correlation is near 0, indicating a co-evolution of performance with firing rate. In low-performance sessions, there is a distinct asymmetry, indicating that neural changes precede behavioral changes. Dotted lines indicate the 99% range of shuffled cross-correlations. The marked point is the approximate center of this asymmetry, at -5 trials, and is above the chance line, indicating statistical significance at the $p < 0.01$ level. **b**, Top, as in Extended Data Fig. 13c, the center of the distribution of path-distance occupancy shifted towards the trial beginning with experience within a session. The effect is more pronounced for sessions with high performance. Middle, same as above but for the distribution of path-distance tuning curve peaks. Bottom, cross-correlation of neural and behavioral experience plots. **c**, Same as **b** but for angle goal distance. **d**, Same as **b-c** but for allocentric goal distance.

Extended Data Fig. 15 Population vector decoding of path distance and allocentric angle.

a, Decoded distance versus true distance for trials 1–15 (left) and trials 16–30 (right). **b**, Path-distance population vector overlap ([Supplementary Information](#)) between entire session activity and activity in trials 1–15 (left) or between trials 1–15 and trials 16–30 (right). Lines and dots mark the smoothed peak correlation on the right-hand plot. Black lines indicate predictive shifts and gray lines indicate postdictive shifts, with a mean value of 15 cm. **c**, Decoded angle versus true angle for trials 1–15 (left) and trials 16–30 (right). **d**, Same as **b** but for angle. The best decoded angles span 0–90°. Right, experiential shift in angle representation was modest and varied as a function of angle (mean -3.2°), which could be due to different turning behavior at specific angles or different turning biases across sessions.

Supplementary information

Supplementary Information

This file contains Supplementary Figs. 1–6 and Supplementary Methods.

Reporting Summary

Rights and permissions

Reprints and Permissions

About this article

Cite this article

Moore, J.J., Cushman, J.D., Acharya, L. *et al.* Linking hippocampal multiplexed tuning, Hebbian plasticity and navigation. *Nature* **599**, 442–448 (2021). <https://doi.org/10.1038/s41586-021-03989-z>

- Received: 14 June 2019
- Accepted: 01 September 2021
- Published: 20 October 2021
- Issue Date: 18 November 2021
- DOI: <https://doi.org/10.1038/s41586-021-03989-z>

Share this article

Anyone you share the following link with will be able to read this content:

[Get shareable link](#)

Sorry, a shareable link is not currently available for this article.

[Copy to clipboard](#)

Provided by the Springer Nature SharedIt content-sharing initiative

This article was downloaded by **calibre** from <https://www.nature.com/articles/s41586-021-03989-z>

| [Section menu](#) | [Main menu](#) |

- Article
- Open Access
- [Published: 27 October 2021](#)

The orbitofrontal cortex maps future navigational goals

- [Raunak Basu](#) [ORCID: orcid.org/0000-0001-8465-0710¹](#),
- [Robert Gebauer¹](#),
- [Tim Herfurth¹](#),
- [Simon Kolb¹](#),
- [Zahra Golipour¹](#),
- [Tatjana Tchumatchenko](#) [ORCID: orcid.org/0000-0001-9137-809X^{1,2}](#) &
- [Hiroshi T. Ito](#) [ORCID: orcid.org/0000-0001-7726-0781¹](#)

Nature volume 599, pages 449–452 (2021)

- 11k Accesses
- 213 Altmetric
- [Metrics details](#)

Subjects

- [Neural circuits](#)
- [Spatial memory](#)

Abstract

Accurate navigation to a desired goal requires consecutive estimates of spatial relationships between the current position and future destination throughout the journey. Although neurons in the hippocampal formation can represent the position of an animal as well as its nearby trajectories^{1,2,3,4,5,6,7}, their role in determining the destination of the animal has been questioned^{8,9}. It is, thus, unclear whether the brain can possess a precise estimate of target location during active environmental exploration. Here we describe neurons in the rat orbitofrontal cortex (OFC) that form

spatial representations persistently pointing to the subsequent goal destination of an animal throughout navigation. This destination coding emerges before the onset of navigation, without direct sensory access to a distal goal, and even predicts the incorrect destination of an animal at the beginning of an error trial. Goal representations in the OFC are maintained by destination-specific neural ensemble dynamics, and their brief perturbation at the onset of a journey led to a navigational error. These findings suggest that the OFC is part of the internal goal map of the brain, enabling animals to navigate precisely to a chosen destination that is beyond the range of sensory perception.

[Download PDF](#)

Main

We trained five rats on a 2-m-long linear maze with ten water delivery sites or wells (Fig. 1a, Extended Data Fig. 1). The rats were required to visit and lick two given wells alternately to obtain water rewards. The licking of the animal was detected by infrared sensors on individual wells, and water was delivered after the correct well was licked for a fixed amount of time (1 s, 1.5 s or 2 s, consistent across trials in a session). After at least six consecutive correct choices, a new pair of wells started to deliver water, enforcing the updating of goal locations. The rats learned this task over 2 weeks. We implanted a tetrode drive into the ventral and lateral parts of the OFC (Extended Data Fig. 2) and collected data from four rats across 18 sessions, each of which comprised 68–328 simultaneously recorded OFC neurons.

Fig. 1: Goal-specific firing of OFC neurons.

 **figure1**

a, Schematic of the task. **b**, Firing of two representative neurons showing spike rasters and rates over position with two running directions in black and grey (left) or over time from lick onset (right). **c**, Firing across trial blocks during running (speed $>10\text{ cm s}^{-1}$) or licking. **d**, Left, well-dependent firing across trial blocks. Middle and right,

invariant firing to the difference in running direction (middle) or starting well (right). **e**, Colour-coded rate plots along the position and navigation phase of the animal. Shown are all rewarded wells approached in the direction of the higher activity of the neuron. **f**, Distribution of peak firing along navigation phase for all OFC neurons encoding position and navigation phase. *Outlier by generalized extreme studentized deviate test (above the threshold of 607.22 neurons at $P = 0.05$). **g**, Pie charts showing the numbers of neurons with spatial and/or navigation phase tuning. **h**, Left, decoding of licking well (target) and other wells (other). Middle, decoding of run-over well against distance (left) and time (right). Right, comparison of decoding between licking and run-over well, showing individual 18 sessions (grey) and means (red). $*P = 1.96 \times 10^{-4}$ in two-sided Wilcoxon signed-rank test. **i**, Decoding of licking well when the corresponding approach direction was excluded from the training of the decoder (left) or when all trials from the corresponding goal well pair were excluded from the training of the decoder (right). In **c**, **d**, **h** and **i**, plots show mean (line) \pm s.e.m. (shaded).

We found that most OFC neurons increased their spiking as the animal approached the goal well, discriminating its location by changing firing rates (Fig. 1b–d). These neurons, however, showed less position-specific firing to the wells that the animal ran over during navigation. These observations were confirmed by plotting firing rates along maze position conjunctively with navigation phase (defined as positional fraction of journey; Fig. 1e–g). As a population, 80.8% of OFC neurons (2,366 of 2,927) exhibited some degree of spatial tuning on the maze ($z > 2.57$ in spatial correlations compared to shuffled activity), but, in most them (86.9%, 2,056 of 2,366), the spatial tuning was also dependent on navigation phase ($P < 0.05$ in spatial correlations compared to activity shuffled across different navigation phases; Extended Data Fig. 3). We further found that, during a random foraging task in an open-field arena, OFC neurons conveyed significantly lower spatial information than neurons in area CA1 of the hippocampus (Extended Data Fig. 4). These results together suggest that most OFC neurons exhibit location-selective firing in conjunction with the demand and phase of goal-directed journey.

Next, we asked how accurately OFC neurons represent the well position. We trained a decoder based on linear discriminant analysis (LDA) using the population activity of OFC neurons in the time range from 0.5 s before to 3 s after lick onset. The trained decoder was then applied to predict the well at which the animal was present ('current' well). The decoder predicted the current well above the chance from 1.7 s before to 6 s after lick onset (Fig. 1h, Extended Data Fig. 5). When the same decoder was applied to the wells that were passed through by the animal, it showed significantly lower performance (Fig. 1h, Extended Data Fig. 6). This result was also supported by poor performance of a decoder trained on the instantaneous position of the animal during running (Extended Data Fig. 6). We confirmed that the decoding of the current well

was possible irrespective of the approach direction of the animal or the starting well (Fig. [1d](#), [1j](#)), suggesting that OFC neurons form a largely viewpoint-invariant coding of spatial positions that are approached as navigational goals.

Persistent goal representation in the OFC

We then asked when the goal well representation develops in the OFC during navigation. We examined the firing rates of individual OFC neurons backwards in time towards the beginning of navigation and discovered that the rates at this time already differentiated the identity of the goal well (Fig. [2a](#)). To confirm this observation at a neural population level, we projected the ensemble activity of OFC neurons on the dimension with maximal goal well separability calculated by LDA and found that the projected activity kept differentiating the next destination throughout navigation (Fig. [2b](#)).

Fig. 2: Persistent goal representation in the OFC.



a, Firing of two representative neurons aligned to motion onset (MO) and lick onset (LO) or throughout navigation on normalized time (right). **b**, Same as **a**, except that the plots are based on ensemble neural activity projected on the axis with maximum goal well separability. **c**, Two representative trials showing the position of

the animal (black) and the decoded well (red; well with maximum decoding probability). **d**, Decoding of goal well (blue) and current well (red), together with the wells next to current goal (magenta) or before goal (cyan), plotted over time from motion onset (left) or positional fraction of journey (right). The inset on the top left shows the displacement of the animal's position. $n = 18$ sessions. **e**, Plot shows the times at which the decoding probability of the goal well first exceeded that of the current well. $n = 18$ sessions. **f**, Decoding of the goal well (as in **d**) compared to chance levels calculated on five null hypotheses (see [Methods](#)). In **a**, **b**, **d** and **f**, plots show mean (line) \pm s.e.m. (shaded). AU, arbitrary units.

Our findings of the OFC's goal representation during navigation, as well as its coding of the position of the animal during reward consumption (Fig. [1h](#)), imply a transition of spatial representation in the OFC before navigation onset. To identify such a transition, we took a decoding approach by training a decoder for goal well identity based on neural activity concatenated between the time segments at the beginning and the end of navigation ([Methods](#)). In individual trials, the decoder that initially indicated the start well of the trial exhibited an abrupt change in representation to the next goal well around the time of motion onset, which was then largely maintained during the entire journey (Fig. [2c](#)). On the trial average, the activity of OFC neurons represented the well at which the animal was present (current well) until 0.7 s before motion onset (Fig. [2d](#), left). However, in contrast to the decay of the current well representation, the activity representing the goal well became significant from 1.1 s before motion onset (Fig. [2d](#), [e](#), Extended Data Fig. [7](#)), reaching a steady peak 2.5 s after the beginning of navigation (Fig. [2d](#), left, Extended Data Fig. [5](#)). The decoding probability plotted along the positional fraction of navigation confirmed that the goal well was persistently represented throughout navigation (Fig. [2d](#), right).

To confirm the decoder's selective representation of goal well over others, we assessed the representations of wells that were passed through by the animal during navigation, particularly the wells that immediately followed the start or preceded the goal along the journey. We found that the decoding probabilities of these wells with the goal well decoder were significantly lower than that of the goal well throughout the course of navigation (Fig. [2d](#)). Additional analyses further confirmed that goal decoding was not due to other task-associated factors (Fig. [2f](#)) and that the transition of representation from the current well to the goal well did not involve sequential activation of neighbouring positions^{[3,10,11](#)} (Extended Data Fig. [8](#)). These results together suggest that the activity of OFC neurons switches their spatial representation from the starting position of the animal to the next destination before navigation onset, subsequently maintaining it throughout navigation.

We further investigated the goal representation in error trials. We applied the goal well decoder trained on correct trials to neural activity at the beginning of error trials and found that it could decode the subsequent incorrect destination of the animal as

accurately as goal wells in correct trials (Extended Data Fig. 5). The activity of OFC neurons thus represents the next target well of the animal irrespective of its correctness, reflecting the animal's decision of goal destination.

Goal coding is orthogonal to OFC dynamics

Although our decoding analysis indicates a persistent goal representation in the OFC, firing rates of individual neurons changed markedly during navigation (Fig. 1b), implying that the encoding of goal locations in the OFC is not through the convergence of neural activity towards a point attractor but likely by dynamic coding evolving over navigation (Fig. 3a). We implemented a principal component analysis (PCA) to obtain reduced dimensions of neural population activity in the OFC. We found that activity trajectories, averaged over trials based on subsequent goals, exhibited similar dynamics while maintaining separation between each other (Fig. 3b). To understand how the goals of individual trials are embedded in activity trajectories, we applied an LDA-based dimensionality reduction approach to obtain the best projections of population activity for goal well selectivity at different times of navigation ([Methods](#), Extended Data Fig. 9). The goal well separation was largely maintained during navigation, albeit it transformed from a compact to a distributed configuration as the animal approached the destinations (Fig. 3c). We also found that the major axis of goal well separation was nearly orthogonal to the direction of activity trajectories (Fig. 3d), suggesting that goal locations are encoded largely independently of the evolution of dynamics. We, therefore, asked whether the dynamics of individual trials could be modelled independently of their goal selectivity. First, the destination-specific activity extracted by LDA was projected back to the original neuronal dimensions, forming time courses of goal-dependent dynamics by minimising activity irrelevant to goal coding (Fig. 3e, left). We then fitted a first-order linear dynamic model on neural activity trajectories of a 2.5-s duration from motion onset to capture the global trend of dynamics irrespective of destinations ([Methods](#)). Finally, the constructed model was fed with the neural activity at motion onset, generating simulated trajectories up to 2.5 s afterwards. We found that the simulated trajectories evolved in a similar manner as the original ones (Fig. 3e, right), which was confirmed by the improvement of goal well decoding over the time course of navigation (Fig. 3f). We further found that our first-order model, trained on correct trials, was also able to simulate the neural activities on error trials, in which the activity evolved to indicate the incorrectly visited destination of the animal (Fig. 3f). OFC neurons thus encode the destination of the animal orthogonally to the ensemble dynamics that evolve, at least in part, deterministically from navigation onset.

Fig. 3: Orthogonal coding of spatial goals to evolving OFC dynamics.

 **figure3**

a, Illustration of dynamic coding. Left, firing of three neurons aligned to motion onset. Right, firing of the same neurons plotted on individual axes of a three-dimensional space, forming similarly shaped activity trajectories separated from each other depending on future goals. **b**, Ensemble activity of OFC neurons in reduced dimensions using PCA plotted separately aligned to motion and subsequent lick onsets (left) or in normalized time (right). Shown are trial averages based on goal wells. **c**,

Ensemble neural activity in individual trials projected on the axes with maximal goal well separability using LDA, calculated at individual time points and reduced to two dimensions using Isomap³⁰. Opaque circles with error bars denote mean \pm s.e.m for each well. **d**, Relationship between the evolution of dynamics and the goal well separability. Top, as in **a**, along with the axis of maximum well separability (first LDA dimension). Instantaneous velocities of neural trajectories are shown with arrows. Bottom, plot shows angular differences (in degrees) between the velocity vectors and the major LDA axis from individual 18 sessions (thin) and means (thick). **e**, Plot shows three principal components (PCs) of neural activity trajectories from individual trials extracted using LDA ([Methods](#)). Left, original trajectories from neural data, separately aligned to motion onsets (thin) and lick onsets (thick). Right, simulated trajectories from the first-order linear dynamic model fed with neural activity at motion onset. **f**, Top, goal decoding from the real (original) and the simulated (model) trajectories. Bottom, destination decoding between correct and error trials from the simulated trajectories. Dashed lines indicate chance levels. In **a** and **f**, plots show mean (line) \pm s.e.m (shaded). $n = 18$ sessions. AU, arbitrary units.

OFC perturbation led to a navigational error

Finally, we asked whether the activity of OFC neurons causally influences the destination of the animal. We first confirmed that pharmacogenetic inactivation of OFC neurons resulted in a significant increase in the animal's incorrect choices of destination (Extended Data Fig. [10](#)). To address whether the effect of perturbation is specific to ongoing navigation, we injected adeno-associated virus (AAV) encoding the excitatory opsin bReaCh-ES-eYFP¹² followed by implantation of optic fibres in the bilateral OFC in three rats (Fig. [4a](#)). We chose the frequency and power of stimulation that elicited reliable spiking in OFC neurons without affecting the motion of the animal (Extended Data Fig. [10](#)). When laser pulses were applied for a 40-s duration, the animals started making more errors immediately after the onset of perturbation (Fig. [4b, c](#)), which gradually subsided after the termination of laser pulses.

Fig. 4: OFC perturbation impairs accurate navigation.

 **figure4**

a, Top, coronal section showing expression of bReaCh-ES-eYFP (green). Dotted white lines indicate the positions of optic fibres. Bottom, plot shows spike rasters and mean rates of a representative OFC neuron during a 6-s laser pulse train (15-ms pulses at 5 Hz). $n = 14$ trials. Scale bar, 2 mm. **b**, Plot shows a representative behaviour of the bReaCh-ES-expressing animal. The position of the animal is plotted over time (black line), together with the licking of the animal at either correct (blue) or incorrect (red) wells. Previous block errors are shown with arrows. **c**, Error rates of the animals before, during and after a 40-s laser pulse train (mean \pm s.e.m.). Errors to the wells rewarded in the previous block are shown separately. $**P < 0.01$ or $*P < 0.05$ in two-sided Wilcoxon signed-rank test with post hoc Bonferroni correction. $n = 12$ sessions from three rats. **d**, Error rates of the animals subjected to a 6-s laser pulse train applied at motion onset (black) or lick onset (grey). Error bars denote s.e.m. $n = 9$ sessions from three rats. $*P = 0.020$ or $**P = 0.008$ in two-sided Wilcoxon signed-rank test.

We then asked whether the effect of perturbation is stronger during the development of goal representation in the OFC. To explore this possibility, we applied laser pulses of 6-s duration either at motion onset or at lick onset (Extended Data Fig. 10) and found that the pulses applied at motion onset caused more errors in the subsequent navigation of the animal (Fig. 4d). This deficit was largely recovered in the immediately succeeding trial, suggesting that the impairment is not due to general loss

of goal memory. The activity of the OFC is thus crucial for determining the next destination of the animal, particularly at navigation onset when a goal representation develops in its ensemble activity.

Discussion

In this study, we identified the OFC as a brain region that represents the subsequent destination of an animal throughout navigation. Neural activity correlated with the goal-directed trajectories of animals has been previously described in the rodent hippocampus in the form of brief sequential firing among place cells^{5,6}. However, this activity encodes not only a particular location of interest but also its nearby positions due to the sequential nature of hippocampal spatial coding¹³, and several studies have cast doubt on its role in determining the destination of animals^{8,9}. Studies in human subjects, by contrast, described the activity modulation in the hippocampus that depends on the next destination instructed by a given cue^{14,15}. It is yet unclear whether this modulation represents the goal location itself or its associated instructive cue or how it can be integrated with a hippocampal spatial map to point to the exact goal position. Goal coding in the OFC is different. The activity of OFC neurons encodes accurate well positions on the maze and exhibits an abrupt transition of encoding position from the location of the animal to its destination without relying on external sensory cues. This goal representation, developed before navigation onset, is then maintained throughout navigation without representing nearby positions or trajectories.

The prefrontal cortex has been considered a key area for navigation¹⁶. Lesioning of its ventromedial region, including the OFC, has been reported to impair accurate targeting to a destination in humans and rats^{17,18}. The activity of the OFC is modulated during goal-directed motion^{19,20} or navigational planning¹⁵, and we discovered, in this study, that it can form a representation of spatial goals. The decision of navigational goal requires a choice among available positions. This is consistent with a previously suggested role for the OFC in choice decisions based on prior history of choices and subsequent outcomes^{21,22,23,24}. The representation of spatial goal, however, needs to satisfy additional cognitive demand for navigation. Although accurate coding of spatial position requires sensory and proprioceptive inputs, the emergence of goal representation, as well as its persistence during navigation, indicate suppression of these inputs along the goal-directed journey. This resistance of goal representation to incoming inputs appears to be achieved by dynamic coding. Unlike place cells¹ or grid cells⁴, OFC neurons discriminate positions in a dynamic manner, whereby neural activity changes during navigation while optimising the separation of encoded destinations. Dynamic coding of behavioural variables has been described in many brain regions and species^{25,26,27,28} and is thought to minimize interference between

orthogonal neural activity subspaces^{28,29}. Goal coding in the OFC might then be used in downstream circuits to form goal-directed trajectories, enabling animals to navigate from one location to another by relying on a cognitive map.

Methods

Subjects

All experiments were approved by the local authorities (RP Darmstadt, protocols F126/1009 and F126/1026) in accordance with the European Convention for the Protection of Vertebrate Animals used for Experimental and Other Scientific Purposes. Nineteen male Long-Evans rats weighing 400–550 g (aged 3–6 months) at the start of the experiment were housed individually in Plexiglass cages (45 × 35 × 40 cm; Tecniplast, GR1800) and maintained on a 12-h light/dark cycle, with behavioural experiments performed during the dark phase. For experiments in the linear maze, the animals were water restricted with unlimited access to food and kept at 90% of their free-feeding body weight throughout the experiment. For recordings in the open-field arena, the animals were food restricted with unlimited access to water and kept at 85–90% of their free-feeding body weight. Four of the rats had tetrodes implanted in the OFC, and one had tetrodes implanted in the hippocampus. Two rats had a silicon probe (Buzsaki64sp, NeuroNexus) implanted in the OFC, which was used for recordings in a modified T-maze task (Extended Data Fig. 5d). Seven rats received AAV injections in the OFC—four of them for designer receptors exclusively activated by designer drugs (DREADD) experiments and three for optogenetic experiments. Five rats, used only for behaviour analysis, received a metal implant on their skull to hold LEDs for position tracking. No statistical method was used to predetermine the sample size.

Surgery, virus injection and drive implantation

Anaesthesia was induced by isoflurane (5% induction concentration, 0.5–2% maintenance adjusted according to physiological monitoring). For analgesia, Buprenovet (buprenorphine, 0.06 mg ml⁻¹; WdT) was administered by subcutaneous injection, followed by local intracutaneous application of either bupivacain (bupivacain hydrochloride, 0.5 mg ml⁻¹, Jenapharm) or ropivacain (ropivacain hydrochloride, 2 mg ml⁻¹, Fresenius Kabi) into the scalp. Rats were subsequently placed in a Kopf stereotaxic frame, and an incision was made in the scalp to expose the skull. After horizontal alignment, several holes were drilled into the skull to place anchor screws, and craniotomies were made for microdrive implantation. The microdrive was fixed to the anchor screws with dental cement, and two screws above the cerebellum were connected to the electrode's ground. All animals received

analgesics (Metacam, 2 mg ml⁻¹ meloxicam, Boehringer Ingelheim) and antibiotics (Baytril, 25 mg ml⁻¹ enrofloxacin, Bayer) for at least 5 d after the surgery.

For tetrode recordings, rats were unilaterally implanted with a microdrive that contained individually adjustable tetrodes made from 17-mm polyimide-coated platinum–iridium (90–10%, California Fine Wire, plated with gold to impedances below 150 kΩ at 1 kHz). The tetrode bundle consisted of 30-gauge stainless steel cannulae, soldered together in circular or rectangular shapes. The drives were implanted in the OFC of the left hemisphere in four rats with the following coordinates and bundle designs: Rat 110 with a 14-tetrode rectangular bundle (anterior–posterior (AP): 2.75–4.5 mm, medial–lateral (ML): 1.5–2.5 mm alongside the anteroposterior axis); Rat 175 with a 28-tetrode rectangular bundle (AP: 2.75–4.9 mm, ML: 1.2–2.7 mm); Rat 182 with a 42-tetrode rectangular bundle (AP: 2.75–5 mm, ML: 1.2–3.0 mm); and Rat 284 with a 42-tetrode circular bundle (AP: 2.75–5.25 mm, ML: 1.0–3.5 mm). Tetrodes were implanted at an initial depth of 2 mm dorsoventral (DV) from the dura and progressively lowered to the final depths of 2.5–4.5 mm. For the recording from neurons in area CA1 of the hippocampus (Extended Data Fig. 4), a circular bundle of 14 independently movable tetrodes was implanted in the right hemisphere (AP: −3.5 mm, ML: 3.5 mm). For the recording from neurons in the OFC in a modified T-maze task (Extended Data Fig. 5d), a silicon probe was implanted in the right hemisphere (AP: 3.5 mm, ML: 2 mm). Experiments began at least 1 week after the surgery to allow the animals to recover.

For optogenetic perturbation of OFC neurons, AAV1-CamKII-bReaCh-ES-EYFP (a gift from K. Deisseroth)¹² was injected into three sites in both hemispheres of the OFC (AP, ML and DV in mm: 3, 3, 4.5; 3.5, 2.8, 4.25; 4, 2.5, 4, respectively). The AAV was injected with an infusion rate of 100 nl min⁻¹ using a 10-ml NanoFil syringe and a 33-gauge bevelled metal needle (World Precision Instruments). After injection was completed, the needle was left in place for 10 min. The volume of 500 nl was injected at each site. Two optic fibres (FP400URT, Thorlabs) were implanted with their tips positioned at approximately 500 μm above the OFC of both hemispheres (AP: 3.5 mm, ML: 2.8 mm and DV: 3.25 mm). The optic fibre in the left hemispheres had two tetrodes attached, with their positions advanced approximately 750 μm from the fibre tip to monitor the neural activity nearby. The virus injection and the optic fibre implantation were performed in the same surgery, and experiments started at least 4 weeks after the surgery.

Behavioural methods

Rats were trained in the 2-m-long linear maze with ten reward wells distributed at an equal distance (20 cm) between each other. The training procedure consisted of three phases. In the first phase, 100 μl of liquid reward (0.3% saccharin) was manually

delivered at two specific wells alternately. Most rats learned to lick wells within 2 d of training. In the second phase, rewards were delivered only after the rat licked the correct wells, but, here, a reward was delivered immediately after the animal's correct lick. The training duration for this phase lasted for 1–7 d, depending on the individual rats. In the final phase, a transition rule was introduced. Once the rat made at least six consecutive correct trials, rewards were delivered in a new pair of wells, which was signalled by LEDs, positioned directly underneath all the ten wells on the maze, together with the delivery of water rewards at the new well pair. These LEDs thus did not give any position information, and the new goal wells were pre-filled with water before the animal's approach. The LEDs turned off once the animal consumed these rewards. Furthermore, the animal was required to keep licking the correct well for a fixed amount of time, defined as lick threshold, for a reward to be delivered. Of all the 18 neural recording sessions, the lick threshold was set to 2 s for 12 sessions, 1.5 s for one session and 1 s for five sessions, respectively (Extended Data Fig. 1). The lick threshold was set to 1 s for all DREADD-mediated silencing, optogenetic perturbation and modified T-maze experiments. The licking of the animal was continuously monitored by infrared sensors (Turck) equipped on individual wells, and, once the duration of the animal's licking exceeded a pre-defined threshold, a tone was generated, followed immediately by the delivery of water with a peristaltic pump (Cole-Parmer). The details of licking behaviours are shown in Extended Data Fig. 1f–h, and the difference of lick threshold did not affect the decoding performance significantly (Extended Data Fig. 1i).

The behavioural analyses (Extended Data Fig. 1) started from the first day of phase 3 training, and each session lasted for 30 min. Neural recording sessions were carried out after the animals reached steady levels of behavioural performance (with stable prior block error rates over a period of three consecutive days—usually achieved within 15 d of training). Trials during the transition to a new well pair were discarded from the analyses. Although one of the rewarded wells in one block could be rewarded again in the immediately succeeding block, this did not affect the learning rate of the animal compared to the blocks where both goal wells were changed (Extended Data Fig. 1j). The number of wells used in each recording session was as follows (out of all ten wells): ten wells in one session, eight wells in five sessions, seven wells in eight sessions and six wells in four sessions. The position and head direction of the animal were monitored with two-coloured LEDs on the head stage at the sampling rate of 25 Hz. All the recordings were performed under a minimum-light condition (no light source in the recording room, with only weak ambient light coming from the adjacent room from computer monitors).

For optogenetic experiments, laser pulses (15-ms width at 6 Hz) were generated from a 561-nm DPSS laser unit (Dragon Laser) for a fixed amount of duration of either 40 s or 6 s. The laser power at the fibre tip in each hemisphere was 1.5 mW. The onset of laser pulses was manually triggered based on the behaviour of the animal on the task,

and the time stamps of the pulses were recorded. Perturbation experiments were performed after the animals reached steady levels of behavioural performance (observed as stable prior-block error rates over 3 d; Extended Data Fig. 10).

Histological procedures

Once the experiments were completed, the animals were deeply anaesthetized by sodium pentobarbital and perfused intracardially with saline, followed by 10% formalin solution. The brains were extracted and fixed in formalin for at least 72 h at 4 °C. Frozen coronal sections were cut (30 µm) and stained using cresyl violet and mounted on glass slides.

Spike sorting and cell classification

All data processes and analyses were performed with MATLAB (MathWorks). Neural signals were acquired and amplified using two or four 64-channel RHD2164 headstages (Intan Technologies), combined with an OpenEphys acquisition system with the sampling rate at 15 kHz. The signals were band-pass filtered at 0.6–6 kHz, and spikes were detected and assigned to separate clusters using Kilosort³¹ (<https://github.com/cortex-lab/KiloSort>) under the parameter settings of the spike threshold at -4 and the number of filters at $2\times$ the total channel number. Each tetrode was independently grouped with ‘kcoords’ parameters, and the noise parameter determining the fraction of noise templates spanning across all channel groups was set to 0.01. The obtained clusters were checked and adjusted manually based on autocorrelograms and waveform characteristics in principal component space, obtaining well-isolated single units by discarding multi-unit activity or noises. Neurons with firing rates less than 0.5 Hz were excluded. Spike times were converted into firing rates, except for the analyses for the open-field experiment (Extended Data Fig. 4) and the conjunctive coding of spatial location and navigation phase (Fig. 1e, Extended Data Fig. 3). The firing rate estimation was performed by convolving spike times by a Gaussian kernel with a bandwidth of 250 ms.

Cell classification

Spatial selectivity

Firing rates of a neuron were assessed at individual spatial bins of 10 cm along the linear maze across trials. For each spatial bin, random sampling was performed 100 times at various epochs of the session, either when the animal was moving (running speed $>10\text{ cm s}^{-1}$) or not moving (running speed $<10\text{ cm s}^{-1}$), obtaining 200 samples of firing rates per spatial bin (Extended Data Fig. 3). By concatenating these samples

across the bins, we created the firing rate distributions of 200 pseudotrials along the maze and evaluated the consistency of spatial tuning by computing pairwise dot products between them. The average of the dot products was considered as a representative value of spatial tuning of the cell. For the corresponding null hypothesis, we shuffled the neural activity between spatial bins for individual pseudotrials and calculated the average dot product between them. This entire process of generation of pseudotrials, as well as calculation of the average dot products for the real and shuffled data, was repeated 1,000 times. The difference between the two distributions was quantified as follows:

$$z = \frac{\mu_r - \mu_s}{\sqrt{\sigma_r^2 + \sigma_s^2}}$$

where μ and σ denote the mean and standard deviation, respectively. Neurons with z -scores exceeding 2.57 (corresponding to $P < 0.01$ in a two-tailed distribution) were categorized as spatially selective. To consider a possible directional tuning of a neuron on the maze, we restricted the analysis to the movement direction with a higher mean firing rate for each neuron.

Among cells categorized as spatially selective, we asked whether spatial tuning of these neurons also depends on the phase of navigation. To address this question, each navigation journey was discretized into eight equidistant positional fractions, and the firing rates at individual fractions or phases were assessed together with the absolute positions of the animal on the maze, by forming a firing rate matrix of phase and position (for example, Fig. 1e, Extended Data Fig. 3). To assess whether a neuron encodes phase and position conjunctively, the firing rate matrix was mean centred (the mean navigation-phase-dependent firing rate was subtracted from each column) and assessed for bias in firing rates relative to navigation phases. This bias was estimated by calculating the Frobenius norm of the mean centred matrix, which is defined as the square root of the sum of squared matrix elements. The statistical significance was assessed by calculating a distribution of Frobenius norms from 1,000 shuffled datasets among eight navigation phases. Neurons with the Frobenius norms exceeding the 95th percentile of the shuffled distribution were considered to encode position and navigation phase conjunctively.

Two-dimensional firing rates and spatial information calculation

The arena (120×120 cm for OFC or 100×100 cm for CA1) was divided into 5×5 -cm spatial bins, and the number of spikes and the overall time spent within individual bins during motion (>7.5 cm s $^{-1}$) was calculated. The firing rate at each bin was estimated

using an adaptive smoothing technique that optimizes the tradeoff between spatial resolution and sampling error³². In brief, for each spatial bin, an expanding circle was constructed until the following criterion was satisfied:

\$\$r > \frac{\alpha}{n_o c c} \sqrt{n_s s p i k e} \}

where $\backslash(r)$ is the radius of the circle in bins, $\backslash(\{ n\} _ \{ \{ \backslash rm\{ o\} \} \{ \backslash rm\{ c\} \} \{ \backslash rm\{ c\} \} \})$ is the number of samples occupied within the radius $\backslash(r)$, $\backslash(\{ n\} _ \{ \{ \backslash rm\{ s\} \} \{ \backslash rm\{ p\} \} \{ \backslash rm\{ i\} \} \{ \backslash rm\{ k\} \} \{ \backslash rm\{ e\} \} \{ \backslash rm\{ s\} \} \})$ is the number of spikes within the radius and $\backslash(\alpha)$ is a constant set to 200,000. Our positional sampling was interpolated to 1-ms resolution. Hence, $\backslash(\{ n\} _ \{ \{ \backslash rm\{ o\} \} \{ \backslash rm\{ c\} \} \{ \backslash rm\{ c\} \} \})$ was the number of milliseconds the animal spent within a circle of radius r centred at the bin. Firing rate (spikes per second) in a given bin was calculated as $1,000 \times \backslash(\{ n\} _ \{ \{ \backslash rm\{ s\} \} \{ \backslash rm\{ p\} \} \{ \backslash rm\{ i\} \} \{ \backslash rm\{ k\} \} \{ \backslash rm\{ e\} \} \{ \backslash rm\{ s\} \} \}) / \backslash(\{ n\} _ \{ \{ \backslash rm\{ o\} \} \{ \backslash rm\{ c\} \} \{ \backslash rm\{ c\} \} \})$. Spatial information for individual neurons in the OFC and CA1 was obtained from the rate maps using the following formula⁵²:

```
$$\sum_{i=1}^N p_i \frac{\lambda_i}{\lambda_i + \lambda_o g_i^2}$$
```

where $\langle N \rangle$ is the total number of spatial bins, $\langle p_i \rangle$ is the probability of occupying the i th bin, $\langle \lambda_i \rangle$ is the firing rate in the i th bin and $\langle \lambda \rangle$ is the overall average firing rate of the neuron. The same formula was used to calculate spatial information of OFC neurons on the linear track.

Well selectivity

The neuron's selectivity for goal well was assessed based on its firing rates for each of 100-ms bins in the time range of -0.5 s to 2 s relative to motion onset of navigation, whereas the selectivity for the animal's licking well (or current well) was assessed from its firing rates in the time range of -0.5 s to 2 s relative to the animal's lick onset. To account for potential confounds of direction-specific firing, we used a two-way ANOVA with the well identity and the direction of the animal's approach as two independent variables and the firing rate as a dependent measure. We used the 'anovan' function of MATLAB and used the type-II sum of squares for individual variables. Based on the P values for the well identity across all time points, we assessed the neuron's selectivity to goal well and current well independently (a neuron can be categorized as both goal well and current well selective).

For the decoding analysis in Figs. 1, 2, we pre-selected neurons for a decoder based on a criterion of $P < 0.05$ at least in one of the time points in the range of -0.5 s to 2 s

relative to the onset of either motion or licking. This procedure excluded neurons that were non-selective for the well identity, reducing the number of uninformative dimensions. For the visualization of neural activity trajectories in PCA-based reduced dimensions in Fig. 3b, we used a more stringent criterion of P values less than 0.01 over at least five consecutive time bins (500 ms) for the goal well selectivity.

Although the well selectivity was separately assessed for the current well or the goal well, we found that $83.03 \pm 1.37\%$ of the goal-well-selective neurons (by the criterion of $P < 0.05$) were also current well selective, and $69.38 \pm 2.55\%$ of the current-well-selective neurons were also goal well selective, suggesting overlaps of the two populations (Extended Data Fig. 3).

Decoding analysis

We applied a decoder based on LDA that assigns individual class probabilities by setting class boundaries between multivariate Gaussian distributions fitted to data. In brief, a dataset from each recording session was divided into a training dataset and a test dataset, and a decoder was constructed from the training dataset by employing multiclass one-versus-one LDA using the ‘fitcecoc’ function of MATLAB with a regularization factor of 0.5 to reduce overfitting. We used uniform priors for all decoders. Next, we used the ‘predict’ function of MATLAB to obtain decoding probabilities of individual wells from the test dataset. This function uses an algorithm described by Hastie and Tibshirani³³ to compute posterior probabilities from the pairwise conditional probabilities obtained using multiclass one-versus-one decoders. The trials during transition phases to new well combinations were excluded, and only correct trials were used for the decoder’s training. The unvisited wells in each session were excluded in the calculations of both decoding performance and its corresponding chance level. A population of neurons used for a respective decoding analysis for current well or goal well were pre-selected based on their well selectivity (using the method described in the previous section) because this procedure improved a decoder’s performance with better generalization to test data (Extended Data Fig. 7c, h), which is likely due to the reduction of unnecessary dimensions from uninformative neurons. For cross-validation of decoding performance, the training data of a decoder comprised all trials except the trial tested with the decoder as well as the one prior to this trial (that is, leave-two-out cross-validation). Additional details specific to each analysis are described in the following sections.

Current well decoding

In the decoding analysis of the animal’s licking well (Fig. 1h,i, Extended Data Fig. 5), the data used for the training of a decoder comprised firing rate vectors of neurons (pre-selected based on their current well selectivity) at individual 100-ms bins in the

range of -0.5 s to 3 s relative to lick onset, resulting in 36 rate vectors for the class label of licking well. This relatively long range of data (-0.5 s to 3 s) was chosen for a better generalization of well decoding over licking time (Extended Data Fig. 5j). Then, by using this decoder, we obtained the decoding probabilities of individual wells for all the 100 -ms bins from -3 s to 6 s relative to lick onset (Fig. 1h, left) or from the beginning (motion onset) to the end (lick onset) of navigation (Fig. 1h, middle). For computing the decoding probability of the well that was run over by the animal, we restricted the analysis on trials when the animal's running speed at the well exceeded 20 cm s $^{-1}$ in a 500 -ms window.

As a control analysis of decoding (Fig. 1h), we tested whether the well decoding depends on the direction of the animal's approach (Fig. 1i, left). We trained a decoder from the data in which particular wells were approached only from one side of the linear maze and then tested the decoding performance when the animal approached the same wells from the other direction. We ensured that the decoder was trained with more than ten trials in which the target well was approached from one direction.

As another control analysis (Fig. 1i, right), we tested the possibility that the well decoding might depend on its paired wells in individual trial blocks. For this aim, we assessed the decoding performance of the wells when they are approached from newly paired wells. We trained a decoder with the data that excluded a trial block of a particular well combination but included the blocks in which the same wells were approached from other paired wells. We then tested the decoding performance of the wells approached from the pairs not used in the decoder's training. The motivation behind this analysis is that, if the well identity is encoded by OFC neurons based on its spatial location, it should be decoded irrespective of its paired wells (or the animal's start positions). The decoding was performed only when the target well was approached by the animal more than ten times in the training dataset.

Goal well decoding

For the decoding of the animal's goal well, we constructed a decoder based on the assumption that the goal well should be represented with the same pattern of neural activity between the beginning and the end of navigation (Fig. 2b). We thus trained the decoder from the data concatenated across two time ranges around motion onset and lick onset. We found that a dimensionality reduction procedure of the neural activity by PCA improved the subsequent decoding performance (Extended Data Fig. 7), likely because this decoding strategy entailed the construction of high-dimensional hyperplanes by concatenating two different time phases of the neural activity, and a dimensionality reduction procedure helped to constrain the hyperplane in a small number of crucial dimensions, thereby improving generalization of the decoder. Before implementing PCA, we used a soft-normalization technique described by

Churchland et al. [34](#) to adjust the range of firing rates across the neural population that were pre-selected based on their goal well selectivity (with the method described in the previous section). We then selected PCA dimensions that explain 85% of the data variance across the entire time duration of a recording session, obtaining the neural population activity in reduced dimensions. For each trial, vectors of the population activity in 100-ms bins were concatenated in the time range of -0.5 s to 0.5 s relative to motion onset, together with that of -0.5 s to 1 s relative to the subsequent lick onset at the destination, forming 27 vectors with the class label of goal well. These time ranges were chosen to capture the neural dynamics from the beginning to the end of navigation (Extended Data Fig. [7f](#)).

The decoding was performed on the test dataset in the time range of either from -2 s to 2.5 s relative to motion onset (Fig. [2d](#), left) or from 1 s before motion onset to the subsequent lick onset at the goal well (Fig. [2d](#), right). The trials in which the goal wells were immediately adjacent to the animal's current wells were excluded from the analysis.

Chance level calculation

We tested a possibility that the goal well decoding could be explained by the neural activity encoding a task-relevant parameter other than the spatial position of goal well. We calculated five chance levels for goal well decoding, each of which corresponds to a specific null hypothesis (Extended Data Fig. [5](#)).

We first tested the possibility that the goal well was not decoded based on its own identity. This possibility was tested by assessing the decoding performance when the well identities were exchanged by shuffling the class labels of training datasets.

We next asked whether the observed goal decoding can be explained by the animal's running direction, speed, acceleration or trajectory length. To test these null hypotheses, we divided the training dataset into multiple groups. For testing the effect of running direction, we split the trials into two groups, each containing trials with the same running direction on the linear maze. Similarly, for testing the effect of trajectory distance, we divided the trials into groups of different trajectory lengths measured in terms of the number of wells between animal's current and goal location; for testing the effect of running speed or acceleration, the trials were categorized into two groups (split across the median; analysis with quartile splits was also performed in Extended Data Fig. [5](#)) according to the animal's running speed or acceleration at motion onset. We then trained a decoder based on the training dataset with the class labels shuffled within individual groups. This procedure provides an estimate of how much well decoding can be possible with the neural activity difference resulting from a given

behavioural parameter (without using precise well labelling for the decoder's training), serving as an additional chance level.

The chance level calculation across all the sessions was implemented as follows. We first performed the decoding of all trials in a session using a decoder with shuffled class labels (as described above) and took the mean of decoding probability of the goal well. This process was repeated 100 times, resulting in a shuffled goal decoding distribution in each session. Examples of goal decoding from individual sessions and their corresponding chance levels (defined as 95th percentile of the corresponding shuffled distribution) are included in Extended Data Fig. 5. The subsequent computation of chance level across all the 18 sessions can intuitively be considered as a procedure to obtain a distribution of the means of 18 independent random variables. We randomly chose one sample from each of the 18 shuffled goal decoding distributions (with 100 samples each) and took their average, obtaining a representative of the session-averaged shuffled decoding probability of the goal well. This procedure was repeated 1,000 times to obtain a distribution of the means of shuffled goal decoding probability across the sessions. The chance level was set at the 95th percentile of the distribution.

The individual chance levels are depicted in Fig. 2f. To calculate the significance level of the decoding analysis in Fig. 2d, we used an aggregate chance level by taking the maximum of the five chance levels at each time point. For the decoding analysis of the animal's licking well (Fig. 1h,i), we used only two null hypotheses by excluding the ones for the animal's running speed, acceleration and trajectory length, as they are relevant only when the decoding includes a navigation phase.

Supervised dimensionality reduction with LDA

LDA was applied for a dimensionality reduction procedure in Figs. 2b, 3c, 3e,f and Extended Data Fig. 9. In contrast to an LDA-based decoder that calculates class boundaries (described in the previous section), the LDA-based dimensionality reduction technique searches for a subspace onto which the projected data exhibit the best separation between categories. The detailed procedures of data matrix manipulations are described step-by-step as follows.

LDA is a supervised linear dimension reduction technique that computes a subspace with the maximum linear separability of data according to class labels. Formally, for C classes, LDA computes at most $C - 1$ eigenvectors corresponding to the eigenvalues of

$$\$\$ \{ (\{ S \} _\{ \backslash rm{w} \}) \} ^\{ -1 \} \{ S \} _\{ \backslash rm{b} \} \} \$\$$$

where $\langle\langle S \rangle\rangle_{\langle\langle \rm{w} \rangle\rangle}$ is the average within-class covariance matrix, and $\langle\langle S \rangle\rangle_{\langle\langle \rm{b} \rangle\rangle}$ is the covariance matrix of class means relative to the mean of all classes. Projecting the data on the subspace constructed by these eigenvectors results in the data with reduced dimensions by maintaining the maximum linear separability between classes. A subspace was calculated at each time point without concatenating the data over time for the analyses in Fig. 3c,e,f and Extended Data Fig. 9.

In the analysis in Fig. 2b, we projected the neural activity on the first LDA dimension (corresponding to the largest eigenvalue) to show the target-well-specific activity during the navigation. To find the common LDA dimensions across navigation, we used the neural activity data around the times of both motion and lick onsets of navigation (the same approach as the goal well decoding described in the previous section).

This procedure was also used to construct goal-well-specific neural trajectories by reducing goal-irrelevant activity (Fig. 3c,e,f, Extended Data Fig. 9). First, we carried out a general de-noising step by projecting neural activity to PCA dimensions that explain 85% of data variance (identical to the step described in the goal decoding section). Next, we applied the LDA-based dimensionality reduction procedure at individual time points of navigation. However, due to high-dimensional input data with a small sample number, LDA might overfit the subspaces resulting in poor generalization. We thus took two approaches to prevent this problem: regularization and cross-validation. For the regularization, we calculated the eigenvectors of the following matrix with a regularization factor:

$$\$\$ \langle\langle S \rangle\rangle_{\langle\langle \rm{w} \rangle\rangle} + \lambda I \rangle^{-1} \times \langle\langle S \rangle\rangle_{\langle\langle \rm{b} \rangle\rangle} \$\$$$

where I is the identity matrix, and λ is the regularization factor set to 1 (different values of λ are tested in Extended Data Fig. 9). For the cross-validation procedure, we estimated LDA subspaces at individual time points of a particular trial from the training dataset excluding this trial (that is, leave-one-out cross-validation).

Because this procedure generated different subspaces (or axes) for individual trials, we projected the activity in the subspaces back to the original neural space common to all trials. For example, supposing that the data comprised d -dimensional neural data with C classes, the processed neural activity at a given time point of a trial was computed by using the following formula:

$$\langle\langle \bf{x} \rangle\rangle = \langle\langle \bf{p} \rangle\rangle \langle\langle \bf{r} \rangle\rangle \langle\langle \bf{o} \rangle\rangle \langle\langle \bf{c} \rangle\rangle = \langle\langle \bf{x} \rangle\rangle - \langle\langle \boldsymbol{\mu} \rangle\rangle \langle\langle \bf{t} \rangle\rangle \langle\langle \bf{r} \rangle\rangle \langle\langle \bf{a} \rangle\rangle$$

$$\{\rm i\}\{\rm n\})\times M\{M\}^+ + \{\boldsymbol{\mu}\}_t\{\rm r\}\{\rm a\}\{\rm i\}\{\rm n\})$$

where $\{\bf x\}$ is a $1 \times d$ vector of the original neural population activity, $\{\boldsymbol{\mu}\}_t$ is a $1 \times d$ vector of the mean neural activity of the training dataset, M is a $d \times (C-1)$ matrix representing a transformation to the subspace computed by the regularized LDA based on the training dataset, M^+ is the pseudo inverse of M and $\{\bf p\}$ is a $1 \times d$ vector of the processed neural activity. This entire procedure resulted in de-noising of neural signals according to LDA-based classification while maintaining the number of input dimensions (illustrated with examples in Extended Data Fig. 9).

Linear modelling of neural dynamics

A regularized first-order linear dynamic model was used to simulate the neural activity dynamics during navigation (Fig. 3e,f). Modelling of a linear dynamic system can be considered a multiple linear regression problem in the following form:

$$\dot{X} = XA$$

in which the matrix A transforms the activity vector to the corresponding velocity vector. The regularized matrix A can be obtained with the following calculation:

$$A = (X^T X + \mu I)^{-1} X^T \dot{X}$$

where X is a data matrix with the activity at different times or trials in the row and the neuronal identities in the column, \dot{X} is the time derivative of X , μ is a regularization factor set to 5 (different values of μ were tested in Extended Data Fig. 9) and I is the identity matrix. For example, in the dataset with p trials, T time bins and d neurons, the matrix X is created by concatenating all $p \times T$ data points, resulting in a $pT \times d$ matrix. Time-derivative components $\{\dot{x}\}_t$ in the matrix \dot{X} were computed as follows:

$$\dot{x}_t = (x_{t+1} - x_{t-1})/2$$

where x_{t+1} and x_{t-1} are the activity vectors at the time step of $t+1$ and $t-1$, respectively. The neural data used for model construction was pre-processed with the LDA-based de-noising approach described in the previous section. To account for non-linear neural trajectories with linear models, we fitted a linear dynamic model at every

500 ms of the neural data. Individual trajectories were simulated using the following equation in an iterative form:

$$\$ \$ \{ \{ \text{\bf{x}} \} \} _ \{ t \} ^ \{ \{ \text{\rm{s}} \} \{ \text{\rm{i}} \} \{ \text{\rm{m}} \} \} = \{ \{ \text{\bf{x}} \} \} _ \{ t-1 \} ^ \{ \{ \text{\rm{s}} \} \{ \text{\rm{i}} \} \{ \text{\rm{m}} \} \} + \{ \{ \text{\bf{x}} \} \} _ \{ t-1 \} ^ \{ \{ \text{\rm{s}} \} \{ \text{\rm{i}} \} \{ \text{\rm{m}} \} \} \times A \$ \$$$

starting with the neural activity at motion onset:

$$\$ \$ \{ \{ \text{\bf{x}} \} \} _ \{ 1 \} ^ \{ \{ \text{\rm{s}} \} \{ \text{\rm{i}} \} \{ \text{\rm{m}} \} \} = \{ \{ \text{\rm{m}} \} \{ \text{\rm{o}} \} \{ \text{\rm{t}} \} \{ \text{\rm{i}} \} \{ \text{\rm{o}} \} \{ \text{\rm{n}} \} \{ \text{\rm{o}} \} \{ \text{\rm{n}} \} \{ \text{\rm{s}} \} \{ \text{\rm{e}} \} \} \\ \{ \text{\rm{t}} \} ^ \{ \{ \text{\rm{d}} \} \{ \text{\rm{a}} \} \{ \text{\rm{t}} \} \{ \text{\rm{a}} \} \} + \{ \{ \text{\bf{x}} \} \} _ \{ \{ \text{\rm{m}} \} \{ \text{\rm{o}} \} \{ \text{\rm{t}} \} \{ \text{\rm{i}} \} \{ \text{\rm{o}} \} \{ \text{\rm{n}} \} \{ \text{\rm{o}} \} \{ \text{\rm{n}} \} \{ \text{\rm{s}} \} \{ \text{\rm{e}} \} \} \\ \{ \text{\rm{t}} \} ^ \{ \{ \text{\rm{d}} \} \{ \text{\rm{a}} \} \{ \text{\rm{t}} \} \{ \text{\rm{a}} \} \} \times A \$ \$$$

where $\{ \{ \text{\bf{x}} \} \} _ \{ t \} ^ \{ \{ \text{\rm{s}} \} \{ \text{\rm{i}} \} \{ \text{\rm{m}} \} \}$ is a simulated neural activity vector at time t (relative to motion onset), and $\{ \{ \text{\rm{m}} \} \{ \text{\rm{o}} \} \{ \text{\rm{t}} \} \{ \text{\rm{i}} \} \{ \text{\rm{o}} \} \{ \text{\rm{n}} \} \{ \text{\rm{o}} \} \{ \text{\rm{n}} \} \{ \text{\rm{s}} \} \{ \text{\rm{e}} \} \}$ is the neural activity population vector at motion onset. We took a leave-one-out cross-validation strategy, in which all the parameters for modelling, de-noising and dimensionality reduction were obtained from the training dataset that excluded a test trial simulated by a model.

Goal decoding of the original and the simulated neural trajectories (Fig. 3f) was performed with the LDA-based decoding procedure described in the previous section, except that the decoders here were trained based on the de-noised neural activity from −0.5 s to 0.5 s relative to lick onset at the goal well. This narrow duration of 1 s was chosen to capture a snapshot of goal representation at lick onset without generalising over time.

Statistical procedures

All statistical tests were two sided and non-parametric unless stated otherwise.

Reporting summary

Further information on research design is available in the [Nature Research Reporting Summary](#) linked to this paper.

Data availability

The datasets used for the figures can be obtained from the authors.

Code availability

MATLAB codes for PCA, LDA (dimension reduction) and Isomap are part of the dimensionality reduction toolbox written by Laurens van der Maaten^{[35](#)}. Other codes can be obtained from the authors.

References

1. 1.

O'Keefe, J. & Dostrovsky, J. The hippocampus as a spatial map. Preliminary evidence from unit activity in the freely-moving rat. *Brain Res.* **34**, 171–175 (1971).

2. 2.

Wood, E. R., Dudchenko, P. A., Robitsek, R. J. & Eichenbaum, H. Hippocampal neurons encode information about different types of memory episodes occurring in the same location. *Neuron* **27**, 623–633 (2000).

3. 3.

Frank, L. M., Brown, E. N. & Wilson, M. Trajectory encoding in the hippocampus and entorhinal cortex. *Neuron* **27**, 169–178 (2000).

4. 4.

Hafting, T., Fyhn, M., Molden, S., Moser, M.-B. & Moser, E. I. Microstructure of a spatial map in the entorhinal cortex. *Nature* **436**, 801–806 (2005).

5. 5.

Pfeiffer, B. E. & Foster, D. J. Hippocampal place-cell sequences depict future paths to remembered goals. *Nature* **497**, 74–79 (2013).

6. 6.

Wikenheiser, A. M. & Redish, A. D. Hippocampal theta sequences reflect current goals. *Nat. Neurosci.* **18**, 289–294 (2015).

7. 7.

Ito, H. T., Zhang, S.-J., Witter, M. P., Moser, E. I. & Moser, M.-B. A prefrontal–thalamo–hippocampal circuit for goal-directed spatial navigation. *Nature* **522**, 50–55 (2015).

8. 8.

Carey, A. A., Tanaka, Y. & van der Meer, M. A. A. Reward revaluation biases hippocampal replay content away from the preferred outcome. *Nat. Neurosci.* **22**, 1450–1459 (2019).

9. 9.

Kay, K. et al. Constant sub-second cycling between representations of possible futures in the hippocampus. *Cell* **180**, 552–567 (2020).

10. 10.

Foster, D. J. & Wilson, M. A. Reverse replay of behavioural sequences in hippocampal place cells during the awake state. *Nature* **440**, 680–683 (2006).

11. 11.

Diba, K. & Buzsáki, G. Forward and reverse hippocampal place-cell sequences during ripples. *Nat. Neurosci.* **10**, 1241–1242 (2007).

12. 12.

Rajasethupathy, P. et al. Projections from neocortex mediate top-down control of memory retrieval. *Nature* **526**, 653–659 (2015).

13. 13.

Buzsáki, G. Space and time: the hippocampus as a sequence generator. *Trends Cogn. Sci.* **22**, 853–869 (2018).

14. 14.

Ekstrom, A. D. et al. Cellular networks underlying human spatial navigation. *Nature* **425**, 184–188 (2003).

15. 15.

Brown, T. I. et al. Prospective representation of navigational goals in the human hippocampus. *Science* **352**, 1323–1326 (2016).

16. 16.

Patai, E. Z. & Spiers, H. J. The versatile wayfinder: prefrontal contributions to spatial navigation. *Trends Cogn. Sci.* **25**, 520–533 (2021).

17. 17.

Vafaei, A. A. & Rashidy-Pour, A. Reversible lesion of the rat's orbitofrontal cortex interferes with hippocampus-dependent spatial memory. *Behav. Brain Res.* **149**, 61–68 (2004).

18. 18.

Ciaramelli, E. The role of ventromedial prefrontal cortex in navigation: a case of impaired wayfinding and rehabilitation. *Neuropsychologia* **46**, 2099–2105 (2008).

19. 19.

Feierstein, C. E., Quirk, M. C., Uchida, N., Sosulski, D. L. & Mainen, Z. F. Representation of spatial goals in rat orbitofrontal cortex. *Neuron* **51**, 495–507 (2006).

20. 20.

Wikenheiser, A. M., Marrero-Garcia, Y. & Schoenbaum, G. Suppression of ventral hippocampal output impairs integrated orbitofrontal encoding of task structure. *Neuron* **95**, 1197–1207 (2017).

21. 21.

Buckley, M. J. et al. Dissociable components of rule-guided behavior depend on distinct medial and prefrontal regions. *Science* **325**, 52–58 (2009).

22. 22.

Walton, M. E., Behrens, T. E. J., Buckley, M. J., Rudebeck, P. H. & Rushworth, M. F. S. Separable learning systems in the macaque brain and the role of orbitofrontal cortex in contingent learning. *Neuron* **65**, 927–939 (2010).

23. 23.

Hirokawa, J., Vaughan, A., Masset, P., Ott, T. & Kepecs, A. Frontal cortex neuron types categorically encode single decision variables. *Nature* **576**, 446–451

(2019).

24. 24.

Ballesta, S., Shi, W., Conen, K. E. & Padoa-Schioppa, C. Values encoded in orbitofrontal cortex are causally related to economic choices. *Nature* **588**, 450–453 (2020).

25. 25.

Elsayed, G. F., Lara, A. H., Kaufman, M. T., Churchland, M. M. & Cunningham, J. P. Reorganization between preparatory and movement population responses in motor cortex. *Nat. Commun.* **7**, 13239 (2016).

26. 26.

Aoi, M. C., Mante, V. & Pillow, J. W. Prefrontal cortex exhibits multidimensional dynamic encoding during decision-making. *Nat. Neurosci.* **23**, 1410–1420 (2020).

27. 27.

Mazor, O. & Laurent, G. Transient dynamics versus fixed points in odor representations by locust antennal lobe projection neurons. *Neuron* **48**, 661–673 (2005).

28. 28.

Machens, C. K., Romo, R. & Brody, C. D. Functional, but not anatomical, separation of ‘what’ and ‘when’ in prefrontal cortex. *J. Neurosci.* **30**, 350–360 (2010).

29. 29.

Parthasarathy, A. et al. Time-invariant working memory representations in the presence of code-morphing in the lateral prefrontal cortex. *Nat. Commun.* **10**, 4995 (2019).

30. 30.

Tenenbaum, J. B. A global geometric framework for nonlinear dimensionality reduction. *Science* **290**, 2319–2323 (2000).

31. 31.

Pachitariu, M., Steinmetz, N., Kadir, S., Carandini, M. & Kenneth D. H. Kilosort: realtime spike-sorting for extracellular electrophysiology with hundreds of channels. Preprint at <https://www.biorxiv.org/content/10.1101/061481v1> (2016).

32. 32.

Skaggs, W. E. & McNaughton, B. L. Theta phase precession in hippocampal neuronal populations and the compression of temporal sequences. *Hippocampus* **6**, 149–172 (1996).

33. 33.

Hastie, T. & Tibshirani, R. Classification by pairwise coupling. *Ann. Statist.* **26**, 451–471 (1998).

34. 34.

Churchland, M. M. et al. Neural population dynamics during reaching. *Nature* **487**, 51–56 (2012).

35. 35.

van der Maaten, L. J. P., Postma, E. O. & van der Herik, H. J. Dimensionality reduction: a comparative review. *Tilburg University Technical Report (TiCC-TR)*. https://lvdmaaten.github.io/publications/papers/TR_Dimensionality_Reduction_Review_2009.pdf (2009).

36. 36.

Kropff, E., Carmichael, J. E., Moser, E. I. & Moser, M.-B. Frequency of theta rhythm is controlled by acceleration, but not speed, in running rats. *Neuron* **109**, 1029–1039 (2021).

37. 37.

Kurth-Nelson, Z., Economides, M., Dolan, R. J. & Dayan, P. Fast sequences of non-spatial state representations in humans. *Neuron* **91**, 194–204 (2016).

38. 38.

Lee, A. K. & Wilson, M. A. Memory of sequential experience in the hippocampus during slow wave sleep. *Neuron* **36**, 1183–1194 (2002).

Acknowledgements

We thank N. Vogt, S. Zeissler, E. Northrup and G. Wexel for animal care; F. Bayer and A. Umminger for building the behavioural mazes; N. Heller for designing electrode interface boards; K. Deisseroth for providing a bReaCh-ES plasmid; G. Laurent and E. M. Schuman for providing valuable comments on the early version of the manuscript; G. Schneider for advice regarding cell type classification; and all members of the Ito laboratory for discussions. This work was supported by the Max Planck Society, the Behrens-Weise Foundation, the Japan Science and Technology Agency (JPMJPR1682), the Human Frontier Research Grant (RGY0072/2018-302), the European Research Council ('NavigationCircuits' Grant Agreement no. 714642) and the Alexander von Humboldt Foundation (Postdoctoral Research Fellowship).

Funding

Open access funding provided by Max Planck Society.

Author information

Affiliations

1. Max Planck Institute for Brain Research, Frankfurt am Main, Germany

Raunak Basu, Robert Gebauer, Tim Herfurth, Simon Kolb, Zahra Golipour, Tatjana Tchumatchenko & Hiroshi T. Ito

2. Institute of Experimental Epileptology and Cognition Research, Life and Brain Center, Universitätsklinikum Bonn, Bonn, Germany

Tatjana Tchumatchenko

Contributions

R.B., Z.G. and H.T.I. designed the experiment. R.B. performed all experiments with help from R.G. on behavioural training, surgery and histology. T.H., S.K. and T.T. advised on decoding methods. R.B. performed all data analysis. R.B. and H.T.I. wrote the manuscript after discussions among all authors. H.T.I. supervised and coordinated the project.

Corresponding authors

Correspondence to [Raunak Basu](#) or [Hiroshi T. Ito](#).

Ethics declarations

Competing interests

The authors declare no competing interests.

Additional information

Peer review information *Nature* thanks Kiah Hardcastle, Hugo Spiers and the other, anonymous, reviewer(s) for their contribution to the peer review of this work.

Publisher's note Springer Nature remains neutral with regard to jurisdictional claims in published maps and institutional affiliations.

Extended data figures and tables

Extended Data Fig. 1 Behavioural performance in the navigation task.

a, Top view photo of the linear maze used in this study. **b**, Mean number of errors committed per trial block during the first 15 days of training. Prior block errors are defined as incorrect licking of wells that were rewarded in the previous block. Current block errors are defined as incorrect licks of the same well from which the animal obtains its most recent reward in the block (by failing to visit its paired well). Topological errors comprise incorrect licks of the wells immediately next to the correct target well (but if this erroneously licked well was rewarded in the previous block, it was classified as prior block error.) The near absence of topological errors implies that animals form a robust spatial map that enables accurate estimation of well positions. **c**, Mean number of successfully completed blocks per session. As the animals learned the task, block transitions occurred quicker, resulting in a steady increase in the number of successfully completed blocks before saturating after 8 days of training. In panels **b-c**, $n = 5$ rats for days 1–12, 4 rats for day 13, and 3 rats for days 14–15. **d**, Average error rates after consecutive correct licks. Numbers in the horizontal axis indicate the number of consecutive correct licks prior to the trial being evaluated (as shown in the schematic on top where blue circles denote correct trials and white circles represent the trial whose outcome was analysed. Data are plotted separately for different stages of training. After five and six consecutive correct trials, the probability of making an error in the subsequent trial was reduced to 6.86% and 8.32%, respectively, and was not significantly different across different stages of training ($p = 0.0261, 0.0006, 0.0416, 0.0476, 0.2074$, and 0.0911 in 1-way ANOVA for error rates following 1–6 consecutive correct trials, respectively; $n = 5$ rats). We thus introduced a block change of well combinations only after the animal made at least six consecutive

correct trials. **e**, Prior block errors were not purely due to the animal's habitual behaviour. We analysed trials in which the same well was rewarded in both previous and current blocks (well A in the scheme) and its paired well in the previous block (well B in the scheme) was in the middle of journey toward the other goal well in the current block (well C in the scheme). The average number of prior block errors in the trained animals proportionally increased as the distance between well B and well C reduced. Dotted line represents the best fit linear regression line (slope: 0.206, $p = 0.02$ from two sided t-statistic with the null hypothesis of zero slope. $n = 13, 9, 6, 12$ sessions from 5 rats for $d = 4, 3, 2, 1$, respectively). **f-h**, Plots showing the distributions of (f) lick durations, (g) time latencies between the end of licking and the onset of motion, and (h) entire times from lick onset to motion onset. Each distribution was further divided into two plots according to the length of lick threshold. The left plots are based on 12 sessions with the lick threshold of 2 s as well as 1 session with the threshold of 1.5 s, and the right plots are on 5 sessions with the threshold of 1 s. Dotted lines represent the medians. **i**, Decoding probability of the well that was approached and licked by the animal (as in Figure 1h) plotted according to different levels of lick threshold ($n = 13$ and 5 for the threshold of > 1 s and $= 1$ s, respectively). Shown are means (line) \pm s.e.m (shaded). **j**, No significant difference in error rates between the two consecutive blocks with a common goal well and those without it. Each dot represents the mean from an individual session ($p = 0.08$ in two-sided Wilcoxon signed-rank test; $n = 18$ sessions from 4 rats). Error bars in panels **c**, **d**, and **e** denote s.e.m.

Extended Data Fig. 2 Tetrode locations and bReaCh-ES-eYFP expression in OFC.

a, Nissl-stained coronal sections of all animals recorded from OFC (4 rats) with tetrode tracks marked with arrows. **b**, Coronal sections showing the expression of bReaCh-ES-eYFP (green) in bilateral OFC of the three animals used for optogenetic perturbation experiments. Dotted white lines indicate the positions of the optic fibres.

Extended Data Fig. 3 Firing properties of individual OFC neurons.

a, Procedure for quantifying spatial selectivity (see [Methods](#)) of OFC neurons. Colour coded firing rates during 200 pseudotrials and their shuffled counterparts are shown in top and middle panels, respectively. First 100 pseudotrials are during stationary periods (speed < 10 cm/s) and the next 100 are during periods of motion (speed > 10 cm/s). Panel on bottom shows the distributions of mean spatial correlations obtained from 1000 original (light grey) and shuffled (dark grey) sets of pseudotrials for this neuron. **b**, Top: three representative neurons that conjunctively encode spatial location and navigation phase. Bottom: three examples of spatially selective neurons that were not influenced by navigation phases. Same convention as in Figure 1e. **c**, Cumulative

frequency of spatial information calculated over firing rates in a 2D space of position \times navigation phase (as in **b**) versus that taking into account only positional differences (and hence averaged across phases) for all 2056 neurons representing position and navigation phase conjunctively. Spatial information in the conjunctive position \times phase space is greater than the one considering positional differences only ($p = 1.78 \times 10^{-180}$ in two-sided Wilcoxon ranksum test). **d**, Peak firing rate of 10 representative neurons during licking. Single dots represent individual trials, and the well identity is colour coded. p-values calculated using one-way ANOVA. **e**, Well-specific but paired-well-independent firing rate of four representative neurons (one from each animal). Same convention as in Figure 1d. **f**, Peak firing rate of 10 representative neurons during -0.5 to 0.5 seconds relative to motion onset. Single dots represent individual trials and are coloured based on the identity of goal well. p-values calculated using one-way ANOVA. **g**, Four representative neurons with goal-well dependent but start-well independent firing at motion onset. p-values calculated using one-way ANOVA. **h**, Session-based summary of the numbers of neurons categorized as active (average firing rate > 0.5), current-well selective, and goal-well selectivite (see [Methods](#)), together with the number of dimensions explaining 85% of the variance of goal-selective neurons (obtained using PCA). **i**, Total numbers of active neurons (average firing rate > 0.5 Hz) during each of the following behavioural phases; running, approach (duration of 500 ms prior to lick onset), and well-licking. **j**, Firing rate plots of the same representative neurons as in Figure 2a with trials averaged (and coloured) based on ‘current’ well. In panels e and g, plots show means (line) \pm s.e.m. (shaded).

[**Extended Data Fig. 4 Low spatial information in OFC neurons.**](#)

a-b, Colour-coded firing rate plots of representative OFC neurons and CA1 neurons during a random foraging task in an open-field arena. **c**, Top: spatial information of individual OFC and CA1 neurons in the random foraging task. Error bars denote s.e.m. Inset shows the distribution of spatial information of the OFC and CA1 neurons. *** $p = 5.76 \times 10^{-20}$, $z = 9.14$ in two-sided Wilcoxon rank-sum test. Bottom: distribution of spatial information of individual OFC neurons during the goal-directed navigation task on the linear maze. Solid and dashed vertical lines indicate the median and mean, respectively. **d**, Stability of spatial tuning during the session. Top: rate maps of two representative neurons, each from OFC and CA1, during the first and second halves of the session. Bottom: histogram of spatial correlations of 70 OFC neurons and 65 CA1 neurons. For each neuron, rate maps were calculated separately for the first and second halves of the foraging sessions, and the correlation between the two position-dependent firing-rate vectors was evaluated (spatial correlation: OFC, 0.19 ± 0.02 , CA1, 0.79 ± 0.02 ; two-sided Wilcoxon rank-sum test: $z = 9.72$, $p = 2.45 \times 10^{-22}$).

[**Extended Data Fig. 5 Validation of goal-well decoding.**](#)

a, Decoding of goal well (blue), current well (red), and previous well (green), in the trials where the animal's next goal and previously-visited well were different due to error trials. $n = 18$ sessions. MO: motion onset. **b**, Decoding of the wells during a 3-well task. Bottom plot shows the decoding probabilities of the wells when the animal's next goal and the previous goal were different. The decoder indicated the animal's next destination but not the previous goal. **c**, Top: decoding on error trials showing the probabilities of current well (red), the animal's next destination visited incorrectly (green), and the correct well according to the task rule (grey), plotted over time (left) or along positional fraction (right). Bottom: decoding of the animal's next destination at motion onset between correct (blue) and error (green) trials. Dots represent individual 18 sessions. $p = 0.372$ in two-sided Wilcoxon signed-rank test. **d**, Top: schematic of the experimental setup and the behaviour paradigm of a continuous alternation task. The correct destination of individual trials switched alternately between Goal 1 and Goal 2. For successful task performance, rats needed to follow the sequence of trajectories outlined by numbers 1 to 4. Two rats were trained with the same strategy as described before⁷, and the performance of both rats reached over 95% accuracy. Bottom: decoding probability of goal well during navigation. Decoding was performed by using a decoder based on quadratic-discriminant analysis that was trained on OFC neural activity during the concatenated time range from -1 s to 1 s relative to motion onset (at the start well) as well as from -2 s to 2 s relative to lick onset (at the goal well). Decoding was restricted to correct trials with trajectory paths 1 and 3 in the top schematic. Each trial was decoded in a leave-one-out cross-validated manner. Decoding performance is plotted across four contiguous time phases: 1) 5 s duration prior to motion onset at the start well, 2) from motion onset to the choice point, 3) from the choice point to lick onset at the goal well, and 4) 3 s duration after lick onset. Due to trial-by-trial variability in the animal's behaviours, the second and third phases are plotted in normalized time for each. Grey line denotes aggregate chance level from well-based and speed-based null hypotheses (see [Methods](#); chance levels for goal distance and direction were not considered because they were identical between the two goal-directed navigations in the maze). The decoding probability of goal well was significantly greater than chance starting from 0.6 s prior to motion onset until 2.6 s after lick onset at the goal well (decoding probability at motion onset: 0.74 ± 0.06 , compared to its chance level of 0.58 ; $n = 4$ sessions from 2 rats). MO: motion onset, CP: choice point, LO: lick onset at goal well. **e**, Schematic of chance level calculation (see [Methods](#)). All five parameters are tested for the goal-well decoding, whereas only the direction and the random well selection were considered for the current-well decoding. **f**, Decoding performance of goal well using the following three kinematic variables together as predictors: acceleration (calculated as in Kropff et al³⁶), speed, and head direction (dotted line). The decoder was separately trained and tested on individual time points. The decoding performance based on the activity of OFC neurons is also included for comparison. Grey horizontal line denotes the times when the goal-decoding performance of the neuron-based decoder was

significantly better than that based on kinematic variables ($p < 0.05$; two-sided Wilcoxon signed-rank test followed by Holm-Bonferroni correction, $n = 18$ sessions). **g**, Top: acceleration at motion onset at individual trials from a representative session plotted as a function of the distance to the goal (measured in a well-interval unit). The regression line best fitting the data is shown with the dotted line. The p-value of the regression slope is shown on top. Bottom: the regression slope between the acceleration at motion onset and the goal distance for all 18 sessions. Red asterisks denote sessions with statistically significant regression slope ($p = 0.0015, 0.0065, 0.0885, 0.3239, 0.8152, 0.1810, 0.0289, 0.0024, 0.0744, 0.0087, 0.0008, 0.0025, 0.0042, 0.0717, 0.9600, 0.2889, 0.9802, 0.9101$, from the t-statistic with the null hypothesis of zero slope without multiple comparison correction). **h**, Goal representation is largely independent of the animal's speed or acceleration. Top left: for testing the effect of the animal's speed at motion onset, we took an approach of grouping based on the animal's running speed, whereby trials were divided into either two or four groups. Top right: we used the same strategy for testing the effect of the animal's acceleration at motion onset. In both cases, we obtained almost the same chance levels between these two grouping strategies. Bottom left: goal decoding probability in trials with quick start using a decoder trained only on trials with slow start. Bottom right: data used in training and testing of a decoder were swapped. **i**, Decoding probabilities of 'current' well at different timepoints. Schematic on top depicts the time durations used for the decoder's training (dark grey lines) with the class label of current well. Left: decoding of current well using the same strategy as used for the goal-well decoding (Figure 2d). Second left: identical to Figure 1h left but is included for comparison. Third and Fourth: decoding of current well relative to lick end and motion onset, respectively. The results together suggest that the current well is only weakly represented in OFC both at motion onset and during navigation, irrespective of the decoding strategy. MO: motion onset, LO: lick onset, LE: lick end. **j**, Decoding of current well as in Figure 1h, but with shorter durations of training data denoted in the schematic on top. **k**, Decoding probabilities and corresponding aggregate chance levels of the current (left 4 plots) or the goal (right 4 plots) well on a representative session from each rat. Same notations as in Figure 1h left or 2d left (trial number for the current or the goal well decoding: Rat 110 session 2, $n = 137$ and 119; Rat 175 session 5, $n = 116$ and 114; Rat 182 session 5, $n = 149$ and 146; Rat 284 session 5, $n = 133$ and 133). In panels **a-d**, **f**, and **h-k**, plots show means (line) \pm s.e.m. (shaded).

Extended Data Fig. 6 Decoding of the animal's position during motion from ensemble activity of OFC neurons.

a-b, Comparison of well representation of OFC neurons during licking versus crossing. **a**, Schematic of two different decoders. Left: a decoder was trained on the neural activity as animals approached and licked a target well (lick decoder). This

decoder is the same as in Figure 1h. Right: another LDA-based decoder was trained on the neural activity as animals crossed a well without licking it (cross decoder).

Training and testing for this cross decoder were performed in a 10-fold cross-validated manner, in which the entire session was divided into 10 equal-duration groups and the neural activity during well crossing from 9 groups were used to train a decoder, while the left-out group was used for testing. **b**, Left: decoding probability of licking well based on the two types of decoders trained during licking (red) or crossing (magenta). Middle two panels: distance (left) and time (right) based decoding of crossing well based on the two decoders. The red traces are identical to those in Figure 1h. Shown are means (line) \pm s.e.m. (shaded). n = 18 sessions. Right: decoding probability of licking well using the decoder trained on the data during well licking, compared with that of crossing well based on the decoder trained on the data during well crossing. Results from individual sessions are shown in small grey circles while larger circles with error bars denote means \pm s.d. (decoding probability of licking well: 0.67 ± 0.07 ; crossing well: 0.41 ± 0.08 ; * $p = 1.96 \times 10^{-4}$ in two-sided Wilcoxon signed-rank test), suggesting that well representation of OFC neural population is particularly strong during licking at goal wells. **c**, Top: decoding probabilities of goal well and its immediately preceding ‘pre-goal’ well when the animal crossed over the pre-goal well. The decoding of pre-goal well was performed using a decoder trained on cross-over wells (as in a–b), whereas goal-well decoding was performed by a decoder trained on a 2 s period prior to lick onset at goal wells. Shown are means (line) \pm s.e.m. (shaded). Bottom: decoding probabilities of pre-goal and goal wells at the time of crossing the pre-goal well. Results from individual sessions are shown in small grey circles while larger circles with error bars denote the means \pm s.d (decoding probability of pre-goal well: 0.37 ± 0.08 ; goal well: 0.59 ± 0.07 ; two-sided Wilcoxon signed-rank test: * $p = 1.96 \times 10^{-4}$). **d**, Schematic of the strategy to decode the animal’s instantaneous position from OFC neural population activity. As the animal perform multiple trial types with various start and goal positions during a session, the entire time duration of the session was first divided into 100 chunks of equal duration, and 10 groups were created by sampling 10 chunks per group randomly (without repetition), which ensure unbiased distributions of spatial bins among groups. To decode the spatial location, we then divided the animal’s position along the linear maze into 5 cm spatial bins. Spatial decoding was carried out on each group using 10-fold cross-validation, in which the neural activity during motion (speed > 10 cm/s) from 9 out of 10 groups was used to train a decoder while that of the left-out group was used for prediction of the rat’s location. Two types of decoding algorithms – LDA and Bayesian – were implemented. For LDA-based decoding, we trained a regularized LDA decoder (see [Methods](#)) with ensemble firing rate vectors at individual 100 ms bins using the class label of spatial bin occupied by the animal. For Bayesian decoding, we first calculated mean firing rates of each neuron at individual positions, and then estimated the posterior probability of the animal’s position at a particular spatial bin in a 100 ms bin using the following formula, $\langle P(\{b\}_{k}) \rangle = C(\{\prod_{i=1}^N (\{b\}_k)^{f_i}\}, f)$

$\{ \}^{\{ \{ s \}_{-i} \}} \{ e \}^{\{ \{ -\sum_{i=1}^N b_{-k}^{[i]} f_i \} \}}$, where b_{-k} is the k^{th} spatial bin, C is a normalizing constant, N is the number of neurons, $b_{-k}^{[i]}$ is the average firing rate of the i^{th} neuron at the k^{th} spatial bin (calculated as the average number of spikes per 100 ms), and s_{-i} is the number of spikes fired by the i^{th} neuron during a given time bin. For both decoding strategies, the spatial bin with the highest probability was assigned as the decoded position. The decoders were trained on the activity of all neurons with mean firing rates greater than 0.5 Hz. **e**, Root mean squared decoding error for each session using the two decoding strategies (average root mean squared error for LDA and Bayesian: 39.51 ± 1.06 cm and 56.41 ± 1.49 cm respectively compared to the well spacing of 20 cm shown in a dotted vertical line; $n = 18$ sessions). **f**, Distribution of absolute decoding errors resulting from Bayesian (left) and LDA based (right) position decoding, shown as thin horizontal lines ranging from 25th to 75th percentile with ticks denoting the median. Each line represents data from one session. **g**, Decoded positions (vertical axis) during a 20 second period (horizontal axis) from four representative sessions. Positions decoded using LDA and Bayesian are shown in blue and red, respectively. **h**, Mean decoding accuracy, defined as a fraction of correctly decoded positions, for every spatial bin from representative sessions. Chance levels for LDA decoders were obtained by shuffling class labels during the decoder's training. This procedure was repeated 100 times, generating a distribution of mean accuracies across spatial bins. Chance level for each bin was set at 95th percentile of this distribution. Similarly, for Bayesian decoding, chance levels were assessed based on shuffled firing rates among spatial bins. **i**, Distribution of decoded positions, shown as thin horizontal lines ranging from 5th to 95th percentile with ticks denoting the median, against the actual spatial location (vertical axis) occupied by the animal. Plots show the results of 4 representative sessions with a decoding strategy based on either LDA (top row) or Bayesian (bottom row).

[Extended Data Fig. 7 Choices of hyperparameters, decoding algorithm, and data range to optimize the goal decoding.](#)

a, Illustration of the impact of dimensionality reduction on goal-well decoding. This strategy, as well as the followings (**b** and **c**), were aimed to reduce the decoder's dimensionality, as a decoder with a large number of parameters results in poor performance on a test dataset in general. Shown in each plot are the mean goal decoding probability and the corresponding chance level based on the data from a representative session (top) or across all sessions (bottom) (see [Methods](#) and Extended Data Fig. 5 for details). We implemented PCA to reduce the data dimensions to different degrees of explained data variance, and assessed the impact of dimensionality reduction on the performance of goal-well decoding. The decoding performance was optimal when the number of chosen dimensions explained 85% of the data variance, in terms of the maximum separation from the corresponding chance level as well as a

small variance of the decoding probability. The decodings were performed with a fixed regularization value of 0.5 on goal-well selective neurons. **b**, Illustration of the impact of regularization. Shown are the decoding performances at three levels of regularization values. We found that the regularizer value of 0.5 has the maximum separation from the corresponding chance level as well as a low variance of the decoding probability. The decodings were performed with reduced dimensions explaining 85% of the data variance on goal-well selective neurons. **c**, Illustration of the impact of pre-selection of goal-well selective neurons. The decoding performance was assessed based on either goal-well selective neurons (left) or all recorded neurons (right). We found that the pre-selection of goal-selective cells achieved better separation from the corresponding chance level. The decoding was performed with the reduced dimensions explaining 85% of the data variance and the regularization value set to 0.5. **d**, Plots show a summary of decoding performance at motion onset relative to the corresponding chance level using different parameters described in **a–c**. * $p < 0.05$, ** $p < 0.01$, and ns ($p > 0.05$). Left: $p = 0.0936, 0.0156, 0.0084$, and 0.9479 ; Middle: $p = 0.0429, 0.0139, 0.0096, 0.0065$, and 0.0279 . Right: $p = 0.0084$, and 0.3061 ; in two-sided Wilcoxon signed-rank test without multiple comparison correction. $n = 18$ sessions. Errorbars denote s.e.m.). **e**, Comparison of decoding performance of goal well between two algorithms, LDA (left) and a support vector machine (SVM, right). For SVM we used a box-constraint of 0.01. Plotted are the decoding accuracy of goal well. For LDA, the predicted well was chosen as the one with the maximum probability. The two algorithms achieved similar decoding performance (the mean accuracy relative to the chance level at motion onset: LDA 0.0365; SVM 0.0432). **f**, Left: performance of decoders trained with different time ranges of neural activity. Four different ranges of the data were used as illustrated on top of each plot (orange bars). We found that the goal decoding improved by concatenating the neural activity at both motion onset and lick onset. Furthermore, the decoding performance at motion onset improved as a longer time range of the data was used for the decoder's training. Interval 3 is the same as in Figure [2d](#). Right: summary of decoding performance at motion onset relative to the corresponding chance level for the four different decoding strategies described in left panel ($n = 18$ sessions, errorbars: s.e.m.). * $p < 0.05$, ** $p < 0.01$, and ns ($p > 0.05$). $p = 0.0176, 0.0642, 0.0084$, and 0.0016 in two-sided Wilcoxon signed-rank test without multiple comparison correction. **g**, Plots showing the times when the decoding probability of the goal well exceeded that of the current well for each of the decoding strategies shown in panel (f) above. Grey diamonds indicate data from individual sessions ($n = 18$ sessions). Light vertical dotted line denotes the mean across sessions (interval 1: 0.12 ± 0.07 s before motion onset; interval 2: 1.24 ± 0.15 s before motion onset; interval 3: 0.93 ± 0.13 s before motion onset; interval 4: 1.12 ± 0.14 s before motion onset). **h**, Decoding probability of the well licked by the animal using only current-well-selective neurons (solid; see [Methods](#) for definition), compared with that from all neurons with the average firing rate greater than 0.5 Hz (dotted), demonstrating the improved decoding

performance by the pre-selection of current-well selective neurons. In panels **a–c, e, f (left)**, and **h**, plots show means (line) \pm s.e.m. (shaded).

Extended Data Fig. 8 Non-sequential transition of spatial representations in OFC.

a, Schematic of the technique to quantify the sequenceness of spatial representations. We here asked if OFC neurons exhibit sequential representations of spatial positions during a transition of their encoding position from the animal's current location to its subsequent goal. We followed the technique described by Kurth-Nelson³⁷, and examined whether the posterior decoding probabilities of wells obtained by the LDA decoder have sequential peaks. For example, when the spatial representation of OFC neurons switched from well 2 to well 6 prior to motion onset, we asked whether peaks of posterior probabilities of wells 3, 4, and 5 were observed in sequential order. We can test this possibility by examining the time lags of cross-correlations of decoding probabilities for individual wells. In the example case, we asked if we observed a consistent time lag for the peaks of cross-correlations between decoding probabilities of well pairs 2 and 3, 3 and 4, 4 and 5, or 5 and 6. We tested a possibility of both forward and reverse sequences (e.g., either from well 2 to well 6 or from well 6 to well 2, in the example). To account for autocorrelations, the difference between forward and reverse correlation is reported. Chance levels of sequenceness were calculated using a non-parametric method suggested by Kurth-Nelson et al³⁷. Briefly, the well identities were shuffled to obtain all possible combinations, for each of which the mean sequenceness was computed. For example, the sequence of wells in trials with the 4-well distance between the start and the goals can be shuffled in 120 different ways in total. Two of them represent the real forward and reverse sequences on the linear maze, and the other 118 are considered shuffled sequences. The maximum and minimum values from these shuffled sequences constitute the two chance levels (positive and negative) across time lags. **b–f**, Verification of the technique on simulated spike trains resembling hippocampal replay events. A virtual agent traversed a 2 meter long linear maze with 10 reward wells (well spacing of 20 cm) bidirectionally for 25 trials at a uniform speed of 25 cm/s. The agent travelled between the positions of 20 cm and 180 cm, thereby encountering wells 2 to 9 in every run. **b**, Top: gaussian spatial tuning curves of 35 simulated neurons. Position and peak firing rate were chosen from a uniform distribution ranging from 5 cm to 185 cm and 8 Hz to 20 Hz respectively. Bottom: spike raster plot of all simulated neurons in one of the simulated journeys from 20 to 180 cm along the maze. Spikes were generated in individual 100 ms bins assuming a Poisson process with the neuron's position-dependent mean firing rates. **c**, Plot shows spike rasters during one replay event, out of 25 simulated events, in which each event comprised sequential representation of well locations from well 2 to well 9. We used a 20-fold time compression to simulate replay events³⁸. Each well was represented for 40 ms, and firing rates of neurons were

stretched over 10 cm from the centre of the well location. **d**, Posterior decoding probabilities of colour-coded individual wells (decoded using LDA, see [Methods](#)) from the representative replay event in **c**. Prior to decoding, spike trains were smoothed with 50 ms Gaussian kernel and binned at 10 ms. To classify a given well identity, the decoder was trained on the neural activity when the agent was within 5 cm of the corresponding well. **e**, Mean sequenceness across all simulated replay events ($n = 25$). As expected, the mean sequenceness exceeds the chance level at a time lag of 40 ms (dotted vertical line) corresponding to the average duration of individual well representations during the simulated replays. **f**, Mean sequenceness during a different simulation where the running speed of the agent was doubled, resulting in each well being represented for 20 ms during replays following a 20-fold compression. Our decoding strategy followed by the sequenceness detection algorithm was still able to detect this short-time sequential representation of positions, although inferring the precise timescale of well transitions appears to be prevented by the width of Gaussian kernel used for smoothing spike trains. **g**, Sequenceness algorithm applied to the posterior probabilities from -2 s to 0 s relative to motion onset from two representative animals. To identify the sequential transition of representation from the current to the goal well at a finer time scale, we binned neural activity into 10 ms time bins. We analysed trials where the start and the goal were separated by 4–7 wells. Plots show the difference between forward and reverse sequenceness for different trajectory lengths in distinct shades of blue along with their corresponding chance levels denoted by dotted lines. No significant sequenceness was observed in the representative animals. **h**, For clarity, the sequenceness for each trial was normalized so that the interval between the corresponding positive and negative chance level lied within 1 and -1 , respectively. Using this normalization strategy, the sequenceness across trials with different distances of journeys could be pooled together. No overall significant forward or reverse sequenceness was observed in any of the four animals used. **i**, Same as in **h** except that the sequenceness was calculated with the middle wells of journey without the current and goal wells in order to exclude possible artefacts due to overrepresentations of these wells. For this analysis, we only focused on trials where starts and goals were separated by 6–7 wells. **j–m**, As sequential transitions in neural states may occur at a finer time scale in the order of a few tens of ms, we reanalysed our neural data by convolving spike trains with a 50 ms Gaussian kernel (rather than 250 ms), which matches the condition of our simulations in **b–f**. **j**, Decoding probability of the goal well relative to motion onset. Goal wells can be decoded greater than chance levels from 1.4 s prior to motion onset. **k**, Plot shows instantaneous firing rates of goal-well selective OFC cells. Firing rates were normalized to the means over the session. Unlike place cells that exhibit elevated instantaneous firing rates during replay events, we did not find any increase in instantaneous firing rates prior to motion onset. **l–m**, the same plots as in **h–i** except for the use of the 50 ms Gaussian kernel. No significant forward or reverse sequenceness was observed. In panels **e–m**, plots show means (line) \pm s.e.m. (shaded).

Extended Data Fig. 9 Choice of hyperparameters and LDA-based denoising strategy for analysing destination-specific neural dynamics.

a, Plots showing neural activity trajectories from individual trials extracted using LDA (as in Figure 3e) from three representative sessions. The trajectories are colour-coded based on the animal's destination. Top: original trajectories from the neural data, separately aligned to motion onset (MO; thin) and subsequent lick onset (LO; thick). Bottom: simulated trajectories with a first-order linear dynamic model based on the neural activity at motion onset. Trajectories aligned to lick onset were omitted from the left panel (Rat 175) to facilitate visualization. **b**, Quantification of the accuracy of first-order linear models. Top: schematic of a random walk model. At each time step, a first-order model predicts a displacement vector based on the activity state at a given time. Iterative additions of these displacement vectors to the neural activity at motion onset result in a predicted neural activity trajectory. We hypothesized that a fair null model to test our first-order model would be a distance-matched random-walk model, in which each displacement vector obtained from the first-order model is randomly rotated, thereby preserving the magnitude of displacement at each time step. Middle: example trajectories generated by the first-order model (left) and its distance-matched random-walk model (right) using data from the same representative session as in Figure 3e. Bottom left: average Euclidean distance between the modelled and the original trajectories (dark, $n = 146$ trials) from the representative session. The light shaded region denotes the full distribution of distances between the original and the simulated trajectories by 1000 random-walk models. Bottom right: normalized average Euclidean distance between the original and the modelled trajectories across all 18 sessions. For each session, all the distances (both the modelled and random trajectories) were normalized to the minimum distance generated by the random-walk models at the time point of 2.5 s after motion onset. Chance level at a given time point for each session was set at the smallest normalised distances between the original and random-walk-model-generated trajectories. **c**, Effect of regularization on LDA-based projections of neural activity from a representative session (same as in Fig. 3). The plots show three principal components (PC) of activity trajectories from individual trials extracted using LDA with different regularization values (see [Methods](#)). The trajectories are colour-coded based on the animal's destination and are separately aligned to motion onset (thin) and lick onset (thick). Insets show the ensemble neural activity in individual trials during one second after the motion onset projected on the axes that maximize the goal separability. The ranges of PC axes are the same across the panels. Absence of regularization caused overfitting, resulting in poor generalization and goal separability. In contrast, a large regularization value (e.g., $\lambda = 10$) separated data primarily based on class means with minimal influence of within-class covariance, resulting in suboptimal separation. We thus chose an intermediate regularization value of 1. **d**, Probability of goal-well decoding from neural trajectories extracted using LDA with three different regularization values. The

decoding strategy was the same as in Figure 3f (also see [Methods](#)). Decoding performance, assessed as the difference between the mean goal decoding probability and the corresponding chance level, was optimal at $\lambda = 1$, which was used in the rest of the analyses. Shown are means (solid) \pm s.e.m. (shaded). n = 18 sessions. e, Neural trajectories from a representative session simulated with a first-order linear dynamical model using three different regularization values. The ranges of axes are the same across the panels. Without regularization, simulated trajectories expanded quickly beyond the range of original neural activity, whereas a high regularization value constrained the models to simulate relatively simple trajectories. We found that regularizer values between 1 and 5 obtained the models that simulate activity trajectories similar to the original data. f, Probability of goal decoding from neural trajectories simulated with different regularization values. Optimal decoding performance was obtained with a regularization value of either 1 or 5, and we thus chose $\mu = 5$ for the rest of the analyses. For the regularization of $\mu = 5$, s.e.m. is not shown in the plot for better presentation of other results, but it is shown in panel i(ii) and Figure 3f. g, Demonstration of the advantages of performing LDA at individual time points based on simulated data. Top: temporal evolution of two groups (red and blue) of Gaussian distributed data evolving with first-order linear dynamics. Data in progressive time steps are coloured with incrementally lighter shades. Middle: data points projected to multiple LDA axes calculated at different time steps, which preserves the dynamics while keeping the separation between the two groups. Bottom: data projected to a single LDA axis calculated from the data across trial durations, which failed to preserve both the dynamics and the optimal group separation. h, Ensemble neural activity from a representative session extracted using different LDA-based denoising strategies (see [Methods](#)): (i) Original neural activity, (ii) Neural activity extracted using multiple LDA subspaces evaluated at individual time points, (iii) and (iv) Neural activity extracted by a single LDA subspace evaluated by concatenating two different time ranges of the neural activity (orange lines). Only neural trajectories aligned to motion onset (MO) are shown. The ranges of axes are the same across the plots. Insets provide magnified views of compact neural activities. Although the activity extraction with a single LDA subspace failed to preserve the original neural dynamics (iii and iv), implementation of multiple LDAs at individual time points succeeded in extracting destination-specific trajectories by preserving the original dynamics (ii). i, Probability of goal-well decoding based on the neural trajectories extracted by individual strategies corresponding to i-iv in h, demonstrating the optimal decoding performance of the time-wise LDA-based extraction method (ii in h).

[Extended Data Fig. 10 DREADDs-mediated manipulation of OFC neurons and additional analyses for optogenetic perturbation experiments.](#)

a, Mean number of errors per block committed by the animals injected with AAV8-hSyn-hM4Di-mCherry (left, n = 4 rats; a gift from Bryan Roth; Addgene viral prep # 44362-AAV8) five days prior to the beginning of perturbation experiments. The volume of 500 nL was injected at eleven sites in the OFC of each hemisphere with the following coordinates (AP, ML, and DV in mm): 2.7, 3.5, 5.2; 3, 2.5, 4.6; 3, 3.8, 4.4; 3.6, 2, 4.2; 3.6, 3.6, 4; 4.2, 1.4, 4.2; 4.2, 2.4, 4; 4.7, 1.6, 3; 4.7, 2.8, 3.5; 5.2, 1.2, 2.6; and 5.2, 2.6, 2.6. To evaluate the effects of manipulation, a microdrive with two circular bundles of 6 movable tetrodes each was implanted bilaterally with the centres of the bundles positioned at 3.5 mm (AP) from bregma and 1.5 mm (ML) from midline. Total errors and the two major error types — prior block errors and current block errors (defined in Extended Data Fig. 1)— are plotted. Shown are means ± s.e.m. **b**, Top: coronal section showing expression of hM4Di-mCherry in bilateral OFC. Bottom: normalized firing rates of OFC neurons over time relative to the subcutaneous injection of Agonist 21 (DREADDs Agonist 21 dihydrochloride, 7.04 mg/mL [20 mM]; Hello Bio at a dose of 6 mg/Kg). Means (solid) ± s.e.m. (shaded) across 100 neurons. **c**, Average speed of the animals expressing hM4Di-mCherry during motion (speed > 10 cm/s) when injected with saline versus Agonist 21. Black oblique lines represent paired sessions (see [Methods](#)). **d**, Plot shows the number of errors per trial block in the saline (grey) or Agonist 21 (red) injected sessions. The animals were injected with Agonist 21 followed by at least 45 min waiting time to allow the drug to reach the brain and take effect before starting the behaviour sessions. On control days, the equal volume of 0.9% saline solution was injected. To evaluate the impact of OFC silencing, the same sequences of well combinations were tested in a pair of saline and Agonist 21 sessions. The two sessions were carried out on consecutive days in a randomized order. All types of errors (left; ***p = 3.08×10^{-5} in two-sided Wilcoxon signed-rank test: $z = -4.16$) and the errors to the wells rewarded in the previous block (right; *** p = 3×10^{-4} in two-sided Wilcoxon signed-rank test: $z = -3.61$,) are shown separately. n = 23 sessions from 4 animals injected with AAV encoding hM4Di-mCherry. **e**, Mean number of errors per block committed by the animals injected with AAV1-CamKII-bReaCh-ES-eYFP five days prior to the start of perturbation experiments. Shown are means ± s.e.m. (n = 3 rats). **f**, Average error rates following consecutive correct licks in a block one day before and after the optogenetic perturbation experiments. The horizontal axis indicates the number of consecutive correct trials prior to the trial being evaluated. All the three animals made no errors after 4 consecutive correct trials, and thus we performed optogenetic perturbations after the first four consecutive correct trials in a block. Furthermore, after the termination of perturbation, the animals still did not make any errors after four consecutive correct trials, suggesting that this criterion is most likely valid during the entire course of perturbation experiments. Shown are means ± s.e.m. (n = 3 rats). **g**, Average running speed of the animals expressing bReaCh-ES-eYFP during the laser pulses of 40-s duration (left; running speed: laser on 33.54 ± 1.18 cm/s, laser off 34.37 ± 0.68 cm/s; p = 0.38 in two-sided Wilcoxon signed-rank test; n = 12 sessions;

analyses were restricted during motion [speed > 10 cm/s]) or 6-s duration (right; running speed: laser on 33.4 ± 0.86 cm/s, laser off 34.85 ± 0.92 cm/s; $p = 0.074$ in two-sided Wilcoxon signed-rank test; $n = 9$ sessions). Each point in the plots represents the average speed from one session. **h**, Histogram of the times of either laser onsets relative to lick onset (left) or laser ends relative to lick end (right) in the experiments with 6 s optogenetic perturbation at lick onset. The vertical axis indicates the number of laser events, and the horizontal axis represents time relative to lick onset (left) and lick end (right). 98% (102 out of 104) of laser onsets occurred after lick onset and 83.65% (87 out of 104) of laser pulses ended before lick end. **i**, Histogram of the times of laser onsets relative to either lick end (left) or motion onset (right) in the experiments with 6 s optogenetic perturbation at motion onset. 91.79% (123 out of 134) of laser onsets occurred after lick end, and 95.52% (128 out of 134) of laser pulses started within 100 ms relative to motion onset. Three laser events that started 5 s after lick end, as well as six laser events that started more than 6 s prior to motion onset, were excluded from the plots.

Supplementary information

Reporting Summary

Rights and permissions

Open Access This article is licensed under a Creative Commons Attribution 4.0 International License, which permits use, sharing, adaptation, distribution and reproduction in any medium or format, as long as you give appropriate credit to the original author(s) and the source, provide a link to the Creative Commons license, and indicate if changes were made. The images or other third party material in this article are included in the article's Creative Commons license, unless indicated otherwise in a credit line to the material. If material is not included in the article's Creative Commons license and your intended use is not permitted by statutory regulation or exceeds the permitted use, you will need to obtain permission directly from the copyright holder. To view a copy of this license, visit <http://creativecommons.org/licenses/by/4.0/>.

Reprints and Permissions

About this article

Cite this article

Basu, R., Gebauer, R., Herfurth, T. *et al.* The orbitofrontal cortex maps future navigational goals. *Nature* **599**, 449–452 (2021). <https://doi.org/10.1038/s41586-021->

04042-9

- Received: 15 March 2021
- Accepted: 20 September 2021
- Published: 27 October 2021
- Issue Date: 18 November 2021
- DOI: <https://doi.org/10.1038/s41586-021-04042-9>

Share this article

Anyone you share the following link with will be able to read this content:

[Get shareable link](#)

Sorry, a shareable link is not currently available for this article.

[Copy to clipboard](#)

Provided by the Springer Nature SharedIt content-sharing initiative

This article was downloaded by **calibre** from <https://www.nature.com/articles/s41586-021-04042-9>

| [Section menu](#) | [Main menu](#) |

- Article
- [Published: 09 November 2021](#)

Temporal controls over inter-areal cortical projection neuron fate diversity

- [Esther Klingler](#)¹,
- [Ugo Tomasello](#)¹ na1,
- [Julien Prados](#) [ORCID: orcid.org/0000-0002-8546-241X](#)² na1,
- [Justus M. Kebschull](#)³ nAff6,
- [Alessandro Contestabile](#) [ORCID: orcid.org/0000-0001-6528-1403](#)¹,
- [Gregorio L. Galiñanes](#)¹,
- [Sabine Fièvre](#)¹,
- [Antonio Santinha](#)⁴,
- [Randal Platt](#)⁴,
- [Daniel Huber](#) [ORCID: orcid.org/0000-0002-0744-7679](#)¹,
- [Alexandre Dayer](#)^{1,2},
- [Camilla Bellone](#) [ORCID: orcid.org/0000-0002-6774-6275](#)¹ &
- [Denis Jabaudon](#) [ORCID: orcid.org/0000-0003-2438-4769](#)^{1,5}

[Nature](#) volume **599**, pages 453–457 (2021)

- 5666 Accesses
- 139 Altmetric
- [Metrics details](#)

Subjects

- [Cell type diversity](#)
- [Neural circuits](#)

Abstract

Interconnectivity between neocortical areas is critical for sensory integration and sensorimotor transformations^{[1,2,3,4,5,6](#)}. These functions are mediated by heterogeneous inter-areal cortical projection neurons (ICPN), which send axon branches across cortical areas as well as to subcortical targets^{[7,8,9](#)}. Although ICPN are anatomically diverse^{[10,11,12,13,14](#)}, they are molecularly homogeneous^{[15](#)}, and how the diversity of their anatomical and functional features emerge during development remains largely unknown. Here we address this question by linking the connectome and transcriptome in developing single ICPN of the mouse neocortex using a combination of multiplexed analysis of projections by sequencing^{[16,17](#)} (MAPseq, to identify single-neuron axonal projections) and single-cell RNA sequencing (to identify corresponding gene expression). Focusing on neurons of the primary somatosensory cortex (S1), we reveal a protracted unfolding of the molecular and functional differentiation of motor cortex-projecting ($\backslash(\backslash\text{vec}\{\{\backslash\text{rm}\{ M\}\}\}\backslash)$) ICPN compared with secondary somatosensory cortex-projecting ($\backslash(\backslash\text{vec}\{\{\backslash\text{rm}\{ S\}\}2\}\backslash)$) ICPN. We identify SOX11 as a temporally differentially expressed transcription factor in $\backslash(\backslash\text{vec}\{\{\backslash\text{rm}\{ M\}\}\}\backslash)$ versus $\backslash(\backslash\text{vec}\{\{\backslash\text{rm}\{ S\}\}2\}\backslash)$ ICPN. Postnatal manipulation of SOX11 expression in S1 impaired sensorimotor connectivity and disrupted selective exploratory behaviours in mice. Together, our results reveal that within a single cortical area, different subtypes of ICPN have distinct postnatal paces of molecular differentiation, which are subsequently reflected in distinct circuit connectivities and functions. Dynamic differences in the expression levels of a largely generic set of genes, rather than fundamental differences in the identity of developmental genetic programs, may thus account for the emergence of intra-type diversity in cortical neurons.

Access options

Subscribe to Journal

Get full journal access for 1 year

\$199.00

only \$3.90 per issue

[Subscribe](#)

All prices are NET prices.

VAT will be added later in the checkout.

Tax calculation will be finalised during checkout.

Rent or Buy article

Get time limited or full article access on ReadCube.

from \$8.99

[Rent or Buy](#)

All prices are NET prices.

Additional access options:

- [Log in](#)
- [Access through your institution](#)
- [Learn about institutional subscriptions](#)

Fig. 1: Postnatal emergence of intracortical connections from S1.

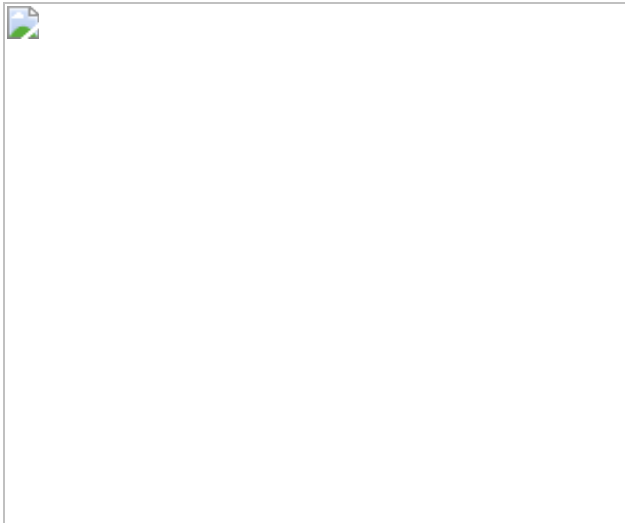


Fig. 2: $\overrightarrow{\{M\}}$ and $\overrightarrow{\{S\}}$ ICPN have distinct maturation paces.

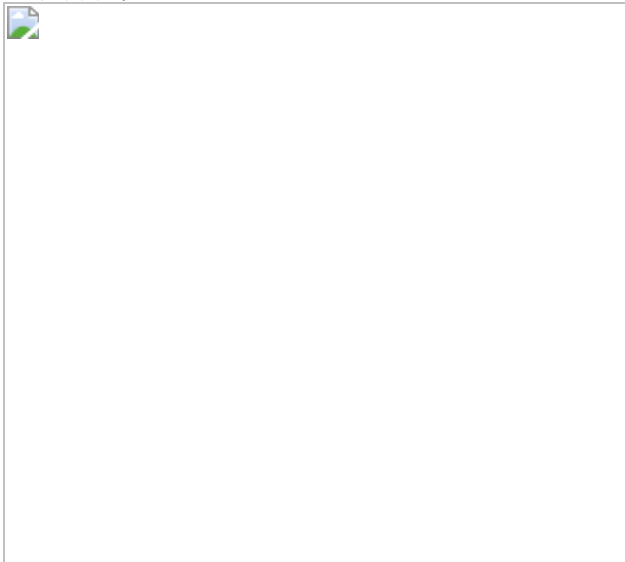


Fig. 3: Postnatal SOX11 expression levels regulate S1 sensorimotor connectivity.

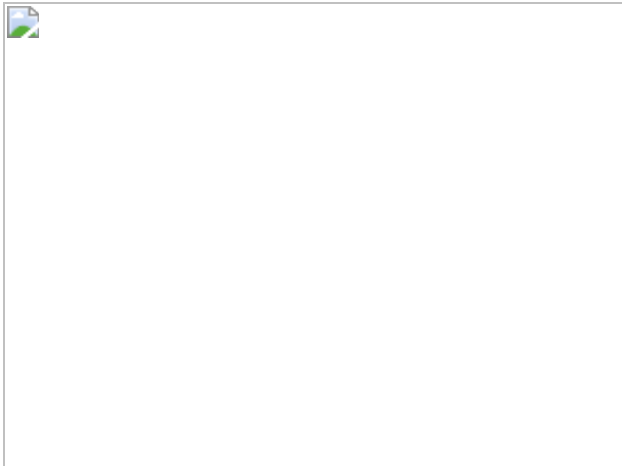
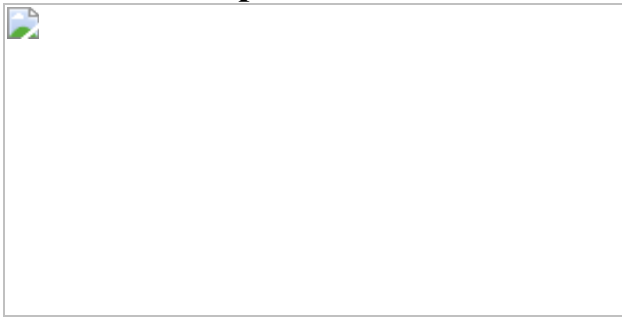


Fig. 4: Subtype-specific ICPN connectivity underlies specific features of sensorimotor exploration.



Data availability

scRNA-seq data have been deposited in the Gene Expression Omnibus (GEO) under the following accessions: MAPseq, [GSE118681](#); Retrobeads: [GSE116944](#); ConnectID: [GSE156080](#).

Code availability

https://github.com/pradosj/docker_sindbis

References

1. 1.

Mao, T. et al. Long-range neuronal circuits underlying the interaction between sensory and motor cortex. *Neuron* **72**, 111–123 (2011).

2. 2.

Chen, J. L., Carta, S., Soldado-Magraner, J., Schneider, B. L. & Helmchen, F. Behaviour-dependent recruitment of long-range projection neurons in somatosensory cortex. *Nature* **499**, 336–340 (2013).

3. 3.

Yamashita, T. & Petersen, C. C. Target-specific membrane potential dynamics of neocortical projection neurons during goal-directed behavior. *eLife* **5**, e15798 (2016).

4. 4.

Glickfeld, L. L., Andermann, M. L., Bonin, V. & Reid, R. C. Cortico-cortical projections in mouse visual cortex are functionally target specific. *Nat. Neurosci.* **16**, 219–226 (2013).

5. 5.

Guo, Z. V. et al. Flow of cortical activity underlying a tactile decision in mice. *Neuron* **81**, 179–194 (2014).

6. 6.

Kwon, S. E., Yang, H., Minamisawa, G. & O'Connor, D. H. Sensory and decision-related activity propagate in a cortical feedback loop during touch perception. *Nat. Neurosci.* **19**, 1243–1249 (2016).

7. 7.

Fame, R. M., MacDonald, J. L. & Macklis, J. D. Development, specification, and diversity of callosal projection neurons. *Trends Neurosci.* **34**, 41–50 (2011).

8. 8.

Sorensen, S. A. et al. Correlated gene expression and target specificity demonstrate excitatory projection neuron diversity. *Cerebral Cortex* **25**, 433–449 (2015).

9. 9.

Tasic, B. et al. Shared and distinct transcriptomic cell types across neocortical areas. *Nature* **563**, 72–78 (2018).

10. 10.

Aronoff, R. et al. Long-range connectivity of mouse primary somatosensory barrel cortex. *Eur. J. Neurosci.* **31**, 2221–2233 (2010).

11. 11.

Zingg, B. et al. Neural networks of the mouse neocortex. *Cell* **156**, 1096–1111 (2014).

12. 12.

Gong, H. et al. High-throughput dual-colour precision imaging for brain-wide connectome with cytoarchitectonic landmarks at the cellular level. *Nat. Commun.* **7**, 12142 (2016).

13. 13.

Chen, X. et al. High-throughput mapping of long-range neuronal projection using *in situ* sequencing. *Cell* **179**, 772–786.e19 (2019).

14. 14.

Peng, H. et al. Morphological diversity of single neurons in molecularly defined cell types. *Nature* **598**, 174–181 (2021).

15. 15.

Yao, Z. et al. A taxonomy of transcriptomic cell types across the isocortex and hippocampal formation. *Cell* **184**, 3222-3241.e26

(2021).

16. 16.

Kebschull, J. M. et al. High-throughput mapping of single-neuron projections by sequencing of barcoded rna. *Neuron* **91**, 975–987 (2016).

17. 17.

Han, Y. et al. The logic of single-cell projections from visual cortex. *Nature* **556**, 51–56 (2018).

18. 18.

Yamashita, T. et al. Membrane potential dynamics of neocortical projection neurons driving target-specific signals. *Neuron* **80**, 1477–1490 (2013).

19. 19.

Yamashita, T. et al. Diverse long-range axonal projections of excitatory layer 2/3 neurons in mouse barrel cortex. *Front. Neuroanat.* **12**, 33 (2018).

20. 20.

Rebsam, A., Seif, I. & Gaspar, P. Refinement of thalamocortical arbors and emergence of barrel domains in the primary somatosensory cortex: a study of normal and monoamine oxidase a knock-out mice. *J. Neurosci.* **22**, 8541–8552 (2002).

21. 21.

Molnár, Z., Kurotani, T., Higashi, S., Yamamoto, N. & Toyama, K. Development of functional thalamocortical synapses studied with current source-density analysis in whole forebrain slices in the rat. *Brain Res. Bull.* **60**, 355–371 (2003).

22. 22.

Wang, C. L. et al. Activity-dependent development of callosal projections in the somatosensory cortex. *J. Neurosci.* **27**, 11334–11342 (2007).

23. 23.

Hand, R. A., Khalid, S., Tam, E. & Kolodkin, A. L. Axon dynamics during neocortical laminar innervation. *Cell Rep.* **12**, 172–182 (2015).

24. 24.

Klingler, E. et al. A Translaminar genetic logic for the circuit identity of intracortically projecting neurons. *Curr. Biol.* **29**, 332–339.e5 (2019).

25. 25.

Telley, L. et al. Temporal patterning of apical progenitors and their daughter neurons in the developing neocortex. *Science* **364**, eaav2522 (2019).

26. 26.

Madisen, L. et al. Transgenic mice for intersectional targeting of neural sensors and effectors with high specificity and performance. *Neuron* **85**, 942–958 (2015).

27. 27.

Quairiaux, C., Megevand, P., Kiss, J. Z. & Michel, C. M. Functional development of large-scale sensorimotor cortical networks in the brain. *J. Neurosci.* **31**, 9574–9584 (2011).

28. 28.

van der Bourg, A. et al. Layer-specific refinement of sensory coding in developing mouse barrel cortex. *Cereb. Cortex* **84**, 401–416 (2016).

29. 29.

Kuwajima, T., Soares, C. A., Sitko, A. A., Lefebvre, V. & Mason, C. SoxC transcription factors promote contralateral retinal ganglion cell differentiation and axon guidance in the mouse visual system. *Neuron* **93**, 1110–1125.e5 (2017).

30. 30.

Paolino, A. et al. Differential timing of a conserved transcriptional network underlies divergent cortical projection routes across mammalian brain evolution. *Proc. Natl Acad. Sci. USA* **117**, 10554–10564 (2020).

31. 31.

Taylor, R. J. et al. Double UP: a dual color, internally controlled platform for in utero knockdown or overexpression. *Front. Mol. Neurosci.* **13**, 82 (2020).

32. 32.

Platt, R. J., et al. CRISPR–Cas9 knockin mice for genome editing and cancer modeling. *Cell* **159**, 440–455 (2014).

33. 33.

Sanjana, N. E., Shalem, O. & Zhang, F. Improved vectors and genome-wide libraries for CRISPR screening. *Nat. Methods* **11**, 783–784 (2014).

34. 34.

Vitali, I. et al. Progenitor hyperpolarization regulates the sequential generation of neuronal subtypes in the developing neocortex. *Cell* **174**, 1264–1276.e15 (2018).

35. 35.

Suter, B. A. et al. Ephus: multipurpose data acquisition software for neuroscience experiments. *Front. Neural Circuits* **4**, 100 (2010).

36. 36.

Golding, B. et al. Retinal input directs the recruitment of inhibitory interneurons into thalamic visual circuits. *Neuron* **81**, 1057–1069 (2014).

37. 37.

Smith, T., Heger, A. & Sudbery, I. UMI-tools: modeling sequencing errors in unique molecular identifiers to improve quantification accuracy. *Genome Res.* **27**, 491–499 (2017).

38. 38.

Li, H. & Durbin, R. Fast and accurate short read alignment with Burrows–Wheeler transform. *Bioinformatics* **25**, 1754–1760 (2009).

39. 39.

Nestorowa, S. et al. A single-cell resolution map of mouse hematopoietic stem and progenitor cell differentiation. *Blood* **128**, e20–e31 (2016).

40. 40.

Subramanian, A. et al. Gene set enrichment analysis: A knowledge-based approach for interpreting genome-wide expression profiles. *Proc. Natl Acad. Sci. USA* **102**, 15545–15550 (2005).

41. 41.

Oberst, P. et al. Temporal plasticity of apical progenitors in the developing mouse neocortex. *Nature* **573**, 370–374 (2019)

Acknowledgements

We thank A. Zador for his contribution to an earlier version of this manuscript and for his sharing of MAPseq mapping reagents; the Genomics Platform and FACS Facility of the University of Geneva; L. Frangeul for her contribution to manuscript preparation and proofreading; A. Benoit for technical assistance; N. Baumann and Q. LoGiudice for assistance with bioinformatics analyses; S. Roig Puiggros for help with schematic designs; all members of the Jabaudon laboratory and E. Azim, V. Castellani, A. Chédotal, C. Desplan and G. Pouchelon for constructive comments on the manuscript. The Jabaudon laboratory is supported by the Swiss National Science Foundation, the Carigest Foundation, the Société Académique de Genève FOREMANE Fund, and the Simons Foundation for Autism Research. E.K. is supported by a grant from the Machaon Foundation. U.T. is supported by Swiss National Foundation Synapsy (grant 51NF40-185897). J.P. is supported by the Public Instruction Department, Geneva. J.M.K. was supported by Boehringer Ingelheim and Jane Coffin Childs postdoctoral funds. D.H. and G.L.G. are supported by the International Foundation for Paraplegia Research and the Swiss National Foundation. A.S. and R.J.P. are supported by the Swiss National Science Foundation (SNF 31003A_175830), ETH Zurich Research Grant (ETH-27 18-2), EMBO Young Investigator Program (4217), Personalized Health and Related Technologies (PHRT), and National Centres of Competence – Molecular Systems Engineering. A.D. was supported by the Swiss National Foundation Synapsy (grant 51NF40-158776). C.B. is supported by the Swiss National Foundation (grant: 31003A_182326) and NCCR-Synapsy.

Author information

Author notes

1. Justus M. Kebschull

Present address: Department of Biomedical Engineering, Johns Hopkins University, Baltimore, MD, USA

2. These authors contributed equally: Ugo Tomasello, Julien Prados

Affiliations

1. Department of Basic Neurosciences, University of Geneva, Geneva, Switzerland

Esther Klingler, Ugo Tomasello, Alessandro Contestabile, Gregorio L. Galiñanes, Sabine Fièvre, Daniel Huber, Alexandre Dayer, Camilla Bellone & Denis Jabaudon

2. Department of Psychiatry, Geneva University Hospital, Geneva, Switzerland

Julien Prados & Alexandre Dayer

3. Cold Spring Harbor Laboratory, Cold Spring Harbor, New York, NY, USA

Justus M. Kebschull

4. Department of Biosystems Science and Engineering, ETH Zurich, Basel, Switzerland

Antonio Santinha & Randal Platt

5. Clinic of Neurology, Geneva University Hospital, Geneva, Switzerland

Denis Jabaudon

Contributions

U.T., A.C., G.L.G. and S.F. performed the experiments. E.K. and J.P. performed the bioinformatics analyses. J.M.K. provided Sindbis virus and shared expertise on MAPseq. A.S. and R.P. designed, cloned and validated sgRNAs and Cas9 vector. E.K. and D.J. wrote the manuscript. U.T., A.C., G.L.G., S.F., J.M.K., D.H., C.B. and A.D. revised and edited the manuscript. We dedicate this manuscript to the memory of Alexandre Dayer, who passed away before completion of this work.

Corresponding author

Correspondence to [Denis Jabaudon](#).

Ethics declarations

Competing interests

The authors declare no competing interests.

Additional information

Peer review information *Nature* thanks the anonymous reviewer(s) for their contribution to the peer review of this work.

Publisher's note Springer Nature remains neutral with regard to jurisdictional claims in published maps and institutional affiliations.

Extended data figures and tables

[Extended Data Fig. 1 MAPseq experimental procedure to study postnatal emergence of inter-areal cortical connectivity.](#)

a, Left, retrograde labeling from M or S2 using green (Gbeads) or red (Rbeads) retrobeads. *Injection site. Center, Gbeads M- and Rbeads S2-inter-areal cortical projection neurons ($\backslash(\backslash\text{vec}\{\{\backslash\text{rm}\{M\}\}\}\backslash)$ and $\backslash(\backslash\text{vec}\{\{\backslash\text{rm}\{S\}\}2\}\backslash)$) ICPN) in S1 at P7 (arrowheads, retrogradely-labeled cells). Right, Illustrations of $\backslash(\backslash\text{vec}\{\{\backslash\text{rm}\{M\}\}\}\backslash)$ and $\backslash(\backslash\text{vec}\{\{\backslash\text{rm}\{S\}\}2\}\backslash)$ ICPN layer positions at P5, P7 and P14 (P5: $n=4$, P7: $n=3$, P14: $n=2$ pups from 2 litters / target; 50 random quantified cells were plotted per condition; dot shades represent the different pups). **b**, Double retrograde labeling using Gbeads in M and alexa 546-conjugated CTB in S2 at P5, P7 and P14 (P5,P14: $n=4$; P7: $n=3$ pups from 2 litters; $n=50$ to 200 $\backslash(\backslash\text{vec}\{\{\backslash\text{rm}\{M\}\}\}\backslash)$ and $\backslash(\backslash\text{vec}\{\{\backslash\text{rm}\{S\}\}2\}\backslash)$ ICPN per pup). Note that the proportion of co-labeled cells (*i.e.* cells projecting to both M and S2) is stable from P5 on (two-way ANOVA test: P value > 0.9999). **c**, Left, MAPseq principle. Center, infected neurons in S1 expressing Sindbis-GFP

14 hours after infection. Arrowhead shows an axon labeled with GFP. Right, *in situ* hybridization at P14 shows barcode-*Gfp* mRNA (level 2 from Fig. 1b). **d**, Microdissections of injection and target sites. **e**, S1 ICPN multiplex projections at P5, P7 and P14 (showing data from Fig. 1c as percent max projection). **f**, Diversity of projection patterns measured by the entropy at each age (see Methods). In black is the value for random patterns (*i.e.* 6 bits / pattern). **g**, Similarity between projection pattern matrices, shown as 1 - relative Kullback-Liebler divergence value (see Methods). Note that P7 and P14 projection pattern matrices display the highest similarity. **h**, First and second targets of ICPN at P5, P7 and P14. ICPN with only one target are represented with same first and second targets. Values are shown as mean \pm s.e.m. (**b**, **h**). Scale bars, 100 μm (**a**, **b**); 300 μm (**c**); 1 mm (**d**). A, auditory cortex; C, contralateral cortex; CTB, cholera toxin B; Gbeads, green retrobeads; Hip, hippocampus; M, motor cortex; P, postnatal day; Rbeads, red retrobeads; S1, primary somatosensory cortex; S2, secondary somatosensory cortex; Sub, subcortical; Str, striatum; Thal, thalamus; V, visual cortex.

[Extended Data Fig. 2 \\(\rightarrow\{\bf{M}\}\\) and \\(\rightarrow\{\bf{S}\}.\{\bf{2}\}\} ICPN have otherwise similar multiplex projection patterns.](#)

a, Cluster analysis of $\left(\vec{\{\rm M\}}\right)$ and $\left(\vec{\{\rm S\}}_2\right)$ ICPN projecting in more than one target at P14 reveals 4 projection patterns ($n = 400 \left(\vec{\{\rm M\}}\right)$ or $\left(\vec{\{\rm S\}}_2\right)$ ICPN). Note the similar distribution of patterns for both populations. **b**, Distribution of P5 and P7 $\left(\vec{\{\rm M\}}\right)$ and $\left(\vec{\{\rm S\}}_2\right)$ ICPN projecting in more than one target in the P14 clusters using k-nearest neighbors (knn; see Methods). Note that $\left(\vec{\{\rm M\}}\right)$ and $\left(\vec{\{\rm S\}}_2\right)$ ICPN show similar patterns at P7 and P14.

[Extended Data Fig. 3 ConnectID data preprocessing and quality controls.](#)

Data presented here are the raw data from the single-cell analysis, and include cells without detected projections in the targets. **a**, Data processing

allowing retrieval of single-cell gene expression and projection(s). **b-f**, Non-filtered barcodes (BC) quality controls in single cells after sequencing error correction (step 5 in **a**) for each pup used in this study ($n = 1859$ cells). **b**, Single cells and their corresponding BC. Each column corresponds to a cell, and each line to a BC sequence. **c**, BC sequence(s) within cells. Number of BC with distinct sequences per cell. Pie chart represents summary of the data. ~80% of the cells express 1 to 4 BC sequences. **d**, BC counts for the top 5 most expressed BC. Box plots indicate median \pm s.d. and interquartile range. **e**, Counts of the most expressed to the less expressed BC for cells with more than 1 BC sequence. **f**, Barcodes across cells. Number of BC sequences found in the top 9 cells (left). 80% of the BC sequences are found in only one cell. Counts for the BC found in several cells from the cell where it is the most abundant to the cell where it is the least abundant (right).

Extended Data Fig. 4 Quality controls of single cells collected 14 hours after Sindbis infection.

a, Fluorescence activated (FAC) sorting of Sindbis-GFP+ / Hoechst+ cells (left), capture and quality controls of single cells in microfluidic wells using brightfield imaging (right). Wells with no cell, several cells, debris or with high mitochondrial reads ($> 30\%$ total mapped reads) were excluded. **b**, Number of mapped reads, of expressed (exprs.) genes, and proportion of mitochondrial (mito.) reads (on total mapped reads) per cell. Bottom right, note that the proportion of mitochondrial reads is not correlated with the viral load (*i.e.* with the number of Sindbis reads) in each cell. Retrogradely-labeled ICPN (Rbeads) collected at P9 were used as control cells for the effect of the viral infection. **c**, Viral load increases with the number of barcode(s) per cell ($n = 2450$ cells). Box plots indicate median \pm s.d. and interquartile range. **d**, Ordinal regression model identifies genes with the strongest weight in distinguishing neurons with a higher viral load from those with a lower viral load. **e**, “least square” fit regression was performed to the expression set using viral load and number of expressed genes as variables to regress. rpm, reads per million.

Extended Data Fig. 5 S1 L2/3 ICPN have highly similar transcriptional identity.

a, Left, UMAP of SSp L2/3 intratelencephalic (IT) neurons and clusters from Yao et al., 2021¹⁵. Right, distribution of cells across clusters. **b**, Distribution of neurons projecting to MOp (corresponding to “M”) or SSs (“S2”) retrogradely labeled (using retrograde AAV2 virus) in the UMAP (left) and within the clusters (right). Note that neurons projecting to MOp or SSs neither belonged to distinct transcriptional cluster nor clustered apart in the L2/3 IT Otof 5 cluster, suggesting that these subtypes have highly similar transcriptional identities. **c**, Top, tSNE representation of P14 neurons after layer microdissection. Bottom, main target and distribution of ConnectID neurons in superficial (SL) versus deep (DL) layers. **d**, Kmeans clustering of single cells based on their tSNE values (left) and distribution of cells in the 4 identified clusters (right). Note that cells cluster based on their age of collection. **e**, Kmeans clustering based on tSNE values calculated independently at each collection age (P7, P9, P14), and distribution of neurons with known projection within these clusters. P7 and P14 cells are from ConnectID experiments, while P9 cells are from both ConnectID and Rbeads experiments (see Methods). Note that developing ICPN are not detectably clustered by their axonal target, but rather by their layer position, as showed at P14 when SL and DL were microdissected. IT, intratelencephalic; L, layer; MOp, primary motor cortex; SSp, primary somatosensory cortex; SSs, secondary somatosensory cortex.

Extended Data Fig. 6 Transcriptional maturation of \(\rightarrow\{\rm{S}\}2\}) and \(\rightarrow\{\rm{M}\}\},\}) ICPN.

a, Pseudo-maturation score calculated for each cell (see Methods). **b**, Expression and number of genes in each wave for $\langle\langle\text{vec}\{\{\text{rm}\{S\}\}2\}\rangle\rangle$ and $\langle\langle\text{vec}\{\{\text{rm}\{M\}\}\}\rangle\rangle$ ICPN. **c**, Gene ontology analysis of genes belonging to each wave in $\langle\langle\text{vec}\{\{\text{rm}\{S\}\}2\}\rangle\rangle$ and $\langle\langle\text{vec}\{\{\text{rm}\{M\}\}\}\rangle\rangle$ ICPN. **d**, Venn diagrams showing shared genes between ontologies. **e**, Distribution of $\langle\langle\text{vec}\{\{\text{rm}\{S\}\}2\}\rangle\rangle$ ICPN wave-defined genes into $\langle\langle\text{vec}\{\{\text{rm}\{M\}\}\}\rangle\rangle$ ICPN waves (left), and of $\langle\langle\text{vec}\{\{\text{rm}\{M\}\}\}\rangle\rangle$ ICPN wave-defined genes

into $\backslash(\backslash\text{vec}\{\{\backslash\text{rm}\{S\}\}2\},\)$ ICPN waves (right) by gene ontology. **f**, Top, expression of axon development- (left), and dendrite- (center) related genes along pseudo-maturation in $\backslash(\backslash\text{vec}\{\{\backslash\text{rm}\{S\}\}2\},)$ and $\backslash(\backslash\text{vec}\{\{\backslash\text{rm}\{M\}\}\})$ ICPN. Bottom, number of genes related to synapse in each wave for $\backslash(\backslash\text{vec}\{\{\backslash\text{rm}\{S\}\}2\},)$ and $\backslash(\backslash\text{vec}\{\{\backslash\text{rm}\{M\}\}\})$ ICPN (left) and synapse-related gene expression along pseudo-maturation in $\backslash(\backslash\text{vec}\{\{\backslash\text{rm}\{S\}\}2\},)$ and $\backslash(\backslash\text{vec}\{\{\backslash\text{rm}\{M\}\}\},)$ ICPN (center) (repeated measures-ANOVA based on a general linear model with Geisser-Greenhouse correction). Right, examples of dynamics of gene expression for 3 classical axon (*Chl1* and *Tubb5*) and dendrite (*Map2*) development-related genes. Dots correspond to single cells.

Extended Data Fig. 7 Functional maturation of $\overrightarrow{\{\backslash\text{rm}\{M\}\}}$ and $\overrightarrow{\{\backslash\text{rm}\{S\}\}2}$ inter-areal cortical projection neurons using calcium imaging upon somatosensory stimulations.

a, Calcium wide-field imaging upon sensory stimulations in Cux2:Cre x GCaMP6s anesthetized pups at P9 and P15. Experimental paradigm and *in situ* hybridization for the *Cre* transcript in Cux2:Cre P28 pup (from the Allen Brain Institute database). **b**, Pooled responses to whisker pad, hindlimb and forelimb stimulations in S1, M, S2, and V at P9 and P15. At P9, response in M was not different than response in V (considered as background value) ($n = 3$ animals / age; two-way ANOVA with Sidak's multiple comparisons test: M versus V: P9: adjusted P value = 0.8421; P14: adjusted P value = 0.0001; S2 versus V: P9: adjusted P value = 0.0174; P14: adjusted P value = 0.0123). Thinner traces represent the values for each individual pup. Grey, stimulation. Pooled responses are either represented by age (top) or by cortical area (bottom). Note the distinct response dynamics at P9 and P15, P15 responses decreasing faster after the stimulation than P9 responses. **c**, Response to whisker pad (top), hindlimb (middle), and forelimb (bottom) stimulations. The absence of response in M at P9 does not depend on the type of stimulation. Scale bar, 100 μm (**a**, top). Fluorescence (F) in targets was normalized to the mean fluorescence in S1. A, auditory cortex; BF, barrel field; FL, forelimb; HL, hindlimb; M,

motor cortex; P, postnatal day; S1, primary somatosensory cortex; S2, secondary somatosensory cortex; V, visual cortex.

Extended Data Fig. 8 Restricted up- and down-regulation of SOX11 in time and space alters intracortical connectivity.

a, *Sox11* is transiently enriched in $\langle \text{vec}(\{\text{rm}\{S\}\})^2 \rangle$ ICPN at P7 (Kolmogorov-Smirnov test: P value < 0.0001), as confirmed at the protein level in $\langle \text{vec}(\{\text{rm}\{S\}\})^2 \rangle$ compared to $\langle \text{vec}(\{\text{rm}\{M\}\}) \rangle$ retrogradely-labeled ICPN ($n = 3$ pups from 2 litters per target; unpaired t -test: P value = 0.0149). Values are shown as mean \pm s.e.m. **b**, Double-UP plasmid control (Ctl) / *Sox11* constructs and Cre-dependent recombination allowing the expression of Scarlet (Ctl) or Scarlet + SOX11 (SOX11). **c**, Left, GFP and Scarlet expression at P14 without (no Cre) or after AAV-pCMV-Cre stereotaxic injection at P0 in putative S1 (pS1). Note the restricted expression of Scarlet in S1 cells, while GFP electroporated cells are found both in S1 and S2. Right, overexpression of SOX11 protein in Scarlet⁺ cells at P5. **d**, Quantification of the number of Cre⁺ cells in S1 at P17 (data are the mean values over 3 sections per pup; unpaired t -test: P value = 0.0808). Note that SOX11 overexpression postnatally does not affect neuron migration or survival. **e**, Left, representative images of Scarlet axons in C and CC. Center, fluorescence-based quantification of the area covered by axonal signal (normalized by the number of Cre⁺ cells in S1) in M, S2, C and CC for each pup (\log_{10} values, see Methods; M: $n = 13$ Ctl, $n = 13$ SOX11; S2: $n = 13$ Ctl, $n = 11$ SOX11; C: $n = 7$ Ctl, $n = 6$ SOX11; CC: $n = 11$ Ctl, $n = 11$ SOX11 pups from 4 litters per condition). Number of brains analyzed differ across targets because in some cases no quantification was possible. Pink dashed line, threshold below which no axon was detected. Right, heatmap of axon signal intensity in M and S2 for each pup. Dark grey, pups for which no axon was detected in the target. Only brains in which S2 and M projections could be assessed are shown here (in two SOX11 cases, only M projections could be assessed). **f**, Co-culture of SOX11-overexpressing and control L2/3 neurons. Left, experimental procedure. Half of the embryos were electroporated with dUP-*Sox11* alone (Ctl) and the other half with dUP-*Sox11* and pCAG:Cre plasmids (SOX11) at E15.5. Control and SOX11 cortical neurons were dissociated and

cultured together at E16.5. Right, at DIV2, axon length was similar in both conditions. Values are shown as mean \pm s.e.m. (unpaired *t*-test: *P* value = 0.3101). **g**, Left, inducible single-guide (sg) RNA against *Sox11* leads to absence of SOX11 expression after AAV-pCMV-Cre stereotaxic injection at P0 in putative S1. Right, representative images of Scarlet⁺ axons in each target and quantification of the axonal phenotype. Scale bars, 100 μ m (**c, e, g** right); 10 μ m (**a, f, g** left). **d, e, g**, Box plots indicate median \pm s.d. and interquartile range. **e, g**, Two-way ANOVA with Sidak's multiple comparisons test: Ctl versus SOX11: M: adjusted *P* value < 0.0001; S2: adjusted *P* value = 0.0008; M versus 2: Ctl: adjusted *P* value = 0.3186; SOX11: adjusted *P* value = 0.0251; Ctl versus *Sox11* sgRNA: M: adjusted *P* value = 0.0833; S2: adjusted *P* value = 0.0339. CC, corpus callosum; DIV, days *in vitro*; dUP, double-UP; E, embryonic day; epo., *in utero* electroporation; M, motor cortex; L, layer; P, postnatal day; S1, primary somatosensory cortex; S2, secondary somatosensory cortex; sfGFP, super-folded GFP.

Extended Data Fig. 9 Altered intracortical somatosensory connectivity impairs exploratory behavior.

a, Trajectories in open-field arena for each pup. The name of each pup is indicated (#). Two different arenas were used accounting for slight differences in trajectory shapes. **b**, SOX11-overexpressing (SOX11) pups display decreased velocity (unpaired *t*-test: *P* value = 0.0355), decreased rearing (unpaired *t*-test: *P* value = 0.0007), increased time immobile (Mann Whitney test: *P* value = 0.0005) but similar time spent in the center of the open-field (unpaired *t*-test: *P* value = 0.9030) or time spent grooming (unpaired *t*-test: *P* value = 0.1990), compared to control pups (Ctl) (*n* = 12 Ctl pups; *n* = 13 SOX11 pups). Box plots indicate median \pm s.d. and interquartile range. **c**, Feature plots of specific behavioral and anatomical parameters. **d**, Correlation between principal component (PC) 1 and the Scarlet axonal signal measured in M for each pup.

Supplementary information

Supplementary Information

This file contains Supplementary Notes 1, 2, including two Supplementary Figures.

Reporting Summary

Supplementary Table 1

ICPN used for MAPseq analyses. $n = 140$ (P5) or 400 (P7; P14) ICPN barcodes (see Methods) per pup ($n = 4$ pups for each age) were randomly selected to avoid any bias due to variability in Sindbis injection site depth. Barcode names are as follows: name of the pup, error-corrected sequence of the barcode, barcode counts and cluster information in S1 injection site (barcode counts before sequencing error correction, number of barcode sequences with less than 3 mismatches, error-corrected barcode counts; see Methods for normalization of barcode counts in targets).

Supplementary Table 2

Distribution of genes in the three transcriptional waves for $\backslash(\backslash\text{vec}\{\{\backslash\text{rm}\{S\}\}2\}\backslash)$ and $\backslash(\backslash\text{vec}\{\{\backslash\text{rm}\{M\}\}\}\backslash)$ ICPN. Normalized transcriptional patterns were clustered in 3 groups (waves) based on their distances along pseudo-maturation using pam function of cluster package ($k = 3$). The average expression pattern was calculated for each cluster and the distances of all transcriptional patterns to this average were calculated. Only genes closely related to a given pattern in both $\backslash(\backslash\text{vec}\{\{\backslash\text{rm}\{M\}\}\}\backslash)$ and $\backslash(\backslash\text{vec}\{\{\backslash\text{rm}\{S\}\}2\}\backslash)$ ICPN were kept for further analyses ($n = 1,293$ genes). Genes in each wave and their ontologies are indicated for both $\backslash(\backslash\text{vec}\{\{\backslash\text{rm}\{S\}\}2\}\backslash)$ and $\backslash(\backslash\text{vec}\{\{\backslash\text{rm}\{M\}\}\}\backslash)$ ICPN.

Supplementary Table 3

Neuron differentiation-, dendrite-, axon development- and synapse- related genes. Gene sets were established using QuickGO gene ontology annotations from EMBL-EBI.

Supplementary Table 4

Differential gene-expression analysis between $\text{vec}(\{\text{rm}\{S\}\}2)$ and $\text{vec}(\{\text{rm}\{M\}\})$ ICPN at P7. Distances between $\text{vec}(\{\text{rm}\{M\}\})$ and $\text{vec}(\{\text{rm}\{S\}\}2)$ ICPN gene-expression profiles along pseudo-maturation were calculated for all genes from wave 1 (that is, genes dynamically regulated along postnatal development, with high expression at P7). Genes with distances > 5.8 between $\text{vec}(\{\text{rm}\{M\}\})$ and $\text{vec}(\{\text{rm}\{S\}\}2)$ ICPN were selected for ontology analyses using GSEA.

Rights and permissions

[Reprints and Permissions](#)

About this article

Cite this article

Klingler, E., Tomasello, U., Prados, J. *et al.* Temporal controls over inter-areal cortical projection neuron fate diversity. *Nature* **599**, 453–457 (2021). <https://doi.org/10.1038/s41586-021-04048-3>

- Received: 27 July 2018
- Accepted: 23 September 2021
- Published: 09 November 2021
- Issue Date: 18 November 2021
- DOI: <https://doi.org/10.1038/s41586-021-04048-3>

Share this article

Anyone you share the following link with will be able to read this content:

[Get shareable link](#)

Sorry, a shareable link is not currently available for this article.

[Copy to clipboard](#)

Provided by the Springer Nature SharedIt content-sharing initiative

This article was downloaded by **calibre** from <https://www.nature.com/articles/s41586-021-04048-3>

| [Section menu](#) | [Main menu](#) |

- Article
- [Published: 29 July 2021](#)

Novel bile acid biosynthetic pathways are enriched in the microbiome of centenarians

- [Yuko Sato](#) [ORCID: orcid.org/0000-0002-2177-5820](#)^{1,2,3 na1},
- [Koji Atarashi](#) [ORCID: orcid.org/0000-0001-5422-0736](#)^{1,2,3 na1},
- [Damian R. Plichta](#) [ORCID: orcid.org/0000-0002-6555-2557](#)^{4 na1},
- [Yasumichi Arai](#)⁵,
- [Satoshi Sasajima](#)^{1,3},
- [Sean M. Kearney](#)^{1,2},
- [Wataru Suda](#)²,
- [Kozue Takeshita](#)^{1,3},
- [Takahiro Sasaki](#)⁶,
- [Shoki Okamoto](#)¹,
- [Ashwin N. Skelly](#) [ORCID: orcid.org/0000-0002-1565-3376](#)¹,
- [Yuki Okamura](#)¹,
- [Hera Vlamakis](#) [ORCID: orcid.org/0000-0003-1086-9191](#)⁴,
- [Youxian Li](#)²,
- [Takeshi Tanoue](#) [ORCID: orcid.org/0000-0003-3639-8834](#)^{1,2,3},
- [Hajime Takei](#)⁷,
- [Hiroshi Nittono](#)⁷,
- [Seiko Narushima](#)^{1,2},
- [Junichiro Irie](#) [ORCID: orcid.org/0000-0003-2662-4121](#)⁸,
- [Hiroshi Itoh](#)⁸,
- [Kyoji Moriya](#)⁹,
- [Yuki Sugiura](#)¹⁰,
- [Makoto Suematsu](#) [ORCID: orcid.org/0000-0002-7165-6336](#)¹⁰,

- [Nobuko Moritoki](#)¹¹,
- [Shinsuke Shibata](#) [ORCID: orcid.org/0000-0002-1185-9043](#)¹¹,
- [Dan R. Littman](#)^{12,13},
- [Michael A. Fischbach](#) [ORCID: orcid.org/0000-0003-3079-8247](#)¹⁴,
- [Yoshifumi Uwamino](#)¹⁵,
- [Takashi Inoue](#) [ORCID: orcid.org/0000-0003-4691-7255](#)¹⁶,
- [Akira Honda](#) [ORCID: orcid.org/0000-0003-0902-8272](#)¹⁷,
- [Masahira Hattori](#)^{2,18},
- [Tsuyoshi Murai](#)⁶,
- [Ramnik J. Xavier](#) [ORCID: orcid.org/0000-0002-5630-5167](#)^{4,19,20},
- [Nobuyoshi Hirose](#)⁵ &
- [Kenya Honda](#) [ORCID: orcid.org/0000-0001-8937-9835](#)^{1,2,3}

Nature volume **599**, pages 458–464 (2021)

- 22k Accesses
- 11 Citations
- 680 Altmetric
- [Metrics details](#)

Subjects

- [Antimicrobial resistance](#)
- [Microbiome](#)

Abstract

Centenarians have a decreased susceptibility to ageing-associated illnesses, chronic inflammation and infectious diseases^{1,2,3}. Here we show that centenarians have a distinct gut microbiome that is enriched in microorganisms that are capable of generating unique secondary bile acids, including various isoforms of lithocholic acid (LCA): iso-, 3-oxo-, allo-, 3-oxallo- and isoallolithocholic acid. Among these bile acids, the

biosynthetic pathway for isoalloLCA had not been described previously. By screening 68 bacterial isolates from the faecal microbiota of a centenarian, we identified Odoribacteraceae strains as effective producers of isoalloLCA both in vitro and in vivo. Furthermore, we found that the enzymes 5 α -reductase (5AR) and 3 β -hydroxysteroid dehydrogenase (3 β -HSDH) were responsible for the production of isoalloLCA. IsoalloLCA exerted potent antimicrobial effects against Gram-positive (but not Gram-negative) multidrug-resistant pathogens, including *Clostridioides difficile* and *Enterococcus faecium*. These findings suggest that the metabolism of specific bile acids may be involved in reducing the risk of infection with pathobionts, thereby potentially contributing to the maintenance of intestinal homeostasis.

Access options

Subscribe to Journal

Get full journal access for 1 year

\$199.00

only \$3.90 per issue

[Subscribe](#)

All prices are NET prices.

VAT will be added later in the checkout.

Tax calculation will be finalised during checkout.

Rent or Buy article

Get time limited or full article access on ReadCube.

from \$8.99

[Rent or Buy](#)

All prices are NET prices.

Additional access options:

- [Log in](#)
- [Access through your institution](#)
- [Learn about institutional subscriptions](#)

Fig. 1: Centenarians have significantly elevated levels of faecal isoLCA, 3-oxoLCA, alloLCA, 3-oxoalloLCA and isoalloLCA.



Fig. 2: Identification of bacterial strains and genes involved in the generation of isoalloLCA and related bile acids.

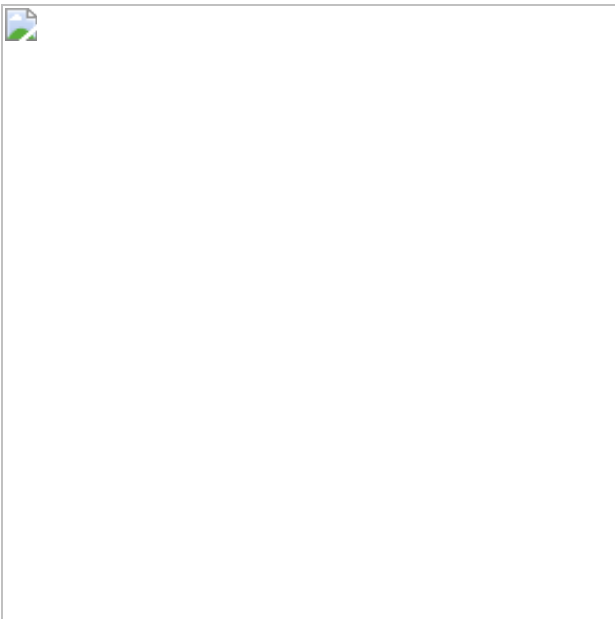


Fig. 3: IsoalloLCA exerts potent antimicrobial activity against Gram-positive pathogens.

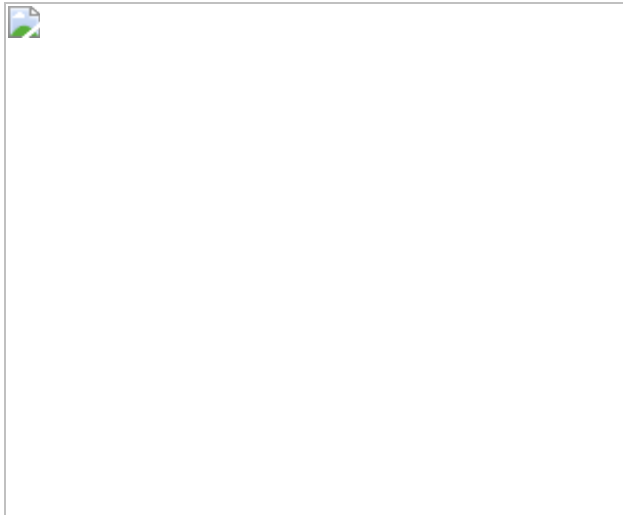
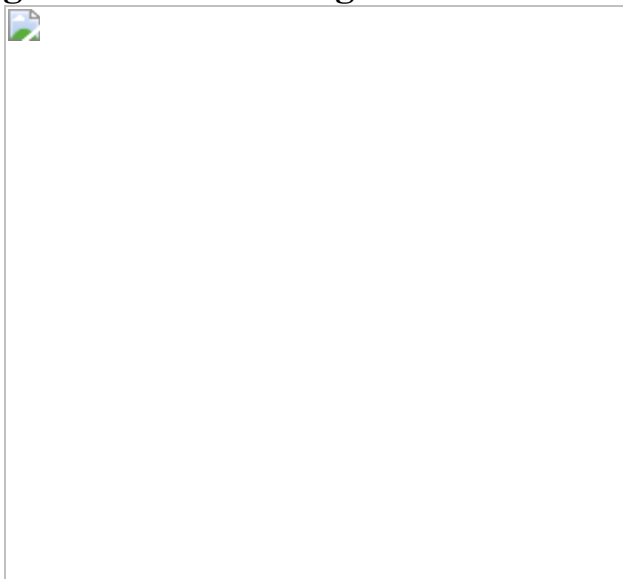


Fig. 4: Association of gut microbiome structure with bile acid profile.



Data availability

Shotgun sequencing data are deposited in NCBI under BioProject [PRJNA675598](#). Genome sequences of the 68 strains isolated from a centenarian and 16S rRNA amplicon sequence data are deposited in the DNA Data Bank of Japan under BioProject [PRJDB11902](#) and [PRJDB11894](#), respectively. LC–MS/MS data are deposited in Metabolomics Workbench (<https://www.metabolomicsworkbench.org/>) under project ID PR001168 with study ID ST001851 for human faeces data and study ID ST001852 for in vitro data. [Source data](#) are provided with this paper.

Code availability

Code for all of the analyses is available on GitHub (<https://gitlab.com/xavier-lab-computation/public/centenarianmicrobiome>).

References

1. 1.
Hirata, T. et al. Associations of cardiovascular biomarkers and plasma albumin with exceptional survival to the highest ages. *Nat. Commun.* **11**, 3820 (2020).
2. 2.
Sebastiani, P. et al. Meta-analysis of genetic variants associated with human exceptional longevity. *Aging* **5**, 653–661 (2013).
3. 3.
Wu, L. et al. A cross-sectional study of compositional and functional profiles of gut microbiota in Sardinian centenarians. *mSystems* **4**, e00325-19 (2019).
4. 4.
Franceschi, C., Garagnani, P., Parini, P., Giuliani, C. & Santoro, A. Inflammaging: a new immune-metabolic viewpoint for age-related diseases. *Nat. Rev. Endocrinol.* **14**, 576–590 (2018).
5. 5.
Bárcena, C. et al. Healthspan and lifespan extension by fecal microbiota transplantation into progeroid mice. *Nat. Med.* **25**, 1234–1242 (2019).
6. 6.

Biagi, E. et al. Gut microbiota and extreme longevity. *Curr. Biol.* **26**, 1480–1485 (2016).

7. 7.

Rampelli, S. et al. Shotgun metagenomics of gut microbiota in humans with up to extreme longevity and the increasing role of xenobiotic degradation. *mSystems* **5**, e00124-20 (2020).

8. 8.

Funabashi, M. et al. A metabolic pathway for bile acid dehydroxylation by the gut microbiome. *Nature* **582**, 566–570 (2020).

9. 9.

Ridlon, J. M., Harris, S. C., Bhowmik, S., Kang, D. J. & Hylemon, P. B. Consequences of bile salt biotransformations by intestinal bacteria. *Gut Microbes* **7**, 22–39 (2016).

10. 10.

David, L. A. et al. Diet rapidly and reproducibly alters the human gut microbiome. *Nature* **505**, 559–563 (2014).

11. 11.

Devlin, A. S. & Fischbach, M. A. A biosynthetic pathway for a prominent class of microbiota-derived bile acids. *Nat. Chem. Biol.* **11**, 685–690 (2015).

12. 12.

Nixon, M., Upreti, R. & Andrew, R. 5 α -Reduced glucocorticoids: a story of natural selection. *J. Endocrinol.* **212**, 111–127 (2012).

13. 13.

Hang, S. et al. Bile acid metabolites control T_H17 and T_{reg} cell differentiation. *Nature* **576**, 143–148 (2019).

14. 14.

Campbell, C. et al. Bacterial metabolism of bile acids promotes generation of peripheral regulatory T cells. *Nature* **581**, 475–479 (2020).

15. 15.

Song, X. et al. Microbial bile acid metabolites modulate gut $ROR\gamma^+$ regulatory T cell homeostasis. *Nature* **577**, 410–415 (2020).

16. 16.

Paik, D. et al. Human gut bacteria produce T_H17 -modulating bile acid metabolites. Preprint at <https://doi.org/10.1101/2021.01.08.425913> (2021).

17. 17.

Li, W. et al. A bacterial bile acid metabolite modulates T_{reg} activity through the nuclear hormone receptor NR4A1. Preprint at <https://doi.org/10.1101/2021.01.08.425963> (2021).

18. 18.

Buffie, C. G. et al. Precision microbiome reconstitution restores bile acid mediated resistance to *Clostridium difficile*. *Nature* **517**, 205–208 (2015).

19. 19.

Begley, M., Gahan, C. G. M. & Hill, C. The interaction between bacteria and bile. *FEMS Microbiol. Rev.* **29**, 625–651 (2005).

20. 20.

Thanissery, R., Winston, J. A. & Theriot, C. M. Inhibition of spore germination, growth, and toxin activity of clinically relevant *C. difficile* strains by gut microbiota derived secondary bile acids. *Anaerobe* **45**, 86–100 (2017).

21. 21.

Honda, A. et al. Regulation of bile acid metabolism in mouse models with hydrophobic bile acid composition. *J. Lipid Res.* **61**, 54–69 (2020).

22. 22.

Holmes, I., Harris, K. & Quince, C. Dirichlet multinomial mixtures: generative models for microbial metagenomics. *PLoS ONE* **7**, e30126 (2012).

23. 23.

Atarashi, K. et al. Ectopic colonization of oral bacteria in the intestine drives T_H1 cell induction and inflammation. *Science* **358**, 359–365 (2017).

24. 24.

Li, D., Liu, C. M., Luo, R., Sadakane, K. & Lam, T. W. MEGAHIT: an ultra-fast single-node solution for large and complex metagenomics assembly via succinct de Bruijn graph. *Bioinformatics* **31**, 1674–1676 (2015).

25. 25.

Hyatt, D. et al. Prodigal: prokaryotic gene recognition and translation initiation site identification. *BMC Bioinformatics* **11**, 119 (2010).

26. 26.

Fu, L., Niu, B., Zhu, Z., Wu, S. & Li, W. CD-HIT: accelerated for clustering the next-generation sequencing data. *Bioinformatics* **28**, 3150–3152 (2012).

27. 27.

Qin, J. et al. A human gut microbial gene catalogue established by metagenomic sequencing. *Nature* **464**, 59–65 (2010).

28. 28.

Li, H. & Durbin, R. Fast and accurate short read alignment with Burrows–Wheeler transform. *Bioinformatics* **25**, 1754–1760 (2009).

29. 29.

Plaza Oñate, F. et al. MSPminer: abundance-based reconstitution of microbial pan-genomes from shotgun metagenomic data. *Bioinformatics* **35**, 1544–1552 (2019).

30. 30.

Li, J. et al. An integrated catalog of reference genes in the human gut microbiome. *Nat. Biotechnol.* **32**, 834–841 (2014).

31. 31.

Segata, N., Börnigen, D., Morgan, X. C. & Huttenhower, C. PhyloPhlAn is a new method for improved phylogenetic and taxonomic placement of microbes. *Nat. Commun.* **4**, 2304 (2013).

32. 32.

Khelaifia, S., Raoult, D. & Drancourt, M. A versatile medium for cultivating methanogenic archaea. *PLoS ONE* **8**, e61563 (2013).

33. 33.

Aziz, R. K. et al. The RAST Server: rapid annotations using subsystems technology. *BMC Genomics* **9**, 75 (2008).

34. 34.

Seemann, T. Prokka: rapid prokaryotic genome annotation. *Bioinformatics* **30**, 2068–2069 (2014).

35. 35.

García-Bayona, L. & Comstock, L. E. Streamlined genetic manipulation of diverse *Bacteroides* and *Parabacteroides* isolates from the human gut microbiota. *mBio* **10**, e01762-19 (2019).

36. 36.

Ferrières, L. et al. Silent mischief: bacteriophage Mu insertions contaminate products of *Escherichia coli* random mutagenesis performed using suicidal transposon delivery plasmids mobilized by broad-host-range RP4 conjugative machinery. *J. Bacteriol.* **192**, 6418–6427 (2010).

37. 37.

Atarashi, K. et al. T_{reg} induction by a rationally selected mixture of *Clostridia* strains from the human microbiota. *Nature* **500**, 232–236 (2013).

38. 38.

Quinn, R. A. et al. Global chemical effects of the microbiome include new bile-acid conjugations. *Nature* **579**, 123–129 (2020).

39. 39.

McDonald, J. A. K. et al. Evaluation of microbial community reproducibility, stability and composition in a human distal gut chemostat model. *J. Microbiol. Methods* **95**, 167–174 (2013).

40. 40.

Claesson, M. J. et al. Gut microbiota composition correlates with diet and health in the elderly. *Nature* **488**, 178–184 (2012).

Acknowledgements

We thank L. Besse for project management and making data available through the SRA and the Broad Institute Genomics Platform and Microbial 'Omics Core for sample processing and sequencing data generation; A. Minowa, M. Asakawa, K. Sugita and members of the JSR-Keio University Medical and Chemical Innovation Center for their technical support; N. Hasegawa, K. Fukunaga, T. Kanai, K. Masaki, S. Azekawa, K. Sasahara, S. Hosomi, M. Shimura and Y. Abe for their assistance in collecting clinical samples; S. Atsushi and members of the Honda laboratory for their suggestions during the course of this studies. K.H. was funded through AMED LEAP under grant number JP20gm0010003, Grant-in-Aid for Specially Promoted Research from JSPS (no. 20H05627), Public/Private R&D Investment Strategic Expansion Program (PRISM) from Cabinet Office of the Government of Japan, the Naito Foundation and the Takeda Science Foundation. The centenarian study was funded by the Japan Ministry of Agriculture, Forestry and Fisheries (M.S.) and Keio Global Research Institute (Y.A. and N.H.). The older-participant recruitment study was funded by a Grant-in-Aid for Scientific Research (no. 18H03055) from the Japan Society for the Promotion of Science and JST Research Complex Program (JP15667051). D.R.P. and R.J.X. were funded by the Center for the Study of Inflammatory Bowel Disease (DK043351), Center for Microbiome informatics and Therapeutics (CMIT) and AT009708. Y. Sato. was supported by the Terumo Life Science Foundation.

Author information

Author notes

1. These authors contributed equally: Yuko Sato, Koji Atarashi, Damian R. Plichta

Affiliations

1. Department of Microbiology and Immunology, Keio University School of Medicine, Tokyo, Japan

Yuko Sato, Koji Atarashi, Satoshi Sasajima, Sean M. Kearney, Kozue Takeshita, Shoki Okamoto, Ashwin N. Skelly, Yuki Okamura, Takeshi Tanoue, Seiko Narushima & Kenya Honda
2. RIKEN Center for Integrative Medical Sciences, Yokohama, Japan

Yuko Sato, Koji Atarashi, Sean M. Kearney, Wataru Suda, Youxian Li, Takeshi Tanoue, Seiko Narushima, Masahira Hattori & Kenya Honda
3. JSR-Keio University Medical and Chemical Innovation Center, Tokyo, Japan

Yuko Sato, Koji Atarashi, Satoshi Sasajima, Kozue Takeshita, Takeshi Tanoue & Kenya Honda
4. Infectious Disease and Microbiome Program, Broad Institute of MIT and Harvard, Cambridge, MA, USA

Damian R. Plichta, Hera Vlamakis & Ramnik J. Xavier
5. Centre for Supercentenarian Medical Research, Keio University School of Medicine, Tokyo, Japan

Yasumichi Arai & Nobuyoshi Hirose
6. School of Pharmaceutical Sciences, Health Sciences University of Hokkaido, Hokkaido, Japan

Takahiro Sasaki & Tsuyoshi Murai
7. Junshin Clinic Bile Acid Institute, Tokyo, Japan

Hajime Takei & Hiroshi Nittono

8. Department of Internal Medicine, Division of Endocrinology,
Metabolism and Nephrology, Keio University School of Medicine,
Tokyo, Japan

Junichiro Irie & Hiroshi Itoh

9. Department of Infection Control and Prevention, The University of
Tokyo, Tokyo, Japan

Kyoji Moriya

10. Department of Biochemistry, Keio University School of Medicine,
Tokyo, Japan

Yuki Sugiura & Makoto Suematsu

11. Electron Microscope Laboratory, Keio University School of Medicine,
Tokyo, Japan

Nobuko Moritoki & Shinsuke Shibata

12. The Kimmel Center for Biology and Medicine of the Skirball Institute,
New York University School of Medicine, New York, NY, USA

Dan R. Littman

13. Howard Hughes Medical Institute, New York, NY, USA

Dan R. Littman

14. Department of Bioengineering, Stanford University, Stanford, CA,
USA

Michael A. Fischbach

15. Department of Laboratory Medicine, Keio University School of
Medicine, Tokyo, Japan

Yoshifumi Uwamino

16. Department of Marmoset Biology and Medicine, Central Institute for Experimental Animals, Kawasaki, Japan

Takashi Inoue

17. Division of Gastroenterology and Hepatology, Tokyo Medical University Ibaraki Medical Center, Ibaraki, Japan

Akira Honda

18. Graduate School of Advanced Science and Engineering, Waseda University, Tokyo, Japan

Masahira Hattori

19. Center for Computational and Integrative Biology, Massachusetts General Hospital, Boston, MA, USA

Ramnik J. Xavier

20. Department of Molecular Biology, Massachusetts General Hospital, Boston, MA, USA

Ramnik J. Xavier

Contributions

K.H., Y. Sato and K.A. planned experiments, analysed data and wrote the paper together with D.R.P., R.J.X., A.N.S. and S.M.K.; Y.A., K.T. and N.H. collected clinical samples; Y. Sato and K.A. performed bacterial experiments; D.R.P., H.V. and R.J.X. performed metagenome analyses; K.A., S.M.K., Y.O., W.S. and M.H. performed whole-genome and meta-16S rRNA gene sequencing and analyses; S. Sasajima, Y. Sato, K.A., H.T., H.N., S.N., Y. Sugiura and M.S. performed metabolomic analysis; T.S., S.O., S. Sasajima and T.M. synthesized chemical compounds; N.M. and S. Shibata. performed electron microscopy imaging; A.H., Y.U., T.I., Y.L., T.T., J.I., H.I. and K.M. provided essential materials; D.R.L. and M.A.F. supervised bacterial experiments.

Corresponding authors

Correspondence to [Ramnik J. Xavier](#) or [Kenya Honda](#).

Ethics declarations

Competing interests

K.H. is a scientific advisory board member of Vedanta Biosciences and 4BIO CAPITAL.

Additional information

Peer review information *Nature* thanks Pieter Dorrestein, Andrew Patterson and the other, anonymous, reviewer(s) for their contribution to the peer review of this work.

Publisher's note Springer Nature remains neutral with regard to jurisdictional claims in published maps and institutional affiliations.

Extended data figures and tables

[Extended Data Fig. 1 Clinical characteristics of centenarians.](#)

a, b, Activities of daily living (ADL) scores assessed via the Barthel index (**a**) and mini-mental state exam (MMSE) scores (**b**) of centenarian (top, ADL, $n = 96$; MMSE, $n = 67$) and older (bottom, ADL, $n = 111$; MMSE, $n = 111$) groups. **c**, Blood tests from centenarian (CE, $n = 146\text{-}150$, orange), older ($n = 111$, blue), and young ($n = 15\text{-}39$, grey) participants; red blood cell (RBC) count; albumin; C-reactive protein (CRP); white blood cell (WBC) count; total protein; blood urea nitrogen (BUN); fasting blood glucose; uric acid; and creatinine. **d**, Faecal lipocalin level of centenarian ($n = 122$), older ($n = 67$), and young ($n = 19$) individuals quantified by ELISA. **e**, Body-mass-index (BMI) values of centenarian ($n = 89$), older ($n = 111$), and young ($n = 39$) individuals. **f**, Percentages of individuals with

medical histories of diabetes mellitus, hypertension, or cancer. Black colour represents affected individuals. Medical history was surveyed from 155–156 centenarian, 110–111 older, and 39 young individuals. In **c–e**, data are mean \pm s.d. *** P < 0.001; ** P < 0.01; * P < 0.05; Kruskal–Wallis with Dunn’s test. ns, not significant. Grey areas within graphs are ranges of normal values.

[Source Data](#)

Extended Data Fig. 2 Gut microbiome signatures in centenarian, older and young Japanese participants based on whole-metagenome shotgun sequencing and de novo assembly analysis.

a, Principal coordinate analysis based on species-level Bray–Curtis dissimilarity from the assembled faecal metagenomes of centenarian [CE, $n = 176$, orange (154 individuals: 3 participants undergoing antibiotic treatment and 3 with insufficient bacterial DNA yield were excluded from the total 160 participants; analysis also included samples collected twice from 20 individuals and three times from 1 individual with an intervening one or two year interval)], older [$n = 110$, blue (110 individuals: 1 participant undergoing antibiotics treatment and 1 participant with insufficient bacterial DNA yield were excluded from 112 participants)], and young [$n = 44$, grey (44 individuals: 3 participants with insufficient bacterial DNA yield were excluded from 47 participants)]. The microbiota composition of centenarians was significantly different from that of both control groups (PERMANOVA false-discovery rate (FDR)-adjusted $P < 0.05$). **b, c**, Relative abundance across phyla. **d**, Shannon diversity index (* $P < 0.05$, linear model). **e–g**, Changes in the relative abundance (RelAb) of gut metagenome species (MSPs) between centenarian, older, and young participants grouped according to the following signatures of differential abundance: 1) ageing signature, 2) rejuvenation signature, and 3) centenarian signature. Each signature is accompanied by models depicting microbial relative abundance patterns in centenarian (C), older (O), and young (Y) groups that would fall into the given signature. Colour scale represents the coefficient from the linear model and indicates enrichment (red) or depletion (blue) of a species in the respective comparisons:

centenarian compared to older, centenarian compared to young, and older compared to young; in each case, the latter group is used as a reference in the model. Differentially abundant species that are significant at FDR

$P < 0.05$ are indicated with asterisks. The first signature ('ageing signature') included taxa whose abundance was increased or decreased with age (**e**).

For example, *Eubacterium siraeum* and undefined Firmicutes species (msp_161, 213) were most abundant in centenarians, followed by the older and then the young controls, whereas *Blautia wexlerae* displayed the opposite trend, being most abundant in young controls, followed by the older participants, and finally the centenarians. These findings are in alignment with previous studies that suggest the relative abundances of these taxa reflect adaptation to ageing, and may be related to physical activity and diet^{3,40}. The second signature ('rejuvenation signature') included taxa whose abundance was similar in centenarians and young controls, but distinct from the older participants (**f**). These species might reflect the maintenance of youth or possess reverse-ageing effects. Notably, *R. gnavus* and *E. lenta* were part of this signature, as they were comparably abundant in both centenarians and young controls. Notably, these species have been implicated in bile acid metabolism, particularly the biosynthesis of iso-bile acids¹¹. The third signature ('centenarian signature') included centenarian-specific taxa whose abundance was significantly different between centenarians and both the older and young control groups, but not between these two control groups (**g**). In the third signature, *Alistipes*, *Parabacteroides*, *Bacteroides* and *Clostridium* species, as well as *Methanobrevibacter*, a predominant archaeon in the human gut, were specifically enriched in centenarians compared with the other groups. One of the most abundant species in centenarians was *C. scindens*. By contrast, key butyrate producers such as *F. prausnitzii* and *E. rectale* were selectively depleted in centenarians. **h, i**, Abundance of genes homologous to the *C. scindens bai* operon in Japanese (**h**) and Sardinian (**i**) centenarian, older, and young age groups. Sardinian centenarians ($n = 19$), older controls ($n = 23$), and young controls ($n = 17$) from the European Nucleotide Archive (accession number PRJEB25514). **c, d, h, i**, Horizontal lines indicate the median; box boundaries indicate the interquartile range; whiskers represent values within $1.5 \times$ the interquartile range of the first and third quartiles. Each circle represents one sample. In **c, e-i**, *FDR-adjusted $P < 0.05$; Wilcoxon rank-sum test. ns, not significant.

[Source Data](#)

Extended Data Fig. 3 The microbiota compositions of centenarians, their lineal descendants and patients with IBD.

Faecal meta 16S rRNA gene sequencing of centenarians (CE, $n = 157$), older participants ($n = 111$), young participants ($n = 40$), lineal relatives of centenarians (CE-L, $n = 22$, 48-95 years old, average 74.7 years old), and patients with IBD (Crohn's disease; $n = 12$, ulcerative colitis; $n = 91$, 15-78 years old, average 49.0 years old) (all Japanese). **a**, PCoA plots based on unweighted UniFrac distance among faecal microbiome of centenarian (orange), older (blue), young (grey), CE-L (yellow), and IBD (red) groups. Note that the microbiota composition of centenarians was distinct from that of patients with IBD. **b-e**, Relative abundance of ASV (amplicon sequence variants) that are significantly enriched in centenarians (**b**); depleted in centenarians (**c**); commonly enriched in both centenarians and their lineal relatives (**d**); and commonly depleted or enriched in both centenarians and young participants (**e**). The closest species of ASVs were assigned using the National Center for Biotechnology Information Reference Sequence (NCBI RefSeq) database. Data are mean \pm s.d. *** $P < 0.001$; ** $P < 0.01$; * $P < 0.05$; Wilcoxon rank-sum test. ns, not significant. Each dot represents an individual.

[Source Data](#)

Extended Data Fig. 4 Faecal short-chain fatty acids and pH in centenarians.

a, GC-MS-based quantification of faecal short-chain fatty acids (SCFAs) from centenarian (CE, $n = 47$, orange), older ($n = 31$, blue), and young ($n = 23$, grey) individuals. Faecal SCFAs are shown in $\mu\text{mol/g}$ wet weight faeces. **b, c**, Faecal ammonia/ammonium (**b**) and faecal pH levels (**c**) from individuals within each group. **d**, Correlation between the levels of secondary bile acids (LCA, 3-oxoLCA, isoLCA, alloLCA, 3-oxoalloLCA, and isoalloLCA) and pH. Each circle represents an individual. Spearman's coefficient (r) and significance (P) were calculated separately for each group. There is significant positive correlation between pH and faecal

alloLCA ($P = 0.0156$), 3-oxoalloLCA ($P = 0.0237$), and isoalloLCA ($P = 0.0034$) in centenarians. In **a-c**, data are mean \pm s.d. *** $P < 0.001$; ** $P < 0.01$; * $P < 0.05$; one-way ANOVA with Tukey's test. ns, not significant.

[Source Data](#)

[Extended Data Fig. 5 Quantification of faecal bile acids by age group.](#)

Faecal bile acid composition of centenarian (CE, $n = 125$, orange), older ($n = 107$, blue), young ($n = 47$, grey), and lineal relatives of centenarians (CE-L, $n = 18$, yellow) were profiled and quantified by LC-MS/MS ($\mu\text{mol/g}$ wet weight faeces). In pilot studies, we found that 94 of 137 examined bile acids were minor components of centenarians' faeces (see Supplementary Table 3). We thus selected the remaining 43 bile acid compounds for follow-up quantitative analysis (see also Fig. 1a). **a**, Multi-dimensional scaling plot using Spearman's correlation highlights differences among the four groups' bile acid profiles. Each circle represents an individual participant from the indicated age group. $P = 4.27 \times 10^{-9}$ for CE versus older; $P = 2.72 \times 10^{-12}$ for CE versus young; $P = 4.18 \times 10^{-6}$ for CE versus CE-L; $P = 0.00123$ for older versus young; Wilcoxon rank-sum test. **b, c**, Average ratio of total primary versus secondary (**b**) and CA- versus CDCA-derived bile acids (**c**). **d**, Sum of conjugated and unconjugated bile acids. **e**, Concentration of each individual bile acid. In **d, e**, each circle represents an individual. Data are mean \pm s.d. *** $P < 0.001$; ** $P < 0.01$; * $P < 0.05$; one-way ANOVA with Tukey's test. ns, not significant. Faecal bile acids are shown in $\mu\text{mol/g}$ wet weight faeces. **f**, Distribution of participants' faecal isoalloLCA concentrations. The median faecal isoalloLCA concentration in centenarians was 19.5 μM , meaning that 63 centenarian samples among 125 (50.4%) had $>19.5 \mu\text{M}$ isoalloLCA. In contrast, only 17 older (15.9%) and 3 young (7.7%) participants were found to have $>19.5 \mu\text{M}$ isoalloLCA.

[Source Data](#)

[Extended Data Fig. 6 Predicted bile acid biosynthesis by gut microorganisms.](#)

a, Biosynthetic pathway of secondary bile acids metabolized by the gut microbiota from primary bile acid chenodeoxycholic acid (CDCA). Responsible enzymes are indicated within boxes. The glycine or taurine conjugated primary bile acids are deconjugated (not depicted) and biotransformed into a variety of secondary bile acids by the gut microbiota. The predominant biotransformation is 7α -dehydroxylation of CDCA by *bai* operon genes, thereby converting it into lithocholic acid (LCA). In addition, bile acids can undergo oxidation and epimerization to generate oxo- (keto-), iso- (3β -hydroxy-), allo- (5α -H-), as well as *cis*- (indicated in a blue box) and *trans*-forms (indicated in a pink box). Brackets indicate predicted pathways to allo-form LCA production. Chemical structures are simplified by depicting only A and B steroid rings. **b**, 3-Oxo- Δ^4 -LCA (also termed 3-oxo-4,5-dehydro-LCA) and 3-oxoalloLCA are structurally similar to testosterone and 5α -dihydrotestosterone (DHT), respectively. Both DHT and 3-oxoalloLCA have A and B steroid rings in a planar (*trans*) conformation (indicated in a pink box). We predicted that alloLCA and isoalloLCA might be generated from 3-oxo- Δ^4 -LCA by the sequential action of a 5α -reductase (5AR) homologue and 3α -HSDH (for alloLCA) or 3β -HSDH (for isoalloLCA), through a 3-oxoalloLCA intermediate (see **a**), analogous to the 5AR-mediated conversion of testosterone into DHT by hydrogenating across the C4-C5 double bond, thereby forcing the A and B steroid rings into a planar conformation. **c**, Biosynthetic pathway of DCA and related bile acids by the gut microbiota based on ref. ¹¹. 3-OxoDCA can be generated from 3-oxo- Δ^4 -DCA by hydrogenation across the C4-C5 double bond such that the C5 hydrogen is in the β position. This reaction is mediated by a 3-oxo- 5β -steroid 4-dehydrogenase (also termed 5β -reductase, 5BR) encoded by the *BaiCD* gene. We predicted that LCA and isoLCA might be generated from 3-oxo- Δ^4 -LCA by the sequential action of a 5BR homologue and 3α -HSDH (for LCA) or 3β -HSDH (for isoLCA), through a 3-oxoLCA intermediate (see panel **a**), mirroring the previously characterized conversion of 3-oxoDCA to DCA or isoDCA. In **a–c**, dashed-wedged lines indicate α -positions of -H and -OH groups, while bold-wedged lines indicate β -positions.

Extended Data Fig. 7 Identification of bile acid-metabolizing bacterial strains isolated from the microbiota of a centenarian.

In vitro bile acid metabolism by 68 CE91-derived isolates using 50 μ M of CDCA (**a**), LCA (**b**), and 3-oxo- Δ^4 -LCA (**c**) as starting substrates in pH 9-adjusted media. Data was obtained by LC-MS/MS analysis of 48 h culture supernatants. A list of the 68 isolated strains is shown in the left panel. The closest species to each isolate was identified based on 16S rRNA sequence similarity to the National Center for Biotechnology Information Reference Sequence (NCBI RefSeq) database. Graphs with red backgrounds indicate *trans*-bile acids and blue backgrounds indicate *cis*-bile acids. Bile acid profiles after culturing in pH 7-adjusted media are shown in Supplementary Fig. 1. **a**, Incubation with CDCA did not result in production of target bile acids in any of the cultures, though *C. scindens* strains 59-60 (St59-60) and *C. hylemonae* St63 were able to produce LCA, albeit at low levels. **b**, When cultured with LCA, *Gordonibacter pamelaeae* St32 and *E. lenta* St33-35 were found to produce 3-oxoLCA and isoLCA, implying carriage of 3 α -HSDH and 3 β -HSDH as predicted in a previous study¹¹. In addition, *Raoulibacter timonensis* St30-31 and Lachnospiraceae spp. St57 were also capable of transforming LCA into 3-oxoLCA, suggesting their possession of 3 α -HSDH, similar to *E. lenta*. **c**, When 3-oxo- Δ^4 -LCA was used as a substrate, 3-oxoLCA accumulated to high levels in the supernatants of *H. hathewayi* St54-55 and Lachnospiraceae spp. St62 cultures, suggesting their carriage of 5BR. Similarly, isoLCA was generated from 3-oxo- Δ^4 -LCA at high levels in *C. innocuum* St51 and Lachnospiraceae spp. St58 cultures, suggesting carriage of 5BR and 3 β -HSDH. It is noteworthy that *P. distasonis* St4-5 converted LCA to 3-oxoLCA and further to 3-oxo- Δ^4 -LCA, as well as 3-oxo- Δ^4 -LCA to isoLCA and LCA, suggesting that these strains possess 3 α -HSDH, 3 β -HSDH, and 5BR. Data are mean + s.d. of duplicate samples and representative of two independent experiments.

[Source Data](#)

[Extended Data Fig. 8 Elucidated biosynthetic pathway of secondary bile acids.](#)

a, Elucidated biosynthetic pathway of secondary bile acids metabolized by CE91-derived bacterial strains. Colour-coded lines indicate in vitro identified metabolic capabilities of each strain. Responsible enzymes are

indicated within boxes. Chemical structures are simplified by depicting only A and B steroid rings. **b**, The genome sequences of 68 isolates from a centenarian (CE91) were determined using PacBio Sequel and Illumina MiSeq sequencers. The gene prediction and annotation of the generated contigs were performed using the Rapid Annotations using Subsystem Technology (RAST) server. Gene clusters containing 5AR (magenta), 5BR (blue), 3 β -HSDH-I (green), and 3 β -HSDH-II (purple) homologues identified in 23 Bacteroidales strains are shown. Note that the gene clusters containing 5AR, 5BR, 3 β -HSDH-I and 3 β -HSDH-II homologues are present in close proximity to genes annotated with tricarboxylic acid (TCA) cycle-related functions (beige) and transporter/efflux system membrane fusion proteins (yellow). Gene homologues are defined as similarity of $<1 \times 10^{-12}$ E-value, $>30\%$ sequence identity, and $>60\%$ query coverage. Arrows represent coding sequences and annotated functions are colour-coded accordingly. Scale bar is 2kb. Note that 3 α -HSDH homologue is not present in any of the 5AR clusters.

Extended Data Fig. 9 Metabolism of LCA-related compounds by Bacteroidales strains and cooperative isoalloLCA production.

a-c, Bacteroidales strains were cultured with 3-oxoalloLCA (**a**), 3-oxoLCA (**b**), or isoLCA (**c**) at a final concentration of 50 μ M in pH 9-adjusted WCA medium. There was substantial substrate specificity and strain-to-strain variation in transformation efficiency. For instance, *P. merdae* St3, *P. distasonis* St4–5, and Odoribacteraceae St21 exhibited strong 3 β -HSDH activity, reflected by both high isoalloLCA production from 3-oxoalloLCA (**a**) and isoLCA production from 3-oxoLCA (**b**), whereas other strains showed less efficient biotransformation or substrate specificity despite carriage of putative 3 β -HSDH genes. The strength of 5BR activity also differed among the strains: *P. merdae* St3, *P. distasonis* St4–5, *B. dorei* St6–7, and *B. uniformis* St10-13 effectively transformed 3-oxoLCA to 3-oxo- Δ^4 -LCA (and further to 3-oxoalloLCA by 5AR), while other strains displayed moderate to weak activity (**b**). *Porphyromonas somerae* St14 lacked a putative 3 β -HSDH gene but was able to generate isoalloLCA from 3-oxoalloLCA nonetheless (**a**), suggesting that it carries a strain-specific gene

with 3 β -HSDH activity. **d**, Co-culture of *P. merdae* St3 or Odoribacteraceae St21 (5BR, 5AR, and 3 β -HSDH encoders) with *E. lenta* St34 (top, green, a 3 α -HSDH and 3 β -HSDH encoder), or *P. distasonis* St4 (bottom, yellow, a 3 α -HSDH, 3 β -HSDH, and 5BR encoder) supplemented with 50 μ M LCA in pH 9-adjusted WCA medium. Notably, co-culture of *P. merdae* St3 and *E. lenta* St34 with LCA resulted in generation of alloLCA in addition to isoalloLCA. **e**, Different combinations of *P. merdae* St3, Odoribacteraceae St21, or *C. scindens* St59 (a *bai* operon encoder capable of converting CDCA to LCA) co-cultured with *E. lenta* St34 (top) or *P. distasonis* St4 (bottom) in the presence of 50 μ M CDCA. In **a–e**, the presence of genes homologous to 5AR, 5BR, 3 β -HSDH-I, 3 β -HSDH-II, 3 α -HSDH, or the *bai* operon in corresponding combinations of strains are indicated as grey boxes within the adjacent charts. Note that the *bai* operon in *C. scindens* contains 5BR and 3 α -HSDH genes. Culture supernatants were collected after 48 h of anaerobic incubation at 37 °C for LC-MS/MS quantification. Data are mean + s.d. of duplicate samples and representative of two independent experiments.

[Source Data](#)

[Extended Data Fig. 10 IsoalloLCA inhibits Gram-positive pathogens.](#)

a, b, Gram-positive (upper) and -negative (lower) pathogens were incubated with varying concentrations of the indicated bile acids under anaerobic conditions at 37 °C in WCA medium until each strain reached stationary growth phase in the control medium (5–75 h). Bacterial growth was determined by OD₆₀₀ measurement. Maximum growth densities (**a**) and growth curves (**b**) of pathogens in varying concentrations of bile acids are shown. Data are mean ± s.d. (error bars shown with fill area). **c**, MIC₉₀ value (minimal inhibitory concentration required to prevent 90% growth) of isoalloLCA for each pathogenic strain was determined by serially diluting the compound and incubating each dilution with the pathogen. Shaded area indicates isoalloLCA concentrations with growth inhibitory effects, and MIC₉₀ is reported inside the shaded box. Data are mean ± s.d. of duplicate samples and are representative of two independent experiments. **d**, In vitro

growth inhibition of *C. difficile* 630 and vancomycin-resistant *E. faecium* (VRE) by co-culturing with CE91-derived isolates in the presence or absence of 12.5 µM 3-oxo- Δ^4 -LCA in WCA medium. Average CFU of overnight cultures are shown ($n = 6$). Data are mean ± s.d. and are representative of two independent experiments. *** $P < 0.001$; Mann–Whitney test (two-tailed) with Welch’s correction. ns, not significant.

Source Data

Extended Data Fig. 11 In vivo suppression of faecal *C. difficile* shedding in *Cyp2a12*^{−/−}*Cyp2c70*^{−/−} mice.

a, b, Faecal and plasma concentrations of isoalloLCA (**a**) and plasma analytes (**b**) from SPF C57BL/6N mice after 14 days on an 0.01%, 0.05%, or 0.1% (w/w) isoalloLCA-containing diet. Plasma analytes from each animal: albumin; aspartate aminotransferase (AST); alanine transaminase (ALT); lactate dehydrogenase (LDH); total bilirubin; cholinesterase; total cholesterol; and total protein. Data are mean ± s.d.; $n = 3$ each; *** $P < 0.001$; ** $P < 0.01$; * $P < 0.05$; one-way ANOVA with Tukey’s test. ns, not significant. **c**, SPF C57BL/6N mice were pretreated with cefoperazone through the drinking water during the period from 7 to 2 days before inoculation and then infected with *C. difficile* 630 by oral gavage on day 0. The mice were subsequently placed on an 0.1% isoalloLCA-containing diet from day 1 to day 3 after infection (p.i.) ($n = 17$ –18 animals each). Faecal *C. difficile* CFUs and isoalloLCA levels throughout the course of infection were determined. Data are mean ± s.d. *** $P < 0.001$; Mann–Whitney test (two-tailed) with Welch’s correction. **d**, Simplified pathway of bile acid metabolism in rodents. In rodents’ livers, CDCA is immediately hydroxylated at the 6 β -position to generate muricholic acids (α - and β -muricholic acids (MCAs)) by CYP2C70, and as such we employed a *Cyp2c70*^{−/−} mouse model. As resulting excessive CDCA causes hepatotoxicity in *Cyp2c70*^{−/−} mice, we cross-bred *Cyp2c70*^{−/−} mice with *Cyp2a12*^{−/−} mice lacking 7 α -rehydroxylation capacity to minimize liver injury. **e–g**, Faecal bile acids of SPF wild-type C57BL/6N mice (WT) and *Cyp2a12*^{−/−}*Cyp2c70*^{−/−} double-knockout (CypDKO) mice ($n = 3$ each) were quantified by LC-MS/MS ($\mu\text{mol/g}$ wet weight faeces). The percent of

each bile acid among total faecal bile acids from each mouse was calculated (**e**). Note that *Cyp2a12^{-/-}**Cyp2c70^{-/-}* double-knockout mice showed elevated levels of LCA and related bile acids. Amount of total faecal bile acids (**f**) and each bile acid (**g**) from each mouse. Data are mean ± s.d. *** $P < 0.001$; ** $P < 0.01$; * $P < 0.05$; one-way ANOVA with Tukey's test. ns, not significant. Each dot represents an individual.

[Source Data](#)

Extended Data Fig. 12 MIC₉₀ of isoalloLCA against gut commensals in WCA and BHI media.

a, Growth inhibitory effect of isoalloLCA on gut commensals in WCA medium. Gram-positive and Gram-negative commensal isolates were selected from our culture collection and incubated anaerobically at 37 °C with the indicated concentrations of isoalloLCA. Bacterial growth was determined by OD₆₀₀ measurement. Each strain was cultured until it reached stationary growth phase in the control medium (7-48 h). Shaded area indicates isoalloLCA concentrations with growth inhibitory effects. MIC₉₀ is shown inside the shaded box. **b**, MIC₉₀ of isoalloLCA against Gram-positive and Gram-negative commensals in WCA and BHI media. **c**, Representative scanning electron microscopy images of *C. difficile* 630, *C. sporogenes*, *C. indolis* and *Clostridium HGF2 (innocuum)* grown in control or 2.5 µM isoalloLCA-containing WCA medium for 5 h. The right panels show the corresponding high-resolution images. Scale bars are 5.0 µm and 1.0 µm. Arrows indicate morphological alterations after isoalloLCA treatment. **d**, The differences in growth inhibitory effect of isoalloLCA between WCA and BHI medium on *C. difficile* 630, *E. faecium* (VRE), *S. dysgalactiae* subsp. *equisimilis* (SDSE), *C. symbiosum*, *C. scindens* and *Clostridium HGF2 (innocuum)*. Data in **a, d** are mean ± s.d. from duplicate samples and are representative of two independent experiments.

[Source Data](#)

Extended Data Fig. 13 The effects of isoalloLCA on the complex gut microbiota.

a, b, f–h, Human faecal samples from healthy young donors (**a, b**) and patients with *C. difficile* infection (CDI) (**f–h**) were incubated for 48 h in modified WCA medium supplemented with 3-oxoLCA, LCA, or isoalloLCA (50 µM). Shannon index of diversity (**a** and **c**) and a compositional shift in the microbiome at the genus level (**b** and **g**) of faecal cultures after secondary bile acid treatment. Each dot in **a** and **f** represents a single donor's faecal culture. ns, not significant by Kruskal–Wallis with Dunn's test. Although α -diversity was not significantly affected, isoalloLCA induced broad changes in microbial community structure, with a significant alteration in the ratio of Gram-negative to Gram-positive bacteria. *C. difficile* CFUs in each CDI microbiota pre- or post- 48 h incubation with medium or secondary bile acids were determined (**h**). Data are mean ± s.d. of duplicate samples. ** $P < 0.01$; * $P < 0.05$; Unpaired t -test. ns, not significant. **c–e**, Correlation between the levels of faecal isoalloLCA and gut MSPs in centenarian (CE, $n = 119$, orange), older ($n = 107$, blue), and young ($n = 39$, grey) participants. Spearman's coefficient (r) and significance (P) for msp_103 *A. putredinis* and msp_095 *O. laneus* (both 5AR and 3 β -HSDH encoders) (**c**), combined *Streptococcus* signal (**d**), and *Streptococcus* species (**e**). Each dot represents an individual. Several *Streptococcus* spp. showed a negative association with isoalloLCA concentration in our cohort.

Source Data

Extended Data Fig. 14 Associations between species encoding cluster V1, V2 or V3, or non-encoders with secondary bile acids.

a, Relative abundance of gut MSPs categorized into clusters V1, V2, and V3 from the assembled gut metagenomes of centenarian (CE, $n = 119$, orange), older ($n = 107$, blue), and young ($n = 39$, grey) groups. **b, c**, Spearman's coefficient (r) and significance (P) between faecal bile acid level and summed relative abundance of cluster V1-, V2-, or V3-encoding species (**b**) and ratio of species encoding clusters V1 and V3 versus V2 from assembled gut metagenomes (**c**). Each dot represents an individual. **d**, Spearman correlation coefficient (r) for each bile acid against species encoding cluster V1, V2, or V3, or non-encoders. Non-encoders that

correlate strongly with bile acid concentration are indicated within a grey circle, and the species are listed.

[Source Data](#)

Extended Data Fig. 15 Stratification into microbial community types with respective microbiome characteristics.

a, Principal coordinate analysis of three microbial community types (1, 2, and 3) stratified using Dirichlet Multinomial Mixtures from the gut microbiomes of centenarian [CE, $n = 176$ (153 individuals)], older ($n = 110$), and young ($n = 44$) individuals. **b**, **c**, Relative abundances across phyla (**b**) and top differentially abundant species from each phylum (**c**) from the assembled gut metagenomes in each community type. Community type 1 is characterized by a high relative abundance of Firmicutes (for example, *Oscillibacter* spp.) and Proteobacteria (for example, *Desulfovibrio* spp.), whereas community type 2 exhibits relative enrichment of Actinobacteria and depletion of Proteobacteria. Community type 3 is structurally similar to type 1, but exhibits a higher abundance of Verrucomicrobia (for example, *Akkermansia* spp.) and Euryarchaeota (for example, *Methanobrevibacter* spp.). **d**, Species harbouring gene clusters V1, V2, and V3 from the assembled gut metagenomes in each community type. Each dot in **c** and **d** represents an individual from the centenarian (orange), older (blue), or young (grey) groups. Horizontal lines indicate the median; box boundaries indicate interquartile range (IQR); whiskers represent values within $1.5 \times$ IQR of the first and third quartiles. Asterisks indicate significantly different abundance in the specified comparison at FDR $P < 0.05$ based on a Wilcoxon rank-sum test. ns, not significant. **e**, Longitudinal change in faecal bile acid composition from the same individual over the course of 1-2 years. Upper numbers indicate collection interval (days). Faecal bile acids were quantified by LC-MS/MS ($\mu\text{mol/g}$ wet weight faeces), and the percent of each bile acid among total faecal bile acids in each sample was calculated. **f**, Stability of microbial community type (1, 2, and 3) in each individual over time.

[Source Data](#)

Supplementary information

Supplementary Information

This file contains Supplementary Figures 1-4, Supplementary Tables 1, 5, 8, 9, and legends for Supplementary Tables 2, 3, 4, 6 and 7.

Reporting Summary

Supplementary Table 2

Quantification of 16 faecal fatty acids by GC-MS.

Supplementary Table 3

A list of 137 bile acid compounds used in this study.

Supplementary Table 4

Genome and 16S rRNA gene sequencing data of 68 CE91-derived isolates.

Supplementary Table 6

Detailed LC-MS/MS setting for *in vivo* samples (48 bile acid compounds) using SCIEX Triple Quad™ 6500+ LC-MS/MS system.

Supplementary Table 7

Detailed LC-MS/MS setting for *in vitro* samples (14 bile acid compounds) using Shimadzu LCMS-8040 system.

Source data

Source Data Fig. 1

[Source Data Fig. 2](#)

[Source Data Fig. 3](#)

[Source Data Fig. 4](#)

[Source Data Extended Data Fig. 1](#)

[Source Data Extended Data Fig. 2](#)

[Source Data Extended Data Fig. 3](#)

[Source Data Extended Data Fig. 4](#)

[Source Data Extended Data Fig. 5](#)

[Source Data Extended Data Fig. 7](#)

[Source Data Extended Data Fig. 9](#)

[Source Data Extended Data Fig. 10](#)

[Source Data Extended Data Fig. 11](#)

[Source Data Extended Data Fig. 12](#)

[Source Data Extended Data Fig. 13](#)

[Source Data Extended Data Fig. 14](#)

[Source Data Extended Data Fig. 15](#)

Rights and permissions

[Reprints and Permissions](#)

About this article

Cite this article

Sato, Y., Atarashi, K., Plichta, D.R. *et al.* Novel bile acid biosynthetic pathways are enriched in the microbiome of centenarians. *Nature* **599**, 458–464 (2021). <https://doi.org/10.1038/s41586-021-03832-5>

- Received: 24 November 2020
- Accepted: 16 July 2021
- Published: 29 July 2021
- Issue Date: 18 November 2021
- DOI: <https://doi.org/10.1038/s41586-021-03832-5>

Share this article

Anyone you share the following link with will be able to read this content:

[Get shareable link](#)

Sorry, a shareable link is not currently available for this article.

[Copy to clipboard](#)

Provided by the Springer Nature SharedIt content-sharing initiative

Further reading

- [Si-Wu-Tang ameliorates fibrotic liver injury via modulating intestinal microbiota and bile acid homeostasis](#)

- Xiaoyong Xue
- , Jianzhi Wu
- , Mingning Ding
- , Feng Gao
- , Fei Zhou
- , Bing Xu
- , Mingjun Lu
- , Jun Li
- & Xiaojiaoyang Li

Chinese Medicine (2021)

- **Role of bile acids and gut bacteria in healthy ageing of centenarians**

- Bipin Rimal
- & Andrew D. Patterson

Nature (2021)

- **Unique bile acid metabolism in centenarians**

- Ursula Hofer

Nature Reviews Microbiology (2021)

Role of bile acids and gut bacteria in healthy ageing of centenarians

- Bipin Rimal
- Andrew D. Patterson

News & Views 06 Oct 2021

| [Section menu](#) | [Main menu](#) |

- Article
- [Published: 21 September 2021](#)

Fc-engineered antibody therapeutics with improved anti-SARS-CoV-2 efficacy

- [Rachel Yamin^{1 na1}](#),
- [Andrew T. Jones ORCID: orcid.org/0000-0002-3739-2322^{1 na1}](#),
- [Hans-Heinrich Hoffmann ORCID: orcid.org/0000-0003-0554-0244²](#),
- [Alexandra Schäfer³](#),
- [Kevin S. Kao¹](#),
- [Rebecca L. Francis¹](#),
- [Timothy P. Sheahan ORCID: orcid.org/0000-0001-9181-2183³](#),
- [Ralph S. Baric ORCID: orcid.org/0000-0001-6827-8701^{3,4}](#),
- [Charles M. Rice ORCID: orcid.org/0000-0003-3087-8079²](#),
- [Jeffrey V. Ravetch ORCID: orcid.org/0000-0003-2024-9041^{1 na2}](#) &
- [Stylianos Bournazos ORCID: orcid.org/0000-0001-5466-5620^{1 na2}](#)

Nature volume 599, pages 465–470 (2021)

- 9933 Accesses
- 3 Citations
- 53 Altmetric
- [Metrics details](#)

Subjects

- [Immunotherapy](#)
- [Viral infection](#)

Abstract

Monoclonal antibodies with neutralizing activity against SARS-CoV-2 have demonstrated clinical benefits in cases of mild-to-moderate SARS-CoV-2 infection, substantially reducing the risk for hospitalization and severe disease^{1,2,3,4}. Treatment generally requires the administration of high doses of these monoclonal antibodies and has limited efficacy in preventing disease complications or mortality among hospitalized patients with COVID-19⁵. Here we report the development and evaluation of anti-SARS-CoV-2 monoclonal antibodies with optimized Fc domains that show superior potency for prevention or treatment of COVID-19. Using several animal disease models of COVID-19^{6,7}, we demonstrate that selective engagement of activating Fcγ receptors results in improved efficacy in both preventing and treating disease-induced weight loss and mortality, significantly reducing the dose required to confer full protection against SARS-CoV-2 challenge and for treatment of pre-infected animals. Our results highlight the importance of Fcγ receptor pathways in driving antibody-mediated antiviral immunity and exclude the possibility of pathogenic or disease-enhancing effects of Fcγ receptor engagement of anti-SARS-CoV-2 antibodies upon infection. These findings have important implications for the development of Fc-engineered monoclonal antibodies with optimal Fc-effector function and improved clinical efficacy against COVID-19 disease.

[Download PDF](#)

Main

Several neutralizing monoclonal antibodies that target the SARS-CoV-2 spike protein have entered clinical testing over the past months, yielding US Food and Drug Administration approval of two monoclonal antibody cocktails—casirivimab and imdevimab, and bamlanivimab and etesevimab—for the treatment of patients with mild-to-moderate COVID-19⁴. In phase II/III studies, these and other monoclonal antibodies that are currently awaiting regulatory approval have demonstrated clear therapeutic benefits in cases of mild-to-moderate COVID-19, reducing the risk for hospitalization^{1,2,3} by more than 80%. These results are in stark contrast to the findings from phase III trials (for example, ACTIV-3 and NCT04501978) that assessed the therapeutic activity of these monoclonal antibodies in hospitalized patients with COVID-19. In all cases, none of the tested monoclonal antibodies offered any therapeutic benefit, even when administered at exceedingly high doses or in combination with remdesivir⁵.

The antiviral activity of IgG antibodies is the outcome of Fab-mediated virus neutralization coupled with the capacity of the Fc domain to mediate effector functions through interactions with Fcγ receptors (FcγRs) expressed on effector leukocytes⁸. FcγR engagement mediates pleiotropic functions, including the clearance of viral

particles⁹, cytotoxic elimination of virus-infected cells¹⁰ and induction of antiviral T-cell responses¹¹. Several reports, using well-defined in vivo models of SARS-CoV-2 infection, have independently demonstrated that the antiviral activity of neutralizing anti-SARS-CoV-2 antibodies depends on Fc–FcγR interactions^{12,13,14,15}. In addition, mechanistic studies have shown that these protective effects are mediated primarily by CCR2⁺ monocytes, as well as cytotoxic CD8⁺ T cells that infiltrate the lung and confer antiviral activities¹². Despite these findings, no studies have tested whether optimization of neutralizing anti-SARS-CoV-2 monoclonal antibodies for enhanced FcγR binding could improve their therapeutic activity, especially in the setting of severe COVID-19. Maximizing the capacity of neutralizing anti-SARS-CoV-2 monoclonal antibodies to engage and activate the appropriate FcγR pathways is expected to lower the monoclonal antibody dose required for the treatment of mild-to-moderate COVID-19, as well as improve their activity in hospitalized patients.

Currently, most monoclonal antibodies in clinical use or development are expressed as human IgG1, which—despite its affinity for activating FcγRs—also exhibits binding to the inhibitory FcγRIIb, thereby limiting protective Fc-effector activities¹¹. In addition, owing to presumptive safety concerns over the capacity of antibodies to exacerbate disease through antibody-dependent enhancement (ADE) mechanisms⁸, several clinical monoclonal antibodies (etesevimab, AZD8895 and AZD1061) have been engineered to lack FcγR-binding activity. However, despite numerous in vivo studies in animal models, there is no evidence for ADE^{12,13,14,15,16}, and therapeutic administration of high doses of convalescent plasma or neutralizing anti-SARS-CoV-2 monoclonal antibodies in patients with COVID-19 has not been associated with worse disease outcomes^{1,2,3,5,17}. Similarly, comparable safety profiles were evident in clinical trials of neutralizing monoclonal antibodies with intact or diminished Fc-effector function^{3,18,19}.

Hamster FcγRs and IgG Fc-domain activity

To assess the role of FcγRs in the monoclonal antibody-mediated protection and develop monoclonal antibodies with superior therapeutic potency, we selected well-established small-animal models of SARS-CoV-2 infection that recapitulate the clinical features of human COVID-19^{6,7,20}. One of these models involves the use of Syrian hamsters (*Mesocricetus auratus*), a species that sustains productive SARS-CoV-2 replication and exhibits evidence of severe disease upon challenge⁶. However, a major obstacle in the study of human IgG Fc-effector activity is the substantial interspecies differences in the affinity of human IgG antibodies for FcγRs expressed by rodent species such as hamsters²¹. We therefore cloned the four classes of hamster FcγRs and characterized their affinities for human, hamster and mouse IgG subclasses and Fc variants (Fig. 1a, b, Extended Data Fig. 1). Comparative analysis of hamster

Fc γ Rs revealed substantial sequence homology to mouse Fc γ Rs, with three hamster Fc γ Rs (Fc γ RI, Fc γ RIII and Fc γ RIV) corresponding to activating Fc γ Rs, whereas Fc γ RIIb represents the sole inhibitory Fc γ R.

Fig. 1: Contribution of Fc-effector function to the protective activity of neutralizing anti-SARS-CoV-2 monoclonal antibodies in hamster infection models.

 figure1

a, Overview of the organization of Fc γ R gene loci in humans, mice and Syrian hamsters. **b**, Fc variants of human IgG1 were evaluated for their affinity for hamster Fc γ Rs. Numbers indicate the fold change in affinity compared with wild-type human IgG1. NDB, no detectable binding. **c**, **d**, Wild-type (WT) and FcR-null (GRLR) variants of REGN monoclonal antibody cocktail (**c**) or S309 monoclonal antibody (**d**) were administered intravenously (5 mg kg^{-1}) to Syrian hamsters 1 day before (prevention model) (**c**) or 1 day after (therapy model) (**d**) intranasal challenge with SARS-CoV-2 (NYC isolate, 10^5 plaque-forming units (pfu)). $n = 9$ hamsters per group for PBS and GRLR-treated, $n = 10$ for wild-type from two independent experiments (**c**); $n = 6$ hamsters per group from two independent experiments (**d**). Hamsters were monitored for weight loss (left) (mean \pm s.e.m.), and lung viral titres (right, analysed on day 7 (**c**) or day 6 (**d**) after infection) were compared between treatment groups by one-way ANOVA (Bonferroni post hoc analysis, adjusted for multiple comparisons). P

values are indicated. **e–g**, SARS-CoV-2-infected hamsters (NYC isolate, 10^5 pfu) were treated on day 1 after infection with Fc variants of the REGN monoclonal antibody cocktail (5 mg kg⁻¹, intravenous injection) exhibiting differential hamster Fc γ R-binding affinity and activating-to-inhibitory (A/I) ratio (calculated on the basis of Fc γ RIV affinity/Fc γ RIIb affinity). Weight loss—plotted over time (mean \pm s.e.m.) (**e**) or as maximum change (**f**)—and lung viral titres, assessed on day 6 after infection (**g**) were compared by one-way ANOVA (Bonferroni post hoc analysis adjusted for multiple comparisons). *P* values are indicated. *n* = 9 hamsters per group for PBS-treated, *n* = 7 for GRLR and GAALIE, and *n* = 5 for V11 from two independent experiments. Red arrow indicates time point of monoclonal antibody treatment post-infection. In box plots, the centre line shows the median, boxes represent the middle quartiles and whiskers show the range of values (minimum to maximum).

Source data.

To assess the contribution of Fc–Fc γ R interactions to monoclonal antibody-mediated protection, we selected neutralizing monoclonal antibodies that are in clinical use or development, including casirivimab and imdevimab (REGN cocktail²²) and S309/VIR-7831²³ (Vir) and expressed them as human IgG1 or as Fc variants with defined affinity for hamster Fc γ Rs. In agreement with recent reports¹², we observed that when monoclonal antibodies are administered prophylactically, Fc-effector function shows minimal contribution to their antiviral activity (Fig. **1c**). By contrast, in the therapeutic setting, wild-type, but not FcR-null (GRLR) variants, are able to suppress lung viremia and prevent weight loss (Fig. **1d**). Because previous studies in mouse models of influenza and HIV-1 infection support a key role for Fc γ RIV in monoclonal antibody-mediated protection^{10,24}, we compared the *in vivo* therapeutic activities of two Fc-domain variants—GAALIE and V11—that exhibit differential hamster Fc γ RIV-binding activity, but comparable affinity for the other hamster Fc γ Rs (Fig. **1b**). Whereas the Fc γ RIV-enhanced variant (GAALIE) demonstrates potent antiviral activity, no therapeutic activity is evident for V11, which exhibits minimal affinity for hamster Fc γ RIV (Fig. **1e–g**).

SARS-CoV-2 in Fc γ R-humanized mice

Although these findings support the importance of Fc–Fc γ R interactions in monoclonal antibody-mediated protection against SARS-CoV-2 infection, their translational relevance is limited, given the structural complexity of the Fc γ R family and the divergence of these receptors between humans and other mammalian species²¹. To address this problem, we previously developed a mouse strain in which only human Fc γ Rs are expressed in a pattern that recapitulates as faithfully as possible the expression pattern in human tissues²⁵. Despite differences in the absolute Fc γ R

expression levels between humans and Fc γ R-humanized mice (for example, the expression of Fc γ RI on neutrophils and Fc γ RIIb on monocytes), this strain represents a suitable platform for studies on human IgG antibody function with translational relevance to humans. Human Fc γ R expression among the various leukocyte populations is stable and does not differ between young and old mice (Extended Data Fig. 2). Infection of old (more than 15-week-old), but not young (7-week-old), Fc γ R-humanized mice with the mouse-adapted SARS-CoV-2 strain MA10⁷ results in challenge-dose-dependent weight loss and mortality (Fig. 2a, b). Recent studies have determined that on day 2 after infection, MA10-infected mice exhibit peak lung viral titres, accompanied by severely compromised pulmonary function and extensive lung histopathologic damage⁷. Histological evaluation of lungs from MA10-infected Fc γ R-humanized mice (more than 15 weeks old) revealed multifocal areas of interstitial pneumonia, extensive inflammatory cell infiltration and occasional necrotic and proteinaceous material and hyalinized membranes within affected alveoli (Extended Data Fig. 3). Such histopathological findings are consistent with those observed in well-established animal models of SARS-CoV-2 infection used extensively in previous studies, and resemble the lung pathology of human COVID-19^{7,12,13,14}. Although it is not classified as a variant of concern, the MA10 strain contains several mutations near the epitopes targeted by monoclonal antibodies currently in clinical use or development. As a result, several of these monoclonal antibodies exhibit significantly reduced neutralizing activity against MA10, which is comparable to that observed for variants of concern such as B1.351 (Extended Data Fig. 4).

Fig. 2: Fc–Fc γ R interactions are required for the therapeutic activity of neutralizing anti-SARS-CoV-2 monoclonal antibodies in mouse infection models.

 **figure2**

a, b, Fc γ R-humanized mice were infected with mouse-adapted SARS-CoV-2 (MA10 strain, 10⁴ pfu, intranasal) and weight loss (mean \pm s.e.m.) was compared in young (7 weeks old; $n = 5$) and older (18 weeks old; $n = 4$) mice (**a**), as well as in mice (16 to 19 weeks old) challenged with the indicated inoculum dose (**b**). $n = 5$ mice per group; $n = 4$ for 10⁴ and 10 pfu dose groups from two independent experiments. **c, d**, The therapeutic activity of REGN monoclonal antibody cocktail (expressed as human IgG1 and administered at 5 mg kg⁻¹ 1 day after infection) was evaluated in Fc γ R-humanized (hFc γ R+) and Fc γ R-deficient (Fc γ R-null) mouse strains challenged with SARS-CoV-2 (MA10 strain, 10⁴ pfu, intranasal). $n = 10$ mice per group (Fc γ R-null); $n = 11$ (PBS)

and $n = 12$ (REGN) mice per group for Fc γ R-humanized mice from two independent experiments. **e, f**, SARS-CoV-2-infected Fc γ R-humanized mice (MA10 strain, 10^4 pfu, intranasal) were treated with wild-type human IgG1 or GRLR variants of REGN monoclonal antibody cocktail 1 day after infection. $n = 8$ (PBS), $n = 5$ (wild-type) and $n = 6$ (GRLR) mice per group from two independent experiments. Weight loss (**c, e**; mean \pm s.e.m.) and survival curves (**d, f**) were compared to the corresponding PBS-treated group by two-way ANOVA (Bonferroni post hoc analysis adjusted for multiple comparisons) and log-rank (Mantel–Cox) test, respectively. P values are indicated. NS, not significant. Red arrow indicates time point of monoclonal antibody treatment post-infection.

[Source data](#).

Fc-effector function in antibody therapy

In a model of monoclonal antibody-mediated therapy, we observed that the REGN monoclonal antibody cocktail (expressed as wild-type human IgG1) confers full protection of Fc γ R-humanized mice when administered at 5 mg kg^{-1} 1 day after lethal challenge with MA10 (Fig. [2c–f](#)). By contrast, no therapeutic activity is evident in mice lacking Fc γ Rs (Fc γ R-null) or when monoclonal antibodies are expressed as variants (GRLR) with minimal affinity for human Fc γ Rs, highlighting the importance of Fc-effector function in the therapeutic activity of neutralizing monoclonal antibodies (Fig. [2c–f](#)). To determine the mechanisms by which human Fc γ Rs contribute to the monoclonal antibody-mediated protection, REGN cocktail monoclonal antibodies were expressed as human IgG1 Fc variants¹¹, and exhibit differential affinities for the various human Fc γ Rs (Fig. [3a](#)). As outlined in Fig. [3b](#), we assessed the therapeutic activity of Fc variants of the REGN monoclonal antibody cocktail at a dose (1 mg kg^{-1}) at which wild-type human IgG1 confers minimal protection (Fig. [3c](#)). Consistent with a protective role for activating Fc γ Rs, Fc variants enhanced for either Fc γ RIIa (GA) or Fc γ RI and Fc γ RIII (ALIE) show a trend of improved therapeutic potency over wild-type IgG1, whereas maximal therapeutic activity was evident only for the GAALIE variant, which is enhanced for both Fc γ RIIa and Fc γ RIII and has reduced affinity for the inhibitory Fc γ RIIb (Fig. [3d, e](#)). These findings suggest that synergy between the two activating Fc γ Rs—Fc γ RIIa and Fc γ RIII—probably accounts for the therapeutic activity of the GAALIE variant, which achieves the same degree of protection as wild-type IgG1, but at a fivefold lower dose. Additionally, the observed differences in the in vivo therapeutic activity among Fc variants could not be attributed to differences in their in vitro neutralization activity, antigen binding specificity or in vivo half-life (Extended Data Figs. [5, 6](#)).

Fig. 3: Selective engagement of activating Fc γ Rs improves the therapeutic activity of anti-SARS-CoV-2 monoclonal antibodies.

 **figure3**

a, Human IgG1 Fc variants with differential affinity for specific classes of human Fc γ Rs were generated for anti-SARS-CoV-2 monoclonal antibodies. Numbers indicate the fold change in affinity compared with wild-type human IgG1. **b–g**, Following the experimental strategy shown in **b**, SARS-CoV-2-infected Fc γ R-humanized mice were treated intravenously at the indicated dose with REGN (**c–e**) or BMS-RU (**f, g**) monoclonal antibody cocktail, or the non-neutralizing monoclonal antibody CR3022 (**h**), expressed as wild-type human IgG1 (blue in **c–h**) or as Fc variants with differential affinity for human Fc γ Rs (magenta in **c–h**). Weight loss (**d**, left, **g**, left, **h**; mean \pm s.e.m.) (**e**; curves for individual mice) and survival curves (**c, d**, right, **f, g**, right) for antibody-treated mice were compared with the corresponding PBS-treated group by two-way ANOVA (Bonferroni post hoc analysis adjusted for multiple comparisons) and log-rank (Mantel–Cox) test, respectively. The fraction of surviving mice is indicated in **e**. *P* values are indicated. **c**, *n* = 6 mice per group from two independent experiments; **d, e**, *n* = 10 mice per group (PBS, GAALIE and GA groups), *n* = 9 (wild-type) and *n* = 11 (ALIE) mice from four independent experiments; **f**, *n* = 8 (PBS and 1 mg kg $^{-1}$) or 9 (10 mg kg $^{-1}$ and 4 mg kg $^{-1}$) mice per group from two independent experiments; **g**, *n* = 7 (GAALIE) or 12 (PBS and wild-type) mice per group from three independent experiments. **h**, *n* = 8 (GAALIE) or 10 (PBS and wild-type) mice per group from two independent experiments. Red arrow indicates time point of monoclonal antibody treatment post-infection.

[Source data](#).

Notably, treatment of MA10-infected mice 1 day after infection with the GAALIE variant was not associated with enhanced disease, when administered at a low dose (1 mg kg $^{-1}$) or at a much higher dose (40 mg kg $^{-1}$) (Extended Data Fig. [7a](#)). At this

higher dose, which is typically used in the clinical setting, FcR-null variants (GRLR) also exhibit full protective activity similar to the GAALIE variants, suggesting that Fc-independent protection could be achieved once neutralizing monoclonal antibodies are administered at sufficiently high doses, as has been documented previously for other viral pathogens²⁴. Similarly, treatment of SARS-CoV-2-infected mice two days after infection, which coincides with the peak of lung viral replication⁷, has no disease-enhancing effects and neither GAALIE nor GRLR variants offer any therapeutic benefit, confirming recent reports showing that the therapeutic window for neutralizing monoclonal antibodies is limited to 24 h after infection²⁶ (Extended Data Fig. 7b).

Similar results were obtained when we assessed the in vivo therapeutic activity of another neutralizing anti-SARS-CoV-2 monoclonal antibody cocktail²⁷ (C135 + C144 (also known as BMS-RU)) currently in clinical development²⁷. When BMS-RU is administered to FcγR-humanized mice at 1 mg kg⁻¹, only GAALIE variants, but not wild-type human IgG1 confer protective activity and prevent disease-induced weight loss (Fig. 3f,g). In contrast to neutralizing anti-SARS-CoV-2 monoclonal antibodies, Fc-engineering of the non-neutralizing anti-receptor-binding domain (RBD) monoclonal antibody CR3022 does not result in improved therapeutic activity, as neither CR3022-GAALIE nor CR3022 protected mice from lethal SARS-CoV-2 challenge (Fig. 3h).

Fc-domain activity in antibody prophylaxis

Our findings in hamsters suggest that when neutralizing monoclonal antibodies are administered prophylactically, Fc–FcγR interactions are not critical for their antiviral activity (Fig. 1c). However, given the substantial interspecies differences in FcγR biology between hamsters and humans, we assessed the contribution of activating FcγR engagement to the monoclonal antibody-mediated prophylaxis of MA10-challenged FcγR-humanized mice (Fig. 4a). When administered at a dose at which wild-type human IgG1 exhibits no protective activity (0.5 mg kg⁻¹) (Fig. 4b), GAALIE variants of the REGN monoclonal antibody confer full protection against lethal SARS-CoV-2 challenge, suggesting that selective activating FcγR engagement could improve the efficacy of neutralizing monoclonal antibodies in both the therapeutic as well as in the prophylactic setting (Fig. 4c).

Fig. 4: Prophylactic activity of anti-SARS-CoV-2 monoclonal antibodies is enhanced by selective engagement of activating FcγRs.

 **figure4**

a–c, The activity of wild-type and GAALIE variants of the REGN monoclonal antibody cocktail was assessed in a model of monoclonal antibody (mAb)-mediated prophylaxis of SARS-CoV-2 infection (**a**). Fc γ R-humanized mice were treated (intravenously) at the indicated dose with REGN monoclonal antibody cocktail expressed as wild-type human IgG1 or as GAALIE variant one day before challenge with SARS-CoV-2 (MA10, 10^4 pfu, intranasal). Weight loss (mean \pm s.e.m.) (**c**, left) and survival curves (**b**, **c**, right) of antibody-treated mice were compared with the PBS-treated group by two-way ANOVA (Bonferroni post hoc analysis adjusted for multiple comparisons) and log-rank (Mantel–Cox) test, respectively. *P* values are indicated. **b**, *n* = 7 mice per group (*n* = 6 mice per group for 2 mg kg $^{-1}$) from two independent experiments; **c**, *n* = 7 (wild-type) or 9 (PBS and GAALIE) mice per group from three independent experiments.

[Source data](#).

Discussion

To maximize the translational relevance of our findings, this study focused on neutralizing anti-SARS-CoV-2 monoclonal antibodies that are currently in clinical use

or development and assessed their in vivo protective activity in mouse strains that recapitulate the unique complexity of human Fc γ Rs²⁵. Challenge of Fc γ R-humanized mice with MA10 results in accelerated weight loss and significant mortality, resembling the clinical manifestations of severe COVID-19. However, such rapid symptomatic disease development limits the therapeutic window for monoclonal antibody treatment and does not allow full unravelling of the mechanisms of COVID-19 disease pathogenesis and the potential immunopathologies due to host immune-related responses. Despite this limitation, we observed that in models of monoclonal antibody-mediated prophylaxis or early treatment, Fc engineering for selective binding to activating Fc γ Rs resulted in an approximately fivefold reduction in the monoclonal antibody dose required to achieve full therapeutic benefit; a finding consistent with our recent in vivo evaluation studies on Fc-optimized anti-influenza virus monoclonal antibodies¹¹. Consistent with previous studies on other viral pathogens, including HIV-1²⁸, influenza²⁴ and Ebola²⁹, our findings suggest that Fc γ R—but not complement pathways—confer monoclonal antibody-mediated protection, as monoclonal antibodies lack protective activity in mice deficient for all classes of Fc γ Rs (Fig. 2c, d). Moreover, Fc variants such as GAALIE, which exhibit diminished C1q-binding activity (Extended Data Fig. 8), demonstrate improved therapeutic efficacy compared with wild-type IgG1.

Analysis of IgG Fc glycan characteristics in hospitalized patients with COVID-19 has previously revealed an association of disease severity with increased levels of afucosylated glycoforms^{30,31}, which exhibit increased affinity for the activating Fc γ RIII¹¹. Although these results suggest a potential pathogenic effect for Fc γ RIII pathways, patients with severe COVID-19 are also characterized by delayed induction of neutralizing antibody responses accompanied by elevated antibody levels³², suggesting that any disease-enhancing effects of afucosylated antibodies might also be related to their poor neutralizing activity³³. However, in our study, we did not observe any pathogenic or disease-enhancing effects of anti-SARS-CoV-2 monoclonal antibodies engineered for enhanced binding to activating Fc γ Rs, irrespective of their neutralizing potency (Fig. 3). It is therefore probable that susceptibility to severe disease is not entirely driven by the Fc γ RIII-binding activity of anti-SARS-CoV-2 IgGs, but rather by multiple, complex immunological determinants.

Despite the successful deployment of highly effective vaccines, neutralizing anti-SARS-CoV-2 monoclonal antibodies are expected to continue to have an important role in virus-containment efforts and the clinical management of COVID-19, especially in high-risk populations and immunocompromised individuals. Although regulatory approval of anti-SARS-CoV-2 monoclonal antibody cocktails has been based on their remarkable clinical efficacy in patients with mild-to-moderate COVID-19^{1,2,3}, none of the currently approved monoclonal antibodies take full advantage of the potential of IgG molecules to mediate protective antiviral Fc-effector functions.

Our findings provide a paradigm for the development of monoclonal antibody-based therapeutics with improved potency and superior therapeutic efficacy against COVID-19 through selective engagement of specific Fc γ R pathways.

Methods

Viruses, cell lines and animals

A P1 stock of the SARS-CoV-2 MA10 strain⁷ was amplified in VeroE6 cells obtained from the ATCC that were engineered to stably express TMPRSS2 (VeroE6-TMPRSS2). To generate a P2 working stock, VeroE6-TMPRSS2 cells were infected at a multiplicity of infection (MOI) of 0.1 pfu per cell and incubated at 37 °C for 4 days. The virus-containing supernatant was subsequently harvested, clarified by centrifugation (3,000g; 10 min), and filtered using a disposable vacuum filter system with a 0.22-μm membrane. Virus stock titres were measured by standard plaque assay on Huh-7.5 cells that stably express ACE2 and TMPRSS2 (Huh-7.5-ACE2/TMPRSS2). In brief, 500 μl of serial tenfold virus dilutions in Opti-MEM were used to infect 4×10^5 cells seeded the previous day into wells of a 6-well plate. After 90 min adsorption, the virus inoculum was removed, and cells were overlaid with DMEM containing 10% FBS with 1.2% microcrystalline cellulose (Avicel). Cells were incubated for 4 days at 33 °C, followed by fixation with 7% formaldehyde and crystal violet staining for plaque counting. To confirm virus identity and evaluate for unwanted mutations that were acquired during the amplification process, RNA from virus stocks was purified using TRIzol reagent (ThermoFisher). In brief, 200 μl of each virus stock was added to 800 μl TRIzol reagent, followed by 200 μl chloroform, which was then centrifuged at 12,000g for 5 min. The upper aqueous phase was moved to a new tube, mixed with an equal volume of isopropanol, and then added to an RNeasy Mini Kit column (Qiagen) to be further purified following the manufacturer's instructions. Viral stocks were subsequently confirmed by Next Generation Sequencing using libraries for Illumina MiSeq.

The SARS-CoV-2 NYC isolate was obtained from a patient's saliva generously provided by A. Viale (Memorial Sloan Kettering Cancer Center) and amplified in Caco-2 cells. This P1 virus was used to generate a P2 working stock by infecting Caco-2 cells at an MOI of 0.05 pfu per cell. Cells were incubated at 37 °C for 6 days before collecting virus-containing supernatant as described above. Similarly, virus stock titres were determined by plaque assay performed on Huh-7.5-ACE2/TMPRSS2 cells. All SARS-CoV-2 experiments were carried out in biosafety level 3 (BSL-3) containment in compliance with institutional and federal guidelines.

VeroE6 cells (ATCC, CRL-1586), Caco-2 cells (ATCC, HTB-37) and Huh-7.5 hepatoma cells³⁴ were cultured in Dulbecco's Modified Eagle Medium (DMEM)

supplemented with 1% nonessential amino acids and 10% fetal bovine serum (FBS). The 293T cells (ATCC, CRL-3216) and HT1080-ACE2 (provided by P. Bieniasz (Rockefeller University)) were maintained in DMEM supplemented with 10% FBS, 50 U ml⁻¹ penicillin and 50 µg ml⁻¹ streptomycin (ThermoFisher). All cell lines were maintained at 37 °C at 5% CO₂. Expi293F cells (ThermoFisher) were maintained at 37 °C, 8% CO₂ in Expi293 expression medium (ThermoFisher) supplemented with 10 U ml⁻¹ penicillin and 10 µg ml⁻¹ streptomycin. Cell lines were not authenticated after purchase. All cell lines tested negative for mycoplasma contamination.

In vivo experiments were approved by the Rockefeller University Institutional Animal Care and Use Committee in compliance with federal laws and institutional guidelines. Hamsters and mice were maintained at the Comparative Bioscience Center at the Rockefeller University at a controlled ambient temperature (20–25 °C) and humidity (30–70%) environment with 12-h dark:light cycle. Golden Syrian hamsters were purchased from Charles River laboratories (strain code 049) and maintained in compliance with USDA regulations. FcγR knockout (mFcγRa^{-/-}; *Fcgr1*^{-/-}) and FcγR-humanized mice (mFcγRa^{-/-}, *Fcgr1*^{-/-}, hFcγRI⁺, hFcγRIIa_{R131}⁺, hFcγRIIb⁺, hFcγRIIIa_{F158}⁺ and hFcγRIIIb⁺) were generated in the C57BL/6 background and characterized in previous studies^{11,25}.

Cloning, expression and purification of recombinant proteins

Human IgG1 Fc-domain variants were generated by site-directed mutagenesis using specific primers as previously described⁹, and recombinant IgG antibodies were expressed and purified using previously described protocols¹¹. Purity was assessed by SDS-PAGE followed by SafeStain blue staining (ThermoFisher), as well as by size exclusion chromatography (SEC) using a Superdex 200 Increase 10/300GL column (GE Healthcare) on an Äkta Pure 25 HPLC system (data analysed using Unicorn v.6.3 software). All antibody preparations were more than 94% pure and endotoxin levels were less than 0.05 EU mg⁻¹, as measured by the limulus amebocyte lysate assay.

The two plasmid-based HIV-NanoLuc-SARS-CoV-2 pseudovirus system³⁵ was provided by P. Bieniasz (Rockefeller University). The *S* gene was modified by site-directed mutagenesis to introduce the amino acid changes present in the MA10 or the B.1.351 strains⁷. SARS-CoV-2 wild-type, MA10 and B.1.351 pseudovirus particles were generated by transfection of the two-plasmid-based system to 293T cells using X-tremeGENE HP DNA transfection reagent (Sigma).

Golden Syrian hamster FcγR cDNA sequences were identified based on the current *M. auratus* genome assembly (MesAur1.0) and recent transcriptomic data³⁶. To validate sequences, hamster FcγR sequences were amplified and sequenced (Genewiz) from

Syrian hamster spleen cDNA (Zyagen) using the following primers: hamster Fc γ RI (5'-GGCGGACAAGTGGTAAATGTCAC-3', 5'-CGGACACATCATTGCTTCAGACTTAAG-3'), hamster Fc γ RII (5'-CTGCTGGACACATGATCTCC-3', 5'-TTAAATGTGGTTCTGGTAATCATGCTCTG-3'), hamster Fc γ RIII (5'-GAGTCTGGAGACACAGATGTTCAAG-3', 5'-CGACGTCATTGTCCCCGAGG-3'), hamster Fc γ RIV (5'-AATGGGTGAGGGTGCTTGAG-3', 5'-GAGGGAATGTTGGGGACAGG-3'). To identify the ectodomain, transmembrane and cytoplasmic domains, Syrian hamster Fc γ R protein sequences were then aligned against annotated mouse Fc γ R protein sequences (Uniprot). Soluble Syrian hamster Fc γ R ectodomains were generated by transient transfection as described above for monoclonal antibodies. Syrian hamster Fc γ R expression plasmids were generated encoding a secretion signal peptide, the predicted Syrian hamster Fc γ R ectodomain, and a C-terminal Strep or His tag. Following transfection of Expi293 cells, recombinant Fc γ Rs were purified from cell-free supernatants by affinity purification using Strep-Tactin Superflow Plus resin (Qiagen) or Ni-NTA Agarose (Qiagen), per manufacturer's instructions. Purified proteins were dialysed into PBS and assessed for purity by SDS-PAGE followed by SafeStain blue staining. Monomeric Fc γ R ectodomains were fractionated from aggregates by SEC on an Äkta Pure system using a Superdex 200 Increase 10/300 GL column (GE Healthcare).

Surface plasmon resonance

All experiments were performed with a Biacore T200 SPR system (GE Healthcare) at 25 °C in HBS-EP⁺ buffer (10 mM HEPES, pH 7.4, 150 mM NaCl, 3.4 mM EDTA, 0.005% (v/v) surfactant P20). IgG antibodies were immobilized on Series S Protein G sensor chip (GE Healthcare) at a density of 2,000 response units (RU). Serial dilutions of recombinant soluble hamster Fc γ R ectodomains were injected to the flow cells at 20 μ l min⁻¹, with the concentration ranging from 1,000 to 15.625 nM (successive 1:2 dilutions). Association time was 60 s followed by a 900-s dissociation step. At the end of each cycle, sensor surface was regenerated with a glycine HCl buffer (10 mM, pH 2.0; 50 μ l min⁻¹, 30 s). Background binding to blank immobilized flow cells was subtracted, and affinity constants were calculated using BIACore T200 evaluation software v.2.0 (GE Healthcare) using the 1:1 Langmuir binding model.

Neutralization assay

Neutralization activity of IgG1 Fc-domain variants was measured as previously described³⁵. In brief, HT1080-ACE2 cells were seeded in 96 U-well black plates 24 h prior to infection with SARS-CoV-2 wild-type, MA10 or B.1.351 pseudoviruses. Pseudovirus particles were pre-incubated with monoclonal antibodies (fourfold serially diluted starting at 10 μ g ml⁻¹) for 1 h at 37 °C and then added to a monolayer

of HT1080_{ACE2} cells. Following a 48-h incubation at 37 °C, cells were carefully washed with PBS and lysed with Luciferase Cell Culture Lysis reagent (Promega) for 15 min. Nano luciferase activity was detected by adding Nano-Glo Luciferase Assay System (Promega) and measured by SpectraMax Plus spectrophotometer (Molecular Devices), using 0.5 s integration time. Data were collected and analysed using SoftMax Pro v.7.0.2 software (Molecular Devices). Relative luciferase units were normalized to those derived from cells infected with the relevant SARS-CoV-2 pseudoviruses in the absence of monoclonal antibodies.

Anti-SARS-CoV-2 RBD ELISA

Recombinant SARS-CoV-2 RBD was immobilized (1 µg ml⁻¹) into high-binding 96-well microtitre plates (Nunc) and after overnight incubation at 4 °C, plates were blocked with PBS plus 2% (w/v) BSA for 2 h. After blocking, plates were incubated for 1 h with serially diluted IgG antibodies or serum samples (1:3 consecutive dilutions in PBS starting at 100 ng ml⁻¹), followed by horseradish peroxidase-conjugated goat anti-human IgG (1 h; 1:5,000; Jackson Immunoresearch). Plates were developed using the TMB two-component peroxidase substrate kit (KPL) and reactions were stopped with the addition of 1 M phosphoric acid. Absorbance at 450 nm was immediately recorded using a SpectraMax Plus spectrophotometer (Molecular Devices) and background absorbance from negative control samples was subtracted. Data were collected and analysed using SoftMax Pro v.7.0.2 software (Molecular Devices).

C1q-binding assay

Human and mouse C1q binding to IgG1 Fc variants was assessed following previously described protocols³⁷. In brief, antibodies were serially diluted (100–0.046 µg ml⁻¹) in PBS and coated overnight (4 °C) onto high-binding 96-well microtiter plates. After washing with PBS + 0.05% Tween-20, plates were blocked with 2% BSA. Normal mouse or human serum (3%) was added and incubated for 60 min with gentle shaking. For the detection of C1q binding, monoclonal mouse anti-C1q antibody (JL-1, Abcam) was added at 0.5 µg ml⁻¹, horseradish peroxidase-conjugated goat anti-mouse IgG was used at a dilution of 1:5,000, and plates were developed and analysed as described above.

Quantification of serum IgG levels

Blood was collected into microvette serum gel tubes (Sarstedt) and serum was fractionated by centrifugation (10,000g, 5 min). IgG levels were determined by

enzyme-linked immunosorbency assay (ELISA) following previously described protocols¹¹.

In vivo SARS-CoV-2 infection models

All animal infection experiments were performed at the Comparative Bioscience Center of the Rockefeller University in animal biosafety level 3 (ABSL-3) containment in compliance with institutional and federal guidelines. Hamsters (6- to 8-week-old males) were anaesthetized with isoflurane (3%) in a VetFlo high-flow vaporizer followed by an intraperitoneal injection of a ketamine (150 mg kg⁻¹) and xylazine (10 mg kg⁻¹) mixture. Hamsters were challenged intranasally with 10⁵ pfu SARS-CoV-2 (NYC isolate, 100 µl viral inoculum). Mice (males or females; 6–7 or 16–22 weeks old) were anaesthetized with a ketamine (75 mg kg⁻¹) and xylazine (15 mg kg⁻¹) mixture (administered intraperitoneally) before challenge with SARS-CoV-2 (MA10 strain, 10⁴ pfu in 30 µl, intranasally).

No statistical method was used to predetermine sample size. On the basis of preliminary studies that determined experimental variation in survival following infection and monoclonal antibody treatment, we performed power calculations and determined that at least $n = 6$ animals per group is sufficient to detect differences among experimental groups (powered at 80% for 5% significance level; survival assessed by log-rank (Mantel–Cox) test).

After infection, animals were monitored daily and humanely euthanized by CO₂ asphyxiation at endpoints authorized by the Rockefeller University Institutional Animal Care and Use Committee, including any of the following: marked lethargy or inactivity, severe respiratory distress or laboured breathing, inability to ambulate or weight loss of greater than 20% of baseline. Animals were randomized on the basis of age, sex and weight. Before treatment, we ensured that the mean weight, sex and age were comparable among the various treatment groups. The treatment groups were not blinded to the personnel involved in monitoring animal survival and weight upon challenge. For antibody-mediated prophylaxis, antibodies were administered intravenously one day before virus challenge, whereas for antibody-mediated therapy, antibodies were administered one day after infection. Antibody dose was calculated in mg kg⁻¹ body weight.

Histological analysis

Lungs from euthanized mice were instilled with 10% neutral buffered formalin and fixed overnight by submersion in 10% formalin. Fixed tissues were embedded in paraffin, sectioned at 4-µm thickness, and stained with haematoxylin and eosin.

Sections of lung were microscopically evaluated by a board-certified veterinary anatomic pathologist and representative images were captured with an Olympus BX45 light microscope using an SC30 camera with the cellSens Dimension software.

Determination of lung viral titres

Hamsters were euthanized at the indicated timepoints following infection and lung weights were recorded. Lungs were lysed in Trizol (ThermoFisher) and dissociated in gentle MACS M tubes using the gentleMACS Octo Dissociator (Miltenyi Biotec). Samples were transferred into Phasemaker tubes (ThermoFisher) and chloroform was added (200 µl chloroform per ml TRIzol). After vigorous shaking, tubes were rested for 5 min and then centrifuged for 15 min at 12,000g at 4 °C. The aqueous phase containing the RNA was transferred into a new tube and RNA extraction was performed by using RNeasy mini kit (Qiagen). SARS-CoV-2 lung titres were determined by quantitative PCR with reverse transcription assay using TaqMan Fast Virus 1-Step Master Mix, specifically designed primers and a TaqMan probe that bind a conserved region in the nucleocapsid gene of SARS-CoV-2 (2019-nCoV_N1-F :5'-GACCCCAAAATCAGCGAAAT-3'; 2019-nCoV_N1-R: 5'-TCTGGTTACTGCCAGTTGAATCTG-3'; 2019-nCoV_N1-P: 5'-FAM-ACCCCCGCATTACGTTGGTGGACC-BHQ1-BHQ1-3'). Quantitative PCR was performed using an Applied Biosystems QuantStudio 6 Flex cycler using the following parameters: 50 °C for 5 min, 95 °C for 20 s followed by 40 cycles of 95 °C for 3 s, and 30 s at 60 °C. Signal from unknown samples was compared to a known standard curve (obtained through BEI Resources, NIAID, NR-52358) and viral titres were expressed as RNA copies per mg tissue.

Flow Cytometry

After lysis of red blood cells (RBC lysis buffer; Biolegend), cells were resuspended in PBS containing 0.5% (w/v) BSA and 5 mM EDTA and labelled with the following fluorescently labelled antibodies (all used at 1:200 dilution unless otherwise stated): anti-human FcγRIIa (clone IV.3)-FITC, anti-human FcγRIIb (clone 2B6)-Dylight650 (used at 5 µg ml⁻¹), anti-B220-AlexaFluor700, anti-Gr1-BrilliantViolet421, anti-CD8β-BrilliantViolet510, anti-human FcγRI (clone 10.1)-BrilliantViolet605, anti-CD3-BrilliantViolet650 (used at 1:100 dilution), anti-CD11b-BrilliantViolet711, anti-CD4-BrilliantViolet785, anti-human FcγRIIIa/b (clone 3G8)-PE, and anti-NK1.1-PE-Cy7. Relevant isotype control antibodies were used and included: mouse IgG1 isotype control-Dylight650 (used at 5 µg ml⁻¹), mouse IgG2b kappa isotype control-FITC, mouse IgG1 kappa isotype control-PE, mouse IgG1 kappa isotype control-BrilliantViolet605. Samples that were stained with isotype control antibodies were also blocked with unlabeled anti-FcγR antibodies as follow: anti-human FcγRI (clone 10.1), anti-human FcγRIIa (clone IV.3), anti-human FcγRIIb (clone 2B6), and anti-

human Fc γ RIIIa/b (clone 3G8) (used at 10 µg ml⁻¹ and incubated for 5 min before staining with fluorescently labelled antibodies). Samples were analysed on an Attune NxT flow cytometer (ThermoFisher) using Attune NxT software v3.1.2 and data were analysed using FlowJo (v10.7) software.

Statistical analysis

Raw data for all main and extended data figures are included in the manuscript as source files. Results from multiple experiments are presented as mean ± s.e.m. One- or two-way ANOVA was used to test for differences in the mean values of quantitative variables, and where statistically significant effects were found, post hoc analysis using Bonferroni (adjusted for multiple comparisons) test was performed. Statistical differences between survival rates were analysed by comparing Kaplan–Meier curves using the log-rank (Mantel–Cox) test. Data were collected and analysed with Microsoft Excel and GraphPad Prism v.9.1 software (GraphPad) and $P < 0.05$ was considered to be statistically significant.

Reporting summary

Further information on research design is available in the [Nature Research Reporting Summary](#) linked to this paper.

Data availability

Raw data for all main and extended data figures are included in the manuscript as source files. [Source data](#) are provided with this paper.

References

1. 1. Chen, P. et al. SARS-CoV-2 neutralizing antibody LY-CoV555 in outpatients with Covid-19. *N. Engl. J. Med.* **384**, 229–237 (2021).
2. 2. Weinreich, D. M. et al. REGN-COV2, a neutralizing antibody cocktail, in outpatients with Covid-19. *N. Engl. J. Med.* **384**, 238–251 (2021).
3. 3.

Gottlieb, R. L. et al. Effect of bamlanivimab as monotherapy or in combination with etesevimab on viral load in patients with mild to moderate COVID-19: a randomized clinical trial. *JAMA* **325**, 632–644 (2021).

4. 4.

Taylor, P. C. et al. Neutralizing monoclonal antibodies for treatment of COVID-19. *Nat. Rev. Immunol.* **21**, 382–393 (2021).

5. 5.

Lundgren, J. D. et al. A neutralizing monoclonal antibody for hospitalized patients with Covid-19. *N. Engl. J. Med.* **384**, 905–914 (2021).

6. 6.

Sia, S. F. et al. Pathogenesis and transmission of SARS-CoV-2 in golden hamsters. *Nature* **583**, 834–838 (2020).

7. 7.

Leist, S. R. et al. A mouse-adapted SARS-CoV-2 induces acute lung injury and mortality in standard laboratory mice. *Cell* **183**, 1070–1085.e1012 (2020).

8. 8.

Bournazos, S., Gupta, A. & Ravetch, J. V. The role of IgG Fc receptors in antibody-dependent enhancement. *Nat. Rev. Immunol.* **20**, 633-643 (2020).

9. 9.

Bournazos, S. et al. Broadly neutralizing anti-HIV-1 antibodies require Fc effector functions for in vivo activity. *Cell* **158**, 1243–1253 (2014).

10. 10.

Lu, C. L. et al. Enhanced clearance of HIV-1-infected cells by broadly neutralizing antibodies against HIV-1 in vivo. *Science* **352**, 1001–1004 (2016).

11. 11.

Bournazos, S., Corti, D., Virgin, H. W. & Ravetch, J. V. Fc-optimized antibodies elicit CD8 immunity to viral respiratory infection. *Nature* **588**, 485–490 (2020).

12. 12.
- Winkler, E. S. et al. Human neutralizing antibodies against SARS-CoV-2 require intact Fc effector functions for optimal therapeutic protection. *Cell* **184**, 1804–1820.e1816 (2021).
13. 13.
- Suryadevara, N. et al. Neutralizing and protective human monoclonal antibodies recognizing the N-terminal domain of the SARS-CoV-2 spike protein. *Cell* **184**, 2316–2331.e2315 (2021).
14. 14.
- Schäfer, A. et al. Antibody potency, effector function, and combinations in protection and therapy for SARS-CoV-2 infection in vivo. *J. Exp. Med.* **218**, e20201993 (2021).
15. 15.
- Ullah, I. et al. Live imaging of SARS-CoV-2 infection in mice reveals neutralizing antibodies require Fc function for optimal efficacy. Preprint at <https://doi.org/10.1101/2021.03.22.436337> (2021).
16. 16.
- Li, D. et al. The functions of SARS-CoV-2 neutralizing and infection-enhancing antibodies in vitro and in mice and nonhuman primates. Preprint at <https://doi.org/10.1101/2020.12.31.424729> (2021).
17. 17.
- Joyner, M. et al. Early safety indicators of COVID-19 convalescent plasma in 5,000 patients. *J. Clin. Invest.* **130**, 4791–4797 (2020).
18. 18.
- Dougan, M. et al. Bamlanivimab plus etesevimab in mild or moderate Covid-19. *N. Engl. J. Med.* **385**, 1382–1392 (2021).
19. 19.
- Wu, X. et al. Tolerability, safety, pharmacokinetics, and immunogenicity of a novel SARS-CoV-2 neutralizing antibody, etesevimab, in Chinese healthy adults:

a randomized, double-blind, placebo-controlled, first-in-human phase 1 study. *Antimicrob. Agents Chemother.* **65**, e0035021 (2021).

20. 20.

Cleary, S. J. et al. Animal models of mechanisms of SARS-CoV-2 infection and COVID-19 pathology. *Br. J. Pharmacol.* **177**, 4851–4865 (2020).

21. 21.

Bournazos, S. IgG Fc receptors: evolutionary considerations. *Curr. Top. Microbiol. Immunol.* **423**, 1–11 (2019).

22. 22.

Baum, A. et al. REGN-COV2 antibodies prevent and treat SARS-CoV-2 infection in rhesus macaques and hamsters. *Science* **370**, 1110–1115 (2020).

23. 23.

Pinto, D. et al. Cross-neutralization of SARS-CoV-2 by a human monoclonal SARS-CoV antibody. *Nature* **583**, 290–295 (2020).

24. 24.

DiLillo, D. J., Tan, G. S., Palese, P. & Ravetch, J. V. Broadly neutralizing hemagglutinin stalk-specific antibodies require Fc γ R interactions for protection against influenza virus in vivo. *Nat. Med.* **20**, 143–151 (2014).

25. 25.

Smith, P., DiLillo, D. J., Bournazos, S., Li, F. & Ravetch, J. V. Mouse model recapitulating human Fc γ receptor structural and functional diversity. *Proc. Natl Acad. Sci. USA* **109**, 6181–6186 (2012).

26. 26.

Martinez, D. R. et al. Prevention and therapy of SARS-CoV-2 and the B.1.351 variant in mice. *Cell Rep.* **36**, 109450 (2021).

27. 27.

Wang, Z. et al. mRNA vaccine-elicited antibodies to SARS-CoV-2 and circulating variants. *Nature* **592**, 616–622 (2021).

28. 28.

Hessell, A. J. et al. Fc receptor but not complement binding is important in antibody protection against HIV. *Nature* **449**, 101–104 (2007).

29. 29.

Bournazos, S., DiLillo, D. J., Goff, A. J., Glass, P. J. & Ravetch, J. V. Differential requirements for Fc γ R engagement by protective antibodies against Ebola virus. *Proc. Natl Acad. Sci. USA* **116**, 20054–20062 (2019).

30. 30.

Chakraborty, S. et al. Proinflammatory IgG Fc structures in patients with severe COVID-19. *Nat. Immunol.* **22**, 67–73 (2021).

31. 31.

Larsen, M. D. et al. Afucosylated IgG characterizes enveloped viral responses and correlates with COVID-19 severity. *Science* **371**, eabc8378 (2021).

32. 32.

Lucas, C. et al. Delayed production of neutralizing antibodies correlates with fatal COVID-19. *Nat. Med.* **27**, 1178–1186 (2021).

33. 33.

Atyeo, C. et al. Dissecting strategies to tune the therapeutic potential of SARS-CoV-2-specific monoclonal antibody CR3022. *JCI Insight* **6**, e143129 (2021).

34. 34.

Blight, K. J., McKeating, J. A. & Rice, C. M. Highly permissive cell lines for subgenomic and genomic hepatitis C virus RNA replication. *J. Virol.* **76**, 13001–13014 (2002).

35. 35.

Schmidt, F. et al. Measuring SARS-CoV-2 neutralizing antibody activity using pseudotyped and chimeric viruses. *J. Exp. Med.* **217**, e20201181 (2020).

36. 36.

McCann, K. E., Sinkiewicz, D. M., Norvelle, A. & Huhman, K. L. De novo assembly, annotation, and characterization of the whole brain transcriptome of male and female Syrian hamsters. *Sci. Rep.* **7**, 40472 (2017).

37. 37.

Pietzsch, J. et al. A mouse model for HIV-1 entry. *Proc. Natl Acad. Sci. USA* **109**, 15859–15864 (2012).

Acknowledgements

We thank P. Smith, E. Lam, R. Peraza, L. Smith, A. M. Mozqueda and T. Martinez for technical assistance and for maintaining and genotyping the mouse colonies used in this study; all the members of the Laboratory of the Molecular Genetics and Immunology (Rockefeller University) for discussions; S. Borghi for providing the recombinant SARS-CoV-2 RBD; P. Bienasz for providing the HT1080-ACE2 cell line and plasmids for generating pseudoviruses; A. Viale for providing the SARS-CoV-2 NYC clinical isolate; A. Ashbrook and G. McNab for advice on handling BSL-3 agents and processing of tissues from infected animals; D. Martinez for technical assistance; S. Carrasco; staff from the Laboratory Comparative Pathology for histopathology support (with funding from NIH Core Grant P30CA008748). Research reported in this publication was supported by the National Institute of Allergy and Infectious Diseases (R01AI137276, R01AI157155, U19AI111825, and R01AI145870) and the Bill and Melinda Gates Foundation (INV-023152). This work was in part made possible with funding from the G. Harold and Leila Y. Mathers Charitable Foundation, the Bawd Foundation and Fast Grants (www.fastgrants.org), a part of Emergent Ventures at the Mercatus Center, George Mason University. We acknowledge support from the Rockefeller University and Vir Biotechnology. The content is solely the responsibility of the authors and does not necessarily represent the official views of the NIH.

Author information

Author notes

1. These authors contributed equally: Rachel Yamin and Andrew T. Jones
2. These authors jointly supervised this work: Jeffrey V. Ravetch and Stylianos Bournazos

Affiliations

1. Laboratory of Molecular Genetics and Immunology, The Rockefeller University, New York, NY, USA

Rachel Yamin, Andrew T. Jones, Kevin S. Kao, Rebecca L. Francis, Jeffrey V. Ravetch & Stylianos Bournazos

2. Laboratory of Virology and Infectious Disease, The Rockefeller University, New York, NY, USA

Hans-Heinrich Hoffmann & Charles M. Rice

3. Department of Epidemiology, University of North Carolina at Chapel Hill, Chapel Hill, NC, USA

Alexandra Schäfer, Timothy P. Sheahan & Ralph S. Baric

4. Department of Microbiology and Immunology, University of North Carolina at Chapel Hill, Chapel Hill, NC, USA

Ralph S. Baric

Contributions

R.Y. designed and performed experiments, generated reagents and analysed the data; A.T.J. cloned and characterized hamster Fc γ Rs, performed binding studies and analysed data; H.-H.H. and A.S. generated and characterized virus stocks; K.S.K. generated reagents, performed in vitro experiments and analysed the data; R.L.F. designed and performed in vivo experiments and generated reagents; T.P.S., R.S.B. and C.M.R. provided intellectual input; J.V.R. designed and directed the study; S.B. designed experiments, analysed data, directed the study and wrote the manuscript with input and edits from all co-authors.

Corresponding authors

Correspondence to [Jeffrey V. Ravetch](#) or [Stylianos Bournazos](#).

Ethics declarations

Competing interests

S.B. and J.V.R. are inventors on a patent (WO2019125846A1) describing the GAALIE variant and its use in therapeutic monoclonal antibodies. C.M.R. and J.V.R. are

members of the scientific advisory board of Vir Biotechnology with equity interests.

Additional information

Peer review information *Nature* thanks Patrick Wilson and the other, anonymous, reviewers for their contribution to the peer review of this work. Peer reviewer reports are available.

Publisher's note Springer Nature remains neutral with regard to jurisdictional claims in published maps and institutional affiliations.

Extended data figures and tables

[Extended Data Fig. 1 Cloning and characterization of the IgG binding activity of hamster Fc \$\gamma\$ Rs.](#)

a, Syrian hamster Fc γ Rs were cloned, and their sequences were determined. The Fc γ R ectodomains are underlined. **b-e**, The affinity of human IgG1 and Fc variants (**b**, **e**, SPR sensorgrams), as well as of mouse (**c**) and hamster (**d**) IgG subclass variants for the various classes of hamster Fc γ Rs was determined by surface plasmon resonance (SPR), using soluble hamster Fc γ R ectodomains. n.d.b., no detectable binding.

[Source data](#)

[Extended Data Fig. 2 Comparison of the Fc \$\gamma\$ R expression levels in the various effector leukocyte populations between young and older Fc \$\gamma\$ R humanized mice.](#)

Fc γ R expression was assessed by flow cytometry in peripheral blood leukocyte populations from young (6-7 weeks old; orange) and older (17 weeks old; blue) Fc γ R humanized mice. **a**, Gating strategy to identify the various leukocyte populations, **b**, Representative histogram overlay plots of Fc γ R expression in young and older Fc γ R humanized mice. Corresponding isotype controls are indicated in lighter shade. **c**, Quantitation of Fc γ R expression (MFI, median fluorescence intensity subtracted from the respective isotype control) in various leukocyte populations. Results are from 4 or 5 mice per group for young and older mice, respectively.

[Source data](#)

[Extended Data Fig. 3 Histopathological analysis of lung tissue from SARS-CoV-2-infected Fc \$\gamma\$ R humanized mice.](#)

Lungs from SARS-CoV-2-infected (MA10 strain, 10^4 pfu, i.n.) Fc γ R humanized mice (16-22 weeks old) were collected on day 4 post-infection and evaluated histologically to assess the pathological changes associated with SARS-CoV-2 infection. **a**, Uninfected mice were characterized by clear alveolar spaces and absence of inflammatory cell infiltrates (low magnification (left panel, 200x); high magnification (center and right panels, 400x). **b**, In contrast, SARS-CoV-2 infection was associated with perivascular and peribronchial mononuclear leukocyte infiltration (200x left; 400x center panel), as well as the presence of macrophages and neutrophils in alveoli and necrotic cellular debris in alveolar spaces (600x, right panel). **c**, In addition, SARS-CoV-2-infected mice exhibited perivenular mixed neutrophilic, histiocytic, and lymphocytic inflammation, reactive endothelium and extravasation of leukocytes (left panel, 400x), as well as foci of interstitial neutrophilic and macrophage inflammation with hemorrhage and single cell necrosis (center and right panels, 400x). Images are representative of one uninfected and six infected mice.

Extended Data Fig. 4 In vitro neutralization activity of anti-SARS-CoV-2 mAbs against SARS-CoV-2 strains.

Neutralization activity of REGN and BMS/RU mAbs (individual mAbs or as a cocktail) against SARS-CoV-2 pseudotyped reporter viruses was measured by *in vitro* neutralization assay. **(a)** *In vitro* neutralization curves and **(b)** IC₅₀ values of REGN (upper panel) and BMS/RU (lower panel) against SARS-CoV-2 WT, MA10, or B.1.351. **(c)** Fold change of SARS-CoV-2_{MA10} and SARS-CoV-2_{B.1.351} IC₅₀ was calculated over WT. n = 1 experiment performed in duplicates. **(d)** Cryo-EM structures of REGN10933 and REGN10987 complexed with SARS-CoV-2 (PDB: 6XDG) or C135 (PDB: 7K8Z) and C144 (PDB: 7K90) complexed with the SARS-CoV-2 spike trimer. Residues within the SARS-CoV-2_{WT} RBD that are mutated in the SARS-CoV-2_{MA10} strain (Q493K, Q498Y, P499T) are indicated in magenta.

[Source data](#)

Extended Data Fig. 5 In vitro neutralization activity and antigenic specificity of Fc variants of anti-SARS-CoV-2 mAbs.

To confirm that changes in the Fc domain have no effect on the neutralization activity and Fab-mediated functions of anti-SARS-CoV-2 mAb, Fc domain variants were characterized in **(a-c)** *in vitro* neutralization assays using SARS-CoV-2_{MA10} pseudotyped reporter viruses and **(d, e)** in ELISA assays using SARS-CoV-2 RBD. n = 1 experiment performed in duplicates. **(a, d)** REGN and **(b, e)** BMS/RU mAb cocktails were expressed as Fc variants and their *in vitro* neutralization activity (**a, b, c**, IC₅₀ values) and **(d, e)** antigenic specificity was compared among Fc variants.

[Source data](#)

Extended Data Fig. 6 In vitro and in vivo stability of Fc variants of anti-SARS-CoV-2 mAbs.

(a) Size-exclusion chromatography (SEC) analysis of Fc variants to determine aggregate formation among Fc domain variants. The SEC elution profiles and abundance (percentage) of monomeric IgG is indicated for the different Fc variants. (b) Fc variants of the REGN mAb cocktail were administered (i.v.; 50 µg) to FcγR humanized mice and antibody serum levels were determined by ELISA at various time points after antibody administration. n= total of 3 mice per group from two independent experiments. Data are mean ± s.e.m.

[Source data](#)

Extended Data Fig. 7 High-dose treatment of SARS-CoV-2-infected FcγR humanized mice with anti-SARS-CoV-2 mAbs Fc variants enhanced for activating FcγR binding is not associated with enhanced disease.

(a) Following the experimental strategy in Fig. 3b, SARS-CoV-2-infected (MA10, 10⁴ pfu, i.n.) FcγR humanized mice (n = 3 for PBS and n = 5 for mAb-treated groups) were treated (i.v.) with 40 mg/kg REGN mAb cocktail expressed as Fc variants with diminished (GRLR) or enhanced activating FcγR binding (GAALIE). (b) SARS-CoV-2-infected mice were treated with 10 mg/kg BMS/RU mAb cocktail expressed as Fc variants GRLR or GAALIE on day 2 post infection. n= total of 10 mice per group for PBS, n = 9 for GAALIE, and n = 6 for GRLR from two independent experiments Weight loss (mean ± s.e.m.) was compared between GRLR and GAALIE-treated groups by two-way ANOVA (Bonferroni post hoc analysis adjusted for multiple comparisons). NS, not significant. Red arrow indicates time point of mAb treatment post-infection.

[Source data](#)

Extended Data Fig. 8 Mouse and human C1q binding of Fc domain variants of IgG1.

The capacity of IgG1 Fc domain variants to interact with mouse (a) and human (b) C1q was assessed by ELISA (n = 1 experiment performed in duplicates). The KA (K322A) variant, which has previously described as a complement-deficient mutant²⁸, was included as control.

[Source data](#)

Supplementary information

[Reporting Summary](#)

[Peer Review File](#)

Source data

[Source Data Fig. 1](#)

[Source Data Fig. 2](#)

[Source Data Fig. 3](#)

[Source Data Fig. 4](#)

[Source Data Extended Data Fig. 1](#)

[Source Data Extended Data Fig. 2](#)

[Source Data Extended Data Fig. 4](#)

[Source Data Extended Data Fig. 5](#)

[Source Data Extended Data Fig. 6](#)

[Source Data Extended Data Fig. 7](#)

[Source Data Extended Data Fig. 8](#)

Rights and permissions

[Reprints and Permissions](#)

About this article

Cite this article

Yamin, R., Jones, A.T., Hoffmann, HH. *et al.* Fc-engineered antibody therapeutics with improved anti-SARS-CoV-2 efficacy. *Nature* **599**, 465–470 (2021).
<https://doi.org/10.1038/s41586-021-04017-w>

- Received: 23 May 2021
- Accepted: 13 September 2021
- Published: 21 September 2021
- Issue Date: 18 November 2021
- DOI: <https://doi.org/10.1038/s41586-021-04017-w>

Share this article

Anyone you share the following link with will be able to read this content:

[Get shareable link](#)

Sorry, a shareable link is not currently available for this article.

[Copy to clipboard](#)

Provided by the Springer Nature SharedIt content-sharing initiative

Further reading

- [**Fc-optimized monoclonal antibodies show superior efficacy**](#)

- Alexandra Flemming

Nature Reviews Immunology (2021)

This article was downloaded by **calibre** from <https://www.nature.com/articles/s41586-021-04017-w>

- Article
- Open Access
- [Published: 03 November 2021](#)

B cell-derived GABA elicits IL-10⁺ macrophages to limit anti-tumour immunity

- [Baihao Zhang](#)¹,
- [Alexis Vogelzang](#)¹ na1,
- [Michio Miyajima](#)¹ na1,
- [Yuki Sugiura](#)² na1,
- [Yibo Wu](#)³,
- [Kenji Chamoto](#)⁴,
- [Rei Nakano](#)⁵,
- [Ryusuke Hatae](#)⁴,
- [Rosemary J. Menzies](#)⁴,
- [Kazuhiro Sonomura](#)⁴,
- [Nozomi Hojo](#)⁶,
- [Taisaku Ogawa](#)⁶,
- [Wakana Kobayashi](#)¹,
- [Yumi Tsutsui](#)¹,
- [Sachiko Yamamoto](#)¹,
- [Mikako Maruya](#)¹,
- [Seiko Narushima](#)¹,
- [Keiichiro Suzuki](#)¹,
- [Hiroshi Sugiyama](#)⁵,
- [Kosaku Murakami](#)⁷,
- [Motomu Hashimoto](#)⁷,
- [Hideki Ueno](#)⁸,
- [Takashi Kobayashi](#)⁹,
- [Katsuhiro Ito](#)^{4,9},
- [Tomoko Hirano](#)⁴,
- [Katsuyuki Shiroguchi](#)⁶,

- [Fumihiko Matsuda⁴](#),
- [Makoto Suematsu²](#),
- [Tasuku Honjo⁴](#) &
- [Sidonia Fagarasan](#) [ORCID: orcid.org/0000-0003-2086-6402^{1,10}](#)

Nature volume **599**, pages 471–476 (2021)

- 18k Accesses
- 1 Citations
- 135 Altmetric
- [Metrics details](#)

Subjects

- [Metabolomics](#)
- [Tumour immunology](#)

Abstract

Small, soluble metabolites not only are essential intermediates in intracellular biochemical processes, but can also influence neighbouring cells when released into the extracellular milieu^{1,2,3}. Here we identify the metabolite and neurotransmitter GABA as a candidate signalling molecule synthesized and secreted by activated B cells and plasma cells. We show that B cell-derived GABA promotes monocyte differentiation into anti-inflammatory macrophages that secrete interleukin-10 and inhibit CD8⁺ T cell killer function. In mice, B cell deficiency or B cell-specific inactivation of the GABA-generating enzyme GAD67 enhances anti-tumour responses. Our study reveals that, in addition to cytokines and membrane proteins, small metabolites derived from B-lineage cells have immunoregulatory functions, which may be pharmaceutical targets allowing fine-tuning of immune responses.

[Download PDF](#)

Main

Lymphocytes are regulated via a variety of receptor interactions with soluble and cell-bound proteins. However, small metabolites derived from immune cells are also abundant in certain tissues, and many may have signalling potential that has yet to be

understood. A growing body of research addresses the flux in metabolic products produced and consumed by different immune cells in various stages of differentiation and activation^{1,2,3}. We hypothesized that water-soluble metabolites can serve as environmental cues, and mediate interactions between immune cells.

GABA is a B cell-associated metabolite

Contrasting homeostatic (non-draining, contralateral; cLN) and activated (draining, ipsilateral; iLN) lymph nodes (LNs) were generated from mice using classic foot-pad immunization with ovalbumin (OVA) protein emulsified in complete Freud's adjuvant (CFA), and subjected to non-targeted profiling of water-soluble metabolites (Fig. 1a). Principal-component analysis revealed that a strong metabolic shift separated iLNs from cLNs in wild-type (WT) mice (Fig. 1b). Pathway analysis of around 200 metabolites with significantly different abundance between iLNs and cLNs revealed that the alanine, aspartate and glutamate pathway was the strongest metabolic feature differentiating resting and activated immune sites (Fig. 1c). Purine and pyrimidine metabolism and the tricarboxylic acid (TCA) cycle were also strongly associated with immune activation (Fig. 1c and Extended Data Fig. 1a).

Fig. 1: Metabolic remodelling of immunized LNs and B cell-dependent GABA production.

 **figure1**

a–e, Mice were injected in the foot pad with OVA + CFA, and iLNs and cLNs were collected for metabolite MS and histology at day 7: WT ($n = 11$), $Cd3^{-/-}$ ($n = 5$), $muMt^{-/-}$ ($n = 4$) and $Rag1^{-/-}$ ($n = 3$). **a**, Immunohistochemistry of B cells (B220), T cells (CD3) and myeloid cells (CD11c). Scale bars, 200 μ m. **b**, Principal-component analysis of metabolites in iLNs and cLNs. PC, principal component. **c**, Pathway analysis of metabolites with significantly different abundance between iLNs and cLNs

in WT mice (two-tailed unpaired *t*-test, $P < 0.05$). **d**, Relative *Cd3*^{−/−} (B cell signature) and *muMt*^{−/−} (T cell signature) iLN metabolites, showing only metabolites that also differed between iLNs and cLNs in WT mice. **e**, GABA levels in the indicated cLNs or iLNs, relative to WT cLNs (data are shown as mean ± s.e.m.; two-tailed unpaired *t*-test: *** $P < 0.001$, **** $P < 0.0001$; NS, not significant). **f**, Correlation of plasma GABA levels with disease activity scores (Simplified Disease Activity Index (SDAI) or Activity Score 28 using C-reactive protein (DAS28-CRP)) and plasma anti-cyclic citrullinated peptide (CCP) antibody levels in patients with rheumatoid arthritis ($n = 138$). Pearson's and Spearman's *r* and *P* values (two tailed) are shown. *n* indicates the number of biological replicates. Data are representative of two experiments (**a–e**). Exact *P* values are provided in the Source Data.

Source data

We assessed the contribution of the main lymphocyte lineages to the metabolic landscape by performing metabolome analyses on activated and resting LNs from immunodeficient mice lacking T cells (*Cd3e*^{−/−}), B cells (*Ighm*^{−/−}; referred to hereafter as *muMt*^{−/−}) or all mature T and B cells (*Rag1*^{−/−}). Despite the presence of many pathogen-associated molecules in CFA expected to stimulate pattern recognition receptors on myeloid cell subsets, the iLN profile of *Rag1*^{−/−} mice was similar to that of cLNs, suggesting that lymphocyte activation is the dominant factor contributing to the metabolic shift in this acute inflammatory model (Fig. [1b](#) and Extended Data Fig. [1a](#)). B cells strongly influenced the immunized LN metabolic landscape, as *muMt*^{−/−} samples were distinct from their WT and *Cd3e*^{−/−} counterparts (Fig. [1b](#)). The neurotransmitter GABA (γ -aminobutyric acid), not previously known to be synthesized by B cells, was identified as the major metabolite upregulated in iLNs in a B cell-dependent manner with respect to both fold change and *P* value (Fig. [1d](#)). GABA was also detected in resting cLNs from WT and *Cd3e*^{−/−} mice, at lower levels (Fig. [1e](#)). However, very little GABA could be detected in LNs from either B cell-deficient mice (*muMt*^{−/−}) or *Rag1*^{−/−} mice, indicating that GABA is a signature B cell metabolite, which was confirmed in random forest algorithm analyses (Fig. [1e](#) and Extended Data Fig. [1c](#)). Imaging mass spectrometry (IMS) confirmed co-localization of GABA and the B cell compartment in iLNs (Extended Data Fig. [1b](#)). In contrast to previous studies^{4,5}, we found a positive correlation of plasma GABA levels with disease activity scores and autoantibody titres in patients with rheumatoid arthritis, suggesting that GABA is indicative of B cell activation in humans (Fig. [1f](#)). Together, the results indicate that GABA synthesis in LNs is enhanced by antigenic stimulation, in a B cell-dependent manner.

B cells synthesize and secrete GABA

GABA is a major inhibitory neurotransmitter regulating inter-neuron communication. Outside the brain, GABA has been detected in the gut, spleen, liver and pancreas^{6,7}. Quantitative measurements in non-immunized WT mice revealed higher amounts of GABA in peripheral and mucosal LNs than in liver or pancreas, supporting the notion that B cell-enriched lymphoid tissues are important sources of GABA production (Extended Data Fig. 2a). However, aside from pancreatic beta cells, the cellular source of GABA outside neurons remains unknown. Although the GABA precursors glutamine and glutamate were abundant in B cells and myeloid cells, B cells were characterized by an enrichment in GABA, in either resting (contralateral) or activated (ipsilateral) popliteal LNs (Fig. 2a). B cells from bone marrow, spleen, Peyer's patches and IgA⁺ plasma cells from the small intestine lamina propria were also characterized by elevated GABA levels (Fig. 2b). Additionally, GABA and other glutamate metabolism components were relatively more abundant in B cells in non-targeted MS analyses of lymphocytes from mouse LNs or peripheral human blood (Extended Data Fig. 2b,c). Analysis of two key enzymes that convert glutamate to GABA showed that transcripts encoding glutamate decarboxylase 67 (GAD67), but not GAD65, were elevated in both mouse and human B cells compared with T cells (Extended Data Fig. 2d,e), suggesting that glutamate metabolism characterizes B-lineage cells in both species.

Fig. 2: Mouse and human B cells synthesize and secrete GABA.

 **figure2**

a, MS analysis of glutamine, glutamate and GABA in purified CD4⁺ T cells, CD8⁺ T cells, CD11b⁺ and/or CD11c⁺ macrophages and dendritic cells (Mf/DC) or B220⁺ B cells from the cLNs and iLNs of immunized WT mice as in Fig. [1a](#) ($n = 3$; ND, not done). **b**, MS-determined GABA levels in B cells from LN ($n = 10$), spleen (SPL; $n =$

4), bone marrow (BM; $n = 3$), Peyer's patches (PP; $n = 4$) and small intestinal lamina propria IgA⁺ plasma cells (SILP IgA⁺ PC; $n = 4$), relative to naive CD4⁺ T cells from the LN of non-immunized WT mice ($n = 13$). **c**, B cells (\pm anti-IgM and anti-CD40) and T cells (\pm anti-CD3, anti-CD28 and IL-2) were cultured with $^{13}\text{C}_5, ^{15}\text{N}_2$ -labelled glutamine for 24 h ($n = 2$) or 72 h ($n = 4$). Isotope-labelled glutamate and GABA were measured by MS in cell lysate or supernatant. **d**, GABA measured by MS in B cells or supernatant after 72 h of treatment with anti-IgM and anti-CD40 ($n = 8$), anti-IgM ($n = 7$) or LPS ($n = 7$), relative to non-stimulated cells ($n = 6$) or as absolute concentration ($n = 5$). **e**, **f**, Human tonsil B cells were stimulated with a mix of anti-IgM and anti-IgG (BCR), CpG (TLR9 agonists), IFN α and IL-2 ($n = 4$) or a mix of IL-21, CD40L and IL-2 ($n = 3$) for 5 d with $^{13}\text{C}_5, ^{15}\text{N}_2$ -labelled glutamine. The percentage of isotope-labelled and unlabelled GABA in cells (**e**) and the level of isotope-labelled GABA in cells and supernatant relative to that in non-stimulated cells (**f**), as measured by MS, are presented ($n = 3$). Significance was calculated by unpaired two-tailed *t*-test (**a**, **b**, **f**), one-way ANOVA (**d**) or two-way ANOVA (**e**): * $P < 0.05$, ** $P < 0.01$, *** $P < 0.001$, **** $P < 0.0001$; NS, not significant;. Data are shown as mean \pm s.e.m. (**a–d**, **f**) or –s.e.m. (**e**). n indicates the number of biological (**a–c**) or technical (**d–f**) replicates. Data are pooled from two (**d**, left) or three (**b**) experiments. Exact P values are provided in the Source Data.

[Source data](#)

Next, B cells were activated in vitro in the presence of $^{13}\text{C}_5, ^{15}\text{N}_2$ -labelled glutamine, and glutamine catabolism and labelled metabolite distribution were traced in cell lysate or supernatant in reference to stimulated T cells. Tracing indicated that glutamine was readily converted to glutamate and used for energy generation, control of reactive oxygen species (ROS) and as a source for carbon and nitrogen for building the biomass in activated B and T cells (Extended Data Fig. [3a,b](#)). However, the abundance of labelled intracellular GABA increased in a time-dependent manner almost exclusively in B cells (Fig. [2c](#)). Labelled glutamine-derived GABA was also detected in B cell media 72 h after stimulation, suggesting that GABA is also released from the cell (Fig. [2c](#)). Other modes of B cell activation, including Toll-like receptor (TLR) stimulation by lipopolysaccharide (LPS) or cross-linking the B cell antigen receptor (BCR) with anti-IgM antibody alone, also induced production and secretion of GABA, albeit to a lesser extent (Fig. [2d](#)). Various modes of stimulation of human tonsil or blood B cells also facilitated the conversion of glutamine to GABA (Fig. [2e](#)) and increased the levels of both intracellular and secreted GABA derived from labelled glutamine (Fig. [2f](#) and Extended Data Fig. [3c](#)). IMS analysis of tonsil confirmed high glutamine and GABA levels in B cell follicles (Extended Data Fig. [3d](#)). The metabolic profile of in vivo and in vitro antigen-exposed lymphocytes indicated that active glutamine and glutamate metabolism contributes to GABA production and secretion in both mouse and human B cells.

B cells limit cytotoxic T cells via GABA

We next addressed the effect of GABA on cellular immune responses, using the MC38 colon carcinoma model in which B cells have been shown to inhibit anti-tumour T cell responses through antigen-non-specific mechanisms^{8,9}. We confirmed that *muMt*^{-/-} mice controlled tumour growth better than their WT counterparts (Fig. 3a). However, implantation of a slow-release GABA pellet led to a significant increase in tumour growth in *muMt*^{-/-} mice compared with mice receiving a placebo (Fig. 3a). *muMt*^{-/-} tumour tissues were enriched in infiltrating CD8⁺ T cells with enhanced cytotoxic and inflammatory properties (Fig. 3b,c, and Extended Data Fig. 4a–c), which was suppressed in *muMt*^{-/-} mice with GABA implants (Fig. 3b,c, and Extended Data Fig. 4a–c). This phenotype was confirmed by gene expression analyses showing that upregulation of tumour necrosis factor (TNF) target gene transcripts characterized CD8⁺ T cells from *muMt*^{-/-} mice, and was considerably reduced by exogenous GABA treatment (Extended Data Fig. 4d). Exogenous GABA did not change tumour growth in WT mice, suggesting that endogenous GABA production (by B cells, macrophages and possibly tumour cells) saturates the system, and additional GABA cannot further impede T cell responses (Fig. 3a). However, picrotoxin, a prototypic GABA_A receptor antagonist, limited tumour growth and enhanced the cytotoxic activity of tumour-infiltrating CD8⁺ T cells in WT mice (Fig. 3d,e). Neither GABA nor picrotoxin treatment affected the proliferation and viability of MC38 cells in vitro (Extended Data Fig. 4e). Together, these results indicate that reduced GABA, or GABA_A signalling, enhances cytotoxic T cell responses and anti-tumour immunity, while secretion of GABA conditions the host towards immune tolerance permissive of tumour growth.

Fig. 3: B cells limit anti-tumour responses via GABA.

 **figure3**

a, MC38 tumour growth in WT or *muMt*^{-/-} mice implanted with GABA (WT, $n = 7$; *muMt*^{-/-}, $n = 8$) or placebo (WT, $n = 8$; *muMt*^{-/-}, $n = 6$) pellets. **b, c**, Flow cytometry quantification of tumour TCR β^+ CD8 $^+$ T cells (WT + placebo, $n = 9$; *muMt*^{-/-} + placebo, $n = 8$; *muMt*^{-/-} + GABA, $n = 10$) (**b**) and intracellular cytokines after re-stimulation (WT + placebo, $n = 4\text{--}5$; *muMt*^{-/-} + placebo, $n = 3\text{--}5$; *muMt*^{-/-} + GABA, $n = 5$) (**c**) on day 7 after MC38 inoculation as in **a**. **d**, MC38 tumour growth in picrotoxin- or DMSO-treated WT mice ($n = 6$). **e**, Flow cytometry of intracellular cytokines in tumour TCR β^+ CD8 $^+$ cells from day 7 as in **d** ($n = 10$). **f**, Hierarchical clustering and heat map of mRNA transcript abundance in TAMs purified at day 7 as in **a** ($n = 6$). Differentially expressed genes in TAMs (DEGs; two-sided Wald test, $P < 0.05$) when comparing placebo-treated WT and *muMt*^{-/-} mice and *muMt*^{-/-} mice treated with GABA or placebo are shown, with DEG annotation analysis comparing the placebo-treated *muMt*^{-/-} and WT groups (right). **g**, Top, z -scores of upregulated genes predicted to be activated by TNF in TAMs from *muMt*^{-/-} mice treated with placebo compared with the WT group for all groups as in **f**; bottom, normalized number of molecules from representative genes ($n = 6$). **h**, DEG annotation analyses

comparing TAMs isolated on day 7 of MC38 growth as in **d** ($n=6$ from four biologically independent mice). Significance was calculated by two-way ANOVA (**a**, **d**), one-way ANOVA (**b**, **c**, **g**) or unpaired two-tailed *t*-test (**e**): * $P<0.05$, ** $P<0.01$, *** $P<0.001$, **** $P<0.0001$; NS, not significant. Data are shown as mean \pm s.e.m. n indicates the number of biological replicates (**a–g**). Data are representative of two experiments (**a**, **c**, **d**) or pooled from two experiments (**b**, **e**). Exact *P* values are provided in the Source Data.

[Source data](#)

GABA_A receptors modulate CD8⁺ T cells

Previous studies have shown that peripheral murine and human lymphocytes express functional GABA receptors^{10,11,12,13,14}. Engagement of ionotropic GABA_A receptor by GABA has been proposed to induce depolarization of membrane potential, leading to inhibition of T cell responses^{10,11,12,15}. We examined the effect of the GABA_A receptor antagonist picrotoxin on intracellular Ca²⁺ concentration, and observed enhanced Ca²⁺ mobilization in mouse CD8⁺ T cells and human Jurkat T cells (Extended Data Fig. 4f). Furthermore, picrotoxin enhanced thapsigargin (TG)-induced store-operated calcium entry in mouse and human T cells (Extended Data Fig. 4g). This confirmed that functional GABA_A receptors on the surface of T cells modulate a pivotal signalling pathway, confirming previous studies suggesting that GABA may directly inhibit CD8⁺ T cells^{16,17}. Purified naive CD8⁺ T cells stimulated in the presence of GABA secreted less inflammatory cytokines, and stimulation in the presence of muscimol, a selective GABA_A receptor agonist, significantly decreased activation and proliferation in a dose-dependent manner (Extended Data Fig. 4h, i). These results indicate that direct signalling via GABA_A receptors is one mechanism by which GABA released by activated B cells may influence the functional properties of nearby T cells.

GABA elicits anti-inflammatory TAMs

Tumour-associated macrophages (TAMs) are known to inhibit anti-tumour immune responses¹⁸. In the MC38 tumour model, macrophage depletion significantly reduced tumour growth in WT mice (Extended Data Fig. 5a, b), consistent with previous studies^{19,20}. Conversely, depletion of macrophages led to an increase in tumour size in *muMt*^{-/-} mice (Extended Data Fig. 5a, b), suggesting that macrophages have distinct immune-regulatory properties in the presence or absence of B cells. The TAM gene transcription profile of *muMt*^{-/-} mice differed significantly from that of WT mice, but

resembled that of WT mice following treatment with exogenous GABA (Extended Data Fig. 5c). Differential gene expression analyses revealed that expression of transcripts related to cytokines, particularly in the TNF signalling pathway, was enhanced in TAMs from placebo-treated *muMt*^{-/-} mice compared with those of WT mice, and this phenotype was significantly disrupted when *muMt*^{-/-} mice were supplemented with GABA (Fig. 3f). Upstream regulator analysis highlighted that many target genes of inflammatory cytokines such as TNF and interferon- γ (IFN γ) with increased expression in *muMt*^{-/-} TAMs were also downregulated by GABA supplementation (Fig. 3g and Extended Data Fig. 5d,e). Conversely, GABA supplementation in *muMt*^{-/-} mice enhanced expression of transcripts related to translation, the cell cycle and energy homeostasis such as oxidative phosphorylation (OXPHOS), which were downregulated in TAMs from *muMt*^{-/-} mice compared with those from WT mice (Fig. 3f and Extended Data Fig. 5f). GABA_A receptor agonists have been shown to diminish the production of inflammatory cytokines by antigen-presenting cells²¹. We found that TAMs isolated from picrotoxin-treated WT mice upregulated expression of transcripts related to calcium signalling and inflammatory cytokines, such as IFN γ -targeted genes (Fig. 3h and Extended Data Fig. 5g). Genes related to translation, the cell cycle and mitochondria and genes targeted by the interleukin-10 receptor (IL-10R) were downregulated by picrotoxin (Fig. 3h and Extended Data Fig. 5g). These results strongly suggest that GABA affects fundamental processes of macrophage physiology and facilitates polarization towards an anti-inflammatory phenotype.

Macrophage conditioning by GABA

Because TAMs are mostly derived from monocytes^{22,23}, we assessed whether GABA influenced differentiation of mouse and human monocytes into macrophages. GABA added to macrophages differentiated under neutral conditions (M-0) increased cell number, cell viability and expression of folate receptor β (FR β), which characterizes anti-inflammatory macrophages²⁴ (Fig. 4a,b, and Extended Data Fig. 6a–c). Gene transcripts related to the cell cycle (such as *Mki67*, *Ccnd1* and *Myc*) and folate metabolism (such as *Folr2*, *Mthfd2* and *Dhfr*) were upregulated by GABA (Extended Data Fig. 6d). Transcriptome and proteome profiling identified a distinct GABA M-0 signature, characterized by activation of pathways related to energy metabolism such as OXPHOS and PPAR signalling and downregulation of pathways related to neuroinflammation and nitric oxide (NO) and ROS production (Fig. 4c). Indeed, real-time measurements confirmed that GABA conditioning increased macrophage bioenergetics, particularly mitochondrial respiration (Extended Data Fig. 6e).

Fig. 4: B cell-derived GABA differentiates anti-inflammatory macrophages, promoting tumour growth.

 **figure4**

a, Quantification of mouse bone marrow or human monocytes cultured in the presence of macrophage colony-stimulating factor (M-CSF) for 6 d (mouse, $n = 6$) or 7 d (human, $n = 5$) with (GABA M-0) or without (M-0) 1 mM GABA. **b**, Flow cytometry of GABA M-0 and M-0 cell viability (assessed with propidium iodide (PI) and

Annexin V, $n = 4$), F4/80, CD68 and FR β (mouse, $n = 3$; human, $n = 5$). **c**, Pathway analysis of mouse GABA M-0 and M-0 transcriptomes ($n = 2$) and proteomes ($n = 3$) (red, upregulated (>0); purple, downregulated (<0)). **d**, Gene expression of mouse M-0 and GABA M-0 cells after 6 h of treatment with IL-10 (M-IL-10 and GABA M-IL-10) ($n = 3$). **e**, Day 7 MC38 tumour monocytes differentiated in vitro into tumour monocyte-derived macrophages (TMDMs) with or without treatment with 1 mM GABA. Immunocytochemistry shows nuclear (TO-PRO-3) localization of total NF- κ B p65 (t-p65) after TNF or IL-1 β stimulation. Scale bars, 100 μ m ($n = 60$). AU, arbitrary units. **f**, MC38 tumour volume in $MbI^{cre/+};GadI^{fl/+}$ ($n = 5$) or $MbI^{cre/+};GadI^{fl/fl}$ ($n = 6$) mice. **g**, Flow cytometry of intracellular cytokines in CD8 $^+$ tumour-infiltrating lymphocytes (TILs) after re-stimulation ($MbI^{cre/+};GadI^{fl/+}$, $n = 4$; $MbI^{cre/+};GadI^{fl/fl}$, $n = 5$). Significance was calculated by two-tailed unpaired *t*-test (**a**, **d**) or two-way ANOVA (**e**, **f**): * $P < 0.05$, ** $P < 0.01$, *** $P < 0.001$, **** $P < 0.0001$; NS, not significant. Data are shown as mean \pm s.e.m. n indicates the number of biological (**c**, **d**, **f**, **g**) or technical (**a**, **b**, **e**) replicates. Data are representative of two (**c** (proteome)) or three (**a** (mouse), **b** (mouse)) experiments. Exact *P* values are provided in the source data.

Source data

Like GABA, IL-10 has also been shown to elicit anti-inflammatory macrophages by metabolic reprogramming promoting OXPHOS²⁵, and is known to be secreted by B cells and IgA $^+$ plasma cells^{26,27}. We observed that the IL-10 receptor A signalling pathway was upregulated in TAMs from WT mice compared with *muMt* $^{-/-}$ mice and downregulated in WT mice by picrotoxin (Extended Data Fig. 5d,g). We next investigated how these two immune-regulatory molecules might influence macrophage generation and function. Monocytes were differentiated in the presence or absence of GABA, followed by the addition of IL-10 to cell cultures (hereafter, GABA M-IL-10 and M-IL-10), before transcriptional, bioenergetic and functional analyses (Extended Data Fig. 7a). Most transcripts of cytokines, cytokine receptors and major histocompatibility complex (MHC) presentation pathway molecules were downregulated by GABA pre-treatment, while IL-10 and OXPHOS transcripts were significantly upregulated (Fig. 4d and Extended Data Fig. 7h). GABA A receptors were involved in these transcriptomic changes, as the addition of picrotoxin partially reverted the effect of GABA on M-IL-10 cells, including IL-10 transcripts (Extended Data Fig. 7h). Real-time PCR and bioenergetic profiling confirmed that combined GABA and IL-10 increased IL-10 transcription and enhanced mitochondrial respiration, indicating generation of macrophages with anti-inflammatory properties (Extended Data Fig. 7b-d). Indeed, M-IL-10 cells conditioned with GABA or B cells significantly suppressed CD8 $^+$ T cell activation in a co-culture assay, reducing granzyme B production and IFN γ and TNF secretion relative to M-IL-10 cells (Extended Data Figs. 7e, f, 8). The inhibitory effect was partially dependent on IL-10,

as IL-10-blocking antibodies restored granzyme B to control levels, without affecting inflammatory cytokine production (Extended Data Figs. 7e, f, 8). In vivo, the transfer of GABA M-IL-10 cells facilitated MC38 tumour growth compared with controls receiving no cells or M-IL-10 cells (Extended Data Fig. 7g).

We next asked whether there is a specific convergence of GABA signalling on the TNF signalling pathway. Monocytes isolated from MC38 tumours were differentiated in vitro in the presence of GABA, before stimulation with TNF or IL-1 β to induce nuclear factor (NF)- κ B activation. GABA greatly reduced the nuclear localization of total p65 induced by TNF, while only partially attenuating its translocation induced by IL-1 β (Fig. 4e). Together, these results indicate that GABA facilitates differentiation, expansion and survival of macrophages with anti-inflammatory properties.

B cell-specific deletion of GAD67

We finally asked whether B cell-specific reduction of GABA synthesis is sufficient to restore anti-tumour responses. Mice carrying a *loxP*-flanked *Gad1* gene encoding GAD67 (*Gad1*^{f/f}) were crossed to transgenic mice with B cell-specific expression of Cre (*Cd79a-cre*; referred to hereafter as *Mb1-cre*) to generate *Mb1*^{cre/+}; *Gad1*^{f/f} mice. *Mb1*^{cre/+}; *Gad1*^{f/f} mice developed normally, and the frequency and number of B cells and their precursors in the bone marrow were similar to those in control *Mb1*^{cre/+}; *Gad1*^{f/f} mice, as were the frequency and number of B and T cell subsets in peripheral lymphoid tissues, the gut and the peritoneal cavity (Extended Data Fig. 9). We confirmed that conditional inactivation of GAD67 in *Mb1*^{cre/+}; *Gad1*^{f/f} mice reduced GABA in B cells to levels similar to those observed in T cells (Extended Data Fig. 10a). *Mb1*^{cre/+}; *Gad1*^{f/f} mice significantly controlled growth of implanted MC38 tumours compared with *Mb1*^{cre/+}; *Gad1*^{f/f} mice (Fig. 4f), with tumour tissues characterized by infiltrating CD8 $^{+}$ T cells with enhanced cytotoxic and inflammatory properties (Fig. 4g and Extended Data Fig. 10b). Together, these results indicate that GABA produced by B cells significantly limits anti-tumour T cell responses.

Discussion

The demands for biomass building and synthesis of effector molecules during immune activation require large adjustments in cell metabolism, and generate countless small molecules. Small metabolites have great evolutionary potential as communication molecules, as they can be synthesized and secreted much more rapidly, using fewer cellular resources, than components of classical cell signalling pathways mediated by cytoplasmic, membrane-bound or secreted proteins. This research builds on a body of work describing GABA acting on mature immune cells, such as CD4 $^{+}$ T cell effector subsets and haematopoietic precursors in the bone marrow. For many of these studies,

the source of GABA remained unclear^{16,28,29,30,31,32,33}. We show that GABA is produced and secreted by both mouse and human B cells, and demonstrate that B cell- or plasma cell-derived GABA is a decisive factor regulating macrophage and CD8⁺ T cell responses and tumour growth in a mouse model of colon cancer.

The presence of IgA⁺ plasma cells expressing PD-L1 and IL-10 within the tumour environment has been linked with poor T cell immunity in human prostatic and liver cancers^{34,35}. Increased tumour-infiltrating IL-10-producing regulatory B cells also correlated with immune evasion in patients with gastric cancer³⁶. We observed little infiltration of tumours by B cells or IgA⁺ plasma cells in the MC38 tumour model, suggesting that B cell conditioning of CD8⁺ T cells or monocytes in this model may occur upstream, during cell differentiation, migration or priming in the LN. However, in human renal cell tumours heavily infiltrated with B cells and IgA⁺ plasma cells, GABA was almost exclusively detected in B cell and IgA⁺ plasma cell areas (Extended Data Fig. 10c), suggesting that GABA produced in the tumour microenvironment may also regulate T cells and monocytes in some settings, perhaps explaining the poor prognosis for renal cell cancers with high infiltration of B-lineage cells³⁷.

The fluctuations in metabolite uptake and secretion that accompany cell activation during immune responses appear to influence both nearby cells and immune outcomes in distant organs. Understanding how intracellular metabolite networks extend into the extracellular milieu to mediate interactions between cells may facilitate development of targeted therapeutic approaches to inhibit tumour cell growth while sparing, or even enhancing, cellular immunity to cancer.

Methods

Mice

muMt^{-/-} (C57BL/6J), *Cd3e*^{-/-} (C57BL/6J)³⁸ *Rag1*^{-/-} (C57BL/6J) and WT mice were bred and maintained under specific-pathogen-free conditions at the RIKEN Center for Integrative Medical Sciences. *MbI*^{cre/+} (C57BL/6J)³⁹ and *Gad1*^{fl/+} (C57BL/6J)⁴⁰ mice were provided by M. Reth (University of Freiburg) and Y. Yanagawa (Gunma University Graduate School of Medicine), respectively. Male *MbI*^{cre/+}; *Gad1*^{fl/+} and female *Gad1*^{fl/+} mice were crossed to generate mice with B cell-specific *Gad1* knockout (*MbI*^{cre/+}; *Gad1*^{fl/fl}) or control mice (*MbI*^{cre/+}; *Gad1*^{fl/+}). Littermate or appropriate age- and sex-matched mice were used for analyses. All animal experiments were conducted in accordance with protocols approved by the Institutional Animal Care and Use Committee at RIKEN.

Human tissue samples

The tonsil samples were collected from donors who (or whose parent(s), in the case of children) provided informed consent on the study, which has been approved by the IRB board at Kyoto University (IRB number: G-1250). Renal cancer samples were collected from the donors who provided informed consent on the study, which has been approved by the IRB board at Kyoto University (IRB number: G-1012).

Foot-pad immunization

Mice were immunized with CFA-emulsified (1:1) OVA in the left foot pad (20 µg per mouse in approximately 20 µl). Seven days later, cLNs and iLNs were isolated for further analyses.

Metabolome analysis

Metabolome analysis was performed as described previously⁴¹. In brief, frozen tissues or cells were homogenized in methanol, followed by addition of chloroform and ultrapure water. After centrifugation and filtration (Ultrafree-MC, UFC3 LCC NB, Human Metabolome Technologies), the solvent was removed using a vacuum concentrator (SpeedVac, Thermo). The concentrated filtrate was used for metabolite analysis. For quantification of GABA, 600 nM of 4-aminobutyric-2,2,3,3,4,4-d6 acids (Sigma-Aldrich) was dissolved in methanol before lysis of the samples.

MetaboAnalystR 5.0 was used for statistical analysis (Auto scaling), enrichment analysis and metabolic pathway analysis to calculate pathway impact values (<https://www.metaboanalyst.ca/home.xhtml>).

Imaging mass spectrometry

On-tissue derivatization of glutamine and GABA was performed as described previously⁴¹. In brief, to perform matrix-assisted laser desorption/ionization (MALDI) MS imaging of amino acids, 5 mg ml⁻¹ of *p*-N,N,N-trimethylammonioanilyl N'-hydroxysuccinimidyl carbamate iodide (TAHS) reagent dissolved in acetonitrile was applied to the surface of thin sections using an airbrush with a 0.2-mm nozzle calibre (Procon Boy FWA Platinum, Mr. Hobby). Tissue sections were incubated for 15 min at 55 °C, followed by application of 2,5-dihydroxybenzoic acid dissolved in acetonitrile containing 0.2% formate. IMS was performed using a MALDI ion trap mass spectrometer (MALDI LTQ XL, Thermo Scientific) equipped with a 60-Hz N₂ laser at 337 nm. The laser scan pitch was set at 40 µm, and the laser was irradiated 50 times for each pixel at a repetition rate of 20 Hz. Mass spectra were acquired in positive-ion mode in conjunction with consecutive reaction monitoring mode. Ion transitions at *m/z*

$323.2 > 177.1$ and $m/z\ 280.2 > 177.1$ (mass window, 0.75 u) were used to detect specific signals of TAHS-derivatized glutamine and GABA, respectively. Acquired data were analysed and ion images were constructed using ImageQuest (version 1.0.1, Thermo Fisher Scientific).

Patients with rheumatoid arthritis

Patients with rheumatoid arthritis were enrolled in the Kyoto University Rheumatoid Arthritis Management Alliance (KURAMA) cohort in 2018. The SDAI and DAS28-CRP scores were used to evaluate disease severity. The levels of anti-CCP antibodies and GABA in plasma were examined. This study complied with the principles of the Declaration of Helsinki and its procedures and protocols were approved by the Medical Ethics Committee of Kyoto University Graduate School and Faculty of Medicine (approval no. R0357). Informed consent was obtained from all participants.

Flow cytometry

Cells were stained with the following antibodies, and flow cytometry was then performed on a BD FACSAria II flow cytometry system (BD Biosciences): anti-CD8a (BioLegend, clone 53-6.7), anti-TCR β (BioLegend, clone H57-597), anti-CD4 (BioLegend, clone RM4-5), anti-CD62L (BioLegend, clone MEL-14), anti-CD11c (BioLegend, clone N418), anti-CD11b (BioLegend, clone M1/70), anti-CD3 ε (BioLegend, clone 145-2C11), anti-CD45.2 (BioLegend, clone 104), anti-granzyme B (BioLegend, clone QA16A02), anti-perforin (BioLegend, clone S16009B), anti-F4/80 (BioLegend, clone BM8), anti-cKit (BioLegend, clone 2B8), anti-SCA-1 (BioLegend, clone D7), anti-CD48 (BioLegend, clone HM48-1), anti-CD150 (BioLegend, clone TC15-12F12.2), anti-CD93 (BioLegend, clone AA4.1), anti-CD38 (BioLegend, clone 90), anti-IFN γ (eBioscience, clone XMG1.2), anti-CD44 (eBioscience, clone IM7), anti-B220 (eBioscience, clone RA3-6B2), anti-TNF (eBioscience, clone MP6-XT22), anti-IgD (eBioscience, clone 11-26c), anti-CD21/CD35 (eBioscience, clone eBio4E3), anti-FOXP3 (eBioscience, clone FJK-16s), anti-CD25 (BD Biosciences, clone PC61), anti-TCR β (BD Biosciences, clone H57-597), anti-IL-2 (BD Biosciences, clone JES6-5H4), anti-CD23 (BD Biosciences, clone B3B4), anti-CD43 (BD Biosciences, clone S7), anti-CD16/32 (BD Biosciences, clone 2.4G2), anti-CD19 (BD Biosciences, clone 1D3), anti-CD5 (BD Biosciences, clone 53-7.3), anti-CD95 (BD Biosciences, clone Jo2), anti- $\gamma\delta$ TCR (BD Biosciences, clone GL3), anti-IgM (SouthernBiotech, polyclonal) and anti-IgA (SouthernBiotech, polyclonal). Apoptotic cells were stained using FITC Annexin V Apoptosis Detection Kit I (BD Biosciences). Proliferating cells were analysed using the CellTrace-Violet Cell Proliferation kit (Thermo Fisher Scientific). To measure intracellular cytokine production, cells were re-stimulated with phorbol 12-myristate 13-acetate (PMA; 50 ng ml $^{-1}$) and ionomycin (500 ng ml $^{-1}$) (Sigma-Aldrich) in the presence of GolgiStop (BD Biosciences) for 4 h. Intracellular

staining was performed using the Fixation/Permeabilization Solution kit (BD Biosciences). Data were analysed with FlowJo software (Tree Star).

Cell sorting

CD4⁺ or CD8⁺ T cells (CD11c⁻CD11b⁻B220⁻ and CD4⁺ or CD8⁺), naive CD4⁺ T cells (CD11c⁻CD11b⁻B220⁻CD8⁻CD4⁺CD44^{low}CD62L⁺), B cells (CD11c⁻CD11b⁻CD4⁻CD8⁻B220⁺) and CD11b/c (B220⁻CD11c⁺ and/or CD11b⁺) cells were sorted from LNs (pooled axillary, brachial and inguinal LNs); follicular (FO) B cells (CD19⁺CD21^{mid}CD23⁺) were sorted from spleen; Peyer's patch B cells (B220⁺IgD^{hi}) and lamina propria IgA⁺ plasma cells (B220⁻IgA⁺) were sorted from small intestine; and bone marrow B cells (B220^{hi}TCRβ⁻) were sorted from the bone marrow of WT mice (Supplementary Fig. 1). Tumour-infiltrating CD8⁺ T cells (CD45⁺TCRβ⁺CD8⁺), monocytes (CD45⁺CD11b⁺F4/80⁻Ly6C^{hi}) and macrophages (CD45⁺CD11b⁺F4/80^{hi}) were sorted 7 d after inoculation with MC38 cells (Supplementary Fig. 2). Fresh human peripheral blood mononuclear cells (PBMCs) were isolated by Ficoll gradient centrifugation. Fresh PBMCs, frozen PBMCs (Lonza) or frozen human tonsil cells were stained with biotin-labelled anti-CD20 (BioLegend, clone 2H7) and anti-CD19 (BioLegend, clone HIB19), and B cells were captured by magnetic selection using anti-biotin MicroBeads (Miltenyi Biotec). T cells were enriched with the Human Pan-T Cell Negative Isolation kit (Miltenyi Biotec).

Real-time PCR

Total RNA was purified using TRIzol reagent (Invitrogen). cDNA synthesis was performed using SuperScript II Reverse Transcriptase (Invitrogen) after DNase I treatment (Invitrogen), and real-time PCR was then run using Thunderbird SYBR Green qPCR mix (Toyobo) and results were analysed with LightCycler 96 SW 1.1 software (Roche). The relative expression levels of mRNAs were normalized to the expression of *Actb* (mouse) or 18S rRNA (human) and are represented relative to control cells. The following primers were used. Mouse primers: *Gad1* (ref. 42): F, 5'-AGGCAGTCCTCCAAGAACCT-3'; R, 5'-CCGTTCTTAGCTGGAAGCAG-3'; *Gad2* (ref. 43): F, 5'-TCAACTAAGTCCCACCCTAAG-3'; R, 5'-CCCTGTAGAGTCAATACCTGC-3'; *Il10* (ref. 44): F, 5'-CAAGGAGCATTGAATTCCC-3'; R, 5'-GGCCTTGTAGACACCTGGTC-3'; *Actb*: F, 5'-CACCTGTGCTGCTACCGA-3'; R, 5'-AGTGTGGGTGACCCGTCTCC-3'. Human primers: 18S rRNA⁴⁵: F, 5'-GGCCCTGTAATTGGAATGAGTC-3'; R, 5'-CCAAGATCCAACACTACGAGCTT-3'; *GAD1* (ref. 46): F, 5'-CGAGTCCCTGGAGCAGATCCTGGTT-3'; R, 5'-GTCAGGCCATTCTCCAGCTAGGCCAATAATA-3'; *GAD2* (ref. 46): F, 5'-

CAACCAAATGCATGCCTCCTACCTCTTCA-3'; R, 5'-TGCCAACTCCAAACATTATCACATGCGCTTCA-3'.

In vitro activation and [$^{13}\text{C}_5, ^{15}\text{N}_2$]glutamine tracing

Mouse T or B cells were purified from LNs with B cell (positive selection) or T cell (negative selection) magnetic beads (Miltenyi Biotec) and cultured for 24 or 72 h in RPMI-1640 (Wako) supplemented with 10% (vol/vol) dialysed FBS (Thermo Fisher Scientific), 1× MEM NEAA, 10 mM HEPES, 50 μM of 2-mercaptoethanol, 1 mM sodium pyruvate, 100 U ml $^{-1}$ penicillin and 100 U ml $^{-1}$ streptomycin. T cells were stimulated with anti-CD3 (2.5 $\mu\text{g ml}^{-1}$; 145-2C11, BD Biosciences) bound to a 96-well plate in the presence of anti-CD28 (2 $\mu\text{g ml}^{-1}$; 37.51, BD Biosciences) and IL-2 (20 ng ml $^{-1}$; R&D Systems). B cells were stimulated with anti-IgM (8 $\mu\text{g ml}^{-1}$; Jackson Immuno Research) alone, anti-IgM (8 $\mu\text{g ml}^{-1}$) plus anti-CD40 (10 $\mu\text{g ml}^{-1}$; BD Biosciences) or LPS (100 ng ml $^{-1}$; Sigma-Aldrich). For [$^{13}\text{C}_5, ^{15}\text{N}_2$]glutamine tracing, glutamine-free medium was supplemented with 2 mM of $^{13}\text{C}_5, ^{15}\text{N}_2$ -labelled l-glutamine (Taiyo Nippon Sanso).

For human B cell culture, PBMCs or tonsil-derived B cells were stimulated with a mix of human IL-21 (50 ng ml $^{-1}$; BioLegend), human CD40L (100 ng ml $^{-1}$; BioLegend) and human IL-2 (10 ng ml $^{-1}$; R&D Systems) or a mix of F(ab') $_2$ goat anti-human IgG/IgM (1 $\mu\text{g ml}^{-1}$; Invitrogen), CpG oligonucleotides (ODN 2006; 4 $\mu\text{g ml}^{-1}$; InvivoGen), human IFN α (1,000 U ml $^{-1}$; R&D Systems) and human IL-2 (10 ng ml $^{-1}$; R&D Systems) as described previously⁴⁷ for 5 d in the medium containing $^{13}\text{C}_5, ^{15}\text{N}_2$ -labelled l-glutamine described above.

Monocyte-derived macrophage culture

Bone marrow cells were isolated from mouse femurs. Red blood cells were removed with lysis buffer (0.15 M NH $_4$ Cl, 1 mM KHCO $_3$, 0.1 mM Na $_2$ EDTA). Monocytes were further purified from bone marrow cells using the EasySep Mouse Monocyte Isolation kit (STEMCELL Technologies). Total bone marrow cells (2×10^6 cells per ml) or purified monocytes (0.5×10^6 cells per ml) were suspended in complete RPMI-1640 (supplemented with 10% (vol/vol) dialysed FBS (Thermo Fisher Scientific), 1× MEM NEAA, 10 mM HEPES, 50 μM of 2-mercaptoethanol, 1 mM sodium pyruvate, 100 U ml $^{-1}$ penicillin, 100 U ml $^{-1}$ streptomycin) with 20 ng ml $^{-1}$ M-CSF (R&D Systems), and seeded on 24-well or 48-well plates. On day 3, non-adherent cells were discarded and adherent cells were further cultured for three more days with fresh medium.

supplemented with 20 ng ml⁻¹ M-CSF. Adherent cells confirmed to be CD11b⁺F4/80⁺ were considered to be mature BMDMs (M-0).

For polarization, M-0 cells were stimulated with 10 ng ml⁻¹ IL-10 (R&D Systems) for 6 h (M-IL-10). For GABA conditioning, 1 mM GABA (Sigma-Aldrich) was added from the start of the cultures, refreshed on day 3 (termed M-0 and GABA M-0) and also during the polarization period (termed M-IL-10 and GABA M-IL-10).

For culture of human monocyte-derived macrophages, human peripheral blood CD14⁺ monocytes (Lonza) were cultured in RPMI-1640 (supplemented with 20% (vol/vol) dialysed FBS (Thermo Fisher Scientific), 1× MEM NEAA, 10 mM HEPES, 50 µM of 2-mercaptoethanol, 1 mM sodium pyruvate, 100 U ml⁻¹ penicillin, 100 U ml⁻¹ streptomycin) with 100 ng ml⁻¹ human M-CSF (R&D Systems) and left untreated or treated with GABA (1 mM) for 7 d. Adherent cells were analysed by flow cytometry.

Co-culture assays

For macrophage–T cell co-cultures, 2 × 10⁴ BMDMs differentiated in the above conditions were seeded together with 5 × 10⁴ sorted CD8⁺ T cells and stimulated for 3 d with anti-CD3 (1 µg ml⁻¹; 145-2C11, BD Biosciences) and anti-CD28 (0.5 µg ml⁻¹; 37.51, BD Biosciences), in the presence or absence of anti-IL-10 blocking antibodies (4 or 10 µg ml⁻¹; JES5-2A5, eBioscience).

For macrophage conditioning with B cells followed by T cell co-cultures, purified LN B cells were stimulated with anti-IgM (8 µg ml⁻¹) plus anti-CD40 (10 µg ml⁻¹; BD Biosciences) for 3 d. Bone marrow cells were differentiated with M-CSF for 1 d, and adherent cells were then cultured with or without activated B cells (1 × 10⁵ cells) for five more days in the presence of M-CSF and further polarized for 6 h with IL-10 (10 ng ml⁻¹). Macrophage–T cell co-cultures were performed as described above. After 3 d of co-culture, CD8⁺ T cells were analysed by flow cytometry, and the concentration of IFN γ and TNF in the supernatant was quantified using the Cytometric Bead Array (CBA) Mouse Th1/Th2/Th17 Cytokine kit (BD Biosciences).

Imaging of NF-κB nuclear translocation

Monocytes (CD45.2⁺CD11b⁺Ly6C^{hi}F4/80⁻) infiltrated into MC38 tumour tissues (day 7) were sorted and differentiated in vitro with or without GABA (1 mM) for 6 d and then seeded onto a 35-mm glass-bottom dish (Iwaki) and analysed by immunocytochemistry as previously described^{48,49}. Cells were stimulated with recombinant mouse TNF (100 ng ml⁻¹) or recombinant mouse IL-1 β (100 ng ml⁻¹) for 30 min. They were then fixed with 4% paraformaldehyde (Nacalai) for 15 min and

processed for immunocytochemistry to examine the intracellular localization of total NF-κB p65. The fixed cells were permeabilized by incubation with 0.2% Triton X-100 (Sigma-Aldrich) for 15 min at 25 °C. Cells were then incubated for 90 min at room temperature with rabbit anti-human total p65 antibody (1:200; clone D14E12, Cell Signaling Technology). After washing with PBS containing 0.2% polyoxyethylene (20) sorbitan monolaurate, cells were incubated with Alexa Fluor 594-conjugated F(ab')₂ fragments of goat anti-rabbit IgG (H+L) (1:1,000; Thermo Fisher Scientific) for 60 min in the dark at 25 °C. Samples were washed three times with PBS containing 0.2% polyoxyethylene (20) sorbitan monolaurate and incubated with TO-PRO-3-iodide (1:1,000; Thermo Fisher Scientific) for 15 min. They were then mounted with ProLong Gold Antifade reagent and visualized using a confocal laser scanning microscope (LSM-510, Carl Zeiss). Co-localization analysis was performed using ZEN software (Carl Zeiss).

Immunofluorescence analysis

For immunofluorescence, tissues were immediately isolated, fixed for 2 h with 4% paraformaldehyde in PBS at 4 °C and soaked in 30% sucrose in PBS overnight at 4 °C. Tissues were then embedded in Tissue-Tek OCT blocks (Sakura) and frozen in liquid nitrogen. The frozen samples were sectioned at a thickness of 10 μm by cryostat (Leica, CM3050S). The following antibodies were used: anti-mouse CD3ε (BioLegend, clone 145-2C11), anti-mouse B220 (eBioscience, clone RA3-6B2) and anti-mouse CD11c (SouthernBiotech, polyclonal). Tissue sections were counterstained with DAPI (Sigma-Aldrich) and mounted with Fluoromount-G antifade reagent (SouthernBiotech).

For human tissue staining, tissues were freshly isolated, embedded in Tissue-Tek OCT blocks (Sakura) or SCEM (SECTION-LAB) and frozen in liquid nitrogen. The frozen samples were sectioned at a thickness of 10 μm by cryostat (Leica, CM3050S). The following antibodies were used for immunohistochemistry staining: anti-human CD68 (eBioscience, clone 815CU17), anti-human CD19 (Abcam, clone EPR5906) and anti-human IgA (SouthernBiotech, polyclonal). Fluorescence images were obtained using a BZ-X700 fluorescence microscope (Keyence).

Extracellular flux analysis

BMDMs differentiated as described above were seeded on Seahorse XF poly(d-lysine)-coated microplates (Agilent) at 1×10^5 cells per well in Seahorse XFp RPMI medium containing 1 mM XFp sodium pyruvate, 2 mM XFp l-glutamine and 10 mM XFp glucose (Agilent) and incubated for 45 min at 37 °C in a non-CO₂ incubator before starting the assay using a Seahorse XFp analyser (Agilent). Oligomycin (1.5 μM), FCCP (2 μM) and rotenone/antimycin A (0.5 μM) were added sequentially, and

the oxygen consumption rate (OCR) and extracellular acidification rate (ECAR) were measured in real time. The maximal respiratory capacity was calculated as (maximum OCR after FCCP injection) – (OCR after rotenone/antimycin A injection).

Measurement of intracellular Ca^{2+} concentrations

Cells were incubated with 2 μM Fluo-3-AM in RPMI supplemented with 10% FBS for 30 min at 37 °C in the dark, washed in PBS and seeded on 35-mm glass-base dishes with Ca^{2+} imaging buffer (120 mM NaCl, 5 mM KCl, 0.96 mM NaH_2PO_4 , 1 mM MgCl₂, 11.1 mM glucose, 1 mM CaCl₂, 1 mg ml⁻¹ BSA and 10 mM HEPES (pH 7.4)) or Ca^{2+} -free imaging buffer (120 mM NaCl, 5 mM KCl, 0.96 mM NaH_2PO_4 , 1 mM MgCl₂, 11.1 mM glucose, 0.5 mM EGTA, 1 mg ml⁻¹ BSA and 10 mM HEPES (pH 7.4)). A confocal laser scanning microscope (LSM510) was used to capture images every 1 s. After baseline image acquisition, cells were stimulated with anti-CD3/CD28 Dynabeads (Thermo Fisher Scientific) or 5 μM thapsigargin (TG). To examine the effects of antagonists for the GABAergic receptor, cells were pre-treated with 100 μM picrotoxin for 5 min. The relative change in intracellular Ca^{2+} concentration ($n = 60$ cells) over time is expressed as the change relative to baseline fluorescence.

Tumour model

The MC38 (mouse colon adenocarcinoma) cell line was originally provided by J. P. Allison (Memorial Sloan Kettering Cancer Center). Mice were implanted subcutaneously with placebo or GABA pellets designed to release GABA over 21 d (31.5 mg per pellet; Innovative Research) or injected intraperitoneally (i.p.) with DMSO or picrotoxin (40 μg per mouse; Abcam) 1 d before intradermal inoculation with 5×10^5 tumour cells in the right flank. DMSO or picrotoxin injection in 200 μl of saline was performed every other day. For macrophage depletion, control liposomes or liposomal clodronate (Hygieia Bioscience) was injected into mice i.p. 1 d before (50 μl per mouse) and on day 6 after (25 μl per mouse) inoculation. For co-injection experiments, MC38 cells (5×10^5 cells per mouse) were injected into mice together with M-IL-10 or GABA M-IL-10 cells (2.5×10^5 cells per mouse) generated in vitro as described above. Tumour tissues were collected on day 7 or day 15 and digested with collagenase (1.5 mg ml⁻¹; Wako) for flow cytometry or sequencing analysis. Tumour volumes were measured with calipers according to the following formula: tumour volume = $\pi \times (\text{length} \times \text{breadth} \times \text{height})/6$.

RNA sequencing

One hundred intratumoural CD45.2⁺TCR β ⁺CD8⁺ T cells and CD45.2⁺CD11b⁺F4/80^{hi} macrophages were purified on day 7 after tumour injection using a FACS Aria III Cell Sorter (BD Biosciences). Cells were collected in SingleCellProtect Single Cell Stabilizing Solution (Avidin) and frozen in liquid nitrogen for digital RNA sequencing⁵⁰. Each library (one per mouse) was sequenced using an indexed pooling method on the MiSeq platform (150 cycles; Illumina kit). Sequencing data were mapped to the mouse genome (mm10 assembly from the UCSC Genome Browser; annotation refFlat from the UCSC Genome Browser) using STAR v.2.5.4b⁵⁰. The normalized number of molecules was calculated using DESeq2 (1.30.1). Genes with significantly different expression (DEGs; two-sided Wald test, $P < 0.05$; average value of normalized number of molecules for all samples > 1 ; $\log_2(\text{fold change}) > 0$ or < 0) were analysed by Ingenuity Pathway Analysis (IPA; Qiagen). DAVID was used for annotation analysis of DEGs (<https://david.ncifcrf.gov/home.jsp>). Principal-component analysis (average value of normalized number of molecules of all samples > 1) was performed through ClustVis (<https://biit.cs.ut.ee/clustvis/>). Sequencing datasets have been deposited in the Gene Expression Omnibus under accession codes [GSE169543](#) and [GSE183246](#).

Gene chip assays

Total cellular RNA was purified using TRIzol (Invitrogen), and the quality was confirmed using Agilent RNA 6000 Pico reagent (Agilent Technologies). The Clariom S Array (Thermo Fisher Scientific) was used to analyse the transcriptome profile (Takara), and data were analysed with Transcriptome Analysis Console Software (Thermo Fisher Scientific) (Supplementary Tables 1 and 2). Pathway analysis was performed using IPA (Qiagen).

Proteome analysis

For preparation of tryptic peptide samples for MS, the phase transfer surfactant method of refs. ^{51,52} was used to prepare BMDM samples for MS, with minor modifications. In brief, cell pellets of 100,000 cells were lysed in 20 μl lysis buffer (100 mM Tris-Cl pH 9.0, 12 mM sodium deoxycholate, 12 mM sodium *N*-dodecanoylsarcosinate, with cOmplete EDTA-free protease inhibitor (Roche)). The protein concentration of each sample was determined using a Pierce BCA Protein Assay kit (Thermo Fisher Scientific). Protein amount varied from sample to sample (3.2–10.0 μg), and the whole amount of each sample was prepared for MS. Samples were reduced with 10 mM DL-dithiothreitol at 50 °C for 30 min, free thiol groups were alkylated with 40 mM iodoacetamide in the dark at room temperature for 30 min and 55 mM cysteine was then added at room temperature for 10 min to quench the reactions. Samples were diluted 1:2.76 with 50 mM ammonium bicarbonate. Lysyl

endopeptidase (FUJIFILM Wako Pure Chemical) and modified trypsin (Promega) were both added at 200 ng, and proteins were digested at 37 °C for 14 h. Tryptic digestion reactions were treated with 1.83 volumes of ethyl acetate and then acidified with trifluoroacetic acid (TFA) to 0.5% (vol/vol) TFA. After centrifugation at 12,000g for 5 min, the upper organic phase containing detergent was discarded and a lower aqueous phase containing digested tryptic peptides was dried using a vacuum centrifuge. The samples were desalted with ZipTip Pipette Tips with 0.6 µl of C18 resin (MilliporeSigma) and dried. Afterwards, samples were dissolved in 10 µl of 0.1% (vol/vol) formic acid and 3% (vol/vol) acetonitrile in water. The peptide concentrations were determined using a Pierce Quantitative Colorimetric Peptide Assay kit (Thermo Fisher Scientific). From each sample, 600 ng of tryptic peptides was measured with MS.

To generate a spectral library, aliquots of tryptic peptides from each sample were combined for a 10-µg tryptic peptide sample, which was fractionated using a Pierce High-pH Reversed-Phase Peptide Fractionation (HPPR) kit, according to the manufacturer's instructions (Thermo Fisher Scientific). For MS, each fraction was dissolved in 6.5 µl of 0.1% (vol/vol) formic acid and 3% (vol/vol) acetonitrile in water and 5.0 µl was measured.

Liquid chromatography and tandem MS (LC–MS/MS) measurements were made using a Q-Exactive Plus Orbitrap mass spectrometer together with a Nanospray Flex ion source (Thermo Fisher Scientific). For LC, an EASY-nLC 1200 system was used (Thermo Fisher Scientific). Solvent A consisted of MS-grade 0.1% (vol/vol) formic acid in water and solvent B consisted of 0.1% (vol/vol) formic acid in 80% (vol/vol) acetonitrile. Samples were measured with a 2-h gradient and a flow rate of 300 nL min⁻¹: the gradient increased from 2% solvent B to 34% solvent B from 0–108 min, then from 34% solvent B to 95% solvent B from 108–110 min and finally to 95% solvent B from 110–120 min to wash the system. Peptides were separated using an analytical column with 3-µm C18 particles, an inner diameter of 75 µm and a length of 12.5 cm (Nikkyo Technos), which was preceded by an Acclaim PepMap 100 trap column with 3-µm C18 particles, an inner diameter of 75 µm and a filling length of 2 cm (Thermo Fisher Scientific). The ion transfer capillary temperature was 250 °C and a spray voltage of 2.0 kV was applied during sample measurement.

To generate a spectral library, the HPPR-fractionated samples were measured with data-dependent acquisition (DDA). Full MS spectra were acquired from 380 to 1,500 *m/z* at 70,000 resolution. The automatic gain control (AGC) target was 3×10^6 , and the maximum injection time (IT) was 100 ms. MS² scans were recorded for the top 20 precursors at 17,500 resolution, and the dynamic exclusion was set to 20 s with the default charge state set to 2. The AGC target was 1×10^5 with a 60-ms maximum IT.

The normalized collision energy was 27% for HCD fragmentation. The intensity threshold was 1.3×10^4 , and charge states 2–5 were included.

To quantify proteins across samples, they were measured with data-independent acquisition (DIA). Data were acquired with one full MS scan and 32 overlapping isolation windows covering the precursor mass range of 400–1,200 m/z . For the full MS scan, the resolution was 70,000, 5×10^6 was the AGC target and the maximum IT was set to 120 ms. DIA segments were acquired at a resolution of 35,000, a 3×10^6 AGC target and an automatic maximum IT. The first mass was fixed at 150 m/z . The normalized collision energy was 27% for HCD fragmentation.

For generation of the spectral library, the eight raw data files obtained from DDA of the HPRP-fractionated tryptic peptides fractions were analysed using Proteome Discoverer version 2.4 (Thermo Fisher Scientific) together with eight raw data files obtained from DDA of eight HPRP-fractionated tryptic peptide fractions derived from BMDM samples, which we had measured previously. The UniProt-reviewed *Mus musculus* (taxon 10090) database was used to process the data files to generate a single results file. Digestion enzyme specificity was set to trypsin (full). Mass tolerance for the precursors was set to 10 p.p.m., and for the fragments the tolerance was 0.02 Da. Carbamidomethylation of cysteine was set as a static modification. Methionine oxidation, N-terminal protein acetylation, methionine loss and methionine loss with N-terminal protein acetylation were set as dynamic modifications. To calculate the false discovery rate (FDR), a concatenated decoy database was used. At both the peptide and protein levels, an FDR of 0.01 was used to filter the search results. To generate the specific spectral library, the results file from Proteome Discoverer was then imported into Spectronaut software (Biognosys).

For quantification of proteins, raw data files from DIA measurements were used to extract protein quantities with the generated spectral library using Spectronaut software (Biognosys). FDR was estimated with the mProphet approach⁵³, and set to 0.01 at both the peptide precursor and protein level⁵⁴. Data filtering parameters for quantification were a q -value percentile fraction of 0.5 with global imputing and cross-run normalization with global normalization on the median. Pathway analysis based on IPA (Qiagen) was performed to analyse significantly differentially expressed proteins (two-tailed unpaired t -test, $P < 0.05$). The MS proteomics data have been deposited to the ProteomeXchange Consortium via the PRIDE⁵⁵ partner repository with the dataset identifier [PXD028403](#).

Statistical analysis

Statistical analysis was performed using Prism (GraphPad) or DESeq2. Analyses were conducted using the Pearson's and Spearman's correlation test, the Wald test, the two-

tailed unpaired Student's *t*-test or repeated-measures ANOVA. *P* value less than 0.05 was considered statistically significant.

Reporting summary

Further information on research design is available in the [Nature Research Reporting Summary](#) linked to this paper.

Data availability

The RNA-seq datasets analysed are publicly available in the Gene Expression Omnibus with accession codes [GSE169543](#) and [GSE183246](#). The proteomics datasets are available via ProteomeXchange with identifier [PXD028403](#). The gene chip datasets are provided in Supplementary Tables 1 and 2. [Source data](#) are provided with this paper.

Code availability

The DESeq2 (1.30.1) package was used to analyse RNA-seq data (<https://bioconductor.org/packages/release/bioc/html/DESeq2.html>).

References

1. 1.

Loftus, R. M. & Finlay, D. K. Immunometabolism: cellular metabolism turns immune regulator. *J. Biol. Chem.* **291**, 1–10 (2016).

2. 2.

Geltink, R. I. K., Kyle, R. L. & Pearce, E. L. Unraveling the complex interplay between T cell metabolism and function. *Annu. Rev. Immunol.* **36**, 461–488 (2018).

3. 3.

Makowski, L., Chaib, M. & Rathmell, J. C. Immunometabolism: from basic mechanisms to translation. *Immunol. Rev.* **295**, 5–14 (2020).

4. 4.

Chen, R. et al. Perturbations in amino acids and metabolic pathways in osteoarthritis patients determined by targeted metabolomics analysis. *J. Chromatogr. B* **1085**, 54–62 (2018).

5. 5.

Zhou, Y. et al. Serum amino acid metabolic profiles of ankylosing spondylitis by targeted metabolomics analysis. *Clin. Rheumatol.* **39**, 2325–2336 (2020).

6. 6.

Tsuji, M. & Nakajima, T. Studies on the formation of γ -aminobutyric acid from putrescine in rat organs and purification of its synthetic enzyme from rat intestine. *J. Biochem.* **83**, 1407–1412 (1978).

7. 7.

Garry, D. J., Sorenson, R. L. & Coulter, H. D. Ultrastructural-localization of γ amino butyric-acid immunoreactivity in B-cells of the rat pancreas. *Diabetologia* **30**, 115–119 (1987).

8. 8.

Zhang, Y., Morgan, R., Podack, E. R. & Rosenblatt, J. B cell regulation of anti-tumor immune response. *Immunol. Res.* **57**, 115–124 (2013).

9. 9.

Akrami, M. et al. Circulation of gut-preactivated naive CD8⁺ T cells enhances antitumor immunity in B cell-defective mice. *Proc. Natl Acad. Sci. USA* **117**, 23674–23683 (2020).

10. 10.

Tian, J., Chau, C., Hales, T. G. & Kaufman, D. L. GABA_A receptors mediate inhibition of T cell responses. *J. Neuroimmunol.* **96**, 21–28 (1999).

11. 11.

Alam, S., Laughton, D. L., Walding, A. & Wolstenholme, A. J. Human peripheral blood mononuclear cells express GABA_A receptor subunits. *Mol. Immunol.* **43**, 1432–1442 (2006).

12. 12.

Bjurstöm, H. et al. GABA, a natural immunomodulator of T lymphocytes. *J. Neuroimmunol.* **205**, 44–50 (2008).

13. 13.

Dionisio, L., Jose De Rosa, M., Bouzat, C. & Esandi Mdel, C. An intrinsic GABAergic system in human lymphocytes. *Neuropharmacology* **60**, 513–519 (2011).

14. 14.

Mendu, S. K., Bhandage, A., Jin, Z. & Birnir, B. Different subtypes of GABA-A receptors are expressed in human, mouse and rat T lymphocytes. *PLoS ONE* **7**, e42959 (2012).

15. 15.

Tian, J. et al. γ -Aminobutyric acid inhibits T cell autoimmunity and the development of inflammatory responses in a mouse type 1 diabetes model. *J. Immunol.* **173**, 5298–5304 (2004).

16. 16.

Soltani, N. et al. GABA exerts protective and regenerative effects on islet beta cells and reverses diabetes. *Proc. Natl Acad. Sci. USA* **108**, 11692–11697 (2011).

17. 17.

Mendu, S. K. et al. Increased GABA_A channel subunits expression in CD8⁺ but not in CD4⁺ T cells in BB rats developing diabetes compared to their congenic littermates. *Mol. Immunol.* **48**, 399–407 (2011).

18. 18.

Noy, R. & Pollard, J. W. Tumor-associated macrophages: from mechanisms to therapy. *Immunity* **41**, 49–61 (2014).

19. 19.

Nandi, B. et al. Stromal CCR6 drives tumor growth in a murine transplantable colon cancer through recruitment of tumor-promoting macrophages. *Oncotarget* **5**, e1189052 (2016).

20. 20.

Ries, C. H. et al. Targeting tumor-associated macrophages with anti-CSF-1R antibody reveals a strategy for cancer therapy. *Cancer Cell* **25**, 846–859 (2014).

21. 21.

Bhat, R. et al. Inhibitory role for GABA in autoimmune inflammation. *Proc. Natl Acad. Sci. USA* **107**, 2580–2585 (2010).

22. 22.

Movahedi, K. et al. Different tumor microenvironments contain functionally distinct subsets of macrophages derived from Ly6C^{high} monocytes. *Cancer Res.* **70**, 5728–5739 (2010).

23. 23.

Shand, F. H. W. et al. Tracking of intertissue migration reveals the origins of tumor-infiltrating monocytes. *Proc. Natl Acad. Sci. USA* **111**, 7771–7776 (2014).

24. 24.

Puig-Kroger, A. et al. Folate receptor β is expressed by tumor-associated macrophages and constitutes a marker for M2 anti-inflammatory/regulatory macrophages. *Cancer Res.* **69**, 9395–9403 (2009).

25. 25.

Ip, W. K. E., Hoshi, N., Shouval, D. S., Snapper, S. & Medzhitov, R. Anti-inflammatory effect of IL-10 mediated by metabolic reprogramming of macrophages. *Science* **356**, 513–519 (2017).

26. 26.

Rojas, O. L. et al. Recirculating intestinal IgA-producing cells regulate neuroinflammation via IL-10. *Cell* **177**, 492–493 (2019).

27. 27.

Meng, L. Z. et al. Bone marrow plasma cells modulate local myeloid-lineage differentiation via IL-10. *Front. Immunol.* **10**, 1183 (2019).

28. 28.

Tian, J. et al. Oral treatment with γ -aminobutyric acid improves glucose tolerance and insulin sensitivity by inhibiting inflammation in high fat diet-fed mice. *PLoS ONE* **6**, e25338 (2011).

29. 29.

Tian, J., Dang, H., Nguyen, A. V., Chen, Z. & Kaufman, D. L. Combined therapy with GABA and *pdroinsulin/alum* acts synergistically to restore long-term normoglycemia by modulating T-cell autoimmunity and promoting β -cell replication in newly diabetic NOD mice. *Diabetes* **63**, 3128–3134 (2014).

30. 30.

Bhandage, A. K. et al. GABA regulates release of inflammatory cytokines from peripheral blood mononuclear cells and CD4 $^{+}$ T cells and is immunosuppressive in type 1 diabetes. *EBioMedicine* **30**, 283–294 (2018).

31. 31.

Januzi, L. et al. Autocrine GABA signaling distinctively regulates phenotypic activation of mouse pulmonary macrophages. *Cell Immunol.* **332**, 7–23 (2018).

32. 32.

Shao, L. et al. The neurotransmitter receptor Gabbr1 regulates proliferation and function of hematopoietic stem and progenitor cells. *Blood* **137**, 775–787 (2021).

33. 33.

Tian, J., Song, M. & Kaufman, D. L. Homotaurine limits the spreading of T cell autoreactivity within the CNS and ameliorates disease in a model of multiple sclerosis. *Sci. Rep.* **11**, 5402 (2021).

34. 34.

Shalapour, S. et al. Immunosuppressive plasma cells impede T-cell-dependent immunogenic chemotherapy. *Nature* **521**, 94–98 (2015).

35. 35.

Shalapour, S. et al. Inflammation-induced IgA $^{+}$ cells dismantle anti-liver cancer immunity. *Nature* **551**, 340–344 (2017).

36. 36.

Murakami, Y. et al. Increased regulatory B cells are involved in immune evasion in patients with gastric cancer. *Sci. Rep.* **9**, 13083 (2019).

37. 37.

Sjoberg, E. et al. A minority-group of renal cell cancer patients with high infiltration of CD20⁺ B-cells is associated with poor prognosis. *Br. J. Cancer* **119**, 840–846 (2018).

38. 38.

Malissen, M. et al. Altered T-cell development in mice with a targeted mutation of the Cd3-ε gene. *EMBO J.* **14**, 4641–4653 (1995).

39. 39.

Hobeika, E. et al. Testing gene function early in the B cell lineage in *Mb1-cre* mice. *Proc. Natl Acad. Sci. USA* **103**, 13789–13794 (2006).

40. 40.

Obata, K. et al. GABA and synaptic inhibition of mouse cerebellum lacking glutamate decarboxylase 67. *Biochem. Biophys. Res. Commun.* **370**, 429–433 (2008).

41. 41.

Miyajima, M. et al. Metabolic shift induced by systemic activation of T cells in PD-1-deficient mice perturbs brain monoamines and emotional behavior. *Nat. Immunol.* **18**, 1342–1352 (2017).

42. 42.

Zeisel, A., Yitzhaky, A., Bossel Ben-Moshe, N. & Domany, E. An accessible database for mouse and human whole transcriptome qPCR primers. *Bioinformatics* **29**, 1355–1356 (2013).

43. 43.

Zhao, C., Driessen, T. & Gammie, S. C. Glutamic acid decarboxylase 65 and 67 expression in the lateral septum is up-regulated in association with the postpartum period in mice. *Brain Res.* **1470**, 35–44 (2012).

44. 44.

Deng, B., Wehling-Henricks, M., Villalta, S. A., Wang, Y. & Tidball, J. G. IL-10 triggers changes in macrophage phenotype that promote muscle growth and regeneration. *J. Immunol.* **189**, 3669–3680 (2012).

45. 45.

Kiselak, E. A. et al. Transcriptional regulation of an axonemal central apparatus gene, sperm-associated antigen 6, by a SRY-related high mobility group transcription factor, S-SOX5. *J. Biol. Chem.* **285**, 30496–30505 (2010).

46. 46.

Gallos, G. et al. Airway epithelium is a predominant source of endogenous airway GABA and contributes to relaxation of airway smooth muscle tone. *Am. J. Physiol. Lung Cell. Mol. Physiol.* **304**, L191–L197 (2013).

47. 47.

Zhang, M. et al. Methionine commits cells to differentiate into plasmablasts through epigenetic regulation of BTB and CNC homolog 2 by the methyltransferase EZH2. *Arthritis Rheumatol.* **72**, 1143–1153 (2020).

48. 48.

Nakano, R., Kitanaka, T., Namba, S., Kitanaka, N. & Sugiya, H. Protein kinase C ϵ regulates nuclear translocation of extracellular signal-regulated kinase, which contributes to bradykinin-induced cyclooxygenase-2 expression. *Sci. Rep.* **8**, 8535 (2018).

49. 49.

Nakano, R. et al. Non-transcriptional and translational function of canonical NF- κ B signaling in activating ERK1/2 in IL-1 β -induced COX-2 expression in synovial fibroblasts. *Front. Immunol.* **11**, 579266 (2020).

50. 50.

Shiroguchi, K., Jia, T. Z., Sims, P. A. & Xie, X. S. Digital RNA sequencing minimizes sequence-dependent bias and amplification noise with optimized single-molecule barcodes. *Proc. Natl Acad. Sci. USA* **109**, 1347–1352 (2012).

51. 51.

Masuda, T., Tomita, M. & Ishihama, Y. Phase transfer surfactant-aided trypsin digestion for membrane proteome analysis. *J. Proteome Res.* **7**, 731–740 (2008).

52. 52.

Masuda, T., Saito, N., Tomita, M. & Ishihama, Y. Unbiased quantitation of *Escherichia coli* membrane proteome using phase transfer surfactants. *Mol. Cell. Proteomics* **8**, 2770–2777 (2009).

53. 53.

Reiter, L. et al. mProphet: automated data processing and statistical validation for large-scale SRM experiments. *Nat. Methods* **8**, 430–435 (2011).

54. 54.

Rosenberger, G. et al. Statistical control of peptide and protein error rates in large-scale targeted data-independent acquisition analyses. *Nat. Methods* **14**, 921–927 (2017).

55. 55.

Perez-Riverol, Y. et al. The PRIDE database and related tools and resources in 2019: improving support for quantification data. *Nucleic Acids Res.* **47**, D442–D450 (2019).

Acknowledgements

We thank all members of the Fagarasan laboratory for discussions. We thank Y. Yanagawa (Gunma University) for *Gad1*^{f/+} mice; M. Reth (University of Freiburg) and T. Kurosaki (IMS RIKEN) for *MbI*^{cre/+} mice; T. Kitami (IMS RIKEN) for the use of the Seahorse Analyser and assistance with Seahorse assays; T. Saito (IMS RIKEN) for the Jurkat cell line; the Iskikawa laboratory (IMS RIKEN) for advice on human tissue staining; M. Li (IMS RIKEN) for help with macrophage cultures; K. Fukuhara (IMS RIKEN) for RNA-seq; and S. Kato for her administrative assistance. This work was supported by the Japan Agency for Medical Research and Development–Core Research for Evolutional Science and Technology (grant 14532135 to S.F.), the Japan Agency for Medical Research and Development-FORCE (grant JP21gm4010008 to S.F.), the RIKEN Aging Project Grant (to S.F.), the Japan Agency for Medical Research and Development–Preliminary Research for Innovative Medical Care (JP21gm6110019 to M. Miyajima), the Japan Society for the Promotion of Science KAKENHI Grant-in-Aid for Challenging Research (Exploratory) (grant 21K19392 to M. Miyajima), the Japan Society for the Promotion of Science KAKENHI Grant

18H05411 (K.S.) and the Yanai Fund (Kyoto University); B.Z., A.V., N.H. and T.O. were supported by the RIKEN Special Postdoctoral Researcher (SPDR) Program. The KURAMA cohort study is supported by a grant from Daiichi Sankyo. The funder had no role in the design of the study, the collection or analysis of the data, the writing of the manuscript or the decision to submit the manuscript for publication.

Author information

Author notes

1. These authors contributed equally: Alexis Vogelzang, Michio Miyajima, Yuki Sugiura

Affiliations

1. Laboratory for Mucosal Immunity, Center for Integrative Medical Sciences, RIKEN Yokohama Institute, Yokohama, Japan

Baihao Zhang, Alexis Vogelzang, Michio Miyajima, Wakana Kobayashi, Yumi Tsutsui, Sachiko Yamamoto, Mikako Maruya, Seiko Narushima, Keiichiro Suzuki & Sidonia Fagarasan

2. Department of Biochemistry and Integrative Biology, Keio University, Tokyo, Japan

Yuki Sugiura & Makoto Suematsu

3. YCI Laboratory for Next-Generation Proteomics, Center for Integrative Medical Sciences, RIKEN Yokohama Institute, Yokohama, Japan

Yibo Wu

4. Center for Genomic Medicine, Kyoto University Graduate School of Medicine, Kyoto University, Kyoto, Japan

Kenji Chamoto, Ryusuke Hatae, Rosemary J. Menzies, Kazuhiro Sonomura, Katsuhiro Ito, Tomoko Hirano, Fumihiko Matsuda & Tasuku Honjo

5. Laboratory of Veterinary Biochemistry, Department of Veterinary Medicine, Nihon University College of Bioresource Sciences, Fujisawa, Japan

Rei Nakano & Hiroshi Sugiya

6. Laboratory for Prediction of Cell Systems Dynamics, RIKEN Center for Biosystems Dynamics Research (BDR), Osaka, Japan

Nozomi Hojo, Taisaku Ogawa & Katsuyuki Shiroguchi

7. Department of Rheumatology and Clinical Immunology, Kyoto University Graduate School of Medicine, Kyoto University, Kyoto, Japan

Kosaku Murakami & Motomu Hashimoto

8. Department of Immunology, Kyoto University Graduate School of Medicine, Kyoto University, Kyoto, Japan

Hideki Ueno

9. Department of Urology, Kyoto University Graduate School of Medicine, Kyoto University, Kyoto, Japan

Takashi Kobayashi & Katsuhiro Ito

10. Division of Integrated High-Order Regulatory Systems, Center for Cancer Immunotherapy and Immunobiology, Kyoto University Graduate School of Medicine, Kyoto University, Kyoto, Japan

Sidonia Fagarasan

Contributions

S.F., B.Z. and A.V. designed the study. B.Z., A.V. and M. Miyajima carried out in vivo and in vitro cell characterization in immunization and tumour experiments. Y.S. and K. Sonomura performed metabolomic studies under the supervision of M.S. and F.M. Y.S. performed tracing experiments and IMS studies on mouse and human tissues. Y.W. performed proteomic studies. K.C., R.J.M. and R.H. contributed to tumour experiments and human blood cell sorting and stimulation under the supervision of T. Honjo. N.H., T.O. and K. Shiroguchi performed 100-cell transcriptome analyses. R.N. performed experiments related to calcium mobilization and NF- κ B activation under the supervision of H.S. W.K., Y.T., S.Y., M. Maruya, S.N. and K. Suzuki provided technical help with mouse generation, phenotyping, analyses and metabolome and transcriptome sample preparation. K.M. and M.H. provided samples and data for patients with rheumatoid arthritis. H.U. provided tonsil samples, and T.K., K.I. and T. Hirano provided renal tumour samples. S.F. supervised the work and analysed data, and S.F., A.V. and B.Z. wrote the manuscript.

Corresponding author

Correspondence to [Sidonia Fagarasan](#).

Ethics declarations

Competing interests

S.F., B.Z. and M. Miyajima, through RIKEN Innovation, have filed a patent application on the methods and findings in this manuscript. The remaining authors declare no competing interests.

Additional information

Peer review information *Nature* thanks Daniel Kaufman, Carola Vinuesa and the other, anonymous, reviewer(s) for their contribution to the peer review of this work. Peer reviewer reports are available.

Publisher's note Springer Nature remains neutral with regard to jurisdictional claims in published maps and institutional affiliations.

Extended data figures and tables

[Extended Data Fig. 1 Metabolic pathways and top metabolites changed by immunization in WT and immunodeficient mice.](#)

a, Pathway analyses of significantly different metabolites (two-tailed unpaired t-test P value < 0.05) between iLN and cLN of WT mice revealed major activation-induced changes in metabolites related to alanine-aspartate-glutamate metabolism, purine-pyrimidine metabolism and TCA cycle. The z -score of all detected metabolites in each of these pathways were plotted to provide an overview of metabolic similarity and variation among different groups of mice. **b**, Imaging mass spectrometry of GABA and immunohistochemical analyses of cLN and iLN of WT mice. **c**, Random forest analysis based on of the metabolites extracted from iLN and cLN of WT mice ($n = 11$), *cd3^{-/-}* ($n = 5$), *muMt^{-/-}* ($n = 4$) and *rag1^{-/-}* ($n = 3$) mice measured by mass spectrometry (MS). n indicates biological replicates. Data are representative of two experiments.

[Source data](#)

Extended Data Fig. 2 GABA concentration in multiple tissues and metabolic signature of B cells in mouse and human.

a, Quantification of GABA in brain, peripheral lymph nodes (pLN) ($n = 6$), mesenteric LN (mLN) ($n = 6$), spleen ($n = 6$), upper and lower segments of the small intestine (SI up and SI low, respectively) ($n = 6$), large intestine (LI) ($n = 6$), liver ($n = 6$), pancreas ($n = 6$), hindlimb skeletal muscle ($n = 6$) and perigonadal fat ($n = 5$) of WT mice measured by mass spectrometry. Box-and-whiskers plots represent the range from the 25th to 75th percentiles (box), the median value (the middle line) and the minimum to maximum value (whiskers). n indicates biological replicates. **b**, Measurement of glutamine, glutamate and GABA by mass spectrometry in *ex vivo*-sorted T or B cells purified by FACS from mouse peripheral lymph nodes and human peripheral blood, relative to matched T cells. **c**, Venn diagrams (upper) and metabolite-set-enrichment analysis (lower panels) showing the significantly different metabolites (two-tailed unpaired t-test P value < 0.05) between *ex vivo*-sorted T and B cells from mice or humans ($n = 5$ (B cells) or 12 (T cells) replicates derived from 5 biologically independent human healthy donors, $n = 10$ or 11(glutamate and GABA in T cells) replicates derived from 6 biologically independent mice). **d, e**, qPCR analysis of GAD67 (*Gad1/GAD1*) and GAD65 (*Gad2/GAD2*) mRNA level in mouse LN-derived T and B cells ($n = 3$) (**d**), or human blood-derived T ($n = 4$) and B cells ($n = 3$) (**e**). * $P < 0.05$, *** $P < 0.0001$ (two-tailed unpaired t-test (**b, d, e**)). Bars represent mean \pm SEM. Data are pooled from four experiments (**a (mouse)**) or representative of two experiments (**d**). Exact P values are in Source Data.

[Source data](#)

Extended Data Fig. 3 $^{13}\text{C}^{15}\text{N}$ -glutamine tracing in mouse and human T and B cells *in vitro*.

Mouse T or B cells sorted from LN were cultured in medium containing $^{13}\text{C}_5^{15}\text{N}_2$ -labeled glutamine (Gln) for 72 h, with or without anti-CD3, anti-CD28 and IL-2 (for T cells), or anti-IgM and anti-CD40 antibodies (for B cells) stimulation. Isotope-labeled or unlabeled metabolites in cells or supernatants were measured by mass spectrometry. **a**, Scheme of metabolism of $^{13}\text{C}_5^{15}\text{N}_2$ -labeled Gln. **b**, Isotopomer analysis of isotope-labeled fraction of the indicated metabolites associated with Gln metabolism in T ($n = 3$) or B cells ($n = 4$) 72 h after stimulation. Inosine monophosphate (IMP), uridine monophosphate (UMP), uridine triphosphate (UTP), cytidine-5'-triphosphate (CTP), aspartate (Asp), isoleucine (Ile), proline (Pro), and tricarboxylic acid cycle (TCA-cycle) related metabolites- alpha-ketoglutarate (αKG), fumarate, malate, citrate, aconitate and isocitrate- are shown. The results are represented as the ratio of isotope-labeled-metabolite in total amount of each metabolite. **c**, Human peripheral blood-

derived B cells were stimulated with a mix of anti-IgM/IgG (BCR), CpG (TLR9 agonists), IFN- α A and IL-2 ($n = 4$) or a mix of IL-21, CD40L and IL-2 ($n = 3$) for 5 days in medium containing $^{13}\text{C}_5\text{ }^{15}\text{N}_2$ -labeled Gln. The level of isotope-labeled-GABA in cell lysate or media is shown, presented relative to non-stimulated cells ($n = 3$). **d**, Imaging mass spectrometry of GABA, glutamine (upper) and immunohistochemical analyses (lower) of human tonsil tissue sections. Scale bar, 1 mm. * $P < 0.05$, *** $P < 0.001$, **** $P < 0.0001$ (two-way ANOVA (b); unpaired two-tailed t-test (c)). Bars represent mean -SEM (b) or +SEM (c). n indicates biological (b) or technical replicates (c). The experiment is performed once (d). Exact P values are in Source Data.

[Source data](#)

[**Extended Data Fig. 4 Functional GABA_A receptors expressed on CD8⁺ T cells.**](#)

WT or *muMt*^{-/-} mice implanted with a pellet containing GABA or a placebo were injected with MC38 tumor cells as in Fig.3a. **a**, Representative immunohistochemistry of tumor sections from the indicated mice groups. **b**, The mean fluorescence intensity (MFI) of granzyme B and perforin in CD8⁺ TILs normalized to the mean WT + placebo value (WT, $n = 9$; *muMt*^{-/-}, $n = 7$; *muMt*^{-/-} +GABA, $n = 10$). **c**, Representative flow cytometry profile of CD8⁺ TILs cells stained as indicated and quantification of the frequencies of TNF- α ⁺ IL-2⁺ or MFI of IL-2 in CD8⁺ TILs, normalized to the mean WT + placebo value (WT, $n = 9$; *muMt*^{-/-}, $n = 9$; *muMt*^{-/-} +GABA, $n = 10$). **d**, The z -score of the transcripts from RNA sequencing of CD8⁺ TILs in each group, all upregulated genes predictively activated by TNF in CD8⁺ TILs of *muMt*^{-/-} + placebo compared to WT group (Wald test $P < 0.05$; two-sided) are selected and plotted for all groups ($n = 6$). **e**, MC38 cells were cultured with GABA or picrotoxin as indicated for 3 days. The number and viability of cells were measured ($n = 4$). **f**, Calcium measurements of mouse CD8⁺ T cells (upper) ($n = 30$) or human Jurkat cell line (lower) ($n = 60$) with and without picrotoxin treatment and stimulated with anti-CD3/CD28 dynabeads. **g**, The analysis of thapsigargin (TG)-induced calcium level of mouse CD8⁺ T cells (upper) ($n = 30$) or human Jurkat cell line (lower) ($n = 60$) with and without picrotoxin treatment in the calcium-free or sufficient medium. **h, i**, Purified naïve CD8⁺ T cells labeled with CellTrace violet dye were cultured for 3 days with or without GABA or muscimol and stimulated with anti-CD3 (1 $\mu\text{g}/\text{ml}$) and anti-CD28 (0.5 $\mu\text{g}/\text{ml}$). The concentration of IFN γ and TNF in supernatants was measured by cytometric bead array, presented as relative to control ($n = 12$ (control), 8 (0.1 μM), 3 (10 μM), 6 (200, 400, 800 μM), 7 (1 mM)) (**h**). Representative quantification analysis for the frequencies of proliferating cells, the MFI of CD25 or CD44 ($n = 3$)

(i). ns: not significant, $*P < 0.05$, $**P < 0.01$, $***P < 0.001$ (one-way ANOVA (**b, c**); two-tailed unpaired t-test (**e, h, i**). Bars represent mean \pm SEM. n indicates biological replicates (**a-d**) or technical replicates (**e-i**). Data are representative of two experiments (**a, e, f, g, i**) or pooled from two experiments (**b, c, h**). Exact P values are in Source Data.

[Source data](#)

Extended Data Fig. 5 Macrophage involvement in MC38 tumor model.

a, b, Macrophage depletion was performed by injection of liposomal clodronate on day -1 and day 6 after MC38 inoculation in WT or *muMt^{-/-}* mice. Tumor volume was monitored at the indicated time points ($n = 9$ (WT control liposomes), 6 (WT liposomal clodronate) or 7) (**a**), flow cytometric analysis was performed on 15 days after tumor inoculation (**b**). **c**, Principal component analysis of transcriptome profile of tumor associated macrophage (TAM) from WT + placebo, *muMt^{-/-}* + placebo or *muMt^{-/-}* + GABA group of mice at 7 days after MC38 inoculation ($n = 6$). **d, e**, Upstream regulator analysis performed by Ingenuity Pathway Analysis (IPA) and based on the differently expressed genes (DEGs) shown for TAM of *muMt^{-/-}* + placebo group compared to WT + placebo group (**d**) or *muMt^{-/-}* + GABA group compared to *muMt^{-/-}* + placebo group (Wald test $P < 0.05$; two-sided) (**e**), $-\log_{10}$ (P value; right-tailed Fisher's Exact Test) and activation z -score of each predicated upstream regulators are plotted (red, transcripts predicted to be activated; blue, transcripts predicted to be inhibited) ($n = 6$). **f**, Oxidative phosphorylation (OXPHOS) pathway related DEGs between WT and *muMt^{-/-}* + placebo group (left), and the transcript level of representative genes (right) ($n = 6$). **g**, Upstream regulator analysis of DEGs in TAM from picrotoxin treatment and their control group 7 days after MC38 tumor inoculation ($n = 6$ from 4 biologically independent animals). $*P < 0.05$, $**P < 0.01$, $***P < 0.0001$ (two-way ANOVA (**a**); one-way ANOVA (**f**)). Bars represent mean \pm SEM. n indicates biological replicates (**a-f**). Data are representative of two experiments (**a**). Exact P values are in Source Data.

[Source data](#)

Extended Data Fig. 6 GABA increases the proliferation, survival and bioenergetics of macrophages differentiated *in vitro*.

a, Scheme of mouse bone marrow (BM)-derived monocytes (Mus-mo), total BM cell or human blood-derived monocytes (Hu-mo) differentiation in the presence of M-CSF without (M-0) or with GABA (GABA-M-0). **b**, The cell number and the ratio of FR β^+ cells in mouse ($n = 2$ (M-0 (middle), 4 (GABA-M-0 (left) or 3) or human monocytes-

derived M-0 ($n = 5$) with or without GABA treatment. **c**, Quantification of the frequencies of propidium iodide (PI)⁺ or ⁻, annexin V⁺ ($n = 4$) and FR β^+ cells ($n = 3$) by flow cytometry in mouse BM-derived M-0 cells conditioned with or without GABA. **d**, Transcripts related to cell cycle and folate metabolism obtained from gene chip analysis of M-0 and GABA-M-0 and represented relative to M-0 ($n = 2$). **e**, Real-time oxygen consumption rate (OCR), maximal respiratory capacity (MRC), and extracellular acidification rate (ECAR) as assessed by Seahorse assay. * $P < 0.05$, ** $P < 0.01$, *** $P < 0.001$, **** $P < 0.0001$ (two-tailed unpaired t-test). Bars represent mean \pm SEM. n indicates biological (**d**) or technical replicates. Data are representative of three experiments (**c, e**). Exact P values are in Source Data. The image of immune cell (Extended Figures) and mouse (Fig. 1a) was created with BioRender.com.

[Source data](#)

[**Extended Data Fig. 7 GABA enhances the anti-inflammatory phenotype of IL-10 polarized macrophages partially via GABA_A receptor signaling.**](#)

a, Scheme of bone marrow cell differentiation in the presence of M-CSF without or with GABA for 6 days, followed by 6 h polarization with IL-10 (M-IL-10 and GABA-M-IL-10). qPCR or gene chip analysis was performed for GABA conditioned macrophages with IL-10 polarization (GABA-M-IL-10) and its control group (M-IL-10) ($n = 3$). **b, c**, *Iil10* mRNA level measured by q-PCR in monocytes ($n = 3$) (**b**) or BM ($n = 4$) (**c**)-derived M-IL-10 and GABA-M-IL-10. Results are represented relative to control group. **d**, Oxygen consumption rate (OCR) of M-IL-10 and GABA-M-IL-10 measured in real time by extracellular flux analyzer. Oligomycin (Oligo), FCCP and rotenone/antimycin A (Rot/AntiA) were added at the indicated time points ($n = 2$). **e, f**, M-IL-10 and GABA-M-IL-10 conditioned macrophages were co-cultured with CD8⁺ T cells stimulated for 72 h with anti-CD3 and anti-CD28 in the presence or absence of anti-IL-10 blocking antibodies (Abs). The percentage of granzyme B⁺ cells in CD8⁺ T cells analyzed by flow cytometry (**e**) and the concentration of IFN γ and TNF in supernatant measured by Cytometric Bead Array (CBA) (**f**) ($n = 6$ (M-IL-10 + CD8⁺), 5 (GABA-M-IL-10 + CD8⁺), 3 (M-IL-10 + CD8⁺ + IL-10 blocking Abs) or 4 (GABA-M-IL-10 + CD8⁺ + IL-10 blocking Abs)). **g**, Tumor volume ($n = 6$) or weight ($n = 4$) of WT mice co-injected with MC38 cells together with in vitro generated M-IL-10 or GABA-M-IL10. **h**, The DEGs representing cytokines and their receptors, MHC molecules and co-factors and OXPHOS between GABA and control (Ctr) group, obtained from gene chip analyses ($n = 3$) and shown for all groups as heatmap. Those genes, which are not differentially expressed between GABA + picrotoxin and Ctr group (two-tailed unpaired t-test; $P > 0.05$), are represented as red color (the transcript level is transformed to z-score). * $P < 0.05$, ** $P < 0.01$, *** $P < 0.001$, **** $P < 0.0001$

(two-tailed unpaired t-test (b, c); one-way ANOVA (f, g (right)); two-way ANOVA (g (left)). Bars represent mean \pm SEM. n indicates biological (g, h) or technical replicates (b-f). Data are pooled from two experiments (c) or representative of two experiments (d-f). Exact P values are in Source Data.

[Source data](#)

Extended Data Fig. 8 Macrophages conditioned by activated B cells suppress the cytotoxic function of CD8⁺ T cells.

a, Scheme of macrophage conditioning with activated B cells followed by polarization with IL-10 (M-IL-10 and B cells-M-IL-10) and co-culture with CD8⁺ T cells stimulated with anti-CD3 and anti-CD28 for 72 h in the presence or absence of IL-10 blocking antibodies (Abs). **b, c**, Representative flow cytometry profiles of CD8⁺ T cells stained for granzyme B and CD25 (b), and quantification of the granzyme B⁺ CD25⁺ cells in CD8⁺ gates (upper graph) or the concentration of IFN γ and TNF in the culture supernatants (lower graphs) ($n = 3$ (M-IL-10 + CD8⁺ +/- IL-10 blocking Abs) or 6 (B-M-IL-10 + CD8⁺ +/- IL-10 blocking Abs)) (c) are shown. ns: not significant, * $P < 0.05$, ** $P < 0.01$, *** $P < 0.001$ (one-way ANOVA). Bars represent mean \pm SEM. Circles on graphs indicate an individual sample. n indicates technical replicates. Data are representative of two experiments. Exact P values are in Source Data.

[Source data](#)

Extended Data Fig. 9 Characterization of precursor cells and immune cell subsets in peripheral organs of *Mb1*^{cre/+}; *Gad1*^{f/f} mice.

a–c, The frequencies and number of the indicated precursor cells ($n = 3$) (a, b) and B cell populations ($n = 4$) (c) in bone marrow from *Mb1*^{cre/+}; *Gad1*^{f/+} or *Mb1*^{cre/+}; *Gad1*^{f/f} mice analyzed by flow cytometry. **d–i**, The frequencies and numbers of the indicated immune cell subsets in peritoneal cavity (PC) ($n = 3$) (d), lymph nodes ($n = 8$) (e), spleen ($n = 3$) (f), Peyer's patch (PP) ($n = 3$) (g), the small intestine lamina propria (SILP) ($n = 3$) (h) and the small intestine epithelial cells (SIE) ($n = 3$) (i) from *Mb1*^{cre/+}; *Gad1*^{f/+} or *Mb1*^{cre/+}; *Gad1*^{f/f} mice analyzed by flow cytometry. ns: not significant (two-tailed unpaired t-test). Bars represent mean \pm SEM. n indicates biological replicates. Data are pooled from two experiments (c, e). Exact P values are in Source Data.

[Source data](#)

Extended Data Fig. 10 Enhanced effector properties of CD8⁺ T cells infiltrating the tumors in *Mb1*^{cre/+}; *Gad1*^{f/f} mice and visualization of GABA in human renal cell cancer infiltrated with B cells and IgA⁺ plasma cells.

a, Intracellular GABA quantitation measured by mass spectrometry in FACS purified T or B cells from the LN of naïve *Mb1*^{cre/+}; *Gad1*^{f/f} or *Mb1*^{cre/+}; *Gad1*^{f/f} mice ($n = 6$ from 3 biologically independent mice). **b**, The numbers of CD8⁺ T cells or frequencies of CD8⁺ T cells in lymphocyte gate and of granzyme B⁺perforin⁺, IFN γ ⁺TNF α ⁺ and TNF α ⁺IL-2⁺ in CD8⁺ T cell gate cells isolated from tumors of *Mb1*^{cre/+}; *Gad1*^{f/f} ($n = 4$) or *Mb1*^{cre/+}; *Gad1*^{f/f} ($n = 5$) mice. **c**, Imaging mass spectrometry of GABA and immunohistochemical analyses of human renal cell cancer tissue sections. Scale bar, 1 mm. ns: not significant, * $P < 0.05$, ** $P < 0.01$, *** $P < 0.0001$ (two-tailed unpaired t-test). Bars represent mean \pm SEM. n indicates biological replicates (**b**). The experiment is performed once (**c**). Exact P values are in Source Data.

[Source data](#)

Supplementary information

[Supplementary Figures](#)

This file contains Supplementary Fig. 1 (Sorting strategies for isolation of immune cells in the peripheral organs) and Fig. 2 (Sorting strategies for isolation of immune cells in tumour tissues).

[Reporting Summary](#)

[Peer Review File](#)

[Supplementary Tables](#)

This file contains Supplementary Table 1 (The datasets of M-0 cells analysed by gene chip assay) and Table 2 (The datasets of M-IL-10 cells analysed by gene chip assay).

Source data

[Source Data Fig. 1](#)

[Source Data Fig. 2](#)

[Source Data Fig. 3](#)

[Source Data Fig. 4](#)

[Source Data Extended Data Fig. 1](#)

[Source Data Extended Data Fig. 2](#)

[Source Data Extended Data Fig. 3](#)

[Source Data Extended Data Fig. 4](#)

[Source Data Extended Data Fig. 5](#)

[Source Data Extended Data Fig. 6](#)

[Source Data Extended Data Fig. 7](#)

[Source Data Extended Data Fig. 8](#)

[Source Data Extended Data Fig. 9](#)

[Source Data Extended Data Fig. 10](#)

Rights and permissions

Open Access This article is licensed under a Creative Commons Attribution 4.0 International License, which permits use, sharing, adaptation, distribution and reproduction in any medium or format, as long as you give appropriate credit to the original author(s) and the source, provide a link to the Creative Commons license, and indicate if changes were made. The images or other third party material in this article are included in the article's Creative Commons license, unless indicated otherwise in a credit line to the material. If material is not included in the article's Creative Commons license and your intended use is not permitted by statutory regulation or exceeds the permitted use, you will need to obtain permission directly from the copyright holder. To view a copy of this license, visit <http://creativecommons.org/licenses/by/4.0/>.

[Reprints and Permissions](#)

About this article

Cite this article

Zhang, B., Vogelzang, A., Miyajima, M. *et al.* B cell-derived GABA elicits IL-10⁺ macrophages to limit anti-tumour immunity. *Nature* **599**, 471–476 (2021). <https://doi.org/10.1038/s41586-021-04082-1>

- Received: 01 April 2021
- Accepted: 28 September 2021
- Published: 03 November 2021
- Issue Date: 18 November 2021
- DOI: <https://doi.org/10.1038/s41586-021-04082-1>

Share this article

Anyone you share the following link with will be able to read this content:

[Get shareable link](#)

Sorry, a shareable link is not currently available for this article.

[Copy to clipboard](#)

Provided by the Springer Nature SharedIt content-sharing initiative

Further reading

- [**GABA molecules made by B cells can dampen antitumour responses**](#)
 - Daniel L. Kaufman

Nature (2021)

[**GABA molecules made by B cells can dampen antitumour responses**](#)

- Daniel L. Kaufman

News & Views 03 Nov 2021

This article was downloaded by **calibre** from <https://www.nature.com/articles/s41586-021-04082-1>

| [Section menu](#) | [Main menu](#) |

- Article
- Open Access
- [Published: 03 November 2021](#)

Cross-HLA targeting of intracellular oncoproteins with peptide-centric CARs

- [Mark Yarmarkovich](#)¹,
- [Quinlen F. Marshall](#) [ORCID: orcid.org/0000-0002-4736-9716](#)¹,
- [John M. Warrington](#)¹,
- [Rasika Premaratne](#)²,
- [Alvin Farrel](#)^{1,3},
- [David Groff](#)¹,
- [Wei Li](#)⁴,
- [Moreno di Marco](#)⁵,
- [Erin Runbeck](#)¹,
- [Hau Truong](#)¹,
- [Jugmohit S. Toor](#)⁶,
- [Sarvind Tripathi](#) [ORCID: orcid.org/0000-0002-6959-0577](#)⁶,
- [Son Nguyen](#) [ORCID: orcid.org/0000-0002-0475-5158](#)⁷,
- [Helena Shen](#) [ORCID: orcid.org/0000-0002-0500-441X](#)¹,
- [Tiffany Noel](#)¹,
- [Nicole L. Church](#)²,
- [Amber Weiner](#)¹,
- [Nathan Kendsersky](#) [ORCID: orcid.org/0000-0003-0132-8748](#)¹,
- [Dan Martinez](#)⁸,
- [Rebecca Weisberg](#)¹,
- [Molly Christie](#)¹,
- [Laurence Eisenlohr](#)⁸,
- [Kristopher R. Bosse](#)^{1,9},
- [Dimiter S. Dimitrov](#) [ORCID: orcid.org/0000-0002-2258-1024](#)⁴,
- [Stefan Stevanovic](#)⁵,
- [Nikolaos G. Sgourakis](#)¹,
- [Ben R. Kiefel](#)² &
- [John M. Maris](#) [ORCID: orcid.org/0000-0002-8088-7929](#)^{1,9}

Nature volume 599, pages 477–484 (2021)

- 19k Accesses
- 227 Altmetric
- [Metrics details](#)

Subjects

- [Cancer immunotherapy](#)
- [MHC class I](#)

Abstract

The majority of oncogenic drivers are intracellular proteins, thus constraining their immunotherapeutic targeting to mutated peptides (neoantigens) presented by individual human leukocyte antigen (HLA) allotypes¹. However, most cancers have a modest mutational burden that is insufficient to generate responses using neoantigen-based therapies^{2,3}. Neuroblastoma is a paediatric cancer that harbours few mutations and is instead driven by epigenetically deregulated transcriptional networks⁴. Here we show that the neuroblastoma immunopeptidome is enriched with peptides derived from proteins that are essential for tumourigenesis and focus on targeting the unmutated peptide QYNPIRTTF, discovered on HLA-A*24:02, which is derived from the neuroblastoma dependency gene and master transcriptional regulator *PHOX2B*. To target QYNPIRTTF, we developed peptide-centric chimeric antigen receptors (CARs) using a counter-panning strategy with predicted potentially cross-reactive peptides. We further hypothesized that peptide-centric CARs could recognize peptides on additional HLA allotypes when presented in a similar manner. Informed by computational modelling, we showed that PHOX2B peptide-centric CARs also recognize QYNPIRTTF presented by HLA-A*23:01 and the highly divergent HLA-B*14:02. Finally, we demonstrated potent and specific killing of neuroblastoma cells expressing these HLAs in vitro and complete tumour regression in mice. These data suggest that peptide-centric CARs have the potential to vastly expand the pool of immunotherapeutic targets to include non-immunogenic intracellular oncoproteins and widen the population of patients who would benefit from such therapy by breaking conventional HLA restriction.

[Download PDF](#)

Main

The curative potential of CAR T cell-based cancer immunotherapies has been established in leukaemias, but their application in solid tumours has been limited by a paucity of known tumour-specific membrane proteins⁵. Although membrane proteins represent up to a quarter of the proteome, only a fraction of these are expressed specifically on tumour cells and not on normal tissues, and a smaller proportion are essential to tumour homeostasis⁶. Rather, most cancer driver proteins reside in the cytoplasm or nucleus of the cell, where they are accessible to the immune system only through presentation of peptides on the major histocompatibility complex (MHC).

MHC class I proteins, encoded by the highly polymorphic human leukocyte antigen (HLA)-A, -B and -C genes, present a snapshot of the intracellular proteome on the cell surface (immunopeptidome) where T cells surveil the peptide–MHC complexes (pMHC) for antigens derived from foreign pathogens. T cell recognition of mutation-derived pMHC neoantigens as non-self is the basis of curative responses achieved through immune checkpoint blockade and complete remissions using adoptive transfer of tumour-infiltrating lymphocytes (TILs)⁷. Nonetheless, only about 5% of these neoantigens are predicted to bind a given HLA allotype⁸, and just 1.6% of neoantigens are reported to be immunogenic⁹. Subclonal mutations and downregulation of mutated non-essential genes further constrain the pool of therapeutically relevant neoantigens, necessitating a mutational threshold for effective neoantigen-based therapies that is not surpassed in most cancers⁹. Tumour cells also present a wide range of unmutated self-peptides on MHC¹⁰ molecules, but these are largely immunogenically silent owing to negative thymic selection of T cells. We hypothesized that a subset of the immunopeptidome consists of tumour-specific peptides derived from essential oncoproteins and that these can be targeted using synthetic peptide-centric CARs (PC-CARs).

Peptides presented in the MHC groove make up only a small fraction of the extracellular pMHC molecular surface. The typical 8–14mer peptide presented on MHC class I comprises only around 2–3% of the amino acids in the pMHC complex and is spatially confined within the adjacent α -helices of the MHC groove, thus posing major challenges for engineering peptide-specific single-chain antibody variable fragment (scFv) binders¹¹. Furthermore, cross-reactivity of engineered receptors with peptides of biophysically similar molecular surfaces presented in normal tissues have resulted in significant toxicity and death^{12,13}.

Neuroblastoma is a childhood cancer derived from tissue of the developing sympathetic nervous system and is often lethal despite intensive cytotoxic therapy¹⁴. These tumours are low in mutational burden¹⁵ and MHC expression¹⁶, making neuroblastoma both a challenging tumour to target with MHC-based immunotherapies and an ideal model for addressing the major problems currently hindering the wider advancement of cancer immunotherapies. As a tumour derived from neural crest

progenitor cells, neuroblastomas express a set of core-regulatory circuit (CRC) transcription factors involved in maintaining cell fate, metabolism, migration, epigenetic states, growth and proliferation⁴. These genes are epigenetically silenced upon terminal differentiation of normal neural tissues, but these developmental pathways are aberrantly hyperactivated in neuroblastoma. Here we present the discovery of recurring lineage-restricted oncoproteins presented on MHC, focusing on immunotherapeutic targeting of the neuroblastoma CRC master regulator PHOX2B using PC-CARs.

Identification of tumour-specific antigens

First, we surveyed the landscape of peptides accessible to T cells by performing MHC capture, peptide elution and liquid chromatography with tandem mass spectrometry¹⁷ (immunopeptidomics) on eight neuroblastoma cell-derived xenografts (CDX) and patient-derived xenografts (PDX) showing a wide range of MHC expression and also encompassing the array of rare recurring mutations found in high-risk neuroblastoma^{18,19} (Fig. 1a, Extended Data Table 1a). We identified a total of 7,608 peptides from 8 tumours (1% false discovery rate (FDR); Supplementary Table 1), finding none of the 4,105 potential 8–14mer neoantigens imputed from tumour mutational data in the immunopeptidome, consistent with expected rates of neoantigen presentation and limited detection using ligandomics in low-mutational tumours²⁰. We first filtered the 7,608 peptides to select HLA binders with sufficient affinity to act as T cell epitopes using a predicted peptide–MHC (pMHC) half-maximal inhibitory concentration (IC_{50}) threshold of 500 nM, yielding 2,286 predicted strong binders. We then filtered for peptides derived from differentially expressed parent genes as determined from RNA-sequencing (RNA-seq) data from 153 neuroblastoma tumours compared with 1,641 normal tissues (from the TARGET²¹ and GTEx¹⁷ databases, respectively), resulting in 61 peptides derived from genes with mRNA expression one log-fold higher in tumour for each normal tissue ($P < 0.01$). Finally, we filtered the remaining tumour peptides against a database of MHC peptides empirically characterized on 190 normal tissues²², removing any peptide with a parent gene that is represented in the normal tissue immunopeptidome. While this last step does not absolutely exclude potential presentation of a peptide in normal tissues, it allowed us to narrow our list to 13 peptides derived from 9 unique genes expressed in neuroblastoma that have not been previously detected in any normal tissue.

Fig. 1: An antigen discovery and prioritization process identifies PHOX2B as a target for immunotherapy.

 **figure1**

a, Summary of tumour-antigen discovery and CAR-engineering workflow: (1) integrated genomics and immunopeptidomics process; (2) target validation; (3) CAR engineering; and (4) cross-HLA tumour killing. **b**, Computational filtering of 9,117 peptide instances identified by immunopeptidomics in primary tumours (1% FDR) resulted in 56 neuroblastoma-specific peptides (33 unique peptides) derived from 29 distinct proteins. **c**, Primary neuroblastoma tumour immunopeptidome compared with 190 normal tissues. Each point on the *x*-axis represents one of 5,832 unique peptides identified in primary tumours, with the proportion of neuroblastoma tumours presenting a given peptide annotated above axis in dark blue and the proportion of normal tissue expressing the identical peptide below the axis in light blue. The green horizontal bar indicates 1,492 peptides not previously observed in the normal tissue immunopeptidome. Parent genes from neuroblastoma-specific peptides resulted in the top two GO enrichment terms: noradrenergic neuron differentiation and sympathetic nervous system development. The arrow denotes 351 recurring peptides presented in neuroblastoma that were not previously detected in normal tissues. **d**, Five antigens differentially expressed in PDX and primary tumours and further prioritized for analysis, HLA allele frequency, relative peptide abundance (percentile rank annotated below pMHC), predicted pMHC-binding affinity, and relevance to neuroblastoma tumourigenesis. **e**, *PHOX2B* expression in RNA-seq data from 153 neuroblastoma tumours versus 1,641 normal tissues in GTEx. *PHOX2B* expression is restricted to tumours, compared with the immunotherapy target HER2 and the neuroblastoma chemotherapy target TOP1 (note differences in the *y*-axis scales). FPKM, fragments per kilobase of transcript per million mapped reads. **f**, Crystal

structure of PHOX2B 9mer QYNPIRTTF (red) refolded with HLA-A*24:02 (grey). **g**, Chromatin immunoprecipitation followed by DNA sequencing (ChIP-seq) of neuroblastoma tissue shows binding of all CRC proteins at the *PHOX2B* locus and association with a H3K27Ac super-enhancer mark. **h**, RNA-seq of fetal tissue shows that *PHOX2B* is expressed in early development and downregulated before birth across seven tissues. Created with BioRender.com.

We then performed immunopeptidomics on eight high-risk diagnostic neuroblastoma primary tumours, focusing on HLA-A*02:01 and HLA-A*24:02 allotypes (Extended Data Table 1a, Supplementary Table 1). Using the same filtering as described for xenograft tumours, we identified 56 peptides (33 unique peptides derived from 29 unique proteins) with strong HLA-binding affinity derived from differentially expressed genes in neuroblastoma and not previously detected in the benign tissue ligandome (Fig. 1b, Extended Data Fig. 1). We confirmed the presence of 7 of the 13 peptides from the xenografts in primary tumours, suggesting that CDX and PDX tumours can be a predictive model for primary tumour ligandomes. Notably, the most enriched gene ontologies of the peptide parent genes not previously observed in the normal-tissue ligandomic dataset were: noradrenergic neuron differentiation ($P = 3.42 \times 10^{-4}$, FDR = 0.0389) and sympathetic nervous system development ($P = 2.95 \times 10^{-5}$, FDR = 0.00665; Fig. 1c, green bar). These findings highlight the distinctiveness of the neuroblastoma ligandome and suggest that MHC-presented peptides are enriched for those derived from aberrantly expressed lineage-restricted genes.

To select those peptides with the highest potential as putative immunotherapeutic targets, we prioritized peptides on the basis of pMHC binding affinity, HLA allele frequency, degree of differential expression of parent genes, relative abundance on MHC as compared to other peptides, recurrence across multiple neuroblastoma tumours and relevance to neuroblastoma biology based on the published literature^{23,24,25}. One peptide each from CHRNA3, GFRA2, HMX1, IGFBPL1, PHOX2B and TH were selected for preclinical development (Fig. 1d, e; Supplementary Table 1). The presence of these peptides in tumours was validated by performing liquid chromatography–mass spectrometry (LC–MS/MS) on synthetic peptides (Extended Data Fig. 2), yielding complete concordance across b and y ions. In addition, we validated the peptide binding to predicted HLA alleles by refolding the pMHC complex and solving the crystal structure of one PHOX2B peptide–HLA-A*24:02 (PDB ID 7MJA) and three IGFBPL1 peptide–HLA-A*02:01 (PDB IDs 7MJ6, 7MJ67 and 7MJ8) protein complexes (Fig. 1f, Extended Data Fig. 3b). Of note, we detected three unique IGFBPL1 peptides as a 9mer, 11mer and 12mer (all with the same core 9mer amino acids) with distinct thermal properties (Extended Data Fig. 3), underscoring the existence of multiple peptides with distinct conformations arising

from the same region of a protein and presenting multiple opportunities for therapeutic targeting²⁶.

We then inferred the ability of a tumour to evade the immune response via downregulation of target genes by examining the binding of neuroblastoma CRC transcription factors (MYCN, ASCL1, HAND2, ISL1, PHOX2B, GATA3 and TBX2; Extended Data Fig. 4a) to the parent gene locus of the prioritized antigens⁴. We found that all six CRC proteins bind regulatory elements at each parent gene locus within H3K27Ac super-enhancer elements (Fig. 1g, Extended Data Fig. 4b), suggesting that transcriptional redundancy and dependency should mitigate the risk of antigen loss in response to immunotherapy owing to downregulation of the parent gene. In addition, we found peptides from each of the six CRC proteins represented in the neuroblastomaimmunopeptidome (Extended Data Table 1b). Indeed, the most significantly enriched gene groups in the immunopeptidome are nucleic acid-binding proteins ($P = 9.5 \times 10^{-17}$; Extended Data Fig. 5c). Finally, we interrogated the dynamics of gene expression during development using temporal transcriptomic data²⁷. Consistent with its function in orchestrating neural crest progenitor development²⁸, PHOX2B is expressed exclusively during fetal development and is completely silenced in normal tissues before birth (Fig. 1h), as are IGFBPL1, TH and CHRNA3 (Extended Data Fig. 6). PHOX2B is a key CRC protein that is among the most specifically expressed genes in neuroblastoma²⁹. PHOX2B expression is not detected in normal tissue, unlike many solid tumour immunotherapy targets, including HER2, and chemotherapy targets in neuroblastoma camptothecin, including TOP1, each of which exhibit significant normal tissue expression (Fig. 1e). PHOX2B expression is routinely used in neuroblastoma diagnostic assays³⁰, is one of two highly penetrant neuroblastoma susceptibility genes³¹, and is the third most significant dependency in neuroblastoma, as reported in DepMap³². Together, these data suggest that PHOX2B is a highly specific tumour antigen in neuroblastoma and an ideal candidate for therapeutic targeting.

Before developing an immunotherapeutic construct targeting the PHOX2B peptide, we validated that low MHC expression in neuroblastoma¹⁶ did not prohibit T cell engagement and activation using an influenza antigen model (experimental details in Extended Data Fig. 7).

PC-CAR T cell engineering for PHOX2B

Owing to the low immunogenicity of self-antigens, we pursued development of scFv-based CARs rather than engineered T cell receptors (TCRs) for PHOX2B after no high affinity TCRs were identified in multiple screens (Extended Data Fig. 8). We reasoned that immunogenicity could be induced to otherwise immunogenically inert pMHCs

using synthetic, peptide-centric receptors. Our first generation of pMHC-directed CARs showed significant cross-reactivity to the MHC, which we were able to abrogate using saturation mutagenesis techniques that also decreased binding affinity (Extended Data Figs. 9–11).

To screen for PHOX2B peptide-specific clones, we next adapted the retained display³³ (ReD) system, a protein-display platform that enables the flow-cytometric selection of pMHC-binding scFvs in permeabilized bacterial cells, with a scFv library containing more than 10^{11} variants. Clones that demonstrated apparent selectivity by flow cytometry were further tested against a panel of 95 unrelated peptides and four highly similar peptides presented on the same HLA allotype to select for clones with the highest selectivity (for example, selective clone 10LH, shown in Fig. 2a), resulting in 25 scFv binders for screening in CAR T constructs. To address cross-reactivity with pMHC in normal tissues, we developed an algorithm to predict potential selective cross-reactive antigen presentation (sCRAP; <https://marisshiny.research.chop.edu/sCRAP/>) on the same HLA allotype (Extended Data Fig. 12), enabling pre-emptive selectivity filtering in early stages of scFv screening without the need of a prior receptor or alanine scan³⁴. We benchmarked the sCRAP algorithm by testing its ability to predict the cross-reactivity of the MAGE-A3 peptide presented on HLA-A*01:01, whose targeting using an affinity-enhanced TCR previously resulted in the fatal cross-reaction with another peptide derived from the TITIN protein presented on HLA-A*01:01 in myocardial tissues¹². We predicted the cross-reactivity of MAGE-A3 with the TITIN peptide as the 4th-ranked prediction out of 1,143,861 potential self-peptides presented in heart tissue (Extended Data Fig. 13).

Fig. 2: Engineering pMHC-specific CAR receptors.

 **figure2**

a, Ranked binding affinity of 10LH scFv to PHOX2B (blue) and a panel of 95 peptides presented on HLA-A*24:02 peptides (orange) demonstrate high target binding and negligible binding to HLA-A*24:02 pMHCs. **b**, Cross-reactivity algorithm identifies CAR constructs with significant off-target binding and informs prioritization of highly selective receptors (selective receptors marked with arrow). Peptide score represents the predicted cross-reactivity based on the amino acid sequences of normal-tissue peptides; overall score is calculated on the basis of peptide score, binding affinity and normal tissue expression; T, peptides reported in the normal tissue immunopeptidome; F, peptides absent in normal immunopeptidome. ND, not determined. **c**, Example counterstaining of top CAR clones with target (x-axis) and off-target (y-axis) peptides on HLA-A*24:02 reveals selective target binding in 10LH and 302LH constructs. **d**, Left, flow cytometry plot of predicted cross-reactive peptides compared with PHOX2B shows cross-reactive binders ABCA8 and MYO7B. Right, flow mean fluorescence intensity (MFI) used to calculate degree of binding relative to PHOX2B in table. **e**, Functional screening of ABCA8 and MYO7B shows CAR killing through ABCA8 only at a supraphysiological concentration of 50 μ M versus through PHOX2B at 0.1 μ M. ABCA8 and MYO7B were not detected in the normal tissue immunopeptidome, and none of the peptides predicted by sCRAP that were detected in the normal immunopeptidome (FDFTI, SLC23A2 and TNS4) show

binding to 10LH. The experiment was performed once on the entire panel of CAR constructs and repeated for 10LH and 302LH on an expanded panel of peptides. **f**, Representative BLItz plot at 200 nM PHOX2B pMHC shows fast on rate for 10LH and 302LH and exceptionally slow off-rate for 10LH ($k_d = 7.6 \times 10^{-4} \text{ s}^{-1}$). **g**, Alanine scan of QYNPIRTTF reveals that mutations in five residues (N3A, I5A, R6A, T7A and T8A) result in significant abrogation of binding to PC-CAR 10LH ($n = 2$; data are mean \pm s.d.). **h**, PHOX2B–HLA-A*24:02 crystal structure paired with alanine scan of 10LH enables mapping of peptide–receptor interface, revealing spatial conformation of five receptor contact residues (left, top view; right, side view of pMHC complex). Created with BioRender.com.

We then screened our panel of PHOX2B-directed CARs against the top seven pMHC predicted by sCRAP (Fig. 2b), allowing us to eliminate cross-reactive CARs and prioritize those with the highest degree of target selectivity (Fig. 2c). Of 25 CARs screened, we selected clone 10LH—which had the highest-specificity profile, showing only two peptides with more than 10% relative binding to 10LH as compared to PHOX2B—for further development (Fig. 2d).

To test the functional significance of the binding to potential off-target pMHCs predicted by sCRAP, we pulsed HLA-matched PHOX2B⁺ SW620 colon adenocarcinoma cells with the PHOX2B peptide and potential cross-reactive peptides across a range of concentrations. Pulsing with the PHOX2B peptide resulted in complete cytotoxicity when co-cultured with 10LH at the lowest tested concentration of 0.1 μM . The 10LH CAR T cells did not induce cytotoxicity with the most cross-reactive predicted peptide ABCA8 at 10 μM , and only induced killing at the supraphysiological concentration of 50 μM . The second most cross-reactive peptide with 10LH (MYO7B) showed no CAR cytotoxicity at concentrations of up to 50 μM (Fig. 2e). Neither ABCA8 nor MYO7B has been detected in normal tissue immunopeptidome¹⁰, and none of the peptides previously detected in the normal tissue immunopeptidome display any cross-reactivity with PC-CAR 10LH (Fig. 2d). These screens demonstrate the utility of sCRAP for pre-emptively identifying off-target effects, efficiently screening their functional consequences and identifying binders with highly selective binding to tumour targets.

The lead scFv 10LH bound PHOX2B pMHC with a dissociation constant K_D of 13 nM and exceptionally slow off rate (k_d) of $7.6 \times 10^{-4} \text{ s}^{-1}$ (Fig. 2f). We next performed an alanine scan for the 10LH CAR, characterizing binding to PHOX2B pMHC with amino acid substitutions at each non-anchor position of the peptide³⁴. The alanine scan revealed significant interactions of the PC-CAR receptor with five out of seven non-anchor residues of the PHOX2B peptide, including key residues protruding from the MHC cleft (interaction interface of 10LH with PHOX2B pMHC mapped on

crystal structures in Fig. 2h), highlighting the superior selectivity of PC-CARs compared with the three or four residues that typically interact with the TCR³⁵.

PC-CAR T cells break HLA restriction

Given the prerequisite of antigen processing and presentation necessary for detection of a given MHC peptide by immunopeptidomics, we hypothesized that identical peptides could be presented on additional HLA allotypes capable of binding a peptide's anchor residues, and that some of these peptides could be presented in a similar enough conformation to be recognized by peptide-centric scFv binders (Extended Data Fig. 14a). We tested this hypothesis using PHOX2B-specific CARs engineered to bind the PHOX2B 9mer presented on HLA-A*24:02 in a peptide-centric fashion. We used our population-scale antigen presentation tool ShinyNAP⁸ to identify additional HLA allotypes that could present the same PHOX2B peptide, identifying 8 additional HLAs predicted to bind the PHOX2B 9mer (Extended Data Fig. 14b). We then used our pMHC structural modelling software, RosettaMHC³⁶, to model the 3D conformation and binding free energy of peptides presented by additional HLA alleles, identifying HLA-A*23:01 and HLA-B*14:02 as top-scoring candidates for recognition by PC-CARs of the PHOX2B peptide originally discovered on HLA-A*24:02 (Fig. 3a, b). After validating binding of QYNPIRTTF to these alternate allotypes (Extended Data Fig. 14c), we measured the ability of 10LH to recognize these pMHCs, finding that in addition to HLA-A*24:02, 10LH binds with high affinity to the PHOX2B 9mer QYNPIRTTF presented by HLA-A*23:01 and HLA-B*14:02 (Fig. 3c). We also found that although QYNPIRTTF binds to HLA-C*07:02, 10LH exhibited 17.4-fold lower binding to HLA-C*07:02, probably owing to a distinct pMHC molecular surface in which the sidechains of the MHC α 2-helix (R151 and Q155) protrude by 15Å at the position axially aligned with the key 10LH binding residues of QYNPIRTTF (I5 and R6) (Fig. 3b). To demonstrate functionally relevant recognition of our prediction of PHOX2B presentation on HLA-A*23:01, we pulsed the HLA-A*23:01 PHOX2B⁻ melanoma cell line WM873 with the QYNPIRTTF peptide, showing induction of antigen-specific killing in peptide-pulsed cells and no cytotoxicity in cells pulsed with mismatched peptide (Extended Data Fig. 14d). HLA-A*23:01 is the most common non-A2 allele in people with African ancestry, highlighting the potential of PC-CARs to expand clinical application to underserved populations. Finally, we reanalysed our immunopeptidomics data, performing a matched peptide analysis to identify lower-confidence potential peptide matches to QYNPIRTTF in additional samples in which the peak was not fragmented. We identified *m/z* matches within 1 min of retention time across 6 out of 8 PDX lines and 7 out of 8 patient samples, each expressing one of the HLA alleles predicted by our analyses, suggesting that this peptide is ubiquitously expressed in neuroblastoma (Extended Data Fig. 14f). These findings warrant additional investigation into cross-

HLA-targeting tumour self-antigens as well as neoantigens and demonstrate the potential to significantly expand the eligible patient population receiving peptide-centric scFv-based immunotherapies.

Fig. 3: Structural basis of CARs binding to PHOX2B peptide presented on multiple HLAs.



a, PHOX2B–HLA-A*24:02 crystal structure and models of PHOX2B in complex with HLA-A*23:01, HLA-B*14:02 and HLA-C*07:02. **b**, The charged and polar R151, Q155 and R69 residues of HLA-C*07:02 align with key 10LH interaction residues I5, R6 and I7 (MHC residues in blue and PHOX2B–10LH interaction residues in red). R151, Q155 and R69 create steric and charged hindrance of key peptide-binding residues. **c**, Staining of the PHOX2B PC-CAR 10LH reveals strong binding to HLA-A*24:02, HLA-A*23:01 and HLA-B*14:02, but not to HLA-C*07:02. CD19, CD19-directed CAR; 10LH, PHOX2B PC-CAR; UT, untransduced T cells. Created with BioRender.com.

PC-CAR T cells selectively eliminate tumours

We next tested the on-target killing potential of 10LH using available HLA-A*24:02 and HLA-A*23:01 neuroblastoma cell lines (SKNAS, NBSD and SKNFI) and

demonstrated complete tumour cell killing and potent IFN- γ release after 24 h at 5:1 effector:target ratio (Fig. 4a–c, Supplementary Video 1). We tested the functional cross-reactivity of PC-CARs against the peptides presented by off-target tissues; PC-CARs showed no activity in three HLA-A*24:02 cell lines that do not express PHOX2B (SW620 colorectal adenocarcinoma, KATO III gastric adenocarcinoma and HEPG2 hepatocellular carcinoma) (Fig. 4a–c, Extended Data Fig. 10b; Supplementary Video 2). To validate the specificity of killing mediated by PC-CARs, we pulsed HLA-matched, PHOX2B-negative cancer cell lines with the PHOX2B peptide as well as forcibly over-expressing PHOX2B. We demonstrated specific killing only in cells pulsed with PHOX2B peptide and those transduced with full length *PHOX2B* mRNA, and not in cells pulsed with non-specific CHRNA3, ABCA8 and MYO7B peptides presented on the same HLA, nor in cells transduced with full length *PRAME* mRNA (Fig. 4d,e), demonstrating that native PHOX2B is processed and presented on MHC, where it is specifically recognized by PC-CARs. To detect PHOX2B pMHC on the cell surface, we generated a tetramerized 10LH scFv and stained on-target and off-target cell lines, which showed significant surface PHOX2B pMHC in neuroblastoma cells and not in HLA-matched controls (Fig. 4f, Extended Data Fig. 15a), suggesting that these reagents have the potential to be used to assess the presence of antigen in biopsied tissue samples. We also found that CARs flagged as cross-reactive by sCRAP demonstrated significant cross-reactivity, validating the functional consequences of cross-reactivities predicted by our algorithm (Extended Data Fig. 15b).

Fig. 4: PHOX2B-specific PC-CAR T cells induce potent tumour killing in vitro and in vivo and break conventional HLA restriction.



a–c, The CAR 10LH induces specific killing and IFN- γ release in neuroblastoma cells expressing HLA-A*24:02 and HLA-A*23:01 and PHOX2B (SKNAS, NBSD and SKNFI), but not in HLA-A*24:02 PHOX2B $^{-}$ non-neuroblastoma tumour cells (SW620, HEPG2 and KATO III), unless PHOX2B peptide is added. No T cell activity was observed in SW620 when pulsed with 10 μ M of the predicted cross-reactive peptides ABCA8 or MYO7B (**b**, **c**). Cytotoxicity was visualized by T cell clustering and cleaved caspase (**a**), relative loss of confluence measured by loss of green fluorescence in GFP-transduced cancer cells in (**b**), and IFN- γ release measured by ELISA (**c**). UT denotes untransduced T cells. Assays performed using T cells from $n = 3$ donors, each in triplicate; data are mean \pm s.d. **d**, Pulsing HLA-A*24:02 PHOX2B $^{-}$ cell line SW620 with 5 μ M PHOX2B induces complete cell killing when co-cultured with 10LH CAR, but no killing when pulsed with 50 μ M CHRNA3. Repeated across 3 experiments. **e**, 10LH CAR specifically and specifically kills SW620 control cells transduced with PHOX2B, but not with PRAME. **f**, Staining cancer cells with tetramerized 10LH scFv enables detection of PHOX2B pMHC on neuroblastoma cells but not in HLA-matched controls. **g**, PHOX2B-specific PC-CAR T cells induce potent tumour killing in mice engrafted with neuroblastoma PDX tumours, including the extremely fast-growing line COG-564x and HLA-A*23:01 line NBSD. $n = 6$ mice enrolled per arm (individual plots shown in Extended Data Fig. 17); data are representative from one of two independent in vivo studies for each PDX line; data are mean \pm s.d. **h**, Treatment with 10LH and 302LH PC-CARs potently upregulate HLA expression in PDX tumours collected from lone mice in each arm reaching tumour burden compared with mice treated with untransduced T cells (COG-564x collected 11 days after treatment; NBSD collected 14 days after treatment for untransduced cells and 17 days after treatment for 10LH and 302LH; both tumours collected from one experiment). Created with BioRender.com.

We next treated immunodeficient mice engrafted with HLA-A*24:02 (SKNAS and COG-564x) and HLA-A*23:01 (NBSD) xenografts with 10^6 10LH- and 302LH-transduced CAR T cells once tumours reached 100–250 mm 3 . Both 10LH PC-CAR-treated and 302LH PC-CAR-treated mice showed complete tumour responses in both HLA-A*24:02 xenografts (Fig. 4g), but only 10LH-treated mice exhibited the response in the HLA-A*23:01 NBSD xenografts. This correlated directly with the relative affinity of these two constructs against the PHOX2B peptide presented on HLA-A*23:01 (Extended Data Fig. 14c), suggesting that a threshold affinity or distinct mode of binding by different scFvs may contribute to the ability to recognize the peptide in slightly altered conformations when presented by different HLA allotypes. We also observed that CAR treatment induced substantial upregulation of MHC in tumours. The COG-564x PDX model was generated from a post mortem blood draw from a patient with high-risk *MYCN*-amplified neuroblastoma who had suffered multiple relapses, and shows an extremely rapid tumour growth rate in mice. In this experiment, one mouse treated with the 10LH construct had a tumour reach

endpoint size of 2 cm³ just one week after PC-CAR T cell therapy and was available for analysis, whereas all other tumours in this arm nearly reached endpoint size and then all regressed (Fig. 4g, Extended Data Figs. 16, 17). The lone COG-564x and NBSD tumours that reached endpoint showed significant PC-CAR T cell infiltrate and marked upregulation of MHC expression compared with endpoint tumours treated with non-transduced CAR T cells (Fig. 4h, Extended Data Fig. 17b). This upregulation is likely to be due to the potent IFN- γ release as measured in vitro, suggesting that these therapies can activate T cells at low antigen density to initiate a feed-forward cascade that increases MHC and antigen presentation.

Discussion

Here we have presented a process for identifying tumour-specific antigens derived from non-mutated oncoproteins, engineering PC-CARs against these tumour self-peptides and screening for cross-reactivity against MHC and the normal immunopeptidome. These methods have resulted in PC-CARs that can induce potent tumour killing across multiple HLA alleles in neuroblastoma and provide a roadmap for addressing the major challenges of therapeutic targeting of intracellular oncoproteins. These approaches demonstrate the value of pairing genomic, transcriptomic, epigenomic and immunopeptidomics datasets of normal and tumour tissues for the discovery of immunotherapy targets, as well as the utility of the ReD system paired with sCRAP to select ultra-rare scFv clones with desired binding and specificity profiles. Targeting of non-immunogenic self-antigens through pMHC-directed PC-CARs can vastly expand the landscape of actionable immunotherapeutic targets and enable the development of personalized immunotherapies in neuroblastoma and other cancers. Owing to the limitations in ionization and canonical search spaces of our immunopeptidomics, the prioritized peptides here are likely to represent only a fraction of potential pMHC complexes available to immunotherapeutic targeting. Neuroblastomas in general, and especially those harbouring *MYCN* amplification³⁷, exist in a highly immunosuppressive tumour microenvironment such that future iterations of PC-CARs may require additional engineering to enable T cells to navigate to the pMHC target. However, our demonstration of significant upregulation of MHC (and thus target) in our models may help alleviate this therapeutic obstacle.

We also highlight the utility of pairing ShinyNAP with RosettaMHC in identifying HLA allotypes capable of presenting identical peptides in a similar conformation. We suggest that these tools, in addition to matched peptide searches of immunopeptidomics data across multiple tumour samples, have the potential to appreciably expand the identification of tumour-specific peptides presented on multiple HLAs. The potential ability to target these antigens beyond canonical HLA restriction can substantially expand the population of patients eligible to receive each PC-CAR construct and reach underserved populations, but this will need to be verified

with other PC-CARs that are in development. The use of the sCRAP algorithm can rapidly exclude constructs with safety liabilities and prioritize those constructs with optimal safety profiles, in contrast to alanine scanning which determines construct-specific cross-reactivities post hoc³⁴.

We demonstrate several distinct advantages of PC-CARs for targeting of MHC peptides compared with TCRs: (1) PC-CARs can be used to target essential unmutated oncoproteins by inducing immunogenicity using synthetic peptide-centric receptors; (2) in contrast to TCRs, peptide-centric receptors are not constrained by the germline-encoded CDR1 and CDR2 interactions with MHC and therefore can be engineered such that these binding loops are able to form additional contacts with target peptides independently of the HLA, allowing us to generate receptors with superior peptide selectivity to that of TCRs; and (3) owing to the lack of CDR1 and CDR2 loop interactions with MHC, PC-CARs can target a peptide presented by multiple HLA alleles, opening up the potential to substantially increase the clinical reach of each construct. Furthermore, PC-CARs may have an advantage over CARs in targeting membrane proteins in their ability to initiate a feed-forward loop of MHC upregulation and increased antigen density. These findings build on recent studies that demonstrate the ability to target neoantigens from mutated TP53 and RAS on MHC using scFv-based approaches and further demonstrate the utility of these approaches in targeting intracellular proteins^{38,39}. We expect that the methods presented here will facilitate the discovery of tumour-specific targets in other human cancers with high unmet need and envision a library of scFv-based synthetic immunotherapies that provides population-scale coverage of HLA genotypes for both neoantigens and self-antigens.

Methods

Neuroblastoma samples and cell lines

Five neuroblastoma cell line xenografts and three patients derived xenografts showing a range of HLA expression by RNA sequencing and immunohistochemistry were selected for the initial immunopeptidomics experiment (Extended Data Table 1). All had whole exome sequencing and single nucleotide polymorphism array data available in addition to RNA-seq data¹⁸. Eight high-risk tumours with a mean mass of 0.56 g ranging from 0.17–1.7 g were obtained from Children's Oncology Group (COG; <https://childrensoncologygroup.org/>) with matched sequencing from TARGET (<https://ocg.cancer.gov/programs/target>). Informed consent from each research subject or legal guardian was obtained for each deidentified tumour and blood sample used in this study through the COG neuroblastoma biobanking study ANBL00B1.

Human-derived neuroblastoma cell lines, including SK-N-AS, SK-N-FI and NB-SD were obtained from the Maris Lab cell line bank. Neuroblastoma cell lines were

cultured in RPMI supplemented with 10% fetal bovine serum (FBS), 100 U ml⁻¹ penicillin, 100 µg ml⁻¹ streptomycin, and 2 mM l-glutamine. Other human cancer cell lines, including Jurkat, SW620, HEPG2 and KATO III were obtained from American Type Culture Collection (ATCC). Jurkat cells were cultured in Iscove's modified Dulbecco's medium (IMDM) supplemented with 10% FBS, 100 U ml⁻¹ penicillin, 100 µg ml⁻¹ streptomycin and 2 mM l-glutamine. SW620 cells were cultured in RPMI supplemented with 10% FBS, 100 U ml⁻¹ penicillin, 100 µg ml⁻¹ streptomycin, and 2 mM l-glutamine. HEPG2 cells were cultured in Eagle's minimum essential medium (EMEM) supplemented with 10% FBS, 100 U ml⁻¹ penicillin, 100 µg ml⁻¹ streptomycin and 2 mM l-glutamine. KATO III cells were cultured in IMDM supplemented with 20% FBS, 100 U ml⁻¹ penicillin, 100 µg ml⁻¹ streptomycin and 2 mM l-glutamine. Packaging cell lines including Platinum-A cells and HEK 293T cells were obtained from Cell BioLabs and ATCC, respectively. Both packaging cell lines were cultured in DMEM supplemented with 10% FBS, 100 U ml⁻¹ penicillin, 100 µg ml⁻¹ streptomycin and 2 mM l-glutamine. All cell lines were grown under humified conditions in 5% CO₂ at 37 °C, and samples were regularly tested for mycoplasma contamination.

Primary human T cells

Primary human T cells were obtained from anonymous donors through the Human Immunology Core at the University of Pennsylvania (Philadelphia, PA) under a protocol approved by the Children's Hospital of Philadelphia Institutional Review Board. Cells were cultured using AIM-V (Thermo Fisher Scientific) supplemented with 10% FBS, 100 U ml⁻¹ penicillin, 100 µg ml⁻¹ streptomycin and 2 mM l-glutamine under humified conditions in 5% CO₂ at 37 °C. T cell donors provided informed consent through the University of Pennsylvania Immunology Core

Isolation of HLA ligands by immunoaffinity purification

HLA class I molecules were isolated using standard immunoaffinity purification as described previously,^{53,54}. In brief, cell pellets were lysed in 10 mM CHAPS/PBS (AppliChem/Lonza) containing 1× protease inhibitor (Complete; Roche). Mouse MHC molecules were removed using a 1 h immunoaffinity purification with H-2K-specific monoclonal antibody 20-8-4S, covalently linked to CNBr-activated sepharose (GE Healthcare). Remaining HLA molecules were purified overnight using the pan-HLA class I-specific monoclonal antibody W6/32 or a mix of the pan-HLA class II-specific monoclonal antibody Tü39 and the HLA-DR-specific monoclonal antibody L243, covalently linked to CNBr-activated Sepharose. MHC-peptide complexes were eluted by repeated addition of 0.2% trifluoroacetic acid (Merck). Elution fractions E1–E4 were pooled, and free MHC ligands were isolated by ultrafiltration using centrifugal

filter units (Amicon; Merck Millipore). MHC ligands were extracted and desalted from the filtrate using ZipTip C18 pipette tips (Merck Millipore). Extracted peptides were eluted in 35 µl of acetonitrile (Merck)/0.1% trifluoroacetic acid, centrifuged to complete dryness and resuspended in 25 µl of 1% acetonitrile/0.05% trifluoroacetic acid. Samples were stored at –20 °C until analysis by LC–MS/MS.

Analysis of HLA ligands by LC–MS/MS

Peptide samples were separated by reversed-phase liquid chromatography (nanoUHPLC, UltiMate 3000 RSLCnano, Dionex) and subsequently analysed in an on-line coupled Orbitrap Fusion Lumos (Thermo Fisher Scientific). Samples were analysed in three technical replicates. Sample volumes of 5 µl (sample shares of 20%) were injected onto a 75 µm × 2 cm trapping column (Acclaim PepMap RSLC, Dionex) at 4 µl min⁻¹ for 5.75 min. Peptide separation was subsequently performed at 50 °C and a flow rate of 300 nl min⁻¹ on a 50 µm × 25 cm separation column (Acclaim PepMap RSLC, Dionex) applying a gradient ranging from 2.4–32.0% of acetonitrile over the course of 90 min. Eluting peptides were ionized by nanospray ionization and analysed in the mass spectrometer implementing the TopSpeed method. Survey scans were generated in the Orbitrap at a resolution of 120,000. Precursor ions were isolated in the quadrupole, fragmented by collision induced dissociation (CID) in the dual-pressure linear ion trap for MHC class I-purified peptides. Finally, fragment ions were recorded in the Orbitrap. An AGC target of 1.5x10⁵ and a max injection time of 50ms was used for MS1. An AGC target of 7x10⁴ and a max injection time of 150ms was used for MS2. The collision energy for CID fragmentation was 35%. For fragmentation mass ranges were limited to 400-650 m/z with charge states 2+ and 3+ for MHC class I.

Synthetic peptides were analyzed using a thirty minute gradient due to the simplicity of the sample. Full scan was acquired in the Orbitrap with a scan range of 300-1200 at 120,000 resolution. The automatic gain control (AGC) target was 5.0 × 10⁵ with a maximum injection time of 50ms. Precursor ions were isolated in the quadropole, fragmented (CID, HCD and ETD) and analysed in the Orbitrap. MS2 were also acquired in the Orbitrap with 30,000 resolution, collision energy of 35%, AGC of 5 × 10⁴, and maximum injection time of 150 ms. Since the discovery analysis were completed using CID, synthetic peptides fragmented with CID were compared for validation.

The mass spectrometry proteomics data have been deposited to the ProteomeXchange Consortium via the PRIDE⁴⁰ partner repository with the dataset identifier PXD027182 and 10.6019/PXD027182

HLA typing

FASTQ files from TARGET DNA and RNA-seq and RNA-seq data from cell lines were processed using PHLAT algorithm, as we previously validated on 15 HLA alleles⁸.

Database search and spectral annotation

Data were processed against the human proteome as compiled in the Swiss-Prot database (<https://uniprot.org>; 27 May 2021; 20,395 reviewed protein sequences contained) using the SequestHT algorithm³ in Proteome Discoverer (v2.1, Thermo Fisher Scientific) software. Precursor mass tolerance was set to 5 ppm, fragment mass tolerance to 0.02 Da. Search was not restricted to an enzymatic specificity. Oxidized methionine was allowed as a dynamic modification. FDR was determined by the Percolator algorithm based on processing against a decoy database consisting of shuffled sequences. FDR was set to 1%. Peptide lengths were limited to 8–14 amino acids for MHC class I. HLA annotation was performed using NetMHC-4.0 for HLA class I. For peptide matching, data was reprocessed using Proteome Discoverer (v2.4, Thermo FisherScientific) using the same parameters but with the addition of the feature mapper node to allow peptide matching between samples. Synthetic peptides were searched using a similar approach but Percolator was replaced with the fixed value PSM validator due to the simplicity of the synthetic peptide sample. Gene Ontology analyses were performed using PANTHER⁴¹ (<http://geneontology.org/>) and *P*-values were calculated using Fischer's exact test.

HLA binding predictions

HLA binding predictions were performed using NetMHC-4.0⁴², NetMHCpan 4.1⁴³, and HLATHENA⁴⁴ on HLA class I.

scFv biopanning and CAR design

scFv binders against MHC presented peptides were retrieved from a large (2×10^{10}) naive phage display scFv library⁴⁵. A competitive panning process was developed to identify specific binders targeting the pMHC based on previous protocols⁴⁶. Biotinylated pMHC monomers (target antigens) and non-biotinylated tetramers (decoy competitors) were obtained from the NIH tetramer core facility. 10^{12} copies of phages were depleted against magnetic beads (Invitrogen Dynabeads MyOne Streptavidin T1) for 30 min before incubation for 1.5 h with 5 µg biotinylated pep-MHC conjugated beads in the presence of 20 µg irrelevant decoy competitors. After incubation, the beads were washed with PBS containing 0.05% Tween-20 (PBST buffer) 5 times followed by two PBS washes. The remaining bound phage were recovered by log-phase TG1 and rescued by M13KO7 helper phage. The amplified phage was collected

the next day by PEG–NaCl precipitation and used for the next round of panning. The target antigen input was decreased from 5 µg for the first round panning to 2 µg and 0.5 µg for the second and third rounds, respectively, and the washing conditions were more stringent along with the panning rounds. After three rounds of panning, polyclonal phage ELISA was performed to evaluate the enrichment. The TG1 cells from the second and third rounds were randomly picked into 96-well plates for soluble expression-based monoclonal ELISA (semELISA), as described previously^{46,47}. Clones producing signals when binding to target antigens and not producing signals when binding the decoy competitors were amplified and sequenced. For protein preparation, these clones were transformed into HB2151 cells for expression, and proteins were purified by one-step Ni-NTA resin affinity. Protein purity and homogeneity were analysed by SDS-PAGE. Protein concentration was measured spectrophotometrically (NanoVue, GE Healthcare). Second-generation CAR constructs were synthesized using scFv sequences with 4-1BB and CD3ζ co-stimulatory domains and cloned into pMP71 vector for screening.

ReD library panning

The Ruby scFv library ($>10^{11}$ diversity) was constructed using fully-germline IGLV3-1 and IGLV6-57 scaffolds paired with theIGHV3-23 scaffold as described³³, with fully synthetic amino acid diversity in both V_L and V_H CDR3 loops.

The Ruby library was panned for two rounds using PHOX2B (43-51) MHC complex bound to MyOne Streptavidin C1 Dynabeads (ThermoFisher, Cat: 65002). Panned library output were transferred into the ReD cell-display platform³³ and cells were permeabilized using 0.5% n-octyl β-d-thioglucopyranoside (Anatrace, catalogue (cat.) no. 0314) and labelled using recombinant PHOX2B pMHC complex ligated to fluorophores excitable by 405 nm and 488 nm lasers. Cells that were positive for target binding were isolated using the FACSMelody sorter (Becton-Dickinson).

After two rounds of positive selection for binding to PHOX2B MHC complex, two further rounds of fluorescence-activated cell sorting (FACS) were conducted using counter-labelled A*24:02 MHC complexes with unrelated peptides. After four rounds of FACS, individual colonies were picked and grown in 96-well plates before scFv induction, cell permeabilization, and PHOX2B MHC labelling and detection by CytoFLEX (Beckman Coulter).

Clones that were identified as binding specifically to the PHOX2B (43–51)–MHC complex were sequenced and unique scFvs were expressed as fusions to the AviTag biotinylation motif in *Escherichia coli*. Biotinylated scFv protein was released by permeabilization with 0.5% n-octyl β-d-thioglucopyranoside and purified to ~90% purity on Nickel NTA agarose resin (ABT, cat. no. 6BCL-NTANi).

Binding kinetics

Affinity measurements were performed using a BLItz system (ForteBio) and analysed using BLItz Pro software. Streptavidin biosensors (ForteBio, cat. no. 18-5019) were loaded with AviTag-biotinylated scFv, blocked with biotin, washed in PBS and then associated with pMHC ligand in PBS.

Steady-state binding assay

An equilibrium binding assay to target pMHCs was also established using MyOne Streptavidin C1 Dynabeads. In brief, 50 µg of Streptavidin C1 Dynabeads were incubated with excess biotinylated scFv before being blocked with free biotin and washed in PBS. Fluorophore-labelled pMHC complex was added to a concentration of 3.5 nM and incubated for 1 h at 4 °C followed by 10 min at 25 °C. Binding of the free MHC complex to the beads was quantified by the CytoFLEX at 488 nm (excitation)/525 nm (emission). Binding was normalized to beads without scFv and with unrelated control MHC complex.

This bead-binding assay was used to quantitate the binding of scFv to MHC complexes with alanine-scan substitutions of the PHOX2B peptides as well as to a plate of 95 unrelated 9mer peptide A*24:02 MHC complexes and the degree of cross-reactivity of binding of MHC complexes with peptides identified as having high homology to the PHOX2B peptide by eXpitope 2.0.

Viral production and transduction of Jurkat and primary T cells

Retrovirus for transduction of Jurkats and primary CD4/8 T cells was produced using Platinum-A (Plat-A) cells, a retroviral packaging cell line. Cells were plated in 6-well plates at 7×10^5 cells per well and transfected with 2.5 µg of the appropriate TCR or CAR construct in the retroviral vector pMP71 using Lipofectamine 3000 (Life Technologies, Invitrogen). After 24 h, medium was replaced with IMDM-10% FBS or AIM-V-10% FBS for Jurkat cells or primary cells, respectively. Supernatants were collected and filtered with 0.2-µm filters after 24 h incubation.

A second-generation lentiviral system was used to produce replication-deficient lentivirus. The day preceding transfection, 15 million HEK 293T cells were plated in a 15-cm dish. On the day of transfection, 80 µl Lipofectamine 3000 (Life Technologies, Invitrogen) was added to 3.5 ml room-temperature Opti-MEM medium (Gibco). Concurrently, 80 µl P3000 reagent (Thermo Fisher Scientific), 12 µg psPAX2 (Gag/Pol), 6.5 µg pMD2.G (VSV-G envelope), and a matching molar quantity of transfer plasmid were added to 3.5 ml room-temperature Opti-MEM medium. Virus

supernatant was collected after 24 and 48 h later and briefly centrifuged at 300g and passed through a 0.45- μ m filter attached to a syringe.

Jurkat cells were plated in 6-well plates pre-treated with 1 ml per well Retronectin (20 mg ml⁻¹, Takara Bio) at 1×10^6 cells per well and spinoculated with 2 ml retroviral supernatant at 800g for 30 min at room temperature. After 24 h, cells were collected, and grown in IMDM-10% FBS.

Primary T cells were thawed and activated in culture for 3 days in the presence of 100 U ml⁻¹ IL-2 and anti-CD3/CD28 beads (Dynabeads, Human T-Activator CD3/CD28, Life Technologies) at a 3:1 bead:T cell ratio. On days 4 and 5, activated cells were plated in 6-well plates pre-treated with 1 ml per well Retronectin (20 mg ml⁻¹, Takara Bio) at 1×10^6 cells per well and spinoculated with 2 ml retroviral supernatant at 2,400 rpm for 2 h at 32 °C. On day 6, cells were collected and washed, beads were magnetically removed, and cells were expanded in AIM-V-10% FBS supplemented with 25 U ml⁻¹ IL-2.

Primary human T cells were thawed and activated in culture for 1 day in the presence of 5 ng ml⁻¹ recombinant IL-7, 5 ng ml⁻¹ recombinant IL-15, and anti-CD3/CD28 beads (Dynabeads, Human T-Activator CD3/CD28, Life Technologies) at a 3:1 bead:T cell ratio in G-Rex system vessels (Wilson Wolf). On day 2, thawed lentiviral vector was added to cultured T cells with 10 μ g ml⁻¹ Polybrene (Millipore Sigma), and 24 h later vessels were filled with complete AIM-V medium supplemented with indicated concentrations of IL-7 and IL-15. On day 10, cells were collected and washed.

Activation beads were magnetically removed, and cell viability was determined before freezing.

Human neuroblastoma cell lines were plated in 6-cm dishes, and 2 ml of thawed lentiviral vector produced with transfer plasmid pLenti-CMV-eGFP-Puro (Addgene plasmid #17448) was added with 10 μ g ml⁻¹ Polybrene (Millipore Sigma). Cells were selected for eGFP expression using flow-assisted cell sorting (BD FACSJazz, BD Biosciences) followed by 1 μ g ml⁻¹ puromycin selection.

sCRAP prediction

Tumour antigens were compared against the entire normal human proteome on the matched HLA (85,915,364 total normal peptides among 84 HLAs). Each residue in the same position of the tumour and human peptides was assigned a score for perfect match, similar amino acid classification or different polarity, scoring 5, 2 or -2, respectively (Extended Data Fig. 12). Similarity scores were calculated based on amino acid classification and hydrophobicity was determined using residues one and three through eight and excluding MHC anchor residues. Next, the maximum normal

tissue RPKM values were identified from 1,643 normal tissues in GTEx. Normal peptides were compared to a database of normal tissue immunopeptidomes⁴⁸. The overall cross-reactivity score for each normal peptide was then calculated using the following equation:

$$\$ \$ \frac{\sum_{i=3}^n P_i}{b \times E_{\max}} \$ \$$$

where n is the peptide length, P_i is the score of each amino acid of the normal peptide as compared to the tumour antigen, b is the pMHC binding affinity of the normal peptide, and E_{\max} is the maximum normal tissue expression

The algorithm is available at <https://marisshiny.research.chop.edu/sCRAP/>.

Tetramer and dextramer staining and flow cytometric analysis

Surface expression and binding of TCR- and CAR-transduced Jurkat cells and primary T cells was measured by staining with PE- or APC-conjugated dextramers carrying NB antigen peptide–MHC (Immudex). Cells were collected from culture, washed with 2 ml PBS at 800g for 5 min, incubated with 1 µl dextramer for 10 min in the dark, washed again, and resuspended in 300 µl PBS for analysis. Typically 5×10^5 cells were used for staining, and analysed on a BD LSR II (BD Biosciences) or an Attune Acoustic Focusing Cytometer (Applied Biosystems, Life Technologies). Flow cytometry data was collected using CytExpert (Beckman Coulter) and FACSDiva (BD Biosciences). Gating strategy for all tetramer and dextramer staining shown in Extended Data Fig. 9f.

Cross-reactivity pMHC screen

Potential cross-reactive peptides (GenScript) were suspended at a 200 µM working concentration. For each test, 0.5 µl of peptide was added to 5 µl HLA-A*24:02 empty loadable tetramer (Tetramer Shop) before incubating on ice for 30 min, or using TAPBR peptide exchange as previously described⁴⁹. Following preparation, pMHC tetramers were used to stain cells (described above). CAR construct cross-reactivity values were determined using Jurkat cells transduced with CAR clones followed by staining with HLA-A*24:02 tetramers loaded with cross-reactive peptides. Mean fluorescent intensity was compared across peptides to determine cross reactivity.

Antigen-specific CD8 T cell enrichment and expansion

Normal donor monocytes were plated on day 1 in 6-well plates at 5×10^6 cells per well in RPMI-10 FBS supplemented with 10 ng ml⁻¹ IL-4 (Peprotech) and 800 IU ml⁻¹ GM-CSF (Peprotech) and incubated at 37 °C overnight. On day 2, fresh

medium supplemented with 10 ng ml⁻¹ IL-4 and 1,600 IU ml⁻¹ GM-CSF was added to the monocytes and incubated at 37 °C for another 48 h. On day 4, non-adherent cells were removed, and immature dendritic cells washed and pulsed with 5 µM peptide in AIM-V-10% FBS supplemented with 10 ng ml⁻¹ IL-4, 800 IU ml⁻¹ GM-CSF, 10 ng ml⁻¹ lipopolysaccharide (Sigma-Aldrich), and 100 IU ml⁻¹ IFN-γ (Peprotech) at 37 °C overnight. Day 1 was repeated on days 4 and 8 to generate dendritic cells for the second and third stimulations on days 8 and 12, respectively.

On day 5, normal donor-matched CD8+ T cells were enriched using protein kinase inhibitor dasatinib (Sigma-Aldrich), dextramers, and anti-PE or anti-APC beads (Miltenyi Biotec) as previously described⁵⁰. Enriched T cells were co-incubated with the appropriate pulsed dendritic cells in AIM-V-10% FBS. The day 5 protocol was repeated on days 8 and 12 using dendritic cells generated on days 4 and 8 for the second and third stimulation, respectively. Expanded T cells were validated for antigen-specificity by staining with the appropriate dextramers and for activation marker 41BB/CD137 (BioLegend).

Antigen-specific T cell sorting, sequencing and cloning

Expanded T cells were stained with CD3, CD8, CD14, CD19, live/dead and matched and mismatched dextramer and single-antigen-specific T cells were sorted using a FACSaria Fusion (BD Biosciences).

Sorted cells were loaded onto 10× Genomics 5' V(D)J chips and libraries prepared according to manufacturer protocols. TCRα/β amplicons were run on MiSeq using 5,000 reads per cell. Sequencing data were processed using Cell Ranger and analysed using Loupe VDJ Browser. TCR alpha and beta chains were codon optimized and synthesized into bicistronic expression cassettes using engineered cysteine residues in the TCR constant domains, using F2A ribosomal skip sites and furin cleavage sites⁵¹. TCR cassettes were cloned into pMP71 retroviral vector.

Incucyte cytotoxicity assay

A total of 0.5×10^5 tumour cell targets were co-incubated with varying ratios of transduced primary cells (5×10^5 , 2.5×10^5 , 1×10^5 , 0.5×10^5 and 2.5×10^4 for 10:1, 5:1, 2:1, 1:1 and 1:2 effector:target (E:T) ratios, respectively) in 96-well plates at 37 °C in the presence of 0.05 µM caspase-3/7 red (Incucyte, Essence BioScience). Plates ran on the Incucyte Zoom or S3 for 24–72 h and measured for apoptosis activity via caspase cleavage and comparison of relative confluency. Following the assay, supernatants were collected for ELISA. Total GFP integrated intensity (Total green calibrated units × µm² per image) was assessed as a quantitative measure of live, GFP+ tumour cells. Values were normalized to the *t*=0 measurement.

Cytokine secretion assays

Cell supernatant collected from cell cytotoxicity assays was thawed and plated in triplicate for each condition. IFN- γ and IL-2 levels were determined using ELISA kits according to the manufacturer's protocol (BioLegend).

Antigen processing and presentation

Neuroblastoma cell lines were titrated with H1N5 influenza virus and infectivity was measured by flow cytometry using virus nucleoprotein (NP) antibody. HLA-A2 neuroblastoma cell lines were cultured with either 5 μ M CEF1 or 50 HAU of H1N5 virus then co-cultured with M1 antigen-specific T cell hybridoma kindly provided by David Canaday⁵². T cell activation was measured using IL-2 ELISA (Abcam).

Expression, refolding, and purification of recombinant peptide and HLA molecules

HLA-A*02:01 and HLA-A*24:02 constructs for bacterial expression were cloned into pET24a+ plasmid. DNA plasmids encoding HLA-A*02:01 (heavy chain), HLA-A*24:02 (heavy chain), and human β 2M (light chain) were transformed into *E. coli* BL21-DE3 (Novagen), expressed as inclusion bodies and refolded using previously described methods⁵³. *E. coli* cells were grown in autoinduction medium⁵⁴ for (16–18 h). Afterward, the *E. coli* cells were collected by centrifugation and resuspended with 25 ml BugBuster (Millipore Sigma) per litre of culture. The cell lysate was sonicated and subsequently pelleted by centrifugation (5,180g for 20 min at 4 °C) to collect inclusion bodies. The inclusion bodies were washed with 25 ml of wash buffer (100 mM Tris pH 8.0, 2 mM EDTA, and 0.01% v/v deoxycholate), sonicated, and pelleted by centrifugation. A second wash was done using 25 ml of Tris-EDTA buffer (100 mM Tris pH 8.0 and 2 mM EDTA). The solution was once again resuspended by sonication then centrifuged. The inclusion bodies were then solubilized by resuspension with 6 ml resuspension buffer (100 mM Tris pH 8.0, 2 mM EDTA, 0.1 mM DTT, and 6 M guanidine-HCl). Solubilized inclusion bodies of the heavy and light chain were mixed in a 1:3 molar ratio and then added dropwise over 2 days to 1 l of refolding buffer (100 mM Tris pH 8.0, 2 mM EDTA, 0.4 M arginine-HCl, 4.9 mM reduced L-glutathione, and 0.57 mM oxidized L-glutathione oxidized) containing 10 mg of synthetic peptide at >98% purity confirmed by mass-spectrometry (Genscript). Refolding was allowed to proceed for 4 days at 4 °C without stirring. Following this incubation period, the refolding mixture was dialyzed into the size-exclusion buffer (25 mM Tris pH 8.0 and 150 mM NaCl). After dialysis, the sample was concentrated first using a LabScale tangential flow filtration system and then using an Amicon Ultra-15 Centrifugal 10 kDa MWCO Filter Unit (Millipore Sigma), to a final volume

of 5 ml. Purification was performed using size-exclusion chromatography on a HiLoad 16/600 Superdex 75 column. After size exclusion, the sample was further purified by anion exchange chromatography using a MonoQ 5/50 GL column and a 0–100% gradient of buffer A (25 mM Tris pH 8.0 and 50 mM NaCl) and buffer B (25 mM Tris pH 8.0 and 1 M NaCl). The purified protein was exhaustively exchanged into 20 mM sodium phosphate pH 7.2 and 50 mM NaCl. The final sample was validated using SDS-PAGE to confirm the formation of a pMHC complex containing both the heavy and light chains.

Differential scanning fluorimetry

To measure the thermal stability of the pMHC-I molecules, 2.5 µM of protein was mixed with 10× Sypro Orange dye in matched buffer (20 mM sodium phosphate pH 7.2, 100 mM NaCl) in MicroAmp Fast 96-well plates (Applied Biosystems) at a final volume of 50 µl. Differential scanning fluorimetry was performed using an Applied Biosystems ViiA quantitative PCR machine with excitation and emission wavelengths at 470 nm and 569 nm, respectively. Thermal stability was measured by increasing the temperature from 25 °C to 95 °C at a scan rate of 1 °C min⁻¹. Melting temperatures (T_m) were calculated in GraphPad Prism 7 by plotting the first derivative of each melt curve and taking the peak as the T_m .

Protein crystallization

Purified HLA-A*02:01–LLLPLLPPL, HLA-A*02:01–LLPPLLPLSP, HLA-A*02:01–LLPPLLPLSPS, HLA-A*02:01–LLPRLPPL and HLA-A*24:02–QYNPIRTTF complexes were used for crystallization. Proteins were concentrated to 10–12 mg ml⁻¹ in 50 mM NaCl, 25 mM Tris pH 8.0, and crystal trays were set up using a 1:1 protein-to-buffer ratio at room temperature. Optimal crystals for HLA-A*02:01–LLLPLLPPL, HLA-A*02:01–LLPPLLPLSP and HLA-A*02:01–LLPPLLPLSPS were obtained with 1 M sodium citrate dibasic, 0.1 M sodium cacodylate pH 6.5. For HLA-A*02:01–LLPRLPPL, diffracting crystals were obtained with 0.2 M magnesium chloride, 0.1 M HEPES pH 7.0, 20 % PEG 6000. HLA-A*24:02–QYNPIRTTF diffracting crystals were obtained with 0.1 M HEPES pH 7.0, 10 % PEG 6000. Diffraction-quality crystals were collected and incubated from the above conditions plus glycerol as a cryoprotectant and flash-frozen in liquid nitrogen before data collection. All crystals used in this study were grown using the hanging-drop vapour-diffusion method. Data were collected from single crystals under cryogenic condition at Advanced Light Source (beam lines 8.3.1 and 5.0.1). Diffraction images were indexed, integrated, and scaled using MOSFLM and Scala in CCP4 Package⁵⁵. Structures were determined by Phaser⁵⁶ using previously published structures of HLA-A*02:01 (PDB ID 5C07)⁵⁷ and

HLA-A*24:02 (PDB ID 3VXN)⁵⁸. Model building and refinement were performed using COOT⁵⁹ and Phenix⁶⁰, respectively.

Homology modelling of p/HLA complexes using RosettaMHC

Three-dimensional structural models of HLA-A*23:01, HLA-B*14:02 and HLA-C*07:02 bound to the peptide QYNPIRTTF were generated using RosettaMHC, an in-house method for modeling the α_1 and α_2 peptide-binding domains of pMHC-I molecules⁶¹. In brief, the amino acid sequences of HLA-A*23:01, HLA-B*14:02 and HLA-C*07:02 were first obtained from the IPD-IMGT/HLA Database⁶². The sequence of HLA alleles of interest was aligned against the sequences of 318 HLA curated template structures available in RosettaMHC. For each allele, all candidate templates were selected according to a 70% sequence identity criterion between aligned residues within the peptide-binding groove (within 3.5 Å of any peptide heavy atom). Generation of 3D models was performed using a Monte Carlo sampling of sidechain rotamer conformations, followed by gradient-based optimization of all backbone and sidechain degrees of freedom. For each peptide–HLA complex, the top 5 models with the lowest Rosetta binding energy were selected as the final structural ensemble. The quality of the final models was assessed using the Molprobity webserver⁶³. Analysis of polar contacts and surface area were performed using the PyMOL Molecular Graphics System, version 2.4.1.

Immunohistochemistry

CD3 (Dako A0452), PHOX2B (Abcam ab183741), and HLA-ABC (Abcam ab70328) antibodies were used to stain formalin fixed paraffin embedded tissue slides. Staining was performed on a Bond Max automated staining system (Leica Biosystems). The Bond Refine polymer staining kit (Leica Biosystems, DS9800) was used. The standard protocol was followed with the exception of the primary antibody incubation which was extended to 1 h at room temperature. CD3, PHOX2B and HLA-ABC antibodies were at 1:100, 1:500 and 1:1,200 dilutions, respectively. Antigen retrieval was performed with E1 (Leica Biosystems) retrieval solution for 20 min (E2 for PHOX2B). Slides were rinsed, dehydrated through a series of ascending concentrations of ethanol and xylene, then coverslipped. Stained slides were then digitally scanned at 20 \times magnification on an Aperio CS-O slide scanner (Leica Biosystems).

Murine PC-CAR T cell preclinical trials

NOD SCID Gamma (NSG) female (6–8 weeks of age) mice from Jackson Laboratories (stock no. 005557) were used to propagate subcutaneous xenografts. All

mice were maintained under barrier conditions and experiments were conducted using protocols and conditions approved by the IACUC at the Children's Hospital of Philadelphia. Treatment was initiated via lateral tail intravenous injection. Dose administered was 100 µl per animal of vehicle or CAR T cells as a single treatment. Treatment was administered at weeks 8–10 when tumour volumes reached 150 mm³ to 250 mm³. Six mice were enrolled per arm based on previous experience and randomized based on tumour size. Mouse technician was blinded to T cell engineering. Tumour volume and survival were monitored bi-weekly measurements until the tumours reached a size of 2.0 cm³ or mice showed signs of graft versus host disease. Animals were removed from study and studies terminated following onset of graft-versus-host disease (GVHD) when animals display hunched posture, rapid breathing, urine staining, weight loss and a body condition score of 2, as determined by visual inspection. Onset of GVHD defined as urine staining and weight loss of 20% or weight loss of 10–15% if accompanied by hunched posture, laboured breathing, or poor body condition.

Statistics and reproducibility

Box and whisker plot representations of data show the median as centre, and 25th percentile and 75th percentile as bounds of boxes for plots shown in Fig. 1e, [Extended Data Figs. 1, 13b](#).

Reporting summary

Further information on research design is available in the [Nature Research Reporting Summary](#) linked to this paper.

Data availability

Neuroblastoma HLA class I immunopeptidomics data is available through PRIDE under accession [PXD027182](#). Sample files are annotated in Supplementary Table 2. Protein structures are available in the Protein Data Bank under accession codes 7MJ6 (HLA-A*02:01–LLLPLLPPL), 7MJ7 (HLA-A*02:01–LLPPLLPLSP), 7MJ8 (HLA-A*02:01–LLPPLLPLSPS), 7MJ9 (HLA-A*02:01–LLPRLPPL) and 7MJA (HLA-A*24:02–QYNPIRTTF). All other data are available within the article and supplementary information files, or by request from corresponding author.

Code availability

The sCRAP algorithm is accessible to the scientific community through a web portal (<https://marisshiny.research.chop.edu/sCRAP/>).

References

1. 1.
Pearlman, A. H. et al. Targeting public neoantigens for cancer immunotherapy. *Nat. Cancer* **2**, 487–497 (2021).
2. 2.
Alexandrov, L. B. et al. Signatures of mutational processes in human cancer. *Nature* **500**, 415–421 (2013).
3. 3.
Leko, V. & Rosenberg, S. A. Identifying and targeting human tumor antigens for T cell-based immunotherapy of solid tumors. *Cancer Cell* **38**, 454–472 (2020).
4. 4.
Durbin, A. D. et al. Selective gene dependencies in *MYCN*-amplified neuroblastoma include the core transcriptional regulatory circuitry. *Nat. Genet.* **50**, 1240–1246 (2018).
5. 5.
Majzner, R. G. & Mackall, C. L. Clinical lessons learned from the first leg of the CAR T cell journey. *Nat. Med.* **25**, 1341–1355 (2019).
6. 6.
Tsherniak, A. et al. Defining a cancer dependency map. *Cell* **170**, 564–576.e516 (2017).
7. 7.
Yossef, R. et al. Enhanced detection of neoantigen-reactive T cells targeting unique and shared oncogenes for personalized cancer immunotherapy. *JCI Insight* **3**, e122467 (2018).
8. 8.
Yarmarkovich, M. et al. Immunogenicity and immune silence in human cancer. *Front. Immunol.* **11**, 69 (2020).

9. 9.

Schumacher, T. N. & Schreiber, R. D. Neoantigens in cancer immunotherapy. *Science* **348**, 69–74 (2015).

10. 10.

Shao, W. et al. The SysteMHC Atlas project. *Nucleic Acids Res.* **46**, D1237–D1247 (2018).

11. 11.

Maus, M. V. et al. An MHC-restricted antibody-based chimeric antigen receptor requires TCR-like affinity to maintain antigen specificity. *Mol. Ther. Oncolytics* **3**, 1–9 (2016).

12. 12.

Linette, G. P. et al. Cardiovascular toxicity and titin cross-reactivity of affinity-enhanced T cells in myeloma and melanoma. *Blood* **122**, 863–871 (2013).

13. 13.

Morgan, R. A. et al. Cancer regression and neurological toxicity following anti-MAGE-A3 TCR gene therapy. *J. Immunother.* **36**, 133–151 (2013).

14. 14.

Matthay, K. K. et al. Neuroblastoma. *Nat. Rev. Dis. Primers* **2**, 16078 (2016).

15. 15.

Pugh, T. J. et al. The genetic landscape of high-risk neuroblastoma. *Nat. Genet.* **45**, 279–284 (2013).

16. 16.

Burr, M. L. et al. An evolutionarily conserved function of polycomb silences the MHC class I antigen presentation pathway and enables immune evasion in cancer. *Cancer Cell* **36**, 385–401.e388 (2019).

17. 17.

Aguet, F. et al. The GTEx Consortium atlas of genetic regulatory effects across human tissues. *Science* **369**, 1318–1330 (2020).

18. 18.

Rokita, J. L. et al. Genomic profiling of childhood tumor patient-derived xenograft models to enable rational clinical trial design. *Cell Rep.* **29**, 1675–1689.e1679 (2019).

19. 19.

Kowalewski, D. J. & Stevanović, S. Biochemical large-scale identification of MHC class I ligands. *Methods Mol. Biol.* **960**, 145–157 (2013).

20. 20.

Bassani-Sternberg, M. et al. Direct identification of clinically relevant neoepitopes presented on native human melanoma tissue by mass spectrometry. *Nat. Commun.* **7**, 13404 (2016).

21. 21.

Ma, X. et al. Pan-cancer genome and transcriptome analyses of 1,699 paediatric leukaemias and solid tumours. *Nature* **555**, 371–376 (2018).

22. 22.

Freudenmann, L. K., Marcu, A. & Stevanović, S. Mapping the tumour human leukocyte antigen (HLA) ligandome by mass spectrometry. *Immunology* **154**, 331–345 (2018).

23. 23.

Raabe, E. H. et al. Prevalence and functional consequence of PHOX2B mutations in neuroblastoma. *Oncogene* **27**, 469 (2007).

24. 24.

Lee, N. H. et al. Clinical significance of tyrosine hydroxylase mRNA transcripts in peripheral blood at diagnosis in patients with neuroblastoma. *Cancer Res. Treat.* **48**, 1399–1407 (2016).

25. 25.

Marachelian, A. et al. Expression of five neuroblastoma genes in bone marrow or blood of patients with relapsed/refractory neuroblastoma provides a new biomarker for disease and prognosis. *Clin. Cancer Res.* **23**, 5374–5383 (2017).

26. 26.

Toor, J. S. et al. A recurrent mutation in anaplastic lymphoma kinase with distinct neoepitope conformations. *Front. Immunol.* **9**, 99 (2018).

27. 27.

Cardoso-Moreira, M. et al. Gene expression across mammalian organ development. *Nature* **571**, 505–509 (2019).

28. 28.

Pattyn, A., Morin, X., Cremer, H., Goridis, C. & Brunet, J.-F. The homeobox gene *Phox2b* is essential for the development of autonomic neural crest derivatives. *Nature* **399**, 366–370 (1999).

29. 29.

Wang, L. et al. ASCL1 is a MYCN- and LMO1-dependent member of the adrenergic neuroblastoma core regulatory circuitry. *Nat. Commun.* **10**, 5622 (2019).

30. 30.

Hata, J. L. et al. Diagnostic utility of PHOX2B in primary and treated neuroblastoma and in neuroblastoma metastatic to the bone marrow. *Arch. Pathol. Lab. Med.* **139**, 543–546 (2015).

31. 31.

Mosse, Y. P. et al. Germline PHOX2B mutation in hereditary neuroblastoma. *Am. J. Hum. Genet.* **75**, 727–730 (2004).

32. 32.

Dharia, N. V. et al. A first-generation pediatric cancer dependency map. *Nat. Genet.* **53**, 529–538 (2021).

33. 33.

Beasley, M. D., Niven, K. P., Winnall, W. R. & Kiefel, B. R. Bacterial cytoplasmic display platform retained display (ReD) identifies stable human germline antibody frameworks. *Biotechnol. J.* **10**, 783–789 (2015).

34. 34.

Kunert, A., Obenaus, M., Lamers, C. H. J., Blankenstein, T. & Debets, R. T-cell receptors for clinical therapy: in vitro assessment of toxicity risk. *Clin. Cancer Res.* **23**, 6012–6020 (2017).

35. 35.

Rudolph, M. G., Stanfield, R. L. & Wilson, I. A. How TCRs bind MHCs, peptides, and coreceptors. *Annu. Rev. Immunol.* **24**, 419–466 (2006).

36. 36.

Nerli, S. & Sgourakis, N. G. Structure-based modeling of SARS-CoV-2 peptide/HLA-A02 antigens. *Front. Med. Technol.*
<https://doi.org/10.3389/fmedt.2020.553478> (2020).

37. 37.

Asgharzadeh, S. et al. Clinical significance of tumor-associated inflammatory cells in metastatic neuroblastoma. *J. Clin. Oncol.* **30**, 3525–3532 (2012).

38. 38.

Douglass, J. et al. Bispecific antibodies targeting mutant RAS neoantigens. *Sci. Immunol.* **6**, eabd5515 (2021).

39. 39.

Hsiue, E. H.-C. et al. Targeting a neoantigen derived from a common *TP53* mutation. *Science*, eabc8697 (2021).

40. 40.

Perez-Riverol, Y. et al. The PRIDE database and related tools and resources in 2019: improving support for quantification data. *Nucleic Acids Res.* **47**, D442–D450 (2019).

41. 41.

Mi, H., Muruganujan, A., Ebert, D., Huang, X. & Thomas, P. D. PANTHER version 14: more genomes, a new PANTHER GO-slim and improvements in enrichment analysis tools. *Nucleic Acids Res.* **47**, D419–D426 (2019).

42. 42.

Nielsen, M. et al. Reliable prediction of T-cell epitopes using neural networks with novel sequence representations. *Protein Sci.* **12**, 1007–1017 (2003).

43. 43.

Reynisson, B., Alvarez, B., Paul, S., Peters, B. & Nielsen, M. NetMHCpan-4.1 and NetMHCIIpan-4.0: improved predictions of MHC antigen presentation by concurrent motif deconvolution and integration of MS MHC eluted ligand data. *Nucleic Acids Res.* **48**, W449–W454 (2020).

44. 44.

Sarkizova, S. et al. A large peptidome dataset improves HLA class I epitope prediction across most of the human population. *Nat. Biotechnol.* **38**, 199–209 (2020).

45. 45.

Zhu, Z. & Dimitrov, D. S. Construction of a large naive human phage-displayed Fab library through one-step cloning. *Methods Mol. Biol.* **525**, 129–142 (2009).

46. 46.

Zhang, M.Y. & Dimitrov, D. S. Sequential antigen panning for selection of broadly cross-reactive HIV-1-neutralizing human monoclonal antibodies. *Methods Mol. Biol.* **562**, 143–154 (2009).

47. 47.

Chen, W., Xiao, X., Wang, Y., Zhu, Z. & Dimitrov, D. S. Bifunctional fusion proteins of the human engineered antibody domain m36 with human soluble CD4 are potent inhibitors of diverse HIV-1 isolates. *Antiviral Res.* **88**, 107–115 (2010).

48. 48.

Shao, W., Caron, E., Pedrioli, P. & Aebersold, R. in *Bioinformatics for Cancer Immunotherapy: Methods and Protocols* (ed. Boegel, S.) 173–181 (Springer, 2020).

49. 49.

Overall, S. A. et al. High throughput pMHC-I tetramer library production using chaperone-mediated peptide exchange. *Nat. Commun.* **11**, 1909 (2020).

50. 50.

Dolton, G. et al. Optimized peptide–MHC multimer protocols for detection and isolation of autoimmune T-cells. *Front. Immunol.* **9**, 1378–1378 (2018).

51. 51.

Yang, S. et al. Development of optimal bicistronic lentiviral vectors facilitates high-level TCR gene expression and robust tumor cell recognition. *Gene Ther.* **15**, 1411–1423 (2008).

52. 52.

Canaday, D. H. Production of CD4⁺ and CD8⁺ T cell hybridomas. *Methods Mol. Biol.* **960**, 297–307 (2013).

53. 53.

Garboczi, D. N., Hung, D. T. & Wiley, D. C. HLA-A2–peptide complexes: refolding and crystallization of molecules expressed in *Escherichia coli* and complexed with single antigenic peptides. *Proc. Natl Acad. Sci. USA* **89**, 3429–3433 (1992).

54. 54.

Studier, F. W. Stable expression clones and auto-induction for protein production in *E. coli*. *Methods Mol. Biol.* **1091**, 17–32 (2014).

55. 55.

Winn, M. D. et al. Overview of the CCP4 suite and current developments. *Acta Crystallogr. D* **67**, 235–242 (2011).

56. 56.

McCoy, A. J. et al. Phaser crystallographic software. *J. Appl. Crystallogr.* **40**, 658–674 (2007).

57. 57.

Cole, D. K. et al. Hotspot autoimmune T cell receptor binding underlies pathogen and insulin peptide cross-reactivity. *J. Clin. Invest.* **126**, 2191–2204 (2016).

58. 58.

Shimizu, A. et al. Structure of TCR and antigen complexes at an immunodominant CTL epitope in HIV-1 infection. *Sci. Rep.* **3**, 3097 (2013).

59. 59.

Emsley, P. & Cowtan, K. Coot: model-building tools for molecular graphics. *Acta Crystallogr. D* **60**, 2126–2132 (2004).

60. 60.

Adams, P. D. et al. PHENIX: a comprehensive Python-based system for macromolecular structure solution. *Acta Crystallogr. D* **66**, 213–221 (2010).

61. 61.

Nerli, S. & Sgourakis, N. G. Structure-based modeling of SARS-CoV-2 peptide/HLA-A02 antigens. *Front. Med. Technol.*
<https://doi.org/10.3389/fmedt.2020.553478> (2020).

62. 62.

Maccari, G. et al. IPD-MHC 2.0: an improved inter-species database for the study of the major histocompatibility complex. *Nucleic Acids Res.* **45**, D860–D864 (2017).

63. 63.

Davis, I. W. et al. MolProbity: all-atom contacts and structure validation for proteins and nucleic acids. *Nucleic Acids Res.* **35**, W375–W383 (2007).

64. 64.

Andreatta, M., Lund, O. & Nielsen, M. Simultaneous alignment and clustering of peptide data using a Gibbs sampling approach. *Bioinformatics* **29**, 8–14 (2012).

65. 65.

Alvarez, B. et al. NNAlign_MA; MHC peptidome deconvolution for accurate MHC binding motif characterization and improved T-cell epitope predictions.

Mol. Cell Proteomics **18**, 2459–2477 (2019).

66. 66.

Sarkizova, S. et al. A large peptidome dataset improves HLA class I epitope prediction across most of the human population. *Nat. Biotechnol.* **38**, 199–209 (2020).

Acknowledgements

This work was supported by a St Baldrick's Foundation-Stand Up to Cancer Dream Team Translational Research Grant (SU2C-AACR-DT-27-17). The St. Baldrick's Foundation collaborates with Stand Up To Cancer. Research Grants are administered by the American Association for Cancer Research, the Scientific Partner of SU2C. Stand Up To Cancer is a program of the Entertainment Industry Foundation administered by the American Association for Cancer Research (J.M.M.). This work was also supported by NIH grants U54 CA232568 as part of the Beau Biden Cancer Moonshot Program (J.M.M.) and NIH R35 CA220500 (J.M.M.), R01 AI143997 (N.G.S.), R35 GM125034 (N.G.S), the Science Center Quod Erat Demonstrandum (QED) program at the Philadelphia Science Center (J.M.M. and M.Y.), the Children's Hospital of Philadelphia Cell and Gene Therapy Collaborative (J.M.M. and M.Y.), and the Giulio D'Angio Endowed Chair (J.M.M.). Diffraction data for protein crystallography were collected at the Advanced Light Source, which is supported by the Director, Office of Science, Office of Basic Energy Sciences, and U.S. Department of Energy, under contract DE-AC02-05CH11231. We thank D. Canaday, A. Wolpaw, E. Hooijberg and H. Goldstein for providing reagents. BioRender.com was used in generating figures.

Author information

Affiliations

1. Division of Oncology and Center for Childhood Cancer Research, Children's Hospital of Philadelphia, Philadelphia, PA, USA

Mark Yarmarkovich, Quinlen F. Marshall, John M. Warrington, Alvin Farrel, David Groff, Erin Runbeck, Hau Truong, Helena Shen, Tiffany Noel, Amber Weiner, Nathan Kendersky, Rebecca Weisberg, Molly Christie, Kristopher R. Bosse, Nikolaos G. Sgourakis & John M. Maris

2. Myrio Tx, Melbourne, Victoria, Australia

Rasika Premaratne, Nicole L. Church & Ben R. Kiefel

3. Department of Biomedical and Health Informatics, Children's Hospital of Philadelphia, Philadelphia, PA, USA

Alvin Farrel

4. University of Pittsburgh, Pittsburgh, PA, USA

Wei Li & Dimiter S. Dimitrov

5. University of Tübingen, Tübingen, Germany

Moreno di Marco & Stefan Stevanovic

6. Department of Chemistry and Biochemistry, University of California Santa Cruz, Santa Cruz, CA, USA

Jugmohit S. Toor & Sarvind Tripathi

7. Massachusetts Institute of Technology, Cambridge, MA, USA

Son Nguyen

8. Department of Pathology and Lab Medicine, Children's Hospital of Philadelphia, Philadelphia, PA, USA

Dan Martinez & Laurence Eisenlohr

9. Perelman School of Medicine at the University of Pennsylvania, Philadelphia, PA, USA

Kristopher R. Bosse & John M. Maris

Contributions

Conceptualization: M.Y. Methodology: M.Y., Q.F.M., J.W., H.S., T.N., E.R., M.d.M., D.M., K.R.B., H.T., L.E., S.T., S.N., A.W., R.W., M.C., D.M., S.S. and D.G.

Immunopeptidomics: M.Y. and M.d.M. scFv screening: R.P., N.L.C., W.L., D.S.D. and B.R.K. Algorithm development: M.Y. and A.F. X-ray crystallography: J.S.T., S.T. and M.Y. Structural modelling, H.T. and M.Y. Analysis: M.Y., Q.F.M., H.T., N.K. and J.M.M. Investigation: M.Y. and J.M.M. Funding acquisition: M.Y., N.G.S. and J.M.M.

Writing: M.Y. and J.M.M. Supervision: M.Y. and J.M.M.

Corresponding author

Correspondence to [John M. Maris](#).

Ethics declarations

Competing interests

J.M.M. and M.Y. have equity stake in Tantigen Bio Inc. and HuLA Therapeutics. Both companies have interest in commercializing technologies described herein. B.R.K. is an employee of and has equity interests in Myrio Therapeutics. R.P. and N.L.C. are employees of Myrio Therapeutics. J.M.M., M.Y. and B.R.K. are co-inventors on a patent filed regarding the PHOX2B PC-CAR.

Additional information

Peer review information *Nature* thanks Lélia Delamarre, Naomi Taylor and the other, anonymous, reviewer(s) for their contribution to the peer review of this work. Peer reviewer reports are available.

Publisher's note Springer Nature remains neutral with regard to jurisdictional claims in published maps and institutional affiliations.

Extended data figures and tables

[Extended Data Fig. 1 Prioritized peptides from immunopeptidome are highly differentially expressed in neuroblastoma.](#)

Differential expression between 153 neuroblastoma tumors from TARGET compared to 1643 normal tissues in GTEx, as described in Fig. [1e](#).

[Extended Data Fig. 2 Validation of antigens discovered by immunopeptidomics using LC/MS/MS of synthetic peptide.](#)

Peptide sequences imputed from immunopeptidomics spectra were synthesized and LC/MS/MS was under matched conditions. Synthetic peptides show complete concordance with tumor-eluted peptides across all b and y ions; masses highlighted in green represent detected peaks corresponding to matched b and y ions found in both tumor-eluted peptide spectra and synthetic peptide spectra.

Extended Data Fig. 3 Crystal structures solved for IGFBPL1 presented as three distinct peptides on HLA-A2.

Crystallographic analysis of IGFBPL1 peptide bound to HLA-A*02:01. a. X-ray structure of HLA-A*02:01 presenting the IGFBPL1 nonameric peptide (LLLPLLPPL), where yellow lines represent polar contacts between the HLA groove and peptide. b. Differential Scanning Fluorimetry (DSF) of HLA-A*02:01 refolded with IGFBPL1 peptides of different lengths. The legend indicates the sequence of the IGFBPL1 peptide and the corresponding melting temperature of the resulting peptide/MHC-I complexes. Mean of triplicate samples reported with error bars representing SD. c. Overlay of IGFBPL1 9mer, 11mer, and 12mer in MHC groove reveals that core peptides and anchor residues are maintained across peptides of varying length, and that additional amino acids in the 11mer and 12mer protrude at C terminus downstream of the L9 anchor position.

Extended Data Fig. 4 Tumor antigens derived from parent genes are under control of neuroblastoma core regulatory circuit.

a. Illustration of core-regulatory circuit in which transcription factors bind to one another's promoters, acting as feed-forward loop b. ChIP Seq data at prioritized neuroblastoma antigens parent gene loci are bound by each of the 7 core-regulatory circuit (CRC) proteins *MYCN*, *ASCL1*, *GATA3*, *HAND2*, *PHOX2B*, *ISL1*, and *TBX2*. All CRC binding sites are associated with a H3K27Ac super-enhancer element.

Extended Data Fig. 5 Properties of neuroblastoma immunopeptidome.

a. Logo plots of peptides eluted from HLA-A2 and HLA-A24 show canonical binding motifs for both alleles⁶⁴. b. Peptides detected by immunopeptidomics are enriched for highly expressed parent genes as compared to the entire cellular transcriptome. c. Gene ontology analysis of the parent genes of peptides of the neuroblastoma immunopeptidome compared to the cellular transcriptome. The most significantly enriched ontology groups are nucleic acid binding proteins (RNA binding protein ontology $p = 1.22e^{-25}$ and nucleic acid binding ontology $p = 9.47e^{-17}$; Fischer's Exact test).

Extended Data Fig. 6 Prioritized antigen parent genes are expressed during tissue development and downregulated in normal tissue after birth.

a-f. Temporal transcriptomic analysis of prioritized neuroblastoma target antigens reveals high expression during development and downregulation prior to birth in the

majority of target genes. Expression shown for each tissue from shown from 4 weeks post-conception to 58-63 years with birth marked by red arrows. PHOX2B (a), TH (b), IGFBPL1 (c), and CHRNA3 (d) exhibit developmentally restricted expression patterns. HMX1 (e) shows expression in testes post-birth. GFRA2 (f) expression in brain may make this target more amenable to targeting by antibody-based therapies that do not cross blood-brain barrier.

Extended Data Fig. 7 Neuroblastoma antigen processing, presentation, and immunogenicity.

a. Schematic of immunogenicity experiment. HLA-A2 neuroblastoma cells were either infected with H1N5 or pulsed with synthetic CEF1 peptide and co-cultured with M1 antigen-specific T cell hybridoma line. T cell activation was evaluated by IL-2 release. **b.** Viral titration of neuroblastoma cells using H1N5 influenza virus measured by FACS staining of viral nucleoprotein expression at 0-200 hemagglutination (HAU). **c.** Experimental schematic of assay: 1) HLA-A2 neuroblastoma cells are pulsed with 5 µM CEF1 peptide and co-cultured with M1 antigen-specific hybridoma and IL-2 release is measured by ELISA; 2) Neuroblastoma cells are infected with 50 HAU of H1N5, co-cultured with M1 antigen-specific hybridoma, measured by IL-2 secretion. Four of seven tested HLA-A*02:01 elicit T hybridoma response when pulsed with CEF1 peptide; three of seven lines induce a response when infected with H1N5 virus. n = 3 independent experiments, each performed in triplicate; plots show mean +/- SD. **d-e.** T hybridoma activation is not associated with HLA expression, but activation is lower in MYCN amplified tumors (MNA) as compared to non-amplified tumors (MNN). Created with BioRender.com.

Extended Data Fig. 8 Detection of tumor self-antigen specific CD8 T cells in normal donors.

a. Gating used to select CD8 T cells. Similar gating strategy was used to select live singlets for Jurkat and primary cells transduced with CAR constructs (without selection for CD3 and exclusion of CD14, CD19, and CD4). **b.** Four normal donors stained with IGFBPL1 dextramer on x-axis and GFRA2 on y-axis shows rare population of antigen-specific cells varying by donor and antigen (left panel showing unstained and right panel showing tetramer stained). **c.** Frequencies and MFIs of antigen specific cells across donors. **d.** Top constructs generated from normal donor-derived antigen-specific TCRs found by single-cell sequencing show range of antigen binding PHOX2B, TH, and IGFBPL1 as compared to DMF5 receptor targeting MART-1. Screening for antigen specific T cells in 3 donors reveals that PHOX2B TCRs have minimal target binding, suggesting that PHOX2B self-antigen is immunogenically silent and warrants targeting using synthetic scFv receptors.

Extended Data Fig. 9 Development of antigen-specific CARs for neuroblastoma antigens.

a. ELISA of PHOX2B scFv A7 using PHOX2B p/MHC and decoy peptide on HLA-A*24:02. **b.** Schematic of second-generation CAR constructs. **c.** A7 CAR transduced into primary CD8 cells binds PHOX2B dextramer but not HLA-A*02:01 dextramer. **d.** A7 CAR preferentially binds PHOX2B dextramer but cross-reacts with mismatched peptides PBK and CHRNA3 on HLA-A*24:02 at high affinity. **e.** A7 CAR potently kills HLA-A*24:02 neuroblastoma lines, but also kills HLA⁺/antigen⁻ tumor cells. **f.** Tetramer and dextramer gating strategy for pMHC staining.

Extended Data Fig. 10 PHOX2B A7 CAR.

a. SKNAS tumor cells co-cultured with A7 CAR shows potent killing. SKNAS cells plated on day 0 (top), non-targeting CAR (left) and A7 CAR (right) added after 18 h; measuring tumor confluence (green) and cleaved caspase (red) on day 2 (bottom) shows tumor outgrowth with non-specific CAR and killing of all tumor cells with A7 CAR. Representative images shown from experiment repeated three times using n = 3 replicates in each experiment. **b.** PHOX2B is expressed in neuroblastoma cell lines (SKNAS, SKNFI, and NBSD), and not in HLA-matched controls (SW620, KATO III, and HEPG2). PHOX2B is expressed in SW620 cells transduced with full-length PHOX2B. For gel source data from single experiment, see Supplementary Fig. 1.

Extended Data Fig. 11 Saturation mutagenesis of A7 construct resulted in single-antigen-specific population.

a-b. Cross-reactive binding to mismatched HLA-A24 peptides. Flow cytometry of Jurkat cells transduced with A7 CAR stained with PHOX2B dextramer on x-axis and mismatched PBK peptide on HLA-A*24:02 on y-axis. **c.** Saturation mutagenesis was performed on CDR loops 1-3 of the heavy chain. Each pool of mutants was stained with target pMHC and counter-stained with mismatched pMHC. Contribution of each CDR binding loop (mutagens labeled CDR loop # - position #) to binding HLA-A*24:02 is shown (green: no contribution to binding; red: significant HLA binding at specific amino acid). Contribution of each position to HLA binding was calculated as follows: $(MFI_{target(mut)} / MFI_{mismatch(mut)}) / (MFI_{target(WT)} / MFI_{mismatch(WT)})$. **d.** Mutations of A7 CAR at CDR3 positions 2 and 3 result in 12.4x and 4.7x shifts towards single specificity, respectively. Double mutation of D3A and R2A resulted in modified A7 CAR with no MHC cross-reactivity and reduced binding to target. Created with BioRender.com.

Extended Data Fig. 12 sCRAP cross-reactivity algorithm.

a. Cross-reactivity algorithm was developed to identify peptides presented on normal tissue with similar biophysical properties to tumor antigens such as to pre-emptively predict cross-reactivities and screen for specificity. **b.** Illustration of peptide scoring system described in methods. **c.** Schematic of algorithm workflow describing how tumor peptides are scored against each peptide predicted to be presented from the normal proteome (totaling 92.4×10^6 potential MHC peptides). Binding affinity is predicted for each normal peptide and maximum gene expression of parent gene are factored into the overall score of each peptide. Peptides are referenced against a normal tissue immunopeptidomics database. Created with BioRender.com.

[Extended Data Fig. 13 pMHC Cross-Reactivity Algorithm sCRAP Predicts MAGE-A3 toxicity through TITIN.](#)

a. Table of top predicted cross-reactive peptides to MAGE-A3 peptide EVDPIGHLY reveals cross-reactivity with Titin peptide ESDPIVAQY ranks 4th out of 1,143,861 potential peptides presented on HLA-A*01:01. **b.** TITIN is highly expressed in GTEx RNA-sequencing of heart (n = 108) and muscle (n = 138) tissues.

[Extended Data Fig 14 Cross-HLA recognition of PHOX2B peptide.](#)

a. Schematic of hypothesis proposing that PHOX2B peptide QYNPIRTTF detected by immunopeptidomics can be presented by additional HLA alleles after undergoing a common antigen processing pathway. **b.** Population-scale presentation across the length of the PHOX2B protein (all potential 9mers on x-axis) generated by ShinyNAP⁸ predicts PHOX2B peptide QYNPIRTTF to be presented by an additional 8 HLA alleles in addition to HLA-A*24:02. Additionally, QYNPIRTTF was found to bind additional common HLA alleles HLA-C*07:01, HLA-C*06:02, HLA-A*29:02, and HLA-A*32:01 using NetMHCPan 4.1⁶⁵ and also predicted by HLATHENA⁶⁶. **c.** Size exclusion chromatography of PHOX2B peptide QYNPIRTTF refolded with HLA-A*23:01, HLA-B*14:0, and HLA-C*07:02 shows formation of stable pMHC complex with each allotype. **d.** PC-CAR 10LH binds PHOX2B on HLA-A*23:01 demonstrates higher binding than 302LH, in concordance with observed *in vivo* activity (Fig. 4g). **e.** 10LH CAR kills HLA-A*23:01/PHOX2B⁻ WM873 cells when pulsed with PHOX2B peptide but not with CHRNA3 peptide n = 2 technical replicates; reported as mean +/- SD. **f.** Matched peptide search identifies unfragmented peaks in additional neuroblastoma tumors (NBSD shown). Unfragmented NBSD peaks are within 0.006 Da m/z of peaks in which PHOX2B peptide QYNPIRTTF was identified by MS/MS in other samples and eluted within one minute of fragmented peaks. While validated MS/MS peaks were found in 2/8 PDX tumors and 2/8 primary tumors, peaks with m/z and retention times matched to validated QYNPIRTTF peaks were identified in 6/8 PDX tumors and 7/8 primary tumors. Created with BioRender.com.

Extended Data Fig. 15 a. Tetramerized 10LH binds to PHOX2B pMHC.

Pulsing SW620 HLA-A*24:02 with 50µM PHOX2B peptide results in 10LH tetrabody binding. **b.** CARs predicted to be cross-reactive show killing in HLA-matched cells. CARs 320LH and 280LH predicted to cross-react with peptides presented on normal tissue demonstrate significant cross-reactivity in HLA-matched SW620 cells. Representative images shown from n = 3 technical replicates.

Extended Data Fig. 16 Immunohistochemistry of tumors collected from mice exceeding tumor burden.

COG-564x tumor-bearing mice treated with 10LH and 302LH PC-CARs show T cell infiltration as measured by CD3, co-localized with loss of PHOX2B target expression and tissue necrosis. No evidence of T cell infiltration observed in mice treated with untransduced T cells. Tumors were collected from one of each mouse in treatment arms reaching tumor burden 11 days after receiving T cells. All other mice in treatment arms went on to achieve complete responses. Images shown from tumors collected from lone mice reaching tumor burden each study arm in single experiment.

Extended Data Fig. 17 PC-CARs result in tumor ablation in mice engrafted with patient-derived xenografts.

a. Tumor regression in individual mice in vivo treated with PC-CARs (n = 6; source data provided in Supplementary Table 3). **b.** COG-564x tumors collected from 302LH PC-CAR-treated mice collected at when mice reached tumor burden on day 11 (left) and endpoint of study on day 38 (right). Though tumors are detectable at endpoint, H&E and PHOX2B staining of 302LH PC-CAR-treated tumors reveals entirely necrotic tissue by endpoint of the study. Single available tumor collected from mouse reaching tumor burden for D11 and single endpoint tumor in one experiment collected for immunohistochemistry shown.

Extended Data Table 1 Antigen discovery strategies in neuroblastoma

Supplementary information

Supplementary Figure 1

The original source images for all data obtained by immunoblotting that show the uncropped form of the gels shown in Extended Data Fig. 10. Gels are labelled according to loading control (Ku80) or experimental samples (PHOX2B).

Reporting Summary

Peer Review File

Supplementary Table 1

Immunopeptidomics data for neuroblastoma PDX/CDX and primary patient tumours. LC/MS/MS proteomics for HLA class I peptides eluted from eight PDX/CDX and eight primary patient tumours using 1% FDR. Peptides are annotated by source protein/gene, tumour line, best predicted HLA binder based on patient HLA class I allotype and predicted binding affinity/rank.

Supplementary Table 2

Annotation of raw sample files uploaded on PRIDE
(<https://www.ebi.ac.uk/pride/archive/projects/PXD027182>).

Supplementary Table 3

Source data for mouse tumour measurements shown in Fig. 4g and Extended Data Fig. 17.

Supplementary Video 1

10LH CAR induces specific killing in SKNAS HLA-A*24:02 PHOX2B⁺ neuroblastoma cells at 5:1 E:T ratio. Cytotoxicity visualized by T cell clustering and cleaved caspase.

Supplementary Video 2

10LH CAR induces no killing in SW620 HLA-A*24:02 PHOX2B⁻ cells expressing at 5:1 E:T ratio. Cytotoxicity visualized by T cell clustering and cleaved caspase.

Rights and permissions

Open Access This article is licensed under a Creative Commons Attribution 4.0 International License, which permits use, sharing, adaptation, distribution and reproduction in any medium or format, as long as you give appropriate credit to the original author(s) and the source, provide a link to the Creative Commons license, and indicate if changes were made. The images or other third party material in this article are included in the article's Creative Commons license, unless indicated otherwise in a

credit line to the material. If material is not included in the article's Creative Commons license and your intended use is not permitted by statutory regulation or exceeds the permitted use, you will need to obtain permission directly from the copyright holder. To view a copy of this license, visit <http://creativecommons.org/licenses/by/4.0/>.

[Reprints and Permissions](#)

About this article

Cite this article

Yarmarkovich, M., Marshall, Q.F., Warrington, J.M. *et al.* Cross-HLA targeting of intracellular oncoproteins with peptide-centric CARs. *Nature* **599**, 477–484 (2021). <https://doi.org/10.1038/s41586-021-04061-6>

- Received: 20 April 2021
- Accepted: 23 September 2021
- Published: 03 November 2021
- Issue Date: 18 November 2021
- DOI: <https://doi.org/10.1038/s41586-021-04061-6>

Share this article

Anyone you share the following link with will be able to read this content:

[Get shareable link](#)

Sorry, a shareable link is not currently available for this article.

[Copy to clipboard](#)

Provided by the Springer Nature SharedIt content-sharing initiative

This article was downloaded by **calibre** from <https://www.nature.com/articles/s41586-021-04061-6>

- Article
- [Published: 10 November 2021](#)

Dietary palmitic acid promotes a prometastatic memory via Schwann cells

- [Gloria Pascual](#) [ORCID: orcid.org/0000-0003-3810-6647¹](#), [na1](#),
- [Diana Domínguez¹](#), [na1](#),
- [Marc Elosúa-Bayes](#) [ORCID: orcid.org/0000-0002-3742-8161²](#),
- [Felipe Beckedorff](#) [ORCID: orcid.org/0000-0001-6735-6851³](#),
- [Carmelo Laudanna](#) [ORCID: orcid.org/0000-0001-8045-320X¹](#),
- [Claudia Bigas¹](#),
- [Delphine Douillet⁴](#),
- [Carolina Greco⁵](#),
- [Aikaterini Symeonidi¹](#),
- [Inmaculada Hernández^{1,2}](#),
- [Sara Ruiz Gil²](#),
- [Neus Prats¹](#),
- [Coro Bescós](#) [ORCID: orcid.org/0000-0002-3865-3037⁶](#),
- [Ramin Shiekhattar³](#),
- [Moran Amit⁷](#),
- [Holger Heyn](#) [ORCID: orcid.org/0000-0002-3276-1889²](#),
- [Ali Shilatifard](#) [ORCID: orcid.org/0000-0002-7490-2854⁴](#) &
- [Salvador Aznar Benitah](#) [ORCID: orcid.org/0000-0002-9059-5049^{1,8}](#)

[Nature](#) volume 599, pages 485–490 (2021)

- 11k Accesses

- 1395 Altmetric
- [Metrics details](#)

Subjects

- [Cancer](#)
- [Metastasis](#)
- [Tumour heterogeneity](#)

Abstract

Fatty acid uptake and altered metabolism constitute hallmarks of metastasis^{1,2}, yet evidence of the underlying biology, as well as whether all dietary fatty acids are prometastatic, is lacking. Here we show that dietary palmitic acid (PA), but not oleic acid or linoleic acid, promotes metastasis in oral carcinomas and melanoma in mice. Tumours from mice that were fed a short-term palm-oil-rich diet (PA), or tumour cells that were briefly exposed to PA in vitro, remained highly metastatic even after being serially transplanted (without further exposure to high levels of PA). This PA-induced prometastatic memory requires the fatty acid transporter CD36 and is associated with the stable deposition of histone H3 lysine 4 trimethylation by the methyltransferase Set1A (as part of the COMPASS complex (Set1A/COMPASS)). Bulk, single-cell and positional RNA-sequencing analyses indicate that genes with this prometastatic memory predominantly relate to a neural signature that stimulates intratumoural Schwann cells and innervation, two parameters that are strongly correlated with metastasis but are aetiologically poorly understood^{3,4}. Mechanistically, tumour-associated Schwann cells secrete a specialized proregenerative extracellular matrix, the ablation of which inhibits metastasis initiation. Both the PA-induced memory of this proneural signature and its long-term boost in metastasis require the transcription factor EGR2 and the glial-cell-stimulating peptide galanin. In summary, we provide evidence that a dietary metabolite induces stable transcriptional and chromatin changes that lead to a long-term stimulation of metastasis, and that this is related to a proregenerative state of tumour-activated Schwann cells.

Access options

Subscribe to Journal

Get full journal access for 1 year

\$199.00

only \$3.90 per issue

[Subscribe](#)

All prices are NET prices.

VAT will be added later in the checkout.

Tax calculation will be finalised during checkout.

Rent or Buy article

Get time limited or full article access on ReadCube.

from \$8.99

[Rent or Buy](#)

All prices are NET prices.

Additional access options:

- [Log in](#)
- [Access through your institution](#)
- [Learn about institutional subscriptions](#)

Fig. 1: OSCC metastatic cells are selectively sensitive to PA and display a metastatic memory.

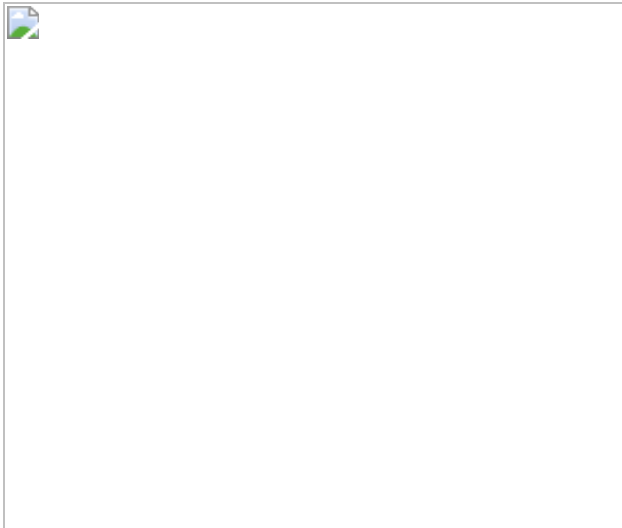


Fig. 2: PA induces stable H3K4me3 chromatin changes in OSCC cells.

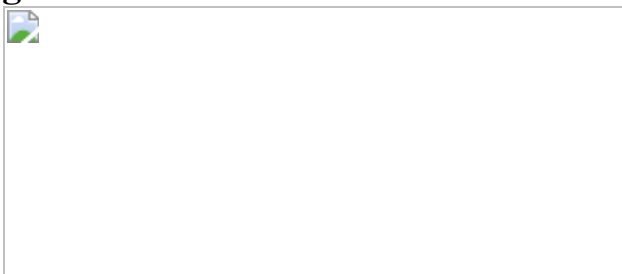


Fig. 3: EGR2 and galanin regulate the palm-oil-diet-induced pro-metastatic memory related to tumour innervation.

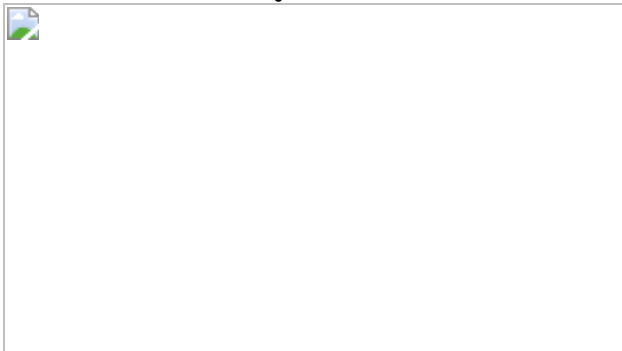
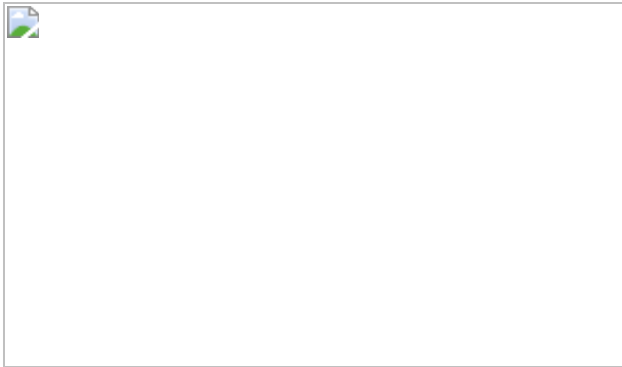


Fig. 4: Tumour cells with a PA-induced metastatic memory display tumour-associated Schwann cell ECM components that can be targeted.



Data availability

All raw data from gene expression RNA microarrays, ChIP-seq, RNA-seq, scRNA-seq, PRO-seq and spatial transcriptomics are available at the Gene Expression Omnibus (GEO) repository under accession code [GSE148321](#). [Source data](#) are provided with this paper.

Code availability

R v.4.0.1 and Python v.3.6.0 were used. All of the code used to analyse the single-cell and positional RNA-seq data are available at GitHub (<https://github.com/MarcElosua/10X-EPID>).

References

1. 1.

Peck, B. & Schulze, A. lipid metabolism at the nexus of diet and tumor microenvironment. *Trends Cancer* **5**, 693–703 (2019).

2. 2.

Pascual, G., Domínguez, D. & Benitah, S. A. The contributions of cancer cell metabolism to metastasis. *Dis. Model. Mech.* **11**, dmm032920 (2018).

3. 3.

Boilly, B., Faulkner, S., Jobling, P. & Hondermarck, H. Nerve dependence: from regeneration to cancer. *Cancer Cell* **31**, 342–354 (2017).

4. 4.

Zahalka, A. H. & Frenette, P. S. Nerves in cancer. *Nat. Rev. Cancer* **20**, 143–157 (2020).

5. 5.

Solans, M., Chan, D. S. M., Mitrou, P., Norat, T. & Romaguera, D. A systematic review and meta-analysis of the 2007 WCRF/AICR score in relation to cancer-related health outcomes. *Ann. Oncol.* **31**, 352–368 (2020).

6. 6.

Pascual, G. et al. Targeting metastasis-initiating cells through the fatty acid receptor CD36. *Nature* **541**, 41–45 (2017).

7. 7.

Lee, C. et al. Tumor metastasis to lymph nodes requires YAP-dependent metabolic adaptation. *Science* **363**, 644–649 (2019).

8. 8.

Rambow, F. et al. Toward minimal residual disease-directed therapy in melanoma. *Cell* **174**, 843–855 (2018).

9. 9.

Haobin, Ye et al. Leukemic stem cells evade chemotherapy by metabolic adaptation to an adipose tissue niche. *Cell Stem Cell* **19**, 23–37.

10. 10.

Abdelmagid, S. A. et al. Comprehensive profiling of plasma fatty acid concentrations in young healthy Canadian adults. *PLoS ONE* **10**, e0116195 (2015).

11. 11.

Feng, R. et al. Free fatty acids profile among lean, overweight and obese non-alcoholic fatty liver disease patients: a case—control study. *Lipids Health Dis.* **16**, 165 (2017).

12. 12.

Nyanbol, Kuol et al. Role of the nervous system in cancer metastasis. *J. Exp. Clin. Cancer Res.* **37**, 5 (2018).

13. 13.

Wang, W. et al. Nerves in the tumour microenvironment: origin and effects. *Front. Cell Dev. Biol.* **8**, 1630 (2020).

14. 14.

Venkatesh, H. S. et al. Electrical and synaptic integration of glioma into neural circuits. *Nature* **573**, 539–545 (2019).

15. 15.

Amit, M. et al. Loss of p53 drives neuron reprogramming in head and neck cancer. *Nature* **578**, 449–454 (2020).

16. 16.

Venkataramani, V. et al. Glutamatergic synaptic input to glioma cells drives brain tumour progression. *Nature* **573**, 532–538 (2019).

17. 17.

Ubink, R., Calza, L. & Hökfelt, T. ‘Neuro’-peptides in glia: Focus on NPY and galanin. *Trends Neurosci.* **26**, 604–609 (2003).

18. 18.

Gresle, M. M. et al. Galanin is an autocrine myelin and oligodendrocyte trophic signal induced by leukemia inhibitory factor. *Glia* **63**, 1005–1020 (2015).

19. 19.

Avgustinova, A. & Benitah, S. A. The epigenetics of tumour initiation: cancer stem cells and their chromatin. *Curr. Opin. Genet. Dev.* **36**, 8–15 (2016).

20. 20.

Schuettengruber, B., Bourbon, H.-M., Di Croce, L. & Cavalli, G. Genome regulation by polycomb and trithorax: 70 years and counting. *Cell* **171**, 34–57 (2017).

21. 21.

Fawcett, J. W., Oohashi, T. & Pizzorusso, T. The roles of perineuronal nets and the perinodal extracellular matrix in neuronal function. *Nat. Rev. Neurosci.* **20**, 451–465 (2019)

22. 22.

Quraishi, S., Forbes, L. H. & Andrews, M. R. The extracellular environment of the CNS: influence on plasticity, sprouting, and axonal regeneration after spinal cord injury. *Neural Plast.* **2018**, 2952386 (2018).

23. 23.

Dzyubenko, E., Gottschling, C. & Faissner, A. Neuron-glia interactions in neural plasticity: contributions of neural extracellular matrix and perineuronal nets. *Neural Plast.* **2016**, 5214961 (2016).

24. 24.

Bartus, K. et al. Large-scale chondroitin sulfate proteoglycan digestion with chondroitinase gene therapy leads to reduced pathology and modulates macrophage phenotype following spinal cord contusion injury. *J. Neurosci.* **34**, 4822–4836 (2014).

25. 25.

McDonald, O. G. et al. Epigenomic reprogramming during pancreatic cancer progression links anabolic glucose metabolism to distant metastasis. *Nat. Genet.* **49**, 367–376 (2017).

26. 26.

Shi, X. et al. The abundance of metabolites related to protein methylation correlates with the metastatic capacity of human melanoma xenografts. *Sci. Adv.* **3**, 11 (2017).

27. 27.

Clements, M. P. et al. The wound microenvironment reprograms Schwann cells to invasive mesenchymal-like cells to drive peripheral nerve regeneration. *Neuron* **96**, 98–114 (2017).

28. 28.

Johnston, A. et al. Dedifferentiated Schwann cell precursors secreting paracrine factors are required for regeneration of the mammalian digit tip. *Stem Cell* **19**, 433–448 (2016).

29. 29.

Ana-Maria, E. et al. Targeting CD36 as biomarker for metastasis prognostic: how far from translation into clinical practice? *BioMed Res. Int.* **2018**, 7801202 (2018).

30. 30.

Gabriele, B. & Sarah-Maria, F. The metabolism of cancer cells during metastasis. *Nat. Rev. Cancer* **21**, 162–180 (2021).

31. 31.

Sundaresan, S. & Abumrad, N. A. Dietary lipids inform the gut and brain about meal arrival via CD36-mediated signal transduction. *J. Nutr.* **145**, 2195–2200 (2015).

32. 32.

Wang, L. et al. A cytoplasmic COMPASS is necessary for cell survival and triple-negative breast cancer pathogenesis by regulating metabolism. *Genes Dev.* **31**, 2056–2066 (2017).

33. 33.

Bledau, A. S. et al. The H3K4 methyltransferase Setd1a is first required at the epiblast stage, whereas Setd1b becomes essential after gastrulation. *Development* **141**, 1022–1035 (2014).

34. 34.

Liu, D., Archer, N., Duesing, K., Hannan, G. & Keast, R. Mechanism of fat taste perception: association with diet and obesity. *Prog. Lipid Res.* **63**, 41–49 (2016).

35. 35.

Yang, P. et al. Dietary oleic acid-induced CD36 promotes cervical cancer cell growth and metastasis via up-regulation Src/ERK pathway. *Cancer Lett.* **438**, 76–85 (2018).

36. 36.

Ubellacker, J. M. et al. Lymph protects metastasizing melanoma cells from ferroptosis. *Nature* **585**, 113–118 (2020).

37. 37.

Vriens, K. et al. Evidence for an alternative fatty acid desaturation pathway increasing cancer plasticity. *Nature* **566**, 403–406 (2019).

38. 38.

Myers, J. N., Holsinger, F. C., Jasser, S. A., Bekele, B. N. & Fidler, I. J. An orthotopic nude mouse model of oral tongue squamous cell carcinoma. *Clin. Cancer Res.* **8**, 293–298 (2002).

39. 39.

Benaich, N. et al. Rewiring of an epithelial differentiation factor, miR-203, to inhibit human squamous cell carcinoma metastasis. *Cell Rep.* **9**, 104–117 (2014).

40. 40.

Schneider, T. E. et al. Measuring stem cell frequency in epidermis: a quantitative in vivo functional assay for long-term repopulating cells. *Proc. Natl Acad. Sci. USA* **100**, 11412–11417 (2003).

41. 41.

Shwartz, Y. et al. Cell types promoting goosebumps form a niche to regulate hair follicle stem cells. *Cell* **182**, 578–593, (2021).

42. 42.

Bhandari, M. et al. Galanin receptor antagonist M35 but not M40 or C7 ameliorates cerulein-induced acute pancreatitis in mice. *Pancreatology* **10**, 682–688 (2011).

43. 43.

Zuber, J. et al. Mouse models of human AML accurately predict chemotherapy response. *Genes Dev.* **23**, 877–889 (2009).

44. 44.

Nowak, J. A. & Fuchs, E. Isolation and culture of epithelial stem cells. *Methods Mol. Biol.* **482**, 215–232 (2009).

45. 45.

Wolock, S. L., Lopez, R. & Klein, A. M. Scrublet: computational identification of cell doublets in single-cell transcriptomic data. *Cell Syst.* **8**, 281–291 (2019).

46. 46.

Hao, Y. et al. Integrated analysis of multimodal single-cell data. *Cell* **184**, 3573–3587 (2021).

47. 47.

Hafemeister, C. & Satija, R. Normalization and variance stabilization of single-cell RNA-seq data using regularized negative binomial regression. *Genome Biol.* **20**, 296 (2019).

48. 48.

Korsunsky, I. et al. Fast, sensitive and accurate integration of single-cell data with Harmony. *Nat. Methods* **16**, 1289–1296 (2019).

49. 49.

Soneson, C. & Robinson, M. D. Bias, robustness and scalability in single-cell differential expression analysis. *Nat. Methods* **15**, 255–261 (2018).

50. 50.

Elosua-Bayes, M., Nieto, P., Mereu, E., Gut, I. & Heyn, H. SPOTlight: seeded NMF regression to deconvolute spatial transcriptomics spots with single-cell transcriptomes. *Nucleic Acids Res.* **49**, e50 (2021).

51. 51.

Bolger, A. M., Lohse, M. & Usadel, B. Trimmomatic: a flexible trimmer for Illumina sequence data. *Bioinformatics* **30**, 2114–2120 (2014).

52. 52.

Li, H. & Durbin, R. Fast and accurate short read alignment with Burrows-Wheeler transform. *Bioinformatics* **25**, 1754–1760 (2009).

53. 53.

Li, H. et al. The Sequence Alignment/Map (SAM) Format and SAMtools. *Bioinformatics* **25**, 2078–2079 (2009).

54. 54.

Zhang, Y. et al. Model-based analysis of ChIP-Seq (MACS). *Genome Biol.* **9**, R137 (2008).

55. 55.

Heinz, S. et al. Simple combinations of lineage-determining transcription factors prime *cis*-regulatory elements required for macrophage and B cell identities. *Mol. Cell* **38**, 576–589 (2010).

56. 56.

R Core Team *R: A Language and Environment for Statistical Computing* (R Foundation for Statistical Computing, 2018);
<http://www.R-project.org/>

57. 57.

Stark, R. & Brown, G. DiffBind: differential binding ChIP-seq peak data. *Bioconductor* 1–27 (2011).

58. 58.

Yu, G., Wang, L. G. & He, Q. Y. ChIP seeker: An R/Bioconductor package for ChIP peak annotation, comparison and visualization. *Bioinformatics* **31**, 2382–2383 (2015).

59. 59.

Chen, E. Y. et al. Enrichr: interactive and collaborative HTML5 gene list enrichment analysis tool. *BMC Bioinform.* **14**, 128 (2013).

60. 60.

Robinson, J. T. et al. Integrative genomics viewer. *Nat. Biotechnol.* **29**, 24–26 (2011).

61. 61.

Douillet, D. et al. Uncoupling histone H3K4 trimethylation from developmental gene expression via an equilibrium of COMPASS, Polycomb and DNA methylation. *Nat. Genet.*
<https://doi.org/10.1038/s41588-020-0618-1> (2020).

62. 62.

Picelli, S. et al. Smart-seq2 for sensitive full-length transcriptome profiling in single cells. *Nat. Methods* **10**, 1096–1100 (2013).

63. 63.

Butler, A., Hoffman, P., Smibert, P., Papalexi, E. & Satija, R. Integrating single-cell transcriptomic data across different conditions, technologies, and species. *Nat. Biotechnol.* **36**, 411–420 (2018).

64. 64.

Trapnell, C. et al. The dynamics and regulators of cell fate decisions are revealed by pseudotemporal ordering of single cells. *Nat. Biotechnol.* **32**, 381–386 (2014).

65. 65.

Gonzalez-Roca, E. et al. Accurate expression profiling of very small cell populations. *PLoS ONE* **5**, e14418 (2010).

66. 66.

Irizarry, R. A. et al. Exploration, normalization, and summaries of high density oligonucleotide array probe level data. *Biostatistics*, **4**, 249–264 (2003).

67. 67.

Chenj, J. et al. ToppGene Suite for gene list enrichment analysis and candidate genes for prioritization. *Nucleic Acid Res.* **37**, W305–W311 (2009).

68. 68.

Berriz, G. F., King, O. D., Bryant, B., Sander, C. & Roth, F. P. Characterizing gene sets with FuncAssociate. *Bioinformatics* **19**, 2502–2504 (2003).

69. 69.

Subramanian, A. et al. Gene set enrichment analysis: a knowledge-based approach for interpreting genome-wide expression profiles. *Proc. Natl Acad. Sci. USA* **102**, 15545–15550 (2005).

70. 70.

Dougherty, J. D. et al. Analytical approaches to RNA profiling data for the identification of genes enriched in specific cells. *Nucleic Acids Res.* **38**, 4218–4230 (2010).

71. 71.

Xu, X. et al. Cell type-specific expression analysis to identify putative cellular mechanisms for neurogenetic disorders. *J. Neurosci.* **34**, 1420–1431 (2014).

72. 72.

Shannon, P. et al. Cytoscape: a software environment for integrated models of biomolecular interaction networks. *Genome Res.* **13**, 2498–2504 (2003).

73. 73.

Zambelli, F. et al. Pscan: finding over-represented transcription factor binding site motifs in sequences from co-regulated or co-expressed genes. *Nucleic Acids Res.* **37**, W247–W252 (2009).

74. 74.

Nagy, A. et al. Validation of miRNA prognostic power in hepatocellular carcinoma using expression data of independent datasets. *Sci. Rep.* **8**, 11515 (2018).

75. 75.

R Core Team *R: A Language and Environment for Statistical Computing* (R Foundation for Statistical Computing, 2008).

76. 76.

Gentleman, R. C. et al. Bioconductor: open software development for computational biology and bioinformatics. *Genome Biol.* **5**, R80 (2004).

77. 77.

Gautier, L., Cope, L., Bolstad, B. M. & Irizarry, R. A., affy—analysis of Affymetrix GeneChip data at the probe level. *Bioinformatics* **20**, 307–315 (2004).

78. 78.

Bolstad, B. M. et al. in *Bioinformatics and Computational Biology Solutions Using R and Bioconductor. Statistics for Biology and Health* (eds Gentleman R. et al.) 33–47 (Springer, 2005).

79. 79.

Eklund, A. C. & Szallasi, Z. Correction of technical bias in clinical microarray data improves concordance with known biological

information. *Genome Biol.* **9**, R26 (2008).

80. 80.

Smyth, G. in *Bioinformatics and Computational Biology Solutions Using R and Bioconductor. Statistics for Biology and Health* (eds Gentleman R. et al.) 397–420 (Springer, 2005).

81. 81.

Benjamini, Y. H. Y. Controlling the false discovery rate: a practical and powerful approach to multiple testing. *J. R. Stat. Soc. B* **57**, 289–300 (1995).

82. 82.

Wu, D. et al. ROAST: rotation gene set tests for complex microarray experiments. *Bioinformatics* **26**, 2176–2182 (2010).

83. 83.

B., Efron, & R., Tibshirani, On testing the significance of sets of genes. *Ann. Appl. Stat.* **1**, 107–129 (2007).

84. 84.

Goeman, J. J., & Bühlmann, P. Analyzing gene expression data in terms of gene sets: methodological issues. *Bioinformatics* **23**, 980–987 (2007).

85. 85.

Ashburner, M. et al. Gene Ontology: tool for the unification of biology. *Nat. Genet.* **25**, 25–29 (2000).

86. 86.

Carlson M. org.Hs.eg.db: genome wide annotation for Human. R package version 3.8.2. (2019).

87. 87.

Carlson M. org.Mm.eg.db: genome wide annotation for Mouse. R package version 3.8.2. (2019).

Acknowledgements

We thank the staff at the histology and genomics facilities of the IRB Barcelona for their assistance in this work; and V. Raker for manuscript editing. Research in the S.A.B. laboratory is supported in part by the European Research Council (ERC) under the European Union's Horizon 2020 research and innovation programme (grant agreement no. 787041), the Government of Cataluña (SGR grant), the Government of Spain (MINECO), the La Marató/TV3 Foundation, the Foundation Lilliane Bettencourt, the Spanish Association for Cancer Research (AECC), the Worldwide Cancer Research Foundation (WCRF) and the BBVA Foundation. D. Domínguez was supported by a La Caixa International Fellowship for Doctoral studies; C. Bigas by an FPI fellowship (MINECO); and I.H. by the EU Horizon 2020 Marie Skłodowska-Curie award (no. 754510). H.H. has received funding from the Ministerio de Ciencia, Innovación y Universidades (SAF2017-89109-P; AEI/FEDER, UE). Studies in A. Shilatifard laboratory related to COMPASS are supported by NCI's Outstanding Investigator Award R35CA197569; other research, by funding from University of Miami Miller School of Medicine, Sylvester Comprehensive Cancer Center, grant R01 GM078455 and DP1 CA228041 from the National Institute of Health (to R.S.), and the National Cancer Institute of the National Institutes of Health (no. P30CA240139; note that the content is solely the responsibility of the authors and does not necessarily represent the official views of the National Institutes of Health). The IRB Barcelona is a Severo Ochoa Center of Excellence (MINECO award SEV-2015-0505).

Author information

Author notes

1. These authors contributed equally: Gloria Pascual, Diana Domínguez

Affiliations

1. Institute for Research in Biomedicine (IRB Barcelona), The Barcelona Institute of Science and Technology (BIST), Barcelona, Spain

Gloria Pascual, Diana Domínguez, Carmelo Laudanna, Claudia Bigas, Aikaterini Symeonidi, Inmaculada Hernández, Neus Prats & Salvador Aznar Benitah

2. CNAG-CRG, Centre for Genomic Regulation (CRG), Barcelona Institute of Science and Technology (BIST), Barcelona, Spain

Marc Elosúa-Bayes, Inmaculada Hernández, Sara Ruiz Gil & Holger Heyn

3. Sylvester Comprehensive Cancer Center, University of Miami Miller School of Medicine, Miami, FL, USA

Felipe Beckedorff & Ramin Shiekhattar

4. Department of Biochemistry and Molecular Genetics and Simpson Querrey Center for Epigenetics, Northwestern University Feinberg School of Medicine, Chicago, IL, USA

Delphine Douillet & Ali Shilatifard

5. Center for Epigenetics and Metabolism, Department of Biological Chemistry, University of California, Irvine, CA, USA

Carolina Greco

6. Department of Oral and Maxillofacial Surgery, Vall D'Hebron Hospital, Barcelona, Universitat Autònoma de Barcelona, Barcelona, Spain

Coro Bescós

7. Department of Head and Neck Surgery, The University of Texas MD Anderson Cancer Center, Houston, TX, USA

Moran Amit

8. ICREA, Catalan Institution for Research and Advanced Studies, Barcelona, Spain

Salvador Aznar Benitah

Contributions

G.P., D. Domínguez and S.A.B. designed the study. C.G. helped to design some of the experiments. G.P. performed all of the in vivo palm oil and olive oil diet studies and analysed the innervation phenotype, including all in vivo transcriptome analyses of tumour and neural compartments (bulk arrays, 10x scRNA-seq and positional RNA-seq). D. Domínguez performed all the in vitro and in vivo epigenetic studies and the mechanistic studies for the Set1A, MLL1 and MLL2 proteins. D. Domínguez and D. Douillet carried out the COMPASS western blotting experiments. G.P. performed the experiments in melanoma. C.L. analysed the scRNA-seq and gene expression data. M.E.-B. analysed the 10x scRNA-seq and the positional RNA-seq data. C. Bigas performed the correlative analyses of the CD36⁺ signature and perineuronal nets in human tumours. M.A. helped to perform the sympathectomy experiments. I.H. and A. Symeodini analysed ChIP-seq data. D. Domínguez performed the in vitro scRNA-seq experiment. S.R.G., I.H. and H.H. contributed to and analysed scRNA-seq data. N.P. characterized histology samples. F.B and R.S. performed some transcriptome analyses. C. Bescós provided the tumour samples to establish the patient-derived VDH15 oral cancer cell line. S.A.B. wrote the manuscript with the input from G.P and D. Domínguez.

Corresponding authors

Correspondence to [Gloria Pascual](#), [Ali Shilatifard](#) or [Salvador Aznar Benitah](#).

Ethics declarations

Competing interests

S.A.B. is a co-founder and scientific advisor of ONA Therapeutics. The other authors declare no competing interests.

Additional information

Peer review information *Nature* thanks Sarah-Maria Fendt and the other, anonymous, reviewers for their contribution to the peer review of this work.

Publisher's note Springer Nature remains neutral with regard to jurisdictional claims in published maps and institutional affiliations.

Extended data figures and tables

Extended Data Fig. 1 Palmitic acid, but not linoleic, oleic or stearic, enhances the metastatic potential of OSCC long term after removing the stimulus.

a, Flow cytometry analysis of *in vitro* cultured SCC-25 cells after 4 days of fatty acid stimulation. The percentage of CD36 membrane expression and cell viability (as measured by DAPI incorporation) are shown. **b**, BLI quantification of lymph node (LN) metastases, showing number and size, from mice inoculated with untreated SCC-25 cells ($n = 17$) or *in vitro* treated with 300 μ M PA ($n = 17$), 50 μ M OA ($n = 10$) or 50 μ M LA ($n = 10$). BLI signals are expressed as the relative normalized photon flux. $P = 0.05$, two-tailed *t*-test. **c**, Frequency of developed LN metastases from animals in b. * $P = 0.01$, ** $P = 0.001$; two-tailed Fisher's exact test. **d**, Flow cytometry analysis of *in vitro* cultured SCC-25 cells immediately after 4 days (4D) PA stimulation or at 14D after PA withdrawal (wdl). The numbers indicate [CD44^{bright}CD36^{bright}] and [CD44^{bright}CD36^{dim}] populations in the represented gate, expressed as percentage of total DAPI-negative cells from *in vitro* cultured cells (samples are representative of $n =$

5 independent experiments). **e**, BLI quantification of primary tumours generated from mice injected with SCC-25 cells *in vitro* 14D after PA withdrawal. The BLI signal is expressed as the relative normalized photon flux. Data are given as the mean and s.e.m. (untreated, $n = 14$; 14D after PA wdl, $n = 14$, $*P = 0.05$, two-tailed *t*-test). **f**, Frequency of developed LN metastases from animals in e ($*P = 0.02$, two-tailed Fisher's exact test). **g**, *ex vivo* BLI lung metastasis quantification of mice injected with VDH-15 cells at 14D fatty acid withdrawal (PA, palmitic acid; SA, stearic acid; OA, oleic acid; LA, linoleic acid). BLI signals are expressed as the relative normalized photon flux. Images are representative of $n = 15$ mice per group. **h**, Frequency of developed lung metastasis of mice injected with SCC-25 after FA withdrawal expressed as percentages ($n = 10$ mice per group, lung metastases: $*P = 0.05$; two-tailed Fisher's exact test). PA/OA denotes a 4-day treatment with palmitic acid followed by a 4-days treatment with oleic acid, followed by 14-day with no fatty acid. **i**, BLI quantification of FACS-sorted and serially-transplanted PT populations (as indicated) from SCC-25 primary recipients. BLI signals are shown as the normalized photon flux ($n = 10$ mice per group. $*P = 0.03$, $**P = 0.05$, $***P = 0.01$; two-tailed *t*-test). **j**, Frequency of developed LN metastases of mice in i ($*P = 0.05$, two-tailed Fisher's exact test).

Extended Data Fig. 2 Tumour cells from palm-oil-fed primary recipient mice display a prometastatic memory in secondary recipient mice in a CD36 dependent manner.

a, Schematic diagram representing the *in vivo* diet experiments in which OSCC that were exposed to a high-fat diet in primary NSG mice recipients were injected into secondary recipients that were maintained on a control diet. At the final point primary tumour (PT) cells were purified by FACS-SORT for molecular characterization (created with BioRender.com). **b**, Flow cytometry analysis of PTs from VDH-15– and SCC-25–injected primary recipients fed a high-fat or control diet, as schematized in a. Numbers indicate [$CD44^{\text{bright}}CD36^{\text{bright}}$] and [$CD44^{\text{bright}}CD36^{\text{dim}}$] populations in the represented gate, expressed as percentages of total DAPI–GFP+Lin– cells. Samples are representative of $n = 3$ independent experiments. **c**, **d**, BLI tumour monitoring of secondary recipients injected with VDH-15–derived cells from primary recipient mice fed with palm oil–

rich, olive oil-rich diet and normal diet (as control). BLI signals are shown as the normalized photon flux ($n = 20$ mice per group, two independent experiments. LN metastasis, $P = 0.04$; lung metastasis, $*P = 0.04$, $**P = 0.007$; two-tailed t -test). **e**, Frequency of developed LN metastases from animals in c expressed as percentage (for LN metastasis, $*P = 0.003$; $**P = 0.02$; for lung metastasis: $*P = 0.01$, $***P = 0.0004$, two-tailed Fisher's exact test). **e, f**, BLI metastasis quantification of secondary recipient mice injected with control pLKO.1 or shCD36 VDH-15- (f) and SCC-25- (g) derived cells from primary recipient mice fed with a high-fat palm oil or a control diet. BLI signals are expressed as the normalized photon flux (for VDH-15, $n = 10$ mice per group; for lymph node and lung met, $*P = 0.04$; n.s., not significant; two-tailed t -test, data are mean \pm s.e.m.; for SCC-25, $n = 20$ mice per group, data from two independent experiments; $*P = 0.03$, $****P < 0.0001$; two-tailed t -test, data are mean \pm s.e.m.). **g**, Frequency of developed metastases from animals in g expressed as percentage (for lymph node met, $***P = 0.003$, $**P = 0.0004$; for lung met, $****P < 0.0001$, two-tailed Fisher's exact test). **h**, *Ex vivo* BLI lung metastasis monitoring from secondary recipient mice injected with control pLKO.1 or shCD36 melanoma-derived cells from primary recipient mice fed with a high-fat palm oil or a control diet. Pictures are representative of $n = 5$ mice per group. **i**, BLI metastasis quantification of animals in i. BLI signals are expressed as the normalized photon flux. ($***P = 0.0009$, $****P < 0.0001$, two-tailed t -test, data are mean \pm s.e.m.).

[Source data](#)

[Extended Data Fig. 3 CD36 blocking metastatic assays and assessment of the impact of PA on the OSCC chromatin landscape.](#)

a, Frequency of developed lung metastasis from secondary mice injected with SCC-25-derived from primary recipient mice fed a normal or palm oil-rich diet; Primary recipients were treated with an anti-CD36 neutralizing antibody (JC63.1) or a control isotype (IgA). Data is expressed as the percentages. ($n = 13$ mice per group; $*P = 0.01$, $*P = 0.03$, two-tailed Fisher's exact test). **b, c**, *ex vivo* BLI imaging and quantification of lung metastasis from VDH-15 secondary recipients injected with a doxycycline-

inducible shCD36 (shCD36 #23 or #76) VDH-15-derived tumour cells from primary recipient mice fed a normal or palm oil-rich diet. The secondary mice were untreated or continuously doxycycline-treated. (Data are mean \pm s.e.m. Images are representative of $n = 10$ mice per group; $*P = 0.01$; $**P = 0.001$; $****P < 0.0001$; two-tailed t -test). **d, e**, TSS-centred heat maps of d) H3K4me1 and e) H3K27me3 non-memory peaks for SCC-25 pLKO.1 14D Untreated and 14D post-PA conditions. **f**, TSS-centred density plot showing the signal of three histone marks of interest (H3K4me3, H3K4me1 and H3K27me3) in the genomic areas where H3K4me3 memory peaks were identified. **g**, ChIP-seq signal TSS-centred distribution plots of H3K4me1 and H3K27ac histone marks used to map enhancer regions in SCC-25 pLKO.1 cells, both at 4D (upper panel) and 14D (bottom panel) time points for Untreated and PA-treated conditions. A total of 2,183 enhancers were mapped. **h**, Volcano plots showing the enhancer regions displaying differential transcription of eRNAs ($FC > +/- 1.6$, $P < 0.05$) at 4D PA (upper panel) or 14D post-PA (bottom panel) according to our Pol II travelling ratio analysis (PRO-seq). Up-/down-regulated eRNAs are coloured in red and blue respectively. **i**, PCA plots of 4D (left) and 14D (right) Untreated/PA-treated H3K9me3 ChIP-seq sSCC-25 pLKO.1 samples. **j**, Images showing representative H3K9me3 neural-related peaks (NRXN3 and GABRG3 genes) lost in 4D PA and 14D post-PA SCC-25 pLKO.1 cells, as compared to control samples.

Extended Data Fig. 4 Surveying *in vitro* and *in vivo* histone methylation PA-driven changes in OSCC cells.

a, PCA plots of 4D/14D Untreated/PA-treated H3K4me3 (left), H3K4me1 (centre) and H3K27me3 (right) ChIP-seq samples of CTRL pLKO.1 SCC-25 cells. On the side, PCA plot of 14D Untreated/PA-treated H3K4me1 ChIP-seq samples of CTRL pLKO.1 VDH-15 cells. **b**, PCA plots of 14D Untreated/OA-treated H3K4me3 ChIP-seq samples of CTRL pLKO.1 SCC-25 (left)/VDH-15 (right) cells. The bottom figures show representative H3K4me3 peaks (NEFM and CHRD1L2 genes) at 14D post-OA for CTRL pLKO.1 SCC-25/VDH-15 cells. **c**, H3K4me3 ChIP-seq from secondary (2ary) primary tumours (PTs) of CTRL pLKO.1 VDH-15 cells upon *in vivo* exposure to Control (CTRL)/Palm oil (PALM)-enriched diets. On the bottom, a table displaying the number of total, differentially up-/down-

regulated H3K4me3 peaks identified when comparing CTRL and PALM diet samples. **d**, Left, TSS-centred heat maps of H3K4me3 memory and non-memory representative peaks for 2ary CTRL/PALM PTs; middle plot, TSS-centred density plot showing the H3K4me3 signal in differential peaks for both conditions assessed; right, representative *in vivo* memory peaks (FABP3, DRGX and CNTFR genes) for both CTRL/PALM tumours (Diff.Bind FDR \leq 0.1). **e**, Venn diagrams showing the overlap between genes harboring total (non-differential) H3K4me3 ChIP-seq peaks for VDH-15 pLKO.1 (left) Untreated 14D and CTRL diet 2ary recipient *in vivo* samples or (right) 14D post-PA and PALM diet 2ary recipient *in vivo* conditions. **f**, Venn diagrams showing the overlap between differential H3K4me3 ChIP-seq peaks-bearing genes for VDH-15 pLKO.1 14D post-PA and PALM diet 2ary recipient *in vivo* conditions. (a,b: *a representation factor* $>/< 1$ indicates *a higher/lower enrichment than expected by chance in gene overlap*; *P-Values were calculated using a hypergeometric test*). **g, h**, Bar plots showing the top biological processes GO terms built by the g) common or h) unique genes indicated in f). Unique refers to the PALM diet 2ary recipient *in vivo* condition. Neural-related terms are highlighted in purple.

Extended Data Fig. 5 Characterizing PA-triggered epigenetic and transcriptional changes and their correlation.

a, Left, PCA plot of 4D/14D Untreated/PA-treated H3K27ac ChIP-seq samples of SCC-25 pLKO.1 cells; middle, TSS-centred density plot showing the H3K27ac signal of all differential peaks in 4D/14D PA samples as compared to their control counterparts; right, Image showing representative H3K27ac peaks (ANGPTL4 gene) gained upon 4D PA treatment in SCC-25 pLKO.1 cells, as compared to the corresponding 14D samples. **b**, Left, plot displaying the three main clusters (0, 1 and 2) detected upon scRNA-seq data *t*-SNE analysis of CTRL pLKO.1 SCC-25 cells after 4D PA exposure. On the side, trajectory plot displaying the predicted Cluster distribution of 4D Untreated/PA-treated individual cells; right, trajectory plot showing the distribution of 4D Untreated (blue)/PA-treated (red) cells and their corresponding clusters. **c**, *t*-SNE plot showing distribution of cells enriched in the 4D PA transcriptional signature; on the side, trajectory plot displaying the predicted distribution of the PA response

score of each cell analyzed; right, bar plot showing the quantification of the Cluster distribution of 4D Untreated/PA-treated cells shown as the proportion of total cells per condition. **d**, Cell cycle Analysis using Propidium Iodide; PI staining. Representative FACS plots displaying the PI cell cycle profiles of both 4/14D Untreated/ PA-treated cells. **e**, Box plots showing the mRNA expression detected by RNA-seq in Untreated and PA-treated SCC-25 pLKO.1 cells at 4D /14D in those regions displaying H3K4me3 PA-driven changes (UP/DOWN in 4D/14D PA box plots *** $P<0.0001$ of a two-tailed t-test).

Extended Data Fig. 6 Tumour cells with a Palm Diet-induced metastatic memory display a neural-related signature.

a, Principal component analysis (PCA) from microarray data of secondary (2ary) recipient-primary tumours (PTs)-sorted [CD36^{bright}CD44^{bright}] or [CD36^{dim}CD44^{bright}]. Diets are indicated as (B) primary recipient mice fed a normal (red), olive oil-rich (green) or palm oil-rich (blue) diet, and secondary mice fed with a normal diet and (A) primary mice fed with a normal diet and secondary mice fed with a palm oil-rich diet (fuchsia). The axis shows the percent variability covered by each of the represented components. **b**, Heat map displaying the DGE levels of 2ary VDH-15–derived PTs with a palm oil memory. CD36b, [CD36^{bright}CD44^{bright}] and CD36d, [CD36^{dim}CD44^{bright}]. **c**, GO and Gene Set Enrichment (GSEA) analysis showing top categories from biological processes that are upregulated in palm oil diet–memory from [CD36^{bright}CD44^{bright}]-sorted populations from secondary PTs. For GO analysis, $FC > 1.5$, $P < 0.05$). **d**, Principal component analysis (PCA) from microarray data of secondary recipient-PTs control pLKO.1– or shCD36 sorted [CD36^{bright}CD44^{bright}] or [CD36^{dim}CD44^{bright}], ±palm oil memory. **e**, Gene Set Enrichment (GSEA) analysis showing top categories from biological processes that were upregulated in palm oil diet–memory from [CD36^{bright}CD44^{bright}]-sorted populations from secondary PTs. **f, g**, Principal component analysis (PCA) and heatmap plot from the microarray data of cells FACS-sorted from secondary PTs from control (pLKO.1) or shCD36 melanoma ± palm oil memory. In f, the axis shows the percent variability covered by each of the represented components. The heat-map plot (g) shows the DEGs in control

(pLKO.1)–palm oil memory PTs as compared to control–normal diet and their correspondence with the gene expression levels from the shCD36–palm oil. **h**, GO and GSEA analysis showing the top biological process categories that were upregulated by a palm oil memory of [GFP+]-sorted populations from secondary recipient, melanoma-derived PTs, as analysed in RNA microarrays. For GO analysis, $FC > 1.5$, $P < 0.05$.

Extended Data Fig. 7 Impact of chemical sympathectomy on metastasis and identification of EGR2 and galanin signalling in tumour cells with a Palm Diet-induced metastatic memory.

a, Diagram of the experimental *setup*. Secondary (2ary) recipient mice were injected on day 0 with OSCC from primary tumours (PTs) ± palm oil memory. 2ary recipients were treated with the neurotoxin 6-hydroxydopamine (6-OHDA; to induce the apoptosis of dopaminergic neurons) or vehicle on days –6, –3 and +3 relative to the day of injection. **b**, Frequency of developed lung metastasis from animals treated as shown in a, expressed as the percentages ($*P = 0.03$, $**P = 0.001$; two-tailed Fisher's exact test). **c**, Tyrosine hydroxylase (TH) immunofluorescence analysis of VDH-15 primary tumours (PTs) from secondary recipients ± palm oil memory after vehicle or 6-OHDA treatment. Nuclei are stained with DAPI. KT-14, cytokeratin 14. Note that 6-OHDA-lesioned-tumours display a marked reduction in the expression level of TH. Images are representative of $n = 3$ biological replicates per group. **d**, Top common predicted binding site motifs in promoter regions of the co-regulated neural-related genes in SCC-25 or VDH-15 primary tumours with a palm memory. Z-scores and P values are shown for each cell line. **e**, Integrative gene set enrichment analysis (GSEA) from PTs of secondary recipients SCC-25–, VDH-15– or melanoma tumour–derived cells ± palm oil memory. The graph shows the biological processes enrichment in palm oil memory compared to control diet. On the right side, detail of the neuropeptide signalling pathway–associated gene-set assayed by integrative GSEA showing galanin (*GAL*) as the top significantly represented gene in palm oil memory tumours. **f**, **g**, PCA plots of differentially bound signal (DBS) regions detected for 4D Untreated/PA-treated EGR2 ChIP–seq samples in f) SCC-25 pLKO.1 and g) SCC-25 CD36-KD cells. **h**, Heat maps showing the EGR2 DBS regions

(differential peaks) detected for 4D SCC-25 pLKO.1 (left) and SCC-25 CD36 KD (right) shown in f) and g) respectively (FDR<0.05).

[Source data](#)

Extended Data Fig. 8 Modulating EGR2 expression to determine its relevance in modulating the OSCC epigenome, transcriptome and metastatic potential.

a, PCA plots of differentially bound signal (DBS) regions detected for 4D (left) and 14D (right) Untreated/PA-treated H3K4me3 ChIP-seq samples in SCC-25 EGR2-KD cells. **b**, Bar plots showing the top biological processes GO terms uniquely down-regulated in 4D PA (upper panel) and 14D post-PA (bottom panel) H3K4me3 ChIP-seq SCC-25 EGR2-KD samples. Neural-related terms are highlighted in purple. **c**, Venn diagrams showing the overlap between *in vivo* proneural-induced gene signatures in secondary OSCC primary tumours with a palm oil memory and the knockdowns, as indicated. **d**, Gene set enrichment analysis (GSEA) showing the negative enrichment of biological processes in secondary PTs derived from SCC-25-shEGR2/PALM vs pLKO.1/control diet or shGAL/PALM vs pLKO.1/control diet. **e**, BLI metastasis quantification of lymph node (LN) and lung of secondary recipient mice injected with primary recipient SCC-25 cells, derived from control (pLKO.1), shRNA-knockdown of EGR2 (shEGR2 #38_9 and shEGR2 #40_9) or shRNA-knockdown of GAL (shGAL #74_4 shRNAs) ± palm oil memory (pLKO.1/control diet, $n = 22$; pLKO.1/PALM, $n = 21$; shEGR2/control diet and shEGR2/PALM, $n = 20$; shGAL/control diet and shGAL/PALM, $n = 10$; in the knockdowns, n reflects number of mice per shRNA used; * $P = 0.01$, two-tailed t -test. Data are the mean ± s.e.m.).

[Source data](#)

Extended Data Fig. 9 Metastatic functional assay after systemic inhibition of galanin signalling through intraperitoneal administration of the pan-galanin receptor inhibitor galantide (M15).

a, Experimental setup of the experiment for galanin receptor inhibition. **b**, **c**, *Ex vivo* BLI lung metastasis (b) and frequency of lung metastasis development (c), expressed as the percentages, from secondary (2ary) recipient mice injected with VDH-15 cells derived from primary recipient mice fed a palm oil-rich diet or a control diet. 2ary recipients were treated with the galanin receptor antagonist galantide (M15) or vehicle as explained in (a) (vehicle-treated, $n = 12$ mice; M15-treated, $n = 15$ mice. * $P = 0.03$; * $P = 0.04$; two-tailed Fisher's exact test).

[Source data](#)

[Extended Data Fig. 10 Elucidating the role of COMPASS methyltransferases in PA-driven OSCC chromatin changes and metastatic abilities.](#)

a, b, Western blot analysis of the COMPASS family of methyltransferases (Set1A/B and MLL1/2) in VDH-15 or SCC-25 pLKO.1 cells that were Untreated, a) 4D after PA treatment or b) 14D after removal of PA. Cells were infected with a non-targeting (nt)-shRNA (pLKO.1). Hsp90 was used as a loading control. **c, d**, PCA plots displaying ChIP-seq for c) MLL1 or d) MLL2 from untreated or 14D post-PA VDH-15 pLKO.1 cells. **e**, Representative peaks from MLL1/MLL2 ChIP-seq of MLL1/MLL2-regulated genes (*HOX* gene cluster) and non-regulated genes (neural-related *CHRD12* gene) for all conditions tested (Untreated/4D PA and 14D post-PA pLKO.1 VDH-15 cells). **f**, PCA plot showing 14D Untreated/PA-treated H3K4me3 ChIP-seq samples of CTRL pLKO.1 and Set1A #42 KD VDH-15 cells. **g**, GO analysis of PA-treated Set1A KD VDH-15 H3K4me3 ChIP-seq samples. The plot shows the top biological processes GO terms significantly down-regulated in Set1A KD #42 samples 14D post-PA exposure when compared to the 14D Untreated samples (Diff. Bind FDR ≤ 0.05). On the side, H3K4me3 peaks of Set1A-regulated neural genes (*CHRD1* and *GRIP2* genes). H3K4me3 representative examples are shown at 4/14D time points for all assessed conditions (CTRL pLKO.1 and Set1A #42 KD VDH-15 cells). **h**, Left, secondary (2ary) recipient orthotopic injections of CTRL pLKO.1 and Set1A #42 KD VDH-15 cells upon *in vivo* exposure to Control/Palm-oil enriched diets in primary recipient mice. The frequency of developed LNmet (at the end-point of the

experiment is shown for all conditions ($n= 10$ mice/group; *LNmets*: *CTRL pLKO.1 CTRL Diet* vs *CTRL pLKO.1 PALM Diet* $n.s= 0.065$, *CTRL pLKO.1 PALM Diet* vs *Set1A KD PALM Diet* $n.s= 0.091$; *n.s.* is not significant Fisher's exact test). Right, frequency of developed LNmets at the end-point of the experiment in lary recipient orthotopic injections of *CTRL pLKO.1/Set1A KD #07 VDH-15* cells 14D post-PA *in vitro* exposure ($n= 20$ mice/group; *LNmets*: *CTRL pLKO.1 UNTR* vs *CTRL pLKO.1 14D post-PA* * $P=0.038$, *CTRL pLKO.1 14D post-PA* vs *Set1A KD 14D post-PA* * $P=0.031$ of Fisher's exact test). For gel source data, see Supplementary Figure 1.

Source data

Extended Data Fig. 11 Tumour cells with a Palm Diet-induced metastatic memory alter the tumour-associated stroma in a CD36-dependent manner.

a, Flow cytometry analysis of SCC-25-primary tumours (PTs) from secondary (2ary) recipients \pm palm oil memory. [GFP-/CD31-/CD45-] tumour stroma-selected cells were purified and processed to perform RNA microarrays. Data are representative of $n= 3$ independent experiments. Numbers indicate the population in the represented gate, expressed as the percentages. **b**, Principal component analysis (PCA) of the microarray data of VDH-15-associated bulk stroma purified from secondary (2ary) recipients. Diet samples are indicated as (B) primary recipient mice fed a normal (red), olive oil-rich (green) or palm oil-rich (blue) diet, and 2ary mice fed with a normal diet and (A) primary mice fed with a normal diet and 2ary mice fed with a palm oil-rich diet (fuchsia). The axis shows the percent variability covered by each of the represented components. **c**, Principal component analysis (PCA) from microarray data of 2ary recipient tumour-associated stroma derived from injection in primary recipients of control (pLKO.1)- or shCD36-VDH-15 or SCC-25 cells, as indicated by the colour-code. The axis shows the percent variability covered by each of the represented components. **d**, Volcano plots for the differential gene expression microarray analysis and GO analysis from a purified tumour stroma from 2ary recipient mice injected with OSCC from PTs \pm palm oil memory. Volcano plots show the up- or downregulated genes in control-

palm oil memory tumours compared to control–normal diet tumours (top) and the expression of these genes in the shCD36–palm oil (lower plot). Data from $n = 2$ biological replicates; fold-change, $FC > 2$, $P < 0.01$. The GO analysis shows the top biological processes categories upregulated in the palm oil memory tumour stroma, $FC > 2$, $P < 0.05$. (Integrated analysis, derived from VDH-15 or SCC-25 cells). **e**, Neural–mouse stromal signature induced in 2ary recipients after orthotopic injection of primary recipient–PT cells, derived from control (pLKO.1), shRNA-CD36, shRNA-EGR2 or shRNA-GAL SCC-25 cell. Each dot in the plot represents a neural gene. **f**, **g**, GSEA showing the negative enrichment of biological processes in neural–mouse stroma associated with 2ary PTs from shEGR2/PALM or shGAL/PALM vs pLKO.1/control diet conditions.

Extended Data Fig. 12 Schwann cell development and neuron projection regeneration are processes enhanced in the stroma of palm-oil derived tumours.

a, Functional network interaction between tumour–mouse stromal palm oil (PALM)–controlled genes and the human OSCC primary tumours with a palm memory. The network graph shows the co-regulated functional nodes of interaction between the two compartments (fold-change, $FC > 1.5$; P value < 0.05). **b**, **c**, 10X single-cell (sc) RNA-seq clustering analysis of the tumour-associated stroma purified from secondary (2ary) oral SCC-25 PTs \pm palm oil memory. The principal component UMAP plot is shown in which the specific cell types have been annotated to each respective cluster. **d**, Overlap analysis represented by Venn diagrams showing the intersection between bulk-stroma palm memory-controlled genes and 10X single-cell (sc) RNA-seq clusters from SCC-25–derived stromal cells in 2ary recipients. Representation factor (RF) and P values are shown for the overlap. Hypergeometric test; estimated number of protein-encoding genes = 25,000.

Extended Data Fig. 13 ECM components related to tumour-associated Schwann cells are increased in palm-oil derived tumours and correlate with CD36+ metastatic signature.

a, b, c, Integrated UMAP cluster visualization, annotated for cell types, of 10X single-cell (sc) RNA-seq data of the tumour-associated stroma purified from secondary (2ary) oral SCC-25 primary tumours (PTs) ±palm oil memory. The UMAP plot shows the expression level and cluster distribution of selected gene markers relative to glial cells and progenitor glia a), specialized extracellular matrix constituent (ECM) b) and nerve injury/ nerve regenerative processes c). **d**, Regression analysis showing the correlation between the long-lasting palm oil–related signature of the OSCC tumours (derived from SCC-25 or VDH-15 cells) or melanoma (501-mel), and the expression of markers related with perineuronal nets (GO:0072534). R-squared coefficients (R) and *P values* are shown for each analysis. **e**, Immunofluorescence analysis of PTs from 2ary recipient mice injected with VDH-15–derived cells from primary recipient ± palm oil memory. Cytokeratin-14 (KT-14) is shown as epithelial marker of OSCCs, and the specialized ECM markers Hyaluronidase 1 (Has1), Tenascin R (TNR) and the glial/Schwann marker s100 are shown as tumour stroma markers. Yellow arrows indicate areas of Has1 positive cells. Dashed lines delimitate the interface between the tumour and the tumour-associated stroma. **f**, Magnification from b) (palm diet memory condition). Note the double labelling of TNR and S100 in the close proximity of the tumour front. Images are representative of $n = 4$ biological replicates.

Extended Data Fig. 14 Spatial transcriptomic analysis of secondary recipient OSCC primary tumours.

a, Images showing Haematoxylin-Eosin (H&E) staining of primary tumours (PTs) from secondary (2ary) recipients injected with control (pLKO.1) and shCD36 SCC-25 cells derived from primary recipient mice fed a normal diet or a palm oil–rich diet. **e**, Spatial transcriptomics analysis of tumours in a) showing the proportion content and spatial distribution of mouse and human transcriptome per spot, the analysis stratification of the tissue as healthy/tumour invasive front/tumour and the proportion content and spatial distribution of the tumour-associated Schwann cells. **c**, Quantitative analysis of the proportional content of tumour-associated Schwann cells within each compartment (healthy/tumour front/tumour) of the PTs from 2ary recipients injected with control (pLKO.1) and shCD36 SCC-25 cells

derived from primary recipient mice fed a normal diet or a palm oil–rich diet.

Extended Data Fig. 15 Immunofluorescent analysis of secondary recipient OSCC primary tumours.

a, b, e, Immunofluorescence analysis and quantification of primary tumours (PTs) from secondary (2ary) recipient mice injected with VDH-15– or SCC-25-derived cells, as indicated, derived from primary recipient mice fed a normal diet, a palm oil–rich or an olive oil–rich diet. Cytokeratin-14 (KT-14) is shown as an epithelial marker of OSCC, and the glial/Schwann markers s100 or GAP43 as a tumour stroma marker. Nuclei are stained with DAPI. Images are representative of $n = 3$ independent experiments. **c**, Graphs showing the values of integrated density of (a, b). ($n = 3$ biological replicates per group; $*P = 0.05$, $****P < 0.0001$; two-tailed t -test). **f**, Immunofluorescence analysis of PTs from M15-treated or vehicle-treated mice \pm palm oil memory. The expression of cytokeratin-14 (KT-14) is shown as an epithelial marker of OSCC, and the glial Schwann cell marker s100 is shown in the tumour-associated stroma. Nuclei are stained with DAPI. Note that the increased expression of s100 in the stroma of palm memory tumours is slightly reduced in the case of M15-treated palm condition.

Extended Data Fig. 16 Enzymatic digestion through chondroitinase ABC (chABC) prevents the increase in metastatic competency induced by palmitic acid in OSCC cells.

a, Western blot analysis of total protein extracted from *in vitro* cultured VDH-15 cells infected with the lentiviral LV-chondroitinase ABC (ch-ABC) vector, showing the overexpression of the chondroitinase ABC enzyme in the infected cells ($n = 2$ replicates per group). **b, c**, Immunofluorescence analysis of primary tumours from secondary recipient mice injected with wild-type VDH-15 (WT) or LV-chondroitinase ABC enzyme (chABC)–derived cells from primary recipient mice fed a normal diet or a palm oil–rich diet. Cytokeratin-14 (KT-14) is shown as epithelial marker of OSCCs, and the specialized ECM markers Versican (Vcan),

Tenascin R (TNR) and the glial/Schwann marker s100 as tumour stroma markers d) or collagen 5A1 (Col5A1) as ECM marker e). Nuclei are stained with DAPI. Images are representative of $n = 3$ biological samples.

Supplementary information

Supplementary Figure 1

Raw images of the western blot experiments presented in Extended Data Figure 10. Pictures of exposed blots for the detection of COMPASS proteins expression in SCC-25 and VDH-15 pLKO.1 cell lines are provided for both the 4 d and 14 d time points, together with information on the molecular mass ladder that was used.

Reporting Summary

Supplementary Table 1

This table is complementary and related to Fig. 1 and Extended Data Figs. 1–3. It contains data about VDH-15 and SCC-25 bioluminescence (BLI) quantification of primary tumours, lymph node and lung metastasis and frequencies of developed primary tumours and metastasis; CD36 membrane expression by FACS profile of primary tumours and in vitro cells.

Supplementary Table 2

This table contains H3K4me3 ChIP-seq differential peaks and annotated genes as well as the corresponding GO analyses for: SCC-25 and VDH-15 pLKO.1 cells 14d after PA (14 d post-PA) samples; VDH-15 pLKO.1 secondary primary tumour samples.

Supplementary Table 3

This table contains H3K4me1 and H3K27me3 ChIP-seq as well as PRO-seq information, including: gene overlap of untreated and PA-treated conditions at both the 4 d and 14 d time points for both H3K4me1 and

H3K27me3 ChIP-seq samples; H3K4me1 ChIP-seq differential peaks and annotated genes for SCC-25 and VDH-15 pLKO.1 cells 14 d post-PA; H3K27me3 ChIP-seq differential peaks and annotated genes for SCC-25 pLKO.1 cells 14 d post-PA; and total and differentially expressed eRNAs as detected by PRO-seq data analysis at both 4 d PA and 14 d post-PA for SCC-25 pLKO.1 cells.

Supplementary Table 4

This table contains information on PA-treated and OA-treated H3K4me3 ChIP-seq samples of both SCC-25 and VDH-15 pLKO.1 cells, including: GO analysis 14 d post-PA H3K4me3 ChIP-seq samples for both SCC-25 and VDH-15 cells; GO analysis 14 d post-OA for H3K4me3 ChIP-seq SCC-25 pLKO.1 samples; GO analysis of H3K4me3 ChIP-seq secondary palm-oil-enriched diet exposed primary tumours; gene overlap of H3K4me3 OA-treated and PA-treated ChIP-seq conditions at the 14 d time point, together with the comparison of total number of differentially expressed peaks 14 d post-PA/OA; gene overlap of H3K4me3 and H3K4me1 or H3K27me3 14 d post-PA ChIP-seq SCC-25 pLKO.1 samples; comparison of the total number of differentially expressed H3K4me1 peaks 14 d post-PA between SCC-25 and VDH-15 pLKO.1 samples; H3K4me3 ChIP-seq differential peaks and annotated genes for SCC-25 and VDH-15 pLKO.1 cells 14 d post-OA and their corresponding GO analyses; and a list of differentially expressed mRNAs as detected by RNA-seq at 4 d and 14 d post-PA as well as the 14 d post-PA corresponding GO analysis.

Supplementary Table 5

This table contains information on PA-treated and OA-treated H3K4me3 ChIP-seq samples of both SCC-25 and VDH-15 pLKO.1 cells, including: GO analysis 14 d post-PA H3K4me3 ChIP-seq samples for both SCC-25 and VDH-15 cells; GO analysis 14 d post-OA for H3K4me3 ChIP-seq SCC-25 pLKO.1 samples; GO analysis of H3K4me3 ChIP-seq secondary palm-oil-enriched diet exposed primary tumours; gene overlap of H3K4me3 OA-treated and PA-treated ChIP-seq conditions at the 14 d time point, together with the comparison of the total number of differentially expressed peaks 14 d post-PA/OA; gene overlap of H3K4me3 and

H3K4me1 or H3K27me3 14 d post-PA ChIP-seq SCC-25 pLKO.1 samples; comparison of the total number of differentially expressed H3K4me1 peaks 14 d post-PA between SCC-25 and VDH-15 pLKO.1 samples; H3K4me3 ChIP-seq differential peaks and annotated genes for SCC-25 and VDH-15 pLKO.1 cells 14 d post-OA and their corresponding GO analyses; and a list of the differentially expressed mRNAs as detected by RNA-seq at 4 d and 14 d post-PA as well as the 14 d post-PA corresponding GO analysis.

Supplementary Table 6

This table contains microarray data, GO and GSEA, and integrative analysis from VDH-15, SCC-25 and melanoma primary tumours from secondary recipients ± palm-oil memory.

Supplementary Table 7

This table contains microarray data, GO and GSEA from melanoma (501mel) primary tumours from secondary recipient ± palm-oil memory.

Supplementary Table 8

This table is complementary and related to Extended Data Fig. 7. It contains data about VDH-15 BLI quantification of primary tumours, lymph node and lung metastasis and the frequencies of developed primary tumours and metastasis.

Supplementary Table 9

This table contains data about: transcription factor binding site analysis in the pro-neural signature of VDH-15 and SCC-25 primary tumours with a palm memory; microarray data and GSEA of SCC-25 shEGR2 and SCC-25 shGAL primary tumours ± palm-oil memory.

Supplementary Table 10

This table contains information on EGR2 ChIP-seq for SCC-25 pLKO.1 and CD36-KD samples, including a comparison of the total number of differentially expressed EGR2 peaks at 4 d PA between SCC-25 pLKO.1 and SCC-25 CD36-KD samples; a comparison of the total number of differentially expressed H3K4me3 peaks at 4 d and 14 d post-PA between SCC-25 CD36-KD samples; gene overlap of H3K4me3 SCC-25 pLKO.1 and EGR2-KD ChIP-seq samples at 4 d and 14 d post-PA, together with the corresponding GO analyses; EGR2 ChIP-seq differential peaks and annotated genes for SCC-25 pLKO.1 at 4 d PA and 14 d post-PA; H3K4me3 ChIP-seq differential peaks and annotated genes for SCC-25 EGR2-KD cells at 4 d PA and 14 d post-PA as well as their corresponding GO analyses; and H3K4me3 ChIP-seq differential peaks and annotated genes for SCC-25 CD36-KD cells at the 4 d PA time point.

Supplementary Table 11

This table is complementary and related to Extended Data Fig. 9. It contains data about VDH-15 BLI quantification of primary tumours, lymph node and lung metastasis, and frequencies of developed primary tumours and metastasis.

Supplementary Table 12

This table contains data of the correlation of *EGR2* or *GAL* expression and the overall survival in different types of tumours.

Supplementary Table 13

This table contains data on MLL1 and MLL2 ChIP-seq experiments as well as in vivo MLL1-KD assays, including information on the total number of differential MLL1 and MLL2 ChIP-seq peaks 14 d post-PA as well as at the corresponding list of differential peaks and annotated genes for SCC-25 pLKO.1 samples; and data on VDH-15 BLI quantification for lymph node metastases 14 d post-PA exposure.

Supplementary Table 14

This table contains data regarding H3K4me3 ChIP-seq experiments together with in vivo assays involving VDH-15 Set1A-KD cells, including H3K4me3 ChIP-seq differential peak GO analysis of VDH-15 Set1A-KD cells 14 d post-PA; and BLI quantification data of VDH-15 pLKO.1 and Set1A-KD primary tumours 14 d post-PA exposure.

Supplementary Table 15

This table contains microarray data, GO and GSEA of bulk tumour-associated stroma from VDH-15 and SCC-25 secondary recipients ± palm-oil memory.

Supplementary Table 16

This table contains data relating to the 10x single-cell analysis of bulk tumour stroma from pLKO.1 and shCD36 SCC-25 secondary recipients ± palm-oil memory; overlap analysis showing the intersection between bulk-stroma palm memory-controlled genes; the 10x scRNA-seq clusters from SCC-25-derived stromal cells in secondary recipients; Palm-oil diet-ECM-related genes.

Supplementary Table 17

This table is complementary and related to Extended Data Fig. 16. It contains data about VDH-15 BLI quantification of primary tumours, lymph node and lung metastasis, and frequencies of developed primary tumours.

Supplementary Table 18

This table contains data about VDH-15 BLI quantification and frequencies of lung metastasis in secondary recipients.

Supplementary Table 19

This table contains Pearson correlation analysis between the CD36⁺ metastatic signature and perineuronal net gene sets in different tumour

types.

Supplementary Table 20

This table contains methods information relating to shRNA sequences, antibodies and Taqman gene expression probes.

Source data

[Source Data Fig. 1](#)

[Source Data Fig. 3](#)

[Source Data Fig. 4](#)

[Source Data Extended Data Fig. 2](#)

[Source Data Extended Data Fig. 7](#)

[Source Data Extended Data Fig. 8](#)

[Source Data Extended Data Fig. 9](#)

[Source Data Extended Data Fig. 10](#)

Rights and permissions

[Reprints and Permissions](#)

About this article

Cite this article

Pascual, G., Domínguez, D., Elosúa-Bayes, M. *et al.* Dietary palmitic acid promotes a prometastatic memory via Schwann cells. *Nature* **599**, 485–490 (2021). <https://doi.org/10.1038/s41586-021-04075-0>

- Received: 03 April 2020
- Accepted: 30 September 2021
- Published: 10 November 2021
- Issue Date: 18 November 2021
- DOI: <https://doi.org/10.1038/s41586-021-04075-0>

Share this article

Anyone you share the following link with will be able to read this content:

[Get shareable link](#)

Sorry, a shareable link is not currently available for this article.

[Copy to clipboard](#)

Provided by the Springer Nature SharedIt content-sharing initiative

This article was downloaded by **calibre** from <https://www.nature.com/articles/s41586-021-04075-0>

- Article
- [Published: 28 October 2021](#)

AKIRIN2 controls the nuclear import of proteasomes in vertebrates

- [Melanie de Almeida](#) ORCID: [orcid.org/0000-0003-4871-2069](#)^{1,2 na1},
- [Matthias Hinterndorfer](#) ORCID: [orcid.org/0000-0003-2435-4690](#)^{1,2 na1},
- [Hanna Brunner](#) ORCID: [orcid.org/0000-0002-3446-3738](#)^{1,2},
- [Irina Grishkovskaya](#) ORCID: [orcid.org/0000-0003-0164-9373](#)¹,
- [Kashish Singh](#) ORCID: [orcid.org/0000-0002-9891-8148](#)^{1 nAff5},
- [Alexander Schleifer](#) ORCID: [orcid.org/0000-0001-6251-2747](#)¹,
- [Julian Jude](#)^{1 nAff6},
- [Sumit Deswal](#)^{1 nAff7},
- [Robert Kalis](#) ORCID: [orcid.org/0000-0001-7553-4806](#)^{1,2},
- [Milica Vunjak](#) ORCID: [orcid.org/0000-0001-6330-363X](#)^{2,3},
- [Thomas Lendl](#) ORCID: [orcid.org/0000-0003-4596-9512](#)¹,
- [Richard Imre](#)¹,
- [Elisabeth Roitinger](#) ORCID: [orcid.org/0000-0002-3405-7801](#)¹,
- [Tobias Neumann](#) ORCID: [orcid.org/0000-0003-3908-4224](#)^{1 nAff8},
- [Susanne Kandolf](#) ORCID: [orcid.org/0000-0002-4007-6283](#)¹,
- [Michael Schutzbier](#)¹,
- [Karl Mechtler](#) ORCID: [orcid.org/0000-0002-3392-9946](#)¹,
- [Gijs A. Versteeg](#) ORCID: [orcid.org/0000-0002-6150-2165](#)³,
- [David Haselbach](#) ORCID: [orcid.org/0000-0002-5276-5633](#)¹ &
- [Johannes Zuber](#) ORCID: [orcid.org/0000-0001-8810-6835](#)^{1,4}

[Nature](#) volume **599**, pages 491–496 (2021)

- 14k Accesses
- 233 Altmetric
- [Metrics details](#)

Subjects

- [Cryoelectron microscopy](#)
- [Functional genomics](#)
- [High-throughput screening](#)
- [Proteasome](#)
- [Protein transport](#)

Abstract

Protein expression and turnover are controlled through a complex interplay of transcriptional, post-transcriptional and post-translational mechanisms to enable spatial and temporal regulation of cellular processes. To systematically elucidate such gene regulatory networks, we developed a CRISPR screening assay based on time-controlled Cas9 mutagenesis, intracellular immunostaining and fluorescence-activated cell sorting that enables the identification of regulatory factors independent of their effects on cellular fitness. We pioneered this approach by systematically probing the regulation of the transcription factor MYC, a master regulator of cell growth^{1,2,3}. Our screens uncover a highly conserved protein, AKIRIN2, that is essentially required for nuclear protein degradation. We found that AKIRIN2 forms homodimers that directly bind to fully assembled 20S proteasomes to mediate their nuclear import. During mitosis, proteasomes are excluded from condensing chromatin and re-imported into newly formed daughter nuclei in a highly dynamic, AKIRIN2-dependent process. Cells undergoing mitosis in the absence of AKIRIN2 become devoid of nuclear proteasomes, rapidly causing accumulation of MYC and other nuclear proteins. Collectively, our study reveals a dedicated pathway controlling the nuclear import of proteasomes in vertebrates and establishes a scalable approach to decipher regulators in essential cellular processes.

Access options

Subscribe to Journal

Get full journal access for 1 year

\$199.00

only \$3.90 per issue

[Subscribe](#)

All prices are NET prices.

VAT will be added later in the checkout.

Tax calculation will be finalised during checkout.

Rent or Buy article

Get time limited or full article access on ReadCube.

from \$8.99

[Rent or Buy](#)

All prices are NET prices.

Additional access options:

- [Log in](#)
- [Access through your institution](#)
- [Learn about institutional subscriptions](#)

Fig. 1: Systematic analysis of MYC regulators.

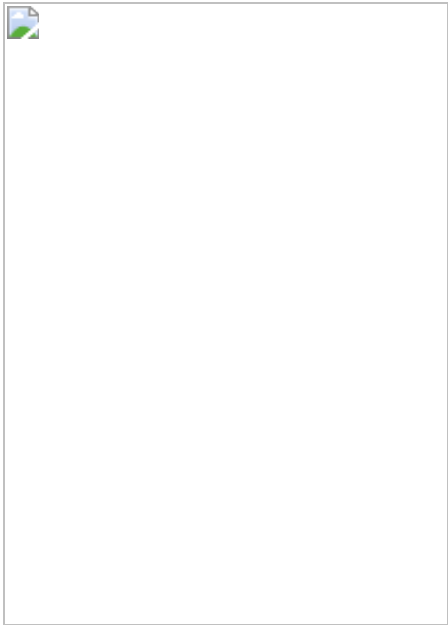


Fig. 2: AKIRIN2 is a critical regulator of MYC.



Fig. 3: AKIRIN2 controls nuclear protein turnover.

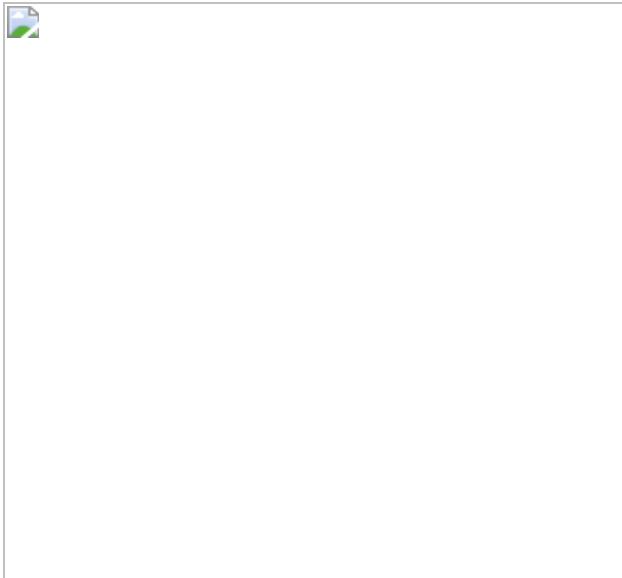


Fig. 4: AKIRIN2 is highly conserved and directly binds the 20S-CP.

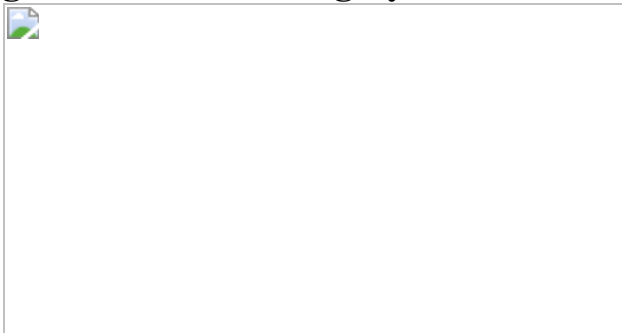
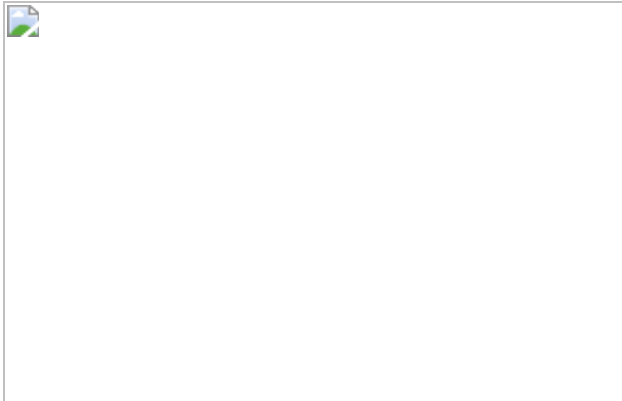


Fig. 5: AKIRIN2 controls nuclear proteasome import.



Data availability

Source data for Figs. 1d, e, 2a, b, 3a, b, d, 4e, f and Extended Data Figs. 2, 4a, b, g, i, 5f, 6d are included in the Supplementary Information files of the manuscript. Raw FASTQ files for RNA-seq analyses are available through

the Gene Expression Omnibus (accession code [GSE15763](#)). Negative staining and cryo-EM density maps are deposited in the Electron Microscopy Data Bank with the accession codes [EMD-11649](#) and [EMD-12341](#), respectively. The atomic model is deposited under Protein Data Bank ID [7NHT](#). Raw micrographs and particle stacks are available in the EMPIAR database ([EMPIAR-10752](#)). TMT quantitative proteomics, V5 and GST co-IP/MS data have been deposited to the ProteomeXchange Consortium PRIDE repository with the accession codes [PXD021898](#), [PXD027184](#) and [PXD027343](#), respectively. Human cancer cell line RNA-seq data were obtained from the ArrayExpress repository (<https://www.ebi.ac.uk/arrayexpress/experiments/E-MTAB-2706>). AKIRIN2 interactors identified in this study were cross-compared to the BioGRID database (<https://thebiogrid.org/120430/summary/homo-sapiens/akirin2.html>). The crystallographic native human 20S proteasome structure used for model building and the cryo-EM structure of the substrate-engaged human 26S proteasome shown for comparison in Extended Data Fig. 7f were obtained from the RCSB protein database (<https://www.rcsb.org/structure/5LE5> and <https://www.rcsb.org/structure/6MSJ>, respectively).

Code availability

Custom code for screen analysis is available on GitHub (<https://github.com/ZuberLab/crispr-process-nf>, <https://github.com/ZuberLab/crispr-mageck-nf>). Custom ImageJ scripts applied for image analysis (see [Methods](#) for details) are available upon reasonable request.

References

1. 1.

Johnston, L. A., Prober, D. A., Edgar, B. A., Eisenman, R. N. & Gallant, P. *Drosophila myc* regulates cellular growth during development. *Cell* **98**, 779–790 (1999).

2. 2.

Sabo, A. et al. Selective transcriptional regulation by Myc in cellular growth control and lymphomagenesis. *Nature* **511**, 488–492 (2014).

3. 3.

Muhar, M. et al. SLAM-seq defines direct gene-regulatory functions of the BRD4–MYC axis. *Science* **360**, 800–805 (2018).

4. 4.

Dang, C. V. *MYC* on the path to cancer. *Cell* **149**, 22–35 (2012).

5. 5.

Hnisz, D. et al. Super-enhancers in the control of cell identity and disease. *Cell* **155**, 934–947 (2013).

6. 6.

He, T. C. et al. Identification of c-MYC as a target of the APC pathway. *Science* **281**, 1509–1512 (1998).

7. 7.

Dani, C. et al. Extreme instability of myc mRNA in normal and transformed human cells. *Proc. Natl Acad. Sci. USA* **81**, 7046–7050 (1984).

8. 8.

Gregory, M. A. & Hann, S. R. c-Myc proteolysis by the ubiquitin-proteasome pathway: stabilization of c-Myc in Burkitt's lymphoma cells. *Mol. Cell. Biol.* **20**, 2423–2435 (2000).

9. 9.

Schwanhausser, B. et al. Global quantification of mammalian gene expression control. *Nature* **473**, 337–342 (2011).

10. 10.

Meyers, R. M. et al. Computational correction of copy number effect improves specificity of CRISPR–Cas9 essentiality screens in cancer cells. *Nat. Genet.* **49**, 1779–1784 (2017).

11. 11.

Dempster, J. M. et al. Extracting biological insights from the Project Achilles genome-scale CRISPR screens in cancer cell lines. Preprint at <https://doi.org/10.1101/720243> (2019).

12. 12.

Michlits, G. et al. Multilayered VBC score predicts sgRNAs that efficiently generate loss-of-function alleles. *Nat. Methods* **17**, 708–716 (2020).

13. 13.

Sears, R., Leone, G., DeGregori, J. & Nevins, J. R. Ras enhances Myc protein stability. *Mol. Cell* **3**, 169–179 (1999).

14. 14.

Welcker, M. et al. The Fbw7 tumor suppressor regulates glycogen synthase kinase 3 phosphorylation-dependent c-Myc protein degradation. *Proc. Natl Acad. Sci. USA* **101**, 9085–9090 (2004).

15. 15.

Inoue, S. et al. Mule/Huwe1/Arf-BP1 suppresses Ras-driven tumorigenesis by preventing c-Myc/Miz1-mediated down-regulation of p21 and p15. *Genes Dev* **27**, 1101–1114 (2013).

16. 16.

Qiao, X. et al. *UBR5* is coamplified with *MYC* in breast tumors and encodes an ubiquitin ligase that limits MYC-dependent apoptosis. *Cancer Res.* **80**, 1414–1427 (2020).

17. 17.

Goto, A. et al. Akirins are highly conserved nuclear proteins required for NF-κB-dependent gene expression in *Drosophila* and mice. *Nat. Immunol.* **9**, 97–104 (2008).

18. 18.

Tartey, S. et al. Akirin2 is critical for inducing inflammatory genes by bridging IκB-ζ and the SWI/SNF complex. *EMBO J.* **33**, 2332–2348 (2014).

19. 19.

Bonnay, F. et al. Akirin specifies NF-κB selectivity of *Drosophila* innate immune response via chromatin remodeling. *EMBO J.* **33**, 2349–2362 (2014).

20. 20.

Fischer, M. Census and evaluation of p53 target genes. *Oncogene* **36**, 3943–3956 (2017).

21. 21.

Stark, C. et al. BioGRID: a general repository for interaction datasets. *Nucleic Acids Res.* **34**, D535–D539 (2006).

22. 22.

Smith, D. M. et al. Docking of the proteasomal ATPases' carboxyl termini in the 20S proteasome's α ring opens the gate for substrate entry. *Mol. Cell* **27**, 731–744 (2007).

23. 23.

Cuylen-Haering, S. et al. Chromosome clustering by Ki-67 excludes cytoplasm during nuclear assembly. *Nature* **587**, 285–290 (2020).

24. 24.

Schmitz, M. H. et al. Live-cell imaging RNAi screen identifies PP2A-B55 α and importin- β 1 as key mitotic exit regulators in human cells. *Nat. Cell Biol.* **12**, 886–893 (2010).

25. 25.

Reits, E. A., Benham, A. M., Plougastel, B., Neefjes, J. & Trowsdale, J. Dynamics of proteasome distribution in living cells. *EMBO J.* **16**, 6087–6094 (1997).

26. 26.

Pack, C. G. et al. Quantitative live-cell imaging reveals spatio-temporal dynamics and cytoplasmic assembly of the 26S proteasome. *Nat. Commun.* **5**, 3396 (2014).

27. 27.

Peters, J. M., Franke, W. W. & Kleinschmidt, J. A. Distinct 19 S and 20 S subcomplexes of the 26 S proteasome and their distribution in the nucleus and the cytoplasm. *J. Biol. Chem.* **269**, 7709–7718 (1994).

28. 28.

Wendler, P. & Enenkel, C. Nuclear transport of yeast proteasomes. *Front. Mol. Biosci.* **6**, 34 (2019).

29. 29.

Palacios, V., Kimble, G. C., Tootle, T. L. & Buszczak, M. Importin-9 regulates chromosome segregation and packaging in *Drosophila* germ cells. *J. Cell Sci.* **134**, jcs258391 (2021).

30. 30.

Budenholzer, L., Breckel, C., Hickey, C. M. & Hochstrasser, M. The Sts1 nuclear import adapter uses a non-canonical bipartite nuclear localization signal and is directly degraded by the proteasome. *J. Cell Sci.* **133**, jcs236158 (2020).

31. 31.

Dominguez, D. et al. A high-resolution transcriptome map of cell cycle reveals novel connections between periodic genes and cancer. *Cell Res.* **26**, 946–962 (2016).

32. 32.

Manasanch, E. E. & Orlowski, R. Z. Proteasome inhibitors in cancer therapy. *Nat. Rev. Clin. Oncol.* **14**, 417–433 (2017).

33. 33.

Parnas, O. et al. A genome-wide CRISPR screen in primary immune cells to dissect regulatory networks. *Cell* **162**, 675–686 (2015).

34. 34.

Brockmann, M. et al. Genetic wiring maps of single-cell protein states reveal an off-switch for GPCR signalling. *Nature* **546**, 307–311 (2017).

35. 35.

Umkehrer, C. et al. Isolating live cell clones from barcoded populations using CRISPRa-inducible reporters. *Nat. Biotechnol.* **39**, 174–178 (2020).

36. 36.

Schambach, A. et al. Lentiviral vectors pseudotyped with murine ecotropic envelope: increased biosafety and convenience in preclinical research. *Exp. Hematol.* **34**, 588–592 (2006).

37. 37.

Wang, T. et al. Identification and characterization of essential genes in the human genome. *Science* **350**, 1096–1101 (2015).

38. 38.

Morgens, D. W. et al. Genome-scale measurement of off-target activity using Cas9 toxicity in high-throughput screens. *Nat. Commun.* **8**, 15178 (2017).

39. 39.

Langmead, B. & Salzberg, S. L. Fast gapped-read alignment with Bowtie 2. *Nat. Methods* **9**, 357–359 (2012).

40. 40.

Liao, Y., Smyth, G. K. & Shi, W. featureCounts: an efficient general purpose program for assigning sequence reads to genomic features. *Bioinformatics* **30**, 923–930 (2014).

41. 41.

Li, W. et al. MAGeCK enables robust identification of essential genes from genome-scale CRISPR/Cas9 knockout screens. *Genome Biol.* **15**, 554 (2014).

42. 42.

Klijn, C. et al. A comprehensive transcriptional portrait of human cancer cell lines. *Nat. Biotechnol.* **33**, 306–312 (2015).

43. 43.

Martin, M. Cutadapt removes adapter sequences from high-throughput sequencing reads. *EMBnet.journal* **17**, <https://journal.embnet.org/index.php/embnetjournal/article/view/200> (2011).

44. 44.

Dobin, A. et al. STAR: ultrafast universal RNA-seq aligner. *Bioinformatics* **29**, 15–21 (2013).

45. 45.

O’Leary, N. A. et al. Reference sequence (RefSeq) database at NCBI: current status, taxonomic expansion, and functional annotation. *Nucleic Acids Res.* **44**, D733–D745 (2016).

46. 46.

Love, M. I., Huber, W. & Anders, S. Moderated estimation of fold change and dispersion for RNA-seq data with DESeq2. *Genome Biol.* **15**, 550 (2014).

47. 47.

Zhu, A., Ibrahim, J. G. & Love, M. I. Heavy-tailed prior distributions for sequence count data: removing the noise and preserving large differences. *Bioinformatics* **35**, 2084–2092 (2019).

48. 48.

Dorfer, V. et al. MS Amanda, a universal identification algorithm optimized for high accuracy tandem mass spectra. *J. Proteome Res.* **13**, 3679–3684 (2014).

49. 49.

Smyth, G. K. Linear models and empirical Bayes methods for assessing differential expression in microarray experiments. *Stat. App. Gene. Mol. Biol.* **3**, Article3 (2004).

50. 50.

Mellacheruvu, D. et al. The CRAPome: a contaminant repository for affinity purification–mass spectrometry data. *Nat. Methods* **10**, 730–

736 (2013).

51. 51.

Schaab, C., Geiger, T., Stoehr, G., Cox, J. & Mann, M. Analysis of high accuracy, quantitative proteomics data in the MaxQB database. *Mol. Cell Proteomics* **11**, M111. 014068 (2012).

52. 52.

Mi, H., Muruganujan, A., Ebert, D., Huang, X. & Thomas, P. D. PANTHER version 14: more genomes, a new PANTHER GO-slim and improvements in enrichment analysis tools. *Nucleic Acids Res.* **47**, D419–D426 (2019).

53. 53.

Altschul, S. F. et al. Gapped BLAST and PSI-BLAST: a new generation of protein database search programs. *Nucleic Acids Res.* **25**, 3389–3402 (1997).

54. 54.

Emms, D. M. & Kelly, S. OrthoFinder: solving fundamental biases in whole genome comparisons dramatically improves orthogroup inference accuracy. *Genome Biol.* **16**, 157 (2015).

55. 55.

Crooks, G. E., Hon, G., Chandonia, J. M. & Brenner, S. E. WebLogo: a sequence logo generator. *Genome Res.* **14**, 1188–1190 (2004).

56. 56.

Katoh, K., Rozewicki, J. & Yamada, K. D. MAFFT online service: multiple sequence alignment, interactive sequence choice and visualization. *Briefings Bioinform.* **20**, 1160–1166 (2019).

57. 57.

Waterhouse, A. M., Procter, J. B., Martin, D. M., Clamp, M. & Barton, G. J. Jalview Version 2—a multiple sequence alignment editor and analysis workbench. *Bioinformatics* **25**, 1189–1191 (2009).

58. 58.

Ishida, T. & Kinoshita, K. PrDOS: prediction of disordered protein regions from amino acid sequence. *Nucleic Acids Res.* **35**, W460–W464 (2007).

59. 59.

Kosugi, S., Hasebe, M., Tomita, M. & Yanagawa, H. Systematic identification of cell cycle-dependent yeast nucleocytoplasmic shuttling proteins by prediction of composite motifs. *Proc. Natl Acad. Sci. USA* **106**, 10171–10176 (2009).

60. 60.

Cuff, J. A. & Barton, G. J. Application of multiple sequence alignment profiles to improve protein secondary structure prediction. *Proteins* **40**, 502–511 (2000).

61. 61.

Drozdetskiy, A., Cole, C., Procter, J. & Barton, G. J. JPred4: a protein secondary structure prediction server. *Nucleic Acids Res.* **43**, W389–W394 (2015).

62. 62.

Lupas, A., Van Dyke, M. & Stock, J. Predicting coiled coils from protein sequences. *Science* **252**, 1162–1164 (1991).

63. 63.

Doblmann, J. et al. apQuant: accurate label-free quantification by quality filtering. *J. Proteome Res.* **18**, 535–541 (2019).

64. 64.

Studier, F. W. Protein production by auto-induction in high density shaking cultures. *Protein Expr. Purif.* **41**, 207–234 (2005).

65. 65.

Sonn-Segev, A. et al. Quantifying the heterogeneity of macromolecular machines by mass photometry. *Nat. Commun.* **11**, 1772 (2020).

66. 66.

Dohmen, R. J. & Scheffner, M. (eds) *Ubiquitin Family Modifiers and the Proteasome* (Springer, 2012).

67. 67.

Besche, H. C., Haas, W., Gygi, S. P. & Goldberg, A. L. Isolation of mammalian 26S proteasomes and p97/VCP complexes using the ubiquitin-like domain from HHR23B reveals novel proteasome-associated proteins. *Biochemistry* **48**, 2538–2549 (2009).

68. 68.

Schorb, M., Haberbosch, I., Hagen, W. J. H., Schwab, Y. & Mastronarde, D. N. Software tools for automated transmission electron microscopy. *Nat. Methods* **16**, 471–477 (2019).

69. 69.

Zivanov, J. et al. New tools for automated high-resolution cryo-EM structure determination in RELION-3. *eLife* **7**, e42166 (2018).

70. 70.

Goddard, T. D. et al. UCSF ChimeraX: meeting modern challenges in visualization and analysis. *Protein Sci.* **27**, 14–25 (2018).

71. 71.

Punjani, A., Rubinstein, J. L., Fleet, D. J. & Brubaker, M. A. cryoSPARC: algorithms for rapid unsupervised cryo-EM structure determination. *Nat. Methods* **14**, 290–296 (2017).

72. 72.

Rohou, A. & Grigorieff, N. CTFFIND4: Fast and accurate defocus estimation from electron micrographs. *J. Struct. Biol.* **192**, 216–221 (2015).

73. 73.

Zivanov, J., Nakane, T. & Scheres, S. H. W. Estimation of high-order aberrations and anisotropic magnification from cryo-EM data sets in RELION-3.1. *IUCrJ* **7**, 253–267 (2020).

74. 74.

Sanchez-Garcia, R. et al. DeepEMhancer: a deep learning solution for cryo-EM volume post-processing. *Commun. Biol.* **4**, 874 (2021).

75. 75.

Schrader, J. et al. The inhibition mechanism of human 20S proteasomes enables next-generation inhibitor design. *Science* **353**, 594–598 (2016).

76. 76.

Pettersen, E. F. et al. UCSF Chimera—a visualization system for exploratory research and analysis. *J. Comput. Chem.* **25**, 1605–1612 (2004).

77. 77.

Murshudov, G. N. et al. REFMAC5 for the refinement of macromolecular crystal structures. *Acta Crystallogr. D Biol. Crystallogr.* **67**, 355–367 (2011).

78. 78.

Kim, D. E., Chivian, D. & Baker, D. Protein structure prediction and analysis using the Robetta server. *Nucleic Acids Res.* **32**, W526–W531 (2004).

79. 79.

Emsley, P. & Cowtan, K. Coot: model-building tools for molecular graphics. *Acta Crystallogr. D Biol. Crystallogr.* **60**, 2126–2132 (2004).

80. 80.

Croll, T. I. ISOLDE: a physically realistic environment for model building into low-resolution electron-density maps. *Acta Crystallogr. D Struct. Biol.* **74**, 519–530 (2018).

81. 81.

Afonine, P. V. et al. Real-space refinement in PHENIX for cryo-EM and crystallography. *Acta Crystallogr. D Struct. Biol.* **74**, 531–544 (2018).

82. 82.

Lukinavicius, G. et al. SiR-Hoechst is a far-red DNA stain for live-cell nanoscopy. *Nat. Commun.* **6**, 8497 (2015).

83. 83.

Dong, Y. et al. Cryo-EM structures and dynamics of substrate-engaged human 26S proteasome. *Nature* **565**, 49–55 (2019).

Acknowledgements

We are grateful to all members of the Zuber and Haselbach laboratories and to A. Pauli, C. Plaschka, T. Clausen, D. Gerlich, M. Petrovic, F. Grebien, N. Brown, G. Winter and M. Petronczki for experimental advice and helpful

discussions. We thank members of the Obenauf, Gerlich, Clausen, Peters and Busslinger laboratories at IMP and IMBA for sharing reagents; K. Aumayr, P. Pasierbeck, the IMP BioOptics flow cytometry, microscopy and image analysis team and T. Kreslavskiy for cell sorting and imaging; G. Dürnberger and A. Lüttig at the IMP/IMBA Protein Biochemistry Core Facility for performing quantitative proteomics and immunoprecipitation mass spectrometry; A. Sommer and the VBCF-NGS team (<https://www.vbcf.ac.at>) for deep sequencing services; the Electron Microscopy Facility team at Vienna BioCenter Core Facilities for negative staining electron microscopy; A. Meinhart for model building advice; O. Kaya for experimental support; the IMP/IMBA Molecular Biology Service for continuous support; and G. Riddihough (Life Science Editors) for help with editing. We acknowledge Diamond Light Source for access and support of the cryo-EM facilities at the United Kingdom's national Electron Bio-imaging Centre (under proposal EM BI25222), funded by the Wellcome Trust, the Medical Research Council and the Biotechnology and Biological Sciences Research Council. This work was funded by a Starting Grant from the European Research Council (ERC-StG-336860) to J.Z., the Austrian Science Fund (SFB grant F4710) to J.Z. and EPIC-XS (project number 823839), funded by the Horizon 2020 Programme of the European Union, to K.M. M.d.A. is the recipient of a DOC fellowship of the Austrian Academy of Sciences. Research at the IMP is generously supported by Boehringer Ingelheim and the Austrian Research Promotion Agency (Headquarter grant FFG-852936).

Author information

Author notes

1. Kashish Singh

Present address: MRC Laboratory of Molecular Biology, Cambridge, UK

2. Julian Jude

Present address: Twist Bioscience, San Francisco, CA, USA

3. Sumit Deswal

Present address: Genome Engineering, Discovery Sciences,
BioPharmaceuticals R&D, AstraZeneca, Gothenburg, Sweden

4. Tobias Neumann

Present address: Quantro Therapeutics, Vienna, Austria

5. These authors contributed equally: Melanie de Almeida, Matthias Hinterndorfer

Affiliations

1. Research Institute of Molecular Pathology (IMP), Vienna BioCenter (VBC), Vienna, Austria

Melanie de Almeida, Matthias Hinterndorfer, Hanna Brunner, Irina Grishkovskaya, Kashish Singh, Alexander Schleiffer, Julian Jude, Sumit Deswal, Robert Kalis, Thomas Lendl, Richard Imre, Elisabeth Roitinger, Tobias Neumann, Susanne Kandolf, Michael Schutzbier, Karl Mechtler, David Haselbach & Johannes Zuber

2. Vienna BioCenter PhD Program, Doctoral School of the University at Vienna and Medical University of Vienna, Vienna BioCenter (VBC), Vienna, Austria

Melanie de Almeida, Matthias Hinterndorfer, Hanna Brunner, Robert Kalis & Milica Vunjak

3. Department of Microbiology, Immunobiology and Genetics, Max Perutz Labs, University of Vienna, Vienna BioCenter (VBC), Vienna, Austria

Milica Vunjak & Gijs A. Versteeg

4. Medical University of Vienna, Vienna BioCenter (VBC), Vienna, Austria

Johannes Zuber

Contributions

M.d.A. and M.H. contributed equally and will be putting their name first on the citation in their CVs. M.d.A., M.H. and J.Z. conceived and planned this project. M.d.A., M.H., H.B. and I.G. designed and conducted experiments with help from M.S., S.K. and E.R. M.d.A., M.H., H.B., I.G., K.S., D.H. and J.Z. analysed and interpreted original data. A.S. performed phylogenetic analyses. T.L. established scripts for imaging analysis. D.H. and K.S. performed the 3D structure reconstruction. T.N. and R.I. performed deep sequencing and mass spectrometry data analyses, respectively. J.J., S.D., R.K. and M.V. established critical reagents and methodology. K.M. and G.V. provided critical input on experimental designs and data analyses. M.d.A., M.H., D.H. and J.Z. co-wrote the manuscript with input from all co-authors.

Corresponding authors

Correspondence to [David Haselbach](#) or [Johannes Zuber](#).

Ethics declarations

Competing interests

J.Z. is a founder, shareholder and scientific advisor of Quantro Therapeutics. J.Z., D.H. and the Zuber and Haselbach laboratories receive research support and funding from Boehringer Ingelheim. J.J. is now an employee of Twist Bioscience and T.N. is now an employee of Quantro Therapeutics. Other authors declare no competing interests.

Additional information

Peer review information *Nature* thanks Roderick Beijersbergen, Cordula Enenkel, Edmond Watson and the other, anonymous, reviewer(s) for their

contribution to the peer review of this work. Peer reviewer reports are available.

Publisher's note Springer Nature remains neutral with regard to jurisdictional claims in published maps and institutional affiliations.

Extended data figures and tables

Extended Data Fig. 1 Engineering and validation of clonal iCas9 cell lines.

a, Schematic of clonal iCas9 cell line engineering and validation. Roman numbers indicate the vectors used for each cell line. In K562, generation of tightly regulatable iCas9 clones required additional suppression of leaky transcription from Tet-responsive promoters via a TetR-KRAB fusion protein. **b–d**, Evaluation of iCas9 function. **b**, Flow cytometric evaluation of inducible Cas9-P2A-GFP (RKO, K562) or -BFP (MIA-PaCa-2) expression in the presence or absence of DOX. **c**, Competitive proliferation assays in iCas9 cells transduced with sgRNAs targeting the core-essential genes *PSMA3* (RKO), *PLK1* (MIA-PaCa-2), or *RPL23* (K562). Percentage of sgRNA⁺ cells was monitored by flow cytometry in the presence or absence of DOX for 10 days. Values are normalized to Day 0. **d**, Evaluation of surface marker editing in iCas9 cells transduced with sgRNAs targeting the surface markers *CD151* (RKO, MIA-PaCa-2) or *CD46* (K562). Editing was evaluated by immunostaining and flow cytometry 48 h after Cas9 induction. **e**, Analysis of *MYC/MYCN* mRNA levels based on⁴². A MYC/MYCN specific antibody was used for the detection of MYC. rtTA3, reverse tetracycline transactivator; DOX, doxycycline; PuroR, puromycin resistance gene; HygroR, hygromycin resistance gene; TRE3G, tetracycline response element; 2A, P2A self-cleaving peptide; GFP, green fluorescent protein; BFP, blue fluorescent protein; APC, allophycocyanin; RPKM, reads per kilo base per million mapped reads.

Extended Data Fig. 2 Identification of MYC regulators in iCas9 screens depends on their turnover and essentiality.

a–b, First timepoints of FACS-based CRISPR MYC-regulator (**a**) and dropout (**b**) screens. **a**, Gene-level sgRNA enrichment in MYC^{lo} (left panels) or MYC^{hi} cells (right panels) over MYC^{mid} (RKO, K562) or unsorted (MIA-PaCa-2) cells and MAGeCK⁴¹ one-sided *P* values. Dashed lines indicate 95th percentile of enrichment and significance (*P* < 0.01). Essential genes based on^{12,37,38} within the scoring window are highlighted in red, 20S-CP subunits in blue. **b**, Gene-level sgRNA depletion in unsorted populations at the first screen timepoint compared to day 0. SgRNAs targeting highly turned-over essential proteins deplete already 2.5 days after Cas9-induction. **c, d**, Second screen timepoints as in **a** and **b**. The identification of MYC regulators at each timepoint depends on their turnover and essentiality. Short-lived essential proteins scored at the first timepoint in FACS-based (**a**) and dropout screens (**b**); however, due to rapid effects on cell viability (**d**), sgRNAs targeting these genes were undetectable at the second timepoint in FACS-based screens (**c**). Conversely, knockout of more stable proteins or protein complexes such as the 20S proteasome had only limited effects in MYC-regulation- (**a**) or dropout- screens after 2.5 days (**b**), while effects were readily detectable 4–5 days post Cas9 induction (**c, d**). The kinetics of gene editing, protein turnover and depletion of sgRNA-expressing cells are further determined by the cellular context, with rapid effects in diploid RKO cells, and delayed effects in hypertriploid K562 and tetraploid MIA-PaCa-2 cells.

Extended Data Fig. 3 AKIRIN2 is an essential regulator of MYC expression.

a–c, Flow cytometric quantification of endogenous MYC protein levels after inducible knockout of MYC regulators in RKO (**a**), MIA-PaCa2 (**b**), and K562 cells (**c**) 1–3 days after Cas9 induction. For MIA-PaCa2 and K562 the timepoint with the maximal effect on MYC protein abundance is shown. RKO maximal timepoints as in Fig. [2c](#). **d–e**, Percentage of cleaved-caspase-3⁺ (**d**) and dead cells (**e**) quantified by flow-cytometry before and 1–3 days after induction of AKIRIN2 knockout. **f**, Competitive proliferation assays. Percentage of sgRNA⁺ iCas9-RKO cells was monitored by flow cytometry in 24 h intervals after Cas9 induction. Values are normalized to Day 0. Data in **a** is representative of three, in **b–c** of two independent

experiments. Data in **d–f** is shown as mean \pm s.d. ($n = 3$ biological replicates). PE, phycoerythrin.

Extended Data Fig. 4 AKIRIN2 regulates nuclear protein turnover.

a–c, Transcriptional changes after acute knockout of AKIRIN2 (**a**) or PSMA3 (**b**). RNA-seq of iCas9-RKO cells was performed 2 (sgAKIRIN2, sgAAVS1) or 3 days (sgPSMA3) after Cas9 induction ($n = 3$ biological replicates). Genes significantly up- or downregulated ($P \leq 0.01$; Benjamini-Hochberg corrected two-sided Wald-test) at least two-fold are highlighted in orange, TP53 target genes according to²⁰ in red. **c**, Principal component (PC) analysis of the 1000 most highly expressed genes. **d, e**, AKIRIN2 and MYC protein half-life quantification. Immunoblot time-series of iCas9-RKO cells treated with cycloheximide (CHX) 2 days after Cas9 induction (**d**) and half-life quantification (**e**) of AKIRIN2 (half-life = 46 min, 95% CI = 37–58 min) and MYC (half-life = 25 and 178 min with 95% CI = 21–31 and 51–238 min in sgAAVS1 control and sgAKIRIN2 cells, respectively). Data is shown as mean \pm s.d. ($n \geq 3$ independent experiments). Dashed lines indicate halflives. **f, g**, Quantitative proteomics following induced AKIRIN2 or PSMA3 knockout. Samples were obtained as described for a-c ($n = 2$ biological replicates). **f**, Principal component analysis of the 1000 most highly expressed proteins. **g**, Scatter plot of transcriptome- versus proteome-changes upon acute AKIRIN2 knockout compared to sgAAVS1 control. AKIRIN2 targets as in Fig. [3a, b](#) (orange; $n = 124$) are upregulated only on protein-, but not on mRNA-level. TP53 target genes as in **a, b** are shown in red. **h**, Western blot of selected AKIRIN2 targets after AKIRIN2 or proteasome knockout. iCas9-RKO cells expressing the indicated sgRNAs were harvested before, and 2 and 3 days after Cas9 induction. **i**, Euler diagram of proteasome targets and AKIRIN2 targets as defined in Fig. [3a, b](#). CI, confidence interval; FC, fold change.

Extended Data Fig. 5 AKIRIN2 is a highly conserved nuclear protein.

a, Alignment of Akirin orthologs from 11 representative model organisms. AKIRIN2 and AKIRIN1 are highly conserved in vertebrates. In invertebrate metazoans, only one Akirin ortholog per species was found, which is more closely related to AKIRIN2 than to AKIRIN1. Colors denote clustal amino acid identity. **b–d**, Knockout-rescue studies evaluating essentiality of AKIRIN2 protein features as in Fig. 4c, d. **b**, Schematic setup of knockout-rescue experiments and *AKIRIN2* cDNA variants, in which sgAKIRIN2 seed and PAM sequences were removed through synonymous mutations. Roman numbers are continued from Fig. 4c. **c**, Competitive proliferation assays of iCas9-RKO cells co-expressing sgAKIRIN2 and the indicated *AKIRIN2* cDNA variant. Cells were monitored using flow cytometry for 10 days after Cas9 induction. Values are normalized to Day 0. Data is shown as mean \pm s.d. ($n = 3$ independent experiments). **d**, Immunoblotting of V5 and AKIRIN2 in iCas9-RKO cells expressing the indicated *AKIRIN2* cDNA variants. **e**, Immunofluorescence localization of AKIRIN2. V5-AKIRIN2 knockout-rescue RKO cells were stained with α -V5 antibody. Images are representative of 3 independent experiments. Scale bar, 15 μ m. **f**, Co-IP/MS of full-length V5-AKIRIN1 purified with α -V5 antibody. Enrichment was calculated over V5-NLS-GFP control (Benjamini-Hochberg corrected limma moderated two-sided *t*-test, $n = 6$ biological replicates from 2 independent experiments).

Extended Data Fig. 6 AKIRIN2 purification and negative staining EM.

a, Schematic four-step purification of recombinant His-GST-AKIRIN2 from *E. coli* (left) and size-exclusion chromatogram (right). Blue bars indicate GST-AKIRIN2 containing fractions analyzed by SDS-PAGE. **b**, SDS-PAGE of eluted fractions. Lower 26 kDa band corresponds to free GST. **c**, **d**, Co-IP/MS of sucrose fractionated proteins co-purified with GST-AKIRIN2 from cytosolic HeLa cell lysate. Experimental setup (c) and normalized protein abundance of selected AKIRIN2-interactors across sucrose fractions (d). 20S-CP and 19S-RP datapoints represent the mean of all 20S-CP and 19S-ATPase and non-ATPase subunits as defined in Fig. 2b, respectively. **e–h**, Negative staining electron microscopy of AKIRIN2-proteasome complexes. Experimental setup (e) and SDS-PAGE (f) of sucrose gradient fractionated proteins co-purified with GST-AKIRIN2 (left)

or GST-UBL (right) from PEG-concentrated HeLa cell lysate. Red boxes indicate fractions used for negative staining electron microscopy (**g**, **h**). 3D reconstructions (**g**) and representative negative stain electron micrograph and 2D class averages (**h**) of 26S proteasome complexes co-purified with GST-AKIRIN2 (left) or GST-UBL (right). Arrows indicate AKIRIN2-specific densities. Data in **a–b** and **f–h** are representative of three independent experiments. Scale bar, 50 nm. SEC, size-exclusion chromatography; EM, electron microscopy; CP, core (proteasome) particle; RP, regulatory particle.

Extended Data Fig. 7 Cryo-EM data processing and analysis of the AKIRIN2-proteasome complex.

a, Representative micrograph and 2D class averages of proteasome complexes co-purified with AKIRIN2. Data is representative of three independent experiments. Scale bar, 50 nm. **b**, Angular distributions of individual particles. **c**, Fourier Shell Correlation (FSC) curve of the refined EM map at 3.2 Å resolution. **d**, Cryo-EM density map of AKIRIN2 bound to the 20S proteasome as in Fig. [4g](#), side view. **e**, **f**, Cryo-EM model of AKIRIN2 bound to the 20S proteasome (**e**) and the substrate-engaged 26S proteasome complex (**f**). Detail views show the binding sites of AKIRIN2. In the active proteasome conformation, the α_3/α_4 pocket (top) and α_2/α_3 pocket (bottom) are occupied by PSMC1 (Rpt2) and PSMC5 (Rpt6), respectively. At a low threshold, the α_1/α_2 pocket also contains a density that may be attributed to the AKIRIN2 C-terminal motif. 20S subunits are shown in blue, AKIRIN2 in red, PSMC1 and PSMC5 in orange, other 19S subunits in transparent white. 26S structure^{[83](#)} was accessed via PDB ID: 6MSJ. FSC, Fourier shell correlation.

Extended Data Fig. 8 AKIRIN2 is a critical mediator of nuclear proteasome import.

a–c, Engineering of 20S proteasome reporter cells. **a**, Schematic of vectors (left) used for PSMB4 knockout-rescue (right). iCas9-RKO cells were co-transduced with an sgRNA targeting *PSMB4* and a cDNA encoding a FLAG-tagged sgRNA-resistant PSMB4-mCherry fusion protein. sgRNA

and cDNA double positive cells were monitored by flow cytometry for 7 days after Cas9 induction. Percentage is normalized to Day 0. **b**, Immunoblot analysis of single cell-derived clonal PSMB4-mCherry reporter cells and WT iCas9-RKO cells. **c**, SDS-PAGE and immunoblot of PSMB4 in WT iCas9-RKO (top) and clonal PSMB4-mCherry reporter cells (bottom) after sucrose gradient fractionation. **d, e**, Representative IF images (**d**) and quantification (**e**) of endogenous PSMA5 (blue) levels in iCas9-RKO cells after induced knockout of AKIRIN2 ($n = 2,729$ cells) or AAVS1 ($n = 3,625$ cells). **f–h**, mCherry-PSMD3 19S proteasome reporter as in **a–c**. **i–j**, Representative confocal images (**i**) and quantification (**j**) of mCherry-PSMD3 signal after induced knockout of AKIRIN2 ($n = 6,858$ cells) or AAVS1 ($n = 7,309$ cells). **k–n**, Nuclear proteasome import (**k, l**) and MYC protein levels (**m, n**) after induced IPO9 knockout. Representative confocal images (**k**) and quantification (**l**) of PSMB4-mCherry signal 7 days after induced IPO9 ($n = 8,055$ cells) or AAVS1 ($n = 8,336$ cells) knockout. Representative flow cytometry histogram of endogenous MYC protein levels 7 days after induced IPO9 knockout (**m**) and fold change compared to sgRNA⁻ cells (one-sided Welch's *t*-test) (**n**). Bars and whiskers represent mean and standard deviation of 3 biological replicates. Nuclei in **e, j, l** were segmented based on DNA channel and signal was normalized to the mean nuclear signal in sgAAVS1 cells. Data in **e, j, l** is shown as mean \pm s.d. ($n = 9$ biological replicates from 3 independent experiments; two-sided Welch's *t*-test). Data in **c, h** is representative of 2 independent experiments. Scale bars, 15 μm . FC, fold change.

Extended Data Fig. 9 AKIRIN2 controls the nuclear re-import of proteasomes following mitosis.

a, Quantification of nuclear PSMB4-mCherry signal in individual dividing iCas9-RKO reporter cells after AKIRIN2 ($n = 38$ cells) or AAVS1 knockout ($n = 27$ cells) as shown in Fig. [5d](#) over time. **b–d**, Time-lapse imaging of mitotic PSMB4-mCherry RKO reporter cells co-expressing IBB-GFP. **b**, Quantification of nuclear PSMB4-mCherry and IBB-GFP signal in dividing reporter cells shown as averaged data (**b**, mean \pm 95% CI, $n = 27$ cells from two independent experiments), individual cell-tracks (**c**), and representative time-lapse images (**d**). Dashed line indicates the onset of IBB-GFP import. DNA was visualized with SiR-Hoechst. Signal intensity is normalized to $t =$

–100 min. Scale bar, 10 µm. **e**, Quantification of MYC-mCherry signal as in **a** after AKIRIN2 ($n = 40$ cells) or AAVS1 knockout ($n = 38$ cells) as shown in Fig. 5f. **f**, Model of post-mitotic nuclear proteasome import mediated by AKIRIN2. Cells undergoing mitotic cell division upon loss of AKIRIN2 give rise to daughter cells that are devoid of nuclear proteasomes. Signal in **a, e** is normalized to mean nuclear signal in sgAAVS1 cells. Pseudotime is normalized to the timepoint of maximal chromatin condensation (**a, e**) or to the onset of nuclear PSMB4-mCherry import (**b, c**).

Extended Data Table 1 Plasmids, sgRNAs and oligonucleotides used in this study

Supplementary information

Supplementary Figs.

This file contains Supplementary Figs. 1–3. Supplementary Fig. 1 contains uncropped images of western blots and SDS gels. Supplementary Fig. 2 shows representative gating strategies for FACS-based MYC regulator screens and flow cytometric analyses. Supplementary Fig. 3 schematically shows cryo electron microscopy image processing and model building.

Reporting Summary

Supplementary Table 1

Raw sgRNA counts of MYC regulator screens. For each screen condition, raw sequencing reads for individual sgRNAs are provided. Reads are not normalized to sequencing depth. Column names are provided in the format cellline_FACSGate_timepoint_replicate.

Supplementary Table 2

MAGECK analysis of MYC regulator screens. Gene-level average, median-normalized \log_2 fold changes, one-tailed logarithmized P values and FDRs calculated by MAGECK v0.5.9. The table contains the merged dataset

representing the minimum P value of both time points, as well as individual datasets for each time point. GO terms are annotated, and genes highlighted and categorized in Fig. 1 and Fig. 2 are indicated. Column names are provided in the format variable_cellline_FACSGate_timepoint.

Supplementary Table 3

Quantitative proteomics and RNA-seq results. Combined table of TMT mass spectrometry and RNA-seq results including normalized protein abundance and mRNA TPM averaged over two or three replicates, respectively, as well as \log_2 fold changes and logarithmized P values (Benjamini–Hochberg-corrected two-tailed limma moderated t -test and Wald test, respectively). Classification into AKIRIN2-responsive and -independent proteasome targets according to Fig. 3 is annotated.

Supplementary Table 4

GO term enrichment analysis of proteasome targets. Results of GO term enrichment analysis of AKIRIN2-responsive and -independent proteasome targets using PANTHER two-tailed Fisher's exact over-representation test with Benjamini–Hochberg multiple testing correction on GO database (release 2020-06-01). Ratio of FDRs (Δ FDR) for AKIRIN2-responsive and -independent genes for each GO term is provided.

Supplementary Table 5

Akirin orthologues. Gene name, species name, primary accession number and protein length in amino acids for 103 Akirin orthologues from 77 different species used for phylogenetic analyses. Consideration of individual orthologues for the different analyses and figures are annotated.

Supplementary Table 6

AKIRIN2 co-immunoprecipitation mass spectrometry results. Normalized, imputed protein abundances identified by co-immunoprecipitation mass spectrometry analysis of V5-AKIRIN2, V5-AKIRIN1, V5-AKIRIN2 Δ YVS

and V5-GFP in RKO cells averaged over six replicates, including \log_2 fold changes and logarithmized *P* values (Benjamini–Hochberg-corrected two-tailed limma moderated *t*-test) as well as mass spectrometric quantification of proteins co-purified with GSTAKIRIN2 from HeLa cell extract after fractionation on a 10–30% sucrose gradient.

Supplementary Table 7

Proteasome subunit nomenclature. Human gene name, common protein nomenclature and chain ID and protein nomenclature used in cryo-EM model of AKIRIN2 bound to the 20S proteasome.

Supplementary Table 8

EM model building statistics. EM data collection and processing statistics for negative stain EM structure of AKIRIN2 bound to the 26S proteasome and data collection, processing, refinement and validation statistics for cryo-EM structure of AKIRIN2 bound to the 20S proteasome.

Supplementary Table 9

Glossary. Abbreviations used in the manuscript and their definitions.

Supplementary Video 1

Live-cell imaging of mCherry–MYC reporter cells. Movie highlights kinetics of MYC stabilization after inducible knockout of *AKIRIN2*, *FBXW7* or the 20S proteasome subunit *PSMA1*. Cells were imaged every 2 h for 96 h. Scale bar, 100 μ m.

Supplementary Video 2

Confocal live-cell imaging of mitotic RKO reporter cells after inducible *AKIRIN2/AAVS1* knockout. mCherryMYC or PSMB4mCherry reporter cells were imaged 15–24 h after induction of *AKIRIN2/AAVS1* knockout and imaged at 5- or 10-min intervals as indicated. mCherry–MYC is shown

in red, PSMB4mCherry in blue and DNA in grey. Scale bar, 10 µm (single cell) and 50 µm (overview, 10 h).

[Peer Review File](#)

Rights and permissions

[Reprints and Permissions](#)

About this article

Cite this article

de Almeida, M., Hinterndorfer, M., Brunner, H. *et al.* AKIRIN2 controls the nuclear import of proteasomes in vertebrates. *Nature* **599**, 491–496 (2021). <https://doi.org/10.1038/s41586-021-04035-8>

- Received: 25 March 2021
- Accepted: 16 September 2021
- Published: 28 October 2021
- Issue Date: 18 November 2021
- DOI: <https://doi.org/10.1038/s41586-021-04035-8>

Share this article

Anyone you share the following link with will be able to read this content:

[Get shareable link](#)

Sorry, a shareable link is not currently available for this article.

[Copy to clipboard](#)

Provided by the Springer Nature SharedIt content-sharing initiative

This article was downloaded by **calibre** from <https://www.nature.com/articles/s41586-021-04035-8>

| [Section menu](#) | [Main menu](#) |

- Article
- [Published: 10 November 2021](#)

Target site selection and remodelling by type V CRISPR-transposon systems

- [Irma Querques](#) ORCID: [orcid.org/0000-0003-1113-2773¹](https://orcid.org/0000-0003-1113-2773)
- [Michael Schmitz](#) ORCID: [orcid.org/0000-0003-3216-7350¹](https://orcid.org/0000-0003-3216-7350)
- [Seraina Oberli](#) ORCID: [orcid.org/0000-0002-3568-7637¹](https://orcid.org/0000-0002-3568-7637)
- [Christelle Chanez](#) ORCID: [orcid.org/0000-0002-3432-4375¹](https://orcid.org/0000-0002-3432-4375) &
- [Martin Jinek](#) ORCID: [orcid.org/0000-0002-7601-210X¹](https://orcid.org/0000-0002-7601-210X)

Nature volume 599, pages 497–502 (2021)

- 4473 Accesses
- 75 Altmetric
- [Metrics details](#)

Subjects

- [Cryoelectron microscopy](#)
- [DNA](#)
- [RNA](#)
- [Small RNAs](#)
- [Transposition](#)

Abstract

Canonical CRISPR–Cas systems provide adaptive immunity against mobile genetic elements¹. However, type I-F, I-B and V-K systems have been adopted by Tn7-like transposons to direct RNA-guided transposon insertion^{2,3,4,5,6,7}. Type V-K CRISPR-associated transposons rely on the pseudonuclease Cas12k, the transposase TnsB, the AAA+ ATPase TnsC and the zinc-finger protein TniQ⁷, but the molecular mechanism of RNA-directed DNA transposition has remained elusive. Here we report cryo-electron microscopic structures of a Cas12k-guide RNA–target DNA complex and a DNA-bound, polymeric TnsC filament from the CRISPR-associated transposon system of the photosynthetic cyanobacterium *Scytonema hofmanni*. The Cas12k complex structure reveals an intricate guide RNA architecture and critical interactions mediating RNA-guided target DNA recognition. TnsC helical filament assembly is ATP-dependent and accompanied by structural remodelling of the bound DNA duplex. In vivo transposition assays corroborate key features of the structures, and biochemical experiments show that TniQ restricts TnsC polymerization, while TnsB interacts directly with TnsC filaments to trigger their disassembly upon ATP hydrolysis. Together, these results suggest that RNA-directed target selection by Cas12k primes TnsC polymerization and DNA remodelling, generating a recruitment platform for TnsB to catalyse site-specific transposon insertion. Insights from this work will inform the development of CRISPR-associated transposons as programmable site-specific gene insertion tools.

Access options

Subscribe to Journal

Get full journal access for 1 year

\$199.00

only \$3.90 per issue

[Subscribe](#)

All prices are NET prices.
VAT will be added later in the checkout.
Tax calculation will be finalised during checkout.

Rent or Buy article

Get time limited or full article access on ReadCube.

from \$8.99

[Rent or Buy](#)

All prices are NET prices.

Additional access options:

- [Log in](#)
- [Access through your institution](#)
- [Learn about institutional subscriptions](#)

Fig. 1: Cryo-EM structure of the *S. hofmanni* Cas12k–sgRNA–target DNA complex.

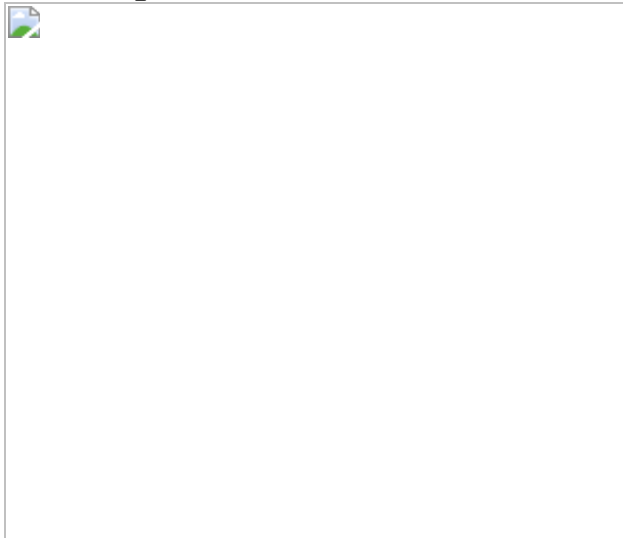


Fig. 2: Cryo-EM structure of the TnsC–dsDNA filaments.

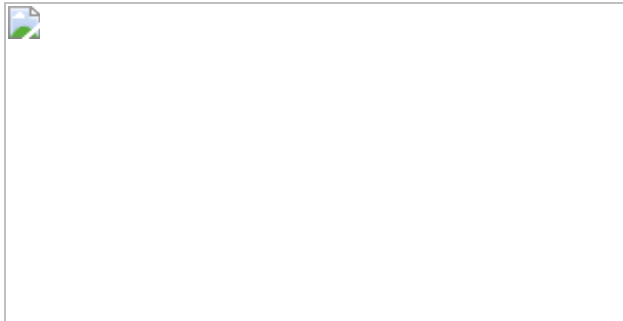


Fig. 3: DNA binding and remodelling by the TnsC filament.

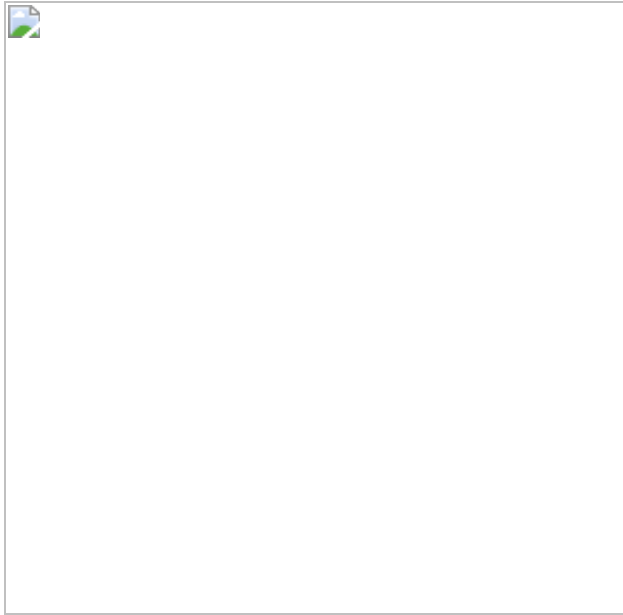


Fig. 4: Functional interactions and roles of ShCAST components.

Data availability

Maps and atomic coordinates of the reported cryo-EM structures have been deposited in the Electron Microscopy Data Bank under accession codes [EMD-13486](#) (*S. hofmanni* Cas12k–sgRNA–DNA complex) and [EMD-13489](#) (Tns-DNA filament), and the Protein Data Bank with accession

codes [7PLA](#) (Cas12k–sgRNA–DNA complex) and [7PLH](#) (Tns–DNA filament). Structure factors and atomic coordinates of the reported X-ray crystallographic structure of TniQ has been deposited in the Protein Data Bank with accession code [7OXD](#).

References

1. 1.
Sorek, R., Lawrence, C. M. & Wiedenheft, B. CRISPR-mediated adaptive immune systems in bacteria and archaea. *Annu. Rev. Biochem.* **82**, 237–266 (2013).
2. 2.
Faure, G. et al. CRISPR–Cas in mobile genetic elements: counter-defence and beyond. *Nat. Rev. Microbiol.* **17**, 513–525 (2019).
3. 3.
Klompe, S. E., Vo, P. L. H., Halpin-Healy, T. S. & Sternberg, S. H. Transposon-encoded CRISPR–Cas systems direct RNA-guided DNA integration. *Nature* **571**, 219–225 (2019).
4. 4.
Petassi, M. T., Hsieh, S. C. & Peters, J. E. Guide RNA categorization enables target site choice in Tn7-CRISPR–Cas transposons. *Cell* **183**, 1757–1771.e1718 (2020).
5. 5.
Peters, J. E., Makarova, K. S., Shmakov, S. & Koonin, E. V. Recruitment of CRISPR–Cas systems by Tn7-like transposons. *Proc. Natl Acad. Sci. USA* **114**, E7358–E7366 (2017).
6. 6.

Saito, M. et al. Dual modes of CRISPR-associated transposon homing. *Cell* **184**, 2441–2453.e2418 (2021).

7. 7.

Strecker, J. et al. RNA-guided DNA insertion with CRISPR-associated transposases. *Science* **365**, 48–53 (2019).

8. 8.

Koonin, E. V., Makarova, K. S. & Wolf, Y. I. Evolutionary genomics of defense systems in Archaea and Bacteria. *Annu. Rev. Microbiol.* **71**, 233–261 (2017).

9. 9.

Peters, J. E. & Craig, N. L. Tn7: smarter than we thought. *Nat. Rev. Mol. Cell Biol.* **2**, 806–814 (2001).

10. 10.

May, E. W. & Craig, N. L. Switching from cut-and-paste to replicative Tn7 transposition. *Science* **272**, 401–404 (1996).

11. 11.

Sarnovsky, R. J., May, E. W. & Craig, N. L. The Tn7 transposase is a heteromeric complex in which DNA breakage and joining activities are distributed between different gene products. *EMBO J.* **15**, 6348–6361 (1996).

12. 12.

Choi, K. Y., Spencer, J. M. & Craig, N. L. The Tn7 transposition regulator TnsC interacts with the transposase subunit TnsB and target selector TnsD. *Proc. Natl Acad. Sci. USA* **111**, E2858–E2865 (2014).

13. 13.

Ronning, D. R. et al. The carboxy-terminal portion of TnsC activates the Tn7 transposase through a specific interaction with TnsA. *EMBO J.* **23**, 2972–2981 (2004).

14. 14.

Stellwagen, A. E. & Craig, N. L. Gain-of-function mutations in TnsC, an ATP-dependent transposition protein that activates the bacterial transposon Tn7. *Genetics* **145**, 573–585 (1997).

15. 15.

Mitra, R., McKenzie, G. J., Yi, L., Lee, C. A. & Craig, N. L. Characterization of the TnsD-attTn7 complex that promotes site-specific insertion of Tn7. *Mob. DNA* **1**, 18 (2010).

16. 16.

Parks, A. R. et al. Transposition into replicating DNA occurs through interaction with the processivity factor. *Cell* **138**, 685–695 (2009).

17. 17.

Wolkow, C. A., DeBoy, R. T. & Craig, N. L. Conjugating plasmids are preferred targets for Tn7. *Genes Dev.* **10**, 2145–2157 (1996).

18. 18.

Halpin-Healy, T. S., Klompe, S. E., Sternberg, S. H. & Fernandez, I. S. Structural basis of DNA targeting by a transposon-encoded CRISPR–Cas system. *Nature* **577**, 271–274 (2020).

19. 19.

Jia, N., Xie, W., de la Cruz, M. J., Eng, E. T. & Patel, D. J. Structure–function insights into the initial step of DNA integration by a CRISPR–Cas–transposon complex. *Cell Res.* **30**, 182–184 (2020).

20. 20.

Li, Z., Zhang, H., Xiao, R. J. & Chang, L. F. Cryo-EM structure of a type I-F CRISPR RNA guided surveillance complex bound to transposition protein TniQ. *Cell Res.* **30**, 179–181 (2020).

21. 21.

Wang, B. B., Xu, W. H. & Yang, H. Structural basis of a Tn7-like transposase recruitment and DNA loading to CRISPR–Cas surveillance complex. *Cell Res.* **30**, 185–187 (2020).

22. 22.

Liu, J. J. et al. CasX enzymes comprise a distinct family of RNA-guided genome editors. *Nature* **566**, 218–223 (2019).

23. 23.

Li, Z. C., N. L. and Peters, J. E. in *Bacterial Integrative Mobile Genetic Elements*. Austin (eds Roberts, A. P. & Mullany, P.) 1–32 (Landes Bioscience, 2013).

24. 24.

Arias-Palomo, E. & Berger, J. M. An atypical AAA+ ATPase assembly controls efficient transposition through DNA remodeling and transposase recruitment. *Cell* **162**, 860–871 (2015).

25. 25.

Mizuno, N. et al. MuB is an AAA+ ATPase that forms helical filaments to control target selection for DNA transposition. *Proc. Natl Acad. Sci. USA* **110**, E2441–E2450 (2013).

26. 26.

Stellwagen, A. E. & Craig, N. L. Avoiding self: two Tn7-encoded proteins mediate target immunity in Tn7 transposition. *EMBO J.* **16**, 6823–6834, (1997).

27. 27.

Greene, E. C. & Mizuuchi, K. Target immunity during Mu DNA transposition. Transpososome assembly and DNA looping enhance MuA-mediated disassembly of the MuB target complex. *Mol. Cell* **10**, 1367–1378 (2002).

28. 28.

Greene, E. C. & Mizuuchi, K. Dynamics of a protein polymer: the assembly and disassembly pathways of the MuB transposition target complex. *EMBO J.* **21**, 1477–1486 (2002).

29. 29.

Park, J. U. et al. Structural basis for target site selection in RNA-guided DNA transposition systems. *Science* **373**, 768–774 (2021).

30. 30.

Swarts, D. C. & Jinek, M. Mechanistic insights into the *cis*- and *trans*-acting DNase activities of Cas12a. *Mol. Cell* **73**, 589–600.e584 (2019).

31. 31.

Anders, C., Niewoehner, O. & Jinek, M. In vitro reconstitution and crystallization of Cas9 endonuclease bound to a guide RNA and a DNA target. *Methods Enzymol.* **558**, 515–537 (2015).

32. 32.

Kabsch, W. Xds. *Acta Crystallogr. D* **66**, 125–132 (2010).

33. 33.

Liebschner, D. et al. Macromolecular structure determination using X-rays, neutrons and electrons: recent developments in Phenix. *Acta Crystallogr. D* **75**, 861–877 (2019).

34. 34.

Terwilliger, T. C. et al. Decision-making in structure solution using Bayesian estimates of map quality: the PHENIX AutoSol wizard. *Acta Crystallogr. D* **65**, 582–601 (2009).

35. 35.

Vonrhein, C., Blanc, E., Roversi, P. & Bricogne, G. Automated structure solution with autoSHARP. *Methods Mol. Biol.* **364**, 215–230 (2007).

36. 36.

Langer, G., Cohen, S. X., Lamzin, V. S. & Perrakis, A. Automated macromolecular model building for X-ray crystallography using ARP/wARP version 7. *Nat. Protoc.* **3**, 1171–1179 (2008).

37. 37.

Emsley, P., Lohkamp, B., Scott, W. G. & Cowtan, K. Features and development of Coot. *Acta Crystallogr. D* **66**, 486–501 (2010).

38. 38.

Afonine, P. V. et al. Real-space refinement in PHENIX for cryo-EM and crystallography. *Acta Crystallogr. D* **74**, 531–544 (2018).

39. 39.

de la Cruz, M. J., Martynowycz, M. W., Hattne, J. & Gonen, T. MicroED data collection with SerialEM. *Ultramicroscopy* **201**, 77–80 (2019).

40. 40.

Punjani, A., Rubinstein, J. L., Fleet, D. J. & Brubaker, M. A. cryoSPARC: algorithms for rapid unsupervised cryo-EM structure determination. *Nat. Methods* **14**, 290–296 (2017).

41. 41.

Bepler, T. et al. Positive-unlabeled convolutional neural networks for particle picking in cryo-electron micrographs. *Res. Comput. Mol. Biol.* **10812**, 245–247 (2018).

42. 42.

Pettersen, E. F. et al. UCSF Chimera—a visualization system for exploratory research and analysis. *J. Comput. Chem.* **25**, 1605-1612 (2004).

43. 43.

Brown, A. et al. Tools for macromolecular model building and refinement into electron cryo-microscopy reconstructions. *Acta Crystallogr. D* **71**, 136–153 (2015).

44. 44.

Chen, V. B. et al. MolProbity: all-atom structure validation for macromolecular crystallography. *Acta Crystallogr. D* **66**, 12–21 (2010).

45. 45.

Prisant, M. G., Williams, C. J., Chen, V. B., Richardson, J. S. & Richardson, D. C. New tools in MolProbity validation: CaBLAM for CryoEM backbone, UnDowser to rethink “waters,” and NGL Viewer to recapture online 3D graphics. *Protein Sci.* **29**, 315–329 (2020).

46. 46.

Krissinel, E. & Henrick, K. Secondary-structure matching (SSM), a new tool for fast protein structure alignment in three dimensions. *Acta Crystallogr. D* **60**, 2256–2268 (2004).

47. 47.

Pettersen, E. F. et al. UCSF ChimeraX: Structure visualization for researchers, educators, and developers. *Protein Sci.* **30**, 70–82 (2021).

48. 48.

Zheng, S. Q. et al. MotionCor2: anisotropic correction of beam-induced motion for improved cryo-electron microscopy. *Nat. Methods* **14**, 331–332 (2017).

49. 49.

Zhang, K. Gctf: Real-time CTF determination and correction. *J. Struct. Biol.* **193**, 1–12 (2016).

50. 50.

He, S. & Scheres, S. H. W. Helical reconstruction in RELION. *J. Struct. Biol.* **198**, 163–176 (2017).

51. 51.

Scheres, S. H. A Bayesian view on cryo-EM structure determination. *J. Mol. Biol.* **415**, 406–418 (2012).

52. 52.

Singleton, M. R. et al. Conformational changes induced by nucleotide binding in Cdc6/ORC from *Aeropyrum pernix*. *J. Mol. Biol.* **343**, 547–557 (2004).

53. 53.

Kelley, L. A., Mezulis, S., Yates, C. M., Wass, M. N. & Sternberg, M. J. The Phyre2 web portal for protein modeling, prediction and analysis. *Nat. Protoc.* **10**, 845–858 (2015).

Acknowledgements

We thank M. Sawicka, L. Loeff and S. Sorrentino (University of Zurich Center for Microscopy and Image Analysis) for assistance with cryo-EM sample preparation and data collection; the Cryo-Electron Microscopy Service Platform at EMBL Heidelberg for instrument access and F. Weis for assistance with data collection; R. Ciuffa for advice on helical reconstruction; M. Pacesa for help with cryo-EM data processing; F. Boneberg and A. Walter for technical assistance; B. Blattmann at the Protein Crystallization Center (University of Zurich) for assistance with crystallization screening; M. Wang, V. Olieric and T. Tomizaki at the Swiss Light Source (Paul Scherrer Institute, Villigen, Switzerland) for assistance with X-ray diffraction measurements; S. Kreutzer and the ETH Genome Engineering and Measurement Lab for assistance with ddPCR assays; G. Riddhough (Life Science Editors) for assistance with manuscript editing. This work was supported by Swiss National Science Foundation Project Grant 31003A_182567 and European Research Council (ERC) Consolidator Grant no. ERC-CoG-820152. I.Q. was supported by FEBS and EMBO (ALTF 296-2020) long-term postdoctoral fellowships. M.S. is a member of the Biomolecular Structure and Mechanism PhD Program of the Life Science Zurich Graduate School. M.J. is an International Research Scholar of the Howard Hughes Medical Institute, and Vallee Scholar of the Bert L. and N. Kuggie Vallee Foundation.

Author information

Author notes

1. These authors contributed equally: Irma Querques and Michael Schmitz

Affiliations

1. Department of Biochemistry, University of Zurich, Zurich, Switzerland

Irma Querques, Michael Schmitz, Seraina Oberli, Christelle Chanéz & Martin Jinek

Contributions

I.Q., M.S. and M.J. conceived the study and designed experiments. I.Q. prepared cryo-EM samples, collected cryo-EM data and determined the structure of TnsC. I.Q. performed crystallization experiments and determined the structure of TniQ. M.S. prepared cryo-EM samples, conducted cryo-EM analysis and determined the structure of Cas12k. M.S. and I.Q. carried out biochemical and ddPCR functional experiments and negative-stain electron microscopy analysis. S.O. expressed and purified TnsC mutant proteins. C.C. assisted with sample preparation for biochemical and ddPCR assays. I.Q., M.S. and M.J. analysed the data and wrote the manuscript.

Corresponding author

Correspondence to [Martin Jinek](#).

Ethics declarations

Competing interests

The authors declare no competing interests.

Additional information

Peer review information *Nature* thanks Hiroshi Nishimasu and the other, anonymous, reviewer(s) for their contribution to the peer review of this work. Peer reviewer reports are available.

Publisher's note Springer Nature remains neutral with regard to jurisdictional claims in published maps and institutional affiliations.

Extended data figures and tables

Extended Data Fig. 1 Cas12k-sgRNA-target DNA complex assembly.

a, Top: Size exclusion chromatography analysis of the Cas12k-sgRNA-target DNA complex. Middle: SDS-PAGE analysis of fractions from a. Proteins were visualised by Coomassie blue staining. Bottom: denaturing PAGE analysis of fractions from a. Nucleic acids were stained with a fluorescent dye (Gel Red). **b**, Representative negative stain EM micrographs of the ShCas12k-sgRNA-dsDNA complex at 68,000x magnification (top) and 180,000x magnification (bottom). Experiment was repeated three times independently with similar results. For gel source data, see Supplementary Fig. 1.

Extended Data Fig. 2 Cas12k cryo-EM image processing workflow and model validation.

a, Cryo-EM image processing workflow for the Cas12k-sgRNA-target DNA complex. Fourier Shell Correlations (FSC) of ShCas12k reconstruction from two independently refined half-maps. The gold-standard cutoff ($FSC = 0.143$) is marked with a blue line. **b**, Final electron density map colored according to the local resolution. **c**, Validation of Cas12k-sgRNA-target DNA structure model.

Extended Data Fig. 3 Structural comparison between Cas12k and CasX.

a, Structural model of Cas12k-sgRNA-target DNA (left) and CasX-sgRNA-target DNA (right, PDB: 6ny2²²) complexes. The structures were superimposed using secondary structure matching⁴⁶ of the RuvC domains and are shown in identical orientations. **b**, Zoom-in views of the tracrRNA-crRNA triplexes.

Extended Data Fig. 4 Structural features and functional analysis of ShCAST sgRNA.

a, Close-up view of the RNA:DNA duplex in proximity of the bridge helix (BH). **b**, Close-up view of the sgRNA-TS DNA heteroduplex in the Cas12k-sgRNA-target DNA complex. **c**, Structural model of the Cas12k sgRNA with detailed views of the 5' terminal segment (top left, 6.6 σ contour level) and the triplex junction (bottom right, 9.0 σ contour level) of the tracrRNA forming ribose-zipper and A-minor interactions, the pseudoknot duplex (bottom left, 9.0 σ contour level) and the central stack junction (top right, 7.6 σ contour level). **d**, Droplet digital PCR (ddPCR)-based analysis of the transposition activity of structure-based sgRNA scaffold mutants in the ShCAST system. Data are presented as mean ± s.d. ($n=3$ biologically independent replicates).

[Extended Data Fig. 5 ShTnsC filament formation and cryo-EM image processing of TnsC-dsDNA helical filaments.](#)

a, Representative negative-stain EM micrographs of TnsC in the presence of a 92-bp dsDNA and ATP or ATPγS. Scale bars, 100 nm. Magnification, 120,000x. Experiment was repeated twice independently with similar results. **b**, Cryo-EM data processing workflow for the TnsC-dsDNA complex. Selected 2D class averages used in image reconstruction and intermediate and final reconstructions are shown. **c**, Fourier Shell Correlations (FSC) of TnsC filament reconstruction from two independently refined half-maps. The gold-standard cutoff (FSC = 0.143) is marked with dashed lines. The resolution value of the FSC corrected curve at this level is indicated. **d**, Structural alignment of the cryo-EM structure of *S. hofmanni* TnsC (blue) and the crystal structure of the *Aeropyrum pernix* ORC2 protein (grey; PDB ID: 1W5T⁵²) used as initial homology model for model building (single protomers). The root mean square deviation (RMSD) between the structures is 1.41 Å over 79 pruned atom pairs, as calculated in Chimera. **e**, Local resolution estimation (Å) for the cryo-EM volumes of the TnsC-dsDNA helical filaments. **f**, Local resolution estimation (Å) of the bound DNA duplex.

[Extended Data Fig. 6 Biochemical analysis of ShTnsC mutants.](#)

a, SDS-PAGE analysis of purified wild type and ATPase activity mutant TnsC proteins. **b**, Representative negative-stain EM micrographs of TnsC

ATPase activity mutants incubated in the presence of dsDNA and ATP or AMPPNP. Magnification, 98,000x. Experiment was repeated twice independently with similar results. **c**, SDS-PAGE analysis of purified wild type and DNA binding mutant TnsC proteins. **d**, Representative negative stain EM micrographs of TnsC in the presence of AMPPNP and dsDNA and with mutations in the DNA binding interface. Magnification, 98,000x. Experiment was repeated twice independently with similar results. **e**, Electromobility shift assay using fluorophore-labeled 27-bp dsDNA in the presence of AMPPNP and either wild type or DNA binding mutant TnsC proteins. -, no protein control. Experiment was repeated twice independently with similar results. For gel source data, see Supplementary Fig. 1.

Extended Data Fig. 7 Role of ShTnsB in ShTnsC filament disassembly and crystal structure of ShTniQ.

a, Representative negative stain EM micrographs of dsDNA-bound TnsC filaments in the presence of TnsB and AMPPNP or ATP. Magnification, 98,000x. **b**, Quantification of filament length in the indicated samples. Data represents the average length \pm s.d. of 50 randomly selected filaments in each sample. Experiment in **a** and quantification in **b** were repeated twice independently with similar results. **c**, Top panel: Domain architecture of TniQ proteins. HTH, helix turn helix motif. wHTH, winged HTH. ZnF, zinc-finger motif. Bottom panel: Structural alignment of the crystal structures of type V *S. hofmanni* TniQ (red) and type I-F *Vibrio cholerae* TniQ (grey and beige protomers; PDB ID: 6V9P¹⁹) (bottom panel). The root mean square deviation (RMSD) between the structures is 1.16 Å over 55 pruned atom pairs, as calculated in Chimera. **d**, Size exclusion chromatography analysis of TniQ. The retention volume corresponds to that of a protein of 12 kDa, as calculated based on molecular weight standards. The theoretical molecular weight of *S. hofmanni* TniQ is 19 kDa.

Extended Data Fig. 8 Mechanistic model of Cas12k-directed transposition.

Schematic diagram depicting transposition of type V-K CRISPR-associated transposons. Cas12k in association with a crRNA-tracrRNA dual guide RNA recognizes target DNA sequences, forming a partial R-loop structure. Full R-loop is formed upon recruitment of TnsC by interactions with DNA-bound Cas12k, which nucleates ATP-dependent formation of a helical filament around structurally remodeled DNA. Filament growth is restricted by TniQ capping the Cas12k-distal end of the TnsC filament. The TnsC filament serves as a recruitment platform for TnsB, which interacts directly with TnsC and stimulates its ATPase activity. This leads to filament disassembly, making DNA downstream of the PAM accessible for transposon insertion. In the post-hydrolysis state, TnsC forms a single-turn helical hexamer around target DNA, possibly acting as a molecular ruler to define the spacing between the Cas12k binding and transposon insertion sites (60-66 nt downstream of the PAM). Image created with BioRender.com and adapted.

Extended Data Table 1 Cryo-EM data collection, refinement and validation statistics for the *S. hofmanni* Cas12k-sgRNA-target DNA and TnsC-dsDNA complexes

Extended Data Table 2 X-ray crystallographic data collection and refinement statistics for *S. hofmanni* TniQ. Values in parentheses are for highest-resolution shell

Supplementary information

Supplementary Figure

This file contains uncropped images of electrophoretic separation assays.

Reporting Summary

Peer Review File

Supplementary Table 1

Oligonucleotides, gBlocks and synthetic genes used in this study.

Rights and permissions

[Reprints and Permissions](#)

About this article

Cite this article

Querques, I., Schmitz, M., Oberli, S. *et al.* Target site selection and remodelling by type V CRISPR-transposon systems. *Nature* **599**, 497–502 (2021). <https://doi.org/10.1038/s41586-021-04030-z>

- Received: 22 June 2021
- Accepted: 16 September 2021
- Published: 10 November 2021
- Issue Date: 18 November 2021
- DOI: <https://doi.org/10.1038/s41586-021-04030-z>

Share this article

Anyone you share the following link with will be able to read this content:

[Get shareable link](#)

Sorry, a shareable link is not currently available for this article.

[Copy to clipboard](#)

Provided by the Springer Nature SharedIt content-sharing initiative

| [Section menu](#) | [Main menu](#) |

- Article
- [Published: 22 September 2021](#)

Nucleation landscape of biomolecular condensates

- [Shunsuke F. Shimobayashi](#)¹,
- [Pierre Ronceray](#) [ORCID: orcid.org/0000-0002-9012-7544](#)^{2,3},
- [David W. Sanders](#) [ORCID: orcid.org/0000-0002-1835-6895](#)¹,
- [Mikko P. Haataja](#) [ORCID: orcid.org/0000-0001-8459-7331](#)^{4,5} &
- [Clifford P. Brangwynne](#) [ORCID: orcid.org/0000-0002-1350-9960](#)^{1,5,6}

Nature volume **599**, pages 503–506 (2021)

- 10k Accesses
- 1 Citations
- 112 Altmetric
- [Metrics details](#)

Subjects

- [Biopolymers in vivo](#)
- [Intrinsically disordered proteins](#)

Abstract

All structures within living cells must form at the right time and place. This includes condensates such as the nucleolus, Cajal bodies and stress

granules, which form via liquid–liquid phase separation of biomolecules, particularly proteins enriched in intrinsically disordered regions (IDRs)^{1,2}. In non-living systems, the initial stages of nucleated phase separation arise when thermal fluctuations overcome an energy barrier due to surface tension. This phenomenon can be modelled by classical nucleation theory (CNT), which describes how the rate of droplet nucleation depends on the degree of supersaturation, whereas the location at which droplets appear is controlled by interfacial heterogeneities^{3,4}. However, it remains unknown whether this framework applies in living cells, owing to the multicomponent and highly complex nature of the intracellular environment, including the presence of diverse IDRs, whose specificity of biomolecular interactions is unclear^{5,6,7,8}. Here we show that despite this complexity, nucleation in living cells occurs through a physical process similar to that in inanimate materials, but the efficacy of nucleation sites can be tuned by their biomolecular features. By quantitatively characterizing the nucleation kinetics of endogenous and biomimetic condensates in living cells, we find that key features of condensate nucleation can be quantitatively understood through a CNT-like theoretical framework. Nucleation rates can be substantially enhanced by compatible biomolecular (IDR) seeds, and the kinetics of cellular processes can impact condensate nucleation rates and specificity of location. This quantitative framework sheds light on the intracellular nucleation landscape, and paves the way for engineering synthetic condensates precisely positioned in space and time.

Access options

Subscribe to Journal

Get full journal access for 1 year

\$199.00

only \$3.90 per issue

[Subscribe](#)

All prices are NET prices.
VAT will be added later in the checkout.
Tax calculation will be finalised during checkout.

Rent or Buy article

Get time limited or full article access on ReadCube.

from \$8.99

[Rent or Buy](#)

All prices are NET prices.

Additional access options:

- [Log in](#)
- [Access through your institution](#)
- [Learn about institutional subscriptions](#)

Fig. 1: Quantifying the nucleation landscape with synthetic condensates.

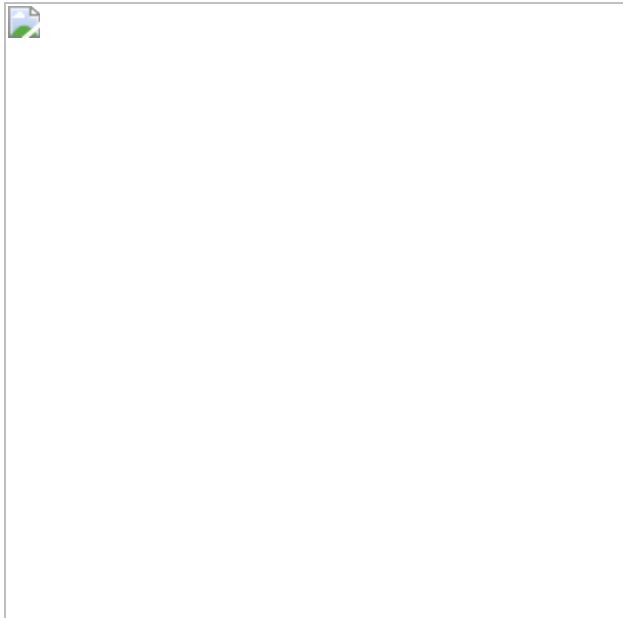


Fig. 2: Engineering the condensate nucleation landscape.

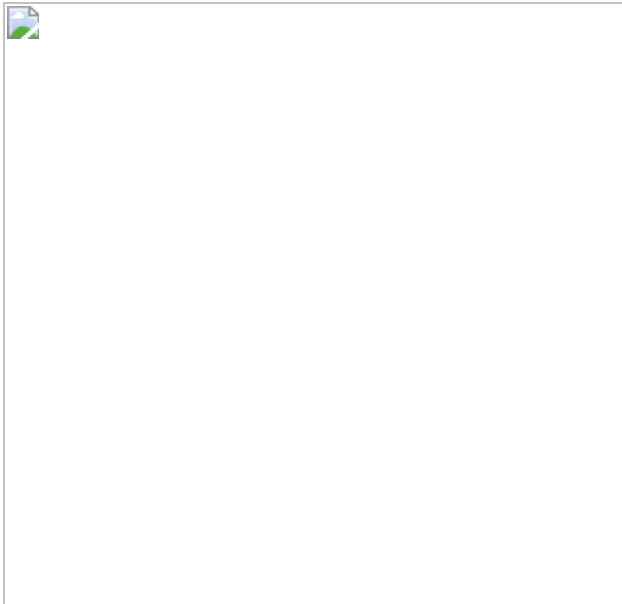
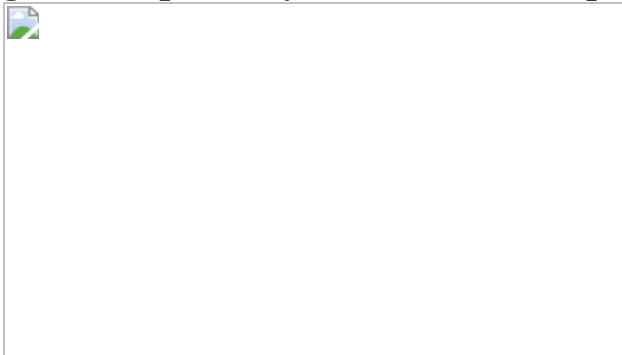


Fig. 3: Temporal dynamics and the specificity of condensate nucleation.



Data availability

Source data for Figs. 1–3 are provided with the paper. All other data are available from the corresponding authors upon reasonable request.

Code availability

Custom code used to process and analyse the images, as detailed in the Methods, is available from the corresponding authors upon reasonable request.

References

1. 1.

Shin, Y. & Brangwynne, C. P. Liquid phase condensation in cell physiology and disease. *Science* **357**, eaar4382 (2017).

2. 2.

Banani, S. F., Lee, H. O., Hyman, A. A. & Rosen, M. K. Biomolecular condensates: organizers of cellular biochemistry. *Nat. Rev. Mol. Cell Biol.* **18**, 285–298 (2017).

3. 3.

Kashchiev, D. *Nucleation* (Elsevier, 2000).

4. 4.

Auer, S. & Frenkel, D. Prediction of absolute crystal-nucleation rate in hard-sphere colloids. *Nature* **409**, 1020–1023 (2001).

5. 5.

Mitrean, D. M. et al. Nucleophosmin integrates within the nucleolus via multi-modal interactions with proteins displaying R-rich linear motifs and rRNA. *eLife* **5**, e13571 (2016).

6. 6.

Sanders, D. W. et al. Competing protein-RNA interaction networks control multiphase intracellular organization. *Cell* **181**, 306–324.e28 (2020).

7. 7.

Martin, E. W. et al. Valence and patterning of aromatic residues determine the phase behavior of prion-like domains. *Science* **367**, 694–699 (2020).

8. 8.

Wang, J. et al. A molecular grammar governing the driving forces for phase separation of prion-like RNA binding proteins. *Cell* **174**, 688–699.e16 (2018).

9. 9.

Bracha, D. et al. Mapping local and global liquid phase behavior in living cells using photo-oligomerizable seeds. *Cell* **175**, 1467–1480 (2018).

10. 10.

Shin, Y. et al. Liquid nuclear condensates mechanically sense and restructure the genome. *Cell* **175**, 1481–1491.e13 (2018).

11. 11.

Wei, M. T. et al. Nucleated transcriptional condensates amplify gene expression. *Nat. Cell Biol.* **22**, 1187–1196 (2020).

12. 12.

Kato, M. et al. Cell-free formation of RNA granules: low complexity sequence domains form dynamic fibers within hydrogels. *Cell* **149**, 753–767 (2012).

13. 13.

Riback, J. A. et al. Composition-dependent thermodynamics of intracellular phase separation. *Nature* **581**, 209–214 (2020).

14. 14.

Rubinstein, M. & Colby, R. H. *Polymer Physics* (Oxford Univ. Press, 2003).

15. 15.

Clouet, E. *Modeling of Nucleation Processes* (ASM Handbook, 2009).

16. 16.

Honerkamp-Smith, A. R., Veatch, S. L. & Keller, S. L. An introduction to critical points for biophysicists; observations of compositional heterogeneity in lipid membranes. *Biochim. Biophys. Acta* **1788**, 53–63 (2009).

17. 17.

Mayoral, E. & Goicochea, A. G. Hyperscaling relationship between the interfacial tension of liquids and their correlation length near the critical point. *Soft Matter* **10**, 9054–9058 (2014).

18. 18.

Lafontaine, D. L., Riback, J. A., Bascetin, R. & Brangwynne, C. P. The nucleolus as a multiphase liquid condensate. *Nat. Rev. Mol. Cell Biol.* **22**, 165–182 (2021).

19. 19.

Cho, W. K. et al. Mediator and RNA polymerase II clusters associate in transcription-dependent condensates. *Science* **361**, 412–415 (2018).

20. 20.

Chong, S. et al. Imaging dynamic and selective low-complexity domain interactions that control gene transcription. *Science* **361**, eaar2555 (2018).

21. 21.

Sabari, B. R. et al. Coactivator condensation at super-enhancers links phase separation and gene control. *Science* **361**, eaar3958 (2018).

22. 22.

Kilic, S. et al. Phase separation of 53 BP1 determines liquid-like behavior of DNA repair compartments. *EMBO J.* **38**, e101379 (2019).

23. 23.

Shevtsov, S. P. & Dundr, M. Nucleation of nuclear bodies by RNA.
Nat. Cell Biol. **13**, 167–173 (2011).

24. 24.

Berry, J., Weber, S. C., Vaidya, N., Haataja, M. & Brangwynne, C. P. RNA transcription modulates phase transition-driven nuclear body assembly. *Proc. Natl. Acad. Sci.* **112**, E5237–E5245 (2015).

25. 25.

Aaron, J. S., Taylor, A. B. & Chew, T. L. Image co-localization—co-occurrence versus correlation. *J. Cell Sci.* **131**, jcs211847 (2018).

Acknowledgements

We thank members of the Brangwynne laboratory for helpful discussions and comments on this manuscript. We thank laboratory members Y. Kim, M. Walls and D. Bracha for providing plasmids. This work was supported by the Howard Hughes Medical Institute, and grants from the AFOSR MURI (FA9550-20-1-0241), and the Princeton Center for Complex Materials, an MRSEC (NSF DMR-2011750). We also thank Princeton’s School of Engineering and Applied Sciences for supporting this work through a Focused Research Team award. S.F.S. is supported by JSPS Postdoctoral Fellowships for Research Abroad. P.R. is supported by the NSF through the Center for the Physics of Biological Function (PHY-1734030), by the French Government programme ‘Investissements d’Avenir’ managed by the French National Research Agency (ANR-16-CONV-0001) and by the Excellence Initiative of Aix-Marseille University —A*MIDEX.

Author information

Affiliations

1. Department of Chemical and Biological Engineering, Princeton University, Princeton, NJ, USA

Shunsuke F. Shimobayashi, David W. Sanders & Clifford P. Brangwynne

2. Center for the Physics of Biological Function, Princeton University, Princeton, NJ, USA

Pierre Ronceray

3. Aix Marseille Univ, Université de Toulon, CNRS, CPT, Turing Center for Living Systems, Marseille, France

Pierre Ronceray

4. Department of Mechanical and Aerospace Engineering, Princeton University, Princeton, NJ, USA

Mikko P. Haataja

5. Princeton Institute for the Science and Technology of Materials, Princeton University, Princeton, NJ, USA

Mikko P. Haataja & Clifford P. Brangwynne

6. Howard Hughes Medical Institute, Princeton University, Princeton, NJ, USA

Clifford P. Brangwynne

Contributions

S.F.S., P.R., D.W.S., M.P.H. and C.P.B. designed the research; S.F.S. and D.W.S. performed the experiments; S.F.S. analysed the data; P.R. and M.P.H took the lead in the theoretical formalism; S.F.S., P.R., M.P.H. and C.P.B. wrote, and all authors reviewed and edited, the paper.

Corresponding author

Correspondence to [Clifford P. Brangwynne](#).

Ethics declarations

Competing interests

C.P.B. is a founder and consultant of Nereid Therapeutics. S.F.S., P.R., D.W.S. and M.P.H. declare no competing interests.

Additional information

Peer review information *Nature* thanks Mike Sleutel and the other, anonymous, reviewer(s) for their contribution to the peer review of this work.

Publisher's note Springer Nature remains neutral with regard to jurisdictional claims in published maps and institutional affiliations.

Extended data figures and tables

[Extended Data Fig. 1 Nucleation process of various endogenous and biomimetic condensates.](#)

a, Time-lapse images of U2OS cells show the nucleation of Cajal bodies (coilin-EYFP) and nuclear speckles (SRRM1-EYFP) in mitosis, DNA repair condensates (miRFP-53BP1) upon 10 µg/ml bleomycin treatment, and engineered FUS condensates. Scale bars, 10 µm. **b**, (i) Number density of condensates, ρ , as a function of time, t , for nucleoli and Cajal bodies in mitosis, stress granules (SGs) upon 400 µM As treatment, and 53BP1 condensates upon 10 µg/ml bleomycin treatment. The nucleation rate, J , is quantified by the slope. Here, $t = 0$ is \(\{ t \} - \{ 0 \} - 5\)) (min). (ii) Mean nucleation rate, J , and its standard deviation for nucleoli ($n = 6$), Cajal bodies ($n = 9$), SGs ($n = 24$) and DNA repair condensates ($n = 9$); $n =$

number of cells. **c**, Schematic diagram of the nucleation process of intracellular condensates.

Extended Data Fig. 2 Quasi-1D nucleation probability.

a, (i) Fluorescence images of U2OS cells expressing HNRNPA1_C-Corelets before and after blue light activation. Scale bar, 10 μm . (ii) Droplet number density as a function of time upon iterative blue-light activation and deactivation. (iii) Quasi-1D nucleation probability $\langle p \rangle_{\{\{\text{rm}\{\text{nuc}\}\}\}^{\{\{\text{rm}\{\text{rel}\}\}\}}}$ in the indicated region which include nucleoli (A) or not (B). **b**, Quasi-1D nucleation probability $\langle p \rangle_{\{\{\text{rm}\{\text{nuc}\}\}\}^{\{\{\text{rm}\{\text{rel}\}\}\}}}$ of U2OS cells expressing FUS_N-Corelets and FUS_N-miRFP-TRF1 in the indicated region ((i) low and (ii) high supersaturation), calculated from five successive activation cycles. Scale bar, 10 μm .

Extended Data Fig. 3 Photo-activated phase separation in nucleus and cytoplasm.

a, Photo-activated phase separation in nucleus. (i) Confocal images of U2OS cells with different expression levels of FUS_N Corelets (FUS_N IDRs (red) and Cores (green)) after light-activation. The cells display nucleation and growth (NG) regimes between the binodal boundary and spinodal region, and spinodal decomposition (SD). Scale bars, 10 μm . (ii) Connected network-like growth and coarsening akin to spinodal decomposition. Scale bar, 10 μm . **b**, Photo-activated phase separation in cytoplasm. (i) Time-lapse confocal images of photo-activated U2OS cells expressing FUS_N-Corelets composed of Core without NLS and FUS_N-mCh-sspb. Scale bars, 10 μm . (ii) Time change of light-induced droplet number density, ρ . The shaded error bars show standard deviation.

Extended Data Fig. 4 Phase separation behaviors of HNRNPA1_C-Corelets.

a, Time-lapse confocal images of photo-activated U2OS cells with different expression levels of HNRNPA1_C-Corelets. Nucleation growth (NG) regime near the binodal boundary (top) and spinodal region (bottom). Scale bars, 10 μm . **b**, Phase diagram of HNRNPA1_C-Corelets as functions of Core concentration and Core-to-IDR ratio ($n = 161$). Solid circles exhibit cells where nucleation growth is observed, while empty triangles and squares show cells where no phase separation and spinodal decomposition are observed, respectively. The colours of solid circles indicate the observed nucleation rate, J . n : number of cells.

Extended Data Fig. 5 Model fit parameters and chi-square values.

a, b, Model fit parameters of $\langle S \rangle^{\langle \text{last} \rangle}$, $\langle \langle \text{rm}\{\kappa\} \rangle \rangle$, $\langle \langle \langle \text{rm}\{\chi\} \rangle \rangle \langle \langle \text{rm}\{\text{red}\} \rangle \rangle^2 \rangle$ for various biomimetic condensates. The errors show the standard errors with 68% confidence intervals of the fits by equation (1). The parameter $\langle \langle \langle \text{rm}\{\chi\} \rangle \rangle \langle \langle \text{rm}\{\text{red}\} \rangle \rangle^2 \rangle^{gg}$ 1) indicates a poor model fit while $\langle \langle \langle \text{rm}\{\chi\} \rangle \rangle \langle \langle \text{rm}\{\text{red}\} \rangle \rangle^2 \rangle \leq 1$) indicates a good model fit. **c**, $\langle S \rangle^{\langle \text{last} \rangle}$ (top) and $\langle \langle \text{rm}\{\kappa\} \rangle \rangle$ (bottom) obtained from fits to equation (1) for FUS_N Corelets with ($n = 23$) or without ($n = 76$) FUS_N (WT) seeds and G3BP1 corelets $\pm 400 \mu\text{M}$ As ($n = 45$). Error bars represent standard fit errors.

Extended Data Fig. 6 Delay time against supersaturation.

Delay time, $\langle t \rangle_0$, against supersaturation, S , for FUS_N-Corelets ($n = 70$), HNRNPA1_C-Corelets ($n = 60$), and FUS_N Corelets plus FUS_N (WT) seeds ($n = 23$) with $1/24 < f < 1/10$. The dashed lines show the best power-law fits. Error bars for $\langle t \rangle_0$ and S show the standard errors of the fits and standard deviation, respectively. n : number of cells.

Extended Data Fig. 7 J against S with various ranges of Core-to-IDR ratio.

Nucleation rate, J , plotted against the degree of supersaturation, S , for (i) FUS_N-Corelets ($n = 26$ for $1/24 < f < 1/18$, $n = 33$ for $1/18 \leq f < 1/12$ and $n = 56$ for $1/12 \leq f < 1/6$) and (ii) HNRNPA1_C-Corelets ($n = 12$ for $1/24 < f < 1/18$, $n = 38$ for $1/18 \leq f < 1/12$ and $n = 18$ for $1/12 \leq f < 1/6$). Error bars for J and S show the standard errors of the fits and standard deviation, respectively. See Extended Data Fig. 5 for model fit parameters and χ^2_{red} . n : number of cells.

Extended Data Fig. 8 Seeded nucleation near the binodal boundary and spinodal region.

Time-lapse confocal images of U2OS cells expressing FUS_N-Corelets and FUS_N-miRFP-TRF1 near the binodal boundary (a) and spinodal region (c). The insets show the regions indicated by the arrows. Scale bars, 10 μm . b, The seeded condensates, which are indicated in a, are enlarged. Scale bar, 1 μm .

Extended Data Fig. 9 Nucleation of FUS_N-Corelets with tyrosine-mutated FUS_N-seeds.

a–c, Fluorescent images of U2OS cells expressing FUS_N-Corelets and FUS_N (-5YS, -27YS)-miRFP-TRF1 or HNRNPA1_C-miRFP-TRF1 before and after blue light activation. The insets and enlarged images show the regions indicated by the squares. Scale bars, 10 μm . Scale bar of the enlarged image, 1 μm . d, Nucleation rate, J , plotted against the degree of supersaturation, S , for FUS_N-Corelets ($1/24 < f < 10$) and FUS_N-Corelets ($1/30 < f < 10$) with FUS_N (-15YS, -27YS)-miRFP-TRF1 ($n = 15$), $\chi^2_{\text{red}} = 12.5$) or HNRNPA1_C-miRFP-TRF1 ($n = 8$). n : number of cells.

Extended Data Fig. 10 Specificity of the nucleation of endogenous condensates.

a, Confocal images of G3BP KO cells expressing G3BP1 corelets and iRFP-tagged FXR1/UBAP2L/LSM14 before and after blue light activation in the absence of As. Scale bars, 1 μ m. **b**, Nucleation rate of endogenous condensates against nominal supersaturation. Nucleation rate, J , plotted against the nominal supersaturation, $\langle S \rangle_{\text{nom}}$, for nucleoli ($n = 6$) and Cajal bodies ($n = 9$) in mitosis and 53BP1 condensates ($n = 9$) upon 10 μ g/ml bleomycin treatment. n: number of cells.

Supplementary information

Supplementary Information

This file contains supplementary text for theoretical discussion and clarification, equations and references.

Reporting Summary

Supplementary Video 1

Live imaging of photo-activated nucleation in nucleus. Live imaging of a U2OS cell undergoing photo-activated nucleation of FUS_N -Corelets upon blue light. Video corresponds to Fig. 1.

Supplementary Video 2

Live imaging of photo-activated nucleation in cytoplasm. Live imaging of a U2OS cell undergoing photo-activated nucleation of FUS_N -Corelets, where core does not have NLS, upon blue light. Video corresponds to Extended Data Fig.3.

Supplementary Video 3

Live imaging of photo-activated network-like coarsening. Live imaging of a U2OS cell undergoing network-like coarsening akin to spinodal

decomposition of FUS_N–Corelets upon blue light. Video corresponds to Extended Data Fig.3.

Supplementary Video 4

Live imaging of seeded nucleation near the binodal line. Live imaging of a U2OS cell undergoing seeded nucleation of FUS_N–Corelets and FUS_N(WT)–miRFP–TRF1 upon blue light. Video corresponds to Fig. 2.

Supplementary Video 5

Live imaging of seeded nucleation near the spinodal region. Live imaging of a U2OS cell undergoing seeded nucleation of FUS_N–Corelets and FUS_N(WT)–miRFP–TRF1 upon blue light. Video corresponds to Fig. 2.

Supplementary Video 6

Live imaging of unseeded nucleation. Live imaging of a U2OS cell undergoing seeded nucleation of FUS_N–Corelets and HNRNPA1_C–miRFP–TRF1 upon blue light. Video corresponds to Fig. 2.

Source data

Source Data Fig. 1

Source Data Fig. 2

Source Data Fig. 3

Rights and permissions

Reprints and Permissions

About this article

Cite this article

Shimobayashi, S.F., Ronceray, P., Sanders, D.W. *et al.* Nucleation landscape of biomolecular condensates. *Nature* **599**, 503–506 (2021).
<https://doi.org/10.1038/s41586-021-03905-5>

- Received: 01 December 2020
- Accepted: 12 August 2021
- Published: 22 September 2021
- Issue Date: 18 November 2021
- DOI: <https://doi.org/10.1038/s41586-021-03905-5>

Share this article

Anyone you share the following link with will be able to read this content:

[Get shareable link](#)

Sorry, a shareable link is not currently available for this article.

[Copy to clipboard](#)

Provided by the Springer Nature SharedIt content-sharing initiative

This article was downloaded by **calibre** from <https://www.nature.com/articles/s41586-021-03905-5>

- Article
- [Published: 27 October 2021](#)

A synthetic antibiotic class overcoming bacterial multidrug resistance

- [Matthew J. Mitcheltree](#) ORCID: [orcid.org/0000-0003-3774-628X¹](https://orcid.org/0000-0003-3774-628X) na1,
- [Amarnath Pisipati¹](#) na1,
- [Egor A. Syroegin](#) ORCID: [orcid.org/0000-0003-2753-3950²](https://orcid.org/0000-0003-2753-3950) na1,
- [Katherine J. Silvestre¹](#),
- [Dorota Klepacki³](#),
- [Jeremy D. Mason](#) ORCID: [orcid.org/0000-0002-1039-0773¹](https://orcid.org/0000-0002-1039-0773),
- [Daniel W. Terwilliger¹](#),
- [Giambattista Testolin](#) ORCID: [orcid.org/0000-0003-0080-0692¹](https://orcid.org/0000-0003-0080-0692),
- [Aditya R. Pote](#) ORCID: [orcid.org/0000-0001-8703-5190¹](https://orcid.org/0000-0001-8703-5190),
- [Kelvin J. Y. Wu¹](#),
- [Richard Porter Ladley](#) ORCID: [orcid.org/0000-0002-3902-8292¹](https://orcid.org/0000-0002-3902-8292),
- [Kelly Chatman⁴](#),
- [Alexander S. Mankin](#) ORCID: [orcid.org/0000-0002-3301-827X³](https://orcid.org/0000-0002-3301-827X),
- [Yury S. Polikanov](#) ORCID: [orcid.org/0000-0002-5064-0327²](https://orcid.org/0000-0002-5064-0327) &
- [Andrew G. Myers](#) ORCID: [orcid.org/0000-0001-9602-6915¹](https://orcid.org/0000-0001-9602-6915)

Nature volume 599, pages 507–512 (2021)

- 24k Accesses
- 1 Citations
- 223 Altmetric
- [Metrics details](#)

Subjects

- [Antibiotics](#)
- [Antimicrobial resistance](#)
- [Structure-based drug design](#)

- [Chemical synthesis](#)
- [X-ray crystallography](#)

Abstract

The dearth of new medicines effective against antibiotic-resistant bacteria presents a growing global public health concern¹. For more than five decades, the search for new antibiotics has relied heavily on the chemical modification of natural products (semisynthesis), a method ill-equipped to combat rapidly evolving resistance threats. Semisynthetic modifications are typically of limited scope within polyfunctional antibiotics, usually increase molecular weight, and seldom permit modifications of the underlying scaffold. When properly designed, fully synthetic routes can easily address these shortcomings². Here we report the structure-guided design and component-based synthesis of a rigid oxepanoproline scaffold which, when linked to the aminoctose residue of clindamycin, produces an antibiotic of exceptional potency and spectrum of activity, which we name iboxamycin. Iboxamycin is effective against ESKAPE pathogens including strains expressing Erm and Cfr ribosomal RNA methyltransferase enzymes, products of genes that confer resistance to all clinically relevant antibiotics targeting the large ribosomal subunit, namely macrolides, lincosamides, phenicols, oxazolidinones, pleuromutilins and streptogramins. X-ray crystallographic studies of iboxamycin in complex with the native bacterial ribosome, as well as with the Erm-methylated ribosome, uncover the structural basis for this enhanced activity, including a displacement of the $\text{m}_2^6\text{A}^{2058}$ nucleotide upon antibiotic binding. Iboxamycin is orally bioavailable, safe and effective in treating both Gram-positive and Gram-negative bacterial infections in mice, attesting to the capacity for chemical synthesis to provide new antibiotics in an era of increasing resistance.

[Download PDF](#)

Main

The rise and dissemination of bacteria resistant to most or all known antibiotics raises concerns of an impending global infectious-disease crisis¹. Any plan to address the problem depends on the discovery of new antibiotics effective against modern bacterial pathogens, but opinions diverge on which strategies can best achieve these discoveries³. For decades, natural products have served as both conceptual and material starting points for antibiotics discovery, but making specific chemical modifications to structurally complex natural products (that is, semisynthesis) is inherently challenging, and the pace of drug discovery by this route has slowed markedly². In an alternative approach, the development of fully synthetic platforms to construct tetracycline⁴, macrolide^{5,6}, group A streptogramin⁷ and arylomycin⁸

antibiotics has enabled deep-seated structural modifications that are not achievable by semisynthesis. These technologies enable chemists to envision and reduce to practice an almost limitless array of design hypotheses. Here we use component-based chemical synthesis to achieve a substantive re-scaffolding of the lincosamide antibiotics, giving rise to a broad-spectrum agent that is effective against a wide range of multidrug-resistant bacterial pathogens.

The ribosome is a major antibiotic target in bacteria, and lincosamides are one of several ribosome-targeting classes that have proved essential to the modern pharmacopeia^{9,10}. Lincomycin (**1**; Fig. [1a](#)), the founding member of the class, was first isolated in 1963 from a Nebraskan soil streptomycete¹¹ and quickly found use in the treatment of streptococcal, pneumococcal and staphylococcal infections. In an early semisynthetic modification of **1**, stereoinvertive deoxychlorination at position C7 of the aminosugar residue resulted in the antibiotic now known as clindamycin (**2**; Fig. [1a](#)), a molecule with improved pharmacokinetic properties and an enhanced spectrum of activity¹² that has largely replaced lincomycin in human medicine¹³. Since the US Food and Drug Administration approved clindamycin in 1970, semisynthetic and fully synthetic approaches to lincosamide discovery have been explored, giving rise to candidates containing six- and seven-membered aminoacyl residues, each with an expanded spectrum of activity^{14,15} (for example, **3**; Fig. [1a](#)) More recently, modifications of the aminosugar residue by semisynthesis have been reported, expanding coverage to certain multidrug-resistant Gram-positive bacteria¹⁶.

Fig. 1: Evolution of a novel antibiotic scaffold.

 **figure1**

a, Chemical structures of lincomycin and clindamycin, and a preclinical antibiotic discovered by Vicuron scientists¹⁵. **b**, The design progression of oxepanoprolinamide antibiotics. Conformational constraint of the C4' substituent within a bicyclic oxepanoprolyl scaffold, together with presentation of a lipophilic group at its 7'

position provided improved activity. **c**, Synthesis of oxepanoprolinamides OPP-**1**, OPP-**2** and IBX (OPP-**3**). Reagents and conditions are as follows: (i) LiHMDS, LiCl; (ii) NaOH, >99% recovery of (*R,R*)-pseudoephedrine; (iii) Boc₂O; (iv) MeI, Cs₂CO₃; (v) allyl ethyl carbonate, Pd(PPh₃)₄; (vi) Hoveyda–Grubbs catalyst I; (vii) LiOH; (viii) 7-Cl-MTL, HATU, Et*i*Pr₂N; (ix) TFA; (x) Pd(OAc)₂, benzoquinone, HBF₄ (aq.); (xi) DAST; (xii) LiHMDS, Comins’ reagent, 51% (plus, separately, 31% Δ6' regioisomer); (xiii) *i*BuMgCl, Fe(acac)₃; (xiv) H₂, Pd(OH)₂/C, 1:1 dr; (xv) BSTFA, TMSI, 17% over 2 steps (plus, separately, the 7'R epimer; 17% over 2 steps).

Clindamycin-resistant bacteria are globally distributed. Acquired resistance to clindamycin most commonly occurs through *N*⁶-dimethylation of 23S ribosomal RNA (rRNA) residue A2058 (nucleotide numbering in this Article refers to *Escherichia coli*) by erythromycin resistance rRNA methyltransferases¹⁷. These enzymes, which are encoded by *erm* genes, give rise to macrolide, lincosamide and streptogramin B (MLS_B) cross-resistance; expression of these genes may be constitutive (c-*erm*), or inducible upon exposure to macrolide antibiotics^{18,19} (i-*erm*). The prevalence of *erm* genes among clinical streptococcal and staphylococcal isolates has led the US Centers for Disease Control and Prevention (CDC) to list MLS_B-resistant pathogens among its most pressing threats in their 2019 report¹. A distinct rRNA methyltransferase, Cfr (encoded by the horizontally transferrable gene *cfr*)²⁰ methylates C8 of the 23S rRNA residue A2503 and confers resistance to phenicol, lincosamide, oxazolidinone, pleuromutilin and streptogramin A^{21,22} (PhLOPS_A) antibiotics as well as 16-membered macrolides²³. Moreover, recent studies have elucidated a third major resistance mechanism affecting the lincosamides, whereby target-protection proteins (for example, LsaA) bind to antibiotic-inhibited ribosomes, evict the drug and in so doing restore protein synthesis^{24,25}. The prevalence of *erm*, *cfr* and target-protection resistance genotypes in staphylococcal, streptococcal and enterococcal clinical isolates, together with the risk of *Clostridium difficile* colitis with the use of clindamycin challenge the continued utility of this antibiotic in patients.

Discovery of oxepanoprolinamides

To enable full structural exploration of the lincosamides, we developed modular synthetic routes to both the aminooctose and aminoacyl residues, then linked these components by amide-bond formation to produce more than 500 antibacterial candidates^{26,27,28,29}. Thus a wide array of structural changes were examined; we observed and report in this Article that bicyclic scaffold modifications of the aminoacyl hemisphere in combination with the aminooctose residue of clindamycin were especially advantageous with respect to antibacterial activity, notably among clindamycin-resistant strains. In brief, the bicyclic scaffold of oxepanoprolinamide **1**

(OPP-1) was conceived to rigidify both the *Cy-endo* proline ring pucker and the extended 4'-*n*-propyl chain of clindamycin as observed when bound to the ribosome³⁰ (Extended Data Fig. 1a). These explorations were inspired and made feasible by a stereoselective aldol reaction developed for a key fragment coupling in the synthesis of macrolide antibiotics⁵. Thus, enolization of (*R,R*)-4, a chiral glycine equivalent³¹, followed by addition of the bis-electrophile 5 led to sequential *syn*-aldol addition, then spontaneous intramolecular *N*-alkylation, furnishing the β-hydroxy proline derivative 6 in a single operation (64% yield, 2.3 g scale) (Fig. 1c). A three-step sequence involving cleavage of the chiral auxiliary (with >99% recovery of pseudoephedrine), *N*-Boc protection, and esterification provided the suitably protected intermediate 7 in 85% overall yield. Construction of the oxepene ring was then achieved through palladium-catalysed O-allylation followed by ring-closing metathesis using the first-generation Hoveyda–Grubbs catalyst³². The target OPP-1 was assembled following an established sequence of saponification, amide coupling to the aminosugar component (7-chloro-1-methylthio-lincosamine, 7-Cl-MTL)³³ and *N*-Boc removal¹⁵.

Microbiological testing of OPP-1 showed it to be comparable in activity to clindamycin (Extended Data Fig. 2a). Substitution of position 7' of the oxepene ring was prioritized next, as molecular modelling suggested that substituents there would project towards a hydrophobic cleft formed by 23S rRNA residues A2451 and C2452 (Extended Data Fig. 1a). Wacker oxidation of intermediate 8 using Grubbs' protocol³⁴ proceeded with complete regioselectivity to provide the 7'-keto product 10 with a yield of 74% (Fig. 1c); this selectivity is thought to arise from the σ-withdrawing effect of the oxygen atom embedded within the 7-membered ring. Deoxydifluorination of intermediate 8 with *N,N*-diethylaminosulfur trifluoride (DAST) followed by the same three-step sequence described earlier provided oxepanoprolinamide OPP-2, which exhibited substantially improved activity against multidrug-resistant Gram-positive strains (*Streptococcus pneumoniae* c-ermA; *Streptococcus pyogenes* c-ermB), as well as against *Klebsiella pneumoniae* (Extended Data Fig. 2a), lending support to our design strategy. Alkyl (and aryl) substitution of position 7' was made possible by non-regioselective enolization of 10 with lithium hexamethyldisilazide (LiHMDS), followed by triflylation with Comins' reagent. The resulting regiosomeric vinyl triflates both served as flexible intermediates for cross-coupling with aryl and alkyl nucleophiles. For example, iron-catalysed coupling of the Δ7' vinyl triflate with isobutylmagnesium chloride³⁵ provided intermediate 12, which upon saponification, amide coupling, non-diastereoselective olefin saturation (~1:1 7'-α:β diastereomeric ratio), *N*-Boc removal and purification by HPLC, provided separately OPP-3 (Fig. 1b) and its less active 7'-β stereoisomer *epi*-OPP-3. We found that, generally, 7'-α-alkyl analogues were more active than their unsaturated and 7'-β stereoisomeric congeners (Extended Data Fig. 2a). This sequence provided a viable discovery route to OPP-3—hereafter termed iboxamycin (IBX)—and other 7'-substituted analogues in amounts

sufficient for minimum inhibitory concentration (MIC) analyses but could not provide sufficient material for in vivo evaluations in animal models of infection. For this purpose, we devised a different sequence to obtain IBX specifically, which produced the antibiotic in multigram quantities and could provide the basis for a manufacturing route³⁶.

IBX overcomes resistance and is effective in vivo

IBX exhibits a broad spectrum of activity when compared with clindamycin and displays an orthogonal resistance profile in side-by-side comparisons with widely prescribed antibiotics (Fig. 2, Supplementary Table 1). Broth culture susceptibility testing revealed that IBX is active against extensively drug-resistant bacterial strains, including ESKAPE pathogens and *erm*-, *cfr*- and *lساA*-expressing strains that are resistant to lincosamide antibiotics (Fig. 2a). For instance, IBX overcame c-*ermB*-mediated resistance in streptococci, an increasingly widespread phenotype³⁷, with MICs at least 1,000× lower than that of clindamycin against *S. pneumoniae* and *S. pyogenes* strains (Fig. 2a,b). Similarly, IBX displayed activity against methicillin-resistant *Staphylococcus aureus* isolates displaying MLS_B and PhLOPS_A cross-resistance phenotypes or expressing *msrA*, the gene encoding the MsrA target-protection protein (Fig. 2a,b). Enterococcal pathogens, which are responsible for widespread and life-threatening healthcare-associated infections³⁸ and are invulnerable to lincosamides, also appear broadly susceptible to IBX: In *Enterococcus faecalis*, IBX overcame intrinsic resistance mediated by the target-protection gene *lساA*³⁹ (Fig. 2a), and displayed MICs $\leq 2 \mu\text{g ml}^{-1}$ against a panel of *Enterococcus faecium* and *E. faecalis* strains with varying resistance to vancomycin, linezolid, doxycycline, azithromycin and levofloxacin (Fig. 2b). IBX exhibited potent activity against *C. difficile* (listed as an urgent threat by the CDC)¹, suggesting it may carry reduced risk of promoting *C. difficile* colitis, but validation of this hypothesis requires further study.

Fig. 2: In vitro and in vivo antibacterial activity of the broad-spectrum antibiotic IBX.

 **figure2**

a–c, MICs in $\mu\text{g ml}^{-1}$ of IBX in standard and multidrug-resistant bacterial strains. **a**, IBX displays a broad antibacterial spectrum of activity, and overcomes *erm*, *cfr* and *lsaA* resistance. *B. fragilis*, *Bacteroides fragilis*; *H. influenzae*, *Haemophilus influenzae*; *K. oxytoca*, *Klebsiella oxytoca*; *S. epidermidis*, *Staphylococcus epidermidis*; *S. haemolyticus*, *Staphylococcus haemolyticus*. Comparisons of IBX with standard antibiotics against clinical Gram-positive (**b**) and Gram-negative (**c**) isolates illustrate the differentiated activity of the oxepanoprolinamide class. CLI, clindamycin; CTR, ceftriaxone; LEVO, levofloxacin; AZM, azithromycin; LNZ; linezolid; VAN, vancomycin; GEN, gentamicin. **d**, Efficacy of IBX in a neutropenic mouse thigh infection model; colours correspond to strains highlighted in **a–c**. Mice received vehicle or IBX intraperitoneally, and bacterial counts were determined 12 h after treatment. Data are mean \pm s.d.; $n = 8$ thighs from 4 mice examined over 2 experiments; two-tailed unpaired Welch's *t*-test. CFU, colony-forming units. **e**, Survival of mice receiving IBX or vehicle following systemic infection with *S. pyogenes*. 3GC-R, third-generation cephalosporin-resistant; CRAB, carbapenem-resistant *A. baumannii*; CRE, carbapenem-resistant Enterobacterales; ESBL, extended-spectrum beta-lactamase; FQ-R, fluoroquinolone-resistant; LNZ-R, linezolid-resistant; MDR, multidrug-resistant; MEC-R, methicillin-resistant; MRSA, methicillin-resistant *S. aureus*; VAN-R, vancomycin-resistant; VRE, vancomycin-resistant *Enterococcus*.

[Source data](#)

IBX showed activity against Gram-negative bacterial isolates, representing a further departure from approved lincosamides. High-priority ESKAPE pathogens such as carbapenem-resistant *E. coli*, *K. pneumoniae* and *Acinetobacter baumannii*, including strains expressing extended-spectrum β-lactamase or aminoglycoside resistance methylase (*arm*) genes, were largely susceptible ($\text{MIC} \leq 16 \mu\text{g ml}^{-1}$; Fig. 2c). In one example, IBX displayed activity against a strain of *E. coli* resistant to cephalosporin, fluoroquinolone, tetracycline and aminoglycoside antibiotics ($\text{MIC} = 8 \mu\text{g ml}^{-1}$; Fig 2c). Clinical strains of *Neisseria gonorrhoeae* were also highly susceptible ($\text{MIC} = 0.125 \mu\text{g ml}^{-1}$; Fig. 2a, Supplementary Table 1). To better understand the basis for this broad-spectrum activity, we determined the MICs of 7'-substituted oxepanoprolinamides, including IBX, in laboratory strains engineered to illuminate the contributions of outer-membrane penetration and transporter-mediated efflux to Gram-negative activity⁶. Whereas clindamycin exhibited activity only against *E. coli* strains with loss-of-function mutations to major efflux transporter (*tolC*) or outer-membrane assembly (*lptD*) genes, we found that, as a class, oxepanoprolinamides were significantly less susceptible to these mechanisms of intrinsic antibiotic resistance (Extended Data Fig. 2b). *Pseudomonas aeruginosa*, while measurably inhibited by IBX ($\text{MIC} = 128 \mu\text{g ml}^{-1}$; Fig. 2a), was comparatively resistant towards the antibiotic, reflecting the unique challenges facing the discovery of antibiotics effective against this pathogen⁴⁰. It is notable that the expanded spectrum of activity of IBX relative to clindamycin is not readily explained by traditional physicochemical predictors of Gram-negative activity such as rotatable-bond count, molecular weight, relative polar surface area or lipophilicity⁴¹. Nor does it reinforce recently advanced rules for Gram-negative accumulation⁴² (see [Supplementary Methods](#)). Nevertheless, we believe that enhanced Gram-negative potency may be realized through optimization of the former metrics within the oxepanoprolinamide class.

To assess the efficacy of oxepanoprolinamide antibiotics, we evaluated IBX in animal models of infection using both Gram-positive and Gram-negative bacteria. Cell culture safety profiling experiments showed that IBX is non-haemolytic and non-toxic towards mammalian cells (concentration causing 50% cell growth inhibition (GI_{50}) > 50 μM, Extended Data Fig. 3a, d–f), and has no effect on membrane integrity or mitochondrial function (Extended Data Fig. 3b, c). In mice, IBX achieved greater exposure than clindamycin, exhibiting an intravenous mean residence time (MRT) of 1.2 h and 24% oral bioavailability (Extended Data Table 1). Next, we studied the efficacy of IBX in a murine neutropenic thigh infection model using standard strains of *S. pyogenes* and *A. baumannii*, a clinical strain of methicillin-resistant *S. aureus*, and a clinical strain of *E. coli* displaying aminoglycoside, tetracycline, fluoroquinolone and third-generation cephalosporin multi-resistance. In each experiment, when compared to vehicle, IBX achieved a statistically significant

reduction in bacterial burden 12 h following treatment (Fig. 2d, Extended Data Fig. 4a–d). Finally, in a model of systemic infection, we studied the ability of IBX to rescue mice from a lethal challenge of intraperitoneally administered *S. pyogenes* ATCC 19606. IBX was well-tolerated at all dose levels in this experiment, and resulted in the rescue of infected mice, with all mice treated with 3 or 10 mg kg⁻¹ IBX surviving (Fig. 2e, Extended Data Fig. 4e). Together, these results illustrate the potential of the oxepanoprolinamide class to provide orally available, broad-spectrum antibiotics effective against a range of resistance mechanisms.

IBX targets wild-type and resistant ribosomes

The remarkable antibacterial profile of IBX prompted us to study its mechanism of action, including the structural basis for its activity against Erm-methylated MLS_B-resistant ribosomes. Broth culture profiling revealed that, like clindamycin, IBX is bacteriostatic but exhibits prolonged effects on bacterial growth following even brief exposure; concentration-dependent cidalty was observed for certain highly susceptible strains (Extended Data Fig. 5). Spontaneous resistance was slow to develop in standard and clinical bacterial strains (approximate frequency of resistance $\leq 10^{-9}$ at 4×MIC; Extended Data Table 2). By contrast, IBX-resistant mutants did emerge in *E. coli* SQ110DTC, a strain specifically engineered for selecting mutations in rRNA that render cells resistant to ribosome-targeting inhibitors⁴³. This strain lacks six out of seven rRNA alleles and the major multidrug efflux pump TolC. When SQ110DTC cells were plated on agar containing IBX, resistant clones with MICs in the range of 2–4 µg ml⁻¹ appeared with a frequency of approximately 10⁻⁸. Of the 14 randomly selected clones we sequenced, all carried the single-nucleotide mutations A2058G or A2059G within the 23S rRNA (Extended Data Table 3), corresponding to base changes in the canonical lincosamide binding site known among clindamycin-resistant bacteria⁴⁴. Notably, mammalian cytosolic and mitochondrial ribosomes carry G2058 residues⁴⁵, explaining the non-toxicity of IBX in human cell culture experiments. These results demonstrated that, like clindamycin, IBX selectively targets the bacterial ribosome and thus has a low potential to select for resistance owing to the redundancy of rRNA genes in the genomes of most bacterial pathogens⁴⁶.

To understand the effect of IBX on ribosomal function, we performed primer extension inhibition analysis ('toeprinting'), an in vitro technique that detects the position of drug-arrested ribosomes on mRNA⁴⁷. Consistent with previous reports⁴³, clindamycin arrested translation at the start codons of the model open reading frames (ORFs), yet allowed a fraction of ribosomes to translate ORFs up to the trap codon, a point at which ribosomes are arrested owing to the lack of isoleucyl tRNA in the in vitro translation system (Extended Data Fig. 6). By contrast, present at the same concentration (50 µM), IBX firmly locked the ribosome at the start codons, allowing

virtually no escape, suggesting that IBX associates more strongly with the ribosome than does clindamycin.

To illuminate the structural basis for this improved activity, we determined the structure of IBX bound to the bacterial ribosome using X-ray crystallography. 70S Ribosomes from the Gram-negative bacterium *Thermus thermophilus* were co-crystallized with IBX, mRNA, non-hydrolyzable aminoacyl-tRNA analogue fMet-NH-tRNA_i^{Met} (located within the P site), and deacylated tRNA^{Phe} (within the A and E sites). The crystals we obtained diffracted to 2.50 Å resolution ([Supplementary Table 2](#)). The unbiased $F_o - F_c$ difference Fourier map revealed positive electron density peaks resembling characteristic chemical features of IBX (Extended Data Fig. [7a, b](#)), and confirmed that the antibiotic binds in the canonical binding pocket within the large ribosomal subunit (Fig. [3a](#)), spanning the peptidyl transferase center (PTC) and extending into the nascent peptide exit tunnel (NPET) ([Supplementary Video 1](#)).

Fig. 3: Structure of IBX in complex with the 70S ribosome, mRNA and tRNAs.

 **figure3**

a, Overview of the IBX binding site in the *T. thermophilus* 70S ribosome viewed as a cross-section through the NPET. Indicated are the 30S subunit (light yellow), the 50S subunit (grey), mRNA (magenta), A-site tRNA (green), P-site tRNA (dark blue) and E-site tRNA (orange). **b, c**, Detail views of IBX bound in the PTC, highlighting hydrogen-bond interactions (dashed lines) and the positioning of the 7'-isobutyl substituent within the A-site cleft formed by 23S rRNA residues A2451 and C2452. **d**, Models of A- and P-site tRNAs from the IBX–ribosome complex (green and blue, respectively) superimposed with those found in the drug-free ribosome (PDB entry 6XHW⁵¹).

The binding of IBX to the functional *T. thermophilus* ribosome complex containing mRNA and tRNAs corresponds closely to the binding of clindamycin to the tRNA-

free ribosome of *E. coli*³⁰ or the large ribosomal subunit of the archaeon *Haloarcula marismortui*⁴⁸ (Extended Data Fig. 7c). As with clindamycin and lincomycin, a network of hydrogen bonds anchors the aminoctose moiety of IBX to NPET nucleotides A2058, A2059, and A2503 (Fig. 3b). Similarly, the cationic aminoacyl residue of IBX occupies a hydrophilic pocket formed by the PTC residues G2061 and U2504 (Fig. 3b), displacing a divalent magnesium ion otherwise observed in the drug-free ribosome^{49,50}. Consistent with our design hypothesis (Extended Data Fig. 1b), the oxepane ring of ribosome-bound IBX overlays closely with the *n*-propyl-group atoms of clindamycin and presents the 7'-isobutyl group for interaction with the A-site cleft formed by 23S rRNA residues A2451 and C2452 (Fig. 3c). This cleft, which normally accommodates the side-chains of incoming amino acids, has a key role in the positioning of aminoacylated 3' ends of A-site tRNAs within the PTC during translation^{49,50}. Electron density corresponding to the CCA terminus of the A-site tRNA is poorly resolved in our structure, suggesting that IBX blocks proper coordination of the aminoacylated 3' end of A-site tRNA (Extended Data Fig. 7d). Notably, the 7'-isobutyl substituent of IBX extends deep enough within the A-site cleft to overlap not only with incoming amino acids (as the *n*-propyl group of clindamycin does, albeit to a lesser extent) but also with the P-site amino acid (Fig. 3d, Extended Data Fig. 7e). As tight coordination and proper placement of the P-site substrate are particularly important at the outset of protein synthesis, these observations, together with the toe-printing results described above, lead us to propose that compared to lincomycin and clindamycin, IBX more readily interferes with translation initiation.

The activity of IBX against bacteria harbouring *erm* resistance genes prompted us to determine the crystal structure of IBX bound to the \(\{\text{m}\}_\{2\}^6\text{A}2058\)-containing ribosome. Erm-mediated methylation of A2058 confers resistance to clindamycin by blocking the association of its 7-Cl-MTL residue with the NPET⁵¹, and because IBX bears the same aminoctose residue, its ability to overcome MLS_B resistance was unexpected. Erm-modified 70S ribosomes with A2058 dimethylation levels of approximately 60% were isolated from *T. thermophilus* cells expressing the *erm* gene from *Bifidobacterium thermophilum*⁵¹. Co-crystallization of these ribosomes with IBX provided crystals diffracting to 2.60 Å resolution ([Supplementary Table 2](#)). Of note, the corresponding electron density map revealed that IBX binds to the methylated ribosome in a manner almost identical to its positioning within the wild-type ribosome, whereas \(\{\text{m}\}_\{2\}^6\text{A}2058\) undergoes a movement of about 2 Å relative to its canonical position to accommodate the antibiotic (Fig. 4). A2058-*N*⁶-dimethylation, together with this previously unknown displacement, disrupts the two hydrogen bonds typically formed between this residue and the aminoctose portion of lincosamides (Fig. 4d); this disruption appears sufficient to destabilize binding of clindamycin to the Erm-modified ribosome. However, new hydrophobic interactions between IBX and the A-site cleft appear to compensate for clashes with the modified nucleobase,

providing sufficient affinity to defeat resistance. Indeed, oxepanoprolinamides' activity against both MLS_B-resistant *S. aureus* and Gram-negative species is governed rather precisely by the length of C7' aliphatic substituents (Extended Data Fig. 2b), lending strong support to the hypothesis that enhanced target engagement underpins the improved activity of the class against multidrug-resistant pathogens. Thus, these results suggest that forming new interactions with the ribosomal A site may prove a general strategy in the design of expanded-spectrum antibiotics capable of defeating methylase-mediated resistance.

Fig. 4: Structure of iboxamycin (IBX) bound to the Erm-methylated 70S ribosome.

 figure4

a, b, Electron density map (blue mesh), contoured at 1.0σ , of IBX (teal) in complex with the Erm-modified *T. thermophilus* 70S ribosome-containing N^6 -dimethylated A2058 residue in the 23S rRNA (**a**), highlighting the interaction with the methyl groups of $\text{m}_2^6\text{A}2058$ (orange) (**b**). **c, d**, Superposition of IBX (yellow) in complex with the WT 70S ribosome containing an unmodified residue A2058 (light blue), and the structure of IBX (teal) in complex with the Erm-modified 70S ribosome containing an $\text{m}_2^6\text{A}2058$ residue (medium blue) (**c**), highlighting hydrogen bonding (dashed lines) (**d**). Note that the position of IBX is almost identical in the two structures, whereas IBX binding to the Erm-modified ribosome causes substantial movement of $\text{m}_2^6\text{A}2058$ from its canonical position (red arrow). WT, wild type.

Conclusion

Using a platform for antibiotics discovery rooted in component-based synthesis and structure-guided design, we identified the emergent oxepanoprolinamide antibiotic class. Departing radically from their lincosamide progenitors, the oxepanoprolinamides overcome Erm-, Cfr- and ABCF-mediated multidrug resistance and display activity against high-priority Gram-positive and Gram-negative pathogens, including multidrug-resistant strains of *S. aureus*, *E. faecalis*, *E. coli*, *K. pneumoniae* and *A. baumannii*. Methodologically, our findings attest to the continued role of empiricism in antibiotics discovery, as the activity of oxepanoprolinamides against posttranscriptionally methylated ribosomes could not have been predicted on the basis of existing antibiotic–ribosome co-crystal structures. Continued refinement of the scaffold, including modifications to the aminoctose residue whose unexpected capacity to displace $\text{m}_2^6\text{A}2058$ we illustrate here, is likely to expand the oxepanoprolinamides’ spectrum of activity further. These findings, together with the safety, pharmacokinetic profile and efficacy of IBX in mouse models of Gram-positive and Gram-negative bacterial infection reaffirm the capacity for chemical synthesis to replenish our antibiotics armamentarium, delivering broad-spectrum agents capable of overcoming increasingly widespread resistance mechanisms.

Methods

In vitro susceptibility

MICs were determined by the broth microdilution method or the agar dilution method following the Clinical and Laboratory Standards Institute (CLSI) guidelines^{52,53,54}. Standard bacterial strains were obtained from American Type Culture Collection

(ATCC). Other bacterial strains were obtained from hospitals and commercial sources, as noted in Supplementary Table 1. Before the start of the MIC experiment, standard and test compound stock solutions were prepared in dimethyl sulfoxide (DMSO, Aldrich D2650) at a stock concentration of $5,120 \mu\text{g ml}^{-1}$. The compound concentration range typically employed for each experiment was 128 – $0.06 \mu\text{g ml}^{-1}$ (2.5% final DMSO concentration). Clindamycin was used as a comparator in all experiments and each experiment was performed in triplicate. Specialized procedures were employed for streptococci, anaerobic species and *N. gonorrhoeae* (see [Supplementary Methods](#) for details). All other bacterial strains were sub-cultured on blood agar plates (tryptic soy agar with 5% sheep blood, Hardy Diagnostics) and incubated overnight at 35°C . Organisms were suspended in cation-adjusted Mueller–Hinton broth (CaMHB, BD 212322) and optical density was adjusted to 0.5 McFarland standard. Suspensions were further diluted to obtain a final inoculum of $5 \times 10^5 \text{ CFU ml}^{-1}$ for broth microdilution experiments. The minimum concentration of compound required to inhibit visible bacterial growth after 24 h of incubation was recorded as the MIC.

Time-kill studies

Time-kill studies were performed using four different concentrations of standard and test compounds (1, 2, 4 and $10\times\text{MIC}$). Experiments were performed in duplicate following CLSI guidelines. An inoculum was prepared in CaMHB containing 0.5×10^6 – $5 \times 10^6 \text{ CFU ml}^{-1}$ of test organism. Cultures were incubated at 37°C in a shaker incubator at 110 rpm; a flask containing bacteria left unexposed to antibiotic was used as untreated control. At time points 0, 1, 3, 6 and 24 h following administration of antibiotic, bacterial counts were determined from each flask by serial dilution and plating on brain heart infusion agar (BD, Sparks, MD). Plates were incubated at 35°C in incubators for 18–24 h to determine bacterial counts.

Compounds exhibiting $\geq 3 \log_{10}\text{CFU ml}^{-1}$ reduction compared to initial counts are considered bactericidal. Compounds exhibiting $\leq 2 \log_{10}\text{CFU}$ reduction, or which maintain counts similar to the initial bacterial counts, are considered bacteriostatic.

Post-antibiotic and post-antibiotic sub-MIC effect

Measurements of post-antibiotic effect (PAE) and post-antibiotic sub-MIC effect (PA-SME) durations were performed according to the methods described by Odenholt-Tornqvist and colleagues⁵⁵. Bacterial strains were cultured overnight on blood agar plates. Optical density was adjusted to 0.5 McFarland standard in CaMHB and suspensions were diluted further into 50-ml sterile Erlenmeyer flasks containing 20 ml CaMHB to achieve a bacterial load of 0.5 – $1 \times 10^6 \text{ CFU ml}^{-1}$. Cultures were then exposed to test and standard antibiotic at 1, 2, 4 and $10\times\text{MIC}$ concentrations for 1 h at

37 °C in a shaker incubator at 110 rpm (0.5% final DMSO concentration). A flask containing the unexposed bacterial strain was left as untreated control. Post-exposure, 100 µl of bacterial culture was diluted in 900 µl of sterile CaMHB; 100 µl of this diluted sample was immediately diluted further in 19.9 ml of sterile CaMHB (1:2,000 final dilution). For PA-SME studies, post exposure and dilution, each flask (except those in the control group) was supplemented with 0.25 and 0.5×MIC per ml of specific antibiotic (0.5% final DMSO concentration). Flasks were incubated at 37 °C in a shaker incubator (110 rpm). Samples (100 µl from each flask per time point) were collected at 0, 1, 3, 6 and 24 h from each flask and were serially diluted. From each dilution, 100 µl and 10 µl from each dilution were plated in duplicate on tryptic soy agar plates. Plates were incubated overnight at 35 °C to determine the bacterial counts (limit of detection = 20 CFU per plate or 2×10^2 CFU ml⁻¹). These counts were plotted against time with linear interpolation between time points to obtain the growth kinetic curves. PAE and PA-SME were determined from these curves using the formulae:

$$\$ \$ \{ \backslash rm\{ P\} \} \{ \backslash rm\{ A\} \} \{ \backslash rm\{ E\} \} = T - C \$ \$$$

where T is the time required for bacteria previously exposed to antibiotic to multiply 1 \log_{10} above counts immediately following dilution, and C is the corresponding time required for untreated culture to do the same; and

$$\$ \$ \text{PA-SME} = \{ T \} - \{ C \} - C \$ \$$$

where T_{pa} is the time taken for bacteria previously exposed to antibiotic and then re-exposed to sub-MIC concentrations to increase 1 \log_{10} above counts immediately following dilution.

Mammalian cell experiments

All cell lines were purchased from ATCC and used at a passage number of no greater than 8; cell lines were not authenticated or tested for mycoplasma contamination. All compounds were dissolved in sterile DMSO to a stock concentration of 20 µM and aliquoted prior to freezing at -20 °C. Aliquots were limited to a maximum of three freeze-thaw cycles. A549 (human pulmonary carcinoma; male) cells were cultured in Dulbecco's Modified Eagle Medium (DMEM) supplemented with 10% fetal bovine serum. K562 (human chronic myelogenous leukaemia; female) cells were cultured in Iscove's Modification of DMEM (IMDM) media supplemented with 10% fetal bovine serum. HCT116 (human colorectal carcinoma; male) cells were cultured in McCoy's 5a (Iwakata and Grace Modification) media supplemented with 10% fetal bovine serum. HepG2 (human hepatocellular carcinoma; male) cells were cultured in Eagle's

Minimum Essential Medium (EMEM) supplemented with 10% fetal bovine serum. All cell cultures were maintained in a 5% CO₂ incubator at 35 °C.

Growth inhibition was studied using the Promega CellTiter-Blue cell viability assay pursuant to the manufacturer's protocol. In brief, cells were harvested, diluted, and mixed with the desired concentration of test compound (or DMSO, used to define 0% growth inhibition). This suspension was then added to a 96-well plate (5×10^4 cells ml⁻¹, 100 µl per well, 5 replicates per test compound), and the plates were incubated for 72 h at 35 °C in a 5% CO₂ incubator. Next, 20 µl of CellTiter-Blue reagent was added to each well and the plates were incubated for 4 h. Plates were read on a SpectraMax i3 plate reader. GI₅₀ values were determined by nonlinear regression using GraphPad Prism and represent the mean of at least three independent experiments.

Mitochondrial toxicity assays^{56,57} were conducted using the Promega Mitochondrial ToxGlo assay, according to the manufacturer's protocol.

Animal studies

Animal experiments were performed at the Biology Research Infrastructure Laboratory of Harvard University following Institutional Animal Care and Use Committee (IACUC)-approved protocols. Animals were maintained in accordance with the recommendations in the Guide for the Care and Use of Laboratory Animals of the National Institutes of Health. Pathogen-free, 5- to 6-week-old, female CD-1 mice weighing 22–26 g were obtained from Charles River Laboratories, Inc. Animals were acclimated for a minimum of three days prior to start of the studies. Mice were caged as a group of four per cage, were housed at 21–23 °C with humidity ranging from 30–70%, were exposed to 12-h light and dark cycles, and were supplied with food and water ad libitum.

Mouse thigh infection studies

Mice were rendered neutropenic by administering cyclophosphamide intraperitoneally, 150 mg kg⁻¹ 4 days prior, and 100 mg kg⁻¹ 1 day prior to infection. Bacterial strains were cultured overnight on agar plates at 35 °C in 5% CO₂. Bacterial inoculum was prepared in sterile brain heart infusion broth (BHIB) and OD was adjusted to 0.1 at 600 nm; the inoculum was further diluted to achieve a bacterial load of 0.5–1 × 10⁷ CFU ml⁻¹. Mice were infected by intramuscular injection of 0.1 ml of inoculum into each thigh (0.2 ml of inoculum was used per mouse). Mice were randomly divided into 4 treatment groups: IBX, comparator antibiotic, vehicle-treated control and untreated baseline. At 2 h post-infection ($t = 0$), the untreated mice ($n = 2$) were

euthanized to obtain pre-treatment bacterial counts, while the others received a single dose of IBX (6 mg ml⁻¹ in 10% Captisol, 250 µl, 60 mg kg⁻¹), comparator antibiotic (clindamycin phosphate, ciprofloxacin, or azithromycin, 6 mg ml⁻¹ in sterile saline, 250 µl⁻¹, 60 mg kg⁻¹), or sterile vehicle (10% Captisol, 250 µl) by intraperitoneal injection. Intramuscular bacterial counts were determined after euthanizing mice from each group ($n = 2$) by CO₂ inhalation. Thighs (4 per time point) were aseptically removed and homogenized in sterile saline, and homogenates were serially diluted and plated (each sample was plated in duplicate). Bacterial counts (log₁₀CFU per thigh) were determined after incubating the plates overnight at 35 °C in 5% CO₂. Each experiment was repeated twice, and mean values were calculated ($n = 16$ counts across 4 biologically independent mice per time point). Because the outcome of the experiment (bacterial counts) was determined by serial dilution, a quantitative technique, blinding was not used. The results of these experiments are displayed in Extended Data Fig. 4.

Mouse systemic infection study

S. pyogenes ATCC 19615 was cultured overnight on blood agar plates in 5% CO₂ at 35 °C before being suspended in BHIB. The optical density of the bacterial suspension was adjusted to 0.1 at 600 nm using sterile BHIB and was then further diluted 1:1 in 10% hog gastric mucin (HGM, type III) to prepare the infecting inoculum in 5% HGM. Mice were infected by intraperitoneal injection of 250 µl infecting inoculum, representing 1–2 × 10⁶ CFU per mouse. Mice were randomly assigned to treatment groups; at time points 1, 5, 17 and 29 h post-infection, mice were administered intravenous infusions of IBX (1, 3 or 10 mg kg⁻¹, 250 µl in 10% Captisol; 8 mice per dose level), clindamycin phosphate (1, 3 or 10 mg kg⁻¹, 250 µl in normal saline; 8 mice per dose level), or vehicle as negative control (10% Captisol, 250 µl; 10 mice). Mice were monitored for survival for seven days following infection. Because the outcome of the experiment (survival) is objective, blinding was not used.

Frequency of resistance

Tripticase soy agar plates containing IBX at concentrations corresponding to 4×MIC, 8×MIC, and 16×MIC were prepared. Bacterial cultures (*S. aureus* ATCC 29213, *S. aureus* ATCC 700699, *E. faecalis* ATCC 29212, *E. faecium* HAV-251, and *K. pneumoniae* ATCC 10031) were prepared by overnight culture, and counts were determined by serial dilution and plating. Bacterial inocula (250 µl, containing approximately 1 × 10⁷, 1 × 10⁸, 1 × 10⁹ or 1 × 10¹⁰ CFU) were spread onto the media plates. The plates were incubated at 37 °C for 72 h and were monitored for the appearance of colonies. The colony appearing after plating 10¹⁰ CFU of *S. aureus*

ATCC 29213 on IBX-containing agar ($4\times$ MIC) was examined further to determine the fold change in antibiotic susceptibility; for details, see [Supplementary Methods](#).

Selection of IBX-resistant mutants in SQ110DTC

Approximately 10^9 CFU (1.2 ml of the exponentially growing cell culture with optical density of $A_{600} = 1.2$), were plated on LB agar plates containing either $0.25 \mu\text{g ml}^{-1}$ or $1 \mu\text{g ml}^{-1}$ of IBX ($\sim 10\times$ or $\sim 30\times$ MIC, respectively). Approximately 20 colonies appeared on both plates after incubation at 37°C for 24 h. The segment of the 23S rRNA gene corresponding to domains V and VI of the 23S rRNA was PCR-amplified from 14 randomly selected colonies using the primers 2020R (CCCGAGACTCAGTGAAATTGAACTC) and L2904 (AAGGTTAACGCTCACGG). PCR products were sequenced using the primer L2667 (GGTCCTCTCGTACTAGGAGCAG).

Toeprinting analysis

The *ermBL* DNA template for toeprinting was generated by a 4-primer cross-over PCR using primers T7, NV1, ermB3-F and ermB3-R. The *ermDL* template was generated in the same way using primers RLR-fwd, RLR-rev, T7-SD-fwd and T7-SD-rev. In vitro translation in the PURExpress system (New England Biolabs) and toeprinting analysis were carried out as described previously⁵⁸. The antibiotics (mupirocin, clindamycin, erythromycin or IBX) were present in the reactions at a final concentration of $50 \mu\text{g ml}^{-1}$.

Primer sequences used for toeprinting are as follows: T7 (TAATACGACTCACTATAGGG); NV1 (GGTTATAATGAATTTGCTTATTAAC); ermB3-F (TAATACGACTCACTATAGGGCTTAAGTATAAGGAGGAAAAAATATGTTGGTA TTCCAAATGCGTAATGTAGATAAAACATCTAC); ermB3-R (GGTTATAATGAATTTGCTTATTAACGATAGAATTCTATCACTTATTCAAAA TAGTAGATGTTTATCTACATTACG); RLR-fwd (GGAGGAAAAAATATGACACACTCAATGAGACTTCGTATTTCCC); RLR-rev (CTATCACTTACAAAGTTGGAAAATACGAAGTCTCATTGAG); T7-SD-fwd (TAATACGACTCACTATAGGGCTTAAGTATAAGGAGGAAAAAATATGACACA CTCAATG); T7-SD-rev (GGTTATAATGAATTTGCTTATTAACGATAGAATTCTATCACTTACAAAGTTG GGAAAAT).

Crystallization of IBX in complex with wild-type and Erm-modified *T. thermophilus* 70S ribosomes

Wild-type 70S ribosomes from *T. thermophilus* (strain HB8) containing unmodified residue A2058 of the 23S rRNA were prepared as described previously⁵⁰. Purification of the Erm-modified 70S ribosomes from *T. thermophilus* (strain HB27 expressing Erm-like enzyme from *B. thermophilum*) containing *N*⁶-dimethylated A2058 residue in the 23S rRNA was accomplished as optimized previously for the wild-type 70S ribosomes from *T. thermophilus*⁵¹. Deacylated tRNA^{Phe} and non-hydrolyzable aminoacylated fMet-NH-tRNA_i^{Met} were prepared as described previously⁵¹.

Complexes of the A2058-dimethylated or unmethylated *T. thermophilus* 70S ribosomes with mRNA, deacylated A-site tRNA^{Phe}, and P-site hydrolysis-resistant aminoacylated fMet-NH-tRNA_i^{Met} were formed as described previously^{49,50,51}. For *T. thermophilus* 70S ribosome complexes with IBX, the antibiotic was included in the crystallization mixture (250 μM each) and then later added to the stabilization buffers (250 μM each). Collection and processing of the X-ray diffraction data, model building, and structure refinement were performed as described in our previous reports^{49,50,51}. Diffraction data were collected at beamlines 24ID-C and 24ID-E at the Advanced Photon Source (Argonne National Laboratory). A complete dataset for each complex was collected using 0.979 Å irradiation at 100 K from multiple regions of the same crystal, using 0.3-degree oscillations. Raw data were integrated and scaled using XDS software⁵⁹ (5 Feb 2021). Molecular replacement was performed using PHASER from the CCP4 program suite⁶⁰ (version 7.0). The search model was generated from the previously published structures of *T. thermophilus* 70S ribosome with bound mRNA and aminoacylated tRNAs (PDB entry 6XHW)⁵¹. Initial molecular replacement solutions were refined by rigid-body refinement with the ribosome split into multiple domains, followed by positional and individual B-factor refinement using PHENIX software⁶¹ (version 1.17). Non-crystallographic symmetry restraints were applied to four parts of the 30S ribosomal subunit (head, body, spur, and helix 44), and four parts of the 50S subunit (body, L1-stalk, L10-stalk, and C-terminus of the L9 protein). Structural models were built in Coot⁶² (version 0.8.2). Structural models and restraints for IBX were generated using PRODRG online software⁶³ (<http://prodrg1.dyndns.org>). The statistics of data collection and refinement are compiled in [Supplementary Table 2](#). All figures showing atomic models were rendered using PyMol software⁶⁴.

Statistical analyses

Statistical analysis was performed using GraphPad Prism. Mouse thigh infection study data (12-h time points) were compared using Welch's two-tailed unpaired *t*-test.

Reporting summary

Further information on research design is available in the [Nature Research Reporting Summary](#) linked to this paper.

Data availability

Coordinates and structure factors are deposited in the RCSB Protein Data Bank with accession codes [7RQ8](#) for the *T. thermophilus* 70S ribosome in complex with IBX, mRNA, deacylated A-site tRNA^{Phe}, aminoacylated P-site fMet-NH-tRNA_i^{Met}, and deacylated E-site tRNA^{Phe}; and [7RQ9](#) for the $\backslash\{ \text{m} \} _ \{ 2 \}^{\{ 6 \}} \text{A} \} 2058 \backslash$ *T. thermophilus* 70S ribosome in complex with IBX, mRNA, deacylated A-site tRNA^{Phe}, aminoacylated P-site fMet-NH-tRNA_i^{Met}. Single-crystal X-ray crystallographic data for compound **6** are deposited at the Cambridge Crystallographic Data Centre under deposition number 2072277. All previously published structures that were used in this work for model building and structural comparisons were retrieved from the RCSB Protein Data Bank under accession codes [6XHW⁵¹](#), [4V7V³⁰](#) and [1YJN⁴⁸](#). [Source data](#) are provided with this paper.

References

1. 1. *Antibiotic Resistance Threats in the United States, 2019* (Department of Health and Human Services, CDC, 2019); www.cdc.gov/DrugResistance/Biggest-Threats.html
2. 2. Wright, P. M., Seiple, I. B. & Myers, A. G. The evolving role of chemical synthesis in antibacterial drug discovery. *Angew. Chem. Int. Ed.* **53**, 8840–8869 (2014).
3. 3. *Scientific Roadmap for Antibiotic Discovery* (Pew Charitable Trusts, 2016); <http://www.pewtrusts.org/antibiotic-discovery>.
4. 4. Charest, M. G., Lerner, C. D., Brubaker, J. D., Siegel, D. R. & Myers, A. G. A convergent enantioselective route to structurally diverse 6-deoxytetracycline antibiotics. *Science* **308**, 395–398 (2005).

5. 5.

Seiple, I. B. et al. A platform for the discovery of new macrolide antibiotics. *Nature* **533**, 338–345 (2016).

6. 6.

Myers, A. & Clark, R. B. Discovery of macrolide antibiotics effective against multi-drug resistant Gram-negative pathogens. *Acc. Chem. Res.* **54**, 1635–1645 (2021).

7. 7.

Li, Q. et al. Synthetic group A streptogramin antibiotics that overcome Vat resistance. *Nature* **586**, 145–150 (2020).

8. 8.

Smith, P. A. et al. Optimized arylomycins are a new class of Gram-negative antibiotics. *Nature* **651**, 189–194 (2018).

9. 9.

Wilson, D. N. Ribosome-targeting antibiotics and mechanisms of bacterial resistance. *Nat. Rev. Microbiol.* **12**, 35–48 (2014).

10. 10.

Lin, J., Zhou, D., Steitz, T. A., Polikanov, Y. S. & Gagnon, M. G. Ribosome-targeting antibiotics: modes of action, mechanisms of resistance, and implications for drug design. *Annu. Rev. Biochem.* **87**, 451–478 (2018).

11. 11.

Mason, D. J., Dietz, A. & De Boer, C. Lincomycin, a new antibiotic. I. Discovery and biological properties. *Antimicrob. Agents Chemother.* 554–559 (1962).

12. 12.

Birkenmeyer, R. D. & Kagan, F. Lincomycin. XI. Synthesis and structure of clindamycin. A potent antibacterial agent. *J. Med. Chem.* **13**, 616–619 (1970).

13. 13.

Phillips, I. Past and current use of clindamycin and lincomycin. *J. Antimicrob. Chemother.* **7** (Suppl. A), 11–18, (1981).

14. 14.

Birkenmeyer, R. D., Kroll, S. J., Lewis, C., Stern, K. F. & Zurenko, G. E. Synthesis and antimicrobial activity of clindamycin analogs: pirlimycin, a potent antibacterial agent. *J. Med. Chem.* **27**, 216–223 (1984).

15. 15.

O'Dowd, H., Erwin, A. L. & Lewis, J. G. in *Natural Products in Medicinal Chemistry* (ed. Hanessian, S.) (Wiley-VCH, 2014).

16. 16.

Hirai, Y. et al. Characterization of compound A, a novel lincosamide derivative active against methicillin-resistant *Staphylococcus aureus*. *J. Antibiot.* **74**, 124–132 (2021).

17. 17.

Leclercq, R. & Courvalin, P. Bacterial resistance to macrolide, lincosamide, and streptogramin antibiotics by target modification. *Antimicrob. Agents Chemother.* **35**, 1267–1272 (1991).

18. 18.

Lai, C. J. & Weisblum, B. Altered methylation of ribosomal RNA in an erythromycin-resistant strain of *Staphylococcus aureus*. *Proc. Natl Acad. Sci. USA* **68**, 856–860 (1971).

19. 19.

Griffith, L. J., Ostrander, W. E., Mullins, C. G. & Beswick, D. E. Drug antagonism between lincomycin and erythromycin. *Science* **147**, 746–747 (1965).

20. 20.

Toh, S. M. et al. Acquisition of a natural resistance gene renders a clinical strain of methicillin-resistant *Staphylococcus aureus* resistant to the synthetic antibiotic linezolid. *Mol. Microbiol.* **64**, 1506–1514 (2007).

21. 21.

Long, K. S., Poehlsgaard, J., Kehrenberg, C., Schwarz, S. & Vester, B. The Cfr rRNA methyltransferase confers resistance to phenicols, lincosamides, oxazolidinones, pleuromutilins, and streptogramin A antibiotics. *Antimicrob. Agents Chemother.* **50**, 2500–2505 (2006).

22. 22.

Giessing, A. M. et al. Identification of 8-methyladenosine as the modification catalyzed by the radical SAM methyltransferase Cfr that confers antibiotic resistance in bacteria. *RNA* **15**, 327–336 (2009).

23. 23.

Smith, L. K. & Mankin, A. S. Transcriptional and translational control of the mlr operon, which confers resistance to seven classes of protein synthesis inhibitors. *Antimicrob. Agents Chemother.* **52**, 1703–1712 (2008).

24. 24.

Crowe-McAuliffe, C. et al. Structural basis of ABCF-mediated resistance to pleuromutilin, lincosamide, and streptogramin A antibiotics in Gram-positive pathogens. *Nat. Comm.* **12** 3577 (2021).

25. 25.

Murina, V., Kasari, M., Hauryliuk, V. & Atkinson, G. C. Antibiotic resistance ABCF proteins reset the peptidyl transferase centre of the ribosome to counter translational arrest. *Nucleic Acids Res.* **46**, 3753–3763 (2018).

26. 26.

Mitcheltree, M. J., Stevenson, J. W., Pisipati, A. & Myers, A. G. A practical, component-based synthetic route to methylthiolincosamine permitting facile northern-half diversification of lincosamide antibiotics. *J. Am. Chem. Soc.* **143**, 6829–6835 (2021).

27. 27.

Mitcheltree, M. J. *A Platform for the Discovery of New Lincosamide Antibiotics*. PhD Dissertation, Harvard University (2018).

28. 28.

Silvestre, K. J. *Design, Synthesis, and Study of Lincosamide Antibiotics Containing a Bicyclic Amino Acid Moiety*. PhD Dissertation, Harvard University (2019).

29. 29.

Moga, I. *Novel Lincosamide Antibiotics Containing an Azepane Amino Acid Moiety*. PhD Dissertation, Harvard University (2019).

30. 30.

Dunkle, J. A., Xiong, L., Mankin, A. S. & Cate, J. H. Structures of the *Escherichia coli* ribosome with antibiotics bound near the peptidyl transferase center explain spectra of drug action. *Proc. Natl Acad. Sci. USA* **107**, 17152–17157 (2010).

31. 31.

Seiple, I. B., Mercer, J. A., Sussman, R. J., Zhang, Z. & Myers, A. G. Stereocontrolled synthesis of *syn*- β -hydroxy- α -amino acids by direct aldolization of pseudoephedrine glycinate. *Angew. Chem. Int. Ed.* **53**, 4642–4647 (2014).

32. 32.

Kingsbury, J. S., Harrity, J. P. A., Bonitatebus, P. J., Jr & Hoveyda, A. H. A recyclable Ru-based metathesis catalyst. *J. Am. Chem. Soc.* **121**, 791–799 (1999).

33. 33.

Magerlein, B. J. & Kagan, F. Lincomycin. 8. 4'-alkyl-1'-demethyl-4'-depropylclindamycins, potent antibacterial and antimalarial agents. *J. Med. Chem.* **12**, 780–784 (1969).

34. 34.

Morandi, B., Wickens, Z. K. & Grubbs, R. H. Regioselective Wacker oxidation of internal alkenes: rapid access to functionalized ketones facilitated by cross-metathesis. *Angew. Chem. Int. Ed.* **52**, 9751–9754 (2013).

35. 35.

Scheiper, B., Bonnekessel, M., Krause, H. & Fürstner, A. Selective iron-catalyzed cross-coupling reactions of Grignard reagents with enol triflates, acid chlorides, and dichloroarenes. *J. Org. Chem.* **69**, 3943–3949 (2004).

36. 36.

Mason, J. D., Terwilliger, D. T., Pote, A. R. & Myers, A. G. Practical gram-scale synthesis of iboxamycin, a potent antibiotic candidate. *J. Am. Chem. Soc.* **143**, 11019–11025 (2021).

37. 37.

Zhao, C. et al. Investigation of antibiotic resistance, serotype distribution, and genetic characteristics of 164 invasive *Streptococcus pneumoniae* from north China between April 2016 and October 2017. *Infect. Drug Resist.* **13**, 2117–2128 (2020).

38. 38.

Weiner-Lastinger, L. M. et al. Antimicrobial-resistant pathogens associated with adult healthcare-associated infections: Summary of data reported to the National Healthcare Safety Network, 2015–2017. *Infect. Control Hosp. Epidemiol.* **41**, 1–18 (2020).

39. 39.

Singh, K. V., Weinstock, G. M., Murray, B. E. An *Enterococcus faecalis* ABC homologue (Lsa) is required for the resistance of this species to clindamycin and quinupristin–dalfopristin. *Antimicrob. Agents Chemother.* **46**, 1845–1850 (2002).

40. 40.

Rice, L. B. Challenges in identifying new antimicrobial agents effective for treating infections with *Acinetobacter baumannii* and *Pseudomonas aeruginosa*. *Clin. Infect. Dis.* **43**, S100–S105 (2006).

41. 41.

O’Shea, R. & Moser, H. E. Physicochemical properties of antibacterial compounds: implications for drug discovery. *J. Med. Chem.* **51**, 2871–2878 (2008).

42. 42.

Richter, M. F. et al. Predictive compound accumulation rules yield a broad-spectrum antibiotic. *Nature* **545**, 299–304 (2017).

43. 43.

Orelle, C. et al. Tools for characterizing bacterial protein synthesis inhibitors. *Antimicrob. Agents Chemother.* **57**, 5994–6004 (2013).

44. 44.

Vester, B. & Douthwaite, S. Macrolide resistance conferred by base substitutions in 23s rRNA. *Antimicrob. Agents Chemother.* **45**, 1–12 (2001).

45. 45.

Böttger, E. C., Springer, B., Prammananan, T., Kidan, Y. & Sander, P. Structural basis for selectivity and toxicity of ribosomal antibiotics. *EMBO Rep.* **2**, 318–323 (2001).

46. 46.

Silver, L. L. Multi-targeting by monotherapeutic antibacterials. *Nat. Rev. Drug Discov.* **6**, 41–55 (2007).

47. 47.

Orelle, C. et al. Identifying the targets of aminoacyl-tRNA synthetase inhibitors by primer extension inhibition. *Nucleic Acids Res.* **41**, e144 (2013).

48. 48.

Tu, D., Blaha, G., Moore, P. B. & Steitz, T. A. Structures of MLS_BK antibiotics bound to mutated large ribosomal subunits provide a structural explanation for resistance. *Cell* **121**, 257–270 (2005).

49. 49.

Polikanov, Y. S., Steitz, T. A. & Innis, C. A. A proton wire to couple aminoacyl-tRNA accommodation and peptide-bond formation on the ribosome. *Nat. Struct. Mol. Biol.* **21**, 787–793 (2014).

50. 50.

Polikanov, Y. S., Melnikov, S. V., Soll, D. & Steitz, T. A. Structural insights into the role of rRNA modifications in protein synthesis and ribosome assembly. *Nat. Struct. Mol. Biol.* **22**, 342–344 (2015).

51. 51.

Svetlov, M. S. et al. Structure of Erm-modified 70S ribosome reveals the mechanism of macrolide resistance. *Nat. Chem. Biol.* (2021).

52. 52.

Methods for Dilution Antimicrobial Susceptibility Tests for Bacteria That Grow Aerobically, Approved Standard 11th edn (Clinical and Laboratory Standards Institute, 2018).

53. 53.

Methods for Antimicrobial Susceptibility Testing of Anaerobic Bacteria; Approved Standard 8th edn (Clinical and Laboratory Standards Institute, 2012).

54. 54.

Performance Standards for Antimicrobial Susceptibility Testing 27th edn (Clinical and Laboratory Standards Institute, 2017).

55. 55.

Odenholt-Tornqvist, I., Löwdin, E., Cars, O. Pharmacodynamic effects of subinhibitory concentrations of β -lactam antibiotics in vitro. *Antimicrob. Agents Chemother.* **35**, 1834–1839 (1991).

56. 56.

Niles, A. L. et al. A homogeneous assay to measure live and dead cells in the same sample by detecting different protease markers. *Anal. Biochem.* **366**, 197–206 (2007).

57. 57.

Marroquin, L. D., Hynes, J., Dykens, J. A., Jamieson, J. D. & Will, Y. Circumventing the Crabtree effect: replacing media glucose with galactose increases susceptibility of HepG2 cells to mitochondrial toxicants. *Toxicol. Sci.* **97**, 539–547 (2007).

58. 58.

Orelle, C. et al. Identifying the targets of aminoacyl-tRNA synthetase inhibitors by primer extension inhibition. *Nucleic Acids Res.* **41** e144 (2013).

59. 59.

Kabsch, W. XDS. *Acta Crystallogr. D* **66**, 125–132 (2010).

60. 60.

McCoy, A. J. et al. Phaser crystallographic software. *J. Appl. Crystallogr.* **40**, 658–674 (2007).

61. 61.

Liebschner, D. et al. Macromolecular structure determination using X-rays, neutrons and electrons: recent developments in Phenix. *Acta Crystallogr. D* **75**, 861–877 (2019).

62. 62.

Emsley, P., Lohkamp, B., Scott, W. G. & Cowtan, K. Features and development of Coot. *Acta Crystallogr. D* **66** 486–501 (2010).

63. 63.

Schuttelkopf, A. W. & van Aalten, D. M. F. PRODRG: a tool for high-throughput crystallography of protein-ligand complexes. *Acta Crystallogr. D* **60**, 1355–1363 (2004).

64. 64.

The PyMOL Molecular Graphics System v.2.0 (Schrödinger, 2017).

Acknowledgements

We thank C.-W. Chen for help with initial X-ray diffraction data collection; M. Svetlov for providing Erm-methylated ribosomes used in our structural studies; D. R. Andes, M. S. Gilmore, F. H. Lebreton, T. J. Dougherty, D. P. Nicolau, P. Courvalin, C. Grillot-Courvalin, H. E. Moser, S. Chiang, B. Wohl, C. Keith, S. Lahiri, R. Duggal and K. M. Otte for their invaluable input in the course of our research; the staff at NE-CAT beamlines 24ID-C and 24ID-E for their help with data collection, especially M. Capel, F. Murphy, I. Kourinov, A. Lynch, S. Banerjee, D. Neau, J. Schuermann, N. Sukumar, J. Withrow, K. Perry and C. Salbego; S.-L. Zheng for X-ray crystallographic data collection and structure determination of compounds **6** and OPP-**3**; D. L. Shinabarger and C. Pillar of Micromyx, L.L.C., W. J. Weiss of the UNT Health Science Center and M. D. Cameron of TSRI Florida for in vitro profiling of compounds. Ligand Pharmaceuticals kindly provided the Captisol used in our mouse experiments. M.J.M. was supported by the National Science Foundation Graduate Research Fellowship

under grant no. DGE1144152. K.J.Y.W. was supported by a National Science Scholarship (PhD) by the Agency for Science, Technology and Research, Singapore. G.T. received postdoctoral support from the Deutsche Forschungsgemeinschaft (TE1311-1-1). This work is based upon research conducted at the Northeastern Collaborative Access Team (NE-CAT) beamlines, which are funded by the National Institute of General Medical Sciences from the National Institutes of Health (P30-GM124165). The Eiger 16M detector on 24ID-E beamline is funded by a NIH-ORIP HEI grant (S10-OD021527 to NE-CAT). This research used resources of the Advanced Photon Source, a U.S. Department of Energy (DOE) Office of Science User Facility operated for the DOE Office of Science by Argonne National Laboratory under Contract No. DE-AC02-06CH11357. Extraordinary facility operations were supported in part by the DOE Office of Science through the National Virtual Biotechnology Laboratory, a consortium of DOE national laboratories focused on the response to COVID-19, with funding provided by the Coronavirus CARES Act. This work was supported by Illinois State startup funds to Y.S.P. and National Institutes of Health R21-AI137584 (to A.S.M. and Y.S.P.), R01-GM132302 (to Y.S.P.), and R35GM127134 (to A.S.M.). A.G.M. gratefully acknowledges support from the LEO Foundation (grant LF18006) and the Blavatnik Biomedical Accelerator at Harvard University.

Author information

Author notes

1. These authors contributed equally: Matthew J. Mitcheltree, Amarnath Pisipati, Egor A. Syroegin

Affiliations

1. Department of Chemistry and Chemical Biology, Harvard University, Cambridge, MA, USA

Matthew J. Mitcheltree, Amarnath Pisipati, Katherine J. Silvestre, Jeremy D. Mason, Daniel W. Terwilliger, Giambattista Testolin, Aditya R. Pote, Kelvin J. Y. Wu, Richard Porter Ladley & Andrew G. Myers

2. Department of Biological Sciences, University of Illinois at Chicago, Chicago, IL, USA

Egor A. Syroegin & Yury S. Polikanov

3. Department of Pharmaceutical Sciences, University of Illinois at Chicago,
Chicago, IL, USA

Dorota Klepacki & Alexander S. Mankin

4. Harvard Center for Mass Spectrometry, Harvard University, Cambridge, MA,
USA

Kelly Chatman

Contributions

M.J.M. identified the oxepanoprolinamide scaffold and the synthetic routes used to prepare analogues OPP-**1**, OPP-**2**, OPP-**4** and OPP-**5**. A.P. designed and performed MIC, TK, PAE, PA-SME and mouse infection experiments. E.A.S. and Y.S.P. designed and performed X-ray crystallography experiments. K.J.S. identified 7'-alkyl oxepanoprolinamides and the synthetic route used to prepare analogues OPP-**6**, *epi*-OPP-**3** and IBX (OPP-**3**) from ketone **10**. D.K. and A.S.M. selected and sequenced IBX-resistant SQ110DTC clones and conducted ribosome toeprinting analysis. M.J.M., K.J.S., J.D.M., D.W.T., G.T., A.R.P. and K.J.Y.W. synthesized and characterized oxepanoprolinamide analogues. A.P. and R.P.L. performed mammalian cell experiments. A.P. and K.C. designed and performed the pharmacokinetic experiments. A.G.M., A.S.M. and Y.S.P. supervised the experiments. All authors interpreted the results. M.J.M, A.G.M, A.S.M, and Y.S.P. wrote the manuscript. All authors discussed the results and commented on the manuscript.

Corresponding authors

Correspondence to [Yury S. Polikanov](#) or [Andrew G. Myers](#).

Ethics declarations

Competing interests

A.G.M., M.J.M., K.J.S., J.D.M. and G.T are inventors in a provisional patent application submitted by the President and Fellows of Harvard College covering antibiotics of the type described in this work. A.G.M., M.J.M. and K.J.S. have filed an international patent application WO/2019/032936 ‘Lincosamide Antibiotics and Uses Thereof’. A.G.M. and M.J.M. have filed an international patent application WO/2019/032956 ‘Lincosamide Antibiotics and Uses Thereof’.

Additional information

Peer review information *Nature* thanks Daniel Wilson, William Wuest and the other, anonymous, reviewer(s) for their contribution to the peer review of this work. Peer reviewer reports are available.

Publisher's note Springer Nature remains neutral with regard to jurisdictional claims in published maps and institutional affiliations.

Extended data figures and tables

[Extended Data Fig. 1 Structure-based design of 7'-substituted oxepanoprolinamides.](#)

a, Superposition of the X-ray crystal structure of ribosome-bound lincosamide antibiotic clindamycin (**2**, blue, PDB entry 4V7V³⁰) with the energy-minimized structure of OPP-1 (green). Note that in this configuration, the C7'-atom of OPP-1 contacts the lipophilic surface of the A-site cleft. **b**, The same structure, overlaid with the X-ray crystal structure of iboxamycin (IBX, yellow) bound to the bacterial ribosome.

[Extended Data Fig. 2 MICs \(μg ml⁻¹\) of antibiotics containing a bicyclic aminoacyl residue.](#)

a, Effects of 7' substitution, ring size, and saturation on antibacterial activity. **b**, Effects of 7'-alkyl substituent chain length on antibacterial activity, including against MLS_B-resistant *S. aureus* and strains of *E. coli* engineered to lack key efflux or outer-membrane assembly machinery. **c**, *ermA/B*, constitutively expressed erythromycin ribosome methylase A/B gene.

[Extended Data Fig. 3 Effects of iboxamycin on mammalian cells.](#)

a, Normalized hemolysis (mean ± s.d.) of human erythrocytes by IBX (n = 3 replicates) and clindamycin (n = 5 replicates) relative to Triton X-100 (n = 45 replicates) measured over one independent experiment. **b, c**, Mitochondrial ToxGlo data showing effects of IBX on HepG2 cellular membrane integrity and ATP production relative to vehicle-treated control (antimycin serves as a positive control for mitotoxicity). Data are mean ± s.d.; n = 3 technical replicates from one independent experiment. **d–f**, Comparison of effects of IBX, clindamycin, doxycycline, and azithromycin on cell viability (CellTiter-Blue). Data are the mean ± s.d. of n = 3

independent experiments performed in technical quintuplicate. Where applicable, GI₅₀ values (μM) are reported beside the dose-response curves.

Extended Data Fig. 4 Efficacy of iboxamycin (IBX) in mouse models of infection. Bacterial counts were quantified in the thighs of neutropenic mice infected with *S. pyogenes* ATCC 19615.

(a), *S. aureus* MRSA HAV017 (b), *A. baumannii* ATCC 19616 (c) or *E. coli* MDR HAV504 (d) treated with IBX, vehicle, or comparator antibiotic at the listed time points post-treatment. Data are mean \pm s.d.; n = 8 thighs from 4 mice examined over 2 experiments, with the exception the sub-set of part c where mice received IBX via intravenous administration (n = 4 thighs from 2 mice examined over a single experiment). e, Mouse survival in an *S. pyogenes* systemic infection model. Abbreviations: AZM, azithromycin; CLI, clindamycin; CPFX, ciprofloxacin; IP, intraperitoneal administration; IV, intravenous administration..

[Source data](#).

Extended Data Fig. 6 Iboxamycin (IBX) efficiently arrests translation at the start codon.

Toeprinting analysis showing sites of IBX-induced translation arrest of ErmBL and ErmDL leader peptides. Because all reactions contained mupirocin, an inhibitor of Ile-tRNA synthetase, the ribosomes that escape inhibition by ribosome-targeting antibiotics are trapped at the codon preceding Ile (black arrowheads). Red arrowheads mark translation arrest at the start codon, while cyan arrowheads denote known erythromycin-induced arrest sites D10 (*ermBL*) and L7 (*ermDL*). Each gel is representative of two independent experiments, for source data see Supplementary Figure 1. ERY, erythromycin; CLI, clindamycin.

Extended Data Fig. 5 Time-kill kinetics, post-antibiotic effect, and post-antibiotic sub-MIC effect data of iboxamycin (IBX) against susceptible strains.

a, Arrayed growth curves for three susceptible strains showing concentration effects on growth inhibition (time-kill), growth kinetics following exposure to antibiotic at 4 \times MIC (PAE), and growth kinetics under sub-MIC concentrations following exposure to antibiotic at 4 \times MIC (PA-SME). Points represent mean values from n = 2 biologically independent experiments. b, Tabulated PAE and PA-SME durations (determined as the difference in time required for bacterial counts to rise 10 \times between

experimental and untreated control arms). Abbreviations: CLI, clindamycin; LNZ, linezolid.

Extended Data Fig. 7 High-resolution electron density maps of iboxamycin (IBX) bound to the bacterial ribosome.

a, b, Unbiased F_o - F_c and $2F_o$ - F_c electron density maps of IBX in complex with the *T. thermophilus* 70S ribosome (green and blue mesh, respectively). The refined model of IBX is displayed in its electron density before (**a**) and after (**b**) the refinement contoured at 3.0σ and 1.5σ , respectively **c**, Superposition of ribosome-bound IBX (yellow) with prior structures of clindamycin bound to the tRNA-free 70S ribosome from eubacterium *E. coli* (blue, PDB entry 4V7V³⁰) or to the 50S ribosomal subunit from archaeon *H. marismortui* harboring the 23S rRNA mutation G2099A (green, PDB entry 1YJN⁴⁸). All structures were aligned based on domain V of the 23S rRNA. **d**, $2F_o$ - F_c electron density map (blue mesh) corresponding to ribosome-bound IBX (yellow), deacylated A-site tRNA^{Phe} (green) and aminoacylated initiator P-site fMet-NH-tRNA_i^{Met} (dark blue). The refined models of tRNAs are displayed in their respective electron-density maps contoured at 1.0σ . In **d**, the entire bodies of the A- and P-site tRNAs are viewed from the back of the 50S subunit, as indicated by the inset. Ribosome subunits are omitted for clarity. Note that IBX binding to the ribosome prevents accommodation of the aminoacyl-bearing CCA-end of the A-site tRNA. **e**, Close-up view of the P-site tRNA CCA-end bearing a formyl-methionyl (cyan) residue. **f**, Detailed arrangement of the hydrogen bonds formed between the aminooctose component of IBX with 23S rRNA residues A2058 and G2505 (light blue).

Extended Data Table 1 Pharmacokinetics of clindamycin and iboxamycin

Extended Data Table 2 Frequency of resistance to iboxamycin in susceptible bacterial strains

Extended Data Table 3 Mutations selected in *E. coli* strain SQ110DTC conferring resistance to iboxamycin

Supplementary information

Supplementary Figure 1

Uncropped mRNA toeprinting gel image.

Reporting Summary

[Peer Review File](#)

[Supplementary Methods](#)

| .docx file | Antimicrobial susceptibility assays; susceptibility testing of a spontaneously resistant mutant; consideration of predictive rules for Gram-negative accumulation; structural basis for Cfr-mediated resistance to lincosamides; chemical synthesis of oxepanoprolinamide analogs.

[Supplementary Table 1](#)

In vitro antibacterial activity of iboxamycin.

[Supplementary Table 2](#)

X-ray crystallographic data for iboxamycin–ribosome complexes.

[Supplementary Video](#)

Illustration of iboxamycin binding to the wild-type ribosome, and iboxamycin-induced displacement of $\text{m}_2^6\text{A}_{2058}$ in the Erm-modified ribosome.

Source data

[Source Data Fig. 2](#)

[Source Data Extended Data Fig. 4](#)

Rights and permissions

[Reprints and Permissions](#)

About this article

Cite this article

Mitcheltree, M.J., Pisipati, A., Syroegin, E.A. *et al.* A synthetic antibiotic class overcoming bacterial multidrug resistance. *Nature* **599**, 507–512 (2021).
<https://doi.org/10.1038/s41586-021-04045-6>

- Received: 01 April 2021
- Accepted: 21 September 2021
- Published: 27 October 2021
- Issue Date: 18 November 2021
- DOI: <https://doi.org/10.1038/s41586-021-04045-6>

Share this article

Anyone you share the following link with will be able to read this content:

[Get shareable link](#)

Sorry, a shareable link is not currently available for this article.

[Copy to clipboard](#)

Provided by the Springer Nature SharedIt content-sharing initiative

Further reading

- [**Synthetic antibiotic fights resistance**](#)

- Sarah Crunkhorn

Nature Reviews Drug Discovery (2021)

[**Bacterial drug resistance overcome by synthetic restructuring of antibiotics**](#)

Research Briefing 27 Oct 2021

This article was downloaded by **calibre** from <https://www.nature.com/articles/s41586-021-04045-6>

- Article
- [Published: 23 September 2021](#)

Architecture and assembly mechanism of native glycine receptors

- [Hongtao Zhu¹](#) &
- [Eric Gouaux](#) [ORCID: orcid.org/0000-0002-8549-2360^{1,2}](#)

Nature volume **599**, pages 513–517 (2021)

- 7275 Accesses
- 46 Altmetric
- [Metrics details](#)

Subjects

- [Cryoelectron microscopy](#)
- [Ion channels in the nervous system](#)
- [Membrane structure and assembly](#)

Abstract

Glycine receptors (GlyRs) are pentameric, ‘Cys-loop’ receptors that form chloride-permeable channels and mediate fast inhibitory signalling throughout the central nervous system^{1,2}. In the spinal cord and brainstem, GlyRs regulate locomotion and cause movement disorders when mutated^{2,3}. However, the stoichiometry of native GlyRs and the mechanism by which

they are assembled remain unclear, despite extensive investigation^{4,5,6,7,8}. Here we report cryo-electron microscopy structures of native GlyRs from pig spinal cord and brainstem, revealing structural insights into heteromeric receptors and their predominant subunit stoichiometry of 4 α :1 β . Within the heteromeric pentamer, the $\beta(+)$ - $\alpha(-)$ interface adopts a structure that is distinct from the $\alpha(+)$ - $\alpha(-)$ and $\alpha(+)$ - $\beta(-)$ interfaces. Furthermore, the β -subunit contains a unique phenylalanine residue that resides within the pore and disrupts the canonical picrotoxin site. These results explain why inclusion of the β -subunit breaks receptor symmetry and alters ion channel pharmacology. We also find incomplete receptor complexes and, by elucidating their structures, reveal the architectures of partially assembled α -trimers and α -tetramers.

Access options

Subscribe to Journal

Get full journal access for 1 year

\$199.00

only \$3.90 per issue

[Subscribe](#)

All prices are NET prices.

VAT will be added later in the checkout.

Tax calculation will be finalised during checkout.

Rent or Buy article

Get time limited or full article access on ReadCube.

from \$8.99

[Rent or Buy](#)

All prices are NET prices.

Additional access options:

- [Log in](#)
- [Access through your institution](#)
- [Learn about institutional subscriptions](#)

Fig. 1: Architecture of native heteromeric and homomeric GlyRs.

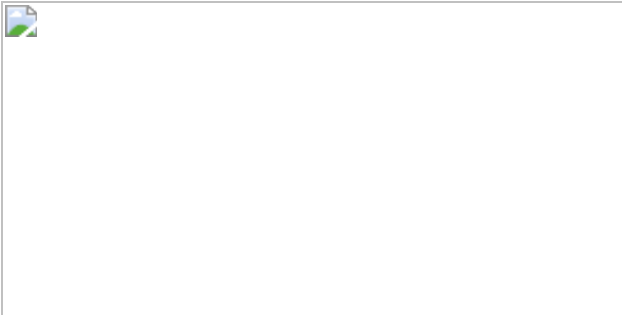


Fig. 2: Inter-subunit interactions.

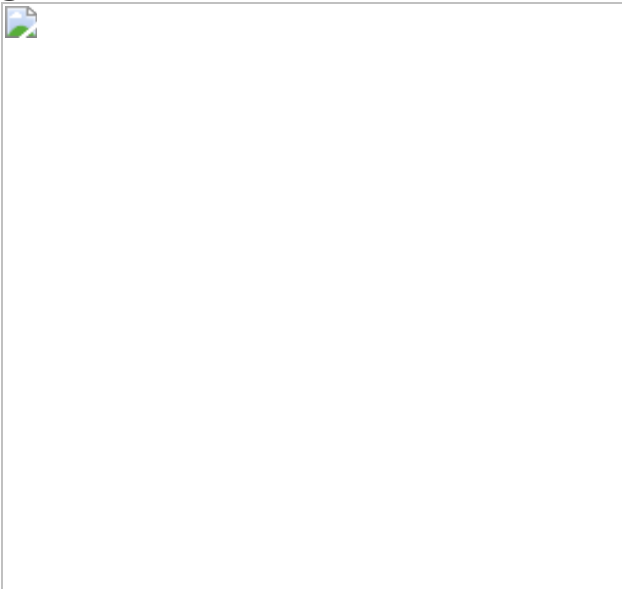
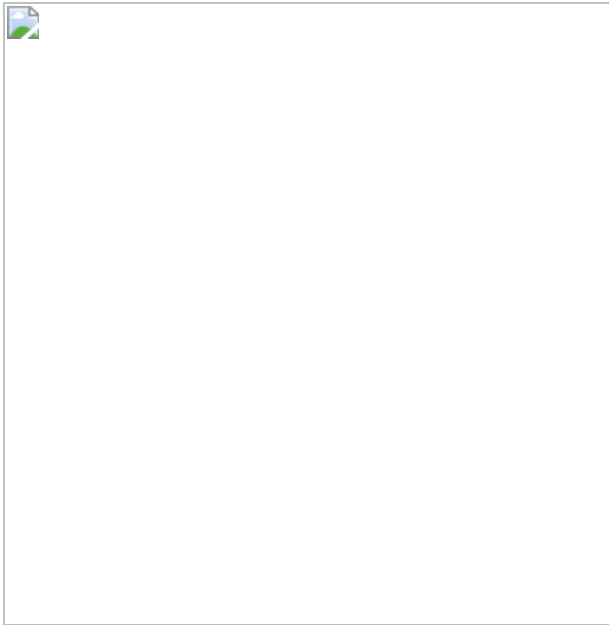


Fig. 3: Homomeric α -assembly intermediates and model for GlyR assembly.



Data availability

The coordinates and volumes for the cryo-EM data have been deposited in the Electron Microscopy Data Bank under accession codes [EMD-23910](#), [EMD-23911](#), [EMD-23912](#) and [EMD-23913](#). The coordinates have been deposited in the Protein Data Bank under accession codes [7MLU](#), [7MLV](#) and [7MLY](#).

References

1. 1.

Legendre, P. The glycinergic inhibitory synapse. *Cell. Mol. Life Sci.* **58**, 760–793 (2001).

2. 2.

Lynch, J. W. Molecular structure and function of the glycine receptor chloride channel. *Physiol. Rev.* **84**, 1051–1095 (2004).

3. 3.

Shiang, R. et al. Mutations in the alpha 1 subunit of the inhibitory glycine receptor cause the dominant neurologic disorder, hyperekplexia. *Nat. Genet.* **5**, 351–358 (1993).

4. 4.

Grudzinska, J. et al. The β subunit determines the ligand binding properties of synaptic glycine receptors. *Neuron* **45**, 727–739 (2005).

5. 5.

Langosch, D., Thomas, L. & Betz, H. Conserved quaternary structure of ligand-gated ion channels: the postsynaptic glycine receptor is a pentamer. *Proc. Natl Acad. Sci. USA* **85**, 7394–7398 (1988).

6. 6.

Yang, Z., Taran, E., Webb, T. I. & Lynch, J. W. Stoichiometry and subunit arrangement of alpha₁beta glycine receptors as determined by atomic force microscopy. *Biochemistry* **51**, 5229–5231 (2012).

7. 7.

Burzomato, V., Groot-Kormelink, P. J., Sivilotti, L. G. & Beato, M. Stoichiometry of recombinant heteromeric glycine receptors revealed by a pore-lining region point mutation. *Recept. Channels* **9**, 353-361 (2003).

8. 8.

Durisic, N. et al. Stoichiometry of the human glycine receptor revealed by direct subunit counting. *J. Neurosci.* **32**, 12915–12920 (2012).

9. 9.

Shan, Q., Han, L. & Lynch, J. W. Distinct properties of glycine receptor β+/α- interface: unambiguously characterizing heteromeric interface reconstituted in homomeric protein. *J. Biol. Chem.* **287**, 21244–21252 (2012).

10. 10.

Shan, Q., Haddrill, J. L. & Lynch, J. W. A single β subunit M2 domain residue controls the picrotoxin sensitivity of $\alpha\beta$ heteromeric glycine receptor chloride channels. *J. Neurochem.* **76** 1109–1120 (2001).

11. 11.

Meyer, G., Kirsch, J., Betz, H. & Langosch, D. Identification of a gephyrin binding motif on the glycine receptor beta subunit. *Neuron* **15**, 563–572 (1995).

12. 12.

Graham, D., Pfeiffer, F., Simler, R. & Betz, H. Purification and characterization of the glycine receptor of pig spinal cord. *Biochemistry* **24**, 990–994 (1985).

13. 13.

Dutertre, S., Becker, C. M. & Betz, H. Inhibitory glycine receptors: an update. *J. Biol. Chem.* **287**, 40216–40223 (2012).

14. 14.

Toyoshima, C. & Unwin, N. Three-dimensional structure of the acetylcholine receptor by cryoelectron microscopy and helical image reconstruction. *J. Cell Biol.* **111**, 2623–2635 (1990).

15. 15.

Yu, H., Bai, X.-c. & Wang, W. Characterization of the subunit composition and structure of adult glycine receptors. *Neuron* **109**, 2707–2716.e6 (2021).

16. 16.

Kuhse, J., Laube, B., Magalei, D. & Betz, H. Assembly of the inhibitory glycine receptor: identification of amino acid sequence

motifs governing subunit stoichiometry. *Neuron* **11**, 1049–1056 (1993).

17. 17.

Yu, J. et al. Mechanism of gating and partial agonist action in the glycine receptor. *Cell* **184**, 957–968.e21 (2021).

18. 18.

Hille, B. *Ion Channels of Excitable Membranes* 3rd edn (Sinauer, 2001).

19. 19.

Kumar, A. et al. Mechanisms of activation and desensitization of full-length glycine receptor in lipid nanodiscs. *Nat. Commun.* **11**, 3752 (2020).

20. 20.

Hibbs, R. E. & Gouaux, E. Principles of activation and permeation in an anion-selective Cys-loop receptor. *Nature* **474**, 54–60 (2011).

21. 21.

Masiulis, S. et al. GABA_A receptor signalling mechanisms revealed by structural pharmacology. *Nature* **565**, 454–459 (2019).

22. 22.

Todorovic, J., Welsh, B. T., Bertaccini, E. J., Trudell, J. R. & Mihic, S. J. Disruption of an intersubunit electrostatic bond is a critical step in glycine receptor activation. *Proc. Natl Acad. Sci. USA* **107**, 7987–7992 (2010).

23. 23.

Phulera, S. et al. Cryo-EM structure of the benzodiazepine-sensitive $\alpha 1\beta 1\gamma 2S$ tri-heteromeric GABA_A receptor in complex with GABA. *eLife* **7**, e39383 (2018).

24. 24.

Kloda, J. H. & Czajkowski, C. Agonist-, antagonist-, and benzodiazepine-induced structural changes in the $\alpha 1$ Met113–Leu132 region of the GABA_A receptor. *Mol. Pharmacol.* **71**, 483–493 (2007).

25. 25.

Liu, S. et al. Cryo-EM structure of the human $\alpha 5\beta 3$ GABA_A receptor. *Cell Res.* **28**, 958–961 (2018).

26. 26.

Walsh, R. M., Jr. et al. Structural principles of distinct assemblies of the human $\alpha 4\beta 2$ nicotinic receptor. *Nature* **557**, 261–265 (2018).

27. 27.

Green, W. N. & Claudio, T. Acetylcholine receptor assembly: subunit folding and oligomerization occur sequentially. *Cell* **74**, 57–69 (1993).

28. 28.

Klausberger, T. et al. Detection and binding properties of GABA_A receptor assembly intermediates. *J. Biol. Chem.* **276**, 16024–16032 (2001).

29. 29.

Blount, P. & Merlie, J. P. Molecular basis of the two nonequivalent ligand binding sites of the muscle nicotinic acetylcholine receptor. *Neuron* **3**, 349–357 (1989).

30. 30.

Hattori, M., Hibbs, R. E. & Gouaux, E. A fluorescence-detection size-exclusion chromatography-based thermostability assay for membrane protein precrystallization screening. *Structure* **20**, 1293–1299 (2012).

31. 31.

Du, J., Lu, W., Wu, S., Cheng, Y. & Gouaux, E. Glycine receptor mechanism elucidated by electron cryo-microscopy. *Nature* **526**, 224–229 (2015).

32. 32.

Kawate, T. & Gouaux, E. Fluorescence-detection size-exclusion chromatography for precrystallization screening of integral membrane proteins. *Structure* **14**, 673–681 (2006).

33. 33.

Goehring, A. et al. Screening and large-scale expression of membrane proteins in mammalian cells for structural studies. *Nat. Protoc.* **9**, 2574–2585 (2014).

34. 34.

Cook, N., Harris, A., Hopkins, A. & Hughes, K. Scintillation proximity assay (SPA) technology to study biomolecular interactions. *Curr. Protoc. Protein Sci. Ch.* **19**, Unit 19.8 (2002).

35. 35.

Cheng, Y. & Prusoff, W. H. Relationship between the inhibition constant (K_I) and the concentration of inhibitor which causes 50 per cent inhibition (I_{50}) of an enzymatic reaction. *Biochem. Pharmacol.* **22**, 3099–3108 (1973).

36. 36.

Mastronarde, D. N. Automated electron microscope tomography using robust prediction of specimen movements. *J. Struct. Biol.* **152**, 36–51 (2005).

37. 37.

Zheng, S. Q. et al. MotionCor2: anisotropic correction of beam-induced motion for improved cryo-electron microscopy. *Nat. Methods* **14**, 331–332 (2017).

38. 38.

Zhang, K. Gctf: Real-time CTF determination and correction. *J. Struct. Biol.* **193**, 1–12 (2016).

39. 39.

Punjani, A., Rubinstein, J. L., Fleet, D. J. & Brubaker, M. cryoSPARC: algorithms for rapid unsupervised cryo-EM structure determination. *Nat. Methods* **14**, 290–296 (2017).

40. 40.

Henderson, R. Avoiding the pitfalls of single particle cryo-electron microscopy: Einstein from noise. *Proc. Natl Acad. Sci. USA* **110**, 18037–18041 (2013).

41. 41.

Jakobi, A. J., Wilmanns, M. & Sachse, C. Model-based local density sharpening of cryo-EM maps. *eLife* **6**, e27131 (2017).

42. 42.

Arnold, K., Bordoli, L., Kopp, J. & Schwede, T. The SWISS-MODEL workspace: a web-based environment for protein structure homology modelling. *Bioinformatics* **22**, 195–201 (2006).

43. 43.

Pettersen, E. F. et al. UCSF Chimera—a visualization system for exploratory research and analysis. *J. Comput. Chem.* **25**, 1605–1612 (2004).

44. 44.

Emsley, P. & Cowtan, K. Coot: model-building tools for molecular graphics. *Acta Crystallogr. D* **60**, 2126–2132 (2004).

45. 45.

Afonine, P. V. et al. Real-space refinement in PHENIX for cryo-EM and crystallography. *Acta Crystallogr. D* **74**, 531–544 (2018).

Acknowledgements

We thank L. Sivilotti, F. Jalali-Yazdi, C. Sun and R. Hallford for discussions and suggestions; L. Vaskalis for assistance with figures; J. Guidry for assisting with the proteomics work; and D. Claxton and D. Cawley for the monoclonal antibody. The LSUHSC Proteomics Core is supported by the Louisiana State University School of Medicine Office of the Dean. A portion of this research was supported by NIH grant U24GM129547 and performed at the PNCC at OHSU and accessed through EMSL (grid.436923.9), a DOE Office of Science User Facility sponsored by the Office of Biological and Environmental Research. This work was supported by NIH grant 5R01 GM100400 to E.G. E.G. is an investigator of the Howard Hughes Medical Institute.

Author information

Affiliations

1. Vollum Institute, Oregon Health and Science University, Portland, OR, USA

Hongtao Zhu & Eric Gouaux

2. Howard Hughes Medical Institute, Oregon Health and Science University, Portland, OR, USA

Eric Gouaux

Contributions

H.Z. performed the experiments. H.Z. and E.G. designed the project and wrote the manuscript.

Corresponding author

Correspondence to [Eric Gouaux](#).

Ethics declarations

Competing interests

The authors declare no competing interests.

Additional information

Peer review information *Nature* thanks Nathan Absalom and the other, anonymous, reviewer(s) for their contribution to the peer review of this work. Peer reviewer reports are available.

Publisher's note Springer Nature remains neutral with regard to jurisdictional claims in published maps and institutional affiliations.

Extended data figures and tables

[Extended Data Fig. 1 Biochemistry results related with native GlyRs.](#)

a, Flow chart for native GlyR purification. **b**, Representative SEC profile for native GlyR in complex with the 3D1 Fab. Inset shows a typical silver staining of sodium dodecyl sulphate-polyacrylamide gel electrophoresis of native GlyR sample for cryo-EM grid preparation. **c**, Results from mass spectrometry (See [Methods](#) for more details). The table shows the identified peptides within the sample and the corresponding proteins with their gene accession numbers. **d**, Western blot analysis of isolated native GlyR eluted from strychnine column using antibodies against α_1 , α_2 , and α_3 . Positive control is the membrane extracts from rat brain. The experiments were repeated two times with similar results. **e**, FSEC profiles for mixing of different concentration of recombinant homomeric α pentamer with 3D1 Fab. **f**, **g**, FSEC profiles for mixing of YFP-tagged homomeric α_1 GlyR (**f**) and CFP-tagged β GlyR (**g**), respectively. **h–j**, Saturation binding of ^3H strychnine to native GlyRs with 3D1 Fab (**h**), recombinant expressed pig heteromeric GlyRs with (**i**) and without 3D1 Fab (**j**), respectively. Results are the average of three replicates and the error bars represent standard error of the mean (SEM) ($n = 3$). **k–m**, The competitive binding of glycine to native GlyRs with 3D1 Fab (**k**), recombinant expressed pig heteromeric GlyR with (**l**) and without 3D1 Fab (**m**), respectively. Results are the average of three replicates and the error bars represent SEM ($n = 3$). The hot ligand used here is ^3H strychnine.

[**Extended Data Fig. 2 3D reconstruction of native GlyRs.**](#)

a, A typical cryo-EM micrograph for native GlyRs. The experiments were repeated three times with similar results. **b**, Selected 2D class averages for native GlyR-Fab complex. **c**, Flow chart for cryo-EM data analysis of native GlyRs. **d**, **f**, **h**, **j**, Local resolution maps for unsharpened heteromeric pentamer (**d**), homomeric α tetramer (**f**), locally refined ECD (**h**) and TMD map (**j**) of homomeric pentamer. **e**, **g**, **i**, **k**, FSC curves for heteromeric pentamer (**e**), homomeric α tetramer (**g**), locally refined ECD (**i**) and TMD map (**k**) of homomeric α pentamer.

[**Extended Data Fig. 3 Representative densities.**](#)

a, b, EM density segments for α .A (**a**) and β (**b**) subunits, respectively. The model is shown in carton representation. The density is shown in surface representation. **c, d**, Representative densities for light (**c**) and heavy chain (**d**) of 3D1 Fab. Regions are numbered. **e, f**, Representative densities for glycosylation on α .A (**e**) and β (**f**) subunits. **g–i**, Representative densities of the binding pockets formed by $\beta(+)$ / α .A $(-)$ (**g**), α .D $(+)$ / $\beta(-)$ (**h**) and α .B $(+)$ / α .C $(-)$ (**i**), respectively. The related key amino acids are labeled. **j, k**, Representative densities for transmembrane helices including M1, M2, M3 and M4 from β (**j**) and α .A (**k**), respectively. All of the isolated densities are contoured at 8σ .

Extended Data Fig. 4 Subunit identities and geometry of GlyR pentamers.

a, b, Comparison of isolated representative densities for α_1 and β subunits contoured at 8σ . Two pairs of representative residues have been selected. These key amino acids are labeled. Black stars highlight the mismatched residues. **c**, Isolated densities with different amino acids between the α_1 and α_2 subunit from native heteromeric and homomeric pentamer maps contoured at 8σ , respectively. **d, f**, ECD (**d**) and TMD (**f**) of heteromeric pentamer shown in cartoon representation. The α subunits are colored in blue and β subunit is in salmon. The centers of mass for ECD and TMD are shown in green and orange, respectively. **e, g**, Schematic diagram illustrating the neighboring distances of centers of mass of heteromeric ECD (**e**) and TMD (**g**), respectively. **h, i**, Schematic diagram illustrating the neighboring distances of centers of mass of homomeric α_1 pentamer ECD (**h**) and TMD (**i**), respectively. **j**, Top-down view of heteromeric GlyR-Fab complex. GlyRs are in cartoon representation, with N-glycans and lipids in sphere representation. 3D1 Fabs, α , β , N-glycans, ligands glycine and lipids are colored in green, blue, salmon, orange, purple and yellow, respectively. All of the distances are denoted in Å.

Extended Data Fig. 5 Binding of 3D1 Fab.

a, d, Side views of 3D1 Fab bound to the isolated α .A (**a**) and α .B subunit (**d**) in carton representation, respectively. **b, c, e**, Close-up view of the

binding site of the region indicated in panel (a) and (d) viewed approximately parallel to the plane of the membrane. The key amino acids involved in interactions are shown in ball-stick representation. The potential hydrogen bonds, cation- π and π - π interactions are indicated in dashed lines. f, Side view of 3D1 Fab bound to the isolated β subunit in cartoon representation. g, Close-up view of the binding site of the region indicated in panel (f) viewed approximately parallel to the plane of the membrane.

Extended Data Fig. 6 Analysis associated with TMD.

a, Sequence alignment of M2 helices among GABAAR, GlyR and GluCl. Higher prime numbers approach ECD, lower prime numbers approach intracellular domain. The -2' position is the first amino acid of M2 helix. Sequence alignment was performed by PROMALS3D. b-d, Isolated M2 helices bound with picrotoxin from GABAAR (b; PDB ID: 6HUG), GluCl (c; PDB ID: 3RI5) and homomeric GlyR (d; PDB ID: 6UD3). The important amino acids 6'T or 2'T interacting with picrotoxin are labeled. The M2 helices and picrotoxin are shown in cartoon and stick representation, respectively. e, f, Isolated M2 helices from native homomeric GlyR (e) and heteromeric GlyR (f), respectively. The 6'T and 6'F are shown in stick representation. The M2 helices are shown in cartoon representation. All distances are denoted in Å.

Extended Data Fig. 7 Structural metrics related with the interfaces.

a-c, View of the interface interactions of native homomeric α_1 pentamer (see Fig. 2c-e). d, The summary of the buried areas for heteromeric pentamer, homomeric α tetramer and homomeric α_1 pentamer. The areas are given in \AA^2 . e, Top down view of heteromeric GlyR in surface and ribbon representation. The glycine molecules are shown in sphere representation. The $\alpha.A$ and $\alpha.D$ are in blue. The β subunit and $\alpha.C$ subunits are colored in salmon and lime, respectively. The boxed areas are enlarged in panels (f) to (h). f-h, Views of the binding pockets at $\alpha.D(+)/\beta(-)$ (f), $\alpha.B(+)/\alpha.C(-)$ (g) and $\beta(+)/\alpha.A(-)$ (h) interfaces, respectively. The glycine molecules are shown in ball-stick representations with oxygen in red, nitrogen in blue and

carbon in green. The possible hydrogen bonds and cation-pi interactions are shown as dashed lines. **i**, Superposition of the orthostatic binding sites. The binding sites are overlapped by the ECD of the principle side subunits. Orange arrows indicate the movement of loop C. **j**, Schematic diagram illustrating the relative positions of the amino acids in the binding pockets. The blue, pink, green and red polygon are created by the connection of the $\text{C}\alpha$ atoms of these crucial amino acids at the $\beta(+)/\alpha.\text{A}(-)$, $\alpha.\text{D}(+)/\beta(-)$, $\alpha.\text{B}(+)/\alpha.\text{C}(-)$ and native homomeric $\alpha(+)/\alpha(-)$ interfaces, respectively. **k–n**, Schematic diagram illustrating the distances and angles related with the interfaces of Cys-loop family members including GABAAR (**k**, PDB ID: 6A96; **l**, PDB ID: 6DW1) and nAChR (**m**, PDB ID: 6CNJ; **n**, PDB ID: 6CNK; see Fig. [2f](#)). The black star indicates the binding pocket bound with ligand. All distances are given in Å and the angles are given in degree.

Extended Data Fig. 8 Results related with assembly intermediates.

a, b, Representative FSEC profiles for recombinantly expressed homomeric GlyR tagged with YFP (**a**) and heteromeric GlyR tagged with CFP on β subunit (**b**), respectively. Melting temperatures (T_m) were determined by fitting the curves to a sigmoidal dose-response equation. **c**, A typical cryo-EM micrograph for recombinant GlyRs. The experiments were repeated three times with similar results. **d**, 2D class averages for recombinant GlyRs bound with 3D1 Fab. **e, f**, Top down and side views for the recombinant heteromeric GlyR map, respectively. **g, h**, Top down and side views for the recombinant homomeric GlyR map, respectively. **i**, Side view of isolated $\alpha.\text{B}-\alpha.\text{C}$ dimer from tetramer. Subunits are shown in cartoon representation. $\alpha.\text{B}$ and $\alpha.\text{C}$ are colored in blue and lime, respectively. The boxed areas are enlarged in panel (**j**) and (**l**). **j, l**, Superposition of the interfaces in the upper ECD (**j**) and the region near loop C (**l**) of $\alpha.\text{B}(+)/\alpha.\text{C}(-)$ interface from homomeric α tetramer, heteromeric pentamer and homomeric pentamer. Orange arrows indicate the displacements of the $\text{C}\alpha$ atoms. **k, m**, Schematic diagram illustrating the relative positions of the amino acids of the homomeric pentamer and tetramer. All distances are given in Å.

Extended Data Table 1 Statistics for 3D reconstruction and model refinement

Extended Data Table 2 Statistics for 2 independent native GlyR single particle data sets

Supplementary information

Supplementary Figures

This file contains Supplementary Figs 1, 2. Supplementary Fig. 1 shows the original gel and original results for the western blots and Supplementary Fig. 2 displays amino acid sequence alignment, secondary structure and posttranslational modifications for pig GlyR α_1 (GlyRA1) and β (GlyRB) subunits.

Reporting Summary

Peer Review File

Rights and permissions

Reprints and Permissions

About this article

Cite this article

Zhu, H., Gouaux, E. Architecture and assembly mechanism of native glycine receptors. *Nature* **599**, 513–517 (2021).

<https://doi.org/10.1038/s41586-021-04022-z>

- Received: 16 May 2021
- Accepted: 15 September 2021
- Published: 23 September 2021

- Issue Date: 18 November 2021
- DOI: <https://doi.org/10.1038/s41586-021-04022-z>

Share this article

Anyone you share the following link with will be able to read this content:

[Get shareable link](#)

Sorry, a shareable link is not currently available for this article.

[Copy to clipboard](#)

Provided by the Springer Nature SharedIt content-sharing initiative

This article was downloaded by **calibre** from <https://www.nature.com/articles/s41586-021-04022-z>

| [Section menu](#) | [Main menu](#) |

Amendments & Corrections

- [**Author Correction: Cotranslational prolyl hydroxylation is essential for flavivirus biogenesis**](#) [21 October 2021]
Author Correction •
- [**Author Correction: Large metallicity variations in the Galactic interstellar medium**](#) [03 November 2021]
Author Correction •
- [**Publisher Correction: An open-access volume electron microscopy atlas of whole cells and tissues**](#) [03 November 2021]
Publisher Correction •
- [**Publisher Correction: Observation of fractional edge excitations in nanographene spin chains**](#) [03 November 2021]
Publisher Correction •
- [**Publisher Correction: A metastasis map of human cancer cell lines**](#) [03 November 2021]
Publisher Correction •
- [**Retraction Note: IspH inhibitors kill Gram-negative bacteria and mobilize immune clearance**](#) [27 September 2021]
Retraction •

- Author Correction
- [Published: 21 October 2021](#)

Author Correction: Cotranslational prolyl hydroxylation is essential for flavivirus biogenesis

- [Ranen Aviner](#)^{1,2},
- [Kathy H. Li](#)³,
- [Judith Frydman](#) [ORCID: orcid.org/0000-0003-2302-6943](#)² &
- [Raul Andino](#) [ORCID: orcid.org/0000-0001-5503-9349](#)¹

Nature volume **599**, page E3 (2021)

- 379 Accesses
- 2 Altmetric
- [Metrics details](#)

Subjects

- [Ribosome](#)
- [Virology](#)

The [Original Article](#) was published on 18 August 2021

[Download PDF](#)

Correction to: *Nature* <https://doi.org/10.1038/s41586-021-03851-2>
Published online 18 August 2021

In the version of this Article initially published, in the Acknowledgements section, the following sentence was missing and has now been included at the end of the section: “J.F. is a CZ Biohub Investigator.” The original Article has been corrected online.

Author information

Affiliations

1. Department of Microbiology and Immunology, University of California, San Francisco, San Francisco, CA, USA

Ranen Aviner & Raul Andino

2. Department of Biology and Genetics, Stanford University, Stanford, CA, USA

Ranen Aviner & Judith Frydman

3. Department of Pharmaceutical Chemistry, University of California, San Francisco, San Francisco, CA, USA

Kathy H. Li

Corresponding authors

Correspondence to [Judith Frydman](#) or [Raul Andino](#).

Rights and permissions

[Reprints and Permissions](#)

About this article

Cite this article

Aviner, R., Li, K.H., Frydman, J. *et al.* Author Correction: Cotranslational prolyl hydroxylation is essential for flavivirus biogenesis. *Nature* **599**, E3 (2021). <https://doi.org/10.1038/s41586-021-04102-0>

- Published: 21 October 2021
- Issue Date: 18 November 2021
- DOI: <https://doi.org/10.1038/s41586-021-04102-0>

Share this article

Anyone you share the following link with will be able to read this content:

[Get shareable link](#)

Sorry, a shareable link is not currently available for this article.

[Copy to clipboard](#)

Provided by the Springer Nature SharedIt content-sharing initiative

This article was downloaded by **calibre** from <https://www.nature.com/articles/s41586-021-04102-0>

- Author Correction
- [Published: 03 November 2021](#)

Author Correction: Large metallicity variations in the Galactic interstellar medium

- [Annalisa De Cia](#) [ORCID: orcid.org/0000-0003-2082-1626¹](#),
- [Edward B. Jenkins](#) [ORCID: orcid.org/0000-0003-1892-4423²](#),
- [Andrew J. Fox](#) [ORCID: orcid.org/0000-0003-0724-4115³](#),
- [Cédric Ledoux](#) [ORCID: orcid.org/0000-0002-7864-3327⁴](#),
- [Tanita Ramburuth-Hurt](#) [ORCID: orcid.org/0000-0003-2597-2415¹](#),
- [Christina Konstantopoulou](#) [ORCID: orcid.org/0000-0002-4690-0157¹](#),
- [Patrick Petitjean⁵](#) &
- [Jens-Kristian Krogager](#) [ORCID: orcid.org/0000-0002-4912-9388¹](#)

[Nature](#) volume 599, page E4 (2021)

- 442 Accesses
- 2 Altmetric
- [Metrics details](#)

Subjects

- [Astrophysical dust](#)
- [Galaxies and clusters](#)
- [Interstellar medium](#)

The [Original Article](#) was published on 08 September 2021

[Download PDF](#)

Correction to: *Nature* <https://doi.org/10.1038/s41586-021-03780-0>

Published online 8 September 2021

In the version of this Article initially published, there was an error in the spelling of an author name. Specifically, Tanita Ramburuth-Hurt's name was initially misspelt as "Ramburuth-Hurt" in the Article. The original Article has been corrected online.

Author information

Affiliations

1. Department of Astronomy, University of Geneva, Versoix, Switzerland

Annalisa De Cia, Tanita Ramburuth-Hurt, Christina Konstantopoulou & Jens-Kristian Krogager

2. Princeton University Observatory, Princeton, NJ, USA

Edward B. Jenkins

3. AURA for ESA, Space Telescope Science Institute, Baltimore, MD, USA

Andrew J. Fox

4. European Southern Observatory, Vitacura, Chile

Cédric Ledoux

5. Institut d'Astrophysique de Paris, Sorbonne Universités & CNRS, Paris, France

Patrick Petitjean

Corresponding author

Correspondence to [Annalisa De Cia](#).

Rights and permissions

[Reprints and Permissions](#)

About this article

Cite this article

De Cia, A., Jenkins, E.B., Fox, A.J. *et al.* Author Correction: Large metallicity variations in the Galactic interstellar medium. *Nature* **599**, E4 (2021). <https://doi.org/10.1038/s41586-021-04146-2>

- Published: 03 November 2021
- Issue Date: 18 November 2021
- DOI: <https://doi.org/10.1038/s41586-021-04146-2>

Share this article

Anyone you share the following link with will be able to read this content:

[Get shareable link](#)

Sorry, a shareable link is not currently available for this article.

[Copy to clipboard](#)

Provided by the Springer Nature SharedIt content-sharing initiative

| [Section menu](#) | [Main menu](#) |

- Publisher Correction
- [Published: 03 November 2021](#)

Publisher Correction: An open-access volume electron microscopy atlas of whole cells and tissues

- [C. Shan Xu](#) ORCID: [orcid.org/0000-0002-8564-7836¹](https://orcid.org/0000-0002-8564-7836),
- [Song Pang](#) ORCID: [orcid.org/0000-0002-7231-4151^{1 nA1}](https://orcid.org/0000-0002-7231-4151),
- [Gleb Shtengel](#) ORCID: [orcid.org/0000-0001-6830-640X^{1 nA1}](https://orcid.org/0000-0001-6830-640X),
- [Andreas Müller^{2,3,4}](#),
- [Alex T. Ritter⁵](#),
- [Huxley K. Hoffman^{6 nAff12}](#),
- [Shin-ya Takemura](#) ORCID: [orcid.org/0000-0003-2400-6426¹](https://orcid.org/0000-0003-2400-6426),
- [Zhiyuan Lu¹](#),
- [H. Amalia Pasolli](#) ORCID: [orcid.org/0000-0003-3899-3530^{1 nAff13}](https://orcid.org/0000-0003-3899-3530),
- [Nirmala Iyer¹](#),
- [Jeeyun Chung^{7,8}](#),
- [Davis Bennett](#) ORCID: [orcid.org/0000-0001-7579-2848¹](https://orcid.org/0000-0001-7579-2848),
- [Aubrey V. Weigel](#) ORCID: [orcid.org/0000-0003-1694-4420¹](https://orcid.org/0000-0003-1694-4420),
- [Melanie Freeman^{1 nAff14}](#),
- [Schuyler B. van Engelenburg](#) ORCID: [orcid.org/0000-0003-2100-3617⁶](https://orcid.org/0000-0003-2100-3617),
- [Tobias C. Walther](#) ORCID: [orcid.org/0000-0003-1442-1327^{7,8,9,10}](https://orcid.org/0000-0003-1442-1327),
- [Robert V. Farese Jr.](#) ORCID: [orcid.org/0000-0001-8103-2239^{7,8}](https://orcid.org/0000-0001-8103-2239),
- [Jennifer Lippincott-Schwartz¹](#),
- [Ira Mellman⁵](#),
- [Michele Solimena](#) ORCID: [orcid.org/0000-0002-3653-8107^{2,3,4,11}](https://orcid.org/0000-0002-3653-8107) &
- [Harald F. Hess](#) ORCID: [orcid.org/0000-0003-3000-1533¹](https://orcid.org/0000-0003-3000-1533)

[Nature](#) volume **599**, page E5 (2021)

- 709 Accesses
- 2 Altmetric
- [Metrics details](#)

Subjects

- [Cell biology](#)
- [Electron microscopy](#)
- [Imaging](#)
- [Neuroscience](#)

The [Original Article](#) was published on 06 October 2021

[Download PDF](#)

Correction to: *Nature* <https://doi.org/10.1038/s41586-021-03992-4>

Published online 6 October 2021

In the version of this Article initially published, there were processing errors in the Supplementary and Extended Data. Specifically, for Supplementary Video 2, the file was damaged and would not render. For Extended Data Fig. 2, the “ $x-z$, $y-z$, $x-y$ ” labels in the lower left of each panel were divergent to the format of similar panels in main text Fig. 2. The changes have been corrected in the online version of the Article.

Author information

Author notes

1. Huxley K. Hoffman

Present address: Department of Cell and Developmental Biology,
University of Colorado Anschutz Medical Campus, Aurora, CO, USA

2. H. Amalia Pasolli

Present address: Electron Microscopy Resource Center, The
Rockefeller University, New York, NY, USA

3. Melanie Freeman

Present address: Advanced Bio-imaging Center, Department of
Molecular and Cell Biology, University of California, Berkeley, CA,
USA

4. These authors contributed equally: Song Pang, Gleb Shtengel

Affiliations

1. Janelia Research Campus, Howard Hughes Medical Institute, Ashburn,
VA, USA

C. Shan Xu, Song Pang, Gleb Shtengel, Shin-ya Takemura, Zhiyuan
Lu, H. Amalia Pasolli, Nirmala Iyer, Davis Bennett, Aubrey V.
Weigel, Melanie Freeman, Jennifer Lippincott-Schwartz & Harald F.
Hess

2. Molecular Diabetology, University Hospital and Faculty of Medicine
Carl Gustav Carus, TU Dresden, Dresden, Germany

Andreas Müller & Michele Solimena

3. Paul Langerhans Institute Dresden (PLID) of the Helmholtz Center
Munich at the University Hospital Carl Gustav Carus and Faculty of
Medicine of the TU Dresden, Dresden, Germany

Andreas Müller & Michele Solimena

4. German Center for Diabetes Research (DZD e.V.), Neuherberg, Germany
Andreas Müller & Michele Solimena
5. Genentech, South San Francisco, CA, USA
Alex T. Ritter & Ira Mellman
6. Molecular and Cellular Biophysics Program, Department of Biological Sciences, University of Denver, Denver, CO, USA
Huxley K. Hoffman & Schuyler B. van Engelenburg
7. Department of Molecular Metabolism, Harvard T.H. Chan School of Public Health, Boston, MA, USA
Jeeyun Chung, Tobias C. Walther & Robert V. Farese Jr.
8. Department of Cell Biology, Harvard Medical School, Boston, MA, USA
Jeeyun Chung, Tobias C. Walther & Robert V. Farese Jr.
9. Howard Hughes Medical Institute, Boston, MA, USA
Tobias C. Walther
10. Broad Institute of Harvard and MIT, Cambridge, MA, USA
Tobias C. Walther
11. Max-Planck Institute of Molecular Cell Biology and Genetics, Dresden, Germany
Michele Solimena

Corresponding authors

Correspondence to [C. Shan Xu](#) or [Harald F. Hess](#).

Rights and permissions

[Reprints and Permissions](#)

About this article

Cite this article

Xu, C.S., Pang, S., Shtengel, G. *et al.* Publisher Correction: An open-access volume electron microscopy atlas of whole cells and tissues. *Nature* **599**, E5 (2021). <https://doi.org/10.1038/s41586-021-04132-8>

- Published: 03 November 2021
- Issue Date: 18 November 2021
- DOI: <https://doi.org/10.1038/s41586-021-04132-8>

Share this article

Anyone you share the following link with will be able to read this content:

[Get shareable link](#)

Sorry, a shareable link is not currently available for this article.

[Copy to clipboard](#)

Provided by the Springer Nature SharedIt content-sharing initiative

This article was downloaded by **calibre** from <https://www.nature.com/articles/s41586-021-04132-8>

- Publisher Correction
- [Published: 03 November 2021](#)

Publisher Correction: Observation of fractional edge excitations in nanographene spin chains

- [Shantanu Mishra](#) ORCID: orcid.org/0000-0002-2900-4203^{1 na1 nAff9},
- [Gonçalo Catarina](#)^{2,3 na1},
- [Fupeng Wu](#)⁴,
- [Ricardo Ortiz](#)³,
- [David Jacob](#)^{5,6},
- [Kristjan Eimre](#) ORCID: orcid.org/0000-0002-3444-3286¹,
- [Ji Ma](#)⁴,
- [Carlo A. Pignedoli](#) ORCID: orcid.org/0000-0002-8273-6390¹,
- [Xinliang Feng](#) ORCID: orcid.org/0000-0003-3885-2703^{4,7},
- [Pascal Ruffieux](#) ORCID: orcid.org/0000-0001-5729-5354¹,
- [Joaquín Fernández-Rossier](#) ORCID: orcid.org/0000-0003-2297-0289² &
- [Roman Fasel](#) ORCID: orcid.org/0000-0002-1553-6487^{1,8}

Nature volume **599**, page E6 (2021)

- 587 Accesses
- 1 Altmetric
- [Metrics details](#)

Subjects

- [Magnetic properties and materials](#)
- [Scanning probe microscopy](#)
- [Surfaces, interfaces and thin films](#)
- [Synthesis and processing](#)

The [Original Article](#) was published on 13 October 2021

[Download PDF](#)

Correction to: *Nature* <https://doi.org/10.1038/s41586-021-03842-3>

Published online 13 October 2021

In the version of this Article initially published, there was an error in Equation (1). Now reading as

$$\hat{H}_{BLBQ} = \sum_i [\vec{S}_i \cdot (\vec{S}_{i+1} + \beta (\vec{S}_i \cdot \vec{S}_{i+1}))^2],$$

the set of round brackets was missing in the originally published version. Further, a placeholder reference was used for ref. 42; the complete citation now reads: “42. Hieulle, J. et al. On-surface synthesis and collective spin excitations of a triangulene-based nanostar. *Angew. Chem. Int. Ed.* <https://doi.org/10.1002/anie.202108301> (2021).” The changes have been made in the online version of the Article.

Author information

Author notes

1. Shantanu Mishra

Present address: IBM Research—Zurich, Rüschlikon, Switzerland

2. These authors contributed equally: Shantanu Mishra and Gonçalo Catarina

Affiliations

1. Empa—Swiss Federal Laboratories for Materials Science and Technology, Dübendorf, Switzerland

Shantanu Mishra, Kristjan Eimre, Carlo A. Pignedoli, Pascal Ruffieux & Roman Fasel

2. International Iberian Nanotechnology Laboratory, Braga, Portugal

Gonçalo Catarina & Joaquín Fernández-Rossier

3. University of Alicante, Sant Vicent del Raspeig, Spain

Gonçalo Catarina & Ricardo Ortiz

4. Technical University of Dresden, Dresden, Germany

Fupeng Wu, Ji Ma & Xinliang Feng

5. University of the Basque Country, San Sebastián, Spain

David Jacob

6. IKERBASQUE, Basque Foundation for Science, Bilbao, Spain

David Jacob

7. Max Planck Institute of Microstructure Physics, Halle, Germany

Xinliang Feng

8. University of Bern, Bern, Switzerland

Roman Fasel

Corresponding authors

Correspondence to [Xinliang Feng](#), [Pascal Ruffieux](#) or [Joaquín Fernández-Rossier](#).

Rights and permissions

[Reprints and Permissions](#)

About this article

Cite this article

Mishra, S., Catarina, G., Wu, F. *et al.* Publisher Correction: Observation of fractional edge excitations in nanographene spin chains. *Nature* **599**, E6 (2021). <https://doi.org/10.1038/s41586-021-04150-6>

- Published: 03 November 2021
- Issue Date: 18 November 2021
- DOI: <https://doi.org/10.1038/s41586-021-04150-6>

Share this article

Anyone you share the following link with will be able to read this content:

[Get shareable link](#)

Sorry, a shareable link is not currently available for this article.

[Copy to clipboard](#)

Provided by the Springer Nature SharedIt content-sharing initiative

This article was downloaded by **calibre** from <https://www.nature.com/articles/s41586-021-04150-6>

- Publisher Correction
- Open Access
- [Published: 03 November 2021](#)

Publisher Correction: A metastasis map of human cancer cell lines

- [Xin Jin](#) [ORCID: orcid.org/0000-0003-4167-1743¹](#),
- [Zelalem Demere¹](#),
- [Karthik Nair¹](#),
- [Ahmed Ali^{1,2}](#),
- [Gino B. Ferraro](#) [ORCID: orcid.org/0000-0002-1587-4259³](#),
- [Ted Natoli¹](#),
- [Amy Deik¹](#),
- [Lia Petronio¹](#),
- [Andrew A. Tang¹](#),
- [Cong Zhu¹](#),
- [Li Wang¹](#),
- [Danny Rosenberg¹](#),
- [Vamsi Mangena](#) [ORCID: orcid.org/0000-0003-2662-0366⁴](#),
- [Jennifer Roth¹](#),
- [Kwanghun Chung](#) [ORCID: orcid.org/0000-0002-8167-3340^{1,4}](#),
- [Rakesh K. Jain](#) [ORCID: orcid.org/0000-0001-7571-3548^{3,5}](#),
- [Clary B. Clish](#) [ORCID: orcid.org/0000-0001-8259-9245¹](#),
- [Matthew G. Vander Heiden](#) [ORCID: orcid.org/0000-0002-6702-4192^{1,2,6}](#) &
- [Todd R. Golub](#) [ORCID: orcid.org/0000-0003-0113-2403^{1,5,6}](#)

[Nature](#) volume 599, page E7 (2021)

- 756 Accesses

- 1 Altmetric
- [Metrics details](#)

Subjects

- [Breast cancer](#)
- [Cancer genomics](#)
- [Cancer models](#)
- [Metastasis](#)

The [Original Article](#) was published on 09 December 2020

[Download PDF](#)

Correction to: *Nature* <https://doi.org/10.1038/s41586-020-2969-2> Published online 9 December 2020

This paper was originally published under standard Springer Nature license (© The Author(s), under exclusive licence to Springer Nature Limited). It is now available as an open-access paper under a Creative Commons Attribution 4.0 International license, © The Author(s). The error has been corrected in the online version of the article.

Author information

Affiliations

1. Broad Institute of MIT and Harvard, Cambridge, MA, USA

Xin Jin, Zelalem Demere, Karthik Nair, Ahmed Ali, Ted Natoli, Amy Deik, Lia Petronio, Andrew A. Tang, Cong Zhu, Li Wang, Danny Rosenberg, Jennifer Roth, Kwanghun Chung, Clary B. Clish, Matthew G. Vander Heiden & Todd R. Golub

2. Koch Institute for Integrative Cancer Research, Department of Biology, Massachusetts Institute of Technology, Cambridge, MA, USA

Ahmed Ali & Matthew G. Vander Heiden

3. Edwin L. Steele Laboratories, Department of Radiation Oncology, Massachusetts General Hospital, Boston, MA, USA

Gino B. Ferraro & Rakesh K. Jain

4. Institute for Medical Engineering and Science, Picower Institute for Learning and Memory, Department of Chemical Engineering, Massachusetts Institute of Technology, Cambridge, MA, USA

Vamsi Mangena & Kwanghun Chung

5. Harvard Medical School, Boston, MA, USA

Rakesh K. Jain & Todd R. Golub

6. Dana-Farber Cancer Institute, Boston, MA, USA

Matthew G. Vander Heiden & Todd R. Golub

Corresponding authors

Correspondence to [Xin Jin](#) or [Todd R. Golub](#).

Rights and permissions

Open Access This article is licensed under a Creative Commons Attribution 4.0 International License, which permits use, sharing, adaptation, distribution and reproduction in any medium or format, as long as you give appropriate credit to the original author(s) and the source, provide a link to the Creative Commons license, and indicate if changes were made. The images or other third party material in this article are included in the article's Creative Commons license, unless indicated otherwise in a credit line to the material. If material is not included in the

article's Creative Commons license and your intended use is not permitted by statutory regulation or exceeds the permitted use, you will need to obtain permission directly from the copyright holder. To view a copy of this license, visit <http://creativecommons.org/licenses/by/4.0/>.

Reprints and Permissions

About this article

Cite this article

Jin, X., Demere, Z., Nair, K. *et al.* Publisher Correction: A metastasis map of human cancer cell lines. *Nature* **599**, E7 (2021).
<https://doi.org/10.1038/s41586-021-04149-z>

- Published: 03 November 2021
- Issue Date: 18 November 2021
- DOI: <https://doi.org/10.1038/s41586-021-04149-z>

Share this article

Anyone you share the following link with will be able to read this content:

[Get shareable link](#)

Sorry, a shareable link is not currently available for this article.

[Copy to clipboard](#)

Provided by the Springer Nature SharedIt content-sharing initiative

This article was downloaded by **calibre** from <https://www.nature.com/articles/s41586-021-04149-z>

- Retraction Note
- [Published: 27 September 2021](#)

Retraction Note: IspH inhibitors kill Gram-negative bacteria and mobilize immune clearance

- [Kumar Sachin Singh¹](#),
- [Rishabh Sharma¹](#),
- [Poli Adi Narayana Reddy²](#),
- [Prashanthi Vonteddu¹](#),
- [Madeline Good²](#),
- [Anjana Sundarajan¹](#),
- [Hyeree Choi¹](#),
- [Kar Muthumani](#) [ORCID: orcid.org/0000-0002-6807-2065¹](#),
- [Andrew Kossenkov³](#),
- [Aaron R. Goldman](#) [ORCID: orcid.org/0000-0001-7605-9592⁴](#),
- [Hsin-Yao Tang](#) [ORCID: orcid.org/0000-0003-1838-018X⁴](#),
- [Maxim Totrov⁵](#),
- [Joel Cassel⁶](#),
- [Maureen E. Murphy²](#),
- [Rajasekharan Somasundaram²](#),
- [Meenhard Herlyn](#) [ORCID: orcid.org/0000-0003-0839-0739²](#),
- [Joseph M. Salvino](#) [ORCID: orcid.org/0000-0002-2184-5980^{2,6}](#) &
- [Farokh Dotiwala](#) [ORCID: orcid.org/0000-0002-7387-2219¹](#)

[Nature](#) volume **599**, page 518 (2021)

- 3097 Accesses

- 18 Altmetric
- [Metrics details](#)

Subjects

- [Antimicrobial responses](#)
- [Bacterial host response](#)
- [Bacterial infection](#)
- [Drug discovery and development](#)

The [Original Article](#) was published on 23 December 2020

[Download PDF](#)

Correction to: *Nature* <https://doi.org/10.1038/s41586-020-03074-x>

Published online 23 December 2020

The authors wish to retract this Article owing to recently uncovered discrepancies between the published Source Data underlying panels in Extended Data Figs. 4, 6 and 7 and the data that were obtained. They have discovered multiple inconsistencies in the data points reported in the published Source Data files. In addition, original source datasets in support of individual panels in Figs. 1, 2 and 4 and Extended Data Figs. 5 and 10 are currently unaccounted for. Together, these issues decrease confidence in the integrity of the experimental findings reported. As such, the authors believe that the most appropriate course of action at this point is to retract this Article in its entirety. The authors sincerely apologize to the scientific community for any confusion and any unintended harm derived from the publication of this paper. All authors agree with the Retraction.

Author information

Affiliations

1. Vaccine and Immunotherapy Center, The Wistar Institute,
Philadelphia, PA, USA

Kumar Sachin Singh, Rishabh Sharma, Prashanthi Vonteddu, Anjana
Sundarajan, Hyeree Choi, Kar Muthumani & Farokh Dotiwala

2. Program in Molecular and Cellular Oncogenesis, The Wistar Institute,
Philadelphia, PA, USA

Poli Adi Narayana Reddy, Madeline Good, Maureen E.
Murphy, Rajasekharan Somasundaram, Meenhard Herlyn & Joseph M.
Salvino

3. Bioinformatics Facility, The Wistar Institute, Philadelphia, PA, USA

Andrew Kossenkov

4. Proteomics and Metabolomics Facility, The Wistar Institute,
Philadelphia, PA, USA

Aaron R. Goldman & Hsin-Yao Tang

5. Molsoft, San Diego, CA, USA

Maxim Totrov

6. Molecular Screening and Protein Expression Facility, The Wistar
Institute, Philadelphia, PA, USA

Joel Cassel & Joseph M. Salvino

Corresponding authors

Correspondence to [Joseph M. Salvino](#) or [Farokh Dotiwala](#).

Rights and permissions

[Reprints and Permissions](#)

About this article

Cite this article

Singh, K.S., Sharma, R., Reddy, P.A.N. *et al.* Retraction Note: IspH inhibitors kill Gram-negative bacteria and mobilize immune clearance. *Nature* **599**, 518 (2021). <https://doi.org/10.1038/s41586-021-03961-x>

- Published: 27 September 2021
- Issue Date: 18 November 2021
- DOI: <https://doi.org/10.1038/s41586-021-03961-x>

Share this article

Anyone you share the following link with will be able to read this content:

[Get shareable link](#)

Sorry, a shareable link is not currently available for this article.

[Copy to clipboard](#)

Provided by the Springer Nature SharedIt content-sharing initiative

This article was downloaded by **calibre** from <https://www.nature.com/articles/s41586-021-03961-x>

Nature Index